

Journal of Acoustic Emission, vol. 35, 2018

Selected Papers from Proc. EWGAE 2018

E W G A E
2018



With the collaboration of



Selected papers are reprinted from the proceedings with generous permission of CETIM and Dr. C. Herve, the Editor.

Contents

Selected Papers from EWGAE 2018

Topical Editors: C. Herve and G. Manthei

- Title preceded with Paper Number
- i Contents
- S1 19 - Combination of vibration analysis & Acoustic Emission measurements to better characterize damage and mechanical behavior of aerospace high speed gear box
Y. Hebrard, A. Proust, M. Batel
- S11 35 - Acoustic Emission for in situ monitoring of laser processing
S. Shevchik, T. Le Quang, B. Meylan, K. Wasmer
- S20 72 - Monitoring of stamping by Acoustic Emission (AE)
A. Saidoun, C. Hervé
- S31 14 - Acoustic Emission monitoring of adhesively bonded wood joints under quasistatic and cyclic fatigue mode II flexure loads using end-notch-flexure specimens
A. J. Brunner, G. Clerc, P. Niemz
- S41 17 - Acoustic Emission analysis during bending tests of timber beams reinforced with carbon fiber composite
F. Rescalvo, C. Abarkane, E. Suárez, A. Gallego
- S49 23- Frequency-Amplitude class of Acoustic Emission for different fracture mechanisms in C/SiC composite
D. Xiao, Y. Gao, L. Jin, F. Meng, N. Li, X. Zhou, Z. Tong, B. Jiang, T. He
- S54 29 - Damage monitoring on a steel truck trailer using parameter-based analysis of Acoustic Emissions
J. V. Pimentel, R. Klemm, M. Dalgic, A. Irretier, K.-L. Krieger
- S62 49 - Structural health monitoring using Acoustic Emission on metallic components in industrial plants
G. Lackner, H. Marihart, G. Schauritsch
- S70 83 - Novel AE monitoring of hydrogen induced damaged vessel and real time alarms. A case study
D. Papasalouros, K. Bollas, I. Ladis, E. Aerakis, A. Anastasopoulos, D. Kourousis
- S79 55 - The influence of source depth and source-to-sensor distance on the AE signal characteristics of damaging events in thin-walled CFRP laminates
B. Kelkel, J. Vogtmann, M. Gurka
- S91 57 - Acoustic Emission behaviour on CFRP with curved fibers
Y. Mizutani, T. Ashizawa, N. Toyama, A. Todoroki
- S98 73 - Use of AE for characterization of damage mechanisms in composite accumulator
O. Colas, C. Briançon, C. Hervé, A. Houssais
- S109 40 - Continuous recording and wireless transmission of AE waveforms by battery powered sensor nodes
K. Ito, M. Enoki
- S114 01- Modal Acoustic Emission analysis of mode-I and mode-II fracture of adhesively-bonded joints
A. Crawford, M. Ghazi Droubi, N. Faisal
- S125 02- On use of signal features for Acoustic Emission source identification in fiber-reinforced composites
M. G. R. Sause
- S137 03- Damage diagnostic and lifetime prognosis for ceramic matrix composite with

- Acoustic Emission during long-term mechanical tests at intermediate temperature
N. Godin, P. Reynaud, G. Fantozzi
- S153 04- Combination of synchrotron computed tomography and Acoustic Emission measurements for cyclic loading of fiber-reinforced composites
P. Potstada, S. Rosini, M. Mavrogordato, I. Sinclair, S. M. Spearing, M. G. R. Sause
- S164 48 - Structural Health Monitoring of composites structures by Acoustic Emission analysis
L. Schubert, E. Schulze, R. Neubeck, B. Weihnacht
- S172 68 - Structural Health Monitoring of composite aerospace structures with Acoustic Emission
M. Lehmann, A. Bueter, O. Schwarzhaupt, C. Contell Asins
- S194 53 - Mechanical and Acoustic Emission characterization of lime-based masonry constituents
N. Shetty, G. Livitsanos, D. Aggelis, D. Van Hemelrijck, M. Wevers, E. Verstryngne
- S204 22 - Characterization of particle impacts using Acoustic Emission
E. Serris, L. Carrillo, A. Valentini
- S214 32 - The sound of metal: Acoustic Emission during the deformation of commercially pure titanium
N. Goossens, M. Seefeldt, M. Wevers
- S227 38- Analysis of kinking and twinning behavior in mg alloys by AE clustering method
M. Enoki, K. Tamura, T. Shiraiwa
- S233 39- Non-threshold Acoustic Emission analysis of damage evolution in pipe segments of steel S355J2H under bending load
F. Baensch, W. Baer, P. Wossidlo, A. Habib
- S241 71 - Galling detection by Acoustic Emission (AE) according to ASTM G98
A. Saidoun, C. Hervé, Y. Chen, T. Lesage
- S250 11-AE monitoring and three-dimensional observation of stress corrosion cracking from corrosion pits
K. Wu, K. Ito, I. Shinozaki, M. Enoki
- S260 18 - Application of Acoustic Emission measurements to monitor the initiation and the propagation of single or multiple Stress Corrosion Cracks (SCC)
O. Al Haj, A. Proust, J. Bolivar, M. Fregonese
- S274 64 - Acoustic Emission from gas bubble nucleation and breaking away from a fl t surface
V. Kietov, M. Mandel, L. Krüger, A. Vinogradov
- S287 75 - New edition of GEA guideline for Acoustic Emission Testing of pressure equipments
C. Di Giulio, C. Hervé
- S295 15 - Use of Acoustic Emission for inspection of various composite pressure vessels subjected to mechanical impact
F. Dahmene, O. Bardoux, S. Bittendiebel, P. Blanc-Vannet, N. Alexandre, F. Nony, M. Barcikowski, A. Maldachowska, M. Panek, P. Sheggem, A. Echtermeyer, K. Lasn
- S306 30 - Detection and identification of low-amplitude Acoustic Emissions during plastic deformation under indentation and scratch testing
A. Danyuk, D. Merson, A. Vinogradov
- S314 33 - When AE (Acoustic Emission) meets AI (Artificial Intelligence) II
K. Wasmer, F. Saeidi, B. Meylan, T. Le Quang, S. A. Shevchik
- S326 65 - AE fracturing modes classification by means of shear tensile source model
M. Petruzalek, T. Lokajicek, T. Svitek, P. Kolar, Z. Jechumtalova, J. Sileny, P. Adamova
- S339 21 - AE sensor sensitivity verification using a stimulated motion verification by laser-

	vibrometry
	H. Vallen
S356	76 - Method for assessing the likelihood of fatigue crack detecting V. Barat, D.V. Chernov, S.V. Elizarov
S369	78 - Statistical non-parametrical algorithm for Acoustic Emission impulses detection adapted on the basis of modal analysis approach V. Barat, D.A. Terentyev, S. Elizarov
S369	09 - Acoustic Emission measurements during a tensile fatigue test in reinforced concrete G. Manthei, M. Koob, J. Minnert
S382	77 - Test of bending reinforced concrete structures by means of Acoustic Emission method S.V. Elizarov, V. Bardakov, A.I. Sagaidak
S390	81 - Assessment of infrastructures by rainy induced AE tomography with wave velocity and attenuation rate T. Shiotani, K. Hashimoto, N. Okude, C. Granier, K. Watabe, H. Takamine
S402	34 - Contouring geodetically accurate Acoustic Emission sources via kernel density estimates P. Gális, V. Kůs
S412	41 - Analysis of AE source location precision for general sensor configurations M. Chlada, J. Kober, Z. Prevorovsky
S419	54 - Time reversal localization of continuous and burst AE sources under noise Z. Prevorovsky, J. Krofta, J. Kober, M. Chlada, M. Mracko
S442	06 Modelling of fiber break as acoustic emission source in single fiber fragmentation test: comparison with experimental results Z. Hamam, N. Godin, C. Fusco and T. Monnier
iv	Conference Proceedings Content
x	Conference Proceedings Authors Index

19 - Combination of vibration analysis & Acoustic Emission measurements to better characterize damage and mechanical behavior of aerospace high speed gear box

Hebrard Yoann¹, Proust Alain², Batel Mehdi²,

¹ SKF Aerospace, 22 rue Brillat Savarin, 26958 Valence, FRANCE
yoann.hebrard@skf.com

²MISTRAS SAS, 27 rue Magellan 94370 Sucy en Brie
alain.proust@mistrasgroup.com

Abstract:

Designed to break the paradigm for efficiency, the new generation of engines promises double-digit reductions in fuel burn, as well as an unparalleled single-leap improvement in emissions and lower noise to fulfil societal environmental objectives for a more sustainable future. The end-use consumer and environmental policy requirements for aircrafts of the next generation translate into components with higher temperature and speed. Furthermore, new instrumentation techniques are needed to closely monitor rolling contact during testing of the next generation of aero engine bearing to check its behavior under the new application condition. Vibration analysis for condition assessment and fault diagnostics is widely used nevertheless interpretation and correlation of collected data is often cumbersome. That is why combination of both techniques giving different types information in two different frequency band can help to understand the behavior of new gear box. This study proposes a correlation between low and high frequency signals with different strategy of signal acquisition and processing. Real time transient analysis with feature extraction can be done in parallel with streaming acquisition. Then pattern recognition of individual AE signal is possible and can be correlated with more traditional analysis based on "multiple chocks" vibration analysis. Continuous monitoring of an aging gear box is giving genuine information on no stationary regime and also time of stabilization. Long term experiments are conducted on damaged and defect free gear boxes at several rotating speed and loading level.

Keywords: Rolling contact monitoring, vibration monitoring, EHL conditions

1. Introduction

Many studies are dealing about the use of vibration to detect fault in gear box and rolling bearings. Some of them are focusing on the use of Acoustic Emission (AE) and vibration for better characterization of the gear box default type. Based on vibration technology the acquisition of raw signal is done by a partial acquisition of the signal at random. AE technology is more focusing on the detection of transient above a predefined threshold in a narrow bandwidth [1,2]. According to the progress of the acquisition system, this study proposes a combination of all these types of acquisition. Wide band sensors offer richer bunch of data allowing us to investigate new methods of processing and default characterization.

The default Characterization we propose will be more than a statistic acquisition but a continuous monitoring.

Acoustic emission (AE) is defined as transient elastic waves generated from a rapid release of strain energy caused by a deformation or damage within or on the surface of a material [4]. This technique is widely used as a non-destructive testing technique for fitness for service evaluation in industrial field. AE is also a powerful tool to characterize and understand damage initiation and propagation. Most of all microscopic mechanisms has been studied and correlated with AE signals as fretting [3]. Many developments in AE technology, mainly developments in AE instrumentation, have occurred in the past ten years.

In this particular investigation, AE appears as the transient elastic waves generated by the interaction of two surfaces in relative motion. The interaction of surface asperities and impingement of the bearing rolling elements over the seeded defect on the outer race will generate AE hits. Due to the high frequency content of the AE transients typical mechanical noise (less than 20kHz) is eliminated.

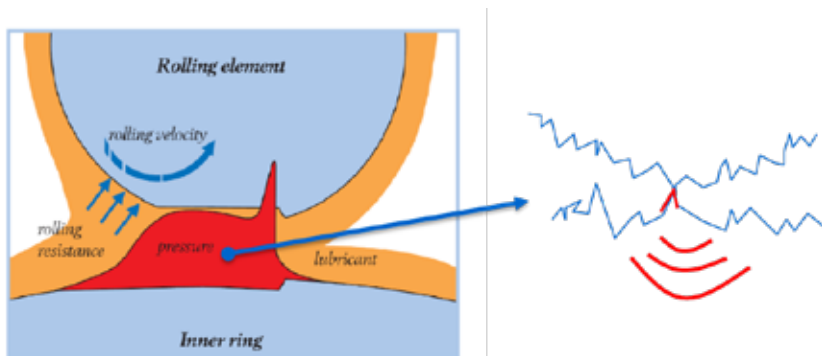


Figure 1: AE signal from asperity in rolling contact

There have been numerous investigations reported on applying AE to bearing defect diagnosis. Roger [5] utilized the AE technique for monitoring slow rotating anti-friction slew bearings on cranes employed for gas production. In addition, successful applications of AE to bearing diagnosis for extremely slow rotational speeds have been reported [6, 7]. Yoshioka and Fujiwara [8, 9] have shown that selected AE parameters identified bearing defects before they appeared in the vibration acceleration range. Hawman et al [10] reinforced Yoshioka's observation and noted that diagnosis of defect bearings was accomplished due to modulation of high frequency AE hits at the outer race defect frequency. The modulation of AE signatures at bearing defect frequencies has also been observed by other researchers [11, 12, 13]. Morhain et al [14] showed successful application of AE to monitor split bearings with seeded defects on the inner and outer races.

This paper investigates the relationship between AE signals for a range of defect conditions, offering a more comparative study than is presently available in the public domain. Moreover, comparisons with vibration analysis are presented. The source of AE from seeded defects on bearings, which has not been investigated to date, is presented showing conclusively that the dominant AE source mechanism for defect conditions is asperity contact.

2. Experimental setup

The bearing test rig employed for this study had an operational speed range of 5000 to 15000 rpm with a maximum load capability of 50kN via a hydraulic ram. The test bearing employed was 3 points contact ball bearing. This bearing type was selected as it allowed defects to be seeded onto the races, furthermore, assembly and disassembly of the bearing was accomplished with minimum disruption to the test sequence. Five calibrated dents were done on the bearing inner ring (rotating). Pure axial loading is applied to the rolling bearing. The defects are located along the predicted rolling raceway path inside the hertz contact zone. Dent length against the rolling velocity are around 200 μ m. The acquisition is performed via a multichannel last generation Mistras AE acquisition system: Express 8.

We have use all capability of this system to record the maximum of information. First, we use continuous energy summation without threshold, which is much accurate than traditional RMS or ASL (RMS with log scale) integration. Then, acquisition of transients based on smart threshold allows us to avoid triggering on continuous signal. It can guaranty a significant hits rate whatever is the level of background continuous AE (fig.2). Manual change of the trigger is not any more require. Transient is characterized by hit and waveform, it can be feed in Noesis, Mistras pattern recognition software for multiparametric evaluation. Express 8 offer also the capability to record streaming (acquisition of raw signal at very high rate and with quasi unlimited buffer) to apply more traditional signal processing often use in vibration but with lower sampling rate.

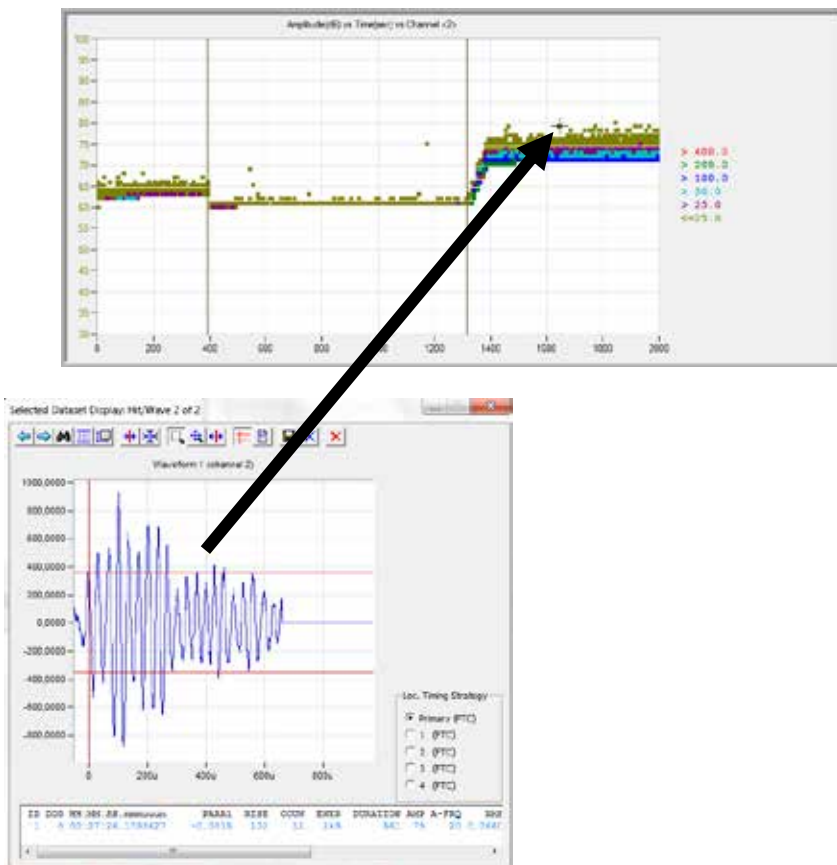


Figure 2: acquisition with smart threshold (above graph) and waveform and hit correspondence (graph below).

The streaming has been also used in parallel without any reduction of performance of traditional AE acquisition. Streaming is a synchronized acquisition of the 4 channels without any threshold. The windows length can be arbitrary of defined like shown in figure 3.

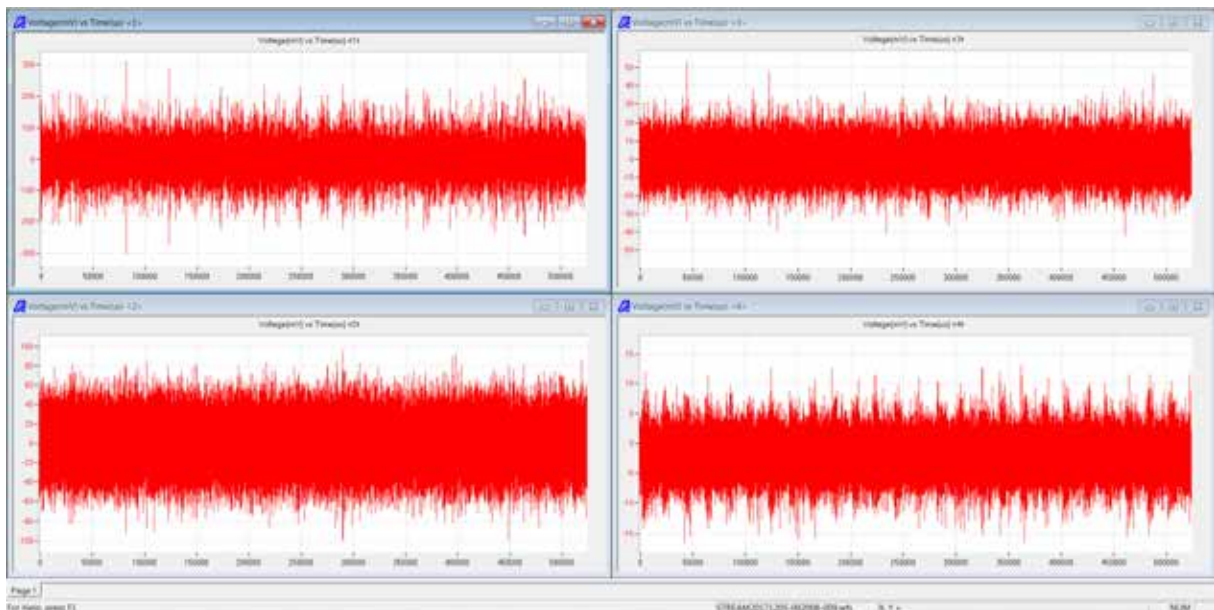


Figure 3: streaming acquisition during 5 sec at 2 Mega sample per second on the four channels.

Three different wideband AE sensors (WD, S9208 and micro 80) are used in parallel with a standard accelerometer Bruel et Kjaer type 4374 (bandwidth 1 to 26KHz 0,5 pC ms⁻²). The calibration curves of these sensors are given in figure 4.

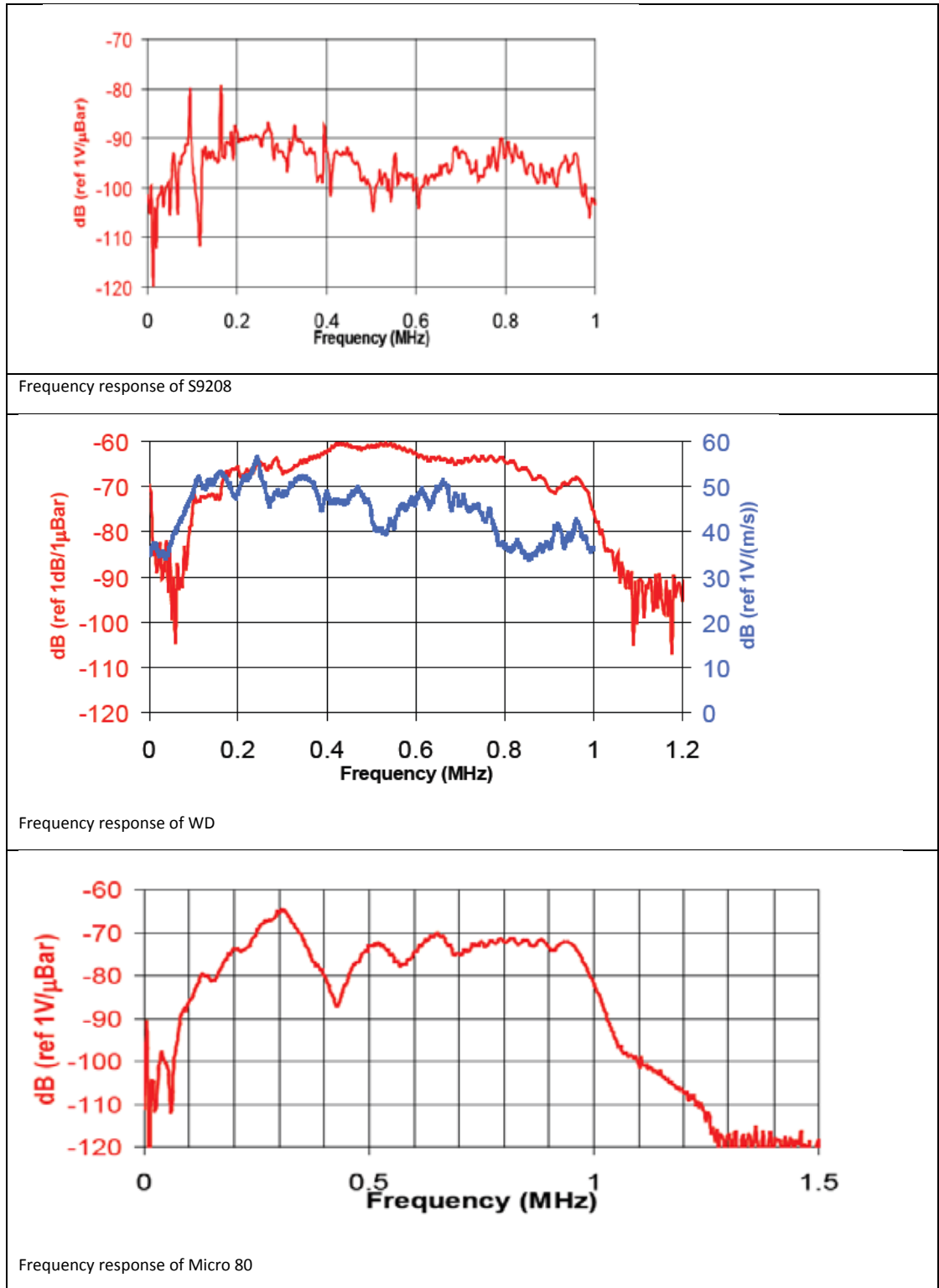


Figure 4: calibration curves of sensors S9203, WD and micro 80.

The sensor must be held in place for the duration of the test. Dry contact between the sensor and the structure does not meet the goal for appropriate wave transmission. For the AE sensors coupling, we used an adhesive tape developed for aerospace industry called "KAPTON" on which the sensor is glued with cyanoacrylate or cement glue. (figure 5). This solution has been successfully tested with cyanoacrylate glue during test space telescope for ASTRIUM under high energetic vibration [15]. The reduction of measured amplitude compare to a traditional grease coupling is less than one dB for Hsu Nielsen source (NF EN1330-9).

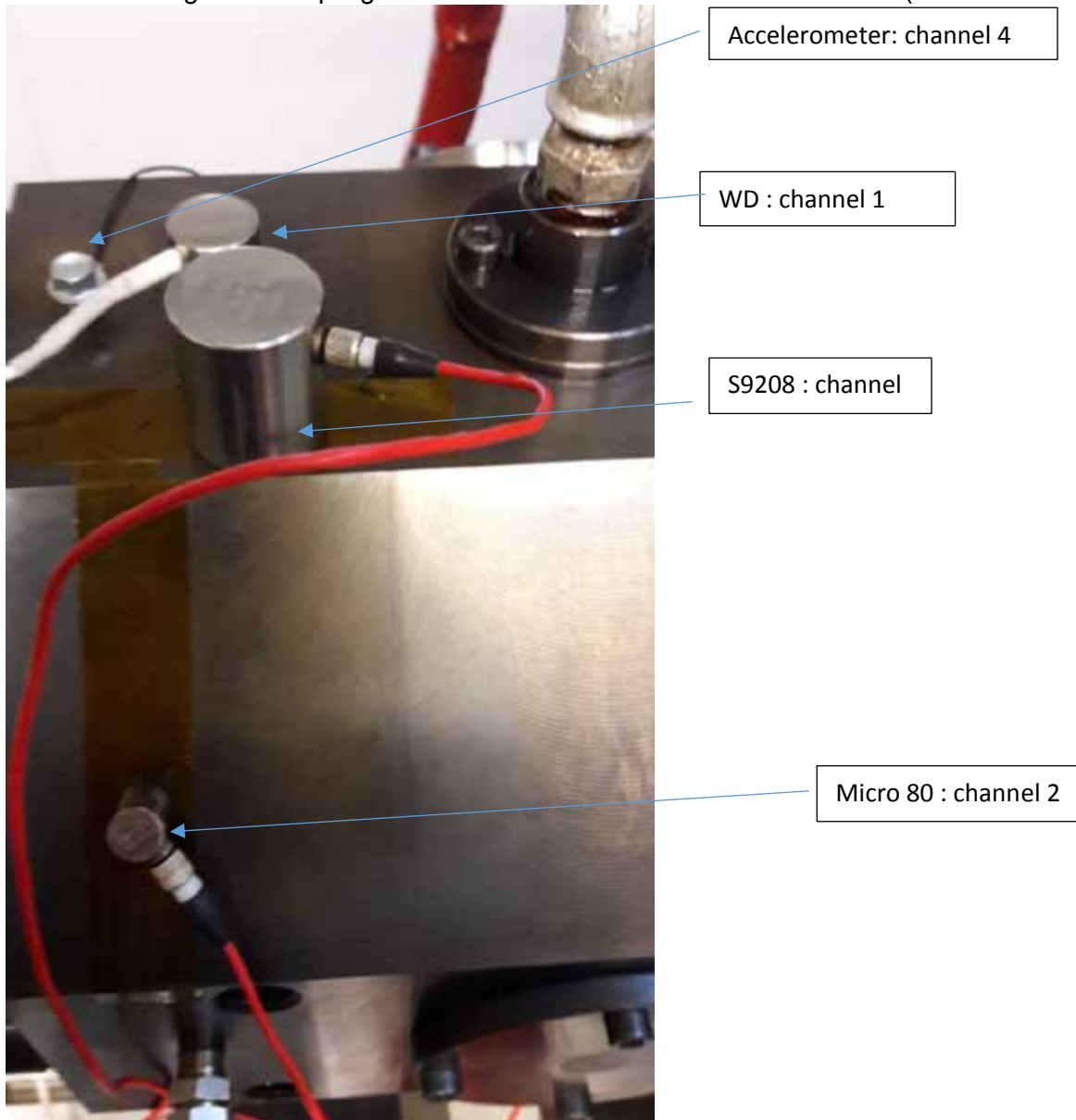


Figure 5: picture of the different sensors used for the monitoring and coupling mode.

3. Results

We performed the same loading sequence for all bearings, see table 1.

Speed (Rpm)	Load (kN)
3000	5
6000	5
11500	5
11500	10
11500	15
11500	20
11500	25
6000	23,5

Table 1: loading sequence for bearing the colors are used to separate the loading sequences.

The four sensors are compared and the WD (channel 1) and micro 80 (channel 2) are giving better results than accelerometer and S9208 to characterized default (fig.6).

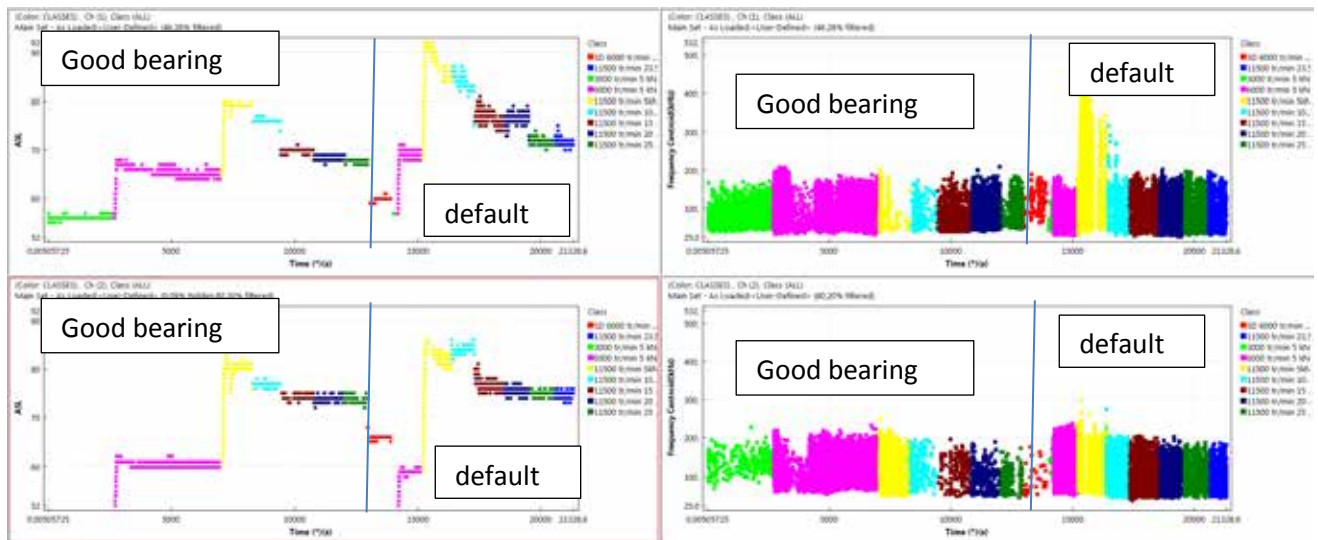


Figure 6: evolution of ASL and frequency centroid versus time with and without default. On the top graph channel 1 (WD) at the bottom channel 2 (Micro 80).

A clear difference of behavior can be seen above 6000 rpm at 5 kN and it enhance at 10 kN on the energy of the AE signals on transients. Also, the center mass of the frequency spectrum

(called frequency centroid) increases a lot for the bearing with default. It exhibits the best power of discrimination using our pattern recognition software. The stabilization of the AE signal takes at least 2 minutes after the loading condition change.

Considering a more standard acquisition mode for channel 1 (WD), on the bearing with default, it can be seen a new pic at 27 kHz at 11500 tr/min and above speed. For another side, the width of the FFT increases as the load increases (fig. 7).

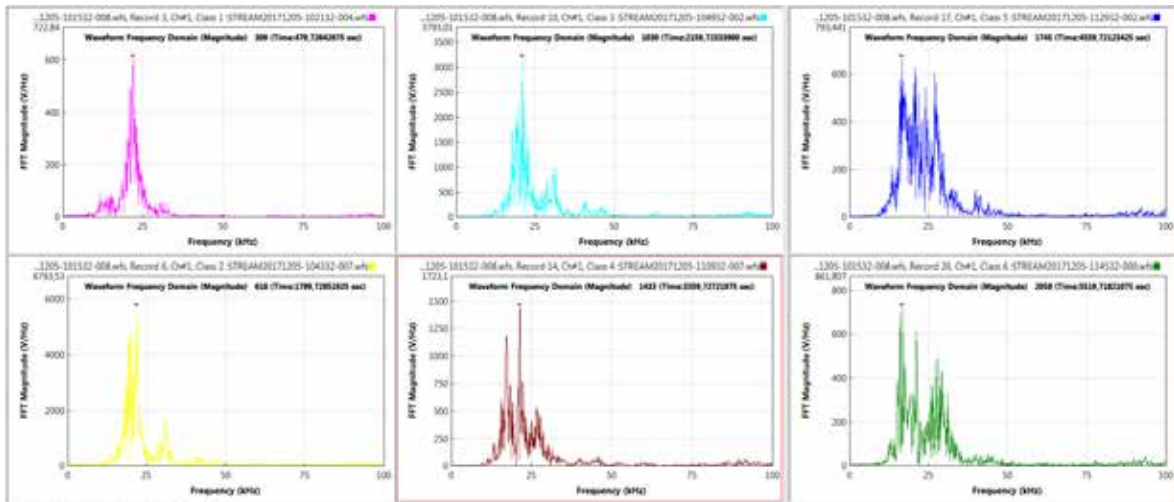


Figure 7 : Fourier transform on 5s files on channel 1 for different cases of load levels and rotating speed.

4. Discussion

The source of AE for seeded defects is attributed to material protrusions above the surface roughness of the outer race. This was established as the smooth defect could not be distinguished from the no-defect condition. However, for all other defects where the material protruded above the surface roughness, AE transients associated with the defect frequency were observed. As the defect size increased, AE ASL, maximum amplitude and kurtosis values increased, however, observations of corresponding parameters from vibration measurements were disappointing. Although the vibration RMS and maximum amplitude values did show changes with defect condition, the rate of such changes highlighted the greater sensitivity of the AE technique to early defect detection.

Again, unlike vibration measurements, the AE transient could be related to the defect source whilst the frequency spectrum of vibration readings failed in the majority of cases to identify the defect frequency or source. Also evident from this investigation is that AE levels increase with increasing speed and load. It should be noted that further signal processing could be applied to the vibration data in an attempt to enhance defect detection.

Techniques such as demodulation, band pass filtering, etc, could be applied though these were not employed for this particular investigation. The main reason for not applying further signal processing to the vibration data was to allow a direct comparison between the acquired AE and vibration signature. From the results presented two important features were noted:

- firstly, AE was more sensitive than vibration to variation in defect size
- secondly, that no further analysis of the AE response was required in relating the defect source to the AE response, which was not the case for vibration signatures.

The relationship between defect size and AE hit duration is a significant finding. In the longer term, and with further research, this offers opportunities for prognosis. AE hit duration was directly correlated to the seeded defect length (along the race in the direction of the rolling action) whilst the ratio of hit amplitude to the underlying operational noise levels was directly proportional to the seeded defect width.

5. Conclusion

It has been shown that the fundamental source of AE in seeded defect tests was due to material protrusions above the mean surface roughness. Also, AE maximum amplitude has been shown to be more sensitive to the onset and growth of defects than vibration measurements.

A relationship between the AE hit duration and the defect length will be established in further posttreatment.

References:

- [1] Raad, A. Sidahmed, B; Early detection of the gear fault – advantage of the acoustic emission technique 25th European conference, Acoustic emission testing; EWGAE; 2002; Prague; 2; II/125-II/130
- [2] Lekou, D.J., Mouzakis, F., Anastasopoulos, A. A., Kourousis, D., Fused Acoustic Emission and Vibration Techniques for Health Monitoring of Wind Turbine Gearboxes and Bearings; Scientific Proceedings of EWEC 2009, pp. 78-82., At Marseille
- [3] Boinet, M. Proust, A., Lenain, J.C., Yantio Njankeu Sabeya, G.R., Paris, J.-Y., Denape, J., Analyse par Emission Acoustique de la dégradation d'un contact sollicité en fretting, Journées Francophone de Tribologie Poitiers, 22–23 mai 2007.
- [4] Mathews, J. R. *Acoustic emission*, Gordon and Breach Science Publishers Inc., New York. 1983, ISSN 0730-7152.
- [5] Roger, L. M., The application of vibration analysis and acoustic emission source location to on-line condition monitoring of anti-friction bearings. *Tribology International*, 1979; 51-59.

[6] Mba, D., Bannister, R.H., and Findlay, G.E. Condition monitoring of low-speed rotating machinery using stress waves: Part's I and II. Proceedings of the Instn Mech Engr 1999; 213(E): 153-185

[7] N. Jamaludin, Dr. D. Mba, Dr. R. H. Bannister Condition monitoring of slow-speed rolling element bearings using stress waves. Journal of Process Mechanical Engineering, I Mech E. Pro. Inst. Mech Eng., 2001, 215(E);, Issue E4, 245-271.

[8] Yoshioka T, Fujiwara T. New acoustic emission source locating system for the study of rolling contact fatigue, *Wear*, 81(1), 183-186.

[9] Yoshioka T, Fujiwara T. Application of acoustic emission technique to detection of rolling bearing failure, *American Society of Mechanical Engineers*, Production Engineering Division publication PED, 1984, 14, 55-76.

[10] Hawman, M. W., Galinaitis, W. S, Acoustic Emission monitoring of rolling element bearings, *Proceedings of the IEEE, Ultrasonics symposium*, 1988, 885-889

[11] Holroyd, T.J. and Randall, N., (1993), Use of Acoustic Emission for Machine Condition Monitoring, *British Journal of Non-Destructive Testing*, 1993, 35(2), 75-78.

[12] Holroyd, T. Condition monitoring of very slowly rotating machinery using AE techniques. *14th International congress on Condition monitoring and Diagnostic engineering management (COMADEM'2001)*, Manchester, UK, 4-6 September 2001, 29, ISBN 0080440363

[13] Bagnoli, S., Capitani, R. and Citti, P. Comparison of accelerometer and acoustic emission signals as diagnostic tools in assessing bearing. *Proceedings of 2nd International Conference on Condition Monitoring*, London, UK, May 1988, 117-125.

[14] Morhain, A, Mba, D, Bearing defect diagnosis and acoustic emission Journal of Engineering Tribology, I Mech E, Vol 217, No. 4, Part J, p 257-272, 2003. ISSN 1350-6501.

[15] Levallois, F., Sobeczko, A., Proust, A., Marlot, D., Lenain J.C. Non-destructive testing of GAIA frame by means of acoustic emission monitoring during launch simulation tests., 30th European Conference on Acoustic Emission Testing & 7th International Conference on Acoustic Emission University of Granada, 12-15 September 2012.

35 - Acoustic Emission for *in situ* monitoring of laser processing

Sergey SHEVCHIK¹, Quang Tri LE¹, Bastian MEYLAN¹, Kilian WASMER¹

¹ Laboratory for Advanced Materials Processing, Empa - Swiss Federal Laboratories for Materials Science and Technology, Feuerwerkerstrasse 39, CH – 3602 Thun, Switzerland; Phone: +41 58 762 62 71; Email: kilian.wasmer@empa.ch

Abstract:

Laser processing is an important technology in industrial manufacture. Today, a standard quality monitoring of the processed workpieces mainly relies on costly X-ray or time consuming post mortem methods. The commercially available *in situ* and real-time monitoring units are also accessible and rely on optical measurements or high resolution imaging of the process zone. Unfortunately, their performance is greatly affected by the plume, formed during the overheating of the material. This limits the detection of defects (e.g. pores) formed inside the workpiece. To bypass the aforementioned limits, we focus on acoustic measurements that are the derivatives of the shockwaves, generated inside the workpiece directly during processing. The measurements are conducted using a high sensitive piezo sensor. The acoustic signals are analysed further by state-of-the-art signal processing. This included a compartment of wavelets and Fourier decompositions, followed by machine learning. The developed methodology is realized in a hardware unit that operates in pseudo real-time. The unit was tested on real welds with various materials. The welding experiments were performed using spot weld, Stepless High-speed Accurate and Discrete One-pulse Weld (SHADOW). The tests were carried out at different laser powers that are closely related to the weld quality. The *in situ* quality control unit demonstrated the capability to classify the weld quality with a confidence level ranged between 82% and 95%. Due to the similar light-matter interaction phenomena, the presented approach and apparatus can also be applied for monitoring other laser-processing technologies, namely: ablation, cutting, drilling and additive manufacturing.

1. Introduction

Laser welding is a rapidly developing technology that becomes an essential part in automobile [1,2], medical [3,4], aerospace [5,6,8] industries and heavy machinery production [8,9]. The advantages of this technology are in relatively low running costs, high processing speed and quality in terms of the mechanical properties of the welded joints [1,5,7]. The growing demand for laser welding requires the development of a reliable *in situ* quality monitoring and control that remains an open topic until today [1]. The challenge in developing such a system is the high complexity in laser-matter interactions [1,5,7]. This happens due to multiple physical phenomena that are present at different time scales affecting the process [5,7]. This complexity may be a reason for the deviations of the real quality from the desired one even in well controlled conditions [1,5,7]. One of the possible causes is the occurrence of pores that are a hidden threat for the mechanical properties of the processed workpieces [1,5,7]. At present, the diagnostic of pores in industrial environment is carried out with several well established methods.

Analysis of the cross-section of the workpieces is one of the most reliable techniques that allows visually inspect the processing results [1]. This method is destructive and time consuming that is obviously not applicable to every single piece in mass production. X-ray imaging is a non- destructive visualization method that allows to search the hidden pores directly inside the workpiece medium [1,10]. The drawback of this approach is the involvement of expensive and very complex equipment. In addition, rather complex image processing algorithms are needed for the search and interpretation of the obtained data. This leads to long computational time of the acquired images. These factors put technical limits on the adaption of this technology for in situ control. At present, this method is only applied for post mortem analysis of workpieces that require long manufacturing time.

The development of a real-time in situ quality control is still pushed by an industrial demand and some new approaches exist but are still at development stage. Image analysis is one of the mostly visible directions due to the availability of the cheap hardware and minimal modifications needed for already existing commercial laser welding systems. In this setup, the images of the process zone are registered in infra-red or visible spectral ranges [1]. The quality inside the workpiece medium is correlated with the surface temperature distributions and/or the geometry of the process zone [1]. The drawback of this approach is due to only surface measurements, while the inside processes remains hidden. In this situation, the aforementioned complexity of the laser-matter interactions [5,7] is, sometimes, responsible for deviations between the surface behavior and the expected behavior inside the medium, thus reducing the precision of this method.

Other methods based on spectroscopy of the evaporated materials from the process zone showed a potential but only for a limited number of applications [1]. High efficiency in detecting the plume and spatter was shown in a number of works [1]. However, those phenomena take place after overheating of the material [11], thus post-factum indicating an uncontrollable development of the process outside the acceptable quality range.

To sum up, the existing approaches for in situ monitoring have forenamed limits. Taking this into account, the present study is based on acoustic emission (AE) that has some advantages due to its nature. AE is a derivative of the elastic shockwaves deformations that take place inside the workpiece [1] and grab the information about the momentary pressure of the liquid/gas material phases inside the process zone onto the solid surrounding [1,7]. This implies direct volumetric measurements of the material behavior inside the process zone. The drawbacks of this approach are in the complexity of the AE signal interpretation. At present, AE proved itself to be a robust method for detection of the plume and spatter [1,5] that are characterized by a higher output intensity of the AE. Those events indicate extreme undesirable process behavior and the detection of the earlier quality critical events, which provide with more decision time, is an open topic. This work is a feasibility study for the detection of the momentary critical events in the AE signals and correlates those with the quality. To do so, we employ the combination of a highly sensitive AE sensor for data collection, and machine learning (ML) for data interpretation. The attraction of ML is in the possibility to create efficient correlation models to recover the links in intricate data, which is the case for laser welding processing inducing AE [1,5]. One additional motivation is given by the successful application of ML in a number of practical applications [12]. In the context of this work, ML was employed as a classification framework of the momentary quality events following the real welding process. The output of the method is a quality map of the entire welded joint with a high spatial resolution.

The hard/soft-ware realization of our approach is a full-fledged prototype of the quality monitoring system. In our setup, additional software was attached to the commercially available laser welding components. The demonstrator operates in pseudo real-time and requires no interventions inside the commercial parts. The data processing proposes a number of unique ML algorithms, the efficiency of which can be tested on the fly, adapting the algorithmic parameters to a specific application.

2. Hardware description

The hardware included a single mode fiber laser source (Fiber laser – StarFiber 150P/300P – long pulse fiber laser systems, Coherent, Switzerland) with a 1070 nm wavelength and peak output light power of 300 kW. The laser source operated in pulse mode with a repetition rate varied in the range of 0.01 – 20 Hz with a spatial Gaussian energy distribution. The output of the laser source was transmitted through a 12 µm core diameter single – mode optical fiber to a laser head. The laser head was a customized version of LASAG PH-10 Wobble (Coherent, Switzerland). Its objective had a focal length of 170 mm that focused the laser light on the sample surface into a spot of 30 µm diameter. The laser head was also equipped with a photodiode that measured the back reflected laser light from the surface of the workpiece. The photodiode was a Ge based with a spectral sensitivity ranged between (1100-1700) nm. Additionally, a narrow band optical filter was placed in front of the photodiode for selective transmittance of the back reflected laser light.

Plates from titanium (Ti) grade 5 with size 2x20x50 mm were used as workpieces. The plates were fixed in an aluminum workpiece-holder, which was placed on a U-521 PILine linear positioning Stage (Physik Instrumente GmbH, Germany). The stage provided the shifts of the workpieces in the direction perpendicular to the laser beam with a tunable velocity between 1 mm/s and 100 mm/s. In this work, the velocity was varied to achieve different welding strategies and qualities and the details are given below.

The laser welding process induced AE, which was recorded by a piezoelectric sensor Pico (Physical Acoustics, USA). The sensitivity range of the AE sensor was in the range of 50 - 1850 kHz. The AE sensor was firmly clamped to the aluminium workpiece-holder in a stationary position throughout all the experiments. The recorded AE signals were digitized by a data acquisition unit from Vallen (Vallen GmbH, Germany) with a sampling rate of 10 MHz. The redundancy in sampling rate was removed later during the signal processing. The data acquisition was triggered by the Ge photodiode of the processing head. At the same time, the acquisition duration was adjusted to the duration of the laser pulse that illuminated the workpiece.

The digitized signals were transmitted to PC where they were stored using the software from Vallen. In addition, the same computer included a specially developed software with the machine learning framework. This software processed the stored AE signals and output the results as a quality map of the weld joint. The quality map was formed as the time ordered sequence of the spatially localized momentary welding events within a single weld. Those momentary events were established before the processing. The general view of the entire setup and the interface of the software with the processing output are shown in Fig. 1.

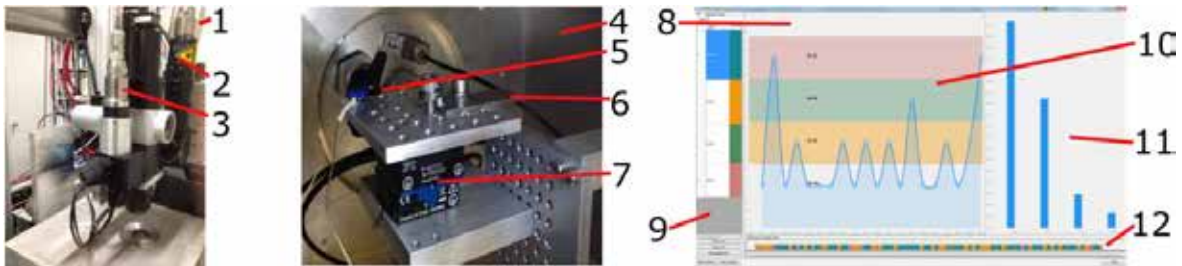


Figure 1: A general view of the setup : 1) the general view of the customized laser head; 2) the optical fiber input from the laser source; 3) the photodiode; 4) the general view of the workpiece placement in the welding chamber; 5) piezo sensor; 6) workpiece from Ti; 7) the moving stage; 8) the interface of the specialized software; 9) the interface panel with the list of the pre-defined momentary welding events and their colour encoding; 10) interface panel with the current momentary classification results; 11) interface panel with the quality statistics; 12) colour encoded quality map of the weld.

The described system allowed realising several welding strategies that are widely used in the industry, namely: i) spot welding and ii) **Stepless High-speed Accurate and Discrete One-pulse Welding (SHADOW)**. The settings of the power of the laser irradiation for both regimes was varied to provoke distinctive welding qualities and the corresponding settings for the power of the laser irradiation were taken from a previous work [11].

Spot welding is the exposure of separate surface areas with short laser pulses that provided deep weld but with a narrow process zone [1,5,11]. To create this regime, the laser pulse duration was fixed at 5 ms whereas the laser power was set to 20W, 40W, 80W and 120W. The sample was moved on a distance of 0.4 mm after each pulse to avoid any overlaps of the heat affected zones. Thirty five pulses for each laser power condition were applied and the corresponding AE signals were used for training of the machine learning classifier.

The welding in a SHADOW regime produces quasi continuous welds from a single pulse. It is distinguished by the lower power consumption while operating during long time periods and provides with less crystallographic changes in heat affected zone [13]. During experiments the welds of 5 mm in length were produced. The irradiated workpieces were shifted at a speed of 100 mm/s under the laser beam and were exposed with a laser pulse duration of 50 ms. The laser power was set to the discrete values of 50W, 100W, 150W, 200W and 250W to provoke different qualities. For SHADOW welding, five welds for each condition were made and used for the training of the machine learning framework. For both welding regimes, the classification tests were performed using real welds that followed after training.

3. Signal processing

All acquired AE signals were recorded in the PC and were processed with a delay of two seconds compare to each laser pulse without data loss. The saved AE signals were recovered and analyzed with our specially developed software one by one according to the time order thus following the actual welding process. For quality classification during spot welding, the entire AE signal from each individual pulse was considered as a single momentary welding event and the AE signals from those were processed entirely. For SHADOW welding regime, the recorded AE signals were evidently of a longer duration. In

this case, those signals were scanned with a running window following the process and splitting the AE signals into a sequence of separate patterns. The processing procedure that is described below was applied to each of such patterns. The typical example of running window processing for SHADOW welding is shown in Fig. 2,a. The time span of the running window was estimated empirically during an exhaustive experimental search. On the one hand, the shorter time span provided a higher spatial resolution in the localization of the local particularities of the weld joint. On the other hand, those were more affected by the noises thus reducing the classification accuracy. It was experimentally estimated that the optimal compromise between those contradicting conditions was with the time span of 1 ms. This time span allowed classifying the weld quality for each 0.1 mm of the weld joint.

The processing of the signals was made in two steps: i) pre-processing and ii) classification. The pre-processing included the computation of two types of features that were compared with each other inside a common machine learning framework. The magnitude spectra of window fast Fourier transform (WFFT) was computed using a Hann window, decomposing the given AE signals in the frequency domain [14]. Then, the wavelet sonograms were computed decomposing the signals in the time-frequency domain [14]. The interest in wavelet application towards this problem was stipulated by wavelet advantages when operating with non-stationary data as compared to the Fourier transforms [14]. The wavelet decomposition is sensitive to the choice of the base (or mother) wavelets. In this study, the search of the suitable base wavelet was performed via an extensive search among the standard wavelets families, including: Daubechies, Symlets, Mexiacan hat, Coiflets, biorthogonal wavelets. The wavelet approximation errors of the collected AE signals were analyzed to make the final choice. Finally, the Daubechies wavelet with 5 vanishing moments was chosen for further analysis as it had the minimum approximation errors.

The construction of the wavelet sonograms was carried out using wavelet packets [14] and the general scheme of this transform is presented in Fig. 2,b. In wavelet transform, the signal is gated through low (h_0 in Fig. 2,c) and high (h_1 in Fig. 2,c) pass filters [14], resulting the extraction of the low and high frequency content. The multi-resolution analysis was achieved by including several decomposition levels, where the same operation is applied to the results of the previous split in the pyramidal way [14] according to the scheme in Fig. 2,c. The relative energies of the low and high frequency components after each such split were computed as: $\rho_{norm\ j,m} = \frac{E_{j,m}}{E_j}$, where $E_{j,m} = \int |d_{j,m}(t)|^2 dt = \sum_k |d_{j,m}|^2$ is the energy of each split and $d_{j,m}$ are the coefficients that are the products of each split and m is the decomposition level. The computed relative energies of narrow frequency bands are localized in the time-frequency domain [14]. The time-frequency ordering of those was used to build the sonograms of the recorded AE signals. An example of such sonogram can be seen in Fig. 2,d.

Two tests were carried out in which the magnitude spectra of the Fourier transform and the wavelets sonograms were the input to the classifier.

The task of the machine learning framework in the context of the present study was to find the unique acoustic signatures of different power regimes. In our setup each power regime was closely related to the quality and the explanations are given in the next paragraph. The classification was made using random forest (RF), which is the state-of-the-art in classification / regression tasks [15,16]. The main attraction of this algorithm towards our problem is its robust operation in the presence of noises, possibilities to build hyperplanes on a data with a complex mutual configuration, insensitivity to outliers and overfitting [16]. RF is

an extension of a bigger family of machine learning algorithms based on decision trees [16] which provides the aforementioned processing advantages. The architecture of decision trees incorporates a number of nodes. Each node splits the data into smaller portions and the need for further splits is decided if the current split fulfils some pre-defined criteria. RF employs the so-called CART (classification and regression trees) [16] in which the gini impurity criteria at each next split is compared with the one of the parent node, thus deciding the needed number of splits for each particular case [15,16].

The general RF architecture includes an ensemble of decision trees, unified into a forest. The processing is carried out by forwarding the input data into a common root of the forest, where it is sub-sampled on each tree individually [15,16]. The final decision is made by voting among all the trees inside the forest after the data propagation through the forest. The outstanding performance of RF is gained due to several novelties that were introduced in its architecture as compared to other ML algorithms. This makes it efficient when operating with real life data. RF does not require any cross validation tests to estimate the tests errors. The corresponding errors are the subject of internal computations (so-called out-of-bag estimates). The algorithm operates well with big dimensions of input variables and, in this case, only important dimensions are selected and further considered for analysis. The individual splits on each tree that followed the gini impurity criteria and the same splits are inhibited for different samples of the datasets. All this preserve RF from overfitting, maximally automatizing the operation of the algorithm and still keeping all the inner parameters accessible.

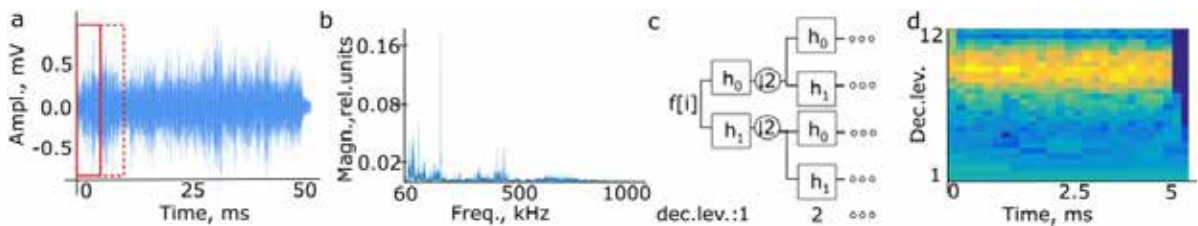


Figure 2: a) The AE signal from the SHADOW welding regime, where the solid and dashed markers show the present and next positions of the running window during processing; b) is the magnitude spectra of the pattern, bounded by the solid marker in a); c) is the wavelet packet transform scheme, where h_0 and h_1 are low and high pass filters correspondently; d) wavelet sonogram, obtained from a pattern, bounded by a solid marker in a).

4. Discussion

The relation of the welding quality to the laser power, provided in our setup, can be observed from the light microscopic images of the cross-sections in Fig. 3. The laser power was modulated during both, spot and SHADOW welds with the discrete laser power mentioned above and the corresponding quality variation, verified in earlier work [11]. The examples are given in Fig. 3,a and b. The microscopic images of the cross-sections for spot and SHADOW regimes were made post-mortem. As seen from the figures, the quality variations are in the welding penetration depth and pores presence. In the images from the figure the melt zone can be observed as a lighter color area inside the material with some textural differences. It is additionally bordered by white solid line in Fig. 3,a for better contrast. As seen for spot welding (Fig. 3,a), the powers of laser of 20W and 40 W corresponded to conduction welding with shallow penetration depths. With the powers of 80W and 120 W, the formation of vapor channel was created (so called keyhole) that resulted deeper penetration depth. The

presence of the key hole can be verified from the aspect ratio of the heat affected zone (HAZ) as is described in [11]. None of the cases in spot welding provoked the formation of pores. For SHADOW welding, the laser powers of 200 W and above were found to be the limit for the creation of pores and evidence of this is seen Fig. 3,b. The detection of pores is challenging as they are located at some depth under the surface. Those are not observable from the surface and carry a hidden threat to the mechanical properties of the workpieces. The laser powers below 200 W were characterized by different penetration depth of the melted material inside the workpiece. The experimental setup presented here provided the repeatability of the results in Fig. 3 during all experiments.

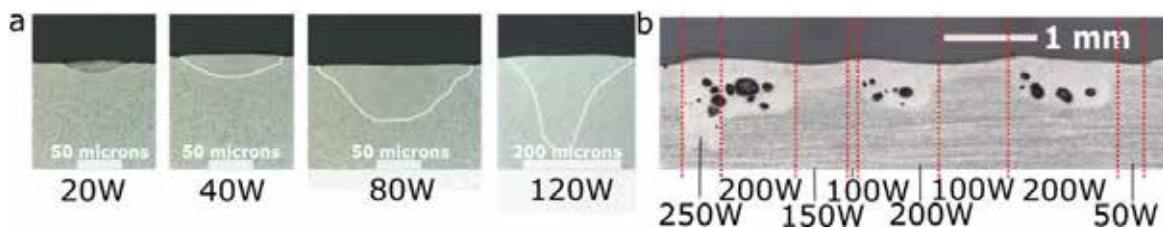


Figure 3: Cross-sections of the workpiece after a) spot and b) SHADOW welding regimes. The markers denote the power of the laser irradiation

The training of the classifier was performed using the preliminary collected dataset. The tests were done afterwards running real welding of workpieces. The results of the tests for spot and SHADOW welds are presented in Tables 1 and 2. The classification results in rows are given versus ground truth in columns. The match of the test results with the ground truth are placed in diagonal cells and highlighted in grey, while the structure of the classification errors is in the non-diagonal row cells.

The classification accuracy for the spot welds ranged from 85 % to 99 % for wavelets (in bold) and from 91 % to 99 % for WFFT [in brackets]. As seen from Table 1, the errors were mainly due to the overlap of the regimes with the neighbored laser power. It is interesting to note that the laser powers below 40 W (co called conduction welding) were classified with a high accuracy. In contrast, the welding regimes with laser power 80 W and 120 W (so called keyhole welding) showed lower accuracies. As seen from Table 1, both categories with high powers showed an overlap between each other's. One explanation can be in the emittance of AE in a broader frequency range while material overheating at higher laser powers that brings to more complex frequency configurations, thus complicating the separation of the data.

The classification accuracy for SHADOW welds varied between 75 % and 95 % for wavelets and 87 % and 98% for WFFT. The lower accuracy as compared to spot welding may be explained by the absorbed energies fluctuations inside a single weld caused by the local optical non-uniformities of the material that caused temperature drops. The errors structure presented in Table 2 showed an overlap between the neighbored values of the laser power which is identical to the situation in Table 1. Also, the greater overlap between 100 W and 150 W can be explained by a smooth border between the two regimes as observed in Fig. 3,b. The overlaps between the regimes with pores formation at 200 W and 250 W in industrial applications do not make a big difference as both are dangerous for the mechanical properties of the processed workpiece. In contrast, the overlap between the laser power with pores at 200 W with the one without at 150 W is relatedly low and is only 5% [-]. This relatively good separation between both regimes with a critical impact on quality demonstrates the applicability of acoustic emissions for quality monitoring. Generally this

processing scheme potentially allows avoiding non-desirable phenomena. However, further optimizations of the algorithms are planned to increase the classification accuracy.

Table 1. Classification accuracy for spot weld, where GT is the ground truth.

GT Test	20 W	40 W	80 W	120 W
20 W	99 [99]	1 [1]	-	-
40 W	1 [1]	99 [99]	-	-
80 W	-	-	85 [92]	15 [8]
120 W	-	-	15 [9]	85 [91]

Table 2. Classification accuracy for SHADOW weld, where GT is the ground truth*

GT Test	50 W	100 W	150 W	200 W	250 W
50 W	95 [99]	5 [1]	-	-	-
100 W	-	75 [87]	25 [13]	-	-
150 W	-	15 [11]	85 [89]	-	-
200 W	-	-	5 [-]	75 [89]	15 [11]
250 W	-	-	-	5 [2]	95 [98]

*the results are given in the format: wavelets [WFFT]

5. Conclusion

This work is a usage of acoustic emission (AE) and machine learning for laser welding quality monitoring. The frequency and time-frequency domains of the AE signals were exploited for signals representations and were the input of the classifier. The test results on real welds showed that this approach is technically feasible for the monitoring of the quality in commercially available laser welding machines. It was approbated on spot and SHADOW welds. The corresponding accuracy rates varied in the ranges of 85 % to 99 % and 75 % to 95 % for both welding regimes respectively. The possibilities to detect potentially dangerous welding regimes that cause the pores formations were shown. The greater error rates were observed as overlaps between the categories at higher laser powers. Mainly those regimes caused the occurrence of overheated material vapors (keyhole). Due to this, the emittance of AE is in a broader frequency range brought to more overlaps between the categories. However, it is important to underline that the regimes with and without pores are still separable with an acceptable precision.

The improvements of the classification confidence may be done with some optimizations of the processing algorithms. Those could be the usage of preliminary preprocessing to capture the training data structure. This is feasible, for example, with spectral graph methods. The extension of the classifier operation in recursive way may bring to higher efficiency as provides with better transients analysis. All this is planned as a future work.

References:

- [1] Stavridis, J., Papacharalampopoulos, A., Stavropoulos, P., Quality assessment in laser welding: a critical review, International Journal of Advanced Manufacturing Technology, Vol. 94, 2018, pp. 1825–1847, <https://doi.org/10.1007/s00170-017-0461-4>
- [2] Kyung-Min, H., Yung, C. S., Prospects of laser welding technology in the automotive industry: A review, Journal of Materials Processing Technology, Vol. 245, 2017, pp. 46-69, <https://doi.org/10.1016/j.jmatprotec.2017.02.008>
- [3] Perveen A., Molardi C., Fornaini C., Applications of laser welding in dentistry: a state of the art review, Micromachines, Vol. 9, 2018, article 209, <https://doi.org/10.3390/mi9050209>

- [4] Besnea D., Dontu O., Spanu A., Rizescu C., Pascu T., Study on laser welding of stainless steel/copper dissimilar materials, IOP conference series: Materials and engineering, Vol.147, 2016, article 012047, <https://doi:10.1088/1757-899X/147/1/012047>
- [5] Behzad F., Steven F. Wayne, G. L., Ebrahim A., A Review on Melt-Pool Characteristics in Laser Welding of Metals, Advances in Materials Science and Engineering, Vol. 2018, 2018, article ID 4920718, <https://doi.org/10.1155/2018/4920718>
- [6] Blackburn, J., Laser welding of metals for aerospace and other applications, In Woodhead Publishing Series in Welding and Other Joining Technologies, edited by M.C. Chaturvedi,, Woodhead Publishing, 2012, pp. 75-108, Welding and Joining of Aerospace Materials, ISBN 9781845695323, <https://doi.org/10.1533/9780857095169.1.75>
- [7] Svenungsson J., Choquet I., Kaplan A.F.H., Laser Welding Process – A Review of Keyhole Welding Modelling, Physics Procedia, Vol. 78, 2015, pp. 182-191, ISSN 1875-3892, <https://doi.org/10.1016/j.phpro.2015.11.042>
- [8] Reitemeyer D., Schultz V., Syassen F., Seefeld T., Vollertsen F., Laser Welding of Large Scale Stainless Steel Aircraft Structures, Physics Procedia, Vol. 41, 2013, pp. 106-111, ISSN 1875-3892, <https://doi.org/10.1016/j.phpro.2013.03.057>.
- [9] Viherva T., Viherva T., Riikonen H., Kujanpaa V., Welding of ship structural steel A36 using Nd:Yag laser and gas-metal arc welding, Journal of laser applications, Vol.12, 5, 2000, pp.185-188, <https://doi.org/10.2351/1.1309549>
- [10] Heider A., Sollinger J., Abt F., Boley M., Weber R., Graf T., High-Speed X-Ray Analysis of Spatter Formation in Laser Welding of Copper, Physics Procedia, vol. 41, 2013, pp. 112-118, <https://doi.org/10.1016/j.phpro.2013.03.058>.
- [11] Vakili-Farahani F., Lungershausen J., Wasmer K., Wavelet analysis of light emission signals in laser beam welding, Journal Laser Application, Vol. 29, 2017, article 22424. <https://doi:10.2351/1.4983507>.
- [12] Shivakumara P.G., Lia H., Knightb K., Georgiou P., Learning from Past Mistakes: Improving Automatic Speech Recognition Output via Noisy-Clean Phrase Context Modeling, February, 2018, arXiv:1802.02607v1
- [13] Kramer T., Olowinsky A.M., Durand F., SHADOW: a new welding technique, Proceedings of the SPIE, vol. 4637, 2002, pp. 545-554
- [14] Mallat S., A wavelet tour of signal processing, 1999, pp. 795
- [15] Breiman, L., Random Forests, Machine Learning, Vol. 45, 2001. <https://doi.org/10.1023/A:1010933404324>
- [16] Rockach L., Maimon O., Data mining with decision trees: theory and applications, 2nd edition, World scientific publishing, 2015, pp. 306

72 - Monitoring of stamping by Acoustic Emission (AE)

Abdelkrim SAIDOUN ¹, Catherine HERVE ¹
¹ CETIM Senlis

Abstract:

The optimization of the shaping processes (stamping, fast cutting, forming, spot welding, machining ...) and the quality of the production are very important in the field of industry. CETIM has been increasingly asked to propose solutions to improve the quality of production while not slowing it down. In this context, MOST "Monitoring of Stamping" has been developed, an online acoustic emission control system that guarantees the quality of production in real time.

The main defects that occurred during the stamping process are the sheet tears. To test the reliability of the MOST system for the detection of this type of defects, various feasibility tests have been carried out on the presses of industrial stamping.

In this study, we show the results of the detection in real time of some representative defects that have been created voluntarily by manufacturers (either by stopping lubrication or by changing the depth punch / mesh ...) by using MOST system.

Key words: stamping, acoustic emission, monitoring of stamping.

Introduction

In a globalized world where the competition is more and more intense, the optimization of the processes of shaping (stamping, fast cutting, trimming, welding by point,) and the quality of the production are the principal preoccupation for the industrialists.

The sheet metal stamping process is one of the most employed manufacturing processes in the automobile and aerospace industries to produce a variety of parts in terms of shape and size. On a mechanical press, the sheet is pressed between the die and the punch is pressed to obtain the required shape. Shearing, bending and drawing are incorporated in the stamping process to produce larger scale components [1]. However, the stability of the metal forming process depends on the parameters of the material and the process. A slight change in a process parameter, such as material properties or lubrication conditions, may result in a defect that could damage the tool, and consequently produce defective parts. For this reason, the monitoring of the manufacturing processes is essential to ensure the safety of the tools as well as the quality of the products.

To monitor manufacturing processes, sensors have been incorporated to monitor mainly the tool wear [2-6]. Considerable condition monitoring studies have also been conducted in the

stamping process using different sensors like strain, audio, borescope, thermocouple, force etc. [7-11]. Sah et al. [12] integrated force sensors into the die to study the contact pressure on the die radius during the forming process. However, high noise produced during the stamping process made the tool wear study complex.

In recent times, authors have attempted to use acoustic emissions to study wear because of its ability to work in the high frequency range (20kHz-2MHz) [13]. Skåre et al. [14] studied the wear and frictional behaviour of high strength steel using acoustic emission. Using AE, Sindi et al. [15] monitored the galling phenomena occurring in forming process on a tribo-test setup. Hase et al. [16] monitored the abrasive and adhesive wear phenomena using acoustic emission on a tribo-test setup.

Unlike the studies mentioned above, which are concerned with the detection of tool wear, MOST (the system developed by the CETIM) use the acoustic emission for the real time detection of tears in stamped parts. In this paper, we present the results of detection feasibility in real time of some representative defects that have been created voluntarily by manufacturers (either by stopping lubrication or by changing the depth punch / mesh ...).

1. Presentation of MOST system

MOST is a monitoring system for industrial processes of forming based on acoustic emission. The tears of sheet metal during the shaping operation are the main defects sought.

MOST can detect the appearance of defects on a production line whose rate varies between 10 and 120 strokes / minute. On the considered presses, the stamped materials vary from aluminum to steel for thicknesses of a few millimeters.

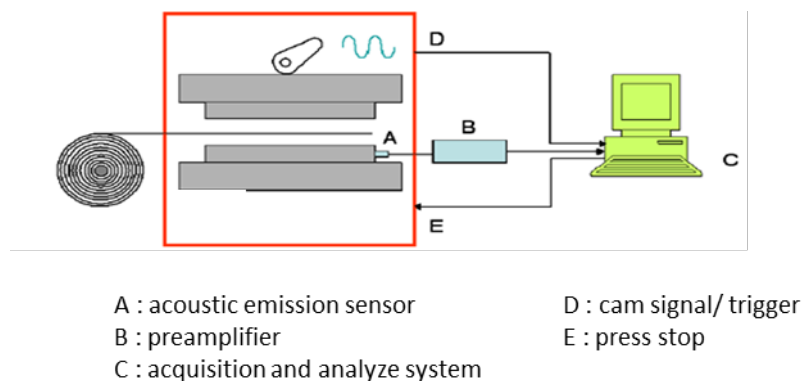


Figure 1. Representation of MOST system

The control protocol via the most system is as follows:

- Implantation of acoustic emission sensors:

The ideal is to place the acoustic emission sensors closer to the stamped part, in order to benefit from maximum detection sensitivity.



Figure 2. Implantation of acoustic emission sensor closer to the stamped part

➤ Determination of the angular window of acquisition:

The acquisition of the acoustic emission data is not done continuously over the cycle, only the acoustic signature of stamping + stripping is recorded in order to limit the noise. Most system is suitable for external triggering via the cam signal.

➤ Acquisition and analysis of acoustic emission data

Once the trigger is correctly set, it is then possible to record the acoustic emission data of the strike as shown in the figure 3. From this record, a processing phase is then performed in order to extract statistical parameters:

- RMS, this parameter reflects the acoustic noise level.
- KTS, this parameter makes it possible to highlight a pulse event of a continuous background noise

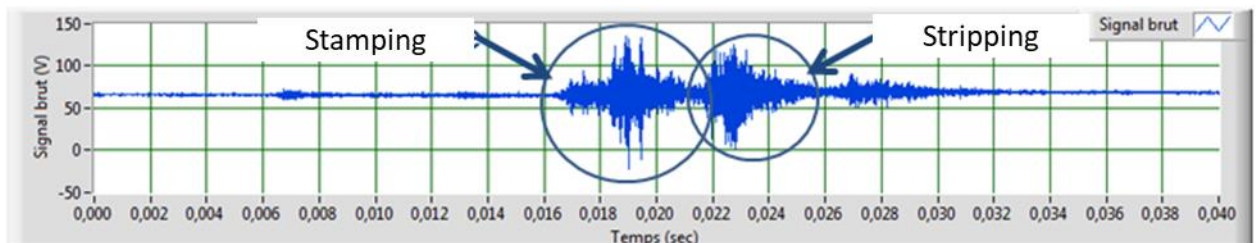


Figure 3. Acoustic emission signal of stamping + stripping

➤ Determination of a criterion of nonconformity

The nonconformity criterion is determined following a learning phase where the level of the two parameters (KTS and RMS) is defined. If one of the two parameters are exceeded, MOST system sends a stop signal to the press automaton.

2. On-line detection of stamping defects by the MOST system

2.1 Industrial feasibility 1

Figure 4.a shows the first case of feasibility by the MOST system. It is an impact observed on the stamped parts. this impact is related to tool wear.

Figure 4.b shows the representative defect voluntarily generated by the manufacturer by correcting the punch in order to increase the penetration.

The parameters of the tests are grouped in table 1:

Material	Inox 1,4307, e = 1,5 mm
Production rate	40 strokes / minute
Press	250T, 13 step tracking tool, punched: Z160 tempered to 58 HRC coated (Same as matrix)
AE sensor	Freq ≈ 200 kHz
Preamplifier	40 dB

Table 1. parameters of the first feasibility test



Figure 4.a. part with a real defect caused by the tool. **b.** part with a defect generated voluntarily by correcting the punch

Figure 5 shows the implantation of the AE sensor close to the stamped parts as explain previously.

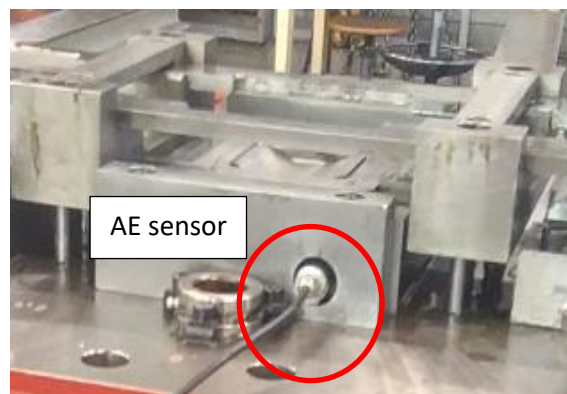


Figure 5. Implantation of AE sensor close to the stamped parts

Figure 6 present the evolution in real time of the KTS as function of the number of stamped parts. A learning phase (test 1 and test 2) was initially carried out on 250 good parts to determine the criterion of nonconformity. The maximum value of the KTS parameter in this phase is 43. The significant increase of the KTS on the series 3 and 4 correspond to the parts produced after rectification of the punch.

MOST was able to detect defective parts of the series (3 and 4) by a significant increase in KTS value.

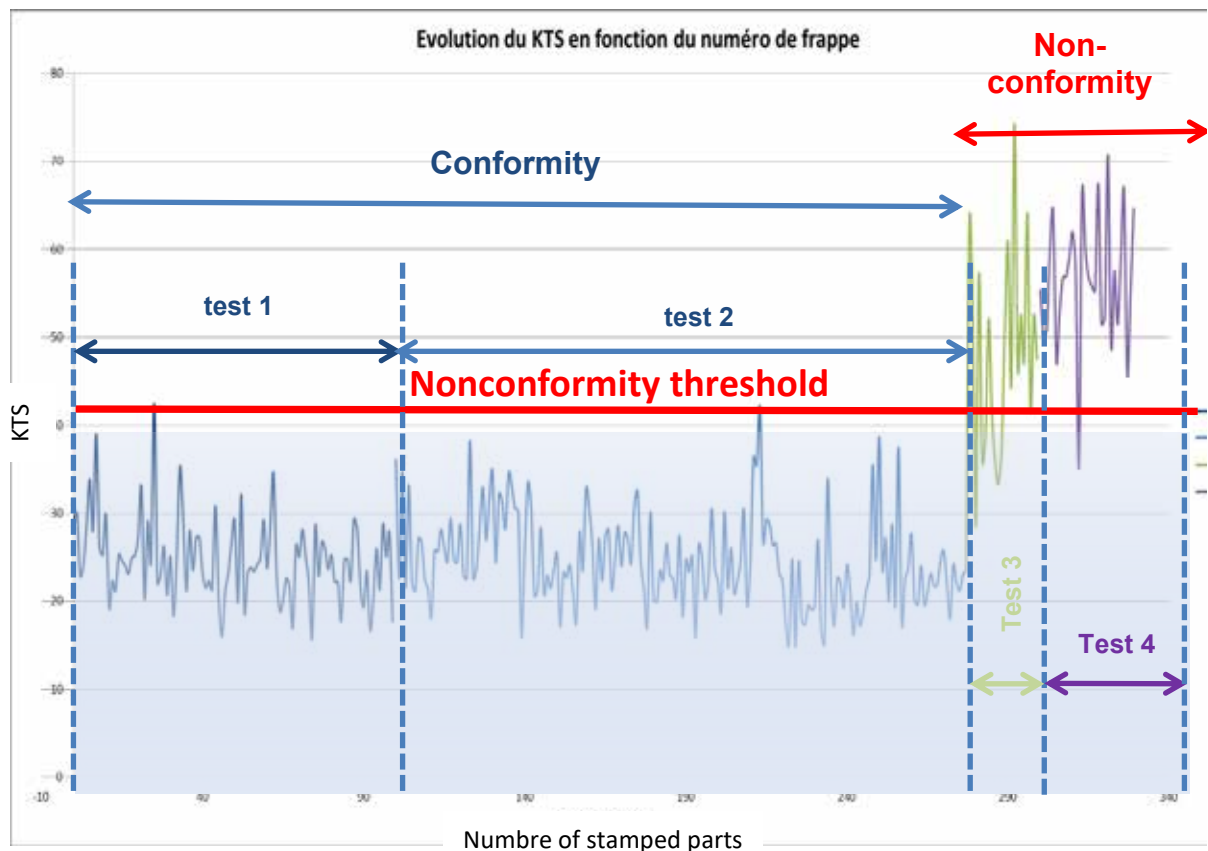


Figure 6. Evolution of KTS as function of the number of stamped parts

2.2 Industrial feasibility 2

Figure 7.a shows the second case of feasibility by the MOST system. It is a tear of the sheet caused by galling.

Figure 7.b shows the representative defect voluntarily generated by the manufacturer by generating impacts on the sheet before the stamping phase.

The parameters of the tests are grouped in table 2.



Figure 7. a. part with a real defect caused by galling. b. part with a defect generated voluntarily by impacting the sheet before the stamping

Material	Standard steel Re= 980 MPa, e = 1 mm
Production rate	18 strokes / minute
Press	300T
AE sensor	Freq ≈ 200 kHz
Preamplifier	40 dB

Table 2. parameters of the second feasibility test

Figure 8 present the evolution in real time of the RMS parameter as function of the number of stamped parts. A learning phase of 50 good parts was carried out to determine the criterion of nonconformity. The maximum value of the RMS parameter in this phase is 29 dB. The significant increase of the RMS on the pieces 58 and 61 correspond to the two defective pieces.

MOST was able to detect defective parts (58 and 61) by a significant increase in RMS value.

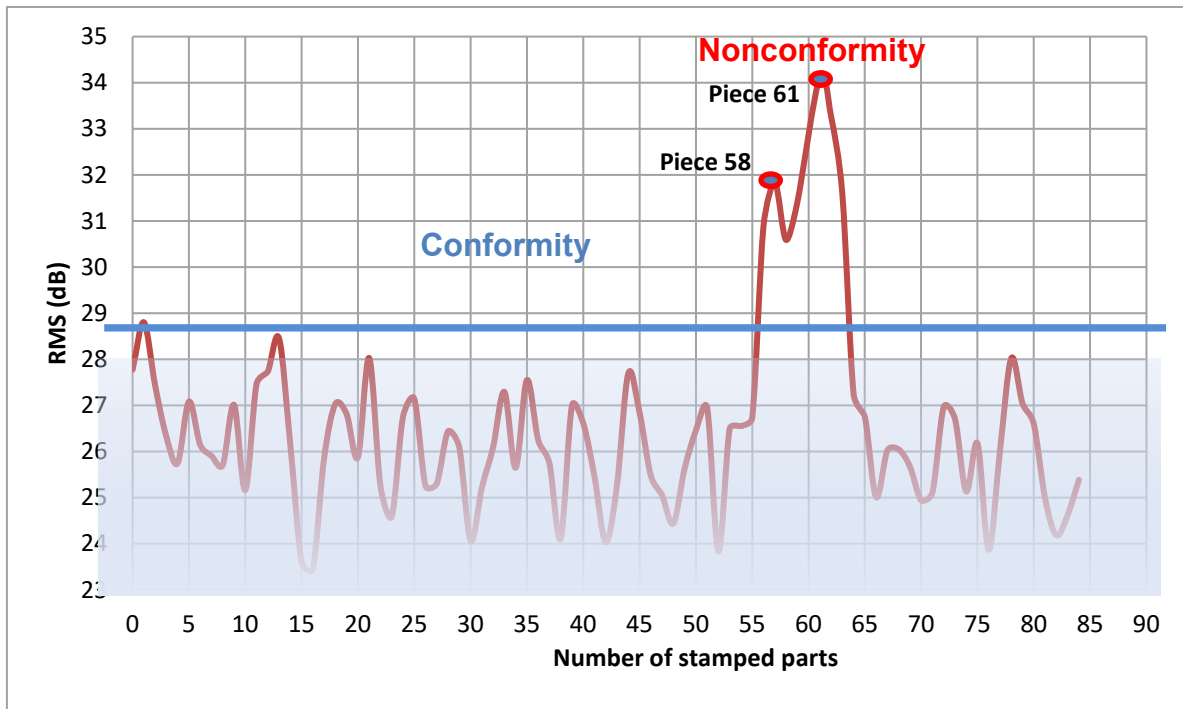


Figure 8. Evolution of RMS as function of the number of stamped parts

2.3 Industrial feasibility 3

The defects observed for this case are shown in figure 9. The factor causing this type of defect is the lack of lubrication in the stamping process. In this case, usually the first defect that appears is the stiction in the stamped parts as shown in the figure 9.a. Then, gradually, the contact between the sheet and the punch / matrix becomes more and more dry which leads to the tearing of the sheet as shown in the figure 9.b.

The aim of the feasibility 3 is to reproduce this defect by stopping lubrication in order to evaluate MOST's ability to detect these defects in real time.

The AE sensor has been installed on the upper part of the tool, close to the stamping section as shown in figure 10.

The parameters of the tests are grouped in table 3.

The different tests carried out in this study are summarized in the table 4. The four first tests aim to determine the threshold of non-conformity and at the same time to verify the reproducibility of the measurements. The lubrication was stopped in the last test in order to generate the defects.

Figure 11 shows the evolution of the RMS parameter (mV) as function of the number of stamped parts for all the series carried out:

- The measurements made on the series (2,3,4,5) corresponding to the production without defects have made it possible to set the reference level of the RMS value (RMS \approx 10 mV);
- It should be noted that measurements made during the learning phase are relatively reproducible;
- The evolution of the RMS for series 6 which corresponds to the phase of generation of defects presents three important steps:
 - **Step 1:** corresponds to the first 15 good pieces. The level of the RMS value is equivalent to the reference threshold. This could be related to the sufficient level of lubricant in the tool mainly in the lubrication rollers;
 - **Step 2:** This is the longest step (835 good pieces approximately). There is a significant increase in the level of RMS (RMS \approx 23 mV). This result could be explained by a lack of lubrication in the stamping process. Thus, the friction is important between the punch-part-matrix and therefore the acoustic noise is higher;
 - **Step 3:** corresponds to the last 28 strikes. It is also the number of pieces cracked. The level of the RMS is even more important (RMS $_{\max}$ \approx 43 mV).

In this study, most allowed not only to detect tears on the stamped parts, but it also allowed to give an indication on the lack of lubricant in the tool according to the first increase of the value of the RMS

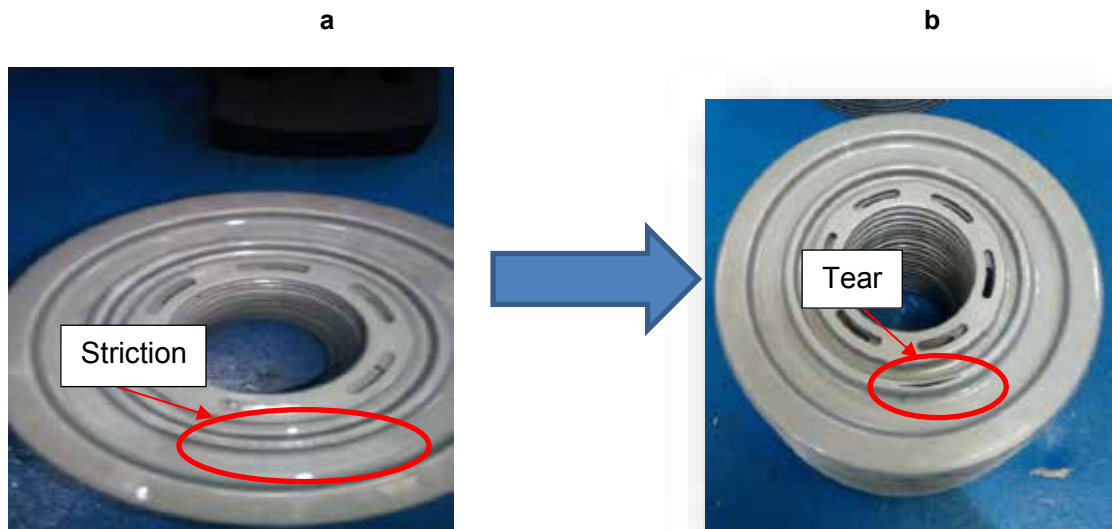


Figure 9. defects caused by a lack of lubrication of the tool. a. striction which appears at fist b. Tear of the the sheet at the second time



Figure 10. Implantation of AE sensor close to the stamped parts

Material	Steel DC04+ZE25, e = 0.6 mm
Production rate	53 strokes / minute
Press	400T
AE sensor	Freq \approx 200- 900 kHz
Preamplifier	40 dB

Table 3. parameters of the second feasibility test

	Conformity of the serie	Nombre of parts	Objectif
Serie 2	No defects	200	Determination of the threshold of nonconformity
Serie 3	No defects	200	Test of reproducibility
Serie 4	No defects	200	Test of reproducibility
Serie 5	No defects	200	Test of reproducibility
Serie 6	No defects	878	Detection of defects

Table 4. summarizing of the tests carried out in this study

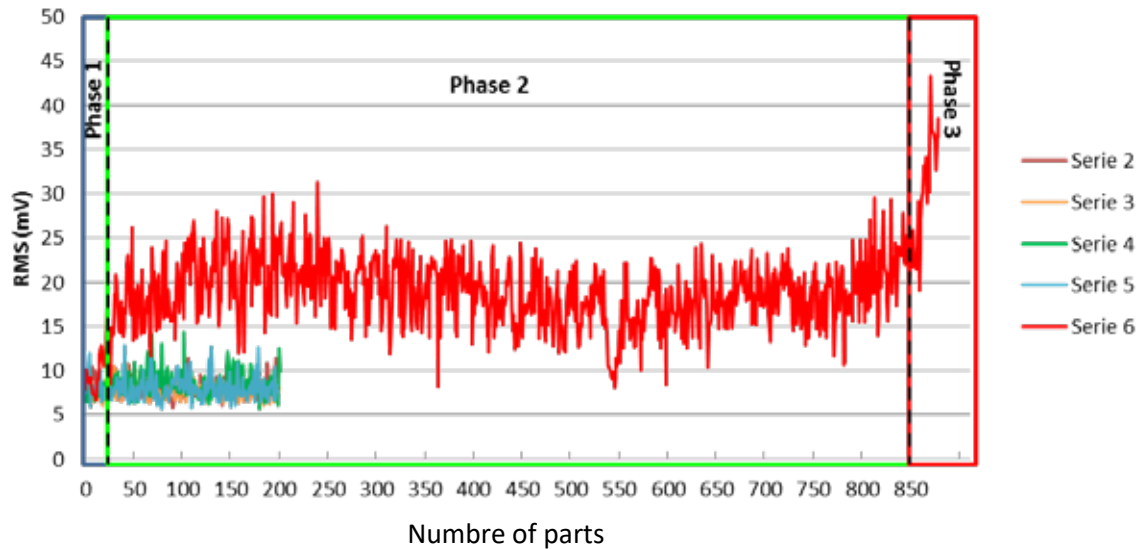


Figure 11. Evolution of the RMS (mV) as function of the number of stamped parts

3. Conclusion

In this paper, the feasibility of detecting defects on stamped parts by the MOST system was studied. Three types of representative defects were analyzed, tool wear, galling and lack of the lubrication.

The results of this study show that the MOST system was able to detect in real time the three types of defects.

The results show also that the KTS parameter is more sensitive to defects related to the tool wear, while the RMS parameter is more sensitive to defects related to galling or a lack of lubrication.

In view of this study, a long-term monitoring test will be conducted to test the robustness of the MOST system under production conditions.

References:

- [1] Sekar, K.V. ed., 2014. *Manuf. Eng. and Tech.* (p. 913). Pearson.
- [2] Govekar, E., Gradišek, J. and Grabec, I., 2000. *Ultrasonic*, 38(1), pp.598-603.
- [3] Grzesik, W. and Bernat, P., 1998. In *International conference AC. 98*, pp. 77-84.
- [4] Li, X., 2002. *Int. J. of Mac. Tools and Manu.* 42(2), pp.157-165.
- [5] Garcia, C., 2005. *J. Mat. Pro. Tech.* 164, pp.1351-1357.
- [6] Burek, J. and Babiarz, R., 1998. In *Int. Conf. on Monitoring and Auto. Supervision in Manuf.-AC. 98*, pp. 41-44.
- [7] Doolan, M., Kalyanasundaram, S., Cardew-Hall, M. and Hodgson, P., 2003. *Jour. of Manuf. Sci. and Eng.*, 125(2), pp.363-368.
- [8] Ubhayaratne, I., Pereira, M.P., Xiang, Y. and Rolfe, B.F., 2017. *Mech. Systems and Signal Proc.* 85, pp.809-826.
- [9] Zhang, G.C., Ge, M., Tong, H., Xu, Y. and Du, R., 2002. *Eng. App. of Artificial Int.*, 15(1), pp.97-104.
- [10] Pereira, M.P. and Rolfe, B.F., 2014. *Jour. of Mat. Proc. Tech.* 214(8), pp.1749-1758.
- [11] Hamedon, Z., Mori, K. and Abe, Y., 2014. *Jour. of Mat. Proc. Tech.*, 214(4), pp.945-950.
- [12] Sah, S. and Gao, R.X., 2011. *The Int. Jour. of Adv. Manuf. Tech.* 55(1-4), pp.121-132.
- [13] Fan-Bean Wu, Jenq-Gong Duh. (2002). *Surf. and Coat. Tech.* Vol 162. pp 106–112.
- [14] Skåre, T. and Krantz, F., 2003. *Wear*, 255(7), pp.1471-1479.
- [15] Sindi, C.T., Najafabadi, M.A. and Salehi, M., 2013. *Tribo. Lett.* 52(1), pp.67-79.
- [16] Hase, A., Mishina, H. and Wada, M., 2012. *Wear*, 292, pp.144-150.

14 - Acoustic Emission monitoring of adhesively bonded wood joints under quasistatic and cyclic fatigue mode II flexure loads using end-notch-flexure specimens

A.J. Brunner¹, G. Clerc², P. Niemz²

¹ Empa, Swiss Federal Laboratories for Materials Science and Technology, Laboratory for Mechanical Systems Engineering, Überlandstrasse 129, CH-8600 Dübendorf, Switzerland

² BFH, Bern University of Applied Sciences, Department of Architecture, Wood and Civil Engineering, Solothurnstrasse 102, CH-2500 Biel/Bienne, Switzerland

Abstract:

Adhesive bonding is becoming more and more important for manufacturing structures or structural elements made from wood. For designing such structures, the performance of adhesives has to be evaluated under quasi-static and cyclic fatigue loading as well as under corresponding fracture loads. The performance of wood glued beams under quasi-static loading is fairly well understood, but their cyclic fracture behavior remains still largely unknown. There are indications from standard tensile shear tests with several types of adhesive that the performance ranking of adhesives under cyclic fatigue loading may differ compared with that observed in the same test under quasi-static loads. Hence, it is of interest whether this is also the case for quasi-static and cyclic fatigue mode II shear fracture. For the mode II shear fracture tests, adhesively bonded joints with wood adherends are prepared with two different adhesives, one a rather brittle (phenol resorcinol formaldehyde) system and one a rather ductile (one component polyurethane) system. These are then compared for their performance under quasi-static and cyclic fatigue mode II in-plane shear fracture loads. Those adhesives are presenting different failure mechanism, for the ductile adhesive the failure will propagate in the interface between wood and adhesive and for the brittle one the crack will mainly run in the wood. For the fracture tests a set-up with four-point end notched flexure specimens is being used, analogous to testing of adhesively bonded polymer composites joints and polymer composite laminates. Selected fracture tests were monitored by acoustic emission for assessing damage evolution due to the mode II in-plane shear fracture loads. The acoustic emission monitoring initially also contributed to identifying shortcomings of a first test set-up that was subsequently modified. The discussion will focus on the comparison between two different types of adhesive and between quasi-static and cyclic fatigue fracture loads.

1. Introduction

Adhesively bonded joints play an increasingly important role in construction with composite materials [1], and, hence, specifically also in civil engineering structures made of wood [2]. Characterizing and comparing the performance of different types of adhesives under various load cases is essential for designing safe and durable wooden structures. A recent comparison between four types of adhesives used in glued lap joints (as defined in [3]) had indicated that cyclic tensile shear fatigue loads yielded differences among the four adhesives that had not become apparent in quasi-static tensile shear tests [4]. Therefore, fracture

mechanics tests under quasi-static and cyclic fatigue loads are performed for a range of different adhesives. The so-called Four-point End-Notched Flexure (4-ENF) test set-up was chosen for comparing quasi-static and cyclic fatigue fracture of adhesively bonded wood joints under in-plane shear (mode II) loading [5]. In this contribution, selected test results will be discussed with an emphasis on acoustic emission (AE) monitoring of the fracture tests.

2. Description of work

The first 4-ENF test set-up (Figure 1 left) was modified in several steps to remove problems observed in preliminary quasi-static and cyclic fatigue tests. While this first set-up worked for quasi-static mode II loading, it was not suitable for cyclic fatigue, since one of the top loading rollers tended to lift-off the wood specimen during the test, also noted acoustically by ear and by periodic AE signal generation. This noise source was removed by introducing a rotating joint to the top loading bar. Later, this was further improved by implementing a universal joint between top loading bar and load cell (Figure 1 right) instead of the uniaxial rotating joint in order to reduce possible moments on the load cell.



Figure 1: Photographs of two versions of the 4-ENF type test-rig, (left) upper loading bar rigidly mounted to the load cell, (right) upper loading bar with rotating joint, the AE sensors are mounted with metal springs.

Beech wood (*Fagus sylvatica* L.) with a density of 714 kg/m^3 at a wood moisture content of 12% was used for the tests. The lumber has no defects such as knots and grain deviation. The length, the width and the height of the specimens correspond, respectively, to the longitudinal, tangential and radial wood orientation (maximal radial orientation of 30°). The planks were first planed to a thickness of 10 mm, a width of 150 mm and a length of 700 mm. The planks were stored for at least two weeks in a climate of 20°C and 65% relative humidity before planing to a thickness of 5 mm and then cut in half. Before the adhesive bonding, a $15 \mu\text{m}$ thick fluoropolymer (ETFE230N) foil was applied between the lamellae on the first 120 mm to simulate a starter crack. Two adhesives are compared in the tests, the first a relatively brittle phenol resorcinol formaldehyde (PRF, trade name «Aerodux 185»), the second a more ductile one-component polyurethane (PUR, trade name «HB110»). The gluing of the two lamellae was done approximately 3-4 hours after the planing according to the gluing parameters described in Table 1 below. Once cured, the front-position of the foil was referenced as position of the crack tip and the crack length was set to 110 mm. The samples

were then cut to a width of 20 mm and a length of 317mm. The adhesively bonded wood joints were stored for several days in the test climate of 23°C and 50% relative humidity before testing.

Adhesive	Hardener	Glue Spread [g/m ²]	Mixture ratio [Adhesive/Hardener]	Pressing time [h]	Pressure [MPa]	Closed assembly time [min]
HB110	-	180	-	10	0.8	10
Aerodux 185	HRP 155	340	100/20	10	0.8	30

Table 1: Processing parameters used in manufacturing the adhesively bonded beech wood joints.

In order to get additional information on the initiation and propagation of the mode II delamination in the adhesively bonded joints, AE monitoring was performed using AE equipment (type AMSY-6 from Vallen Systeme GmbH) with resonant AE sensors (type SE 150-M from Dunegan Engineering Corp.) as well as one broad-band AE sensor (type S9208 from Physical Acoustics Corp.). The AE sensors were connected to the data acquisition via preamplifiers (type AEP-3 from Vallen Systeme GmbH) with a hardware high-pass frequency filter of 30 kHz, a low-pass of 1'000 kHz and a gain of 34 dB. Figure 2 shows a schematic of the 4-ENF test specimen with the geometry and dimensions used in the test series, including the positions of the seven AE sensors for monitoring the damage development during the fracture tests. Please note that the distance between the top loading rollers (100 mm) of the 4-ENF test rig did not correspond to either one third or one half of the distance between the bottom support rollers, i.e., were different from the spans usually recommended for the tests [5]. This was due to the fact that the top loading bar had to leave space for the AE sensors mounted on the adhesive joint. A silicone-free vacuum grease was used as coupling agent and the AE sensors were mounted by metal clamps (shown in Figure 1 right). AE data acquisition settings were: threshold 40 dB_{AE}, duration discrimination time 400 μs, and rearm time 1 ms (except for preliminary tests with rearm time of 3.23 ms). For the acquisition of full waveforms (with the broad-band AE sensor only) sampling at 5 MHz and 4'096 samples (corresponding to roughly 820 microseconds) with a pretrigger of 200 samples (40 microseconds) was chosen.

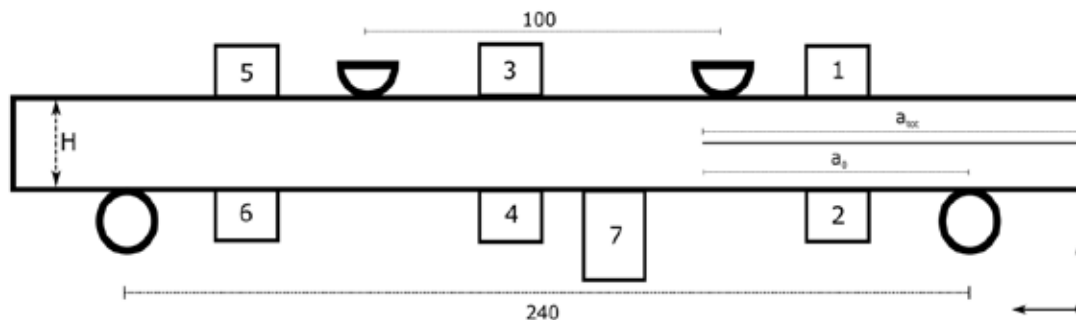


Figure 2: Schematic of the 4-ENF type specimen for mode II (in-plane shear) quasi-static and cyclic fatigue fracture testing of adhesively bonded wood joints. The positions of the AE sensors and the specimens dimensions are also shown ($H = 10 \text{ mm}$, $a_{tot} = 110 \text{ mm}$, a_0 approximately 70 mm).

The load tests were performed on a servo-hydraulic test machine (type 1237 from Instron) equipped with a 1 kN load cell (mounted below the 25 kN load cell). The quasi-static tests

were performed under displacement control at 1 mm/min and the cyclic fatigue tests also under displacement control at 5 Hz; starting from a displacement level selected from the load-displacement curve by setting a displacement ratio of 0.1 between upper and lower limit). Load and displacement signals from the test machine were also recorded synchronously with the AE data (sampling-rate around 40 Hz). There were preliminary, quasi-static compressive tests at 0.1 mm/min with limited displacements for determining the compliance of the test set-up in which the wood joint was replaced by a steel bar, and calibration tests with different length of the starter crack between the bottom support rollers for determining the delamination length from specimen compliance. A travelling optical microscope was used to visually observe the delamination during the fracture tests.

3. Results

Focusing on the information from the AE monitoring of the tests, the evaluation of the fracture toughness for the comparison between the adhesives (the main goal of the tests) will not be discussed here. Figure 3 shows examples of the linear AE signal source location plots from quasi-static flexure testing, one for each adhesive type. The auto-calibration signals of the AE equipment were used to determine the signal speed for the linear AE signal source location by adjusting the signal speed until the location of the recorded signals matched the known sensor positions. The values of the signal speed obtained varied between about 400 and 500 cm/ms with an average around 425 cm/ms.

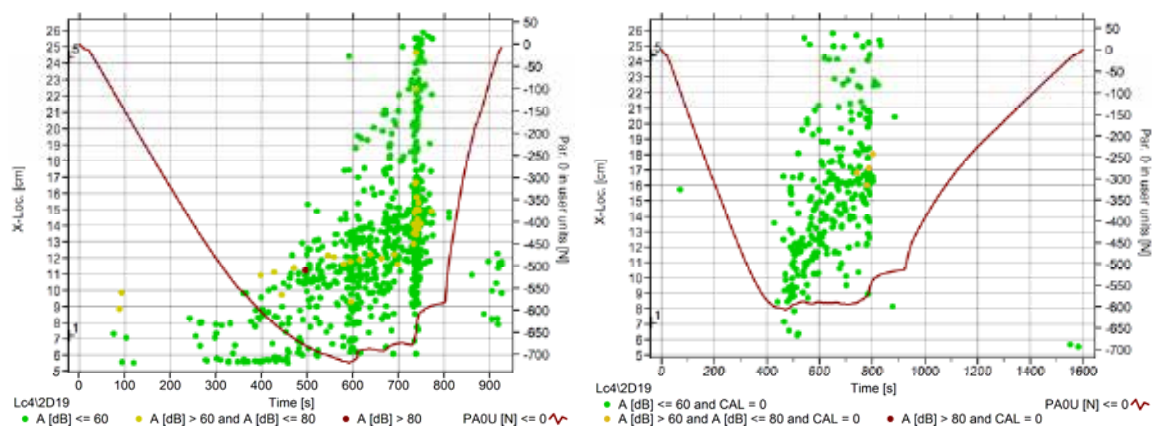


Figure 3: AE linear signal source location (color-coded for AE signal amplitude) of quasi-static tests (under displacement control at 1 mm/min) using the AE sensors on the compression side (top) and the load curve for the 4-ENF specimens with (left) PRF and (right) HB110 adhesive.

It can be noted that the non-linear point in the load curves indicating the initiation of the delamination corresponds fairly well to the onset of significant AE. As a trend, the more brittle adhesive (PRF) yields more AE signal source locations than the more ductile one (HB110). For the PRF-type joint (Figure 3 left), the AE signal amplitudes above 60 dB_{AE} roughly indicate the position of the delamination tip as a function of time. These positions are also consistent with the visual observation of the delamination propagation on the edge of the specimens. For the more ductile adhesive (HB110), the AE signal source locations do not highlight the tip of the delamination as clearly as for the more brittle adhesive. The AE signal amplitudes recorded during delamination propagation in this case (Figure 3 right) are essentially all below 60 dB_{AE}. For the PRF-type joint, the cluster of AE signal source locations extending over most of the distance between the two sensors at about 740-750 s is likely due

to tensile damage in the (bottom) wood beam occurring before the loading was stopped (Figure 4). This tensile damage in the wood also yielded audible cracking noise. The respective AE signal source cluster is even more pronounced when plotting the signal source location data from the tensile, i.e., the bottom side of the joint. The located signals yield even higher AE signal amplitudes than the locations from the compressive (top) side. The scattered AE signal source locations beyond the tip of the delamination after about 500 s (Figure 3 left) are likely due to precursors of the macroscopic tensile damage. Similar AE signal source locations beyond the tip of the delamination for the HB110 adhesive joint possibly indicate that some damage is also initiating there. However, tensile damage was not noted and was not visible when inspecting the specimen after the test. It has to be noted, however, that contributions from friction signals (e.g., from the contact between test-rig and joint or from slight relative movement between sensor and coupling surface due to specimen bending) to both location plots cannot be excluded.



Figure 4: Photographs of the PRF-type joint showing signs of tensile failure (highlighted by black zig-zag-type marks) on the bottom side after quasi-static testing, on the edge, the delamination is visible as well.

Since the 4-ENF setup inevitably involves some friction between the support and loading rollers and the wood joint, the AE signals are further analyzed using selected AE signal parameters. Figure 5 shows plots of AE signal duration (logarithmic scale) versus AE signal amplitude (linear scale), again for both types of adhesive. This plot has been shown to allow for rough identification of AE signal source mechanisms in fiber-reinforced polymer composites [6], such as, e.g., mechanical rubbing (low amplitude, broad range of durations), delamination (intermediate amplitudes, high durations), fiber breakage (high amplitude range and high durations), electromagnetic interference (intermediate amplitude, short durations). This approach has also been used by Schubert et al. [7] for identifying AE signal source mechanisms in a full-scale wind rotor blade test. Even though the AE signal parameter areas for different mechanisms may overlap to some extent, it is likely that “low” amplitude signals (e.g., about 40-45 dB_{AE}) for all durations observed (up to about 1'000 μs in Figure 5) indicate friction or rubbing. The other parameter ranges are then attributed to crack or delamination propagation and fiber breaks (in the case of laminates). That possibly also holds for wood as

a natural fiber-reinforced composite material, if the delamination damage develops in the adherend rather than in the adhesive or at the interface between wood and adhesive.

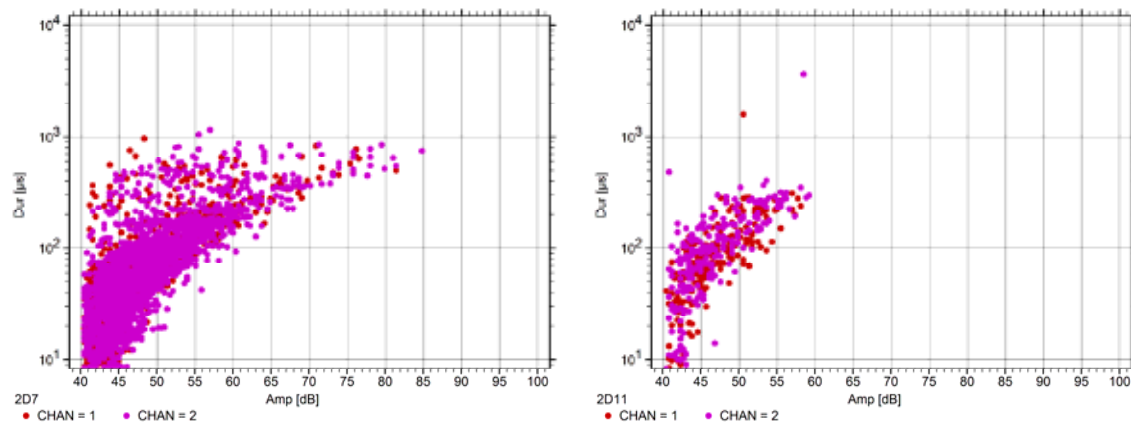


Figure 5: AE signal parameter plots (duration versus amplitude) of quasi-static tests using the AE sensors located near the starter crack tip of the 4-ENF specimens with (left) PRF and (right) HB110 adhesive (following [6]).

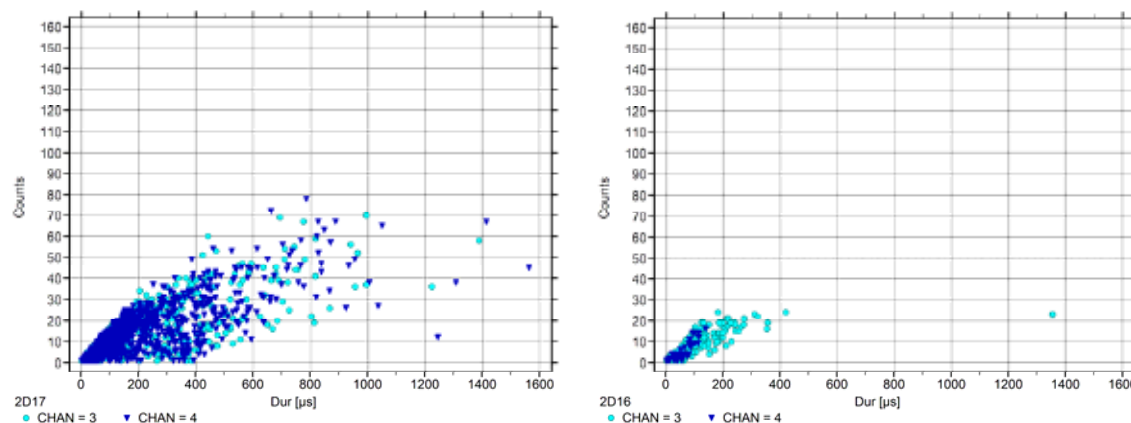


Figure 6: AE signal parameter plots (counts versus duration) of quasi-static tests using the 150 kHz resonant AE sensors located in the delamination propagation zone of the 4-ENF specimens (between the top loading rollers) for (left) PRF and (right) HB110 adhesive.

As already seen in the AE signal source location plots (Figure 4), the HB110 adhesive joint yields less source locations and less AE signals (Figure 5) than the PRF adhesive joint. This can be attributed to the difference in adhesive properties, the more ductile adhesive (HB110) yields less signals and/or lower amplitude signals when failing, resulting in fewer data being recorded. Figure 6 shows another set of AE signal parameters (counts versus duration) that also yields information on the type of source mechanism. Typically, signals with low number of counts at relatively long duration correspond to signals with significant low frequency partial power in their Fourier Transform power spectra. The example for the PRF adhesive (Figure 6 left) has much more AE signals with durations between about 200 and 600 microseconds and less than 20 counts than that for the HB110 adhesive (Figure 6 right). Please note that the plots in Figure 6 show channels 3 and 4, i.e., sensors located in the delamination propagation zone. The same parameter plots for the other sensor pairs (channels 1 and 2 located in the starter crack range; and channels 5 and 6 located in the uncracked part of the adhesive joint) show less signals in this parameter range (low number

of counts and long duration). Comparing the two types of adhesive, these plots are consistent with the signal parameter analysis shown in Figure 5, i.e., a larger amount of friction signals for the PRF-type joint.

The dynamic load-signal (cycling at 5 Hz under displacement control) as a function of test duration shown in Figure 7 on the right indicates a decreasing trend of the maximum compressive load with time. This is due to the increasing compliance of the specimen, i.e., a reduction in flexural rigidity with increasing delamination length.

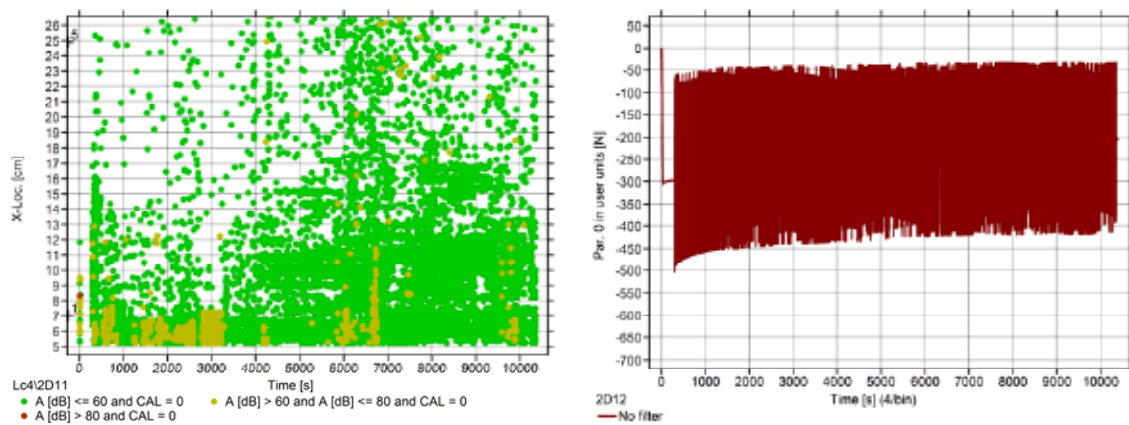


Figure 7: (left) AE linear signal source location (color-coded for AE signal amplitude) of dynamic 4-ENF tests at 5 Hz using the AE sensors on the compression side and (right) load curve for the 4-ENF specimen with the PRF adhesive.

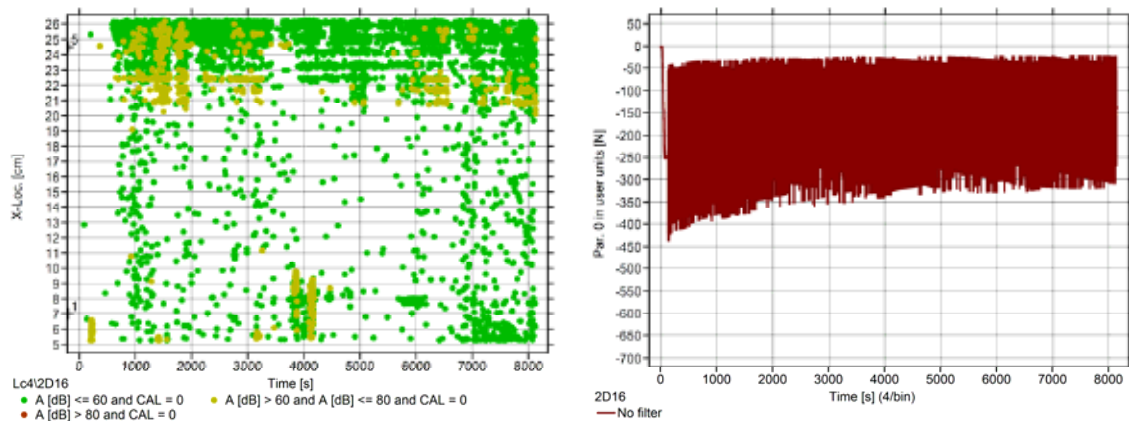


Figure 8: (left) AE linear signal source location (color-coded for AE signal amplitude) of dynamic 4-ENF tests at 5 Hz using the AE sensors on the compression side and (right) load curve for the 4-ENF specimen with the HB110 adhesive.

The duration versus amplitude plots for the two types of adhesive joints tested under mode II cyclic fatigue fracture load at 5 Hz (Figure 9) differ less in the amount of signals than for the respective quasi-static tests (Figure 5). Interpreting the signals with amplitudes below 45 dB_{AE} again as being mainly due to friction, the HB110 adhesive joint yields more friction signals and with durations extending up to 2-3 ms rather than 1 ms for the PRF type joint, and this in spite of the lower total number of cycles applied (PRF 50'000 cycles, HB110 40'000 cycles).

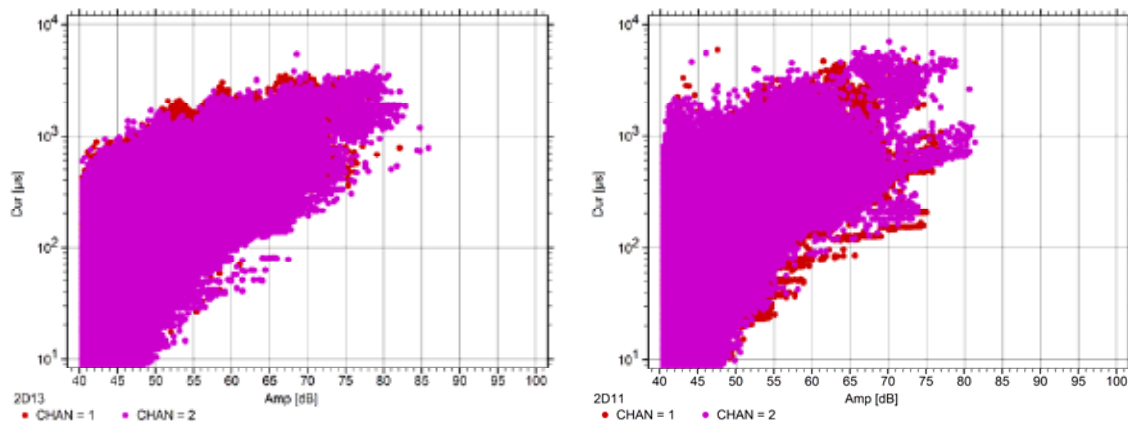


Figure 9: AE signal parameter plots (duration versus amplitude) of quasi-static tests using the AE sensors located near the starter crack tip of the 4-ENF specimens with (left) PRF and (right) HB110 adhesive (following [6]).

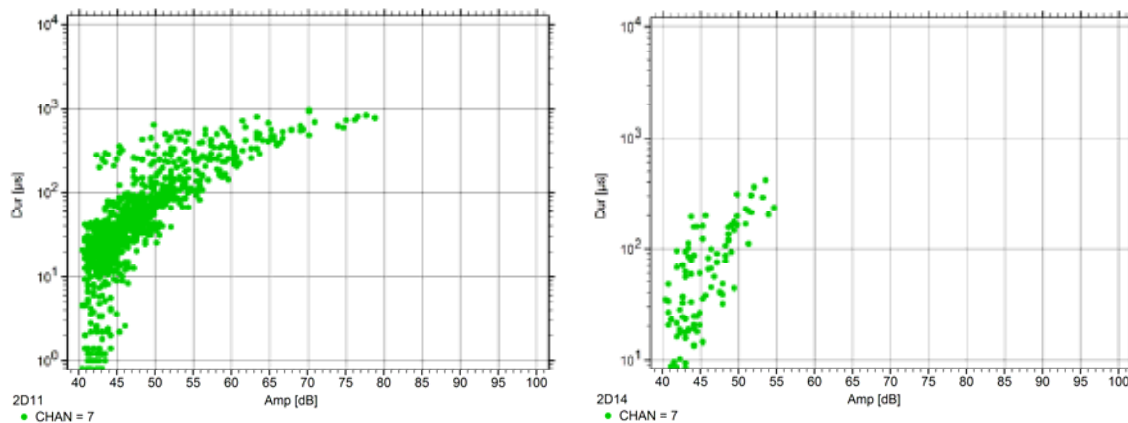


Figure 10: AE signal parameter plots (duration versus amplitude) of quasi-static tests using the broadband AE sensor in the propagation zone of the delamination for (left) PRF and (right) HB110 adhesive (following [6]).

4. Discussion

The AE monitoring of the quasi-static and cyclic mode II (in-plane shear load) fatigue fracture tests yields additional information for interpreting the damage induced in adhesively bonded wood joints under quasi-static and cyclic fatigue in-plane shear (mode II) fracture loads. Linear AE signal source location yields indications of delamination propagation with time for comparison with the visual observation on the edge of the joints. From this, the average delamination propagation speed can be calculated. AE signal source location also yields indications of damage initiation in the wood adherends of the adhesive joints beyond or outside the propagating delamination that cannot be detected by visual observations.

The rather dense set of AE signal locations toward the undamaged end of the HB110-type specimen in Figure 8 is tentatively attributed to friction from slight movement of the specimen on the support during cyclic loading. For confirming this, AE signal source mechanisms should be identified.

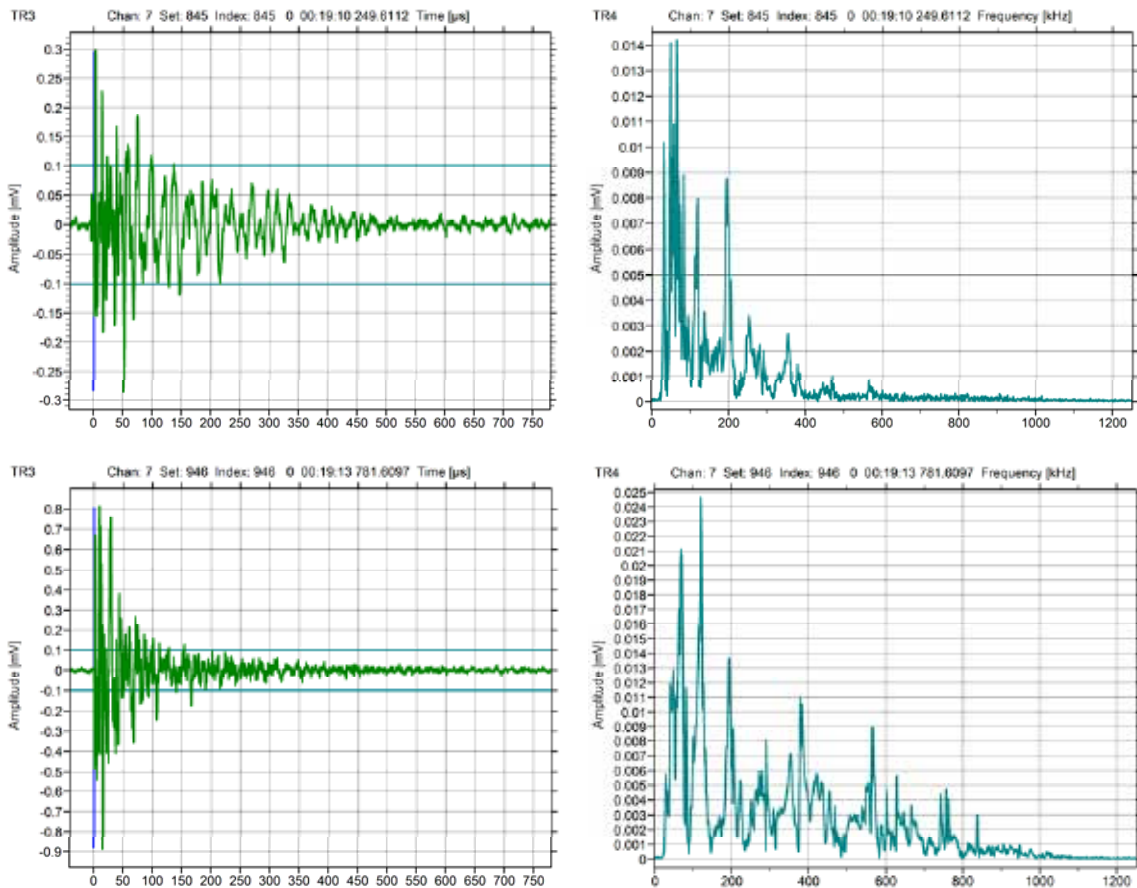


Figure 11: Selected AE waveforms and Fast Fourier Transform power spectra for one PRF adhesive joint from the broad-band AE sensor mounted in the propagation zone of the delamination.

Therefore, for further analysis of the possible different source mechanisms, recorded AE waveforms are briefly discussed as well. Figure 10 shows the duration versus amplitude plots for the broad-band AE sensor (channel 7) for the two types of adhesive. As for the signals recorded with resonant type AE sensor, the more ductile adhesive (HB110) yields significantly less signals than the more brittle one (PRF). Figure 11 shows selected AE waveforms and Fourier Transform power spectra of signals recorded with the broad-band AE sensor on the PRF adhesive joint. As expected, the AE signals with low amplitude or low counts, and intermediate duration, respectively show larger low frequency partial power contributions than AE signals with higher amplitude and counts for comparable signal duration.

In the cyclic fatigue fracture loading tests, likely, noise sources such as, e.g., friction between test-rig and specimen, seem to dominate the recorded AE. It is planned to investigate this in more detail by applying pattern recognition approaches, e.g., as described in [8,9].

5. Conclusion

Examples of AE monitoring and analysis of mode II fracture tests on adhesively bonded wood joints indicate that the adhesive type has a significant effect on the amount as well as on the parameters of the recorded AE signals. AE further provides a perspective for

comparison between quasi-static and cyclic fatigue fracture behavior of adhesively bonded wood joints made with different adhesive types. Differences observed in the power spectra from AE waveforms recorded with a broad-band AE sensor during quasi-static tests suggest that pattern recognition approaches (e.g., similar to those described in [8,9]) should be allowed to discriminate between different AE signal source mechanisms, possibly also for the cyclic fatigue fracture tests. This will be further investigated.

Acknowledgment

Contributions of Ms. Magdalena Pérez-Galmés to the design and modification of the 4-ENF test rig as well as to data analysis; and test machine setup and control by Mr. Daniel Völki are gratefully acknowledged.

References:

- [1] Vassilopoulos, A.P., Fatigue and fracture of adhesively bonded composite joints: behavior, experiments, simulation and modeling, Woodhead Publishing, Series in Composites Science and Engineering, Number 52, 2015, ISBN 978-0-857098-06-1.
- [2] Vallée, T., Tannert, Th., Fecht, S., Adhesively bonded connections in the context of timber engineering – A Review, *The Journal of Adhesion*, Vol. 93(4), 2017, pp. 257-287.
- [3] DIN-EN-302-1 Adhesives for load-bearing timber structures – Test methods – Part 1: Determination of longitudinal tensile shear strength (German version), 2013, pp. 1-13.
- [4] Bachtiar, E.V., Clerc, G., Brunner, A.J., Kaliske, M., Niemz, P., Static and dynamic tensile shear test of glued lap wooden joint with four different types of adhesives, *Holzforschung*, Vol. 71(5), 2017, pp. 391-396.
- [5] Yoshihara H., Mode II R-curve of wood measured by 4-ENF test, *Engineering Fracture Mechanics*, Vol. 71, 2004, pp. 2065–2077.
- [6] Gostautas, R.S., Identification of Failure Prediction Criteria using Acoustic Emission Monitoring and Analysis of GFRP Bridge Deck Panels, Kansas Department of Transportation, Report No. K-TRAN: KU-02-1, 2007, pp. 1-71.
- [7] Schubert, L., Schulze, E., Frankenstein, B., Source mechanisms of acoustic emissions as an indicator of injury during a full scale fatigue test of a wind turbine rotor blade, *Proceedings of the 8th International Conference on Structural Dynamics, EURO DYN 2011*, G. De Roeck, G. Degrande, G. Lombaert, G. Müller (eds.) ISBN 978-90-760-1931-4, 2011, pp. 3462-3468.
- [8] Sause, M.G.R., Gribov, A., Unwin, A.R., Horn, S., Pattern recognition approach to identify natural clusters of acoustic emission signals, *Pattern Recognition Letters*, Vol. 33(1), 2012, pp. 17-23.
- [9] Sause, M.G.R., Horn, S., Quantification of the Uncertainty of Pattern Recognition Approaches Applied to Acoustic Emission Signals, *Journal of Nondestructive Evaluation*, Vol. 32, 2013, pp. 242–255.

17 - Acoustic Emission analysis during bending tests of timber beams reinforced with carbon fiber composite

Francisco J. Rescalvo¹, Chihab Abarkane¹, Elisabet Suarez¹, Antolino Gallego¹

¹ University of Granada, Dept. of Applied Physics, Building Engineering School,
Granada, Spain, antolino@ugr.es

Abstract:

This paper proposes the monitoring of old timber beams with natural defects (knots, grain deviations, fissures and waness), reinforced with carbon composite materials (CFRP). Reinforcement consisted of the combination of a CFRP laminate strip and a CFRP fabric discontinuously wrapping the timber element. Monitoring considered the use and comparison of two types of sensors: strain gauges and multi-resonant acoustic emission (AE) sensors. AE data analysis propose two main steps: 1) A filtering of signals based on the root mean squared of the waveforms; 2) The use of partial spectral ratio corrected by the attenuation characteristics of the material, to identify damage mechanisms. Results demonstrate that: 1) the mechanical behaviour of the beams can be considerably improved by means of the use of CFRP (160% in bending load capacity and 90% in stiffness; 2) Acoustic emission sensors provide valuable information for damage assessment and its location during operation in real wood structures.

1. Introduction

The use of FRP for retrofitting and repair of wooden structures as an alternative material to steel has been booming for several years. Its high strength and deformability and the low weight added to the structure are its main attractions. In particular, the use of carbon fiber pultruded laminates and fabrics (CFRP), already at reasonable and competitive prices in the market, provide excellent results in terms of strength, stiffness and ductility.

Numerous experimental, analytical and numerical works have demonstrated the high capacity for retrofitting and repair conferred by different layouts of CFRP [1-14]. However, at present, the use of codes and standards for the calculation and design of FRP reinforcement systems on timber beams, unlike in the case of concrete, are still scarce or nonexistent. This gap generates in the professionals of architecture and civil engineering and in the owners of wooden structures, both private and administrations that own many historic buildings, certain reluctance to use them.

To generate confidence about its operation in situ, as well as to do a continuous follow-up that establishes the pertinent structural alerts, the in-situ and real-time monitoring of structures [15] is an efficient strategy (Structural Health Monitoring), which can be of great utility to the case of FRP-retrofitted or repaired timber structures. In particular, acoustic emission (AE) method is an efficient technology for structural monitoring especially suitable for this purpose [16-18]. There are just one, as far as the authors of this work know, previous publications about the AE monitoring of timber structures reinforced with CFRP [19]. The method has been, however, widely used for wood and CFRP, individually [20-25]. There are also some works on the AE monitoring of concrete elements retrofitted with CFRP [26-30].

In the case of wood, however, two problems arise when applying this technique: a) Its high heterogeneity, which confers a very high distortion to the waves. Multiple reflections and other propagation phenomena of the wave, alter in a very considerable way the shape of the wave, making its ulterior analysis very complicated and unreliable; b) The

high attenuation of the material, which entails a closer location of the sensors, and the almost losing of information at higher frequencies.

To overcome both inconveniences, this work proposes a double strategy for the AE data analysis. Firstly, all the AE data analysis is done only on a very narrow window of the signal, just after the threshold crossing, including only one cycle of the waveform. This action largely avoids the effect of reflections and other propagation phenomena. Secondly, the proposed method includes a correction of the signal in the frequency domain, which attempts to compensate the attenuation losses.

Using this double strategy, the work proposes the use of signals whose spectral energy is predominant within a band of high frequencies, correlating these signals as coming from the resin-wood failure (precursor of CFRP-wood delamination). The appearance, detection and location of these AE signals serve as a real-time alert of final element failure. The proposed methodology has been validated on two different retrofitting layouts, providing successful AE results in both cases.

2. Description of work

All the timber beams used in this work were extracted from the last rehabilitation carried out on the roof of the Faculty of Law of the University of Granada. They are *pinus sylvestris* beams from the forests of the south of Spain, which had been in service for more than 200 years. They were cut and sanded with a final cross-section of $(147 \pm 11) \times (222 \pm 6) \text{ mm}^2$ and a length of $4500 \pm 2.4 \text{ mm}$.

In particular, six beams were reinforced with CFRP by using two different layouts named as LR (longitudinal) and BR (braided), respectively. They are represented in Fig. 1. Furthermore, two beams without reinforcement (NR) were used as control specimens. As is shown in Fig. 1, the width of the CFRP lamella for both layouts was set at $w_{frp} = 100 \text{ mm}$. In the case of the BR layout, the CFRP fabric height was set at $h_{frp} = 150 \text{ mm}$ and the length of each piece of fabric was set at $l_{frp} = 100 \text{ mm}$.

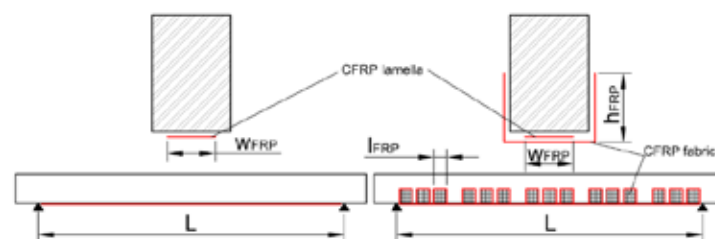


Fig. 1. LR (left) and BR (right) reinforcement layouts

AE data analysis

The acoustic attenuation of the six beams was measured before the mechanical tests. To do that, one AE sensor was placed at the center of six intervals of length $[-60, 60] \text{ cm}$. *Pencil lead break* tests (PLBs, using 0.5 mm 2H leads) were carried out at each particular point every 20 cm on the central line of the lateral face of the beam, according with the standard ASTM E976. Three PLBs were done at each point, and the peak amplitude in dB of each recorded AE signal was obtained. Fig. 2 describes the attenuation tests.

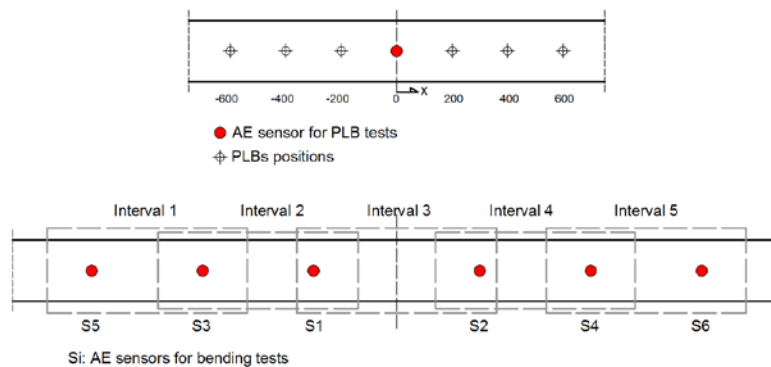


Fig 2. Attenuation tests procedure

A Vallen Systeme AMSY-5 equipment was used to acquire the AE signals. Multi-resonant VS45-H sensors with a sensitivity within the frequency range 25-500 kHz (Fig. 3), were used. As it can be seen, two of the main resonances are located around 100 kHz (low frequency) and 300 kHz (high frequency), respectively. The sampling frequency for the waveforms recording was established at 5 MHz, and the number of samples was set at 4096 with a pre-trigger of 300 samples.

Big attenuation values and very relevant differences between all the specimens is obtained. It is basically due to the big differences in density and number and position of defects of each specimen. Similarly, a no symmetric attenuation pattern is obtained respect to the central position of the sensor, demonstrating the enormous heterogeneity of the used wood.

For ulterior data analysis of the AE signals during the mechanical tests (Section 3), it was required to evaluate and quantify the attenuation in the two particular frequency bands, B_1 and B_2 . To do that, the RMS for each band was calculated. Only the first cycle of the signal just after the first threshold crossing, W_0 : [0 - 20] μ s, was used for the calculation of the spectral energy. This very narrow temporal window was selected in order to avoid as much as possible the influence of the different reflections and other propagation effects of the wave on the calculation of the spectral energy. This strategy was already follow for some of the authors in a previous work [31]. More precisely, the used bands were

- a) **Band (B_1):** [60 - 120] kHz. Low frequencies. $RMS_0(B_1)$.
- b) **Band (B_2):** [270 - 330] kHz. High frequencies. $RMS_0(B_2)$.

AE data analysis was carried in four steps, described as follows.

Step 1. Filtering of miss-recorded signals. Due to the avalanche of generated AE signals, some of them were miss-recorded. Basically, they were signals recorded with a large period of low amplitude before the arrival time. In order to filter automatically the miss-recorded signals, two temporal windows were considered in each signal. Then, the root mean squared (RMS) of each signal in both temporal windows W_1 ($RMS(W_1)$) and W_2 ($RMS(W_2)$) was calculated. Using the difference between $RMS(W_1)$ and $RMS(W_2)$, only the signals fulfilling the RMS_{12} criterion were considered as properly acquired and passing the filter for ulterior data analysis in step 2.

Step 2. Source linear location. By means of the classical AE source location theory [16-18], linear location of the passing signals was carried by using the 6 used sensors. Thus, for each particular AE event the coordinate x between two sensors was obtained.

Step 3. Attenuation correction. For the first-hit of the located events in Step 2, the spectral energy at each frequency band, $RMS_0(B_1)$ and $RMS_0(B_2)$ in decibels was calculated. Using the location of each event, x , and the attenuation fitting curves, for each frequency band, $f_-(x)_{B_1}$ and $f_+(x)_{B_1}$ for B_1 and $f_-(x)_{B_2}$ and $f_+(x)_{B_2}$ for B_2 , a corrected spectral energy was calculated. The corrected RMS was named as $RMSC_0(B_1)$ and $RMSC_0(B_2)$, respectively.

Step 4. Classification of events. During the last step, a classification of passing signals in two groups was carried out, according to the relative importance of its corrected spectral energy. More precisely, passing signals were classified in Group 1 as predominant low-frequency signals and in Group 2 as predominant high-frequency signals, respectively (Eqs. 1-2), i.e.

$$\text{Group 1} \rightarrow \text{If } RMSC_0(B_1) > RMSC_0(B_2) \quad (1)$$

$$\text{Group 2} \rightarrow \text{If } RMSC_0(B_2) > RMSC_0(B_1) \quad (2)$$

Mechanical testing with acoustic emission monitoring

All the beams were subjected to monotonic 3-point bending test until failure. Displacement rate was 1.5 mm/min. Tests were carried out on a hydraulic machine from the company SERVOSIS S.L., model CH4·ST·100, with a span between supports set at 4000 mm.

In addition, all specimens were continuously monitored by the acoustic emission method, by using six multi-resonant VS45-H sensors. For these tests, the pre-trigger was established at 500 samples. The acquisition threshold was set at 32.1 dB and a 34 dB gain preamplifier was used. The AE sensor was coupled with silicone grease and fixed with a magnetic holder to the specimen.

3. Results and discussion

Fig. 3 shows the stress as a function of time during the bending test on the eight monitored specimens. In the case of non-retrofitted beams (NR) the final failure was totally brittle. For the case of the beams with LR retrofitting layout, the stress curve shows a slight plastic range, although the final failure was also brittle. On the other hand, the three beams retrofitted with the BR layout had a much more ductile behavior, with a gradual and stepped decreasing of the loading capacity. For LR beams, although the knots still remain as sensitive areas, the final failure occurs due to delamination between the CFRP laminate and wood. In the case of the BR layout, the purpose of the fabric is to prevent the resin-wood failure and the subsequent delamination. Therefore, when a particular stress level is reached, the fabric begins to work, thus avoiding the delamination. The failure that causes the first loading decay occurs when this adhesion fails, i.e. when wood-resin breakage occurs.

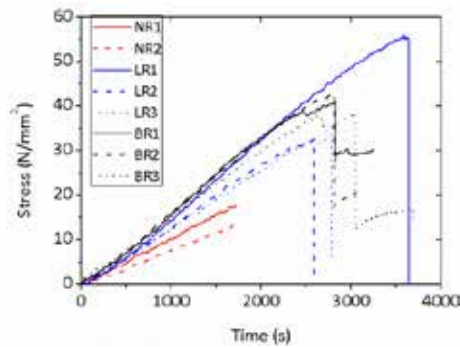


Fig. 3. Stress versus time for all the tested beams. Red: Non-reinforced beams (NR). Blue: Longitudinal reinforced beams (LR). Black: Braided reinforced beams (BR).

Fig. 4 represents the cumulative AE events grouped as explained in Section 2, for three particular beams of each group (NR, LR and BR). In all cases, it is observed that Group 1 events (in which low frequencies predominate) are much more numerous than Group 2 events (in which high frequencies predominate). It is also observed that the events of Group 1 do not show any special change when the element is close to reach the maximum load. However, in many cases, the events of Group 2 show a substantial increase when the load is close to its maximum value. This indicates that Group 2 events can be relevant to predict the final failure of the element in advance.

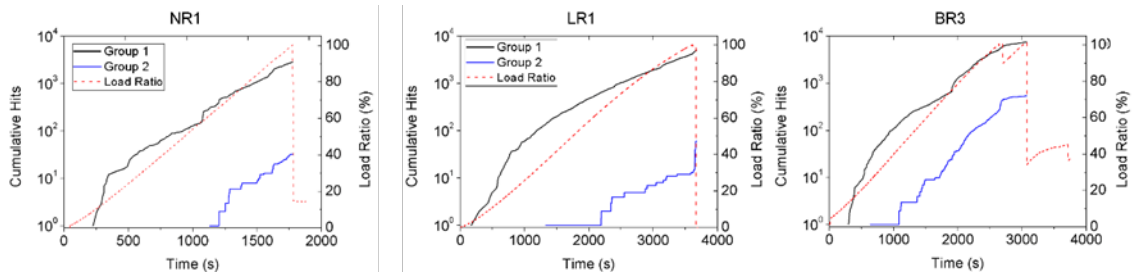


Fig. 4. Cumulative AE events versus time for an example of non-reinforced (NR), longitudinal reinforced (LR) and braided reinforced (BR) beam.

For this reason, Fig. 5 shows the location results of the Group 2 AE events along each tested specimen. The red dots represent the position of the sensors. Each blue dot in the graphs represents a localized event. The figures represent the peak amplitude of each localized event versus its position along the monitored area of the beam (the coordinate origin is at the center of the beam). The green lines correspond to the cracks in the wood, whereas the areas where breakage between wood and resin was observed are shown in orange color. The black areas correspond to the CFRP laminate that did not delaminate, while gray areas with black dots correspond to the zones where CFRP-wood delamination occurred.

In general, fewer events and shorter pick amplitudes are observed for the non-reinforced beams (NR) than for the reinforced beams (LR and BR). This indicates that the events of Group 2 can be mainly associated with resin-wood breakage (precursors of CFRP-wood delamination).

In the case of the beams retrofitted with the CFRP laminate (LR beams), it is observed that Group 2 events (especially those with a greater peak amplitude) are mostly and more clearly located in the area where the resin-wood breakage occurred. This area was

where the final CFRP-wood delamination began, leading to the fragile failure of the element.

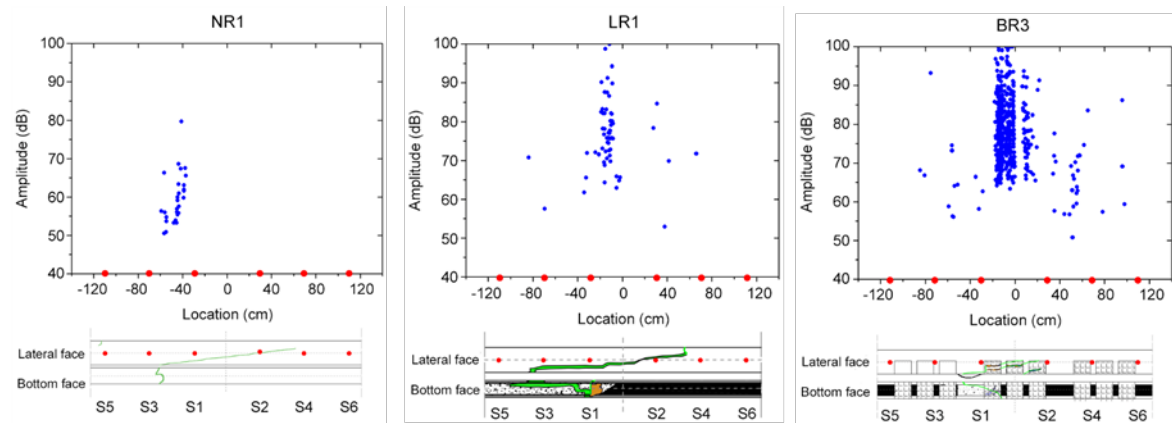


Fig. 5. AE linear location of events (Group 2) during the bending test for an example of non-reinforced (NR), longitudinal reinforced (LR) and braided reinforced (BR) beam.

A similar result is observed for beams reinforced with laminate and fabric (BR). For the three beams, the cracks of the wood were concentrated at the central part of the element, subjected to greater stresses. It can be clearly seen that the AE events are located mainly in this central area of the beam, which is an excellent correlation between AE location and damage location. In addition, the highest concentration of events for the beam BR3 is located in the interval $[-20, 0]$ cm, just at the resin-wood breakage area and precursor of lamella CFRP-wood delamination.

4. Conclusion

The work proposes the use of acoustic emission technique for the early detection of delamination between CFRP and wood, applicable to the case of retrofitted or repaired wooden beams with CFRP material. This analysis consisted on the following steps:

- Elimination of erroneously recorded AE signals, by comparing the temporal RMS of the signals in two different time windows.
- Calculation of the spectral RMS in a very narrow time window of the AE signals in two particular frequency bands. This minimizes the influence of the reflections of the acoustic waves and other propagation effects.
- Correction of the spectral energy of the AE signals by means the attenuation curves empirically determined.
- Clustering of signals into two groups, according to the value of the corrected spectral energy in two frequency bands: Group 1 (low frequencies are predominant) and Group 2 (high frequencies predominant). It has been shown, that if the attenuation correction is not carried out, no signals of Group 2 are found, due to the strong attenuation in wood material.

It has been shown that Group 1 events undergo virtually no change when the specimen is close to the final failure. However, in general, the events of Group 2 suffer a considerable increase. It has been corroborated that the location of the Group 2 events correlates very well with the location of the wood-resin break zones, which are the precursors of delamination failure between the CFRP sheet and the wood. This check has been made both on reinforced beams only with CFRP laminate (in which delamination is a critical aspect) and beams reinforced also with CFRP fabric.

References:

- [1] Parisi MA, Piazza M, Restoration and strengthening of timber structures: Principles, criteria, and examples, *Pract Period Struct Des Constr*, Vol 12(4), 2007, pp: 177-85.
- [2] de Jesus AM, Pinto JM, Morais JJ, Analysis of solid wood beams strengthened with CFRP laminates of distinct lengths, *Constr Build Mater*, Vol 35, 2012, pp: 817-28.
- [3] Nowak TP, Jasieńko J, Czepiżak D, Experimental tests and numerical analysis of historic bent timber elements reinforced with CFRP strips, *Constr Build Mater*, Vol 40, 2013, pp: 197-206.
- [4] de la Rosa García P, Escamilla AC, García MNG, Bending reinforcement of timber beams with composite carbon fiber and basalt fiber materials, *Compos Pt B-Eng*, Vol 55, 2013, pp: 528-36.
- [5] Yang Y-l, Liu J-w, Xiong G-j, Flexural behavior of wood beams strengthened with HFRP, *Constr Build Mater*, Vol 43, 2013, pp: 118-24.
- [6] Solarov R, Glišić M, Glulam beams reinforced with FRP strips and their application in architecture, *Spat*, Vol 32, 2014, pp: 1-6.
- [7] D'Ambrisi A, Focacci F, Luciano R, Experimental investigation on flexural behavior of timber beams repaired with CFRP plates, *Compos Struct*, Vol 108, 2014, pp: 720-8.
- [8] Ansell MP, Hybrid wood composites—integration of wood with other engineering materials, *Wood Compos*, 2015, pp: 411-26.
- [9] Biscaia HC, Cruz D, Chastre C, Analysis of the debonding process of CFRP-to-timber interfaces, *Constr Build Mater*, Vol 113, 2016, pp: 96-112.
- [10] Vanerek J, Smak M, Kusak I, Misak P, Durability of FRP/wood bonds glued with epoxy resin, *Mater Tehnol*, Vol 51(6), 2017, pp: 889-95.
- [11] Biscaia HC, Chastre C, Cruz D, Viegas A, Prediction of the interfacial performance of CFRP laminates and old timber bonded joints with different strengthening techniques, *Compos Pt B-Eng*, Vol 108, 2017, pp: 1-17.
- [12] Rescalvo FJ, Valverde-Palacios I, Suarez E, Gallego A, Experimental Comparison of Different Carbon Fiber Composites in Reinforcement Layouts for Wooden Beams of Historical Buildings, *Materials*, Vol, 10 (10), 2017, pp: 1113.
- [13] Rescalvo FJ, Valverde-Palacios I, Suarez E, Gallego A, Experimental and analytical analysis for bending load capacity of old timber beams with defects when reinforced with carbon fiber strips, *Compos Struct*, Vol 186, 2018, pp: 29-38.
- [14] Rescalvo FJ, Suarez E, Abarkane C, Cruz-Valdivieso A, Gallego A, Experimental validation of a CFRP laminated/fabric hybrid layout for retrofitting and repairing timber beams, *Mech Adv Mater Struct*, 2018, pp: 1-8.
- [15] Rescalvo FJ, Valverde-Palacios I, Suarez E, Roldán A, Gallego A, Monitoring of carbon fiber-reinforced old timber beams via strain and multiresonant acoustic emission sensors, *Sensors*, Vol 8(4), 2018, pp: 1224.
- [16] Ibrahim M, Nondestructive testing and structural health monitoring of marine composite structures, *Marine Applications of Advanced Fibre-Reinforced Composites: Elsevier*; 2016, pp, 147-83.
- [17] Grosse CU, Ohtsu M, *Acoustic emission testing: Springer Science & Business Media*, 2008.
- [18] Mizutani Y, *Practical acoustic emission testing, Tokyo2016*.
- [19] Ono K, Application of acoustic emission for structure diagnosis, *Diagnostyka*, Vol 2 (58), 2011, pp: 3-18.
- [20] Degala S, Rizzo P, Ramanathan K, Harries KA, Acoustic emission monitoring of externally bonded FRP-reinforced concrete, In: Kundu T, editor, *Health Monitoring of Structural and Biological Systems 2008*.

- [21] Pullin R, Eaton MJ, Pearson MR, Pollard C, Holford KM, Assessment of bonded patch bridge repairs using acoustic emission and acousto-ultrasonics, In: Uhl T, editor, Structural Health Monitoring, 2012, pp: 57-65.
- [22] Ono K, Gallego A, Research and applications of AE on advanced composites, 30th European Conference on Acoustic Emission Testing, Granada 2012.
- [23] Dahmene F, Yaacoubi S, El Mountassir M, Bendaoud N, Langlois C, Bardoux O, On the modal acoustic emission testing of composite structure, Compos Struct, Vol 140, 2016, pp: 446-52.
- [24] Diakhate M, Angellier N, Pitti RM, Dubois F, On the crack tip propagation monitoring within wood material: Cluster analysis of acoustic emission data compared with numerical modelling, Constr Build Mater, Vol 156, 2017, pp: 911-20.
- [25] Kolanu NR, Raju G, Ramji M, Experimental and numerical studies on the buckling and post-buckling behavior of single blade-stiffened CFRP panels, Compos Struct, 2018.
- [26] Degala S, Rizzo P, Ramanathan K, Harries KA, Acoustic emission monitoring of CFRP reinforced concrete slabs, Constr Build Mater, Vol 23 (5), 2009, pp: 2016-26.
- [27] Verbruggen S, Aggelis DG, Tysmans T, Wastiels J, Bending of beams externally reinforced with TRC and CFRP monitored by DIC and AE, Compos Struct, Vol 112, 2014, pp: 113-21.
- [28] Choi W-C, Yun H-D, Acoustic emission activity of CFRP-strengthened reinforced concrete beams after freeze–thaw cycling, Cold Reg Scienc Tech, Vol 110, 2015; pp: 47-58.
- [29] Diakhaté M, Bastidas-Arteaga E, Pitti RM, Schoefs F, Cluster analysis of acoustic emission activity within wood material: Towards a real-time monitoring of crack tip propagation, Eng Fract Mech, Vol 180, 2017, pp: 254-67.
- [30] Tayfur S, Alver N, Tanarlan HM, Ercan E, Identifying CFRP strip width influence on fracture of RC beams by acoustic emission, Constr Build Mater, Vol 164, 2018, pp: 864-76.
- [31] Martínez-Jequier J, Gallego A, Suárez E, Juanes FJ, Valea Á, Real-time damage mechanisms assessment in CFRP samples via acoustic emission Lamb wave modal analysis, Compos Pt B-Eng, Vol 68, 2015, pp: 317-26.

23 - Frequency-Amplitude class of Acoustic Emission for different fracture mechanisms in C/SiC composite

Xiao Denghong¹, Gao Yong^{1,2}, Jin Liang¹, Meng Fanchao¹, Li Naitian¹, Zhou Xiaohong¹, Tong Zongkai¹, He Tian², Jiang Bo³

¹ Beijing Electro-Mechanical Engineering Institute, Beijing 10074, P. R. China

² Beihang University, Beijing 10079, P. R. China

³ Shenyang Aerospace Xinguang Group Co., LTD

Abstract:

Acoustic emission (AE) registration is a useful methodology, which allows “hearing” and registering damage during loading of a specimen or a part. It is a challenge to determine connection between acoustic emission (AE) events and the corresponding damage modes. In the present study AE events registered during static loading of a C/SiC laminate are correlated to actual damage. The friction and cracks in the C/SiC laminate and localized delimitations are distinguished. AE events are classified according to the amplitude and centroid frequency of the signal into high frequency ,low frequency – low amplitude and low frequency – high amplitude clusters. The first (high frequency) AE events are assumed to be connected to friction. The second (low frequency – low amplitude) are assumed to be connected to formation and propagation of cracks, and the later (low frequency – high amplitude) are assumed to be connected to fiber breakage. The study validates use of Frequency-Amplitude class of AE for identification of damage models in C/SiC laminates and find out the load when each damage model first emerge.

1. Introduction

Due to its high temperature resistance, C/SiC is widely used in aerospace applications, especially in some high temperature resistant structures [1], such as the spacecraft rudder surface [2]. Due to lack of plastic deformation, ceramic matrix composites have high brittleness and may cause sudden damage under external loads. The use of suitable non-destructive testing methods to detect the damage of the C/SiC structure will play a key role. NASA puts advanced nondestructive testing methods in a very important position in its advanced ceramic matrix composite structural plans [3]. C/SiC composite Damage will lead to strong acoustic emission [4]. Acoustic emission signals contain important information about structural damage, such as the location of damage, severity and type of damage [5]. Therefore, for certain C/SiC structure, this paper uses the relationship between the frequency and amplitude of the center of mass of acoustic emission signals received to classify and recognize acoustic damage.

2. Structural static test and data collection

Here, the acoustic emission monitoring technology is applied to the damage analysis of the C/SiC structure during the static loading process. Six acoustic emission sensors were

arranged on the upper surface of the structure and two sensors are arranged on the lower surface of the structure. The location is shown in Figure 1.

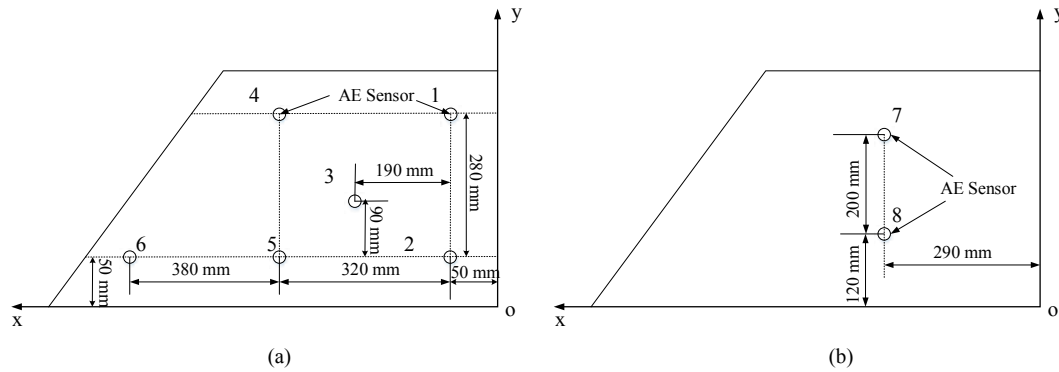


Fig. 1 Arrangement of acoustic emission sensors: (a) upper surface; (b) lower surface

The threshold is set to 200 mV, and the resulting cumulative energy of the acoustic emission signals received by the eight sensors is shown in Table 1. It can be seen that the accumulative energy of the acoustic emission signal received by the No. 8 sensor is the largest, and the damage position of the test piece is closest to the No. 8 sensor. Therefore, the following section mainly analyzes the acoustic emission signal received by the No. 8 sensor.

Table 1 cumulative energy of acoustic emission signals received by eight sensors

Sensors number	1	2	3	4	5	6	7	8
cumulative energy	0.12	1.30	9.54	36.26	10.17	5.17	26.20	39.77

3. Acoustic emission data analysis

The cumulative energy and loading load of the acoustic emission signal received by the No. 8 sensor over time are shown in FIG. 2 . It can be seen from Fig. 2 that the accumulative energy of the acoustic emission signal received by the No. 8 sensor gradually increases with the increase of the loading load, and the accumulated energy suddenly increases to the maximum slope when the applied load causes the test piece to be destroyed. Therefore, the moment of destruction of the test piece can be judged based on the cumulative energy change of the acoustic emission signal. However, the cumulative energy of the acoustic emission signal can only be seen at a time when the degree of damage of the test piece is relatively large, and it cannot be judged when the damage has just started and the type of damage. Therefore, the relationship between the amplitude of the acoustic emission signal and the center-of-mass frequency is studied in this paper to solve the problem of determining the type of damage and the moment of initial damage.

The relationship between the centroid frequency and amplitude of the acoustic emission signal received by the No. 8 sensor is shown in Fig. 3. It can be seen from Fig. 3 that the relationship between the mass center frequency and amplitude can be clearly divided into three categories, namely the high-frequency sound at 600 kHz. The transmitted signal is a low-frequency, low-amplitude acoustic emission signal and a low-frequency, high-amplitude acoustic emission signal with an amplitude of 7000 mV. The resulting changes in the centroid frequency of the three types of acoustic emission signals over time are shown in Fig. 4.

It can be seen from Figure 4 that the first type of high-frequency AE signals is mainly concentrated in the later stage of the test, and the frequency will be higher during the period when the test pieces are destroyed. This article observes the time-domain diagram of acoustic emission signals during the destruction stage of the test pieces. It has been found that there are a large number of signals with high center-of-gravity frequencies. At this time, since the damage expansion is severe, a large number of fibers break, and the acoustic emission band of fiber breakage is high, so the center-of-gravity frequency of the damage acoustic emission signal increases at this time. The second type of low-frequency and low-amplitude acoustic emission signals appeared at the beginning of the test and existed throughout the entire test. Therefore, such acoustic emission signals can be regarded as the generation of micro-cracks in the test piece. The third type of low-frequency, high-amplitude acoustic emission signals are generated in large quantities before the test piece is destroyed. Therefore, such acoustic emission signals can be regarded as a matrix fracture. At this time, the center-of-focus frequency of the acoustic emission is not high, but the energy of the acoustic emission event is significantly increased. high. Then find the time when the three types of damage begin to occur. The time for the first type of large-scale fiber breakage signal to be generated is 964s, and the corresponding load is 120%; the time for the second kind of microcrack signal to start is 98s, corresponding to The load is 50%; the time for the third type of matrix fracture signal to start generating is 829s, and the corresponding load is 80%.

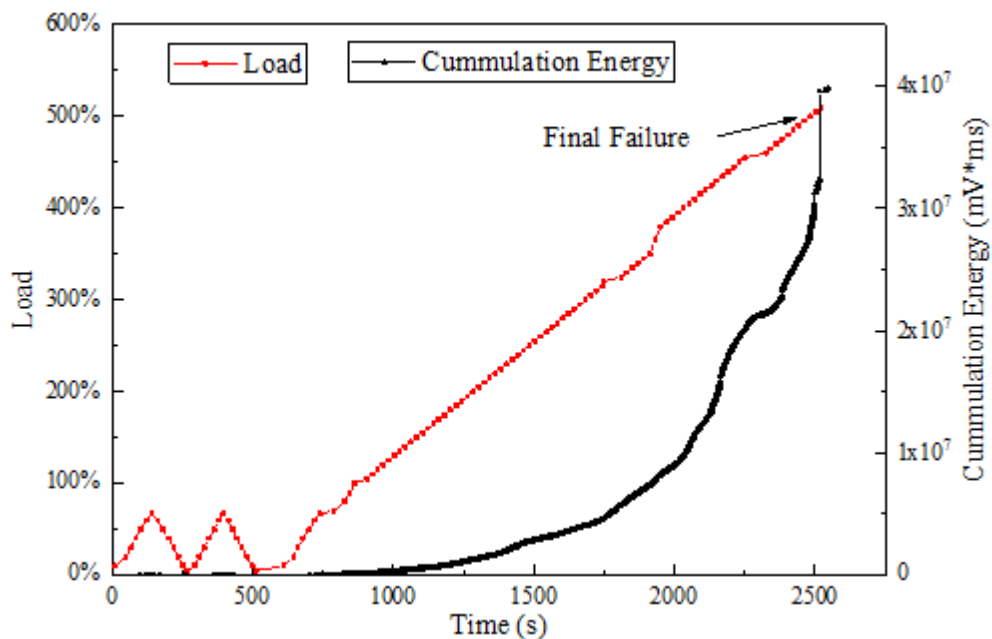


Fig. 2 The cumulative energy by No. 8 sensor during Loading process

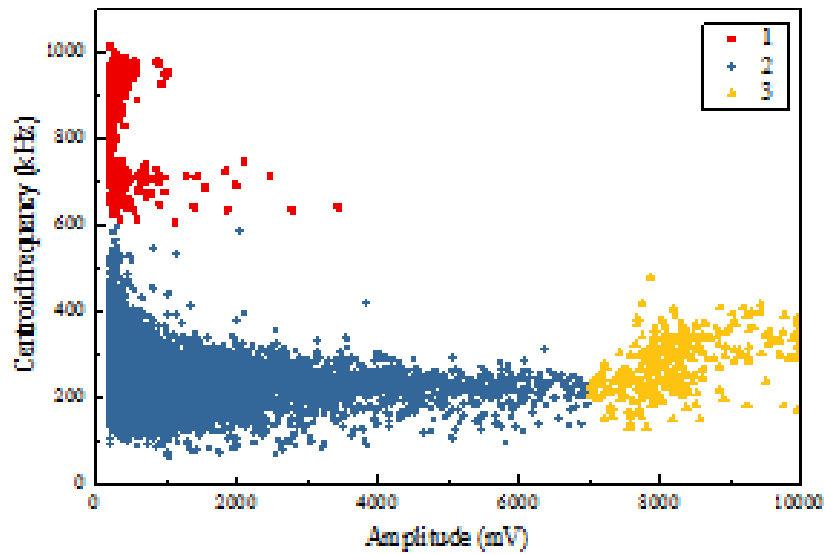


Fig. 3 Relationship between centroid frequency and amplitude of acoustic emission signal received by No. 8 sensor

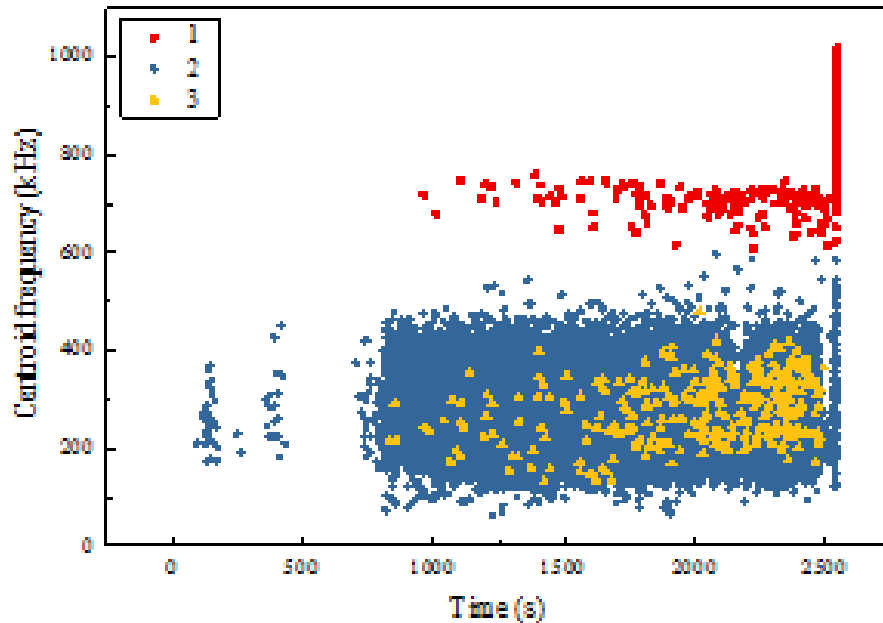


Figure 4 Occurrence time of three types of acoustic emission events

4. Conclusion

In this paper, we use acoustic emission to study the damage characteristics of a C/Sic composite structure during static experiments. Based on the relationship between the frequency and amplitude of the center of the acoustic emission signal, acoustic emission events can be divided into three categories: high frequency with low amplitude, low-frequency with low-amplitude and Low-frequency. The main damage characteristics of the

three types of acoustic emission events are determined. The research results of this paper can provide reference for the damage monitoring of this kind of structure.

References:

- [1] Xiang Y., Chen Z. H., Cao F., High-temperature protective coatings for C/SiC composites, *Journal of Asian Ceramic Societies*, Vol. 2 , 2014, pp.305–309.
- [2] Natalie D. S., High-temperature modal survey of a hot-structure control surface, 27th International Congress of The Aeronautical Sciences, 2010.
- [3] Advanced Ceramics Technology Roadmap—Charting Our Course, Sponsored by United States, Advanced Ceramic Association, U.S. Department of Energy, Prepared by Energetics, Incorporated and Richerson and Associates, 2000.
- [4] Chomiot N. C., Fleischmann P., Fougeres R., Fiber Break Characterization by Acoustic Emission in a Single SiC Aluminum Matrix Model Composite, *Progress in acoustic emission VI*, The Japanese Society for NDI, 1992: 567-574.
- [5] Madaras E. I., Winfree W. P., Prosser W. H., Nondestructive Evaluation for the Space Shuttle’s Wing Leading Edge, 41st AIAA/ASME/SAE/ASEE Joint Propulsion Conference & Exhibit 10-13 July 2005, Tucson, Arizona

29 - Damage monitoring on a steel truck trailer using parameter-based analysis of Acoustic Emissions

João Vitor Pimentel¹, Rolf Klemm¹, Munip Dalgic², Andree Irretier², Karl-Ludwig Krieger¹

¹Institute of Electrodynamics and Microelectronics (ITEM),
University of Bremen, Bremen, Germany

²Leibniz Institute for Materials Engineering (IWT),
University of Bremen, Germany

Abstract:

The structural health of a solid body can be monitored by detecting acoustic emissions (AE) that indicate the occurrence and/or propagation of fractures. Continuous monitoring is possible with vibroacoustic sensors that generate electric signals in response to structure-borne sound. However, damage detection and identification in real time imposes performance challenges on the sensor system that must be solved so that it can acquire and process the signal of interest.

In this work, piezoelectric sensors were connected a prototyping unit to continuously monitor a steel semitrailer structure subjected to fatigue tests. From previous tests on sample structures, signals in frequencies of up to several hundred kHz were expected to be associated with the emergence of cracks. At the required sampling frequencies, it was not possible to record, display or transmit the measurement data for external or post-processing. A parametric analysis was therefore carried out, whereby the vibrations were processed in 5 ms bursts. In such an implementation, the raw measured data is never made available. It could nevertheless be processed in real-time in order to calculate parameters that enabled damage monitoring.

The paper describes the parametric analysis used for online monitoring of the structure under test. The hardware implementation of the sensor system is described and results are compared with post-processed results of raw data to validate the online analysis.

1. Introduction

Structural health monitoring techniques based on acoustic emission (AE) detection are used in a wide range of applications, from buildings to aircraft. Such monitoring relies on the detection of AE events caused by crack formation or propagation in the material. The first challenge to the success of a quasi-passive AE-based condition monitoring system is to properly acquire relevant vibroacoustic data, since AE signals can have very low amplitudes relative to unavoidable background noise. In general, one-time events (such as catastrophic failures) generate stronger and clearer signals than progressive damage (such as caused by fatigue). Moreover, the characteristics of an AE signal, both in time and in the frequency domain, depend on the type of event that caused it as well as on the geometry and mechanical properties of the medium where it propagated. The second challenge is, therefore, to properly identify an AE event within the vibroacoustic data, which is particularly

difficult if there is no prior knowledge of where a fracture is likely to emerge, or of what kind of damage may occur in the structure.

The work presented here was carried out in the scope of the research project *TraZu (Electronic Condition Monitoring System for Predictive Maintenance of Semitrailers)*. The project focuses on semitrailers used in the transportation industry, which saw in 2016 an increase of 3.5 billion tonnes in the amount of goods transported by road within Germany alone [1]. There is a constant demand for ever-lighter structures, to be in operation as often as possible, carrying as close to its load limit as permitted, and often above it. Making the load-bearing structures of transport vehicles lighter can increase payload, but also the risk of damage to which these vehicles are already subjected in normal operation [2,3]. In Figure 1 examples are shown of damages to a semitrailer frame which most likely occurred progressively, but too fast to be found by regular periodic maintenance [4].



Figure 1. Damages to semitrailers at junction plate (left) and transverse beam (right)

The goal of the research project is a predictive maintenance system (illustrated in Fig. 2), a crucial part of which is the damage detection based on AE detections by decentralised sensor units. Specific parts of the semitrailer were chosen for monitoring taking into account the likelihood of structural damage occurring in their vicinity and on previous studies of the propagation of structure-borne sound on the frame [5]. The electrical signal from each sensor first goes through a signal conditioning stage (including pre-filtering and analog-to-digital conversion). The digital data is then delivered to a sensor controller unit, which performs the damage detection. These three stages comprise a decentralized sensor unit (DSU). Each DSU reports its results to the central electronics unit, which interprets these data taking into consideration complementary data received from the telematics unit – environmental data, vehicle information such as speed and load, etc. The end user (e.g. the driver or the fleet management) can also configure the damage detection via the telematics user interface.

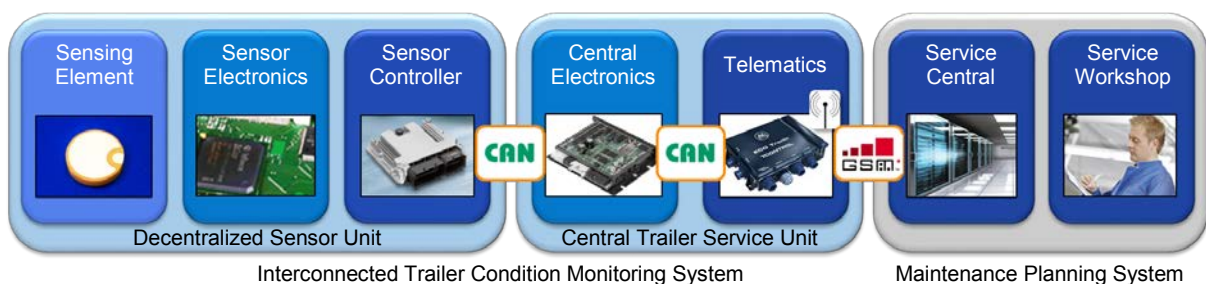


Figure 2. Overview of the predictive maintenance system

In previous works, the authors have demonstrated the validity of the AE-based damage detection strategies used in preliminary examinations of test specimens in controlled environments (static tensile tests and fatigue tests) and how they can be correlated to damage in a real semitrailer structure in operation [6–9]. Among the results of these first studies was the determination of a range of frequencies corresponding to the signals of interest (i.e. acoustic emissions due to fractures in the material). It became clear that for the relatively high frequencies involved (ca. 150–500 kHz), real-time processing of the raw data would impose severe performance challenges to the equipment. Therefore, a parametric analysis was favoured for the damage monitoring.

In parametric damage monitoring, a probable AE event is typically detected when the monitored signal exceeds a certain voltage threshold. A sample of a certain length of the signal is then quickly processed so that predefined parameters, also called “features”, are calculated. The raw measurement data is discarded and only the values of the features obtained is used for further analysis of the event, e.g. to confirm whether it corresponds to an acoustic emission or to identify its source. Classical features of an AE signal (see 10) include:

- Maximum – peak amplitude within the sampled window;
- Rise time – time from the first crossing of the threshold until the maximum is reached;
- Fall time – time from the maximum until the last threshold crossing within the window;
- Duration – time between first and last threshold crossings, equals rise + fall times;
- Counts – number of times the threshold is crossed during the sampled window.

These are illustrated in Fig. 3 over a sample of a real detection captured during preliminary tests. The parameter *counts* is omitted for visual clarity.

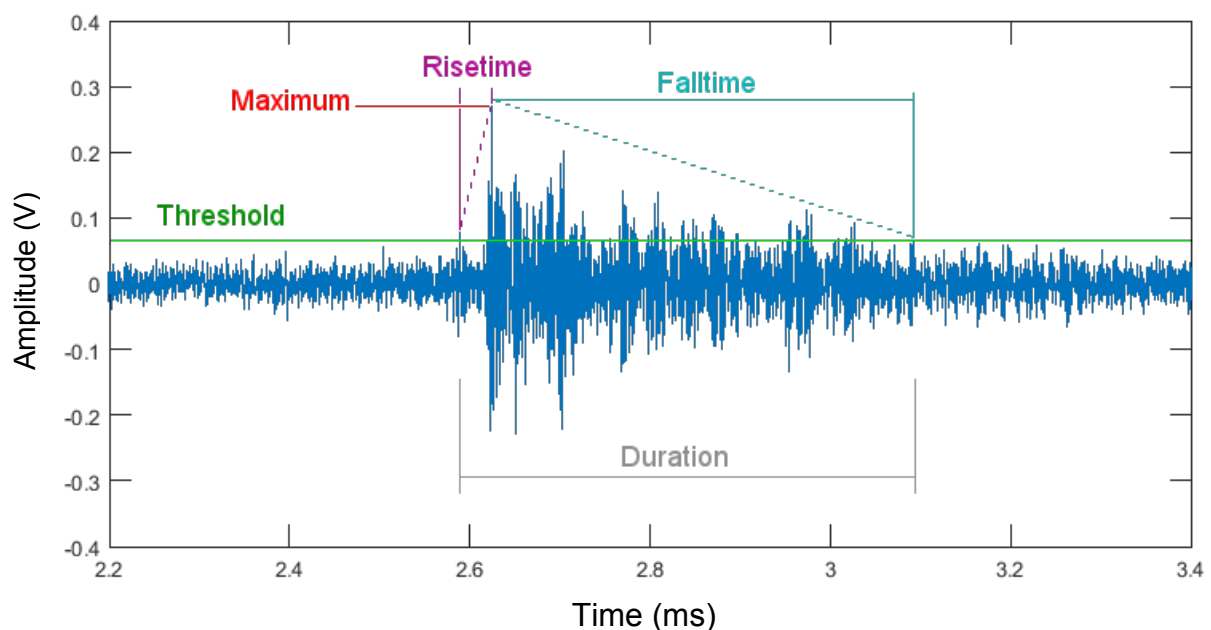


Figure 3. Classical features in AE testing

The classical features listed above were used in this work, as described in the following sections. In the system, these are called “low-end” features, to differentiate them from the secondary or “high-end” features calculated later. For brevity, they will be referred to here only as “features”, since further stages of the damage monitoring system fall out of the scope of this publication.

2. Description of work

During the development of the damage detection algorithm, Hsu-Nielsen tests were used to simulate acoustic emissions on samples of various geometries, all out of S700 MC steel, 4 mm thick. The algorithms were then tested during the fatigue test of a larger longitudinal section of semitrailer chassis (length 3.5 m, width 2.5 m) comprising the region corresponding to all three axles. The second (middle) axle was mounted. The testing machine varied the force applied to the axle between a minimum F_L and a maximum $F_H = 10 \cdot F_L$ at a frequency of 2 Hz. The forces were progressively increased in different phases of the test, with F_H in the range 46–110 kN, until a crack could be clearly seen and its propagation observed. Structure borne-sound was measured using four VS150-RIC piezoceramic sensors (Vallen Systeme), placed on the longitudinal beams on either side of the semitrailer structure, adjacent to crossbeam junctions near the first and second axles. Measurement data was acquired for post-processing using a PicoScope 5444B (pico Technology). For the online monitoring, a MicroLabBox (dSPACE) was used as a real-time data processing unit.

Models were built in MATLAB/Simulink so the algorithms developed until then could be implemented in a real-time application on the MicroLabBox. The analog-to-digital converter (ADC) class 1 of the MicroLabBox has a fixed vertical resolution of 16 bits and a configurable sampling rate of up to 1 Msps. Considering the range of frequencies of interest, the upper limit was desired. However, although the ADC can sample the signal within 1 μ s, the time needed for data from the ADC to be made available to the running application can be close to 3 μ s. Hence it was not possible to implement the algorithms developed for post-processing in an online manner.

A solution was to build the application using the burst conversion mode, whereby the ADC samples at 1 Msps and after 5 ms (i.e. 5000 samples) sends a hardware interrupt signal and makes the whole 5000-sample burst available to the application as a vector X of values x_i indexed from 1 to 5000. Both the interrupt block and the ADC subsystem, which delivers the sampled vector as well as a binary status signal, are part of the group *Input* on Fig. 4. Additionally, a switch signal is used to determine whether detections will be triggered based on an amplitude threshold value p_a or on a variance threshold p_v . The trigger switch and threshold values can be set by the user in real-time, and are thus part of the group *Input*.

The interrupt signal is used in the MATLAB/Simulink model to trigger a subsystem (in the group *Detection*), which takes the newly available data and compares it to the chosen threshold p . If $x_i \geq p_a$ for any i , or if $\text{Var}(X) \geq p_v$, depending on the chosen threshold, a detection signal is set to 1; otherwise, it is set to 0. This signal is used to trigger other parts of the model. The parameter *counts* can be directly obtained as the number of indices i where $x_i \geq p_a$. Furthermore, the first and last such indices, denoted as a and z respectively, are carried over to the subsystem in the *Low-End Features* group and used to determine the *duration* feature of the signal. With the index m of the maximum value within the vector, the *rise* and *fall* times also follow as $r = m - a$ and $f = z - m$ respectively. In the model, *duration*, *rise* and

fall are given by an integer number of samples, instead of a floating-point value of time; with a predefined sample rate, the actual times can be calculated directly. Although not strictly necessary, the calculated features are then set as model outports, so they can be easily visualised in a real-time application running on the dSPACE software in a host-PC connected to the MicroLabBox. To save the generated features (and some additional control signals) for later analysis, the USB Flight Recorder functionality is used (group *USB Recorder*). Chosen variables are saved automatically and periodically to a USB mass storage device connected to the MicroLabBox according to the sample time of their tasks in the model. The application can still run with no USB connected, but then no data is saved. The USB flight recorder is used only as a means to analyse the results a posteriori, and has no corresponding functionality in the planned monitoring system described above.

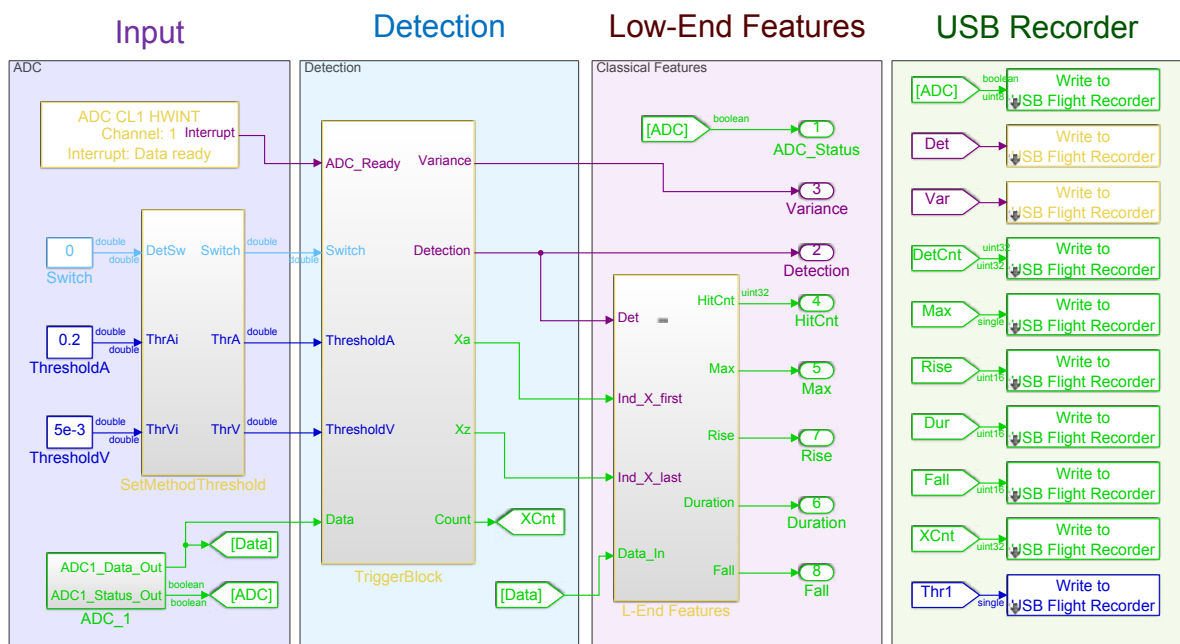


Figure 4. Simulink model of the first stages of the detection algorithm

In accordance with the system structure, the features generated so far are then packed into CAN messages (configured in a separate .dbc file and controlled by pre-built Simulink blocks) and sent out along with a detection ID. The CAN communication is out of the scope of this paper. However, it should be said that these messages are not periodic, but rather triggered by the detection signal.

The graphic user interface developed for the online detection monitoring is shown in Fig. 5. The GUI allows the user to configure the damage detection in real time via adjustable values of threshold as well as the input gain of the ADC and other visualization tools, e.g. the LEDs that show when a certain number N of events was detected within a certain period T . The interface reports detections clearly as they happen. An “event detected” means that the set threshold was overcome, and does not take into account the features calculated. These are shown to the user (although not readable in Fig. 5) along with the status of their respective CAN messages, to confirm that they were sent to the next stage of the monitoring system.

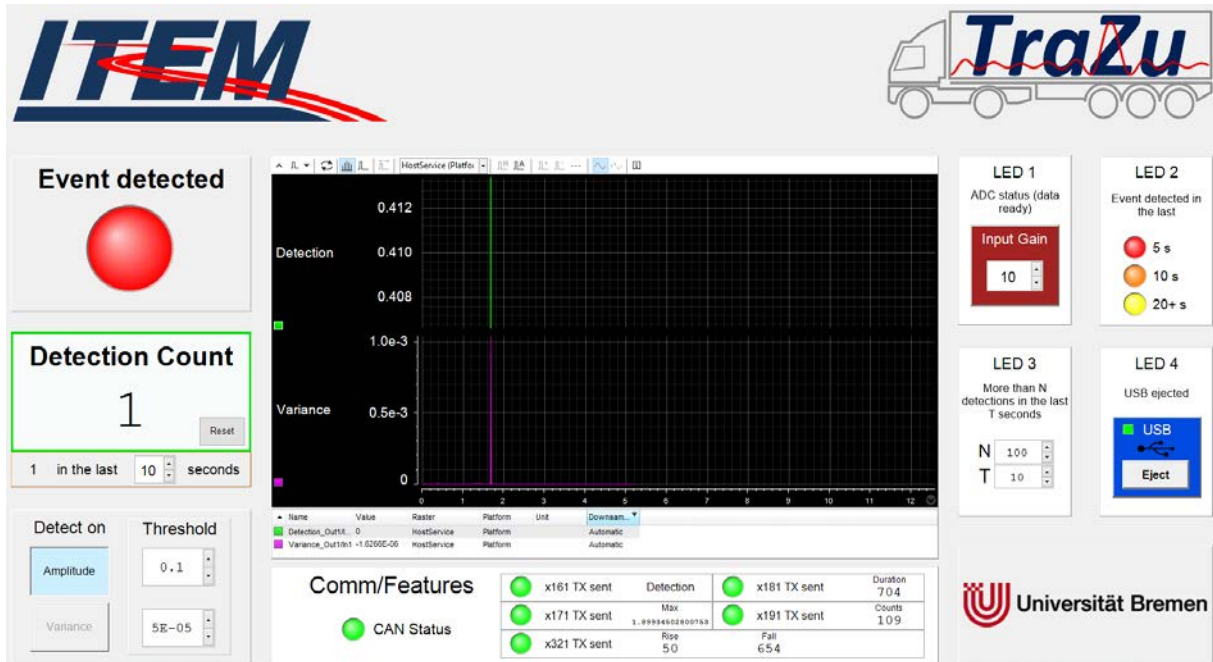


Figure 5. Graphic User Interface for the AE event detection in the MicroLabBox

3. Results and Discussion

The results of AE monitoring during the fatigue test of the larger semitrailer structure, described in the previous section, was compared to the outcome obtained with post-processing of the corresponding measurement data. Moreover, visual inspection of the trailer, as well as strain gauge data, were used to assess the online feature-based monitoring. Due to the length of the test, selected periods were considered for this evaluation. The results in Fig. 6 correspond to one of the last phases of the fatigue test, with an applied force of 110 kN. Towards the end of the period shown (at a point in time highlighted in red) the crack was already visible. The left-hand y-axis corresponds to the number of events detected during that phase (plotted in blue), while the right-hand y-axis corresponds to the *counts* parameter in each burst. From the figure it is already apparent that periods of rapid increase in the number of events correlated to high values of *counts* in each event. A rapid increase in event detections can be associated to either crack initiation or, especially, rapid crack propagation [9,11]. Therefore, this result indicates a significance of *counts* as a valid analysis parameter in the system presented.

Another example of validation of the feature generation was obtained later, after the macroscopic crack had already been verified. Crack propagation gauges were placed over the fracture so that its progression could be tracked in 100- μ m steps. While the rate of propagation was roughly 100 μ m/h most of the time, there were “jumps” during which the crack grew by several hundred microns within an hour. In Fig. 7, the maximum voltage in the burst is plotted against the total number of load/unload cycles of the fatigue test until that moment. The parameter was saved periodically in the USB flight recorder. For the large time scale displayed, it is not possible to differentiate between subsequent data points, especially since at this stage in the test AE events were frequent, resulting in a rapid variation between high and low values of the *maximum* parameter. Nevertheless, it can be seen that the high

value is relatively stable at ca. 1.8 V, except for a significant rise between approx. 4.579 and 4.581 million cycles, as well as a few spikes around the same time. Nearly all significant variations in the *maximum* value occur within a period (highlighted in green) when the crack propagation rate rose from ca. 100 $\mu\text{m}/\text{h}$ to 336 $\mu\text{m}/\text{h}$. Fig. 7 is thus shown as another example of a clear change in the value of the features that can be strongly correlated to crack formation or propagation verified by other means. The sudden drop in the *maximum* value at the point highlighted in red marks the time at which the testing machine was turned off and the test was stopped.

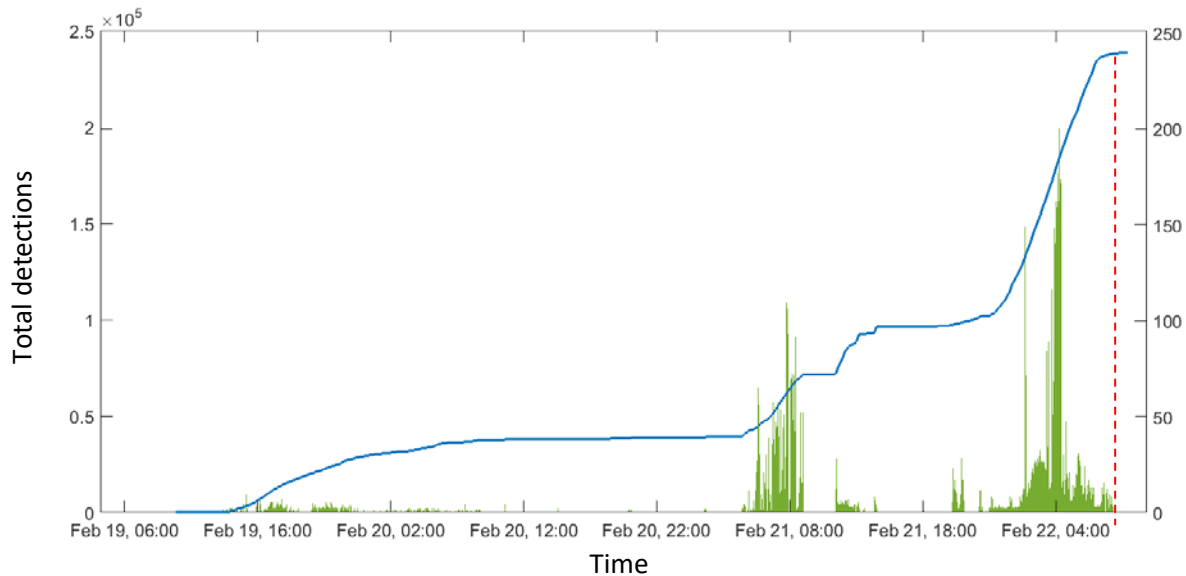


Figure 6. Blue (left-hand y axis): cumulative number of events detected.
Green (right-hand y axis): counts per burst.

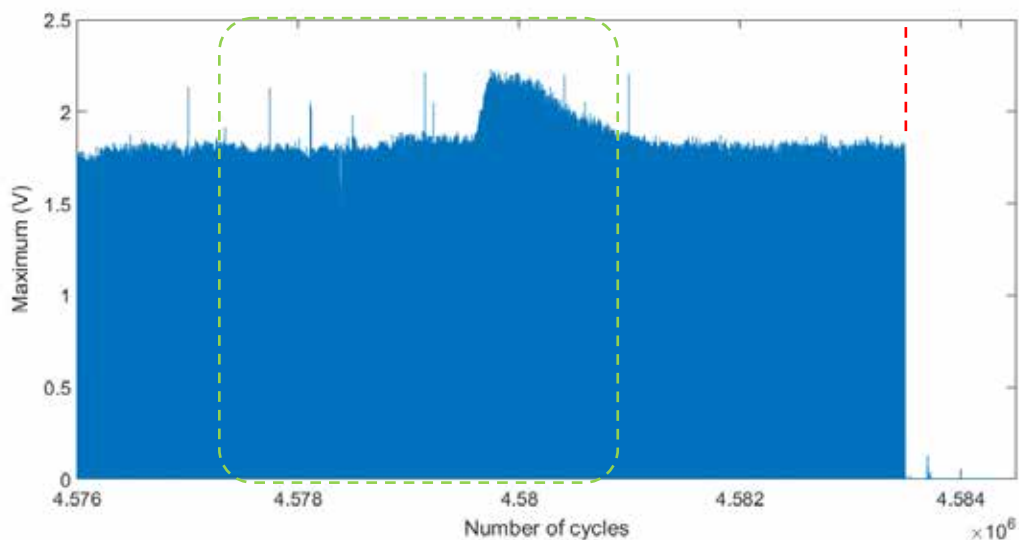


Figure 7. Maximum voltage in a burst for the last hours of the test. Area highlighted in green corresponds to an increase in the crack propagation rate. Red dashed line indicates test stopped.

4. Conclusion

The first stages of a parametric damage monitoring system for semitrailer structures based on acoustic emission were implemented on a MicroLabBox. Due to the technical impossibility of delivering raw measurement data to the further stages of the system, the structure-borne sound acquired by the sensors were digitized using burst conversion mode, which resulted in some restrictions to the signal processing. The approaches taken to implement the AE detection were described in this work, including the generation of classical features. The applicability of the features to the desired application was verified during fatigue tests, the results of which were analysed by various methods. Other stages of the damage monitoring system will be presented in future work.

References:

- [1] Federal Federal Statistical Office, Goods transport in 2016: volume of transport at record high again, Press Release 057, 2017.
- [2] Bathias, C., There is no infinite fatigue life in metallic materials, *Fatigue Fract Eng Mater Struct*, Vol. 22, 1999, pp 559–565
- [3] Fatemi, A. and Yang, L., Cumulative fatigue damage and life prediction theories: a survey of the state of the art for homogeneous materials, *Int J Fatigue*, Vol. 20, 1998, pp 9-34
- [4] Gesamtvorhabenbeschreibung Elektronisches Zustandsüberwachung zur vorbeugenden Wartung von Trailern (TraZu), 2015
- [5] Klemm, R., Harmstorf, J., Pimentel, J.V., and Krieger, K.-L., Untersuchung der Körperschallausbreitung auf einem LKW-Trailer mit Hilfe von Hsu-Nielsen Tests, *Proc. Deutsche Jahrestagung für Akustik (DAGA)*, 2018
- [6] Pimentel, J.V., Klemm, R., Dalgic, M., Irretier, A., and Krieger, K.-L., Automatic detection of fractures during tensile testing using vibroacoustic sensors, *Proc. 3rd International Electronic Conference on Sensors and Applications (ECSA)*, 2016
- [7] Pimentel, J.V., Klemm, R., Dalgic, M., Irretier, A., Zoch, H.-W., and Krieger, K.-L., Monitoring crack formation in metal structures with a percussion-inspired detection method, *Proc. IXth NDT in Progress*, pp 67-74, 2017
- [8] Klemm, R., Pimentel, J.V., Krieger, K.-L., Irretier, A., and Dalgic, M., Entwicklung eines echtzeitfähigen Sensorsystems zur frühzeitigen Erkennung von Rissen an Trailerrahmen, *Proc. 5th International Commercial Vehicle Technology Symposium (CVT)*, 2018
- [9] Klemm, R., Pimentel, J.V., Dalgic, M., Irretier, A., and Krieger, K.-L., Early detection of fatigue cracks in truck trailer structures by acoustic emission testing, *Proc. 12th European conference on Non-Destructive Testing (ECNDT)*, 2018
- [10] Shiotani, T., Parameter Analysis, in: Grosse, C.U., and Ohtsu, M. (Eds), *Acoustic Emission Testing: Basics for Research - Applications in Civil Engineering*, Springer-Verlag, 2008, pp. 41-51
- [11] Kohn, D.H., and Ducheyne, P., Acoustic emission during fatigue of Ti-6Al-4V: incipient fatigue crack detection limits and generalized data analysis methodology, *J Mat Sci*, Vol. 27, 1992, pp. 3133-3142

49 - Structural health monitoring using Acoustic Emission on metallic components in industrial plants

Heribert Marihart ¹, Gerald Lackner ¹, Gert Schauritsch ¹

¹ TÜV AUSTRIA, Austria, tph@tuv.at

Abstract:

The Structural health monitoring (SHM) is a method to safeguard the integrity of metallic components or component assemblies during service. This process involves a continuous or periodic measurement, the extraction or selection of degradation-relevant data and the statistical analysis to determine the actual state of the system condition. Acoustic emission (AE) monitoring detects and locates potential defects in plant components like piping and pressure vessels. An essential advantage of acoustic emission is that it allows assessing the components regarding evolving defects, leaks or even active corrosion during operation. Therefore, acoustic emission qualifies excellently as a tool for structural health monitoring.

The sensors of the monitoring system have to be mounted at preselected positions of the metallic structure and a tailored data analysis programme evaluates the incoming signals to provide a reliable statement regarding the structural health. Individually designed alarm and warning criteria enable corrective actions to prevent that the observed degradation evolves to failure.

In order to meet the requirements of customers from the oil and gas industry or the energy generation industry, TÜV AUSTRIA developed a monitoring technique for hot and cold surfaces including a methodology for collecting, transferring, storing and evaluating the measuring data.

This paper contains case studies where structural health monitoring with acoustic emission is used to provide an alternative to the regular requalification procedure of the monitored metallic pressure equipment.

1. Introduction

The performance of a conventional water pressure test indicates total failure in the form of visible deformation or leakage. A conventional acoustic emission testing (AT) is used as a periodic inspection method for the condition assessment of metallic pressure equipment. Accompanying pneumatic or hydraulic pressure tests are generally performed up to 1.1 times of the design pressure of metallic pressure equipment, while the acoustic emission testing provides a statement regarding the structural integrity of the item under test and can also detect early failure mechanisms. A relevant issue of AT is that the pressurization is performed with the operating medium. In contrast to hydrostatic testing no hazardous waste will be produced. Furthermore residual humidity may induce or facilitate failure mechanism. Therefore plant operators avoid complex cleaning and drying procedures which would be required after completion of the test. Acoustic emission testing is appealing for industry and enables the plant operators to optimize the plant availability with low operating costs for the recommissioning of the pressure equipment after the inspection test.

Structural health monitoring by means of acoustic emission is the next milestone in AT history. The pressure equipment operational parameters, such as working pressure, temperature or cycles should be recorded during the performance of the pressure test with AE. The monitoring period for SHM can either be discontinuous (e.g. 3 days 4 times per year) or continuously.

In general information regarding the current conditions of the metallic components in industrial plants is of vital importance for every plant operator. Therefore, one main task of the maintenance department is to take proper actions for ensuring secure operation. As an illustration, there are a lot of different methods on the non-destructive testing sector, to estimate the duration of a service period for pressure equipment, which are provided by TÜV AUSTRIA. Hence, there is increased attention on structural health monitoring using acoustic emission. Precise information regarding the actual conditions of the metallic components would enable the maintenance department to point out the components which should be repaired or when they should be replaced. That would give an economic advantage by preventing a shutdown of entire industrial plants and enable an appropriate repair.

2. Acoustic Emission Monitoring Concept

The main function of structure health monitoring is to merge the AE-data with the operating parameter (pressure, temperature, volumetric flow rate...) in the measuring system (see figure 1). Subsequently these monitoring data will be stored and can be analysed with dedicated software (e.g. Vallen Systeme "Automation Manager"). The automation manager has an online access to the measurement data. For example, if certain criteria are exceeded, an alarm message is sent if necessary per email and a test report is created over a predefined inspection period.

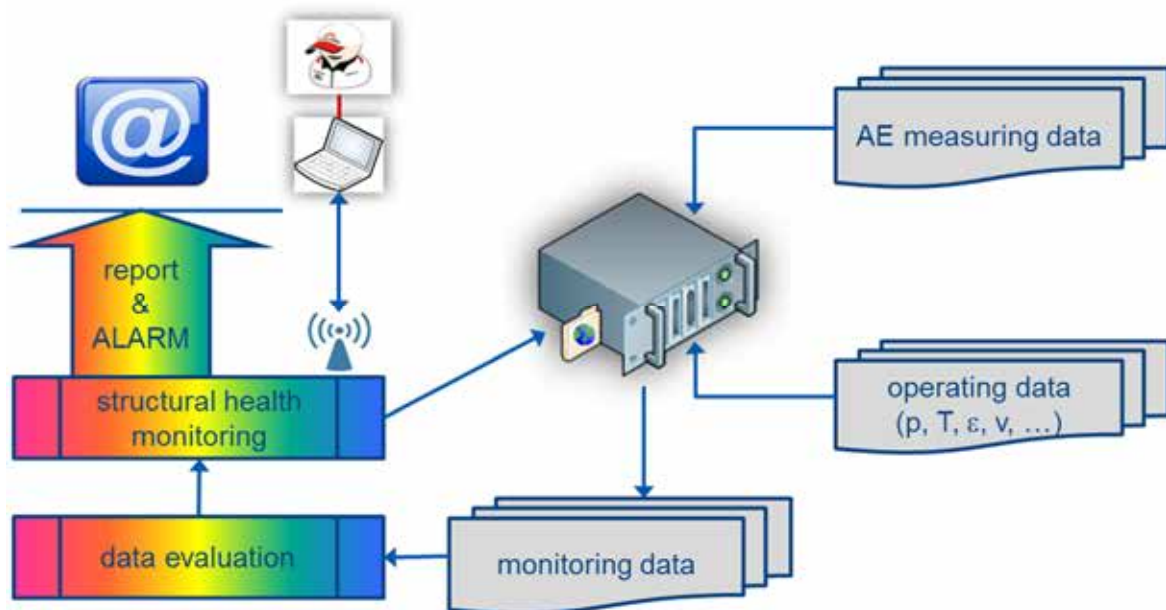


Figure 1: Acoustic emission monitoring concept

Two kinds of sensors will be applied in these use cases. Standard sensors VS150-RIC from Vallen Systeme with a temperature range up to 60 °C are mounted on the metallic surface of the pressure equipment. For a temperature, up to 180 °C, VS150-BD-V01 sensors are

mounted directly on the tested surface. For temperature ranges above 180 °C, a specifically designed waveguide device is applied between the test surface and the acoustic emission sensor. The VS150-BD-V01 sensor is certified for hazardous areas and is connected to the AMSY-6 measuring system with a 20-meter hazardous-certified coax cable and an AEP3-BD-V01 preamplifier.

The sensitivity of each measuring chain is checked with the Hsu-Nielsen source before the test. The AE system is an AMSY-6, which can acquire AE data and waveform data simultaneously for each channel. It has an internal pulsing unit, which sends on request an electric pulse to a sensor. That electric pulse is transformed into an acoustical pulse by the sensor. The other sensors may detect the sent pulse after propagation in the metallic structure. The AE system measures the time period from the emitting to the receiving sensor and that together with the distance between emitter and receiver gives the speed of sound. This pulsing function, defined as “Auto Pulsing”, will also be used to check the functionality and sensitivity of the measuring chain before, during and after the 24h-AE-measurements.

The software for data acquisition, visualisation and frequency analysis is also provided by Vallen Systeme. With VisualAE™ evaluation data files can be created concerning to the metallic pressure equipment, the respective relevant operational parameters (pressure, temperature, strain, volumetric flow rate...), cluster evaluation factor (CEF) [1] and external data (weather data).

“Automation Manager”, the software used for structural health monitoring with acoustic emission is also provided by Vallen Systeme. For a better comparison 24h measurements will be saved with previously configured data acquisition and visualisation files. With the “Auto Pulsing” function mentioned before the measuring chain is checked at certain intervals. If a previously defined deviation of AE parameters occurs, an alarm should be sent as a result [2]. Similarly, previously set limits of the acoustic emission results can trigger alarms. Consequently, digital inspection reports will be created. The structure health monitoring could be performed discontinuous or continuous.

3. Examples of monitored metallic Components

- Urea plant (passivation air cylinder, figure 2)



Figure 2: AET application on passivation air cylinder (urea plant)

The entirety of the structure of the passivation air cylinder can be monitored by an application of acoustic emission testing. As an example, for a simple standard sensor arrangement, 3 sensors must be applied linear on the 660-mm diameter cylinder in figure 2. The used sensor is the VS150-RIC, which has a resonant frequency of 150 kHz. The sensitivity of each measuring chain is checked with the Hsu-Nielsen source before the test. The “Auto Pulsing” function of the Vallen Systeme was executed before and after a 24h-AE-measurement and periodically in a 6 hours cycle. This functional check of the AE measuring chain was appended to each 24h-AE-measurement inspection report (see figure 3). The AE system is an AMSY-6, which can acquire AE data and waveform data simultaneously for each channel and is able to intercommunicate with the “Automation Manager” software.

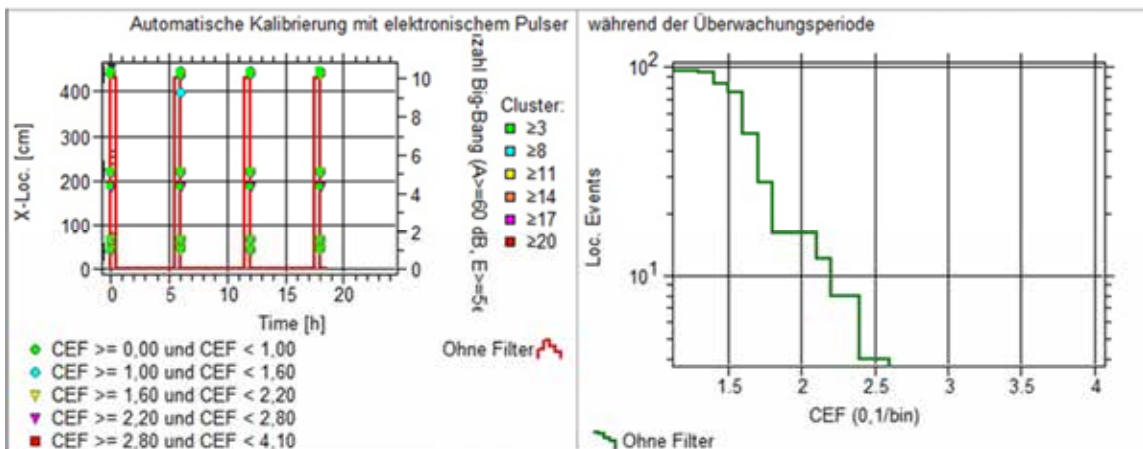


Figure 3: Auto Pulsing on passivation air cylinder

While the pressure equipment was in operation the 24h-AE measurement was recorded with the operation pressure as external parameter. For the passivation air cylinder SHM used acoustic emission was done discontinuous 3 days 4 times per year.

- Urea plant (Nitrogen cylinders, figure 4)

The same sensor arrangement as the passivation air cylinder was applied for this both nitrogen cylinders. Those metallic pressure equipment are exposed to environmental impacts. Thus, the external parameters were enhanced with the data of the weather station for a profound analysis. The monitoring time was also the same: discontinuous 3 days 4 times per year.

- Preheater for fuel gas in gas-fired power station (figure 5)



Figure 4: SHM on nitrogen cylinders

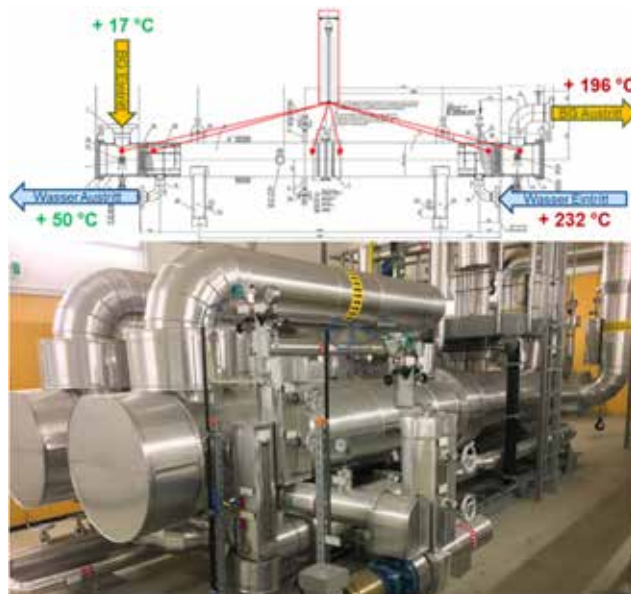


Figure 5: SHM on preheater for fuel gas in gas-fired power station

- Main steam distributor (figure 6)

The main steam distributor should give an example of the application of an acoustic emission monitoring system during operation at temperatures up to 170 °C. A sensor arrangement with 5 sensors must be applied linear on the 450-mm diameter cylinder in figure 6. Whereas 3 sensors were mounted directly with magnet holder and 2 further sensors were mounted between those 3 sensors with a waveguide technique. For this example, external parameters are temperature, pressure and volumetric flow rate. The electrical signal of these 3 parameters was fed directly into the acoustic emission system.



Figure 6: SHM on main steam distributor

4. Results

The verification of the structural integrity while the metallic component is in operation was implemented by the evaluation of a 24h-AE-measurement and provides further information: Existence of active AE-sources caused by the act of defect-mechanism in the structure, grading of the intensity of the AE-sources during the applied pressurisation and localisation of the AE-sources in space of the whole structure.

Moreover, in respect of safety-relevant measures the early recognition potential of AET in contrast to alternative test methods is from vital importance, especially to the common hydraulic pressure test (water pressure test). This also includes an early detection at approximately 30 % of the load of the component failure for ductile materials. Also, possible defect-mechanisms can be observed in a microscopic range.

Figure 7a) shows the cluster evaluation factor (CEF) and the pressure versus time of measuring. This graph gives conclusions about the load profile; it shows minimum- & maximum- working-pressure, and pressure intervals during operation of the metallic component. The cluster evaluation factor is applied for on-line evaluation of located events. The CEF calculation is based on prototype data acquired on structures with known defects. The evaluation range of CEF start from 0 (no located events = 0 severity) up to 4 (very high severity).

At the example of the passivation air cylinder the traceable, active AE-sources are located among the sensors xd4 and xd5 at the range between 380 and 400 cm (see figure 7b).

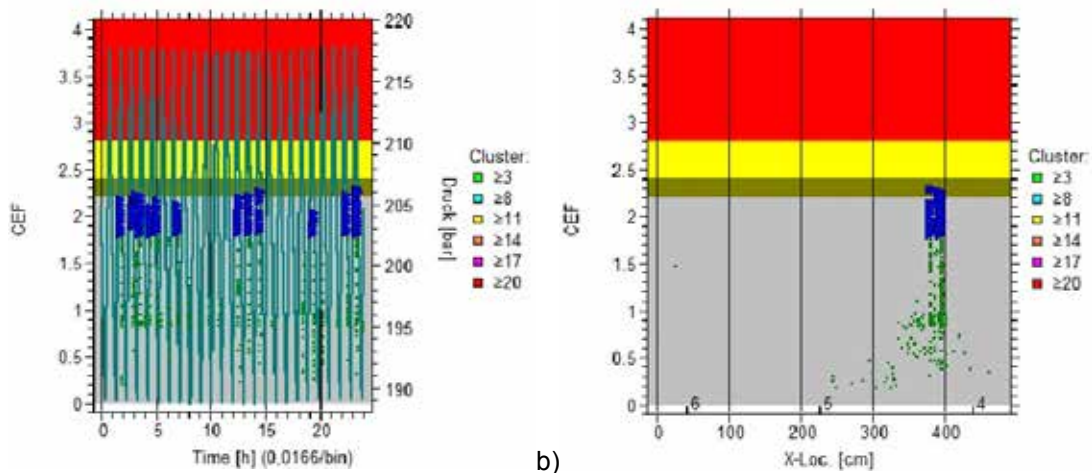


Figure 7: Evaluation of passivation air cylinder
a) CEF and pressure vs. time, b) CEF vs. X-Location.

Exactly on this position the mounting ring is fitted. Therefore, this area was verified on the cylinder with an ultrasonic test. This inspection method exhibits no noticeable indications. Hence, the result suggests that the activity of the acoustic emission was caused by mechanical friction between the mounting ring and the passivation air cylinder.

The important advantage of the monitoring inspection report is the history of those 12 x 24h-AE-measurements which could be compared easy. An equally important reason to realise SHM is the adequately long monitoring period of about 290 h compared to one hour of a conventional acoustic emission test. The project target was the extension of the service period till to next inspection (one year).

5. Conclusion

Structure health monitoring using acoustic emission on metallic components will become an increasingly role on non-destructive testing sector. The system effectiveness of new industrial plants is growing and the knowing of the actual conditions of the metallic components in industrial plants is of vital importance for every plant operator.

Conventional acoustic emission tests will be more popular because they are performed with the process medium, but this method must take a requalification. The test performance must realise during a planned shut-down and usually on pressure equipment in ambient conditions. Often the prevailing test requirements do not represent the operating conditions or only in a limited way. Also, the material is sometimes not sufficiently loaded as in operation, for example material properties modify with temperature.

In case if points which mention above should be relevant, acoustic emission monitoring could be the solution. However, the degradation of the material happens normally during operation nevertheless not during testing. Consequently, structure health monitoring using AET is recording during operation and as a result it is a measurement of the degradation process. Considering this analytic data, the "Automation Manager" makes it possible to send a warning if defect-mechanism occurs as early as possible. Moreover, for a measurement during operation, no further time must be spent for testing in a shut-down. Additionally, in

case of severe degradation, the scheduled operation time can be observed with acoustic emission monitoring to safeguard the time till to replacement of the metallic component.

This enables further improvements of customer specific implementation of SHM using acoustic emission, which shall foster a broad acceptance of acoustic emission by equipment users/operators.

References:

[1] TSCHELIESNIG, Peter; SCHAURITSCH, Gert: Inspection of LPG vessels with AE examination. *Journal of Acoustic Emission*, Vol. 18, 2000, p. 138 – 143

[2] G. Schauritsch, “Schallemissionsprüfung an einem rissbehafteten Flüssiggaslagerbehälter –Ergebnisse zum Nachweis der Verfahrenseignung”, *Proceedings of 18. Kolloquium Schallemission*, Vortrag #03, 2011.

83 - Novel AE monitoring of hydrogen induced damaged vessel and real time alarms. A case study

Dimitrios Papasalouros¹, Konstantinos Bollas¹, Ioannis Ladis¹, Eleftherios Aerakis¹,
Dr. Athanasios Anastasopoulos¹, Dimitrios Kourousis¹

¹ Mistras Group Hellas ABEE, Athens, Greece

Abstract

Hydrogen induced cracking (HIC) damage is a common damage mechanism, expected typically in vessels in severe wet H₂S service. It can occur at relatively low temperatures, as the atomic hydrogen is concentrated at the impurities within the steel. The occurring damage is mostly cumulative and it can be manifested in various types such as blistering, step-wise cracking or stress-oriented cracking. As such, the qualitative and quantitative evaluation of structural integrity of any vessel possibly suffering from wet hydrogen damage is of great concern from a safety, environmental and financial point of view. In the present paper, results of the application of real-time AE monitoring of a HIC damaged area of a thick-walled amine absorber in severe wet H₂S service are presented. The damaged area was found during a routine UT inspection. UT and AE trials were performed in order to fine-tune and maximize the effectiveness of the application. This resulted in a unique correlation database from which monitoring criteria were developed, that greatly maximized the AE location performance and minimized the false alarms due to the noisy environment. Major benefits of the AE monitoring application include an overall increase of health and safety, as well as minimum down-time for the refinery until a full vessel replacement becomes possible.

1. Introduction

Acoustic Emission [1][2] has been successfully applied for the integrity assessment of static structures such as pressure vessels and storage tanks during both in-service and hydrostatic tests for a wide range of manufacturing materials. Extensive testing of such equipment has led to the development of AE testing procedures, evaluation criteria and international standards [3][4]. In addition to that, industry applied procedures, such as MONPAC & IPAC [9][10] for pressure vessels, extended the codes' pass-fail assessment to quantitative evaluation of fault severity and criticality, providing the industry with a tool for 100% evaluation of the vessel, capable of giving early warning of developing defects, increasing, thus, the operational safety.

In areas with high stress concentration and where local strength may lead to crack propagation, as in the case of step wise cracking HIC or SOHIC (Figure 1), local monitoring

can be performed. Many variables, like temperature, contaminations, microstructure etc., may affect and thus differentiate the final damage.

Although surface breaking cracks are visible, their detection may be performed with various other NDT techniques like UT (TOFD-PA), EC, PT or RT. Many of these methods may also provide information about the crack size, position and orientation.

In cases where the primary interest is the crack growth and its criticality in relation with the variation of operating conditions, continuous AE may be used by utilizing the stochastic stimulation of the structure (varying pressure, temperature variations etc.) [6]. In this paper, a novel adaptation of the method and application of real-time alarm criteria over a noisy environment is presented. This was possible due to the unique AE & UT findings correlation database. The continuous monitoring was able to provide an early indication of possible damage accumulation in severely damaged areas.

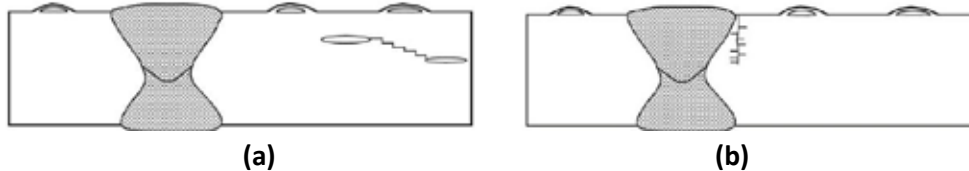


Figure 1 – (a) Stepwise Indication - HIC (b) Through Thickness Indication in HAZ – SO-HIC [6]

2. Case Study: HIC Monitoring of Amine Absorber

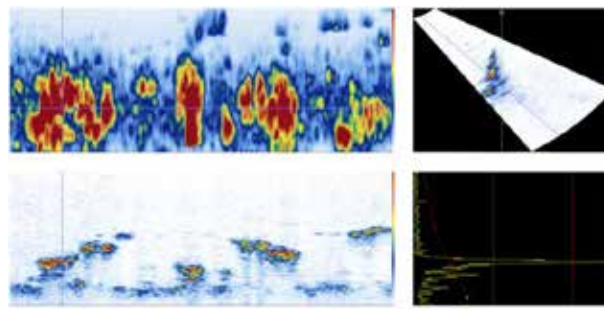
During a routine internal inspection, a large number of surface breaking blisters was found on the internal surface of the 91mm-thick column (Figure 2) with an operational temperature of 60°C. These indications appeared just above the operational water level, on the internal surface of the 2nd course of the column. Subsequent base metal and weld ultrasonic (UT) inspection with phased arrays (PA), as indicated by [6] were performed in sampled areas of the column. UT inspection showed unexpected scattered indications in both areas (HAZ & base metal).

The indications that were discovered were ranging from planar to step-wise (Figure 3a). Some larger clustered axial-oriented indications were also discovered that appeared as through-thickness damage (Figure 3b). The presence of these indicated that the damage was already in an advanced state.

To this respect, the planning for continuous monitoring was established due to the criticality of the column regarding its structural integrity condition as well as its impact on the general safety during subsequent operation, until its replacement.



Figure 2 –Internal Surface Condition



(a)

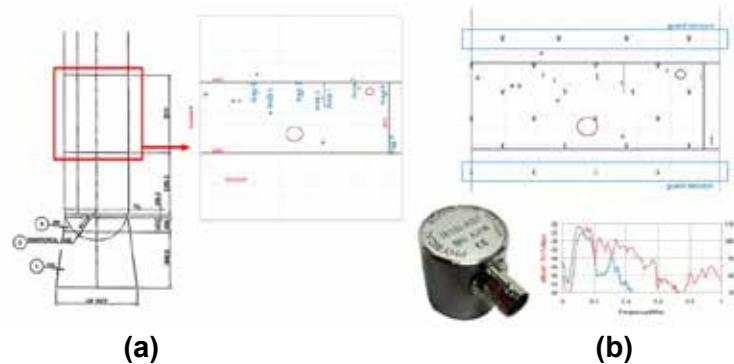


(b)

Figure 3 – (a) Step-wise damage (b) Through-thickness damage indication

3. Setup

Eight areas (1–8) with larger clusters of identified damage were selected for monitoring as being the most critical. Area 6, was selected as a reference since it was damage-free (Figure 4a).



(a)

(b)

Figure 4 – (a) Monitoring areas 1-6 (b) Sensor layout, PAC R15i-AST, probes frequency response

In total, twenty-two (22) R15i AE sensors, with a 150 kHz resonant frequency and integral preamplifier, were mounted around the 2nd course in triangular formation (Figure 4b), where the first and last four sensors were used as guards, in order to exclude operational or other activity not correlated with the damaged areas. These were mounted after the column was brought back to service.

The sensors were mounted with high-temperature couplant and magnetic holders (Figure 5a). The connection to the more centralized junction boxes (Figure 5a) was performed via coaxial cables that were shielded inside elastic tubing (Figure 5b).

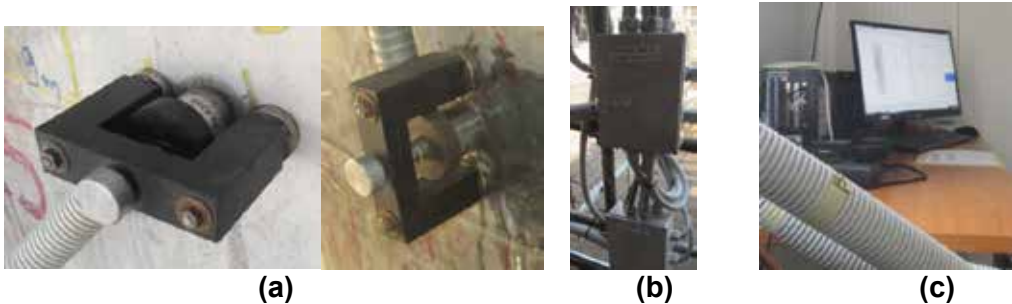


Figure 5 – (a) Sensor mounting (b) Junction box (c) Cable routing and μSamos Express-8 AE monitoring workstation

From each of the junction boxes the coaxial cables were routed to a nearby shielded isobox where the physical connection with the system (Figure 5c) was established. All routing to the system was performed via larger diameter elastic tubing to shield the cables against the elements.

4. Attenuation Measurements & Location Verification

AE signal attenuation measurements (Figure 6a) were performed along the axial direction, circumferential direction and 45° angle from the circumferential direction. As is often observed in thick vessels, the signal attenuation was relatively low (65 dBae at 500cm from an AE probe). In this respect, it was expected that the predefined tight array of Acoustic Emission probes would greatly increase the event detection capability of the resulting setup.

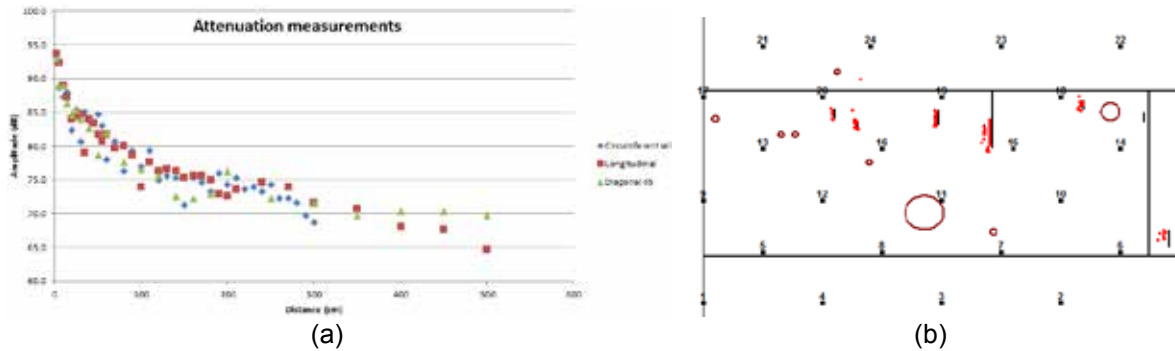


Figure 6 – (a) Attenuation measurements in 3 directions (b) Hsu-Nielsen sources location results

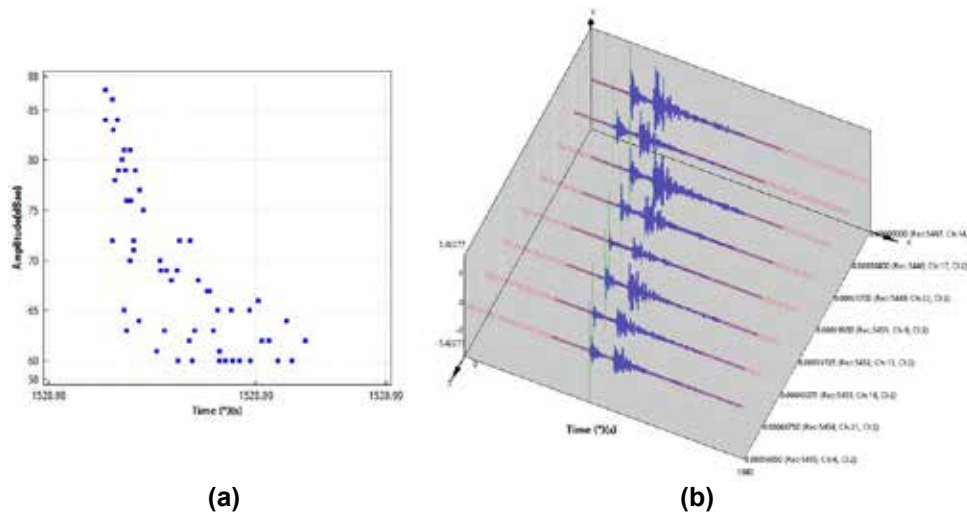


Figure 7 – (a) Event due to a HN source (b) Resulting waveforms from the first 8 hits acquired

This was verified with the application of Hsu-Nielsen sources along the axial direction of each of the areas of interest. The raw results are shown in Figure 6b. There is a clear distinction between the sources located at area 1 and 2 which shows that the effective spatial resolution of the setup was at least 10cm (distance between Areas 1 & 2). Moreover, the effectiveness and performance of the resulting setup during the noisy service time was maximized by utilizing a higher amount of AE hits for the location algorithm [21].

5. System Functionality and Sensitivity Verification

For any monitoring scheme, safeguards and system checks must be enforced in order to maintain a high confidence level for the functionality of the system. For these reasons, daily routines were performed in order to ensure that the system was functioning properly and the sensitivity of the probes was not degraded due to the operation of the column or exposure to the elements.

This was achieved by using the Auto Sensor Test (AST) feature of the MISTRAS µSamos Express-8 boards in predefined and/or random intervals and the results were cross-referenced with the reference AST results acquired when the probes were initially mounted. The AST feature data comparison shows of the difference of AE features between two data

sets. The comparison of the newer AST measurements (when performed) with the reference AST measurements was automatically performed by the system each time new AST data was available. Graphs from AST trials showing typical AE features for each probe are shown in Figure 8a. In addition, for system performance, the Average Signal Level (ASL - Figure 8b) of each channel was continuously monitored in order to have clear indications about any abrupt operational changes or external noise that could contaminate the acquired data.

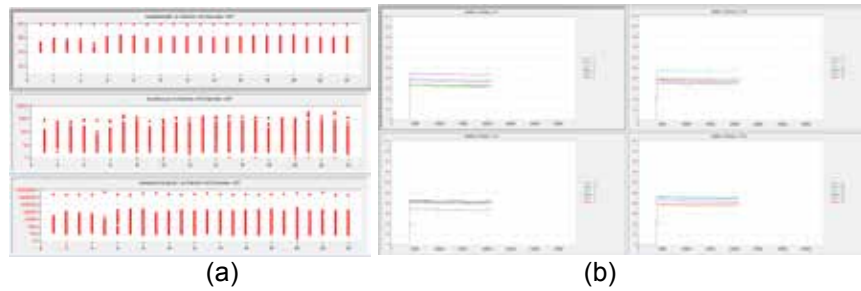


Figure 8 – (a) Example of AST measurements for all 22 mounted AE probes (b) ASL measurements

In the rare case that a sensor’s response was degraded from its average behavior and sensitivity, local crew was performing the necessary adjustments.

6. Data Evaluation and Reporting AE Results Grading

Daily evaluation and reporting of acquired data was decided due to the criticality of the situation and the massive amount of acquired data. AE and UT phased array trials were performed in order to develop a unique correlation database. Upon the completion of trials and by using the resulting database the real-time alarm criteria were greatly improved and fine-tuned in order to be used in real-time alarms. The number of false alarms during continuous monitoring was greatly reduced, thus maximizing the effectiveness of the monitoring. A confidential list of Events Cluster Activity, Amplitude and Energy Criteria and time compensation/normalization was agreed with the client, upon the completion of initial trials. The typical daily report contained the cluster activity grading of the monitored areas assigned into 4 categories (Table 1a).

TYPE	Alarm/Evaluation Cluster Criteria				Channels Criteria
CLUSTER THRESHOLD	Summary of Alarms/Evaluation criteria	ABOVE THRESHOLD	ADVISORY	WARNING	per Channel
ADVISORY			CRITICAL		
WARNING	Day Of Week DD/MM/YY				
CRITICAL					

Table 1 – (a) Cluster activity grading categories (b) Daily/weekly reported cluster activity

In addition, a summary weekly report was generated at the end of each week (Table 1b).

7. Monitoring and Real Time Alarms

24/7 remote access to the μ Samos Express-8 AE Monitoring Workstation was available through a high speed internet connection. Daily reports of operational parameters of the column and weather conditions were correlated in order to filter the data. AEWIN software was used for automated located data clustering during acquisition (Figure 9). The alarm generation according to the aforementioned categories and criteria was subsequently triggered.

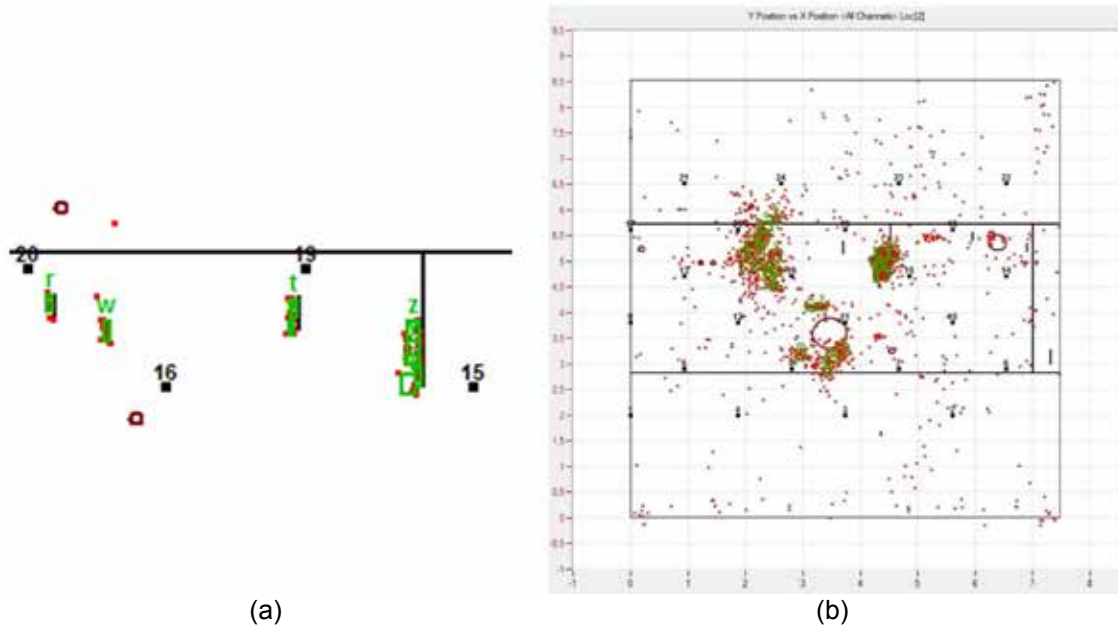


Figure 9 – (a) Example of automated clustering (b) Real-time automated clustering

An interesting observation is that there is significant located AE event clustering, in the areas of interest.

8. Discussion & Conclusions

In general, this novel AE monitoring method of verified HIC damaged areas, offers the unique opportunity for asset owners to be informed rapidly and continuously, with minimum interference, about the condition of the structural integrity of critical assets that need to operate at their design limits.

Results of the test can be given almost immediately, upon the alarm triggering, with full evaluation within hours after, thus providing a great assistance to the general operations regarding the asset.

More specifically, safety and operational risks are minimized and operational efficiency is increased, therefore minimum downtime is guaranteed.

Location optimization using high-density AE probe arrays shows a highly promising contribution to the early detection of damage areas even in case that were not identified

previously. This was shown in (Figure 9b) where the area between probes 6, 7 and 11 was not initially selected for monitoring. However from the initiation of AE monitoring the resulted large AE event cluster that was located, change the criticality of this area. and additional UT-PA follow up that was performed revealed many smaller critical indications.

Finally, all the above advantages can be further exploited by installing permanent AE monitoring systems with remote access functionality, in order to assess the structural integrity of assets during in-service operation and/or prolonged time periods. Typical systems of this magnitude are already successfully monitoring critical assets, thus greatly promoting the minimization of safety risks and the increase of operational efficiency.

References

- [1] Pollock A. A., 1989, "Acoustic Emission Inspection", Metals Handbook, 9th Edition, Vol. 17, ASM International, pp. 278-294.
- [2] Vahaviolos S. J., 1996, "Acoustic Emission: A new but sound NDE technique and not a panacea", in NDT, eds. D. Van Hemelrijck & A. Anastasopoulos, Balkema, pp. 101-115.
- [3] ASME, Section V, Article 12, 1988, "Acoustic Emission Examination of Metallic Vessels During Pressure Testing".
- [4] ASTM E 569, 2002, "Standard Practice for Acoustic Emission Monitoring of Structures During Controlled Stimulation".
- [5] Fowler T. J., Blessing J. A., Conlisk P. J. and Swanson T. L., 1989, "The MONPAC System", Journal of Acoustic Emission, Vol. 8, Number 3.
- [6] American Petroleum Institute (API) 571-1, FFS-1, 2016
- [7] Fixed Equipment in the Refining Industry RECOMMENDED PRACTICE 571, FIRST EDITION, 2003
- [8] MONPAC Procedure for Acoustic Emission Testing of Metal Tanks/Vessels, August 1992.
- [9] "Selection of 5 papers on MONPAC technology and applications", Journal of Acoustic Emission, 1989, Vol. 8, No.3 July-September, pp.1-33.
- [10] ASME, Section V, Article 12, "Acoustic Emission Examination of Metallic Vessels During Pressure Testing", 2015.
- [11] ASTM E569-13, "Standard Practice for Acoustic Emission Monitoring of Structures During Controlled Stimulation".
- [12] EN 15495:2007, "Non Destructive testing - Acoustic emission - Examination of metallic pressure equipment during proof testing - Zone location of AE sources".
- [13] EN 14584:2013, "Non-destructive testing - Acoustic emission - Examination of metallic pressure equipment during proof testing - Planar location of AE sources".

- [14] C. R. Heiple and S. H. Carpenter, "Acoustic Emission Produced by Deformation of Metals and Alloys – A Review", *Journal of Acoustic Emission*, Volume 6, Number 3, 1987.
- [15] Anastasopoulos A. and Tsimogiannis A., 2004, "Evaluation of Acoustic Emission Signals During Monitoring Of Thick-Wall Vessels Operating At Elevated Temperatures", *J. of Acoustic Emission*, Vol. 22, pp 59-70.
- [16] Carlos M. F., Wang D., Vahaviolos S., Anastasopoulos A., 2003, "Advanced acoustic emission for on-stream inspection of petrochemical vessels", in "Emerging Technologies in NDT", Editors D. Van Hemelrijck, A. Anastasopoulos, N. Melanitis, *Proceedings 3rd International Conference On Emerging Technologies In Non Destructive Testing*, 26–28 May 2003, Thessaloniki, A. A. Balkema, Netherlands 2004, pp. 167-172.
- [17] Anastasopoulos A., 2004, "Pattern Recognition Techniques for Acoustic Emission based Condition Assessment of Static Equipment in the Refining Industry", *Progress in Acoustic Emission XII*, JSNDT, pp.411-418.
- [18] Tsimogiannis A., Anastasopoulos A., Kouroussis D., 2002, "Stainless Steel Vessel, Tank and Pressure Equipment Structural Integrity Evaluation", 2nd Balkan Conference of B.S.N.D.T. Athens, November 2, 2002.
- [19] M.F.Carlos, D.Wang, S.Vahaviolos, A. Anastasopoulos, "Advanced Acoustic Emission for On-stream Inspection of Petrochemical Vessels", *Proceedings of the 3rd International Conference on Emerging Technologies in NDT*, A. A. Balkema, Netherlands 2004, ISBN 90 5809 645 9 (Volume)-. 90 5809 645 7(CD), pp. 167-172.
- [20] Noesis V9, Pattern Recognition Software, Mistras Group Hellas ABEE.
- [21] Aewin Software for Express-8 E5.90, Mistras Group Inc., U.S.A.

55 - The influence of source depth and source-to-sensor distance on the AE signal characteristics of damaging events in thin-walled CFRP laminates

Benjamin Kelkel¹, Julia Vogtmann¹, Martin Gurka¹

¹ Institut für Verbundwerkstoffe GmbH, Kaiserslautern, Erwin-Schrödinger-Straße,
67663 Kaiserslautern

Abstract:

The identification of damaging events in fiber-reinforced plastics (FRP) based on their acoustic emissions (AE) has been a vivid field of research for more than 25 years. Damage classification has been carried out by correlating damage patterns with single or multiple features from the time and frequency domain of the corresponding AE. Features such as maximum amplitude, peak frequency and Weighted peak frequency were used as indicators to distinguish between the various damaging events in FRP. However, classification results among authors partly contradicted each other and transferability of results has therefore been questioned. Besides the differences in measurement equipment (e.g. sensor, amplifier) and specimen design (e.g. geometry, layup) the effect of source depth and source-to-sensor distance on the resulting signal characteristics has been pointed out as another possible cause for the ambiguity in classification results. In this study, acoustic emissions are systematically produced in various depths and distances to the AE sensors during quasi-static tensile testing of bidirectional CFRP laminates with 0/90/0 and 90/0/90 layup in order to investigate the influence of source depth and source-to-sensor distance on the signal characteristics of fiber and matrix fracture. The results underline the impact of source depth and source-to-sensor distance on the resulting AE features and visualize the limitations of AE for damage classification in CFRP.

1. Introduction

Multiaxial carbon fiber reinforced plastics (CFRP) show gradual failure characteristics with high complexity due to their inherent heterogeneous structure and the various types of damaging mechanisms. Understanding this failure process is the key for exploiting the full potential of CFRP for structural lightweight applications. Acoustic emission (AE) analysis has been utilized to characterize damage progression through the detection and analysis of released acoustic emissions from crack initiation and development during mechanical testing. Source identification has been realized through the correlation of single or multiple features from the time and frequency domain of released acoustic emissions with the occurring damaging mechanisms [1-7]. In this context, unsupervised and supervised clustering methods such as k-means or self-organizing maps have been commonly utilized to find similarities in extracted features in a multidimensional feature space and thereby identify the acoustic signatures of damaging mechanisms [8,9]. However, the transferability of the findings has been questioned since ambiguous results for the acoustic signatures of damaging modes such as fiber and matrix fracture have been published [10]. Recent studies pointed out the importance of the source-to-sensor distance and source depth on the acoustic footprint of matrix cracks in thin-walled CFRP [10-12]. They proved that matrix cracks can excite low- as well as high-frequent

acoustic emissions depending on the source depth. This contradicts the general believe that only fiber cracks will produce acoustic emissions with high frequency content. The cause lies in the excitation of the fundamental guided wave modes and their characteristics. Whereas a spontaneous in-plane deformation in the center plane of a plate results in a symmetric wave mode, an in-plane excitation outside the plane of symmetry will yield a dominant antisymmetric wave mode. Since both modes vary in attenuation, wavelength and group velocity, AE signal analysis with a constant time window will result in variations in frequency content and extracted parameters. Hamstad et. al simulated this change in modal content in an aluminum plate and thereby proved the importance of source depth on the resulting acoustic wave [13]. Maillet et. al pointed out that limitations have to be given regarding the source-to-sensor distance in order to allow for valid damage classification in CFRP [11]. The strong attenuation of the acoustic waves in CFRP has a major impact on the frequency content of the detected waves and thereby impedes source identification.

This study focusses on the influence of source-to-sensor distance and source depth on the acoustic waves and damage classification. Specimens are designed to systematically produce fiber and matrix fracture during quasi-static tensile loading in various depths and distances to the sensors.

2. Description of work

Specimen

Mechanical testing was performed on CFRP laminates with 0/90/0 and 90/0/90 layup that were manufactured with SGL Prepreg T700 12K 50C/EP322 according to the recommended cure cycle. The layup was chosen to systematically produce fiber break and transverse matrix cracking in different depths during tensile loading in 0° direction. Based on the design from [14] the specimens were cut on a CNC milling machine to the dimensions shown in figure 1. The tailored shape thereby promotes the occurrence of damaging events and respective acoustic emissions in the mid-section. The nominal thickness of the specimens was 0.73 ± 0.03 mm with a fiber volume content of around 53%. Tapered (+45/-45)_s GFRP laminates were used as end taps in order to avoid early failure in the gripping area.

Experimental Setup

Mechanical testing was performed on a universal testing machine with hydraulic clamps. The specimens were fixed with a clamping length of 215 mm and loaded in tension with a rate of 1 mm/min. AE analysis was performed with Vallen AMSY-5 system and four AE Sensors. The inner VS900 sensors (1 & 2) were used for evaluation while the outer VS150 sensors (3 & 4) served as guards to filter noise from the gripping area. The AEP4 was set up as preamplifier for every channel with a gain of 34 dB. The sensors were coupled with silicon grease and fixed with spring clamps.

For data acquisition, a sample rate of 10 MS/s (0.1 μ s) with 4096 samples per set and 1024 pre-trigger samples was selected. Hit definition was based on a fixed Threshold of 60dB and a duration discrimination and rearm time of 100 μ s. Frequency evaluation was constrained through a bandpass filter from 25 to 850 kHz.

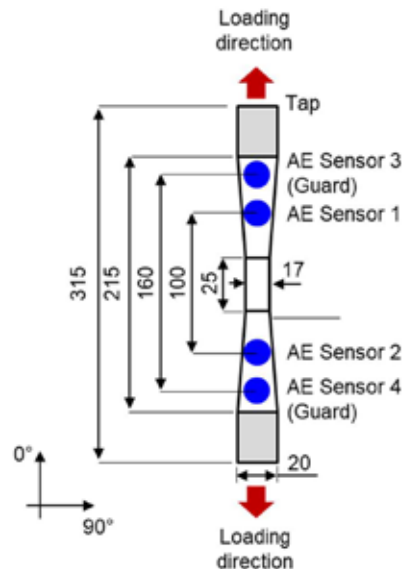


Figure 1: Specimen dimensions and experimental setup for the quasi-static tensile testing of CFRP coupons

Data Evaluation

Acoustic events were defined based on differences in time of arrival between triggering channels. For event localization, the threshold-based arrival time were adjusted through the Akaike Information criterion (AIC) picker [15]. The S0 mode was assumed to be the triggering mode of each event with an estimated velocity of 2500 and 5000 m/s in the 0° direction for the 90/0/90 and 0/90/0 specimen respectively. Data evaluation was constrained to the area between the inner sensors. Acoustic emissions outside this area were filtered out by considering only those events that were localized in this area and triggered one of the inner sensors (1 & 2) first. Feature extraction was performed with the remaining events in the frequency domain based on the Fast Fourier Transform of the time signal in a fixed evaluation window that spanned 1536 samples, starting 512 samples before the trigger and ending 1024 samples after. The features are based on Sause et. al [7] and are listed in table 1. In order to identify the damaging mechanisms, a cluster analysis was performed in the AE feature space by fitting a variable number of gaussian mixed models to the data set. The definition of the number of gaussians was based on the results of former work [7,8].

AE Features	Abbreviation	Unit
Partial Power 1, 0 to 200 kHz	PP1	-
Partial Power 2, 200 to 400 kHz	PP2	-
Partial Power 3, 400 to 600 kHz	PP3	-
Partial Power 4, 600 to 800 kHz	PP4	-
Partial Power 5, 800 to 1000 kHz	PP5	-
Frequency centroid	f_c	kHz
Peak frequency	f_p	kHz
Weighted peak frequency	f_{wp}	kHz

Table 1: Extracted Features from the frequency domain of AE signals (See Reference [7])

3. Results

Influence of source depth

Among the extracted AE features, the combination of Partial Power 1 with Weighted peak frequency was found to visualize patterns in the data sets the best way. The results of the cluster analysis for the data sets of both specimen types can be seen in figure 2. Only the features of the first hit of each event were selected for analysis. Three clusters could be identified for the 0/90/0 specimen, whereas four clusters were visible in the 90/0/90 data set. However, after investigating the time and frequency domain of signals from cluster 3, it was found that low frequency noise and electromagnetic interference were responsible for the formation of this additional cluster of 90/0/90. Cluster 3 was therefore not considered for further analysis.

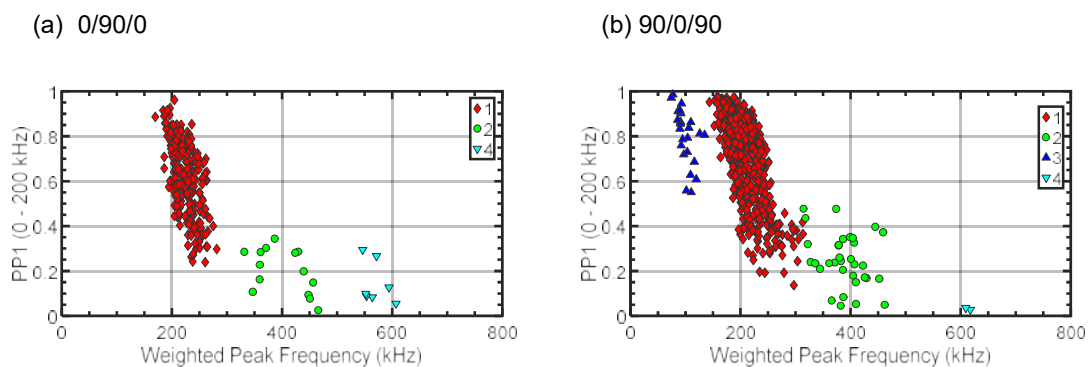


Figure 2: Signal classification through AE Features Partial Power 1 (-) and Weighted peak frequency (kHz) of 1st Hit of events for specimen 0/90/0 (a) and 90/0/90 (b) with color coded classes

The partitions of both data sets resemble each other. The shapes as well as the positions of clusters 1, 2 and 4 are similar for specimen 0/90/0 and 90/0/90. However, the quantity of AE data from each cluster differs as can be seen in figure 3 on a logarithmic scale. Whereas specimen 90/0/90 shows a higher number of events in classes 1 and 2, there are more events of class 4 found for specimen 0/90/0.

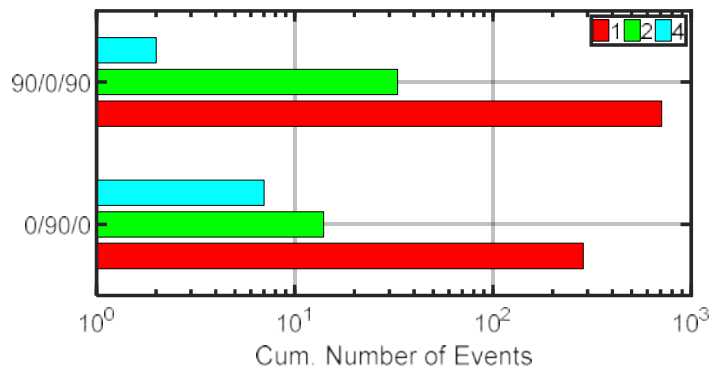
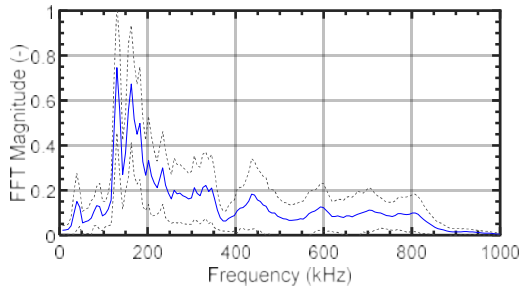


Figure 3: Cumulative number of events in the classes 1, 2 and 4 for the 90/0/90 and 0/90/0 specimen

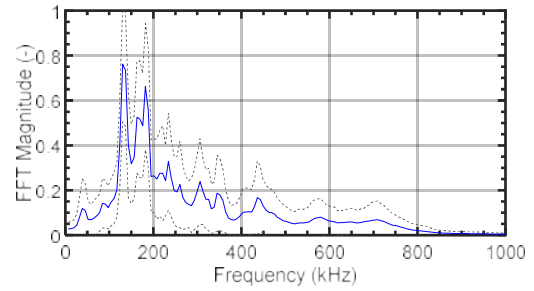
In the next step, the frequency spectra of all three classes were inspected furthermore. For comparability, a representative spectrum for each class was created by standardizing every single spectrum by its maximum value and averaging these spectra class wise. The results can be seen in figure 4 where the average spectra for each class (blue line) are visualized along with their standard deviation (black dotted line) for both specimens.

Classes 1 and 2 of both specimens show a similar frequency distribution. However, specimen 0/90/0 shows more magnitude in the frequency region above 800 kHz in both classes. This is highlighted furthermore in figure 5, where Partial Power 5 is displayed against Weighted peak frequency. In the frequency spectra of class 4 additional dissimilarities can be found between both specimens. Whereas some peaks can be found in both spectra, specimen 90/0/90 shows one pronounced peak between 550 and 600 kHz that is not as prominent in specimen 0/90/0. Furthermore, there is no hard drop in magnitude after the peak at around 700 kHz for the 90/0/90 specimen. Instead, it seems like there are multiple peaks following the major peak at 700 kHz where there is only one around 800 kHz for the 0/90/0 specimen.

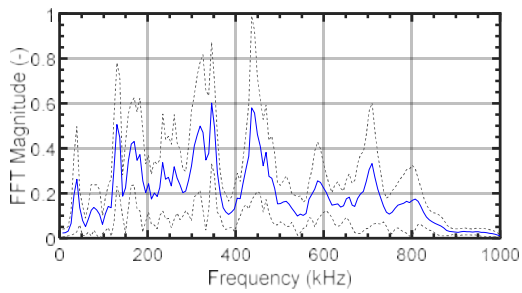
(a) Class 1, 0/90/0



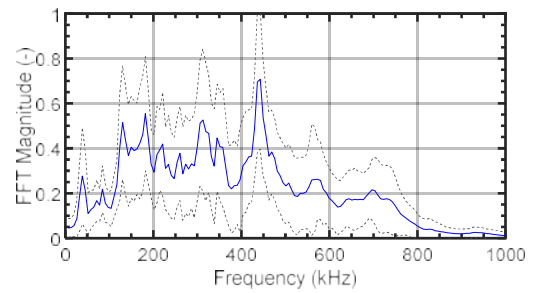
(d) Class 1, 90/0/90



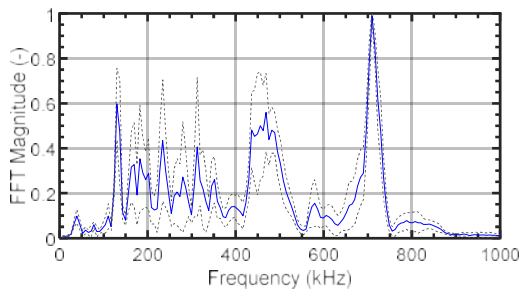
(b) Class 2, 0/90/0



(e) Class 2, 90/0/90



(c) Class 4, 0/90/0



(f) Class 4, 90/0/90

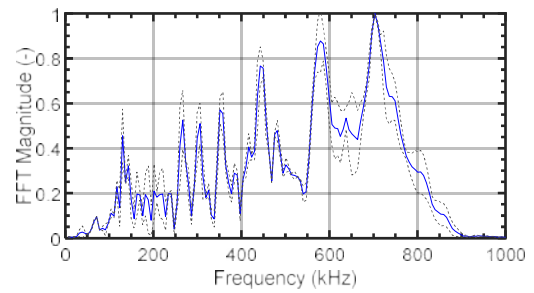


Figure 4: Standardized and averaged Fourier transforms of acoustic emission signals (blue line) from classes 1, 2 and 4 from specimen 0/90/0 (a,b,c) and 90/0/90 (d,e,f) along with their standard deviation (black dotted line)

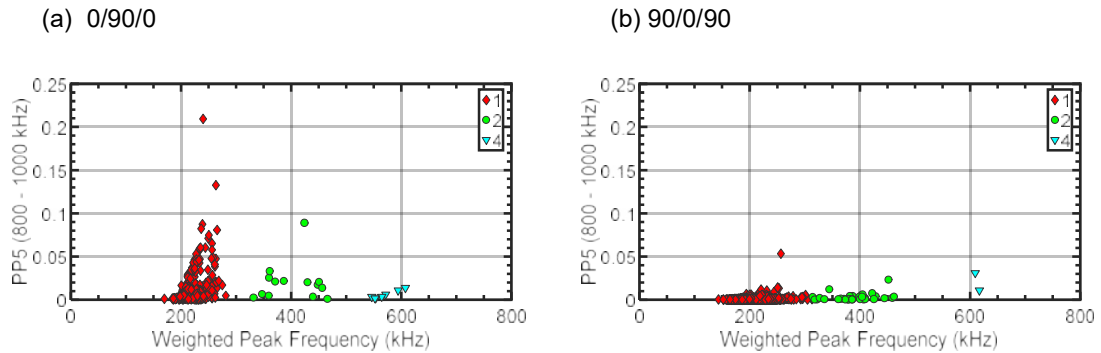


Figure 5: Partial Power 5 (-) and Weighted peak frequency (kHz) of 1st Hit of events for specimen 0/90/0 (a) and 90/0/90 (b) with color coded classes

Quasi-static tensile testing – Influence of source-to-sensor distance

The influence of source-to-sensor distance on the ability to identify clusters in AE features and distinguish between damaging mechanism can be seen in figure 6 where Partial Power 1 and Weighted peak frequency are displayed for the first and second Hit of an event that differ in 100 mm propagation path at maximum. Except for cluster 1, the shape and position of the clusters varies. An increase in Partial Power 1 and a decrease in Weighted peak frequency can be observed for the AE events of cluster 2 and 4. As a result, separation between the clusters gets lost and events would have gotten misclassified if AE features from the 2nd Hit of each event were taken for cluster analysis.

For a closer look on the development of AE features the change in Weighted peak frequency as a function of source-to-sensor distance is illustrated in figure 7. For both specimens a decrease in Weighted peak frequency can be observed for events from the classes 2 and 4 with increasing source-to-sensor distance. These charts allow the estimation of a maximum source-to-sensor distance for proper cluster separation. In the case of the 90/0/90 specimen, this critical distance lies between 60 and 80 mm. For the 0/90/0 specimen, the critical distance is hard to estimate due to the lack of data points between 20 and 80 mm. In contrast to the events from other classes, events from class 1 don't show a trend in the change of Weighted peak frequency in relation to source-to-sensor distance.

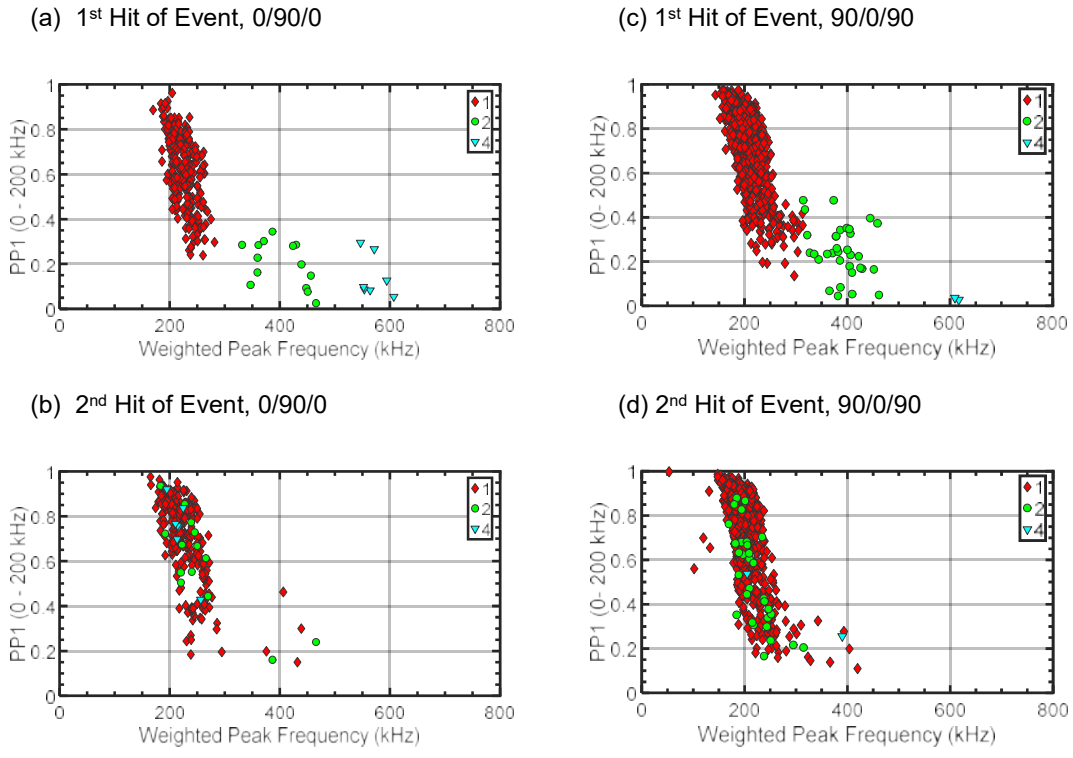


Figure 6: Signal classification through AE Features Partial Power 1 and Weighted peak frequency of 1st and 2nd Hit of events for specimen 0/90/0 (left side) and 90/0/90 (right side)

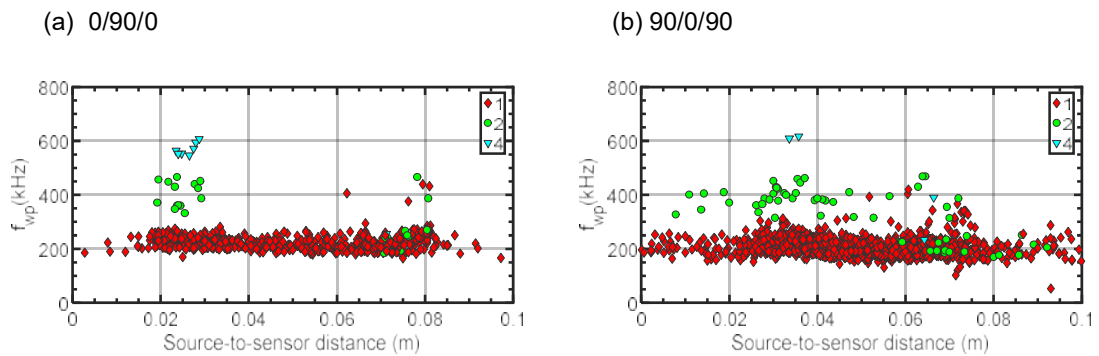


Figure 7: Change in Weighted peak frequency as a function of source-to-sensor distance for specimen 0/90/0 (left side) and 90/0/90 (right side). The colors represent the classes

4. Discussion

Influence of source depth

According to several authors the source depth influences modal as well as frequency content of the resulting acoustic emissions and should therefore affect the acoustic signature of fiber break and matrix cracking in the selected specimen layups [10-13]. Regarding class 1 and 2 a higher frequency content was observed for the events from 0/90/0 compared to 90/0/90. If we assign cluster 1 with matrix fracture as suggested by Sause et. al [7], the change in frequency content of cluster 1 could be attributed to the variation in source depth of transverse matrix cracking. The reason for an increase in frequency content could be found in the change of modal content. According to Hamstad et. al, an in-plane excitation outside of the axis of symmetry leads to the formation of a dominant antisymmetric wave mode whereas an in-plane excitation in the plane of symmetry results in a purely symmetric mode [13]. Since transverse matrix cracking represents an in-plane source for wave excitation, the resulting acoustic emission should carry a dominant antisymmetric mode in the 90/0/90 and a dominant symmetric mode in the 0/90/0 specimen. By looking at the continuous wavelet transforms of exemplary events from class 1 of both specimens, one can see the differences in modal content.

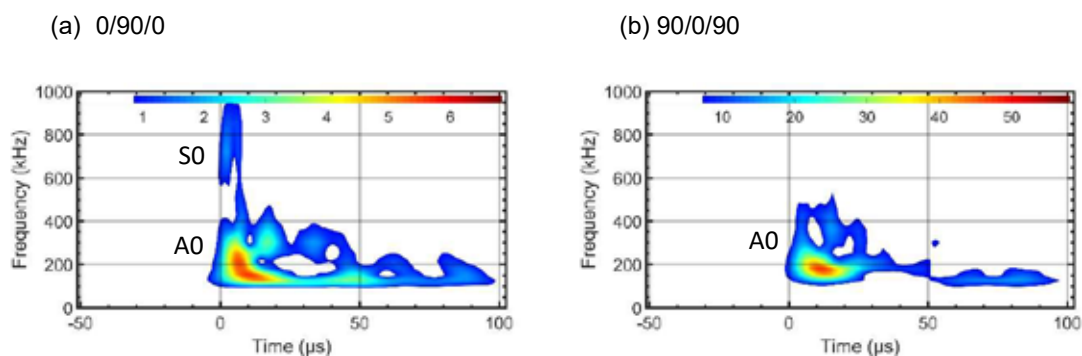


Figure 8: Continuous wavelet transforms of exemplary signals of class 1 from specimen 0/90/0 (left side) and 90/0/90 (right side)

A change in modal content doesn't have to result in a change in frequency content. However, there are three reasons for it:

1. Both modes show differences in dispersion behavior which affect the temporal duration of the wave package as a function of propagation path. When taking a constant time window for AE evaluation and feature extraction, the result will depend on the excited mode and the source-to-sensor distance, leading to differences in frequency content and related features.
2. There are differences in the attenuation behavior of the symmetric and antisymmetric wave mode that will lead to variations in frequency content depending on the source-to-sensor distance and the propagation direction in CFRP [16-18]
3. Both modes show a different wavelength at a given frequency, which leads to variations in the sensors response due to the aperture effect [19]. Since the wavelength is in the order of the sensor diameter this can have a significant effect on the frequency content and the resulting features.

In general, the combination of all three effects will determine the resulting changes in frequency content when modal content of the excited wave varies.

In this study, transverse matrix cracking in the 0/90/0 specimen lead to a higher magnitude above 800 kHz compared to the 90/0/90 specimen. These changes in frequency content could result from the formation of a strong S0 mode that is excited through transverse matrix cracking in the center layer of the 0/90/0 specimen. Since the S0 mode shows a lower attenuation in CFRP compared to the A0 mode [16-18], the high frequency content in the acoustic signal is more likely to be sustained over the propagation path. Furthermore, the S0 mode shows a higher wavelength at a given frequency compared to the A0 mode which results in a higher critical frequency for signal attenuation due to the aperture effect of the piezoelectric sensor.

Regarding the events of cluster 4, we also observed changes in the frequency content between both specimen. If we assign cluster 4 to fiber breaking, as suggested by Sause et. al [7], we can explain the changes in frequency content again with a change in modal content that results from the variation of source depth of fiber breaking. For the 90/0/90 specimen fiber breaking takes place predominantly in the middle layer (the plane of symmetry), promoting the formation of a symmetric wave mode whereas fiber breaking in the 0/90/0 specimen should excite a more prominent antisymmetric wave mode. Again, differences in the attenuation factors as well as in wavelengths of both modes are responsible for the observed changes in frequency content.

Due to the aperture effect and the differences in wavelength of both modes, different peaks in the frequency spectra can form from a broadband signal that can be assigned to the S0 and A0 mode respectively. This was observed in figure 4 and can be validated by looking at exemplary signals in more detail. If the sensor dimensions and the wavelength of the modes are known, the characteristic peaks could be determined and serve as indicators for the S0 to A0 ratio that could again yield information about the source depth.

Influence of source-to-sensor distance

In figure 7, events from classes 2 and 4 showed a decreasing trend in Weighted peak frequency with increasing source-to-sensor distance. After around 60 to 80 mm of propagation path in the 90/0/90 specimen, acoustic events from the two classes could not be separated from events of class 1 anymore. This could result from the strong attenuation of lamb waves in CFRP compared to metallic structures [16-18].

The Weighted peak frequency of events from each class is affected differently by the source-to-sensor distance. The highest loss in Weighted peak frequency can be observed for events from class 4 for both specimen. This is due to the higher frequency content in acoustic signals of class 4 because attenuation increases with frequency. The events of class 1 seemed to be unaffected by the source-to-sensor distance. This behavior can be explained with the strong resonance of the AE sensors around 140 kHz. The low-frequency events of class 1 are mainly characterized by this resonance which represents a stable peak frequency over the source-to-sensor distance. Hence, frequency centroid shows only slight changes as well so that the Weighted peak frequency of events from class 1 stays stable over the source-to-sensor distance.

To quantify the reduction in Weighted peak frequency as a function of source-to-sensor distance and thereby define limitations for source identification in CFRP, more specimens will be included in future analysis.

5. Conclusion

In this study, the influence of source depth and source-to-sensor distance on acoustic signal characteristics of damaging events in CFRP was studied. The specimens were designed to promote the generation of fiber breaking and transverse matrix cracking during quasi-static tensile loading in various depths and distances to the sensors. The authors could show that the source depth as well as the source-to-sensor distance have a significant impact on the frequency content of the acoustic signals. Regarding the influence of source depth, a variation of S0 to A0 ratio in relation to source depth was suggested to be the cause for the observed changes in frequency spectra. Both modes vary in group velocity, wavelength and attenuation behavior and therefore yield different frequency spectra. The role of the aperture effect was underlined in this context. In terms of source-to-sensor distance, the authors could show that propagation distances of 60 to 80 mm are sufficient for misclassification of AE signals in the CFRP specimens under investigation. In the future work, the limitations for damage identification will be investigated in more detail in order to increase the awareness of the influences of source depth and source-to-sensor distance in AE analysis.

References:

- [1] Crivelli, D., Guagliano, M., Eaton, M., Pearson, M.R., Al-Jumaili, S.K., Holford, K.M., Pullin, R., Localisation and identification of fatigue matrix cracking and delamination in a carbon fibre panel by acoustic emission, *Composites: Part B*, Vol. 74, 2015, pp. 1-12
- [2] McCrory, J.P., Al-Jumaili, S.K., Crivelli, D., Pearson, M.R., Eaton, M., Featherston, C.A., Guagliano, M., Holford, K.M., Pullin, R., Damage classification in carbon fibre composites using acoustic emissions: A comparison of three techniques, *Composites: Part B*, Vol. 68, 2015, pp. 424-430
- [3] Gutkin, R., Green, C.J., Vangrattanachai, S., Pinho, S.T., Robinson, P., Curtis, P.T., On acoustic emission for failure investigation in CFRP: Pattern recognition and peak frequency analyses, *Mechanical Systems and Signal Processing*, Vol. 25, 2011, pp. 1393-1407
- [4] Kempf, M., Skrabala, O., Altstädt, V., Acoustic emission analysis for characterization of damage mechanisms in fibre reinforced thermosetting polyurethane and epoxy, *Composites: Part B*, Vol. 56, 2014 pp. 477-483
- [5] Liu, P.F., Chu, J.K., Liu, Y.L., Zheng, J.Y., A study on the failure mechanisms of carbon fiber/epoxy composite laminates using acoustic emission, *Materials and Design*, Vol. 37, 2012, pp. 228-235
- [6] Martínez-Jequier, J., Gallego, A., Suárez, E., Juanes, F.J., Valea, Á, Real-time damage mechanisms assessment in CFRP samples via acoustic emission Lamb wave modal analysis, *Composites: Part B*, Vol. 68, 2015, pp. 317-326

- [7] Sause, M.G.R., Müller, T., Horoschenkoff, A., Horn, S., Quantification of failure mechanisms in mode-I loading of fiber reinforced plastics utilizing acoustic emission analysis, *Composites Science and Technology*, Vol. 72, 2012, pp. 167-174
- [8] Sause, M.G.R., Gribov, A., Unwin, A.R., Horn, S., Pattern recognition approach to identify natural clusters of acoustic emission signals, *Pattern Recognition Letters*, Vol. 33, 2012, pp. 17-23
- [9] Godin, N., Huguet, S., Gaertner, R., Integration of the Kohonen's self-organising map and k-means algorithm for the segmentation of the AE data collected during tensile tests on cross-ply composites, *NDT&E International*, Vol. 38, 2005, pp. 299-309
- [10] Baker, C., Morscher, G.N., Pujar, V.V., Lemanski, J.R., Transverse cracking in carbon fiber reinforced polymer composites: Modal acoustic emission and peak frequency analysis, *Composites Science and Technology*, Vol. 116, 2015, pp. 26-32
- [11] Maillet, E., Baker, C., Morscher, G.N., Pujar, V.V., Lemanski, J.R., Feasibility and limitations of damage identification in composite materials using acoustic emission, *Composites: Part A*, Vol. 75, 2015, pp. 77-83
- [12] Oz, F.E., Ersoy, N., Lomov, S.V., Do high frequency acoustic emissions events always represent fibre failure in CFRP laminates?, *Composites: Part A*, Vol. 103, 2017, pp. 230-235
- [13] Hamstad, M.A., O' Gallagher A., Gary J., A wavelet transform applied to acoustic emissions signals : Part 1 : Source identification, *Journal of Acoustic Emission*, Vol. 20, 2002, pp. 39-61
- [14] AVK Expert task force: Standardization of continuous fibre reinforced thermoplastics
- [15] Kurz, J.H., Grosse, C.U., Reinhardt, H.W., Strategies for reliable automatic onset time picking of acoustic emissions and of ultrasound signals in concrete, *Ultrasonics*, Vol. 43, 2005, pp. 538-546
- [16] Neau, G., Lamb waves in anisotropic viscoelastic plates. Study of the wave fronts and attenuation, Phd Thesis, 2003
- [17] Calomfirescu, M., Lamb Waves for Structural Health Monitoring in Viscoelastic Composite Materials, Phd Thesis, 2008
- [18] Su, Z., Ye, L., Identification of Damage Using Lamb Waves, *Lecture Notes and Applied Computational Mechanics*, Vol. 48, 2009
- [19] Miller, R.K., McIntire, P., American Society for Nondestructive Testing, *Nondestructive testing handbook (2nd Edition)*, Vol. 5, 1987

57 - Acoustic Emission behaviour on CFRP with curved fibers

Yoshihiro MIZUTANI¹, Takeshi ASHIZAWA¹, Nobuyuki TOYAMA², Akira TODOROKI¹

¹ School of Engineering, Department of Mechanical Engineering, Tokyo Institute of Technology, JAPAN

² Research Institute of Measurement and Analytical Instrumentation, National Institute of Advanced Industrial Science and Technology (AIST), JAPAN

Abstract:

Application of CFRP to the industrial field is expanding and acoustic emission testing (AT) is utilized for some applications. In this paper, possible problems that may cause when AE testing is applied to CFRP components with curved fibers are discussed based on the previous author's paper about ultrasonic propagation in CFRPs. It was concluded that the AE amplitude has a potential to be highly affected by the location of AE sensors on the components. It is also noted that general AE source location algorithm cannot be applied for this kind of materials in some cases since shortest path from AE source to AE sensor are varied with the position on the components

1. Introduction

Carbon fiber reinforced plastics (CFRP) are widely used for structural components in industrial fields. Acoustic emission testing (AT) is sometimes used for structural health assessment of CFRP components together with other inspection methods. As CFRP is anisotropic material, AE propagation behavior is different from that in isotropic material. Figure 1 shows propagation direction of phase velocities and group velocities of AE in CFRPs when AE propagates as bulk waves. Relationship between phase velocities and group velocities of bulk wave can be found in the basic acoustic textbook, such as reference 1. Rhee et al. [2] reported that this relationship could be applied for lamb waves when Fd (Frequency \times Thickness) value is less than 0.7 for S_0 -mode, and between 0.2-0.7 for A_0 -mode. The authors investigated amplitude of Lamb wave AE that propagates in CFRP according to this relationship [3].

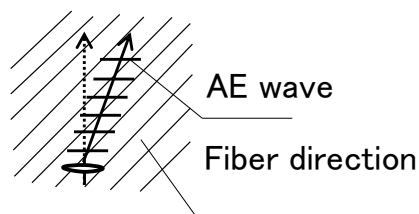


Figure 1 Propagation direction of phase velocities and group velocities in CFRPs. Dotted arrow shows phase velocities direction, Solid arrow shows group velocities direction

Figure 2 shows normalized amplitude distributions of Lamb wave AE generated with dipole source in Cross-ply CFRP [0/90]_{2s} with $Fd=0.64$ for S_0 -mode and $=0.32$ for A_0 -mode. Material properties used for the calculation are shown in Table 1. As shown in the figures, amplitudes of Lamb wave AE highly change with propagation direction and this phenomenon is different from that in isotropic materials.

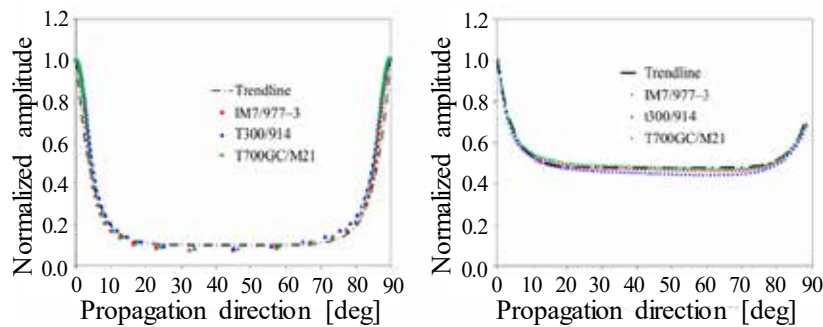


Figure 2 Relationship between normalized amplitude and propagation direction of Lamb wave AE in cross-ply CFRP generated with dipole source. (Left: $Fd=0.64$ for S_0 -mode, Right: $Fd =0.32$ for A_0 -mode)[3]

Table 1 Stiffness Matrix used for calculating amplitude distributions

	C_{11}	C_{22}	C_{33}	C_{23}, C_{32}	C_{31}, C_{13}	C_{12}, C_{21}	C_{44}	C_{55}, C_{66}
IM7/977-3	178.2	14.44	14.44	8.119	8.347	8.347	3.161	6.1
T300/914	143.8	13.3	13.3	6.5	6.2	6.2	3.6	5.7
T700GC/M21	123.44	11.54	11.54	6.35	5.55	5.55	2.6	4.6

Unit: GPa

On the other hand, there are curved structures made of CFRPs as shown in Figure 3. There are several published papers discussing elastic wave propagation behavior in CFRP with curved fibers [4-6]. However, these studies focused on guided waves and the CFRP specimens are curved with curvature of structures. Then the elastic waves are affected not only by curved fibers but also by curved boundaries of structures. The authors investigated elastic wave behavior of thick CFRP with curved fiber by both the numerical analysis and by the experiment [7]. In this paper, the results from reference 7 are introduced and the effects for the AE testing are discussed.

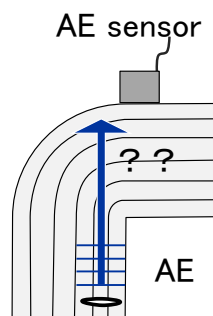


Figure 3 Thick CFRP component with curved carbon fibers

2. Numerical simulation in reference 7

In the reference 7, 2D analyses of bulk elastic wave propagation in CFRP with curved fibers were conducted using the finite difference method. A plane strain condition was assumed. The numerical simulations were performed in the cylindrical ($r-\theta$) coordinate system to incorporate the curvature of the principal axis. The fiber direction is correspond with the θ -axis of the cylindrical coordinate system. Figure 4 shows the analysis model. r_1 , r_2 , Δr , $\Delta\theta$ in the figure are 0.1[m], 1[m], 1.75×10^{-3} [m] and 1.75×10^{-3} [rad] respectively. Figure 5 shows description of AE source used for the simulation. Detailed condition of the simulation is shown in reference 7.

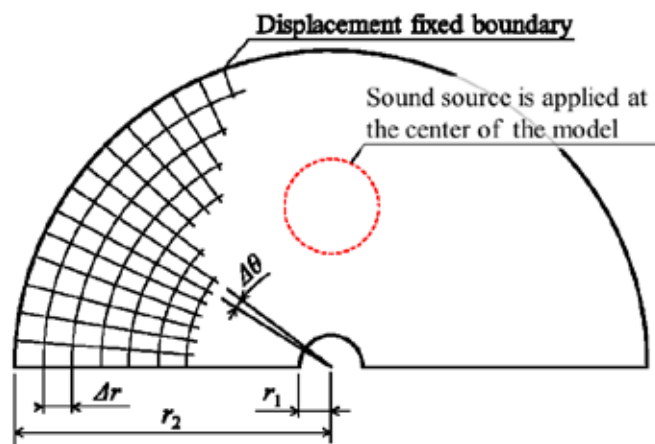


Figure 4 Analysis model of elastic wave in the cylindrical coordinate system [7]

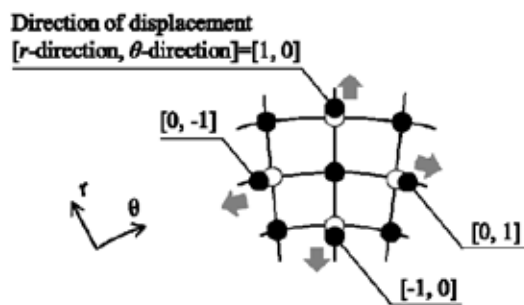
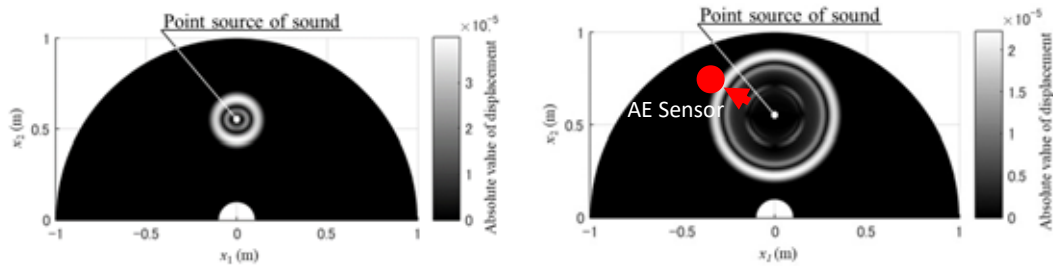


Figure 5 Description the quasi-point source of sound [7]

3. Amplitude of AE

Figure 6 and 7 shows simulation result from reference 7. The figures show the absolute value of displacement in color. Figure 6 shows results for isotropic aluminum specimen and 7 for CFRP with curved fibers which explained in chapter 2. Direction of continuous fibers are shown in the figure. In the original our paper, only the wave propagation was focused and acoustic emission issue was not taken into account. Then, in this paper, we assume the point sources in the figures as the source of AE and discuss the amplitude dependence to the location of AE sensors.

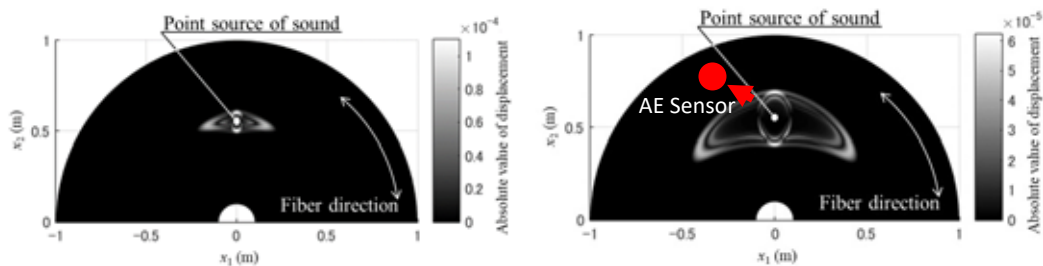
As shown in the figure 6, when the material is isotropic aluminum, AE propagate concentrically from the source. As a result, when the AE is detected by AE sensors, AE amplitude (dB_{AE}) is same when the distance between the source and AE sensor is constant.



(a) 8000 steps, 26.6 μ s (b) 18000 steps, 59.8 μ s

Figure 6 The result of the numerical simulation for aluminum. The point sound source was applied at the center of the model [7]

On the other hand, as shown in Fig. 7, when the material is CFRP with curved fibers, AE generated from the source propagates under the influence of the curved fiber and does not propagate concentrically. Though, AE amplitude detected by AE sensor highly influenced by the location of AE sensor.



(a) 8000 steps, 26.6 μ s (b) 18000 steps, 59.8 μ s

Figure 7 The result of the numerical simulation for CFRP, T700GC/M21. The point sound source was applied at the center of the model [7]

When the material is an isotropic material as shown in Fig. 6, the AE signal amplitude depends only by the magnitude of the damage at the source and the distance from the source to the AE sensor, so the AE signal amplitude is used as an important AE parameter for evaluating scale of fractures at the source. However, when the material is an anisotropic material as shown in Fig. 7, the AE signal amplitude varies greatly depending not only by the

propagation distance but also by the position of the AE sensor, so special caution must be taken when using the AE signal amplitude for evaluating the damage scale.

It is also noted that, special care is required to determine the location of AE sensor since AE is difficult to transmit in directions other than along the fibers. For example, when considering a CFRP component having curved fibers with drilled hole as shown in Fig.8, it is recommended to attach the AE sensor at position A or B rather than position C and D as AE propagates along fibers. Such consideration is particularly necessary when the direction of the fiber does not follow the outer shape of the structure, and it is assumed that it will become more important issue in the future as the number of continuous fiber CFRP products made with 3D printers increases [8].

Even the stacking sequence of CFRP components are quasi-isotropic, such as $[0_i/45_i/90_i/45_i]_{sym.}$, similar consideration may necessary when the wavelength of the AE is much smaller than the thickness of the components as AE propagates only the upper surface of the components.

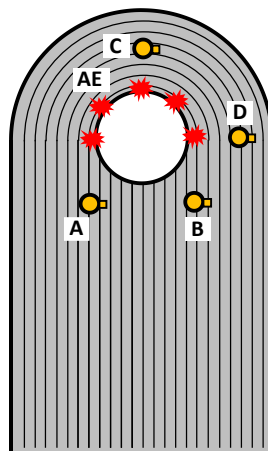


Figure 8 Suitable AE sensor locations (A and B) on CFRP with curved fibers

4. Source location of AE

Source location of AE is important issue for AE testing. Even the fibers in CFRP are straight, special consideration is required for the accurate source location [9][10]. When the CFRP components includes curved fibers, propagation path for the minimum arrival time becomes not the straight line between AE source and AE sensors. It makes difficult to conduct source location in such kind of the components. As in the previous chapter, consider a CFRP in which fibers are arranged concentrically around the origin. Figure 9 comes from reference 11 from author's research group and shows wave front of elastic waves when the waves are

generated not from the origin of the fibers. AE sensor and path-A and -B in the figure are overlapped with original figures. In this paper, the source of the elastic waves (indicated as "Point source of sound" in the figure) is considered as the source of AE. Dotted line in the figure shows shortest path of AE from the source of AE.

When AE sensor is attached at the position in the figure and the material is isotropic, shortest path to arrive AE sensor is path-A in the figure. In such case, it is easy to conduct the source location by traditional source location algorithm. However, in this case (material is CFRP with curved fibers), path-B becomes the shortest path for the AE. Since the shortest path from the source to the AE sensor changes complicatedly depending on the combination of these two parameters, it is difficult to estimate the AE source accurately.

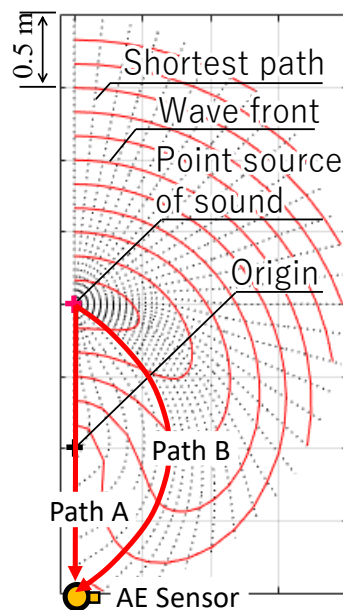


Figure 9 Shortest path for the AE in the CFRP with curved fibers [11]

5. Conclusion

In this paper, based on the previous author's paper of elastic wave propagation analysis in CFRP with curved fibers, we raised the potential problems when the AE testing is conducted for such kind of materials. Followings are main possible problems for the AE testing. It may be required to solve these problems when we apply AE testing for CFRP with curved fibers adequately.

- 1) AE signal amplitude depends not only by the magnitude of damage occurrence at the AE source but also by the positional relationship between the AE sensor and the source
- 2) For an isotropic material, the shortest path that AE reaches from AE source to AE sensors is straight line connecting these two points, although, in a CFRP with curved fibers, shortest path becomes curved line and the pass changes in complicated manner by the position between the AE sensor and the AE source. Though, traditional source location algorithm cannot be applied in this case.

References:

- [1] Auld, B. A., Acoustic fields and waves in solids, 1, 2: John Wiley&Sons Inc., 1973
- [2] Rhee, S. H., Lee, J. K. and Lee, J. J., The group velocity variation of Lamb wave in fiber reinforced composite plate, *Ultrasonics*, Vol. 47, 2007, pp. 55-63.
- [3] Mizutani, Y., Miki, T., Suzuki, Y. and Todoroki, A., Amplitude of AE propagating in laminated FRP plates, *Progress in Acoustic Emission XVIII*, 2016, pp.491-496.
- [4] Towfighi, S., Kundu T. and Ehsani M., Elastic wave propagation in circumferential direction in anisotropic cylindrical curved plates, *J. Appl. Mech.*, Vol. 69, No.3, 2002, pp.283-291.
- [5] Leutenegger, T. and Dual J., Detection of defects in cylindrical structures using time reverse method and a finite-difference approach, *Ultrasonics*, Vol. 40, 2002, pp.721-725.
- [6] Gsell, D. and Dual J., Non-destructive evaluation of elastic material properties in anisotropic circular cylindrical structures, *Ultrasonics*, Vol. 43, 2004, pp.123-132.
- [7] Ashizawa, T., Mizutani, Y., Toyama, N., Todoroki, A. and Suzuki, Y., Numerical analysis and experimental observation of ultrasonic wave propagation in CFRP with curved fibers, *Composite Structures*, Vol. 194, 2018, pp.316-327
- [8] Matsuzaki, R., Ueda, M., Namiki, M., Jeong, T., Asahara, H., Horiguchi, K., Nakamura, T., Todoroki, A. and Hirano, Y., Three-dimensional printing of continuous-fiber composites by in-nozzle impregnation, *Scientific reports*, 2016, doi: 10.1038/srep23058
- [9] Yamada, H., Mizutani, Y., Nishino, H., Takemoto, M., Ono, K., Lamb wave source location of impact on anisotropic plates, *Journal of AE*, Vol. 18, 2000, pp.51-60
- [10] Kurokawa, Y., Mizutani, Y., Mayuzumi, M., Real-Time Executing Source Location System Applicable to Anisotropic Thin Structures, *Journal of Acoustic Emission*, Vol.23, 2005, pp.224-232
- [11] Ashizawa, T., Numerical simulation to analyze ultrasonic waves in CFRP having concentric fibers, *NIMS Week 2017, academic symposium*, 2017, T83

73 - Use of AE for characterization of damage mechanisms in composite accumulator

Oriane COLAS¹, Catherine HERVE², Christophe BRIANCON¹, Alain HOUSSAIS³

¹ CETIM, 74 route de la Jonelière, 44000 NANTES

² CETIM, 52 Avenue Félix Louat, 60300 SENLIS

³ PARKER OLAER, 16 Rue de Seine, 92700 COLOMBES

Abstract:

This study presents the results of a collective study performed at CETIM for industrials of the hydraulic transmissions profession. The purpose is to develop an accumulator made of composite material, carbon fiber and thermosetting resin, and to characterize the behavior of this accumulator by both static and cyclic pressure tests.

Knowledge of the damage mechanisms evolution occurring during these tests is studied by Acoustic Emission monitoring combined by strain gage measurements.

The AE monitoring results are compared to the failure criteria used in the design model in order to correlate the different damage mechanisms occurring in each layer with the detected AE signals.

Further mechanical tests were carried out on samples taken from accumulators tested at different pressure levels. Visual observations by video camera combined with AE data recording during these tests validated the identification and the progression of the different damage mechanisms in different layers.

1. Introduction

In the scope of hydraulic transmission needs, a study is currently conducted at CETIM to better understand damage mechanisms of accumulators made from carbon fiber-reinforced thermosetting matrix. For that purpose, several accumulators and more specifically their pressure envelopes, have been designed, manufactured and tested. This paper is mainly focused on the results of the static tests. The tests were divided in two parts; operational tests with proof testing at different pressure levels and residual mechanical characterization with tensile tests on samples cut from tested accumulator. The aim of the tests analysis is to characterize the behavior of the structure during the proof test through AE monitoring and strain measurement combined with ultrasonic inspection performed before and after the proof test. The mechanical tests are then performed in order to give the residual strength in axial direction and the damage mechanisms are observed with a camera combined with AE monitoring.

2. Description of work

2.1 Accumulator design

The accumulator is composed of a 5 mm plastic liner, a 6 mm layer of composite material and 2 metallic nozzles. The working pressure of the accumulator is 300 bar. The composite design is made up of 6 different orientation layers (circumferential and helicoïdal layers) containing various ply number. Each ply is composed of epoxy resin and carbon fiber with a fiber volume fraction of 50%.

Six accumulators have been manufactured by filament winding process.

2.2 Proof tests

Different proof pressure levels have been applied in order to analyze their influence on the accumulator damage mechanisms. The tests have been performed at P_s (300bar), $1,5P_s$ (450 bar) and $2P_s$ (600bar) (Table 1). The test device consists of a water booster with a range of 0-1000 bar. The proof test cycle used is presented Figure 1.

Accumulator reference	Proof test pressure (bars)
ESP8	300
ESP9	450
ESP12	600
ESP13	450

Table 1: Proof test description

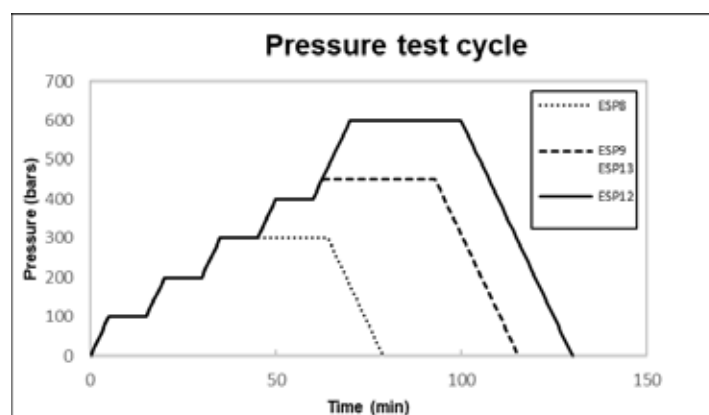


Figure 1: Pressure test cycle

A strain measurement has been performed with 4 unidirectional strain gages located around a circumference on the center of the accumulator (90° apart). The strain measured is the circumferential strain.

All the proof tests are monitored by Acoustic emission. Ten sensors are located on the accumulator as described in Figure 2. They are 150kHz resonant sensors, coupled by cement to the composite surface.



Figure 2: Sensor implantation

Non-destructive inspection is performed before and after the proof test by phased array ultrasonics.

2.3 Mechanical tests

The tensile mechanical tests are performed to determine the residual mechanical characteristics in axial direction on tested accumulators. To do this, specimens are taken from the central part along the axis of the accumulator, their location being determined from AE and ultrasonic inspection results .

The tensile tests are realized with a tensile test machine equipped with self-fastening hydraulic clamps. Tabs are glued on the specimens to the specimens so as to obtain a flat surface in contact with the hydraulic jaws. The test velocity is 1 mm/min according to the ISO527-4, the strain measurement is performed by an extensometer and there is a monitoring by acoustic emission (Figure 3).

These tests do not stress the composite in the main direction of stress induced by internal pressure, i.e. in the circumferential direction. Nevertheless, they provide valuable information on the pressure damage induced in the helicoïdal layers.



Figure 3: Tensile test configuration

3. Results

3.1 Proof tests results

3.1.1 acoustic emission analysis

The first step of the analysis is to evaluate the AE signal evolution during the tests in terms of activity (hit number) and intensity (hit amplitude or energy).

- Global analysis with acoustic energy parameter

It can be seen on Figure 4 that signal energy for high amplitudes signals (superior to 85 dB) increases regularly with the pressure with local acceleration around 150 to 200 bar and after 400 bars (cumulative energy slope changes suddenly after these steps).

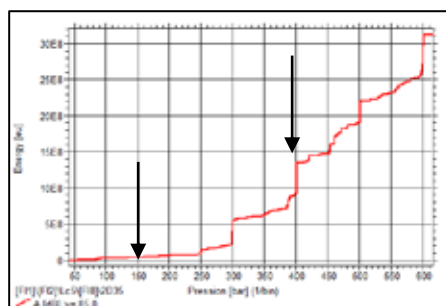


Figure 4: AE cumulative energy for high amplitude signals

These punctual accelerations can be linked to the progression of the damages during the pressure holds. The acceleration for high amplitude signal is sudden compare to lower amplitude signals acceleration (Figure 5). This can be explained by the fact that high amplitude signals correspond to high energy damage phenomena such as fiber strand breaks, which occur randomly.

Another observation linked to the signal amplitude is that for the 4 accumulator the signal amplitude doesn't exceed the following values:

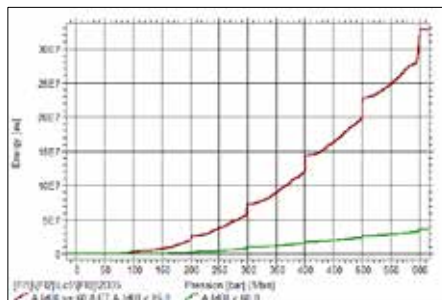


Figure 5: AE cumulative energy for medium (brown) and low (green) amplitude signals

- 70dB for the 100 bar increase
- 80 à 85dB for the 200 bar increase
- 90dB for the 300 bar increase
- 95dB for the 400 bar increase

These characteristics have been observed on all the 4 accumulators. What can be also noted is that the accumulators have the amount of acoustic emission activity related to the same pressure level. The results for 400 bars are shown below in Figure 6.

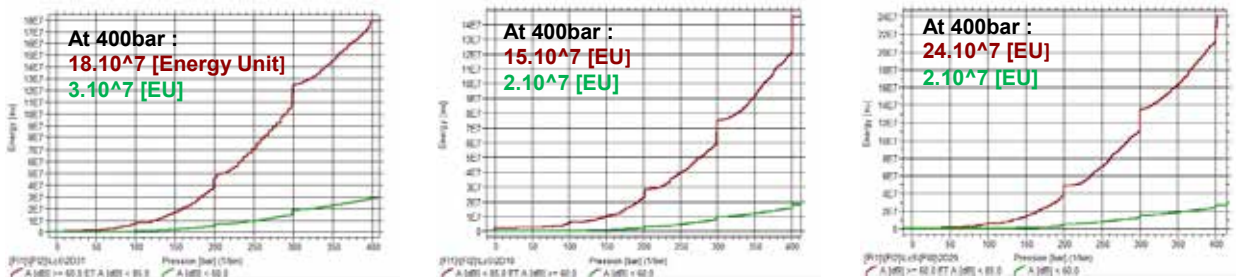


Figure 6: AE cumulative energy for low and medium amplitude signals

Given the energy evolution and the signal amplitude progression, these two parameters could be linked in order to define a damage starting point. This will have to be consolidated by further tests leading to critical damages and their impact on signal energy level.

- Local analysis

Zonal analysis makes it possible to identify the areas where acoustic emission is concentrated. In the conducted tests, several areas were identified, principally on the bottom shell junctions and on the center of the shell (Figure 7). These observations helped us to select the mechanical tests and micrographic observation samples.

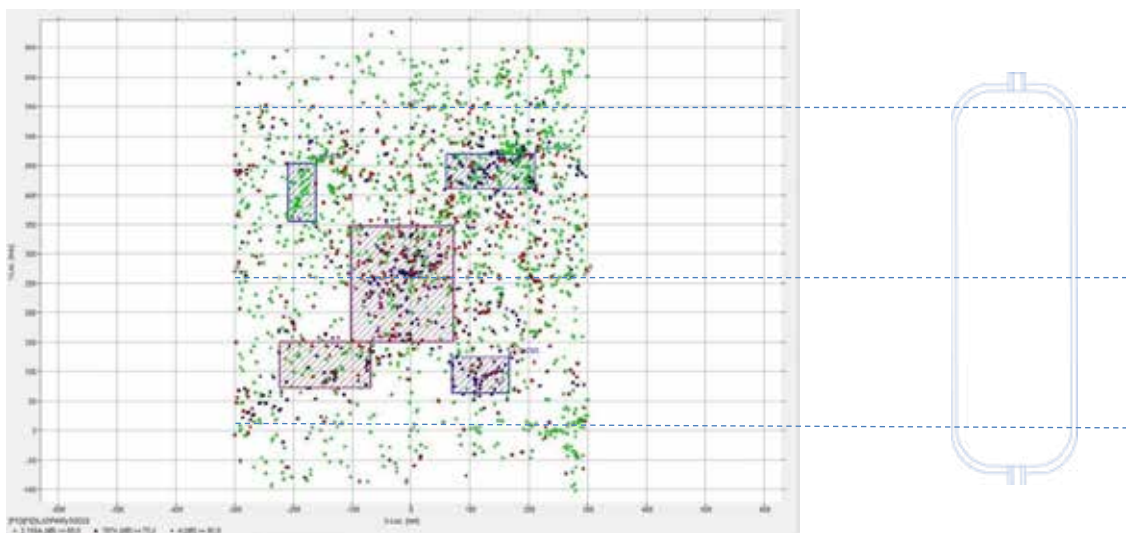


Figure 7: Zonal analysis of the accumulator ESP12

Pressure holds analysis

The AE activity during the different holds (10 min for intermediate holds every 100 bar and 30 min for the final hold) has been analyzed. From the 400 bar steps, the acoustic activity doesn't decrease during the holds but has a stable level. No activity increase was detected during the holds, which means that there is no significant damage progression occurring when the accumulator is stabilized in pressure.

3.1.2 ultrasonic testing analysis

The ultrasonic inspection of the 4 accumulators showed that there was no significant evolution of the indications initially detected, knowing that the purpose of the inspection is to detect defects such as delamination. Moreover, no significant defects created by the proof

test was detected, which means that proof test until 600 bar doesn't lead to severe damages between the composite layers.

3.1.3 micrographic analysis

For the accumulator tested at 300 bar, matrix cracking is observed in the helicoidal layers. A more severe damage is noted in the layer $\pm 10^\circ$ compare to the $\pm 30^\circ$ and $\pm 55^\circ$ layers. The $\pm 10^\circ$ layer presents over the thickness cracks whereas discontinuous cracks are in the $\pm 30^\circ$ and $\pm 55^\circ$ layers (Figure 8).

For the accumulators tested at 450 bars, the cracking state of the $\pm 10^\circ$ layer is more severe than for the 300 bar accumulator, particularly due to cracks appearing through all the thickness (Figure 8). The cracks from the $\pm 30^\circ$ et $\pm 55^\circ$ seem also more developed in length and density.

As for the 600 bar accumulator, the cracking in the $\pm 10^\circ$ layer is comparable to the one present in the 450 bar accumulator. The cracks in the $\pm 30^\circ$ $\pm 55^\circ$ layer are also more developed.

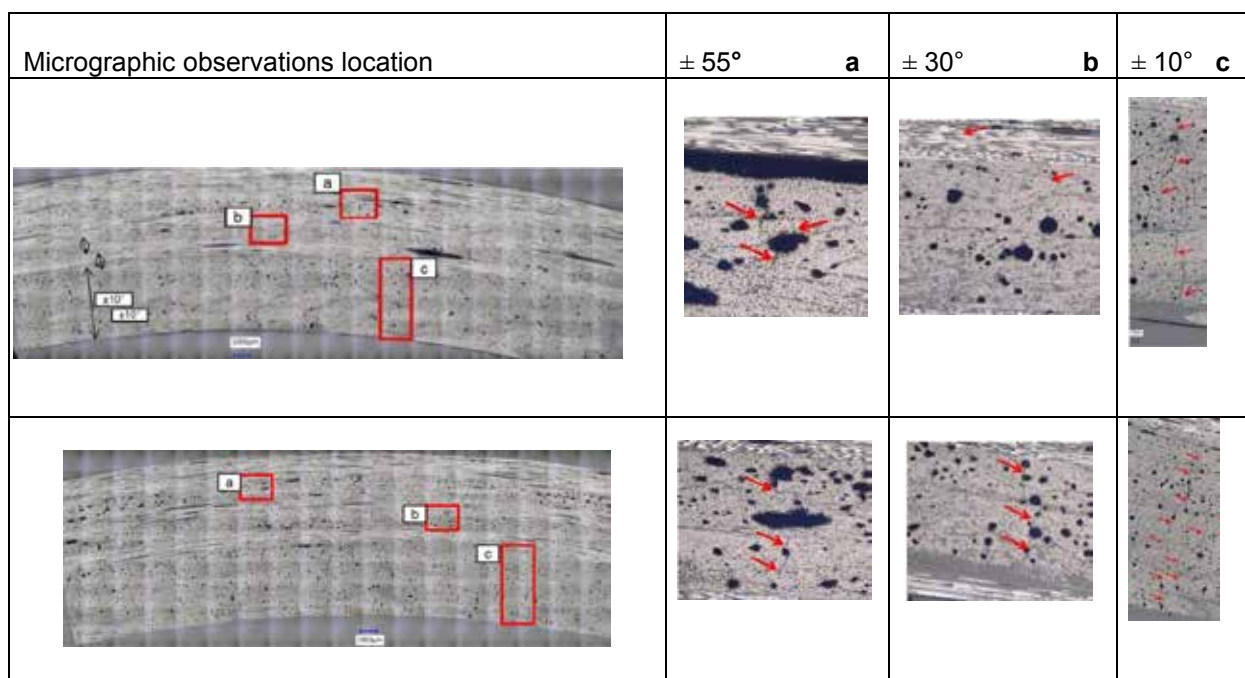


Figure 8: Micrographic observations

3.2 Mechanical tests results

3.2.1 residual strength

The tensile tests show a decrease of 19-22% of material stiffness after the tests at 300 and 450 bar. This can be explained by the transverse cracking observed in the helicoidal layers.

The stiffness decrease doesn't generate a decrease on the residual strength which means that the high energy AE signals detected before 450 bars don't affect the breaking load.

3.2.2 damage mechanisms

During the tensile tests, a monitoring by AE and a camera gave us information about the chronology of damage occurring during the load increase.

What has been observed thanks to the camera is that the onset of damage occurs with transverse cracking in the $\pm 90^\circ$ plies around 57MPa (13kN) (Figure 9). Then these cracks multiply and at 271MPa (65kN) the damage of intern plies oriented at $\pm 10^\circ$ begins. Internal damage continued to propagate until the final failure at 340MPa (82kN). Then, a delamination propagates along the oriented plies. All the specimen tested (x21) have a similar behavior.

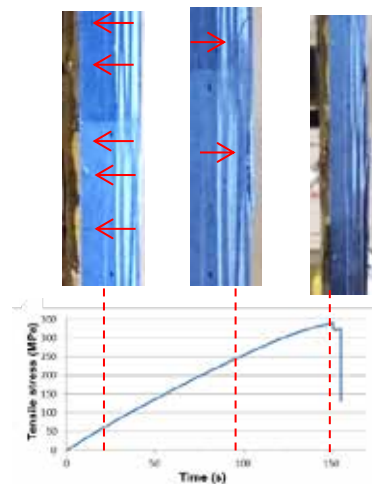


Figure 9 : Tensile test damage mechanisms Top: damage visual observation Bottom: load increase

The AE data have been analyzed in parallel and what can be noted is that before the final failure of the specimen, two AE accelerations occur. The first one happens around 10kN and the second one between 70 and 80kN (Figure 10). These two accelerations could be linked with the initiation of damages in the $\pm 90^\circ$ and $\pm 10^\circ$ layers as described above.

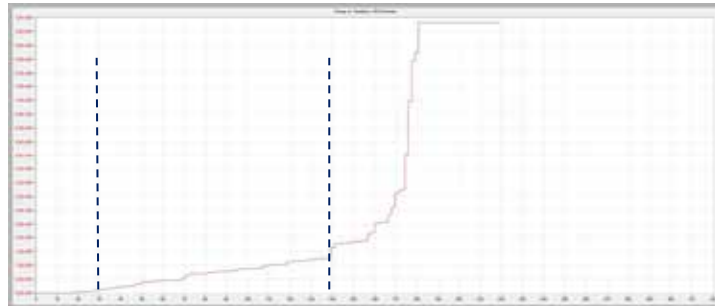


Figure 10 : AE energy cumulate for tensile tests

4. Discussion

The different results obtained by the tests lead were brought together with the design criteria, the Hashin criteria. Hashin criteria is used to determine the criticality of tensile loads for unidirectional fibers [reference?]. The criteria allow to differentiate the damage mechanisms of:

- tensile fibre breakage
- compression fibre breakage
- tensile matrix breakage
- compression matrix breakage

Once the value of the criteria reaches 1 for each damage mechanism, the break is likely to occur. For 300 and 450 bars levels an evaluation of this criteria has been realized.

At 300 bar, this criteria shows the following:

The helicoidal ply $\pm 10^\circ$ is in a breaking state which means that the fibre transversal strain exceed the layer transversal strain. The $\pm 30^\circ$ layer has a high probability of through thickness cracks. The $\pm 55^\circ$ has also a probability of cracks presence.

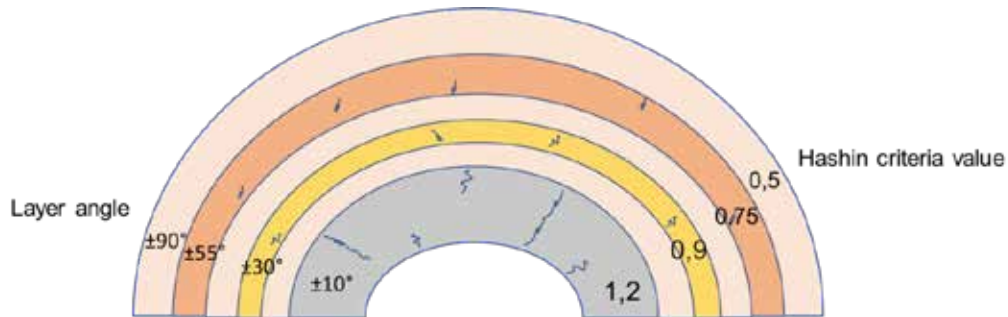


Figure 11 : Overview of accumulator layers with Hashin criteria evaluation for a proof test pressure of 300 bar

This Hashin criteria observations can be linked to the experimental results. Indeed, the AE data showed that an acceleration of acoustic activity took place around 200 bar which means that some damage mechanisms have already appeared and are propagating until reaching the proof test pressure. In addition to that, micrographic observations validate the fact that there is damage in the $\pm 10^\circ$ layer but also in the $\pm 30^\circ$ and $\pm 55^\circ$ layers.

At 450 bar, the criteria has evolved:

The helicoidal ply $\pm 10^\circ$ must have several through thickness cracks, and the first through thickness cracks appear in the $\pm 30^\circ$ layer. In the $\pm 55^\circ$ layer the cracks are longer and denser.

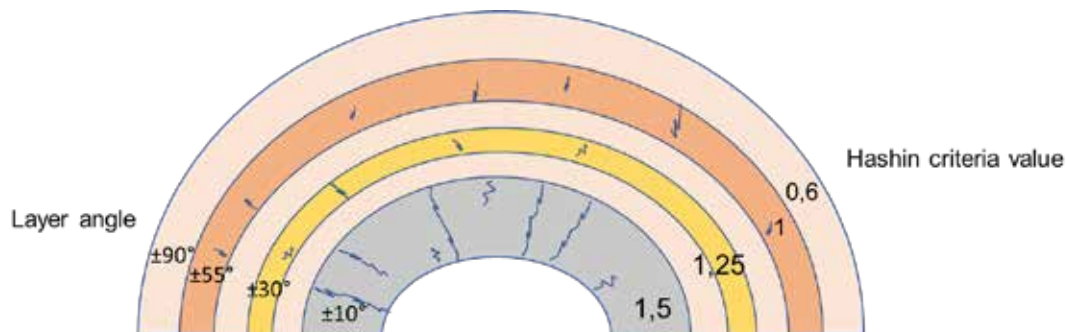


Figure 12: Overview of accumulator layers with Hashin criteria evaluation for a proof test pressure of 450 bar

In the case of the accumulator tested at 450 bar, the experimental results can also be linked with the Hashin criteria. In micrographic observations cracks through the thickness of the layer at $\pm 10^\circ$ are more numerous. In the $\pm 30^\circ$ and $\pm 55^\circ$ layers, cracks are denser and have a higher length than in the accumulator tested at 300 bar. Moreover, AE signal amplitude are getting higher which may correspond to the multiplication of through thickness cracks.

5. Conclusion

The present project has given us an approach on how to study the behavior under pressure of a composite material accumulator. As far for the Acoustic Emission analysis is concerned, the energy criteria have given us important information about the evolution of the damages during the proof tests. Moreover, the possibility to locate the areas where the activity was the most intense was also an asset to evaluate the zones with the highest stress and to analyze

them after with micrographic observations and tensile tests. AE provides valuable information for the manufacturer in evaluating the safety and the residual life of this pressure equipment.

The micrographic observations were useful to link the AE observations with the Hashin design criteria evaluation and so to the actual damage mechanisms occurred during the proof tests. (It gave a good information of what had been induced by the proof tests).

The possibility of performing tensile tests allowed to give information of the criticality of the damage present in the accumulators.

40 - Continuous recording and wireless transmission of AE waveforms by battery powered sensor nodes

Kaita Ito¹, Manabu Enoki²

¹ National Institute for Materials Science

² The University of Tokyo

Abstract:

AE streaming *i.e.* continuous recording of AE waveform is effective for monitoring under a noisy environment such as materials processing because an optimized digital noise filter can be designed from the real measurement result. For real-time denoising of AE streams, a PC-level high performance CPU and a number of cables are needed for power supply and communication for conventional AE streaming. However, complicated cabling among the measurement equipment, amps and sensors often disturb the materials processing. Therefore, a wireless AE streaming system is strongly demanded. In this study, such a wireless system was developed. A battery-powered small sensor node continuously acquires AE waveform and transmits it to a base station via broadband wireless network such as IEEE802.11ac (Wi-Fi). The whole waveform analysis is conducted in the base station which includes a high performance computer. An in-process defect monitoring during friction stir welding (FSW) was conducted as a test of the developed system. AE sensors were attached to the FSW machine and moved on the specimen. Four channels AE stream with 4 MHz of sampling frequency and 14 bit resolution was acquired, transmitted and analyzed in real-time. AE events due to joining defect were successfully detected and located. The measurement noise in the developed wireless sensor node was much lower than the conventional wired system because the sensor nodes were electrically insulated.

1. Introduction

Since the AE method detects the occurrence of microfracture inside the material in real time, it is an effective method not only for health monitoring of structures but also for process monitoring of material manufacturing. Continuous acquisition *i.e.* streaming of AE waveforms is effective for noise reduction and AE event detection under noisy environments. For more than a decade, the authors have developed “Continuous Wave Memory” (CWM) system which specialized for measurement and analysis of continuous AE waveforms, considering the importance of streaming in process monitoring.[1][2] Furthermore, it has been applied to various materials manufacturing processes including thermal spraying [2] and welding. However, since the equipment for material manufacturing process often has many moving parts and large monitoring object, it is troublesome to handle a large number of cables for power supply and signal transmission between the AE measuring devices, amps and sensors. Therefore, the authors have developed wireless CWM.

Although the wireless AE measuring devices already exist, they were difficult to deal with continuous waveforms. In recent years, calculation efficiency (performance per watt) and

wireless communication performance of small computers for IoT (Internet of Things) device are dramatically improving. However, analysis of continuous AE waveforms is still too heavy load for such small computer. Therefore, in order to realize wireless CWM, performance of high speed wireless communication was expected. The wireless sensor node *i.e.* slave machine only performs continuous waveform measurement and separated from the master unit with sufficient computing performance and storage capacity.

2. Development of sensor node of wireless CWM

AE streaming is roughly divided into three steps as acquiring, recording, and analyzing of continuous waveforms. Since the AE wave generally includes signal components of about 1 MHz at the maximum, at least 2 MHz of sampling frequency is required. The resolution of a typical A/D (analog-to-digital) converter is 10 to 16 bits *i.e.* one sample data is 2 bytes, therefore the required data rate is 4 MB/s/ch. This data rate can be sufficiently written continuously even with an internal storage of a sensor node likes microSDHC card. However, it is not practical to store continuous AE waveforms with several hundreds of gigabytes in one measurement in memory cards for each sensor node. Next, consider analysis of continuous AE waveform. When digital noise filtering with a large amount of calculation is conducted by the built-in CPU of the sensor node, the power consumption becomes unacceptably large. On the other hand, power consumption can be reduced by using DSP (Digital Signal Processor) or FPGA (Field-Programmable Gate Array) for filtering. However, it is difficult for these processors to change the analysis method frequently. Finally, consider transmission of continuous AE waveforms. The recent high speed Wi-Fi (IEEE 802.11ac) can obtain an effective speed of 25 MB/s (200 Mbps) even with a low theoretical speed of 433 Mbps. Since four access points with no frequency bands overlapping are allowed in Japan, continuous transmission of several tens of channels of continuous AE waveforms is estimated to be possible.

From the above consideration, the wireless sensor node only acquires the continuous waveform. Waveforms are transmitted to the master unit in real time via Wi-Fi, recording and analysis are performed in this master unit. By using the conventional CWM as the master unit, the development man-hours are kept down and high compatibility with conventional wired CWM system is maintained. An IoT board STEMLab 125-14 board by Red Pitaya team was adopted as the sensor node. Figure 1 shows a schematic diagram of the data flow of the wireless CWM system, figure 2 is a photo of the wireless sensor node and table 1 shows the specifications of the wireless sensor node. Because the A/D converter is high resolution (14 bits) and the voltage range can be narrow as ± 1 V, preamplifier was not necessary. The highest sampling frequency of the built-in A/D converter of STEMLab 125-14 is 125 MHz. However, this is the instantaneous highest speed which valid only for a short time burst transfer. Then, a preliminary experiment was conducted to investigate the upper limit frequency for continuous measurement without any data lost. As a result, the effective maximum was about 4 MHz (125 MHz / 32). The sampling data was acquired from the FPGA by ARM CPU and transmitted to the master unit by IEEE 802.11ac Wi-Fi. At this time, a microSDHC card was used as a cache in the sensor node to prepare for temporal destabilization of wireless communication in environments with many metal equipment and other Wi-Fi devices like factory and laboratory. The acquired continuous AE waveform were recorded and analyzed with Intel CPU on the master unit.

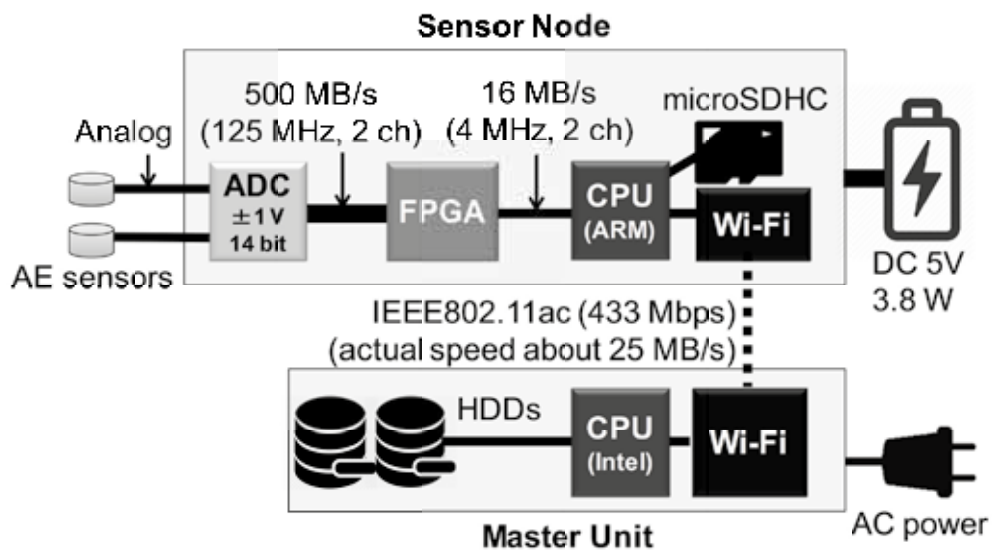


Figure 1. Schematic diagram of the data flow of the wireless CWM system

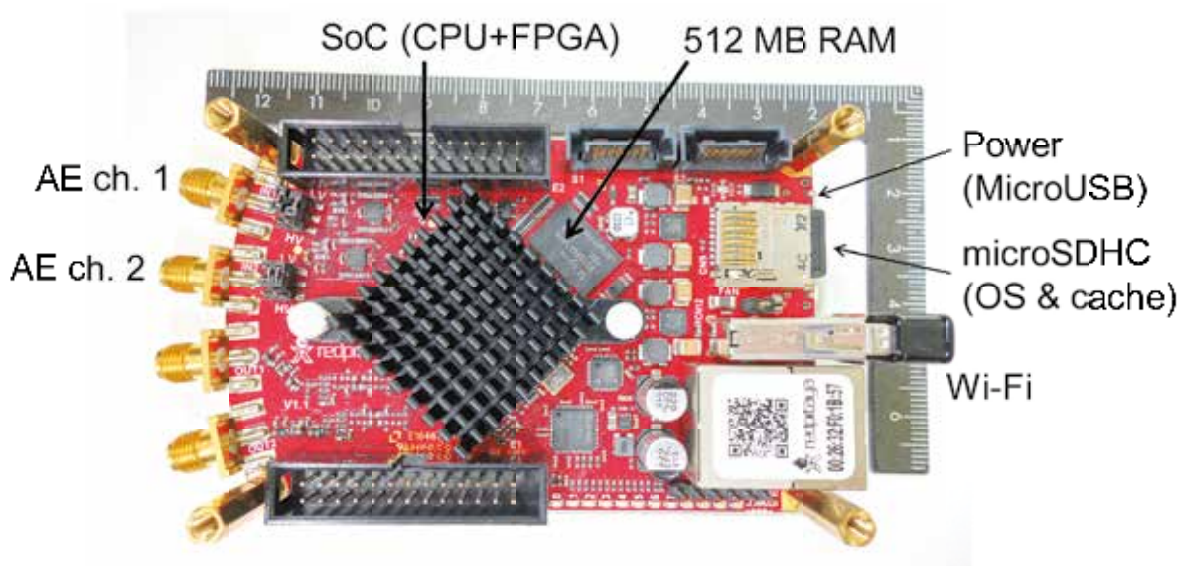


Figure 2. Photo of the wireless sensor node (STEMlab125-14 board)

Table 1. Specifications of the wireless sensor node

Channels	2 ch
Max. Sampling Freq. for continuous recording	about 4 MHz
Voltage range	± 1 V or ± 20 V
A/D resolution	14 bit
Power consumption	3.5 W
Footprint	107 mm \times 60 mm
Weight (without battery)	90 g

3. Demonstration Experiments of wireless CWM

For demonstration of the wireless CWM, AE measurement during FSW (Friction Stir Welding) was performed. Figure 3 shows a schematic diagram of the FSW experiment. The specimen was two flat plates of flame-resistant magnesium alloy with 200 mm long × 70 mm wide × 2.0 mm thick. A rotating steel tool was inserted into the specimen and moved along the butting line. During the FSW process, specimen softened in the solid phase and was joined by plastic flow. At this time, if there was excess or deficiency in heat input, a welding defect occurred and AE was generated. Because of the heat due to the welding, four heat resistant AE sensors (type AE254SMH177 by Fuji Ceramics) were placed so as to surround the welding part. These sensors were fixed to the FSW tool holder and moved on the specimen while adsorbed to the sample by magnetic force of the neodymium magnet. Ch. 1 and ch. 2 were connected to the conventional wired CWM via the type 9913 preamplifier (20 dB amplification) manufactured by NF corporation, ch. 3 and ch. 4 were connected to the wireless sensor node. The sampling frequency was set to about 2 MHz (125 MHz / 64) and it was well above the sensor's resonant frequency of 250 kHz. After the continuous waveform recording, the same high-pass filter with a cutoff frequency of 100 kHz was applied to each waveform on the wired and wireless sides.

A typical waveform of the AE event part is shown in figure 4. Although the absolute value of the amplitude varied depending on the presence or absence of the amplifier, almost the same waveform was acquired. A notable difference between the wired and wireless sides was the presence or absence of electrical noise. In wired measurement, electrical noise was likely to intrude into the A/D converter because the all electrical devices *i.e.* sensors, amps, PC for CWM and even the FSW machine were electrically conducted via the commercial power supply line. In addition, when electric noise invaded the AE sensor and vibrated the piezoelectric element, noise with a waveform similar to an AE event that rapidly rose and gradually attenuated was generated. On the other hand, in the wireless measurement, the sensor node was touching on the specimen via the sensor, but no electrical noise was found since there was no electrical path through the sensor node.

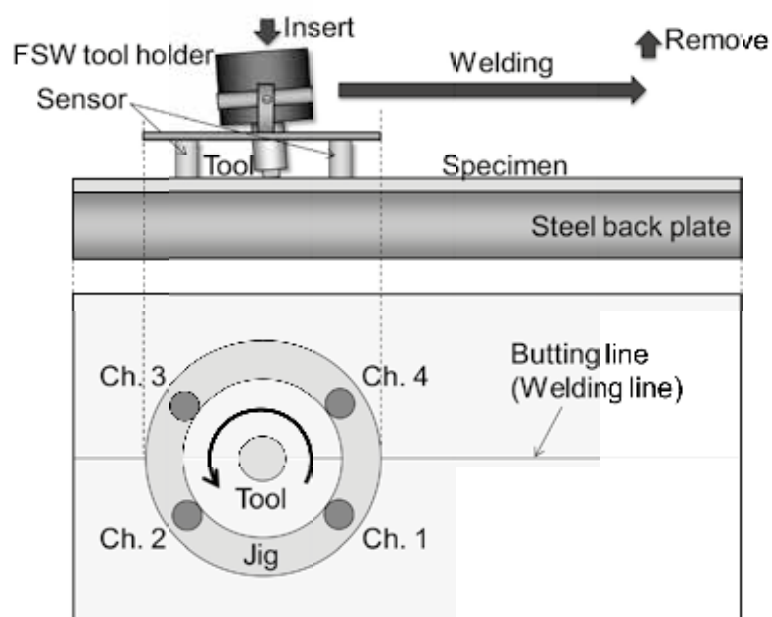


Figure 3. Schematic diagram of the FSW experiment

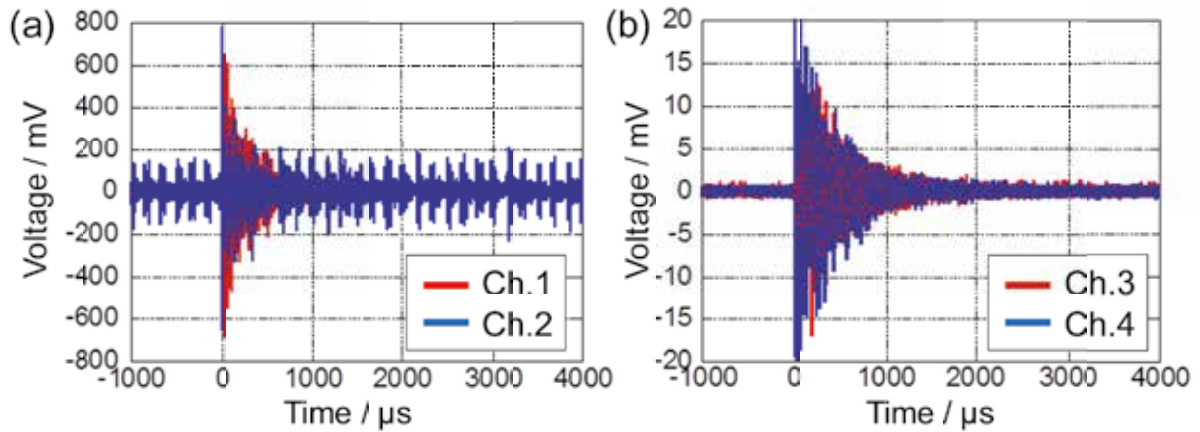


Figure 4. Typical waveform of an AE event recorded by (a) wired and (b) wireless CWM

4. Conclusion

- A battery-powered wireless sensor node with AE streaming function was developed. All waveforms with 16 MB/s of data rate (2 ch, 4 MHz, 2 Bytes/sample) per node could be transferred to the master unit via Wi-Fi.
- Monitoring of FSW process could be performed with high S/N ratio since the developed wireless sensor node was not easily invaded by electrical noise.

Acknowledgement:

This research was supported by JSPS KAKENHI (Grant-in-Aid for scientific research) No. 17K14820 and research grants from NEDO, the MORITANI Foundation and the Light Metal Education's Foundation. Also, the authors are grateful to Mr. Makoto Katayama and Mr. Kazuki Takahashi of the University of Tokyo and Dr. Eitaro Yukutake of Industrial Technology Innovation Center of Ibaraki Prefecture

References:

- [1] Ito, K., Enoki, M., Acquisition and Analysis of Continuous Acoustic Emission Waveform for Classification of Damage Sources in Ceramic Fiber Mat, *Materials Transactions*, vol. 48, 2007, pp. 1221-1226.
- [2] Ito, K., Kuriki, H., Araki, H., Kuroda, S., Enoki, M., Detection of Segmentation Cracks in the Top Coat of Thermal Barrier Coatings during Plasma Spraying by Non-Contact Acoustic Emission Method, *Science and Technology of Advanced Materials*, vol. 15, 2014, pp.035007.

01 - Modal Acoustic Emission analysis of mode-I and mode-II fracture of adhesively-bonded joints

Alasdair R. Crawford, Mohamad G. Droubi, Nadimul H. Faisal

SCHOOL OF ENGINEERING, ROBERT GORDON UNIVERSITY, GARTHDEE
ROAD, ABERDEEN, AB10 7GJ, UK

Abstract:

Acoustic emission (AE) testing has previously been demonstrated to be well suited to detecting failure in adhesively-bonded joints. In this work, the relationship between the fracture-mode of adhesively-bonded specimens and the acoustic wave-modes excited by their failure is investigated. AE instrumented Double-Cantilever-Beam (Mode-I fracture) and Lap-Shear (Mode-II fracture) tests are conducted on similar adhesively-bonded aluminium specimens. Linear source-location is used to identify the source-to-sensor propagation distance of each recorded hit, theoretical dispersion curves are used to identify regions of the signal corresponding to the symmetric and asymmetric wave modes, and peak wavelet-transform coefficients for the wave-modes are compared between the two fracture-modes. It is demonstrated that while both fracture-modes generate AE dominated by the asymmetric mode, the symmetric mode is generally much more significant during Mode-II fracture than Mode-I. While significant scatter and overlap in results prevents the ratio of peak-wavelet transform coefficients from being a robust single classifier for differentiation between fracture-modes in most cases, other modal analysis methods, or integration of this parameter into multi-parameter methods in future work may result in more reliable differentiation. Understanding of the wave-modes excited by the different fracture-modes also has implications for source-location, as identification of the correct modes is critical for selection of suitable wave velocities.

1. Introduction

Structural adhesive bonding is increasingly being utilized across a wide range of industries, such as the aerospace, renewable energy, marine and automotive industries. Adhesives offer a variety of advantages over more conventional mechanical fastening methods, including improved stress distribution, low weight, corrosion resistance, damping properties and the ability to join dissimilar materials and composites. They are however susceptible to defects introduced throughout manufacture and service life which can lead to catastrophic failure. These defects can include disbonds or weak “kissing” bonds, introduced by surface contamination of the adherends, voids, due to inadequate quantities of adhesive or air entrapment during lay-up, porosity, due to volatiles or entrained air, cracks, due to thermal shrinkage or applied stressed in service, and poor cure, occurring from improper mixing or inadequate thermal exposure [1].

Due to these potential defects, non-destructive testing (NDT) and condition monitoring is vital if adhesives are to be used in safety critical applications. Acoustic Emission (AE) testing has been well proven in its ability to detect adhesive failure and, particularly for large structures, the ability to provide continuous real-time monitoring over a large area is advantageous and makes AE an appealing technique to complement more conventional NDT techniques, such as ultrasound and resonant-frequency based methods.

Multiple studies of adhesively bonded joints have demonstrated the ability of AE to detect initiation and propagation of debonding and adhesive cracking through the correspondence between AE and drops in load during various fracture tests [2-5], while studies such as those by Croccolo and Cuppini [6] have demonstrated the ability to predict the final failure load of a joint, based on the acoustic emissions at lower load. Differentiation between debonding and adhesive cracking has also been achieved by Galy *et al.* [3] through clustering based on typical AE parameters, while work by Bak and Kalaichelvan [7] used peak-frequency analysis to differentiate between the failure mechanisms of adhesive failure, light fiber tear failure and fiber tear failure during lap-shear tests of composite specimens.

Dzenis and Saunders [8] successfully utilized the statistical pattern recognition software Vallen VisualClass to differentiate between Mode-I (crack opening), Mode-II (shear) and Mixed-mode fatigue failures of adhesively bonded joints. While it was demonstrated that differentiation between fracture-modes was possible, the method used, and results reported provided little insight into the fundamental differences between the recorded waveforms. The differentiation between fracture-modes is extremely valuable in the case of adhesive bonds, as there is vast disparity in the strength of bonds dependent on the loading orientation. For this reason, most adhesively bonded joints are designed to be loaded predominantly in Mode-II, and application of unexpected Mode-I loadings may therefore lead to catastrophic failure. The study will look further into the differences in AE occurring from different fracture-modes.

It has been demonstrated by Gorman [9], amongst others, that the orientation of an AE source affects the amplitudes of the wave-modes propagating from it. In-plane sources are seen to create a greater extensional/symmetric wave-mode, while out-of-plane sources are seen to create a greater flexural/asymmetric wave-mode. This finding has been previously used in modal AE analysis of composites to aid in differentiation between delamination (out-of-plane) and fiber-breakage or matrix cracking (in-plane) [10-11]. Understanding of the wave-modes generated is also crucial for accurate source location. Due to differing propagation velocities, it is critical that velocities used in calculating source-location correspond to the wave-modes for which arrival times have been detected.

The aim of this study was to investigate the wave-modes generated by Mode-I and Mode-II fracture of adhesively-bonded joints and to identify whether modal analysis has the potential to discriminate between fracture-modes in a similar manner to which it has been used to discriminate between failure mechanisms of composites. To achieve this, AE instrumented Double Cantilever Beam (DCB) (Mode-I) and Lap-Shear (LS) (Mode-II/Mixed-mode) tests have been conducted on adhesively-bonded aluminum specimens and the resulting AE analysed, using continuous wavelet-transforms and theoretical dispersion curves to identify the resulting wave-modes.

2. Experimental Setup

2.1 Specimen preparation

Both specimen types were manufactured from 3.175 mm x 50 mm HE30TF aluminium bar. Adherends were cut to 300 mm long for the DCB test, and 360 mm long for the lap shear test. Specimen widths and lengths were chosen to be as large as was practical for the available test equipment, to minimize the effects of edge-reflections in the results, and to allow significant propagation distance for the wave modes to separate through dispersion. The adhesive bonding process consisted of surface preparation, adhesive application and curing. The specimens were initially rinsed with acetone, before being abraded with P400 grade abrasive

paper, rinsed with acetone again, and then cleaned with Loctite SF 7063. Silicone grease was then carefully applied to a 60 mm long region of the DCB specimens to prevent bonding and thus create a pre-crack. Loctite EA 3430, a relatively brittle two-part epoxy adhesive, was then applied through a mixer-nozzle to the bond areas of one adherend for each of the specimens. The bond area for the DCB specimens covered the entire specimen, aside from the pre-crack, while the bond area for the shear specimens was a 50 mm x 50 mm square, located 70 mm from the ends of the adherends. Small 0.5 mm thick aluminium shims were then added into the adhesive to maintain a uniform bond thickness as the other adherends were placed on top. Once assembled, weights totaling 4 kg were added on top of each specimen and they were left to cure for a minimum of five days, at an average temperature of 19°C and humidity of about 20%.

2.2 Mechanical testing

Both types of specimen were tested using an Instron 3382 universal testing machine (UTM), controlled through BlueHill 3 software. Loading blocks were bonded to the DCB specimens to allow them to be mounted to the machine in custom made yokes. Lap shear specimens had tabs bonded to each end and were then clamped into the machine using 50 mm mechanical jaws. The loading rates used were 0.5 mm/min, based on ASTM D5528 – 01 [12], and 1.3 mm/min, based on ASTM D1002-10 [13], for the DCB and lap shear specimens respectively. DCB tests were run up to a crosshead displacement of 10 mm, while lap shear tests were run until complete failure was achieved. Each test was conducted four times to ensure repeatability.

2.3 Acoustic emission setup

Two Physical Acoustics Micro80D differential sensors were used. These were connected to a PC with a NI PCI-6115 DAQ through; Physical Acoustics 2/4/6 variable-gain pre-amplifiers (set to 60dB), an in-house built signal-conditioning unit (providing an additional 12dB gain), and a NI BNC-2120 shielded connector block. The system was operated through LabVIEW software, with the signals being recorded continuously at 2.5 MHz and saved in *.tdms format. Signal processing and analysis was conducted after testing, using MATLAB.

The sensor locations used were both on the same sides of the specimens. On the DCB specimens, as indicated in Figure 1, one sensor was located at the end of the pre-crack, and the other 10 mm from the end of the specimen. On the lap shear specimens, illustrated in Figure 2, the sensors were located either side of the bond area, at distances of 90 mm and 200 mm away from the center of the bond area. Sensors were coupled to the specimens with a layer of silicone grease and secured using aluminium adhesive tape. As well as recording AE, a video camera was used to record crack propagation for the DCB test to verify the position of the crack-front. This approach could not be used effectively for the shear specimens due to the speed of their failure.

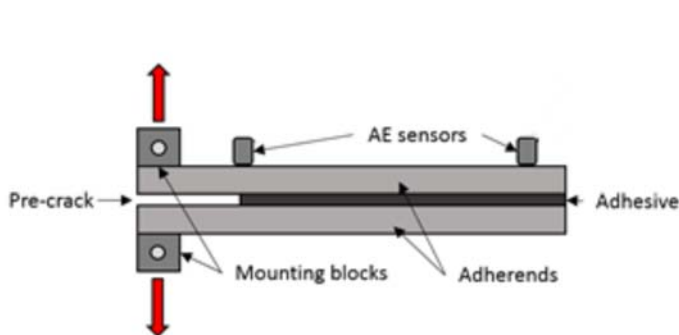


Figure 1. Double Cantilever Beam experimental schematic (not to scale)

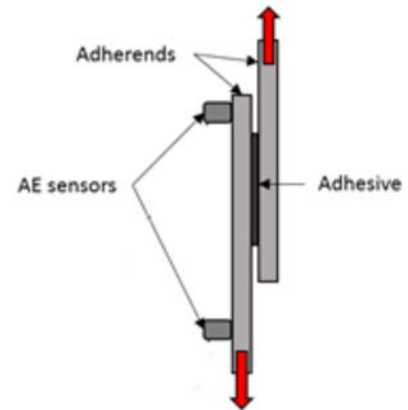


Figure 2. Lap Shear experimental schematic (not to scale)

3. Signal processing

As the system was recording continuously, the initial step was to isolate hits for further analysis and to discard the noise. This was achieved by averaging the RMS value of the signal over 200 data points, to create something similar in form to the upper wave envelope, and then applying upper and lower thresholds. Hits of significant amplitude were identified by crossings of the upper threshold. The start and end of the hit were then identified by the nearest crossings of the lower threshold before and after this point. Threshold values were set at 0.05 V and 0.15 V, chosen based on the level of noise present in the recorded signals.

The identified hits were transformed into the time-frequency domain by continuous wavelet transform. In this case the Gabor wavelet was used, as this provides the best combination of time and frequency resolution. An example of this transformation from time to time-frequency domain is illustrated in the upper panels of Figure 3. Arrival times, corresponding to the A_0 mode at 300 kHz, were determined as the first peak in the 300 kHz band of the wavelet transform to exceed 70% of the maximum WT coefficient. These arrival times, and the separation distance between the sensors, were used to estimate the linear source location of each hit, and therefore the propagation distance from the source to each of the sensors. Hits located as occurring from outwith the potential bond regions of the specimens were excluded from further analysis.

Based on the identified propagation distances, the arrival times of both the S_0 and A_0 wave-modes are calculated using the theoretical dispersion curves for the adherends (generated by Vallen Dispersion software). The central panel of Figure 3 shows these dispersion curves, modified by the propagation distance, overlaid on the wavelet transform plot of the signal. This allows certain peaks in the wavelet transform plot to be attributed to these wave-modes.

To allow quantitative analysis of the contributions of each wave-mode, the corresponding peaks within a certain frequency band were extracted. The frequency band around 300 kHz was chosen as it is close to the resonant peak of the sensor and contains significant content from both wave-modes. There is also significant enough dispersion at this frequency to differentiate between the wave-modes in the time-domain. The lower panel of Figure 3 shows

the WT coefficients in the 300 kHz band with the S_0 and A_0 peaks marked. The ratio between the amplitudes of these peaks was then used to investigate the difference between the fracture-modes. In a small number of hits the wave-modes could not be clearly identified or separated due to factors such as overlapping of hits, in such cases the hits were excluded from further analysis.

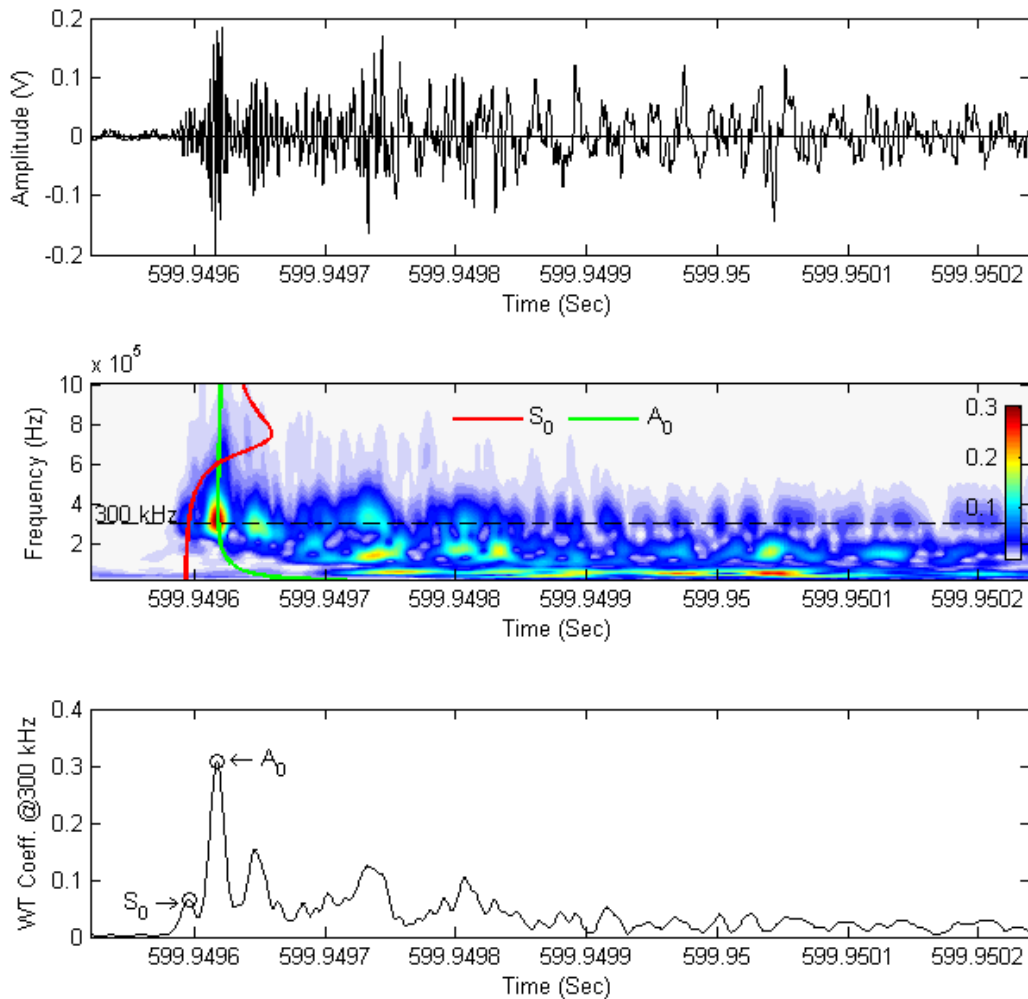


Figure 3. Example of signal-processing method. Top: Original AE signal. Middle: Wavelet Transform plot with overlaid dispersion curves indicating symmetric (S_0) and asymmetric (A_0) wave-modes. Bottom: Wavelet Transform coefficients for 300 kHz frequency band, with S_0 and A_0 peaks marked.

4. Results

4.1 Load results

Typical examples of the loading curves and AE source location results for the tests are shown in Figure 4. As expected, the loading characteristics of the two specimen types vary significantly. The DCB tests result in an approximately linear increase in load as the adherends deflect elastically in the pre-crack region until the maximum load is reached. This is followed by multiple small drops in load as the adhesive fails in sections, and small rises in load between these, as the adherends elastically deform again. The lap-shear tests however, exhibit an

approximately linear region of elastic deformation up to their maximum load, followed by sudden complete failure in which the adherends completely separate. The maximum loads withstood by the two specimens should be noted, as the DCB specimens withstood loads in the region of only 50 N, while maximum loads applied to the lap-shear specimens were in the region of 2000 N. This disparity highlights the potential importance of being able to discriminate between fracture-modes during condition monitoring.

4.2 Failure mechanisms

The main failure mechanism observed in all specimens was adhesive failure, with the adhesive layer separating from one adherend as the bond between adhesive layer and adherend failed, while remaining bonded to the other adherend. In the DCB specimens, and to a lesser extent in two of the lap-shear specimens, some adhesive cracking was also found. In some regions the adhesive failure would occur at the interface with the upper adherend, and in other regions it would occur at the lower adherend. The result being that the adhesive layer cracked between these regions, allowing sections of the adhesive to remain attached to either adherend. Figure 5 shows annotated examples of the failure mechanisms present in both types of specimen.

4.3 Acoustic emission source locations

In both specimen types, a small number of hits were recorded during the initial linear portion of the loading. Most hits however, correspond to significant drops in load as the adhesive fails. In the DCB specimen hits are spread throughout the test as crack slowly propagates through the specimen, whereas in the lap-shear test, AE activity is concentrated around the moment of final failure. The AE source locations identified in the DCB tests generally correspond well with the visually observed crack-front recorded with the video-camera, with the hits initially being centered around the tip of the 60 mm pre-crack and then progressing further along the specimens as the crack opens. While the AE source location results generally correspond well, there is some variation and scatter which is believed to be due to a combination of the following factors; the crack-front will not be uniform due to the inhomogeneous bond quality, so the location of the crack-front recorded at one side will not necessarily be accurate through the entire specimen width. The use of a linear source-location method, as opposed to 2D or 3D, will also generally result in a small level of error as not all hits will occur directly between the sensors. In the lap-shear specimens hits are concentrated within the bond area, as would be expected, although some hits are identified as occurring out with the bond area. This may again be due to the limitations of linear source-location but may also be due in some cases to the incorrect identification of arrival times due to interference between overlapping hits, a problem which can also occur in the DCB specimens but is much more prominent in the lap-shear tests due to the limited time in which the hits all occur.

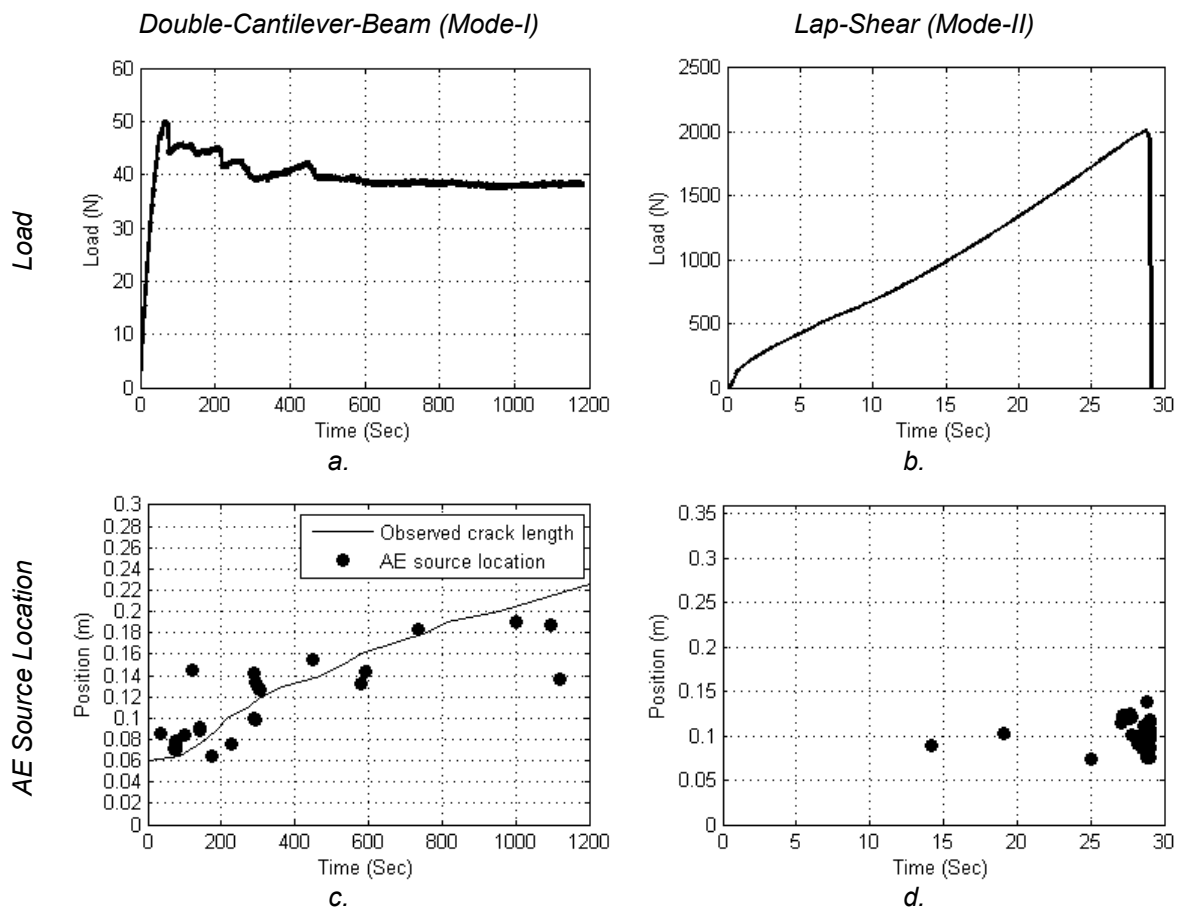


Figure 4. Examples of loading curves and source locations. (a) Loading of DCB test. (b) Loading of lap-shear test. (c) AE source location and visually observed crack length for DCB test. (d) AE source location for lap-shear test.

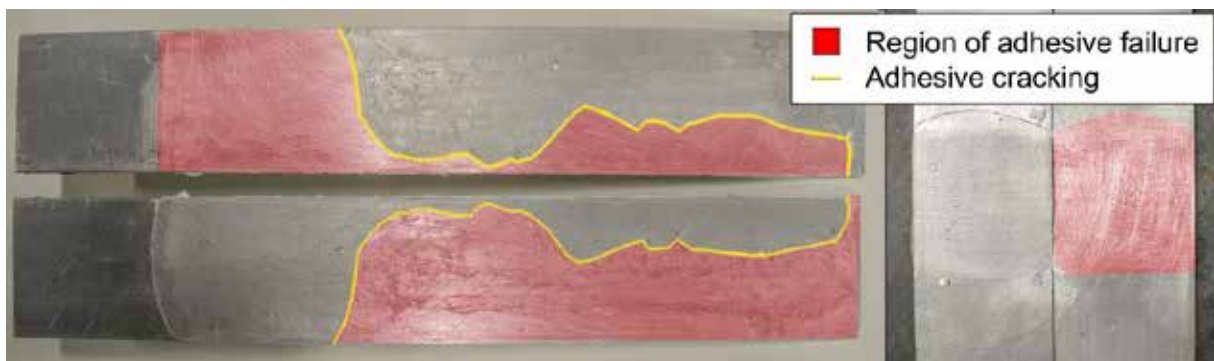


Figure 5. Example of failure mechanisms observed. Left: DCB specimen showing adhesive failure and cracking of the adhesive layer. Right: Lap-shear specimen showing only adhesive failure.

4.4 Modal acoustic emission analysis

The resulting ratios of the peak wavelet-transform coefficients corresponding to the S_0 and A_0 wave-modes are presented in Figure 6. Both fracture-modes can result in a wide range of S_0/A_0 ratios being generated. For the DCB tests, values range from 0.0169 to 0.4178 with an overall

mean and standard deviation of 0.085 and 0.0848 respectively. Lap-shear tests produced values ranging from 0.0616 to 0.7197 and with an overall mean and standard deviation of 0.1902 and 0.1425.

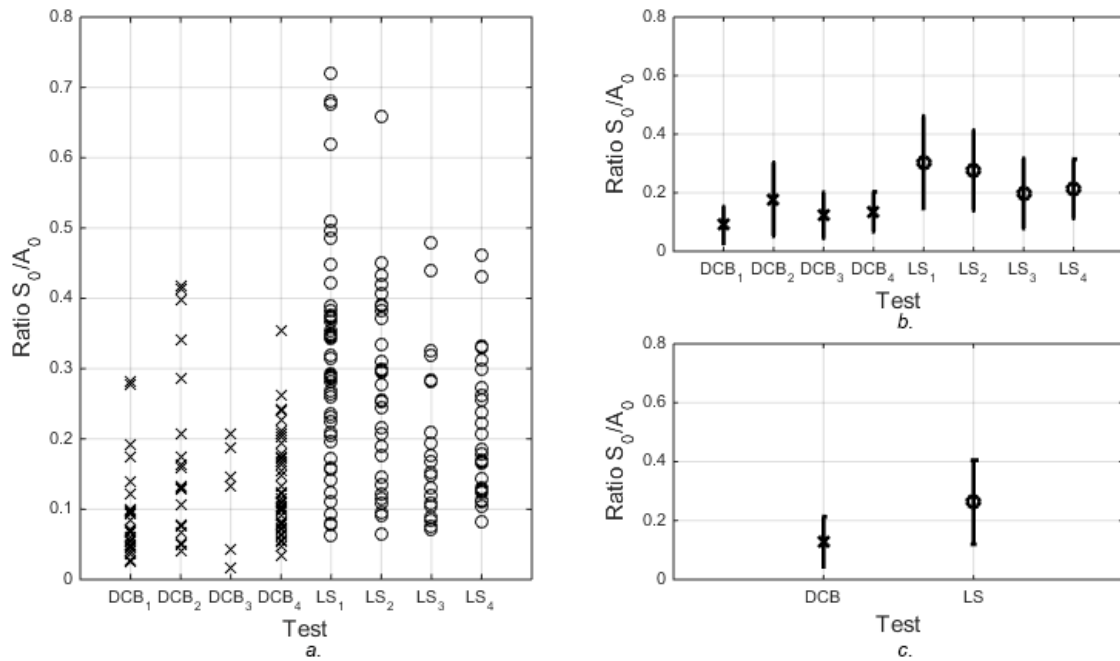


Figure 6. Ratios of peak wavelet-transform coefficients at 300 kHz corresponding to S_0 and A_0 wave-modes. (a) All hits analysed. (b) Mean and std. deviation for each test. (c) Overall mean and std. deviation for the two test types.

5. Discussion

The WT coefficient peak ratios show that in both tests the A_0 mode is dominant and that there is significant overlap between the sets of results. There is however a clear trend indicating that the S_0 mode is generally greater in the Mode-II lap-shear tests than in the Mode-I DCB tests. This result appears to be in line with previous work, as Mode-I failure creates a clear out-of-plane source, very similar to the delamination of composites, which has previously been shown to create a dominant A_0 component.

While the loading in the Mode-II test is applied in-plane with respect to the adherends, any failure occurring at the interface with the adhesive is occurring at the surface of the adherend rather than near the mid-plane, as can be the case for other in-plane sources previously investigated, such as fiber-failure or matrix cracking in composites. It has been previously demonstrated by Hamstad *et al.* [14] that while a signal generated by an in-plane source located on the mid-plane will be dominated by the symmetric mode, the same source, applied away from the mid-plane, can create a signal dominated by the asymmetric mode. This provides some explanation as to why both fracture-modes result in signals dominated by the asymmetric mode, despite the loading orientation. Additionally, a lap-shear test is technically not a pure Mode-II test, while the loading is predominantly in shear, bending of the adherends can result in a small Mode-I crack-opening component, making it Mixed-mode and potentially contributing further to the generation of the A_0 mode.

As both fracture-modes have a significantly higher amplitude A_0 than S_0 mode, a suitably chosen threshold can be used to consistently select the arrival time of the A_0 mode, without risk of accidental selection of the S_0 arrival time. If the Mode-II tests had resulted in a greater S_0 component, then a more sophisticated method would be necessary to select arrival times and calculate source locations.

The results presented by Dzenis and Saunders [8], analysed using Vallen VisualClass, clearly demonstrated the possibility to differentiate between fracture-modes using AE, they did not however provide much insight into the fundamental differences in the signals which allowed this differentiation. The results presented in this work indicate that it is likely that the difference in wave-modes excited during their tests will have been one of the significant factors contributing to the differentiation which was achieved, while other differences may have also occurred from features such as the specimen geometries causing variation in attenuation and reflections. An increased understanding of these factors allowing differentiation will be beneficial if attempts are made to utilize these techniques on full scale structures, rather than small laboratory specimens, as any method used will need to suitably account for the dispersion, attenuation and reflection which will be present in larger structures with potentially irregular geometries.

The use of the WT peak ratio as a classifier to differentiate between fracture-modes may be feasible when considering multiple hits, i.e. an entire test, however due to significant variation between hits, and the overlap between tests, it would not be possible in most cases to identify fracture-mode based on a single hit. Future work should therefore consider either; other methods to assess the modal content of the signals which may yield clearer discrimination, or, combining this parameter with others to form a more robust method of discrimination.

Differentiation between hits occurring from the adhesive failure and cracking of the adhesive layer has not yet been attempted within this study, and it is recognized that results for each test may include hits from both failure mechanisms which may exhibit different characteristics. Future work should address this issue by conducting tests capable of isolating each of these failure mechanisms to identify the defining characteristics of AE occurring

6. Conclusion

The aim of this study was to investigate, for the first time, the AE wave-modes generated by Mode-I and Mode-II fracture of adhesively-bonded joints (aluminium metal-to-metal) and to identify whether modal analysis has the potential to discriminate between fracture-modes in a similar manner to which it has been used to discriminate between failure mechanisms of composites. Differentiation between fracture-modes is particularly important in adhesive joints due to the vast disparity in strength between joints in Mode-I and Mode-II loading, assessment of loading conditions through AE could therefore provide a very useful tool for structural health monitoring. Understanding of the wave-modes generated by different fracture-modes is also important for accurate source location. Due to the differing propagation velocities of the modes, it is critical that the velocity used in source location calculations corresponds to the wave-mode for which arrival times have been detected. From the work conducted, the following has been concluded:

- Use of linear source location to identify propagation distances and theoretical dispersion curves to identify arrival times, has successfully identified regions of the time-frequency domain corresponding to the fundamental S_0 and A_0 modes.

- Modal analysis, based on investigation of the amplitude-ratio of peaks in the continuous wavelet-transform corresponding to the S_0 and A_0 modes, has revealed clear differences between Mode-I and Mode-II/Mixed-mode fracture. While signals from both fracture-modes are dominated by the A_0 mode, the S_0 mode is generally greater in the Mode-II tests than in the Mode-I.
- As the amplitude of the A_0 mode is consistently higher than that of the S_0 mode, a suitably chosen threshold can be used as a reliable method to select the arrival time of the A_0 mode for the purposes of source location.
- Analysis of the amplitude-ratio of wavelet-transform peaks corresponding to the wave-modes has been demonstrated to reveal differences between the fracture-modes when considering each test. However, due to the variation between hits within each test, and the overlap between results from the two test types, it is generally not possible to distinguish between fracture-modes based on a single hit. Future work should therefore focus on investigation of other methods to assess modal content of the signals or on utilizing the wavelet peak ratio in combination with other parameters to provide a more robust classifier.

References:

- [1] R. D. Adams, "Nondestructive Testing," in *Handbook of Adhesion Technology*, Oxford, Springer, 2011, pp. 1050-1067.
- [2] M. G. Droubi, A. Stuart, J. Mowat, C. Noble, A. K. Prathuru and N. H. Faisal, "Acoustic emission method to study fracture (Mode-I, II) and residual strength characteristics in composite-to-metal and metal-to-metal adhesively bonded joints," *The Journal of Adhesion*, 2017.
- [3] J. Galy, J. Moysan and A. Y. N. M. N. El Mahi, "Controlled reduced-strength epoxy-aluminium joints validated by ultrasonic and mechanical measurements," *International Journal of Adhesion and Adhesives*, vol. 72, pp. 139-146, 2017.
- [4] M. G. Droubi, J. McAfee, H. R. C. S. Walker, C. Klaassen, A. Crawford, A. K. Prathuru and N. H. Faisal, "Mixed-mode fracture characteristics of metal-to-metal adhesively bonded joints: experimental and simulation methods," in *Structural Integrity Procedia*, Funchal, 2017.
- [5] K. Senthil, A. Arockiarajan and R. Palaninathan, "Experimental determination of fracture toughness for adhesively bonded composite joints," *Engineering Fracture Mechanics*, no. 154, pp. 24-42, 2016.
- [6] D. Croccolo and R. Cuppini, "A methodology to estimate the adhesive bonding defects and the final releasing moments in conical joints based on the acoustic emissions technique," *International Journal of Adhesion & Adhesives*, no. 26, pp. 490-497, 2006.
- [7] M. K. Bak and K. Kalaichelvan, "Evaluation of Failure Modes of Pure Resin and Single Layer of Adhesively Bonded Lap Joints Using Acoustic Emission Data," *Transactions of the Indian Institute of Metals*, no. 68, pp. 73-82, 2015.

- [8] A. Dzenis and I. Saunders, "On the possibility of discrimination of mixed mode fatigue fracture mechanisms in adhesive composite joints by advanced acoustic emission analysis," *International Journal of Fracture*, no. 117, pp. 23-28, 2002.
- [9] M. R. Gorman, "AE Source Orientation by Plate Wave Analysis," *Journal of Acoustic Emission*, vol. 9, no. 4, pp. 283-288, 1991.
- [10] J. Martínez-Jequier, A. Gallego, E. Suárez, F. J. Juanes and Á. Valea, "Real-time damage mechanisms assessment in CFRP samples via acoustic emission Lamb wave modal analysis," *Composites Part B: Engineering*, vol. 68, pp. 317-326, 2015.
- [11] M. Surgeon and M. Wevers, "Modal analysis of acoustic emission signals from CFRP laminates," *NDT & E International*, no. 32, pp. 311-322, 1999.
- [12] ASTM International, "D5528-01 Standard Test Method for Mode I Interlaminar Fracture Toughness of Unidirectional Fiber-Reinforced Polymer Matrix Composites," ASTM International, West Conshohocken, 2007.
- [13] ASTM International, "D1002-10 Standard Test Method for Apparent Shear Strength of Single-Lap-Joint Adhesively Bonded Metal Specimens by Tension Loading (Metal-to-Metal)," ASTM International, West Conshohocken, 2010.
- [14] M. A. Hamstad, A. O'Gallagher and J. Gary, "A wavelet transform applied to acoustic emission signals: Part 1: Source Identification," *Journal of Acoustic Emission*, no. 20, pp. 39-61, 2002.

02 - On use of signal features for Acoustic Emission source identification in fibre-reinforced composites

Markus G. R. Sause¹

¹ University of Augsburg, Institute for Materials Resource Management, Mechanical Engineering, D-86135 Augsburg

Abstract:

In the past, many approaches were proposed to perform the task of acoustic emission based source identification in fibre-reinforced composites. Almost all identification attempts make use of feature values to act as representation of the recorded acoustic emission signals. The typical features are classified in two primary categories, one to express the intensity / energy of the signal and one to describe the frequency characteristic of the signal. Both categories are used to classify signals into microscopic failure mechanisms such as matrix cracking, fibre breakage and many more. To this end, various approaches used either energetic or frequency features or a mix of both. This contribution takes a closer look at the relationship between acoustic emission signals and their feature values and assesses their relation to acoustic emission source mechanics. This provides guidance on the reliability of acoustic emission features for source identification procedures and points out some key aspects for successful classification attempts.

1. Introduction

Failure of composite materials during mechanical loading is a complex phenomenon starting on the microscopic level. At exposure to increased load, small flaws start to grow into larger ones, escalating over several orders of magnitude, which finally coalescent into macroscopic failure. Each microscopic (and macroscopic) crack progression generates acoustic emission (AE). The multitude of different cracks occurring in composites have been categorized and listed several times (i.e. [1], [2]). In the context of AE, it is most noteworthy that all of these different cracks result in detectable AE signals. Among other things, the detectability will depend on the distance between source position and the sensor position. One intrinsic challenge is to deal with the variety of terminology used in the past to categorize the different failure mechanisms in composites. Still there is no consensus on how many different AE source mechanisms can be distinguished in a particular test setup. However, in the past decades there have been many attempts to distinguish between the different AE source mechanism as occurring in composites [3-20]. Basic distinction is made between work that has applied model specimens to establish prototype signals for each source type, approaches that are using validation of signal classes by microscopic evidence and approaches using numerical or analytical modelling to assist in the interpretation.

The aim of this contribution is to review the reliability of particular AE parameters (features) applied to perform source identification in fibre-reinforced composites.

2. Experimental

As described in more detail in [10], [12], a four-point bend test was combined with multi-resonant type WD sensors to detect the AE generated during damage initiation and progression. For acoustic coupling Baysilone silicone grease of medium viscosity was used, the mechanical contact was provided by two clamps. To decrease detection of friction noise a bandpass ranging from 20 kHz up to 3 MHz was used. The AE waveforms were recorded using a PCI-2 data acquisition system with 40 dB_{AE} preamplification and the software AEWIn (Physical Acoustic Ltd.) with a threshold of 40dB_{AE} and a sampling rate of 10 MS/s. This will provide some representative AE data for further discussion and only acoustic emission sources located between the two upper supports are considered for the following analysis.

To analyse the crack formation inside the material, high-resolution computed tomography was used. The Nanotom m system (General Electric) was applied with 50 kV tube voltage and 200 µA tube current using a voxel resolution of 5.2 µm. This provides a way of volumetric measurement of the typical crack dimensions found after four-point bending in a composite material.

After extraction of classical signal features out of the first 100 µs after signal arrival (definition of features see Appendix C in [2]), the feature dataset is ready for analysis by pattern recognition methods. In figure 1, a typical result from a hierarchical clustering using the agglomerative tree linkage [21] is shown for one representative dataset resulting from loading the specimens to failure. This statistical data analysis method applies the Ward-algorithm (also known as “sort algorithm” or “agglomerative tree linkage”) and groups the AE features according to their similarity based on a minimum variance criterion [19], [22]–[25]. High numerical values indicate an equal relevance to describe the underlying data structure. In the example of figure 1, the feature “energy” and “signal strength” link at a value of approximately one, so they essentially provide the same information, i.e. they are highly correlated.

For composite materials, this feature dendrogram (example see figure 1) often splits in two branches that link at relatively low levels. One branch is primarily composed of features related to the “energetic quantities”, such as energy, amplitude, signal strength, but it also includes features related to the amplitude. One such example is the duration of the signal (louder signals take longer to fall below threshold). Similar, the rise time and the counts to peak correlate with the strength of the signals as increased amplitudes may cause an earlier onset above threshold level.

The other branch of the feature dendrogram typically holds the features, related to frequency information of the AE signals. Besides the obvious frequency measures, this chart reveals the high correlation between counts and the average frequency, as the latter is based on the former value (see Appendix C in [2] for precise definition).

As this kind of behaviour seems to appear in many AE datasets of composites, this indicates that there is a distinct difference in the descriptive capabilities of both branches. Therefore, this motivates the organization of this work in two sections, one dealing with a review of “energetic” AE features and one dealing with a discussion of “frequency” AE features.

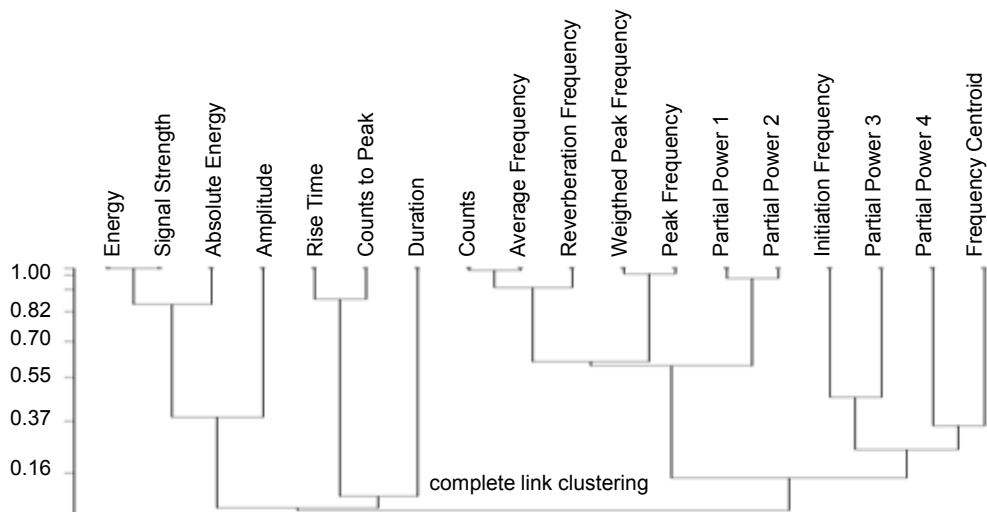


Figure 1. Hierarchical clustering of dataset using the Ward-algorithm (agglomerative tree linkage).

3. Energetic AE signal features

Several fundamental acoustic emission theories aim to establish a relationship between the AE source type, the properties of the fracturing homogeneous isotropic solids and the resulting AE signal [2]. Composite materials are, dependent on the observation scale, significantly different to that, i.e. they are only homogeneous on the macroscopic scale where they may be approximated as homogeneous anisotropic solids. Nevertheless, the key principles of these theories are still found to be still valid for composite materials [2].

One of the common results of all the theories mentioned above is that they expect a proportionality between the size of a crack growth a and the AE signal amplitude U . The theory of Lysak would propose $U \propto a^{3/2}$ for the case of a “crack-through” and $U \propto a$ for an internal “penny-shaped” crack [22]. Green and Zerna reported a $U \propto a$ relationship for a crack-through process [26]. Investigations by finite element modeling recently confirmed the relationship $U \propto a^{3/2}$ for a crack-through process in a homogeneous material, while results from internal cracks apparently obey the $U \propto a$ relationship [2].

The theory of Ohtsu and Ono uses the moment tensor representation for AE sources, which generally states $U \propto \Delta V$, with ΔV being the internal volume produced by the crack growth [23], [24]. Similar, the theory of Scruby and Wadley would predict the proportionality $U \propto \Delta V$, given the dynamics of the crack process are unchanged when comparing different crack sizes [2], [27], [28].

3.1. Matrix cracking and interfacial failure

In a composite, the expected variation of crack sizes for “matrix cracking” ranges from fairly small length scales in the order of 1 μm to 10 μm (cf. figure 2a) to reasonably macroscopic sizes such as several 100 μm to some 1 mm (cf. figure 2b). In [29] polymer fracture was even measured to generate one huge signal for final fracture at several centimetres of length scale.

The theories quoted above allow estimating an increase of the corresponding acoustic emission signal amplitude by three orders of magnitude. This corresponds to a dynamic range of the corresponding AE signal amplitudes of at least 60 dB (1µm to 1mm internal cracks). Furthermore, for a typical composite, there is no expectation of distinct crack sizes, as larger “matrix cracks” do not necessarily need to grow at once, but may show several intermediate rests. This will result in more than one AE signal for one such macroscopic crack. Accordingly, the distribution of crack lengths for source types such as “matrix cracking” and “interfacial failure” is not discrete. This is different in some cases, when the typical extent is geometrically limited in one more directions (e.g. because of ply structure, bundle distances, or other). Thus, in [30] it was demonstrated, that the average signal amplitude of matrix cracking is related to the thickness of the failing plies. Similar, findings in [31] indicate, that matrix cracking in fibre yarns causes characteristic acoustic emission energies.

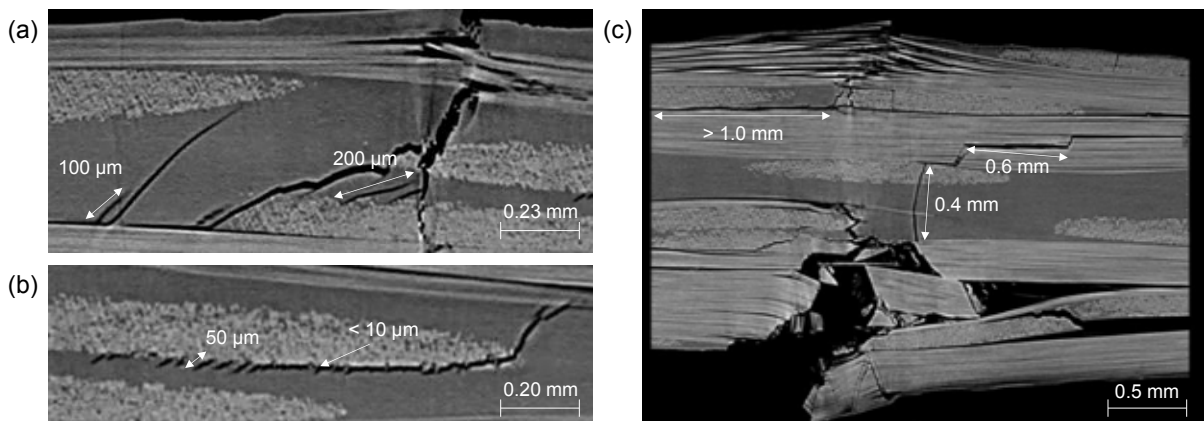


Figure 2. Computed tomography image of crack network on microscale (a and b) and on macroscale (c) taken from damage region of four-point bending sample of [10], [12].

Nevertheless, for the majority of composites, there is no general discretization of crack dimensions for matrix cracking and interfacial failure, but a homogeneous distribution of crack length sizes. Hence, it appears invalid to detect the occurrence of either “matrix cracking” or “interfacial failure” based on a particular amplitude range unless the microstructure explicitly forces discrete size distributions.

3.2. Fibre breakage

Another type of failure mechanism frequently interpreted in terms of its expected AE signal amplitude is fibre breakage. Essentially, contradicting proposals have been made that either concluded $U_{fiber} \gg U_{matrix}$ or $U_{fiber} < U_{matrix}$.

Based on the theories mentioned in section 3.1, the decisive factor for the size of the AE amplitude is the ΔV -value. Due to the fibre diameters, the crack area is well defined for carbon fibres (5 µm to 10 µm) or glass fibres (10 µm to 50 µm). For fibres failing under tensile load, the additional contribution to ΔV is the extension along the fibre axis. The amount of this extension in load direction relates to two factors, namely (i) the amount of elastic energy stored before fibre failure and (ii) the confinement effect of the surrounding fibres and matrix. The first

contribution implicitly relates the amount of extension to such factors as the fibres tensile strength (or their fracture toughness). Hence, a larger ΔV expects for a stronger fibre. In addition, a stronger AE signal is expected for a 10 μm diameter cracking fibre vs. a 10 μm diameter cracking matrix polymer. Assuming typical fibre and matrix failure strength values (50 MPa polymer vs. 5 GPa fibre) and applying the theoretical relationships above, for the same cross-sectional area this results in 100 times larger AE signal amplitude and accordingly $U_{fiber} < U_{matrix}$. Note that this description does not take into account potential additional contributions to ΔV due to matrix cracking and debonding surrounding the fibre filament. This might well lead to additional contributions to the fracture surface normal to the tensile load (i.e. factor of 2 – 4 as estimated from computed tomography images, cf. figure 3).

A primary difference to the discussion of amplitude distribution of section 3.1 is the discrete size distribution expected for fibre breakage. As demonstrated e.g. by [32] the single filament failure initiates long before ultimate failure and does not necessarily result in cascades of fibres failing simultaneously. For constant cross-section and constant fibre strength, a discrete AE energy release is theoretically expected. However, this discrete energy smoothens out due to the cross-section distribution of the fibre filaments and the Weibull strength distribution of the filaments.

Single filament testing sometimes is used to demonstrate that fibre breakage AE signals have very strong amplitudes. As sketched in figure 3, the confinement of the failing filament is substantially different in single filament testing vs. a real composite. In the case of the free filament, the crack faces may move independently in each direction, reaching many millimetres or even centimetres. For fibre failure inside a composite material, the surrounding fibres and matrix (in case they do not fail simultaneously) confine the movement of the breaking fibre. In this case the resulting movement along the axis could be quantified using in-situ computed tomography analysis to be less than 5 μm as seen in figure 3-b [33]. Thus, the resulting ΔV is more than three orders of magnitude smaller than for single filament testing. Based on the theories stated above this would result in a corresponding reduction of AE signal amplitudes of up to 90 dB_{AE}. The same change in energy release was also consistently found in finite element modelling for the case of free fibre filaments in [33] and for confined fibres in [2].

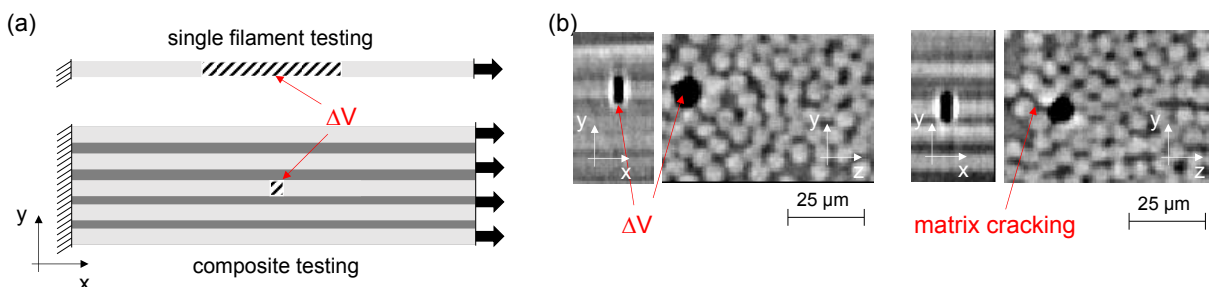


Figure 3. Schematic difference in ΔV for single filament testing vs. fibres confined within composite material (a) and experimental measurement of ΔV using high-resolution computed tomography at 0.4 μm voxel size (b).

Other indications that fibre breakage signals from composites (confined condition) show relatively low amplitudes were recently provided by Lomov et al. and Swolfs et al. [30], [31]. They compared theoretical predictions for first fibre filament failure based on classical Weibull theory to the corresponding onset of AE signals. Overall, the predicted onset of the weakest fibre filaments systematically preceded the measured AE onset. This indicates that the AE signals of the weakest fibres possibly fall below the experimentally used detection threshold. This was additionally verified by finite element modelling of fibre breakage with varying tensile strength following a Weibull-type strength distribution in [2].

As baseline of all these considerations above, the dominating factors for the AE signal amplitude (and hence energy) are the size of the crack as well as the amount of elastic energy stored immediately before fracture.

4. Frequency AE signal features

In contrast to the energetic AE signal features, there are several established ways to compute frequency information to represent the recorded AE signals. The three different features “Initiation-“, “Reverberation-“ and “Average-Frequency” are used to provide an estimate of the characteristic frequency before and after the peak-maximum and of the complete signal (see Appendix C in [2] for precise definition). These features are no exact frequencies since they rely on the number of signal threshold crossings, which is a discrete and often error-prone count, thus resulting in relatively inaccurate nominal frequencies.

A significantly better approach is to compute the Fast-Fourier-Transformation (FFT) of the AE signal. The “Peak-frequency” f_{peak} is the frequency value of maximum intensity in the spectrum. The “Frequency Centroid” $f_{centroid}$ characterizes the frequency content of an AE signal in a similar way as the centre of mass describes the properties of geometric object with uniform density. Thus, it is an independent evaluation of the characteristic average frequency of the signal and is generally not equal to the “Peak-frequency”. Another means of representing the signals frequency spectrum is the definition of different “Partial Power” levels. They measure the signals frequency contribution within a given interval and represent the frequency distribution of the AE signal by more than only one characteristic value. Hence, they usually are defined for subdivisions of a certain frequency range of interest, e.g. 150 kHz intervals ranging from $f_{start} = 0$ kHz to $f_{end} = 1200$ kHz (see Appendix C in [2]).

Another sophisticated approach is to extract the frequency information from time-frequency transformations. Using such concepts based on wavelets [34] or kernel convolution procedures such as those proposed by Choi and Williams [35] this allows to obtain additional frequency features. For the discrete wavelet transformation, the intensity of the decomposition levels has been proposed as features to describe the AE signal [36], [37].

Similar as for the energetic features, established theories allow raising some expectations for the resultant frequency spectrum of a particular source mechanism in a fibre reinforced composite. All of the established theories assume a source function, which is due to a rapid internal displacement [19], [22]–[24] and has been recently confirmed by fracture mechanics

based numerical modelling [33]. Typically, this is a step function as seen exemplarily in figure 4-a for two typical rise-times. In this simple source representation, the governing factor to judge on the source dynamics is the rise-time of the internal displacement. However, the rise-time is not identical to the time the crack needs to propagate. In [2], [33] the duration for crack growth was found to be substantially shorter than the rise-time of the source function with the additional dynamics caused by inertia effects and by the vibration of the crack faces, as well as propagating surface waves. Nevertheless, a simple FFT of the two exemplary source functions of figure 4-a reveals the corresponding bandwidth of the AE source and is plotted in figure 4-b. Naturally, faster internal displacement generates broader bandwidth, i.e. causes excitation of higher frequencies. Similar, the slower internal displacement causes reduced bandwidth of the source.

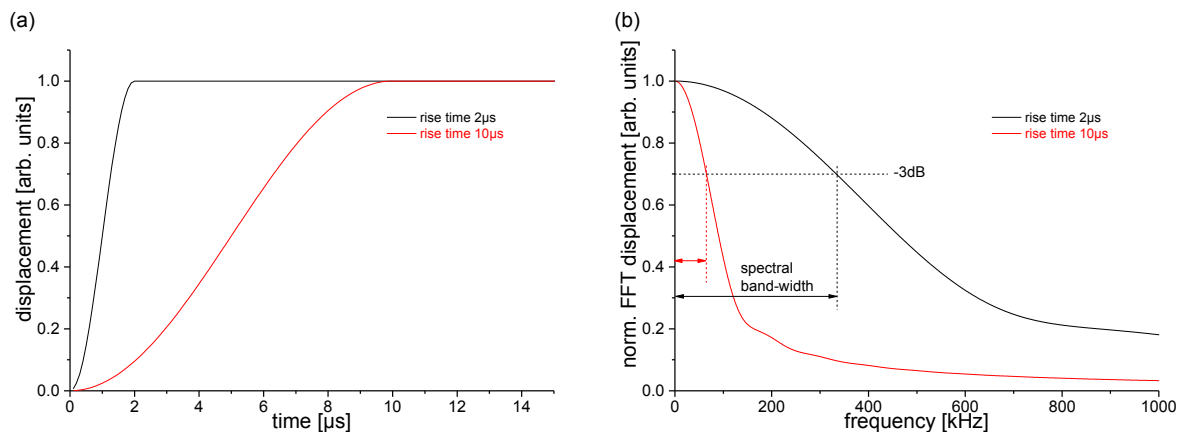


Figure 4. Scheme of source function (a) and corresponding spectral bandwidth estimated from -3dB drop (b).

4.1 Dynamics of source mechanisms in composites

Based on these considerations, the discussion now focuses on the expected dynamics for different source mechanisms. In general, the duration for a singular crack event (from initiation to rest) links to two factors. This is (i) the ductility/brittleness of the material and (ii) the geometry/extension of the crack growth. The first item directly links to the crack propagation speed. As has been discussed by Scruby [25], depending on the applied load and the material properties, cracks may potentially reach their ultimate propagation speed limit, which is the Rayleigh wave speed. The second item relates to the geometric boundary conditions posed for the crack growth. At constant speed, larger crack length will need longer to form than shorter crack length, hence adding to the overall rise-time of the source. Potentially there is a fixed upper limit to this duration of growth, as cracks in composites can be geometrically confined due to sizes of the plies or due to the overall dimension of the sample (width, thickness, ...).

For failure mechanisms such as matrix cracking or delamination the basic expectation for broad crack length distributions has already been discussed in section 3.1. Based on the above considerations, this would expect a broad distribution of source rise-times for these cases.

Likewise, for discrete crack dimensions as for fibre breakage, a discrete rise-time distribution is expected.

However, reinforcement fibres such as glass or carbon fail more brittle than typical matrix polymers and also exhibit up to one order of magnitude higher Rayleigh velocities (e.g. glass 3000 m/s, carbon 5000 m/s, polymer 500 m/s) as can be calculated from the materials Young's modulus, density and Poisson's number when using the Bergman approximation [38].

Hence, generally the rise-time of the source function is significantly shorter for failure of the reinforcement fibres than for a comparable failure size of a matrix polymer. Accordingly, nominally larger crack increments as for matrix cracking and interfacial failure will reduce the bandwidth further compared to the fibre breakage bandwidth.

4.2 Transfer of frequency information from source to sensor

Although, the source dynamics govern the bandwidth of the source and the spectrum itself seems to be fairly flat with frequency (cf. figure 4-b), there are several factors which affect the propagation of frequency information from source to sensor. One example obtained from FEM calculus to demonstrate the severity of these effects shows figure 5.

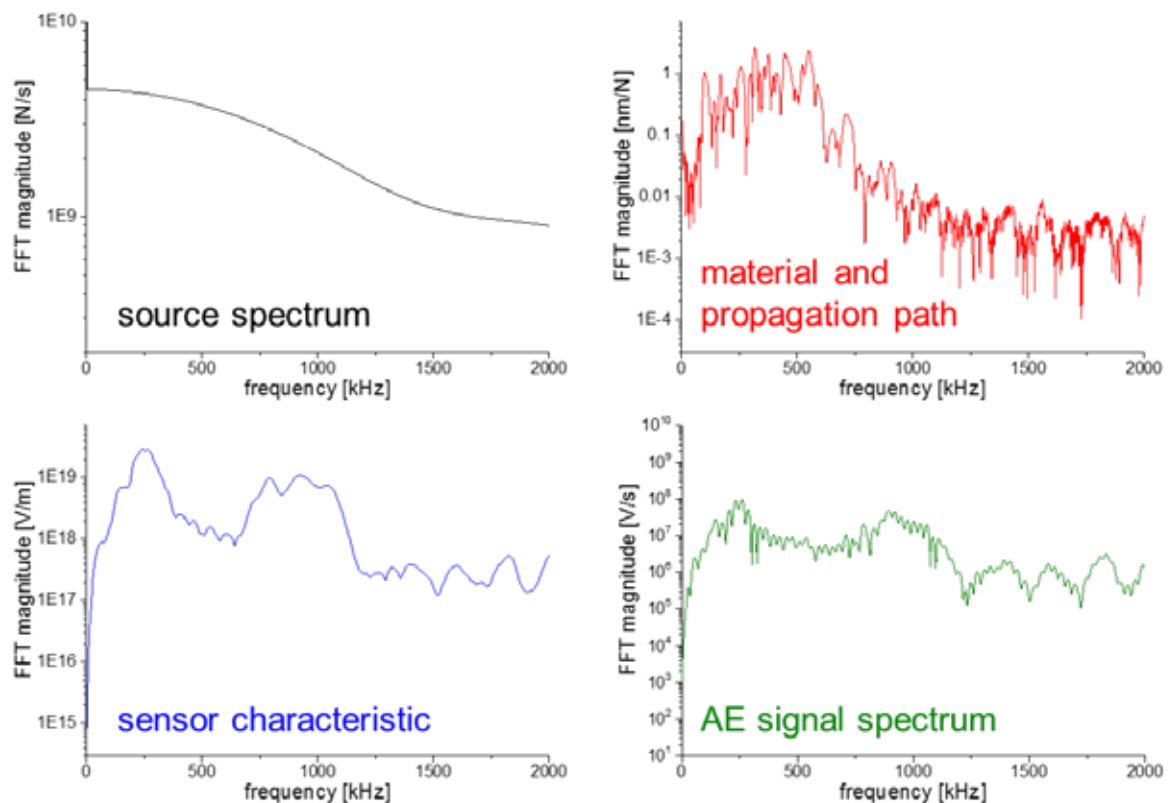


Figure 5. Transmission characteristics of sensor, material and propagation path and their influence on generation of AE signal spectrum in relation to source spectrum.

The first non-linear transmission is the formation of guided waves in a typical thin-walled composite plate. As discussed in [2], the formation of plate waves comes with particular frequency regions, that allow preferential transmission of the signal. Correspondingly, some frequency ranges transmit badly, resulting in a significant change of the frequency spectrum. The particular frequency values for preferential transmission depend mostly on the thickness of the plate and the material properties. This guided wave propagation also leads to formation of some of the characteristic peaks in the FFT spectrum of the final AE signal. Another important source of non-linear transmission is the sensing system used. Especially for the typical commercial sensor systems (resonant or multi-resonant designs), this results in additional reduction of bandwidth or may cause characteristic peaks in the frequency spectrum, which are owed to the internal sensor resonances (cf. figure 5).

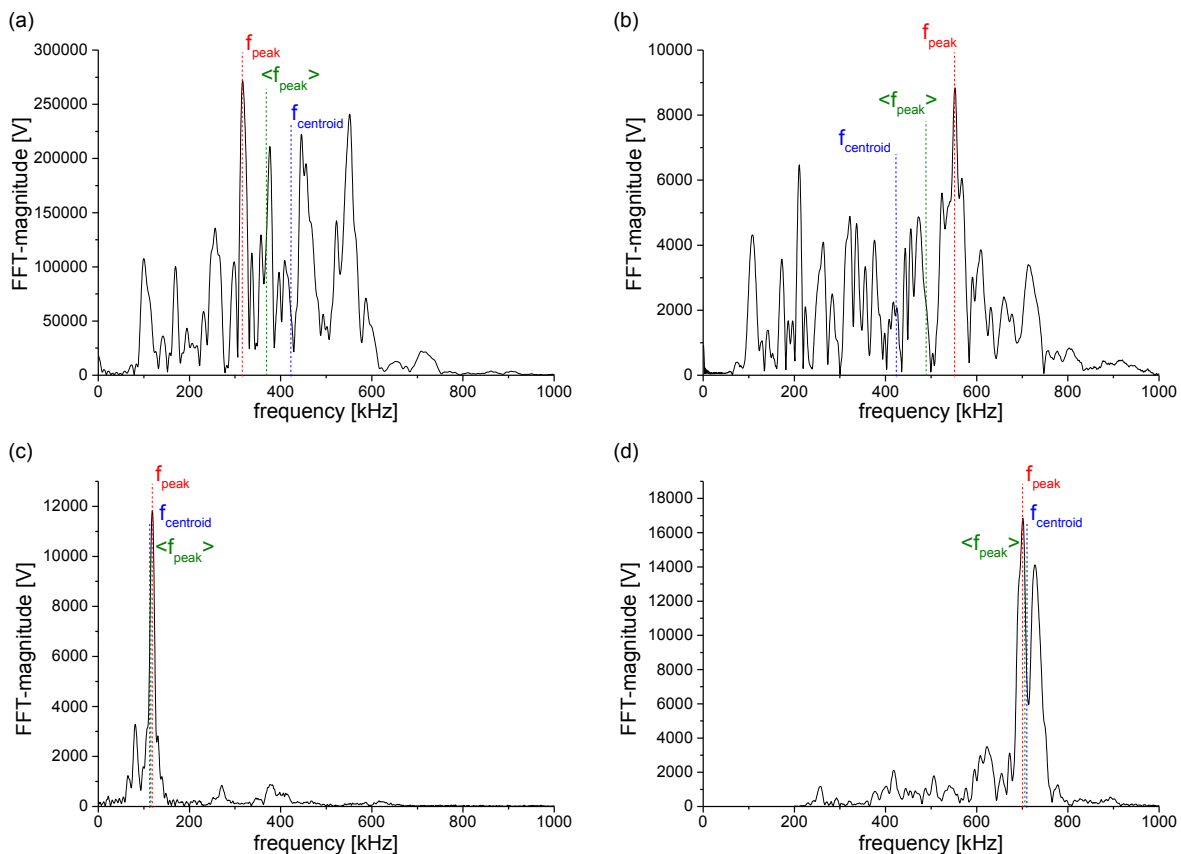


Figure 6. Comparison of frequency representation for four AE signals (a-d) using Peak-frequency f_{peak} , Frequency Centroid $f_{centroid}$ and Weighted Peak-Frequency $\langle f_{peak} \rangle$.

As seen in figure 5, the frequency information of the AE source maps not well to the acquired electrical AE signal. In particular, features such as the “Peak-frequency” usually link either to the sensor resonances or to the frequency ranges of preferential transmission of the guided waves. Thus, it does not seem appropriate to use such features to distinguish failure mechanisms based on their absolute frequency values. Typically, a choice to distinguish a mechanism of e.g. ≤ 137 kHz is either due to the sensor used or due to the material investigated.

To remove the sensor and material bias implicit to the frequency features, the use of relative features, such as the “Weighted Peak-Frequency” $\langle f_{peak} \rangle$ or “Partial Powers” was proposed [11]. As the aim of all the frequency features is to best represent the frequency spectrum, consider the four examples shown in figure 6. Visually, one would state close similarity between the spectra of figure 6-a and 6-b and high dissimilarity between spectra of figure 6-c and 6-d. Accordingly, frequency parameters should be representative numerical values for this observation. Using the f_{peak} feature this works well for the bottom case, resulting in a difference of 600 kHz. However, the upper case results in a difference of 240 kHz for visually similar spectra. Accordingly, absolute values of the f_{peak} feature do not suffice in this case.

The $f_{centroid}$ feature is less susceptible to the occurrence of peaks in the spectrum as it is obtained from an averaging of the full spectrum. However, the disadvantage of this is the reduced sensitivity to relative changes of frequency spectra. Although the example spectra of figure 6-a and 6-b are similar, they still do have different weight at low and high frequencies. Still the $f_{centroid}$ is numerically almost identical for both spectra. This lack of sensitivity of the $f_{centroid}$ feature is quite typical as the basic “finger-print” of the spectrum originates to a significant extent from constant contributions, such as sensor characteristics and guided wave propagation (cf. figure 5). Therefore, the $f_{centroid}$ feature by itself is not very useful to capture small changes relative to the average frequency content.

As result of these observations, the combination of both features into the $\langle f_{peak} \rangle$ feature was proposed [11]. As square-root combination of both other features, it retains the good discriminative capability of the f_{peak} , but is also susceptible to small changes in frequency spectrum (cf. figure 6-a and 6-b) without being too susceptible to the resonance frequencies of AE sensor or the material.

5. Conclusion

Based on the presented considerations it hardly seems applicable to perform source identification in composite materials based on energetic features unless there is a discrete size distribution expected for one mechanism. In specific cases this can be justified (i.e. matrix cracks all growing the full height and width within a ply at once). In a general situation, there is no expectation for a discrete distribution of AE signal amplitudes for one of the failure mechanisms in a composite. Instead, especially for “matrix cracking” and “interfacial failure” a wide distribution of AE signal amplitudes is expected, which cover several orders of magnitude. Thus, the AE signal amplitude and energetic features should be interpreted more in terms of strength or severity of the failure mechanism other than a feature to distinguish failure mechanisms.

In order to perform source identification, frequency features were found to provide better discriminative capabilities. The AE signals bandwidth directly relates to the duration of the crack growth. In fibre-reinforced composites, the different failure mechanisms show characteristic crack durations, which originates from the speed of the crack propagation and the typical crack length of the different mechanisms (specifically for fibre breakage). However,

the transfer of the information of the source bandwidth to corresponding AE features suffers from resonances of the structure and the sensor. To overcome the associated issues in evaluation of the frequency spectra the “weighted Peak-Frequency” was proposed. In combination with other frequency features such as the “Partial Powers” and multi-variant data analysis (e.g. by pattern recognition methods [12]) this appears as best approach to meaningful AE source identification in fibre-reinforced composites, as the reliability of a single AE feature is not significant enough to allow this complex task.

References:

- [1] E. Greenhalgh, *Failure Analysis and Fractography of Polymer Composites*. Oxford/Cambridge/New Delhi: Woodhead Publishing Limited, 2009.
- [2] M. G. R. Sause, *In Situ Monitoring of Fiber-Reinforced Composites*, vol. 242. Cham: Springer International Publishing, 2016.
- [3] A. A. Anastassopoulos and T. P. Philippidis, “Clustering Methodology for the Evaluation of Acoustic Emission from Composites,” *J. Acoust. Emiss.*, vol. 13, 1995.
- [4] T. Philippidis, V. Nikolaidis, and A. Anastassopoulos, “Damage Characterisation of C/C laminates using Neural Network Techniques on AE signals,” *NDT&E Int.*, vol. 31, 1998.
- [5] J. M. Richardson, R. K. Elsley, and L. J. Graham, “Nonadaptive, semi-adaptive and adaptive approaches to signal processing problems in nondestructive evaluation,” *Pattern Recognit. Lett.*, vol. 2, no. 6, 1984.
- [6] E. Vi-Tong and P. Gaillard, “An algorithm for non-supervised sequential classification of signals,” *Pattern Recognit. Lett.*, vol. 5, no. 5, 1987.
- [7] S. Huguet, N. Godin, R. Gaertner, L. Salmon, and D. Villard, “Use of acoustic emission to identify damage modes in glass fibre reinforced polyester,” *Compos. Sci. Technol.*, vol. 62, 2002.
- [8] C. R. Ramirez-Jimenez, N. Papadakis, N. Reynolds, T. H. Gan, P. Purnell, and M. Pharaoh, “Identification of failure modes in glass/polypropylene composites by means of the primary frequency content of the acoustic emission event,” *Compos. Sci. Technol.*, vol. 64, 2004.
- [9] A. Marec, J.-H. Thomas, and R. Guerjouma, “Damage characterization of polymer-based composite materials: Multivariable analysis and wavelet transform for clustering acoustic emission data,” *Mech. Syst. Signal Process.*, vol. 22, pp. 1441–1464, 2008.
- [10] M. G. R. Sause, F. Haider, and S. Horn, “Quantification of metallic coating failure on carbon fiber reinforced plastics using acoustic emission,” *Surf. Coatings Technol.*, vol. 204, no. 3, 2009.
- [11] M. G. R. Sause and S. Horn, “Simulation of Acoustic Emission in Planar Carbon Fiber Reinforced Plastic Specimens,” *J. Nondestruct. Eval.*, vol. 29, no. 2, 2010.
- [12] M. G. R. Sause, A. Gribov, A. R. Unwin, and S. Horn, “Pattern recognition approach to identify natural clusters of acoustic emission signals,” *Pattern Recognit. Lett.*, vol. 33, no. 1, 2012.
- [13] D. D. Doan, E. Ramasso, V. Placet, L. Boubakar, and N. Zerhouni, “Application of an Unsupervised Pattern Recognition Approach for AE Data Originating from Fatigue Tests on CFRP,” in *31st Conference of the European Working Group on Acoustic Emission*, 2014.
- [14] A. A. Anastassopoulos, V. N. Nikolaidis, and T. P. Philippidis, “A Comparative Study of Pattern Recognition Algorithms for Classification of Ultrasonic Signals,” *Neural Comput. Appl.*, vol. 8, 1999.
- [15] P. Yu, V. Anastassopoulos, and a. N. Venetsanopoulos, “Pattern recognition based on morphological shape analysis and neural networks,” *Math. Comput. Simul.*, vol. 40, 1996.
- [16] F. Baensch, M. G. R. Sause, A. J. Brunner, and P. Niemz, “Damage evolution in wood – pattern recognition based on acoustic emission (AE) frequency spectra,” *Holzforschung*, vol. 69, no. 3, 2015.
- [17] V. Kostopoulos, T. Loutas, A. Kontsos, G. Sotiriadis, and Y. Pappas, “On the identification of the failure mechanisms in oxide/oxide composites using acoustic emission,” *NDT E Int.*, vol. 36, no. 8, 2003.
- [18] R. de Oliveira, O. Frazão, J. L. Santos, and A. T. Marques, “Optic fibre sensor for real-time damage detection in smart composite,” *Comput. Struct.*, vol. 82, no. 17–19, 2004.
- [19] M. Giordano, L. Condelli, and L. Nicolais, “Acoustic emission wave propagation in a viscoelastic

- plate," *Compos. Sci. Technol.*, vol. 59, 1999.
- [20] J. Bohse, "Acoustic emission characteristics of micro-failure processes in polymer blends and composites," *Compos. Sci. Technol.*, vol. 60, 2000.
- [21] B. S. Everitt, *Cluster Analysis*, 3rd ed. John Wiley & Sons Inc., New York, 1993.
- [22] M. V. Lysak, "Development of the theory of acoustic emission by propagating cracks in terms of fracture mechanics," *Eng. Fract. Mech.*, vol. 55, no. 3, 1996.
- [23] M. Ohtsu and K. Ono, "A generalized theory of acoustic emission and Green's function in a half space," *J. Acoust. Emiss.*, vol. 3, 1984.
- [24] M. Ohtsu and K. Ono, "The generalized theory and source representation of acoustic emission," *J. Acoust. Emiss.*, vol. 5, 1986.
- [25] C. B. Scruby, "Quantitative acoustic emission techniques," *Nondestruct. Test. Vol. 8*, 1985.
- [26] A. E. Green and W. Zerna, *Theoretical Elasticity*. New York, USA: Oxford University Press, 2002.
- [27] M. G. R. Sause and A. Monden, "Comparison of Predicted Onset of Failure Mechanisms By Nonlinear Failure Theory and By Acoustic Emission Measurements," in *16th European Conference on Composite Materials*, 2014.
- [28] C. B. Scruby, H. N. G. Wadley, and J. J. Hill, "Dynamic elastic displacements at the surface of an elastic half-space due to defect sources," *J. Phys. D. Appl. Phys.*, vol. 16, no. 6, 2000.
- [29] S. O. Gade and M. G. R. Sause, "Measurement and Study of Electromagnetic Emission Generated by Tensile Fracture of Polymers and Carbon Fibres," *J. Nondestruct. Eval.*, vol. 36, no. 1, 2017.
- [30] S. Lomov, M. Karahan, A. Bogdanovich, and I. Verpoest, "Monitoring of acoustic emission damage during tensile loading of 3D woven carbon/epoxy composites," *Text. Res. J.*, vol. 84, no. 13, 2014.
- [31] Y. Swolfs, I. Verpoest, and L. Gorbatikh, "Issues in strength models for unidirectional fibre-reinforced composites related to Weibull distributions, fibre packings and boundary effects," *Compos. Sci. Technol.*, vol. 114, 2015.
- [32] A. E. Scott, M. Mavrogordato, P. Wright, I. Sinclair, and S. M. Spearing, "In situ fibre fracture measurement in carbon-epoxy laminates using high resolution computed tomography," *Compos. Sci. Technol.*, vol. 71, no. 12, Aug. 2011.
- [33] M. G. R. Sause and S. Richler, "Finite Element Modelling of Cracks as Acoustic Emission Sources," *J. Nondestruct. Eval.*, vol. 34, no. 1, 2015.
- [34] M. A. Hamstad, "Comparison of Wavelet Transform and Choi-Williams Distribution to Determine Group Velocities For Different Acoustic Emission Sensors," *J. Acoust. Emiss.*, vol. 26, 2008.
- [35] H.-I. Choi and W. Williams, "Improved Time-Frequency Representation of Multicomponent Signals Using Exponential Kernels," *IEEE Trans. Acoust. Speech Signal Process.*, vol. 37, no. 6, 1989.
- [36] L. Angrisani, P. Daponte, and M. D'Apuzzo, "A method for the automatic detection and measurement of transients. Part I: the measurement method," *Measurement*, vol. 25, no. 1, 1999.
- [37] G. Qi, A. Barhorst, J. Hashemi, and G. Kamala, "Discrete wavelet decomposition of acoustic emission signals from carbon-fiber-reinforced composites," *Compos. Sci. Technol.*, vol. 57, 1997.
- [38] R. H. Bergman, R. A. Shahbender, E. H. Bergman, R. A. Shahbender, R. H. Bergman, and R. A. Shahbender, "Effect of Statically Applied Stresses on the Velocity of Propagation of Ultrasonic Waves," *J. Appl. Phys.*, vol. 29, no. 12, p. 1736, Jun. 1958.

03 - Damage diagnostic and lifetime prognosis for ceramic matrix composite with Acoustic Emission during long-term mechanical tests at intermediate temperature

Nathalie Godin, Pascal Reynaud, Gilbert Fantozzi

University of Lyon, INSA Lyon, MATEIS, UMR 5510, 69621 Villeurbanne cedex

Abstract:

Damage of composite materials is a key factor for the durability in service. It is therefore essential to define the most suitable damage indicators and to develop models to estimate the Remaining Useful Lifetime from analysis of precursor events resulting from damage. Acoustic emission is relevant to the development of the Prognostic and Health Management because it allows knowing the state of damage of a composite structure in real time. This work is dedicated to lifetime prediction using AE for long-term tests on CMC during static and cyclic fatigue tests. New indicators of damage have been defined, based mainly on acoustic energy analyses. These indicators highlight critical times (around 50 % of the composite lifetime) allowing an evaluation of the remaining lifetime. A linear correlation is observed between these critical times and the lifetime duration. For a prognostic phase, the results obtained with this empirical law are compared to those obtained with a power law such as a Benioff law. Moreover, the clustering of acoustic emission, using a random forest approach, makes possible to identify the mechanism responsible for this critical time. For the static fatigue test, the critical time around 50 % correspond to the delayed failure of fibres.

1. Introduction

Ceramic matrix composites (CMCs) are very attractive candidates for civil aircrafts applications because of their excellent creep resistance, high-temperature strength and lightweight [1-2]. Even though both fibre and matrix are made of brittle materials (mostly Carbon and Silicon Carbide), CMCs can reach relatively high strain-to-failure due to energy dissipation through multiple matrix cracking, deviation of cracks at the fibre/matrix interface or propagation into a multi-layered matrix. Matrix cracking is then the first main damage mechanism occurring. However, the composite failure is driven by physicochemical degradation of the fibres that includes both effects of stress redistribution during damaging of matrix and interface and effects of oxidation. The various phenomena that are involved in the damage process make the lifetime prediction of this type of material a very challenging work. Here, the objective is to develop a new approach based on acoustic emission monitoring that would allow real-time prediction of the Remaining Useful Lifetime (RUL) of CMCs during fatigue tests. The aim of prognostics is to make remaining useful lifetime previsions [3-6]. Prognostics is a natural extension of structural health monitoring where the user is not only concerned with detecting, locating and identifying damage but also determining the RUL long before failure. The RUL or the TTF (Time To Failure) can be defined as duration between the time t (after detection of the damage) and the time when the damage will reach its critical threshold. It is a continuous process and predictions must be regularly updated as the system health state changes (Fig.1). A diagnosis phase and a prognostic phase can thus be distinguished. The diagnosis phase must be able to detect, locate, identify the damage and assess its severity. The prognosis

phase, based on the results of the diagnosis and on models, makes it possible to evaluate the residual lifetime. Acoustic emission allows reaching this objective, as this technique allows the health of an entire structure regardless of its size to be monitored. The analysis of the collected data can be used to discriminate the sources of damage (matrix cracks, fibre breaks, fibre/matrix decohesion, delamination...) [7-9] and to measure the kinetics of the various degradation mechanisms. In addition, an estimate of the composite materials remaining lifetime can be considered based on a real-time tracking of the damage recorded by EA. In this context, two approaches based on two complementary analyses of acoustic activity are developed:

(1) a collective and cooperative analysis of all the collected signals. The idea is to predict the lifetime of a part in service by analysing its behaviour by monitoring the acoustic emission during the load. The rupture can then be predicted by looking at the cooperative aspect, synthesizing all the information contained in the events in a global way.

(2) an individual analysis of the signals: the objective of this analysis is to associate each EA signal with the generated damage mechanism. This allows, in real time, identifying the type of damage that occurs and to quantify its severity.

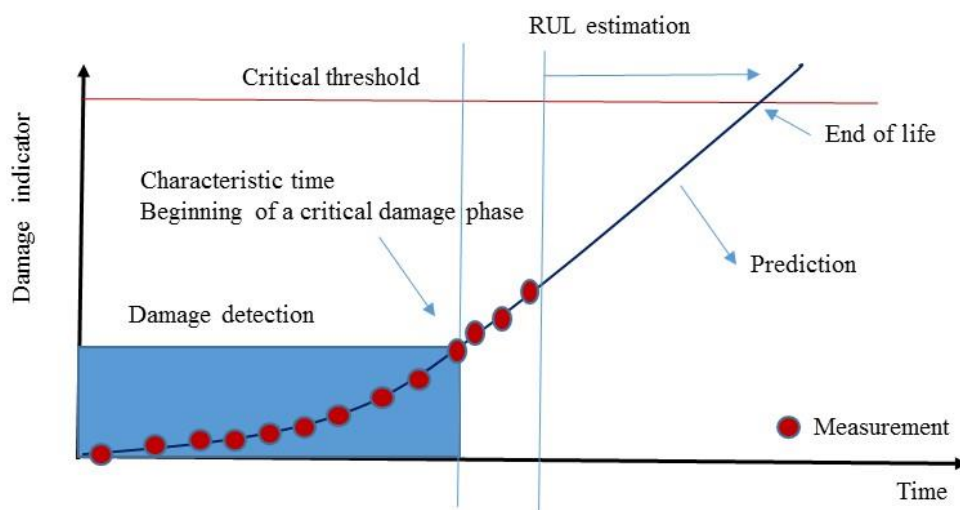


Figure 1: Prediction of lifetime of Ceramic Matrix Composite during long-term mechanical tests

2. Description of work

2.1 Materials, mechanical tests and AE monitoring

Fatigue tests have been realized at a temperature of 450°C or 500 °C under air. The material is a ceramic matrix composite reinforced with Nicalon SiC fibres, coated with PyC and embedded in a self-healing [Si-B-C] matrix, manufactured by SAFRAN CERAMICS. The reinforcement architecture is a stack of several layers of 2D satin fabrics linked together by strands of fibres in the third direction. In this study, all the specimens have a dog-bone shape with a thickness of 4 mm and a gauge section of 60 mm x 16 mm. For static fatigue tests, specimens were first loaded at constant loading rate of 1kN/min, and periodically (every 6 or

12 hours) unloading-reloading cycles were carried out in order to determine the secant elastic modulus. Cyclic fatigue tests were conducted under a tensile/tensile sinusoidal loading with constant amplitude and a frequency of 2 Hz. Strain is measured using by an extensometer.

Two piezoelectric sensors (Micro80, Mistras Group) are maintained on the specimen surface. Medium viscosity vacuum grease is used to ensure a good coupling between the specimen and sensors. Each sensor is connected to the data acquisition system (PCI2, Mistras Group) via a preamplifier with a 40 dB gain and 20-1200 kHz bandwidth (Mistras Group). The position of a detected source can be determined linearly knowing the wave velocity in the material.

2.2 Damage indicators

Most of the damage indicators are based on the investigation of the AE energy. It is generally accepted that the energy of an AE signal includes the energy released by the source at crack initiation. The following equation is proposed to describe the energy of recorded AE signals (for instance, at sensor 1) received from the source n [10-11]:

$$E_i(n) = E_s(n) \cdot A_i \cdot e^{-B(L+x(n))} \quad (1)$$

$E_s(n)$ is the energy released at source n in the form of elastic waves. A_i is the proportion of source energy that is recorded by sensor i . It is a constant characteristic of sensor. $L + x(n)$ is the distance of propagation from source n to sensor 1 ($2L$ being the distance between sensors). The attenuation coefficient B is related to the propagation medium, which is subjected to changes due to damage evolution.

The source energy is then defined as the square root of the product of the amounts of energy received at both sensors for each source:

$$E_{eq} = \sqrt{E_1 \times E_2} = E_s(n) \cdot A_1 \cdot A_2 \cdot e^{-BL} \quad (2)$$

where L is the distance between sensors. B is related to the propagation medium but it is supposed independent of the source energy.

2.2.1 Identification of attenuation parameters

To evaluate energy attenuation [10], the ratio of AE signal energies recorded at both sensors is calculated for each source n . For an easier identification of attenuation coefficient B , $X(n)$ is defined as the natural logarithm of this ratio. From Equation 1 for the both sensors, it comes:

$$X(n) = \log \frac{E_1(n)}{E_2(n)} = \log \frac{A_1}{A_2} - 2 \cdot B \cdot x(n) \quad (3)$$

Estimation of attenuation coefficient B is performed as follows. Attenuation is evaluated for a given time interval using the median values of $X(n)$ in every space interval (width: 10 mm, overlapping: 5 mm). Each median value of $X(n)$ corresponds to a few hundred AE sources located in the same space-time interval. The linear approximation is repeated in consecutive

time intervals. Each time interval corresponds to 2000 AE sources. At every increment of 500 sources, a new time interval is considered. The overlapping is set in order to accurately monitor evolution of both attenuation parameters.

2.2.2 Coefficient of emission R_{AE}

The energy of the recorded AE events represents a part of the elastic energy released by CMC specimens. Thus, the evolution of elastic energy released by analysing the energy of AE events may be investigated [12]. The coefficient of emission R_{AE} is defined as the increment of energy ΔE recorded during an increment of time Δt , divided by the total energy emitted during the initial loading of the sample:

$$R_{AE} = \frac{1}{E_{loading}} \frac{\Delta E}{\Delta t} \quad (4)$$

where $E_{loading}$ is the cumulative AE energy for all the signals recorded during the initial loading up to the nominal load of the test, ΔE is the cumulative AE energy for all signals recorded during the interval $[t; t + \Delta t]$.

2.2.3 The severity

In this study, the energy rather than the signal strength is used to define the severity. It is defined as the average energy.

$$S_r = \frac{1}{J} \sum_{m=1}^{m=J} E_m(n) \quad (5)$$

J is an empirical constant.

2.2.4 The coefficient R_{LU}

The indicator denoted R_{LU} , is defined by the ratio of the liberated energy during the loading part of a cycle and the energy recorded during the unloading part of this cycle [13].

2.2.5 Coupling between mechanical data and AE data

AE data and mechanical information can be analysed independently. However, combination of mechanical energy (U_m) and acoustic energy (U_{AE}) denoted Sentry Function (F), initially introduced by Minak [14], can be used in order to obtain a better damage characterization:

$$F = \ln \frac{U_m(x)}{U_{AE}(x)} \quad (6)$$

where $U_m(x)$, $U_{AE}(x)$ and x are respectively the strain energy, the cumulated acoustical energy and the strain of the tested material. It is defined as soon as the first acoustical event is recorded. Strain energy is calculated by measuring the area under the force-displacement curve. To determine only the effects of tension, unloading/loading loads are not taken into account. This global function is calculated every k acoustic sources ($k \sim 0.1\%$ of number of

signals). Sudden drops of the function may be related to the occurrence of a significant internal material damage.

2.3 Power law : Time to failure estimation

Benioff's law [15] (the sum of the square root of the energy released for sequential earthquakes) has been suggested for precursory phenomena of large earthquakes, increasing as an inverse power law of time before a main shock.

$$\Omega(t) = \sum_{i=1}^{N(t)} \sqrt{E_i} = \Omega_R + C(t_R - t)^{1-\gamma} \quad (7)$$

where E_i is the seismic energy release of the i^{th} precursory earthquake and $N(t)$ is the number of precursory earthquakes considered up to time t . Ω_R is the value of $\Omega(t) = \sum_{i=1}^{N(t)} \sqrt{E_i}$

when $t = t_R$, t_R is the failure time. $C = -\frac{\phi}{1-\gamma}$ is negative, $1-\gamma$ is an exponent and ϕ is a constant. Based on Eq. (7), the increase of AE collected during fatigue is analysed. E_i is the energy of the i^{th} AE signal detected and $N(t)$ is the number of AE signals recorded and located along the gauge length until time t .

2.4. Supervised Classification with a random forest algorithm: identification of the acoustic signature

A supervised classification technique can also be used to analyse AE signals recorded during fatigue of CMC composites. This technique requires a database of signals that have been labelled: the training set. This training set was created by merging data collected during tensile test. As described in the previous paper [16], the analysis of AE signals, observation of microstructures and analysis of the mechanical behaviour of the composite led to the identification of 4 types of AE signals and to the following labelling of classes:

Class A: cluster A contains signals from two damage mechanisms, which are chronologically well separated: seal coat cracking and tow breaks,

Class B: cluster B contains also signals from two damage mechanisms, which are chronologically well separated: longitudinal matrix cracking and individual fibre breaks in the fracture zone just before failure,

Class C: Cluster C contains signals with relatively short duration, short rise time and low amplitude when compared to the others: transversal matrix cracking,

Class D: this cluster is the last one to be activated, it becomes more active as strain increases, and the D-type signals have a longer rise time when compared to other signals: sliding at fibre/matrix interfaces, fibre/matrix debonding.

An additional class denoted E was introduced into the library [13]. It corresponds to signals recorded under fatigue, during unloading steps of cycles after the cycle 2000 and for applied stresses lower than $\sigma_{max}/2 - 10$ MPa. These signals are associated to the friction generated in cyclic fatigue.

In order to establish the training set of labelled signals for the supervised analysis, the same amount of signals (2000 signals) in each class (A, B, C, D and E) was used. This training set included all the damage modes that may operate in this composite. The supervised classification is based on a random forest algorithm [17]. During the testing phase, each AE signal runs down each tree of the forest, leading to T votes. The final decision can be obtained by two different ways. The first one is simply the usual majority voting (MV) rule. In this work, a second decision rule is introduced called security voting (SV) rule. In this special rule, one given AE signal is assigned to a specific class if more than 51% of the total number of trees voted for that class and the second class the most represented following the votes has to gather no more than 30 % of the votes [13].

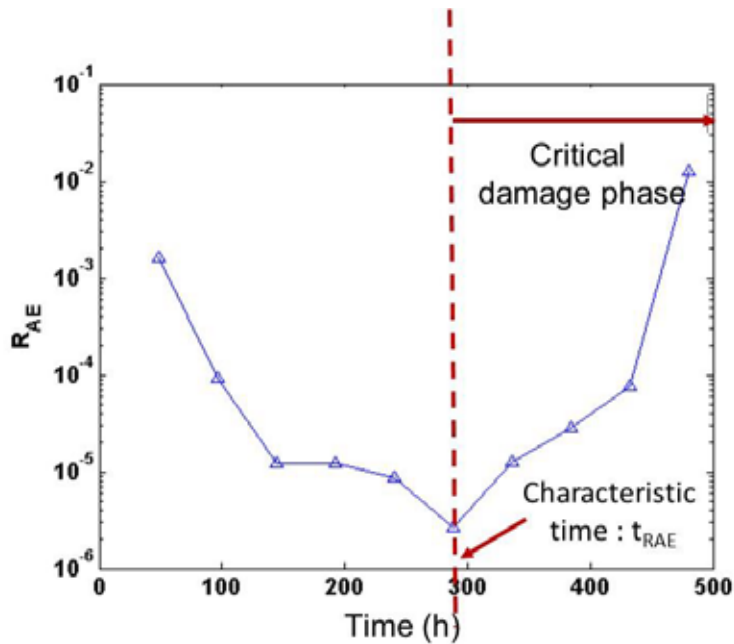
3 Results

3.1 Identification of a critical time during static fatigue test

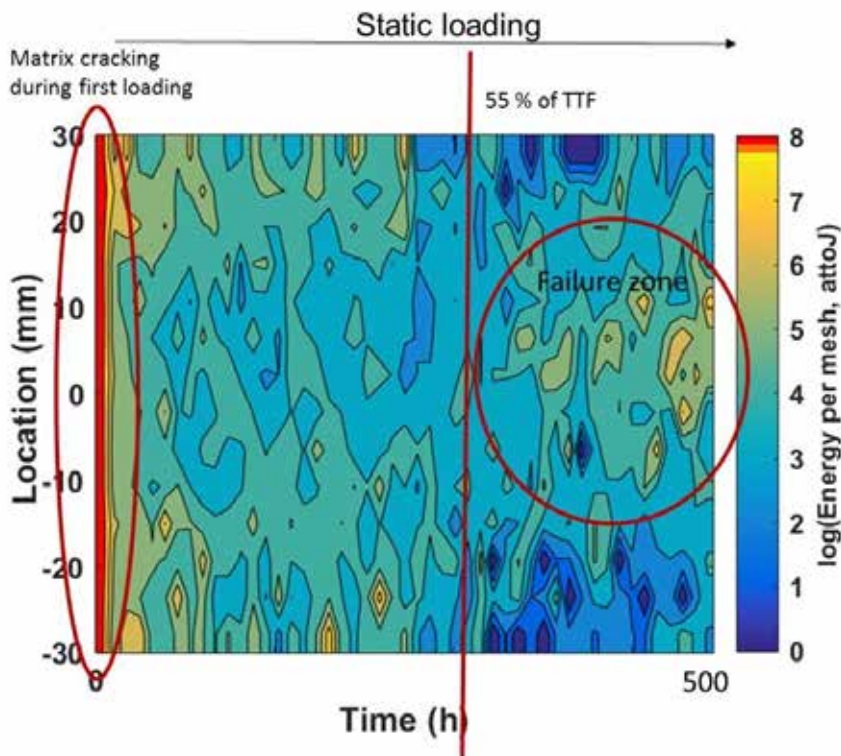
The evolution of R_{AE} coefficient versus time is given in Fig. 2a. R_{AE} coefficient decreases first, down to a minimum value, and then increases up to the failure of the composite [12]. On average, the minimum of R_{AE} appeared at 55% of the rupture time. The representation of AE sources localization during the static fatigue tests reveals that the energy is mainly located near the failure zone after 55 % of the total test duration certainly due to the beginning of fibre breaks (Fig. 2b). The colour scale corresponds to the recorded acoustical energy for the events recorded in a mesh defined in the plane “position” versus “time”. During the first part of the static fatigue test, the recorded energy is distributed along the gauge length certainly associated to the evolution of interfaces. The restart of activity prior to final rupture may be attributed to the avalanche fibres ruptures, controlled by the oxidation of fibres and by the recession of interfaces.

Attenuation coefficient B [11] increases significantly during the first half of tests and reaches a plateau value at approximately 40% of the rupture time (Fig. 3a). At the same time, a slight increase of the damage parameter D can be observed. Fig. 3b shows the evolution of attenuation coefficient B during the tensile test carried out at 450°C. A slight increase is observed until 0.2 % certainly due to the matrix cracking. Thus, attenuation coefficient B remains relatively constant until 0.4 %. Behind this value, a significant increase is observed certainly due to the cracks opening and the evolution of interphases. Moreover, attenuation coefficient B decreases during unloading and increases back to its previous maximum value at the end of reloading. Therefore, attenuation coefficient B , during static loading, is mainly

sensitive to matrix crack opening. The plateau observed on the evolution of attenuation coefficient B indicates that matrix crack opening gets to an equilibrium state around 50% of the rupture time. The significant increase of matrix crack opening observed before 50% of the rupture time is attributed to oxidation of carbon in the interphase causing an increase in length of the debonded region of fibres in the vicinity of matrix cracks. Beyond 50% of the rupture time, the oxygen flux, determined by the degree of matrix crack opening, controls the rate at which fibres break by subcritical crack growth. The sentry function (Fig 3c) mainly sensitive to the matrix cracking does not bring further information.

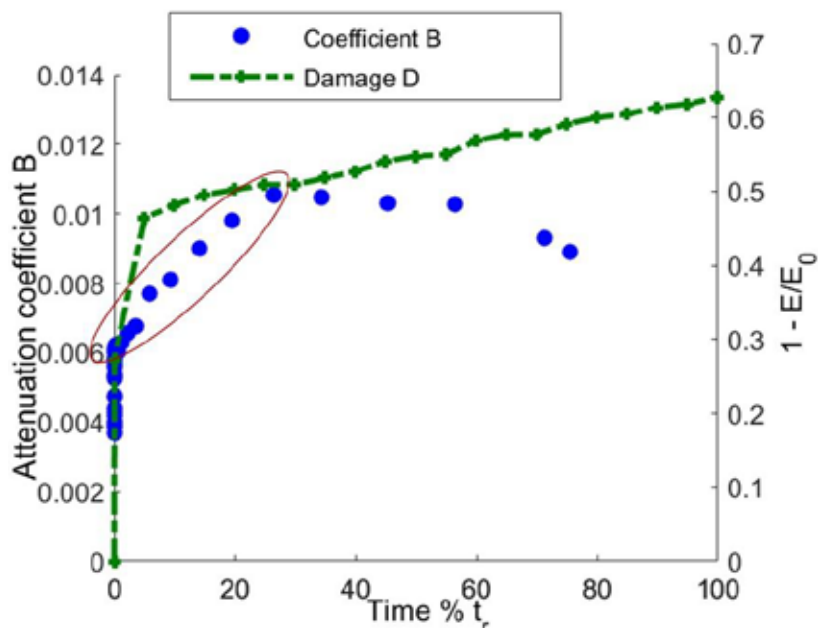


a)

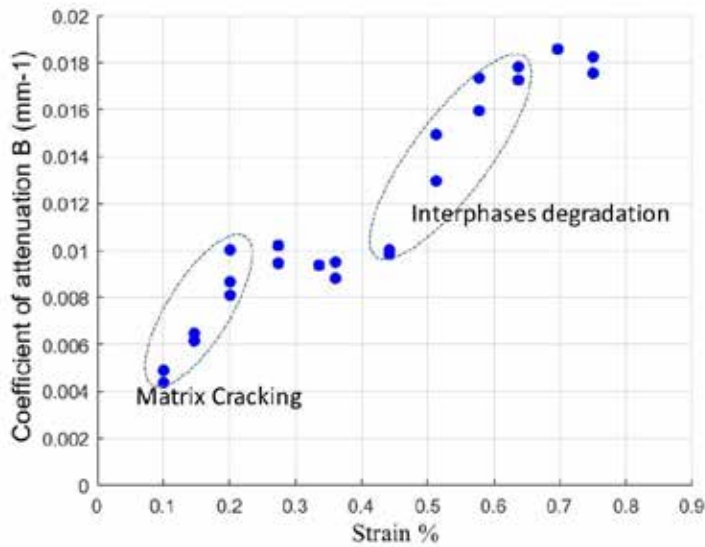


b)

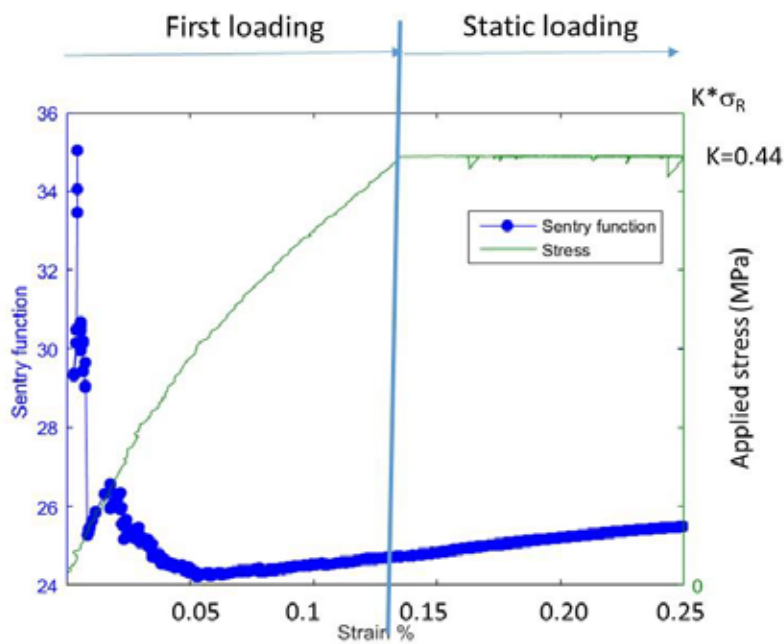
Figure 2 : a) Evolution of the coefficient R_{AE} and b) Location of the acoustic emission signals and the recorded energy versus time for a static fatigue test at 500 °C and $\sigma_{applied}/\sigma_r=0.44$, the colour scale represents the recorded energy in a mesh.



a)



b)



c)

Figure 3: a) Evolution of the coefficient of attenuation B and the damage parameter D versus time during a static fatigue test at 500 °C ($\sigma_{\text{applied}}/\sigma_{\text{T}}=0.44$). b) Evolution of the coefficient B versus strain during a tensile test at 450°C and c) Stress/Strain curve and evolution of the sentry function versus strain during a static fatigue test at 500 °C ($\sigma_{\text{applied}}/\sigma_{\text{T}}=0.44$).

3.2 Identification of a critical time during cyclic fatigue test

The evolution of the coefficient R_{AE} is very different during cyclic fatigue test from that observed in static fatigue (Fig.4). A minimum value. Is not observed. A significant change of slope takes place for all mechanical tests at approximately 20 % of the total test duration [13]. This characteristic time could certainly be used in order to evaluate time to failure. Moreover, it is interesting to notice that the coefficient R_{LU} highlights two characteristic times before 50% of rupture time (Fig. 4), the coefficient R_{LU} is again upper to 1 after the last characteristic time. After this characteristic time, the increase of the coefficient R_{LU} is linked to a significant increase of the severity of the signals recorded during the loading part (Fig. 4). While for the signals recorded during the unloading phases, the severity remains constant. Moreover, the coefficient R_{LU} goes through a minimum around 25 % of rupture time. It is interesting to notice that the coefficient R_{LU} highlights two characteristic times around 25 % and 50% of rupture time. Indeed the coefficient R_{LU} is again upper to 1 beyond this characteristic time [13].

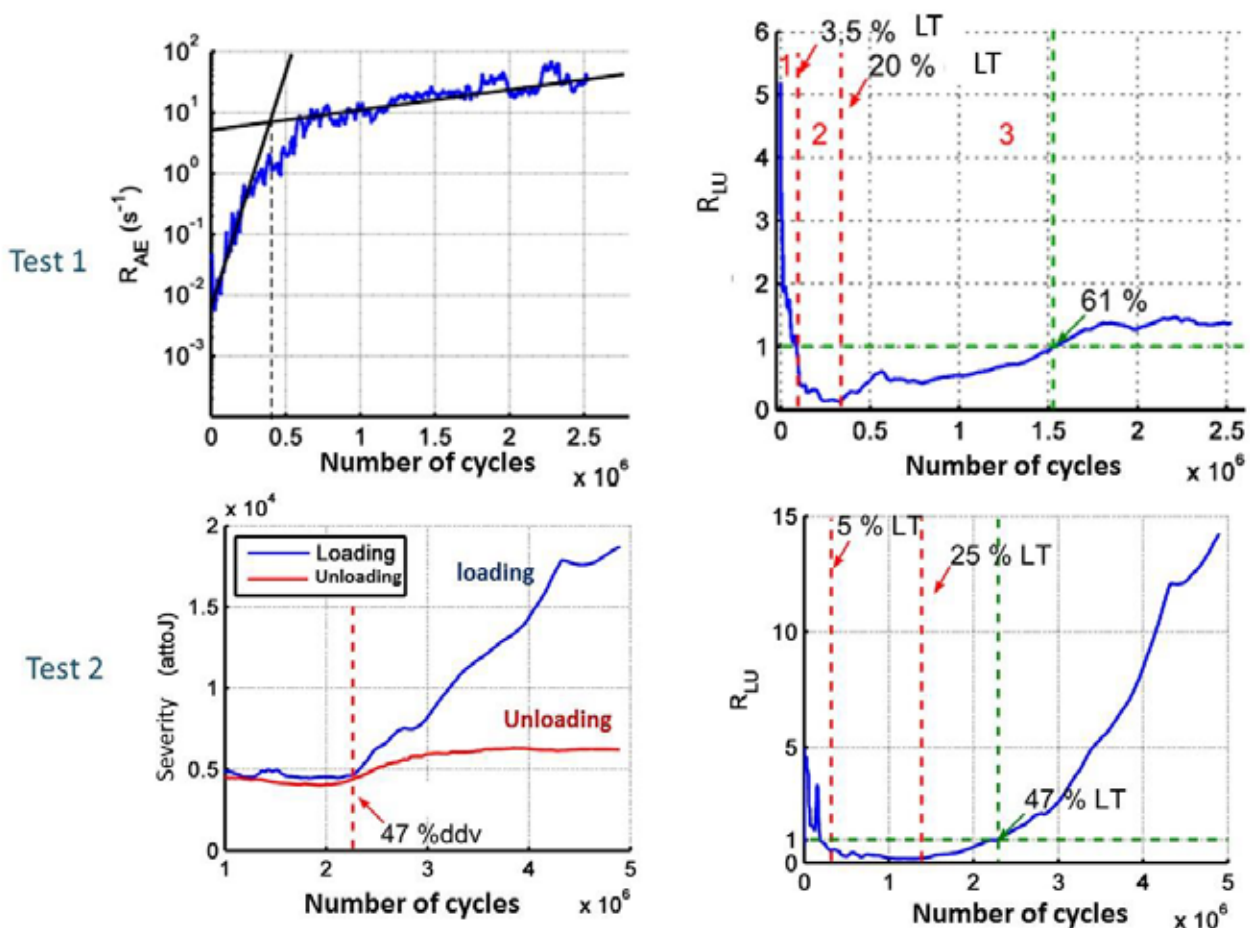


Figure 4: Evolution with the number of cycles of the coefficient R_{AE} , the coefficient R_{LU} . (LT lifetime) and the severity for two different cyclic fatigue tests at for a cyclic fatigue test at constant amplitude ($\sigma_{max}/\sigma_r=0.36$).

3.3 Link with the damage mechanism

The coefficient R_{AE} is calculated for the several damage mechanisms identified with clustering analysis of AE data for the static fatigue tests (Fig. 5). The coefficients obtained for the two classes A and B go through a minimum, contrary to those of classes C and D. It may be noticed that the minimum of the coefficient R_{AE} is observed only for clusters A and B corresponding to fibres breaks during the second part of the test around 55 % of the rupture time.

The cluster analysis with random forest algorithm pointed out various damage mechanisms generated by cyclic loading during the loading phase (Fig. 6). First with the cluster E, it is possible to eliminate friction. With the supervised clustering, the cluster A is mainly recorded at the end of the test around 90 % of the total test duration and the signals are attributed to the breaks of fibres. The cluster B associated with the matrix cracking in the longitudinal yarns is significantly activated very early towards 25 %. Hence, with this analysis a link is established between the characteristic time at 25 % and the beginning of the matrix cracking [13]. Nevertheless, it is not possible with this analysis to make a link with the second characteristic time around 50 % and the damage mechanisms. It may be due to the fact that only 50 % of the signals are kept after the application of the security voting.

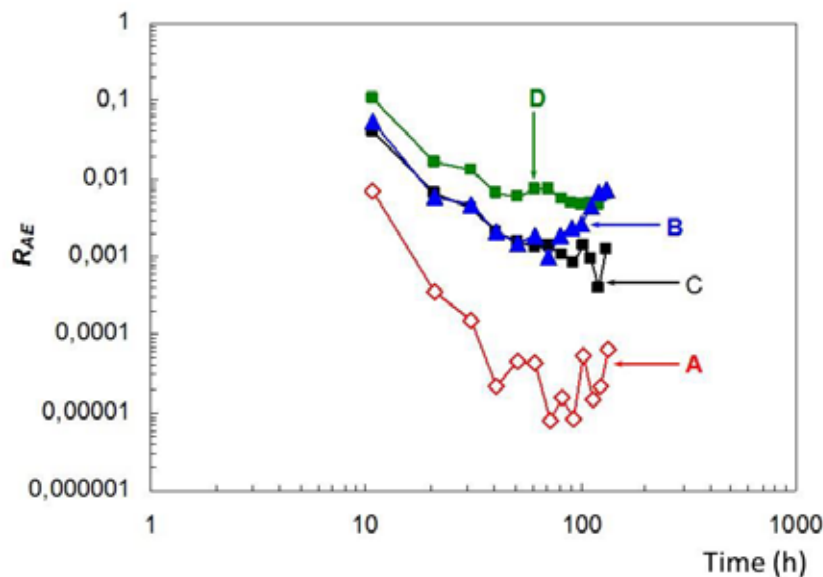


Figure 5 : Evolution of the RAE coefficient for the four clusters identified during static fatigue test

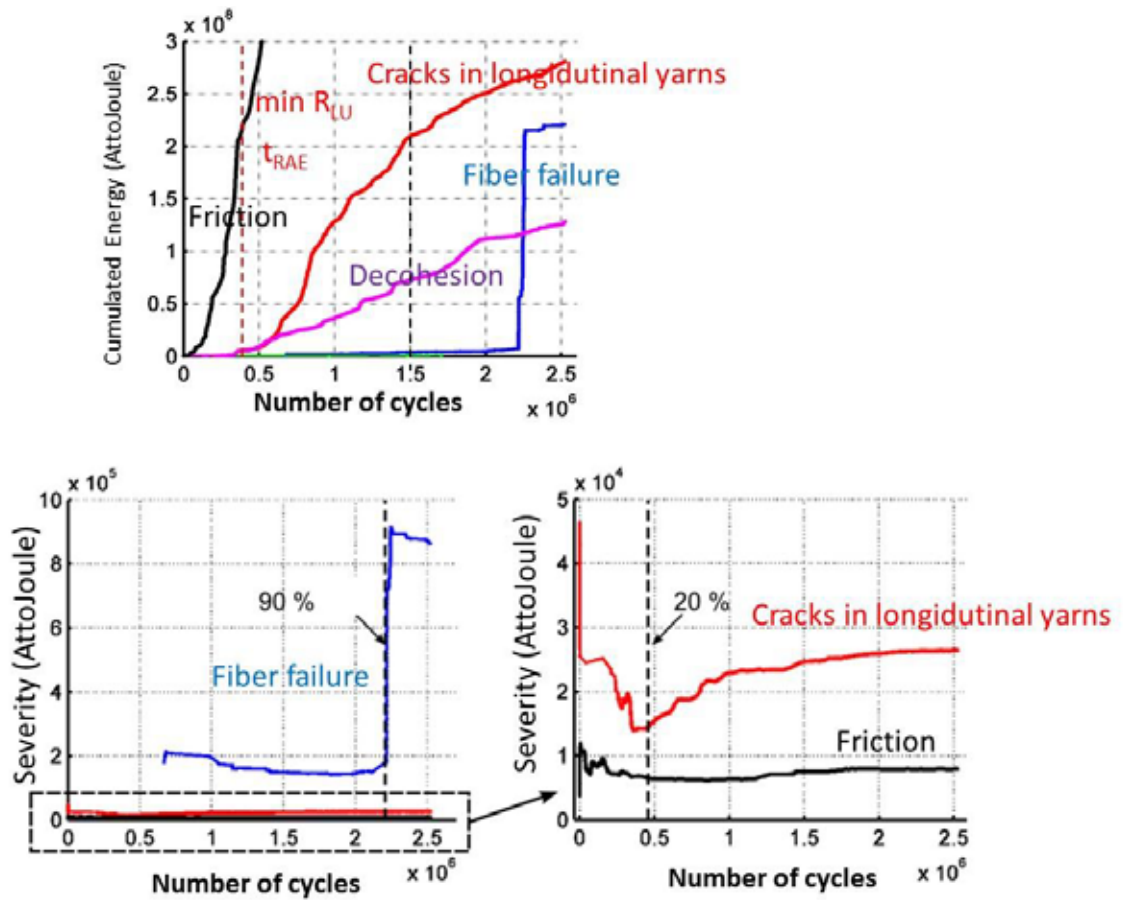


Figure 6 : Evolution of the activity of several damage mechanisms during the loading phase of a cyclic fatigue test.

3.4 Remaining Useful Lifetime obtained with acoustic emission for the static fatigue tests

Beyond this critical time, the criticality of the liberated energy can be modelled by a power law such as the Benioff law in order to evaluate the time to failure for the static fatigue test [12]. For this estimation, it is necessary to fit all the data collected between the time t_{RAE} and the rupture time in order to evaluate the exponent m . In fact, this value is very scattered. In this context, it is very difficult to calibrate the law with a specific test (table 1).

The time t_{RAE} presents a very interesting correlation with the lifetime duration of the test (Fig. 7) also for the tests conducted at 500 °C and 450 °C. The slope of the linear fit is equal to 1.49. Another time may be introduced, based on the investigation of the evolution of the coefficient B denoted t_B . It corresponds to the time at which a significant change is observed in the evolution of B during the static loading. A second linear correlation may also be observed between this time t_B and the lifetime duration. Nevertheless, this time is very difficult to detect in real time and its evaluation presents uncertainty.

T (°C)	$\sigma_{applied}/\sigma_r$	t_R (exp) Experimental values (h)	m
500	0.95	42	0.49
500	0.79	136	0.35
500	0.67	195	0.27
500	0.44	480	0.53
450	0.71	372	0.50
450	0.62	591	0.52

Table 1 : Exponent (m) for the Benioff law for the static fatigue tests conducted at 450 °C and 500°C.

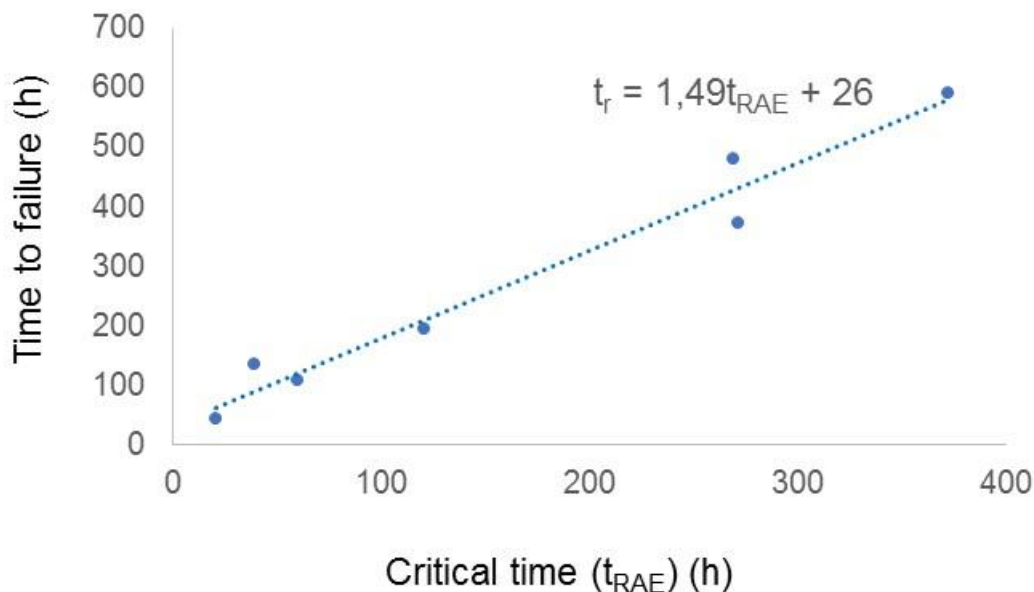


Figure 7 : Correlation between the characteristic time t_{RAE} , obtained with the minimum of the coefficient of emission, and the experimental time to failure.

The linear correlation confirms [6] that the characteristics time indicates the beginning of the avalanche fibres ruptures, controlled by the oxidation of the fibres and by the recession of interfaces, slowed down by the self-healing matrices. With this characteristic time, it is possible to estimate the remaining lifetime with the following equation:

$$t_{r(RAE)} = 1.49t_{RAE} + 26 \tag{8}$$

The results are summarized in the Table 2. The estimated TTF are denoted $t_{R(RAE)}$. The correlation between the experimental values and the predicted values is good when the ratio $\sigma_{applied}/\sigma_R$ is lower than 0.7 whereas large inaccuracies can occur for high $\sigma_{applied}/\sigma_R$ ratio.

T (°C)	$\sigma_{applied}/\sigma_r$	t_R (exp) Experimental values (h)	Lifetime estimation (h)
			$t_{R(RAE)}$ (eq. 8)
500	0.95	42	61
500	0.71	109	115
500	0.79	136	131
500	0.67	195	206
500	0.44	480	425
450	0.71	372	386
450	0.62	591	571

Table 1 : Comparison between the estimated time to failure and the experimental time to failure obtained with the two methods.

3.5 Limitation of this approach :

In these studies, the wave from the source is altered during propagation and this aspect is not taken into account. Indeed, the signal is modified during propagation (mode conversion, reflections, dispersion) and then by the acquisition system. Aggelis [18] shows that the separation distance of the sensors is a paramount importance and it should be taken into account. The analyzed parameters are highly dependent on the material properties, the structure geometries, the sensor, the detection and the analysis system. In addition, the state of damage of the material can affect AE signals [19-20] and the recorded energy. The geometry of the sample is also an important parameter [21]. These aspects need to be included in a modelling work in order to establish a quantitative link between the acoustic energy and the energy released by the source.

4 Conclusion

This paper focuses on the investigation of the damage during fatigue (static and cyclic) tests of CMC at intermediate temperature. Some new damage indicators are defined based on AE energy activity. These new AE indicators show the evolution of damage during long-term tests. AE is a powerful method to identify critical times and to predict the remaining lifetime. An empirical relation based on the critical time t_{RAE} is defined, which allows prediction of the time-to-rupture. These results offer very interesting perspectives. Now, it is necessary to investigate the effects of the size of the specimens in order to apply this method to real parts. Future work will focus on the introduction of new predictive laws beyond this characteristic time in order to evaluate the remaining lifetime.

5. Acknowledgments

The collaboration with SAFRAN Ceramics is gratefully acknowledged.

References:

- [1] Dalmaz A, Reynaud P, Rouby D, Fantozzi G & Abbe F. Mechanical behaviour and damage evolution during fatigue at high temperature of a 2,5D Cf/SiC composite. *Composite Science and Technology* 1998; 58: 693-699.
- [2] Lamon J. Micromechanics-based approach to the mechanical behavior of brittle matrix composites. *Composites Science and Technology* 2002; 58 : 2259-2272.
- [3] Loutas T, Eleftheroglou N, Zarouchas D. A data-driven probabilistic framework towards the in-situ prognostics of fatigue life of composites based on acoustic emission data. *Composites structures Composite Structures* 2017 ;161 : 522–529.
- [4] Suresh Kumar C, Arumugam V, Sengottuvelusamy R et al. Failure strength prediction of glass/epoxy composite laminates from acoustic emission parameters using artificial neural network, *Applied Acoustics* 2017; 115 : 32-41.
- [5] Eleftheroglou N; Loutas T. Fatigue damage diagnostics and prognostics of composites utilizing structural health monitoring data and stochastic processes; *Structural Health Monitoring* 2016; 15 (4) : 473-488.
- [6] Godin N, Reynaud P, Fantozzi G. Contribution of AE analysis in order to evaluate time to failure of ceramic matrix composites *Engineering Fracture Mechanics*
<https://doi.org/10.1016/j.engfracmech.2018.03.006>
- [7] Godin N, Reynaud P, Fantozzi G. Acoustic emission and durability of composites materials, Book published by ISTE-Wiley editions, N° ISBN : 9781786300195, 2018.
- [8] Sause M., “In situ monitoring of fiber-reinforced composites : Theory, basic concepts, methods, and applications” Springer series in materials science 242, 2016.
- [9] Ramasso E., Placet V., Boubakar L. , Unsupervised Consensus Clustering of Acoustic Emission Time-Series for Robust Damage Sequence Estimation in Composites, *IEEE Transactions on Instrumentation and Measurement*, vol 64, p. 3297-3307, 2015.
- [10] Maillet E, Godin N, R'Mili M, et al., Real-time evaluation of energy attenuation: A novel approach to acoustic emission analysis for damage monitoring of ceramic matrix composites, *Journal of the European Ceramic Society*. 2014, 34 (7) :1673-1679.
- [11] Godin N, Reynaud P, R'Mili M, Fantozzi G. Identification of a Critical Time with Acoustic Emission Monitoring during Static Fatigue Tests on Ceramic Matrix Composites: Towards Lifetime Prediction, *Appl. Sci.* 2016; 6 (2) : article number 43
- [12] Momon S, Moevus M, Godin N, R'Mili M, Reynaud P, Fantozzi G, Fayolle G. Acoustic emission and lifetime prediction during static fatigue tests on ceramic matrix composite at high temperature under air. *Comp: Part A* 2010;41:913-18.

- [13] Racle E, Godin N, Reynaud P and Fantozzi G. Fatigue Lifetime of Ceramic Matrix Composites at Intermediate Temperature by Acoustic Emission, *Materials* 2017; 10 (6) article number 657.
- [14] Minak G; Morelli P; Zucchelli A. Fatigue residual strength of circular laminate graphite–Epoxy composite plates damaged by transverse load. *Compos. Sci. Technol.* 2009; 69 :1358–1363.
- [15] Bufe CG, Varnes DG. Predictive modeling of the seismic cycle of the Greater San Francisco Bay Region; *Journal of Geophysical Research* 1993; 98 : 9871-83
- [16] Moevus M, Godin N, R'Mili M, Rouby D, Reynaud P, Fantozzi G, Fayolle G. Analyse of damage mechanisms and associated acoustic emission in two SiC/[Si-B-C] composites exhibiting different tensile curves. Part II: Unsupervised acoustic emission data clustering. *Comp Sci Technol.* 2008; 68 (6): 1258-1265.
- [17] Morizet N., Godin N., Tang J., Maillet E., Fregonese M., Normand B., Classification of acoustic emission signals using wavelets and Random Forests : Application to localized corrosion. *Mechanical Systems and Signal Processing*, 2016, Volumes 70–71, pp. 1026-1037
- [18] Aggelis D.G. Shiotani T. Papacharalampopoulos A. and Polyzos D. The Influence of propagation path on elastic waves as measured by acoustic emission parameters. *Structural Health Monitoring* 11(3), 359-366 (2011)
- [19] Kharrat M., Placet V., Ramasso E. and Boubakar L., “Influence of damage accumulation under fatigue loading on the AE-based health assessment of composite material: Wave distortion and AE-features evolution as a function of damage level”. *Composites Part A: Applied Science and Manufacturing*, in press, <http://doi.org/10.1016/j.compositesa.2016.03.020>, 2016
- [20] Carpinteri A., Lacidogna G., Accornero F., Mpalaskas A.C, Matikas T.E., Aggelis D.G., “Influence of damage in the acoustic emission parameters”, *Cement and concrete composites* 44, p. 9-16, 2013.
- [21] Le Gall T., Godin N., Monnier T., Fusco C. and Hamam Z. “Acoustic Emission modeling from the source to the detected signal: model validation and identification of relevant descriptors, *Journal of Acoustic Emission*, vol 34, 2016

04 - Combination of synchrotron computed tomography and Acoustic Emission measurements for cyclic loading of fibre-reinforced composites

Philipp Potstada¹, Sebastian Rosini², Mark Mavrogordato², Ian Sinclair², S. Mark Spearing², Markus G. R. Sause¹

¹ University of Augsburg, Institute for Materials Resource Management, Mechanical Engineering, D-86135 Augsburg

² University of Southampton, Faculty of Engineering and the Environment,

Abstract:

During incremental load-unload cycles of fibre-reinforced materials, the re-initiation of acoustic emission below the previously reached load is frequently observed. This is known as the Felicity effect and its physical origin has been discussed in the community for several decades. The principal explanations for this effect are the rubbing together of existing crack faces which thus act as tribological acoustic emission sources or the initiation of new damage because of material stress-relaxation during the unloading phase. We conducted combined acoustic emission measurements and high-resolution synchrotron computed tomography experiments on a carbon fibre / epoxy prepreg system. Samples were prepared as double-edge notched tensile specimens with [± 45 0 ± 45], [0 90₃ 0] and [90 0₃ 90] layups. At a voxel resolution of 1.625 μ m, we were able to visualize the growth of damage as a function of applied load/unload steps in a sequence of volume images. With the simultaneously acquired acoustic emission signals, this allows identification of the origin of the source volumetrically, as three volumes were taken per load step *in situ*. These investigations are part of an ongoing measurement campaign and represent a first interpretation towards the physical origin of the early acoustic emission onset in fibre-reinforced materials. This provides a first step to reveal the origin of the Felicity effect in fibre-reinforced materials.

1. Introduction

Fibre-reinforced polymer composites are used in transport applications because of their strength/weight and stiffness/weight ratios to reduce component weight, and hence to provide greater fuel efficiency and lower emissions. However, predicting damage formation and progression remains challenging, so conservative design levels are used and safety-relevant components need to be re-qualified frequently.

Acoustic emission (AE) sensing represents a core non-destructive testing technology for composite materials in transport applications, in which transient elastic waves, linked to sudden stress redistribution phenomena (such as micro-cracking, interface sliding) are used to detect and quantify damage processes. In many safety-critical applications of fibre-reinforced polymers such as pressure vessels, aerospace structures and similar, qualification and re-qualification of components makes use of the measurement of the so-called Felicity ratios (FR) as introduced by Timothy Fowler [1].

In his pioneering work, Joseph Kaiser demonstrated for metallic materials, that AE usually starts after exceeding the previous load level [2]. However, as first pointed out by Timothy Fowler, in fibre-reinforced polymers, the AE signals usually initiate at lower load levels than

those previously achieved [1]. After almost 40 years of scientific debate [3]–[10], no convincing experimental evidence has hitherto been provided that clearly explains the source of such early AE signals in FRPs and thus explains why these materials apparently violate the Kaiser effect [1].

In the scientific community there are essentially two principal ways of interpreting this early onset of AE:

1. Microscopic relaxation, viscoelastic behaviour and “settling” of the material cause local stress levels, that are sufficient to initiate new damage at macroscopic load levels, lower than those previously reached;
2. Stick-slip friction (rubbing) of existing crack walls causes AE, which is not related to any microscopic or macroscopic damage formation.

As stick-slip friction is a well-known source of AE, it cannot be excluded, that all or part of the early AE originates from this source. Revealing that such non-damage related AE acts as an indicator for the structural integrity of a fibre-reinforced polymer would immediately question the validity of current testing routines, as accept / reject decisions are then taken based on friction signals, not damage growth. In addition, the formation of new microscopic damage as consequence of local stress redistribution is another aspect, which is rarely taken into account in structural analysis and definition of test procedures.

Previous work using synchrotron radiation computed tomography (SRCT) has demonstrated that damage mechanisms, such as individual fibre fractures, matrix cracking, and other damage mechanisms can be reliably located and quantified [11], [12]. Thus, with the ability to observe visually the initiation and growth of new damage at low load levels and to distinguish this versus the relative movement of crack walls due to stick-slip friction we expect to make a key contribution to this scientific and engineering question.

This paper presents initial data demonstrating that it is possible to acquire AE-signals during an *in situ* SRCT loading experiment at the European Synchrotron Radiation Facility (ESRF) in Grenoble France. In this study, we present first results to correlate the AE signals recorded during load/unload cycles of a carbon/epoxy material with the occurrence of microscopic damage identified by SRCT.

2. Experimental

For the experiments at the ESRF, the microtomography beamline ID19 was chosen in order to provide optimal image fidelity at the resolution required. For the *in situ* acquisition, a combination of a MISTRAS PCI-2 AE-system and a modified DEBEN CT5000 tensile stage proven in previous studies was used [13], [14]. The AE measurement chain consists of a miniature multi-resonant sensor HD2WD from MISTRAS. Two AE sensors were used to allow a one-dimensional AE source localization. The acquired signals were amplified by a MISTRAS 2/4/6 pre-amplifier and were subject to a built-in analogue 20-1200 kHz band-pass-filter. Preamplifiers were mounted on the rotation table close to the *in situ* tensile load stage. The amplified AE signal was led outside the experimental hutch using a standard RG58 coaxial cable, which connects to the PCI-2 acquisition card. The acquired signals were recorded with the MISTRAS software AEwin™.

The load was applied by a commercial CT5000 DEBEN™ U.K. *in situ* tensile stage connected via the associated controller box to a standard PC using software provided by DEBEN™ U.K.

While the drive unit and the load cell of the tensile stage remained unmodified relative to the commercial setting, the load introduction concept of the specimen was modified (see Figure 1).

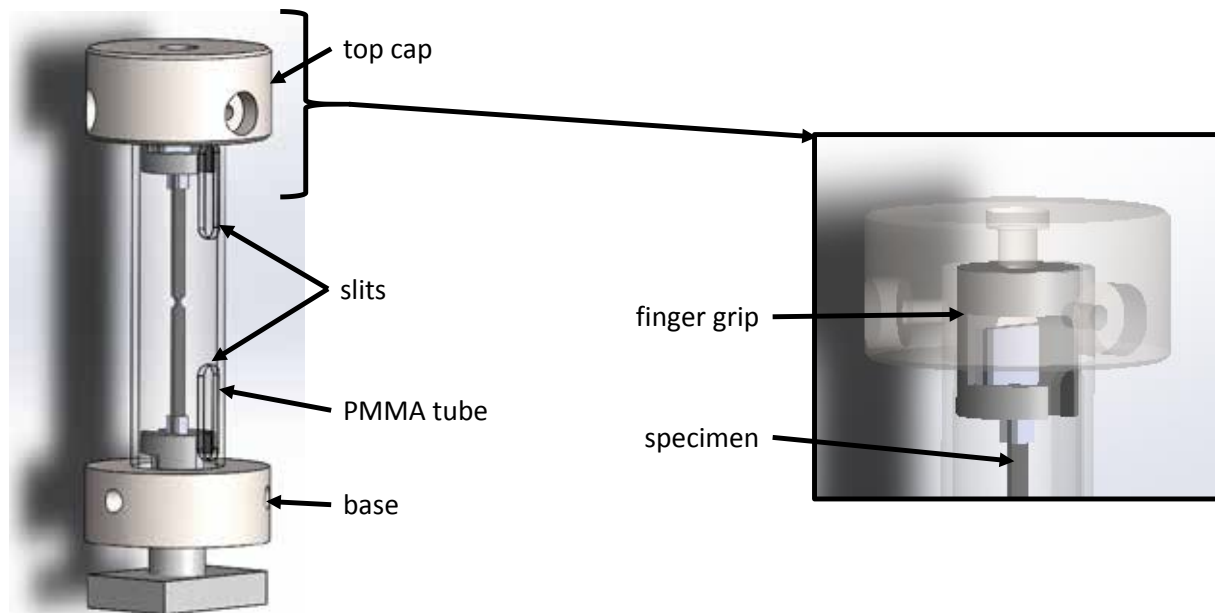


Figure 1. Modified part of the in situ tensile stage with finger grip clamping system and PMMA tube with two inserts for acoustic emission sensors cables.

The load was introduced via a finger grip system, which ensures a simple assembly of the specimen and a proper load transfer into the specimen after reaching a slight pre-load. The upper finger grip was statically fixed in a top-cap, which transferred the load via a PMMA tube into a custom-made frame of the tensile stage. To ease assembly of the PMMA tube, it was held in position with three screws. For synchronous evaluation of mechanical load and acoustic emission data, the current force values were fed into the AE system by a proportional analogue voltage signal.

Based on the explanations in Section 1, to reveal the origin of the Felicity effect, it is necessary to induce step-wise crack growth and potential friction effects during load-unload experiments. Accordingly, we used three different multi-angle layups, which allow growth of a crack network before ultimate failure of the specimen. In addition, based on the layup we also expect a certain likelihood of mutual crack interaction and the occurrence of crack surface friction. Based on earlier investigations by Wright *et al.* [15], we prepared double edge notched tensile specimens via waterjet cutting from $[\pm 45 \ 0 \ \pm 45]$, $[0 \ 90_3 \ 0]$ and $[90 \ 0_3 \ 90]$ laminate plates. All laminates were produced from carbon/epoxy prepreg, Sigrafil™ CE1250-230-39 following the material supplier's specifications. T-shaped aluminium tabs were adhesively bonded to the specimen specimen ends. A grinding and cleaning phase on the contact surface between tabs and coupons took place before application of fast curing methyl-methacrylate adhesive. To ensure adhesion and mechanical stability of the AE sensors on the specimens, holders were fabricated out of polylactide by additive manufacturing and attached tightly to the specimens using rubber rings. To obtain a repeatable and correct positioning of the support structure, the holders include four integrated dowel pins (as indicated in Figure 2).

At the beginning of each test, three pencil lead breaks (PLB) were performed at the base of the tensile stage to ensure a sufficient coupling of the AE-sensors to the specimen. The setting used for the AE-acquisition for both sensors were a threshold of 35dB_{AE} at 40dB_{AE} pre-amplification and a Peak Definition Time (PDT) of 10µs, a Hit Definition Time (HDT) of 80µs and a Hit Lockout Time (HLT) of 300µs. The AE signals were acquired with a sampling rate of 10 MS/s.

After a satisfactory pre-check, the AE-acquisition was started. A first SRCT scan was collected to record the initial (undamaged) specimen volume. To ensure a proper alignment of the specimen in the beam path, a load of 15 N (representing a small percentage of the sample ultimate tensile strength) was applied. At this load level, no pre-damage was observed. The drive unit was switched off and the cross-head position was kept constant by the self-locking mechanics of the loading stage. The scan was performed continuously with beam energy of 19.5 keV. During each tomographic scan, 2996 projections with an exposure time of 50 ms were collected at a detector distance of 50 mm. The voxel size was 0.65 µm.

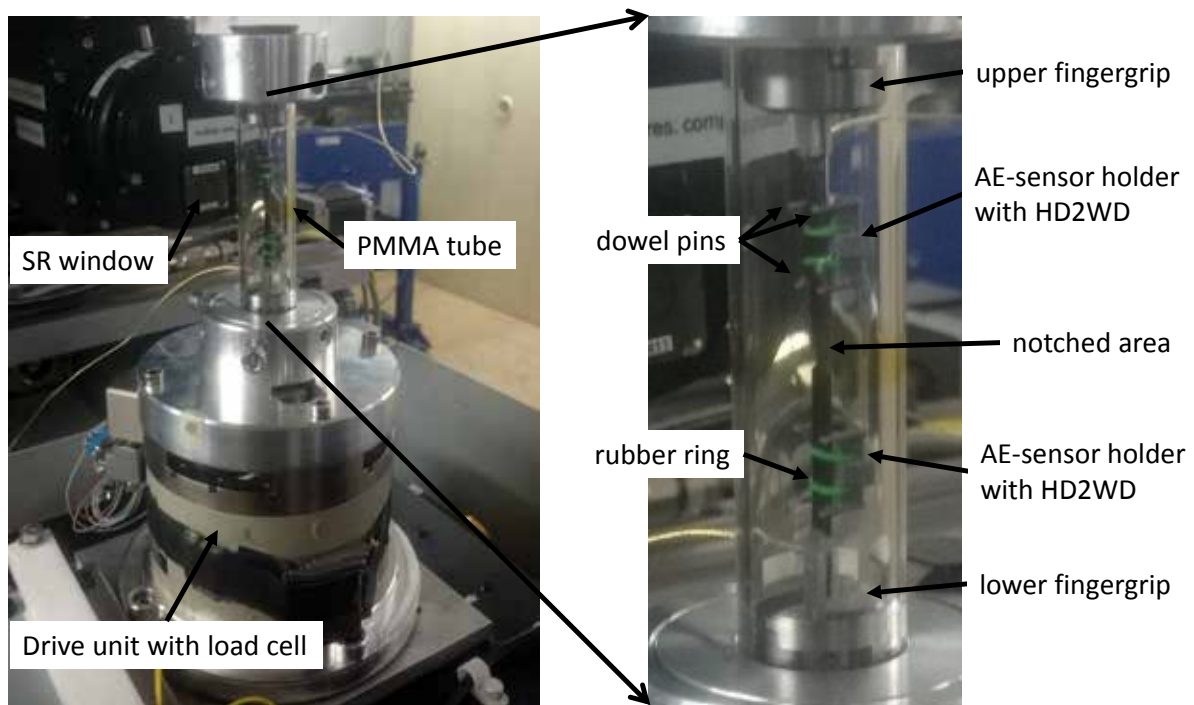


Figure 2. In situ tensile stage with installed specimen and AE sensors ready for testing.

For the evaluation of the Felicity effect, load/unload experiments are carried out at a constant displacement rate of 0.2 mm/min. Typically, the load is increased to some nominal target value L_1 , then reduced and increase again to a higher value L_2 . This is continued for increasing loads until the material fails at a value L_{max} . At the first occurrence of significant acoustic emission during the reload cycle, the load level B_2 is defined. This allows calculation of the Felicity ratio FR for the second load cycle according to $FR = B_2/L_1$. In order to reveal the origin of the Felicity effect, we follow a slightly modified load schedule in this investigation. Other than pre-defined step-wise increased loading, test were interrupted after the occurrence of a sequence of acoustic emission signals (e.g. > 5 signals). After reaching this peak load, the specimens are unloaded by 10% of the peak load. Two more load/unload cycles are carried out with the same peak load as seen in the examples of Figures 6-8. This allows the virgin Felicity ratio to be determined at each load level and to distinguish this from subsequent loading to the same

load level. At each plateau phase seen in Figures 6-8, additional SR scans are taken to assess the occurrence of damage progression. Two more peak load increments are carried out for each sample to induce a certain amount of damage progression. For the three different sample types, the ultimate tensile strength was calculated as 577 MPa for $[\pm 45 \ 0 \ \pm 45]$, 736 MPa for $[0 \ 90_3 \ 0]$ and 1046 MPa for $[90 \ 0_3 \ 90]$ layups.

2.1. Acoustic emission evaluation

For the acquired AE signals, a feature extraction routine was performed. Besides the common AE feature values of amplitude, energy, duration, also the partial powers of six equal frequency ranges of 150 kHz width, ranging from 0 MHz to 1 MHz were calculated out of the first 35 μ s after the arrival time. The arrival time was calculated using the Akaike information criterion (AIC) [16]. In addition, spectral feature values, such as the weighted peak frequency and frequency centroid were calculated from FFT spectra of the signals (see [17] for precise definition of features). A first data reduction was carried out to remove erroneous AE signals resulting from driver motor control signals. These were easily identified based on their unique frequency characteristics and their time of occurrence of the direction of load reversal.

Furthermore, AE sources were localized using a classical Δt -based algorithm considering the given geometry of the specimen and the sensor positions. The velocity of sound was measured for each material using time-of-flight tests on the raw material plates before cutting the test geometries. Only the AE-signals localized within 50 ± 3 mm around the notch centre were used for the following evaluation. This limitation is necessary to conform with the observation volume of the SR scans, i.e. to reach an equivalent data basis for both methods.

A pattern recognition approach following [18] was performed using a Gustafson-Kessel algorithm allowing a maximum number of $P = 6$ clusters and a minimum number of $M = 4$ features for 12 previously selected list of frequency features K . The selected features are reverberation frequency, average frequency, initiation frequency, partial power 1-6, peak frequency, frequency centroid and weighted peak frequency. Similar to other specimens tested in this experimental setting [19], two clusters are identified in this optimization procedure. Based on conclusions of earlier investigations [17], [20], [21] and direct validation within [19], these are ascribed to the occurrence of fibre breakage (high frequency cluster) and to the occurrence of matrix cracking and interfacial related mechanisms (low frequency cluster).

For the evaluation of the Felicity ratio, a modified procedure originally published in [4], [22] was proposed to stabilize the numerical values [23]. In contrast to this, for this investigation, we use the most conservative approach and take the load level of the first acoustic emission signal as the onset value for the definition of the Felicity ratio. Additionally, we distinguish between signals of both clusters, e.g. we calculate separate Felicity ratios for fibre breakage and matrix cracking / interfacial failure related AE signals.

2.2. SRCT evaluation

Ten scans of the same region of interest (showed in Figure 4) were collected, while the specimens were increasingly loaded (and strains increased). To ensure at a micro-metre scale that the same region could be investigated while damage progressed, a registration of the scanned volumes was made by visual inspection. The user was asked to recognise a unique feature (e.g. a particular pattern in the top view of the fibres) and to record the position of this feature in all the scanned volumes. Based on this, all the volumes were cropped and aligned to a same position along the specimen length. All the scans were loaded onto the software

VGStudio MAX™ and the volume recorded at the highest strains was observed first. Cracks were visually detected and segmented using a growth segmentation tool available within the software. The user was able to identify the most developed cracks and reduce the time needed to investigate the volumes at lower strains as the centroids of the segmented cracks had approximately the same coordinates in all the registered volumes. By visual check and use of the automated growth segmentation tool it was then possible to record the evolution of a particular crack. An example of a crack detected with the automated tool is shown in Figure 3 where both the contours of the less and more developed crack are shown respectively in dark and lighter cyan.

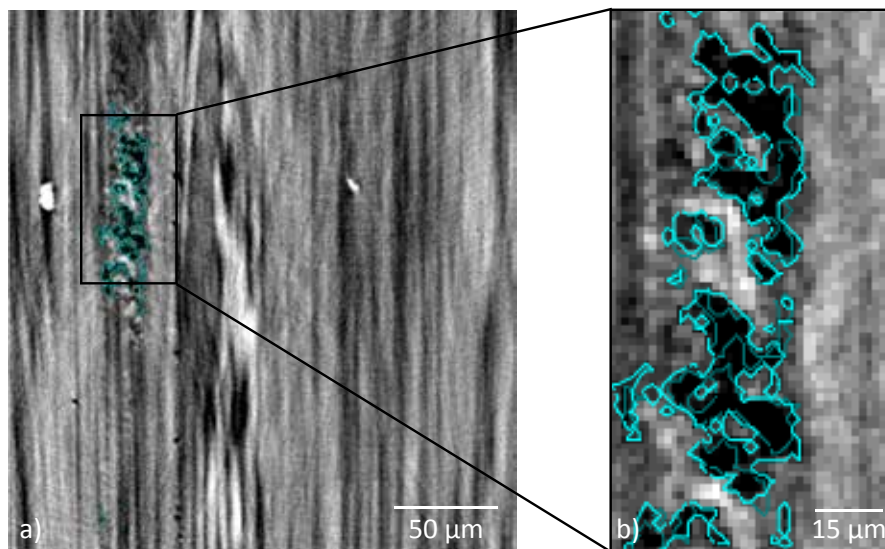


Figure 3. a) Crack evolution as identified on a single slice of the highest strains scanned volume
b) zoomed region showing in black the crack at the highest strains with its contours in light cyan. In darker cyan, the contours of the same less developed crack as detected with the growth segmentation tool in a scanned volume at lower strains.

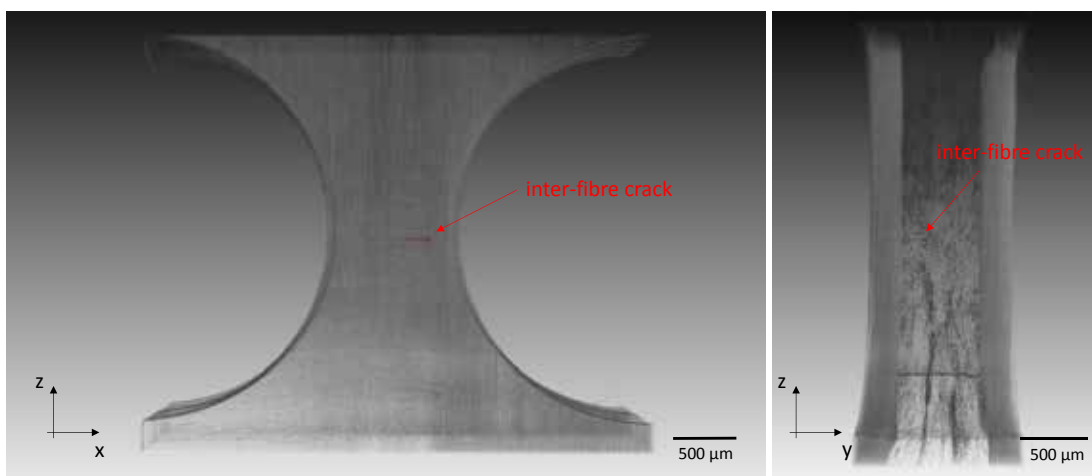


Figure 4. Frontal (left) and lateral (right) view of the region of interest, kept the same for all the scanned volumes. The inter-fibre crack is shown in red as identified in the highest strains scans. The combined use of a visual approach and an automated growth segmentation tool on VGStudio MAX™ allowed the user to identify the crack evolution from lower to higher strains.

3. Results

In the following, the results of the *in situ* investigations are presented, using combined AE and SRCT measurements, distinguished based on the stacking sequence used.

3.1. Layup [0 90₃ 0]

As the first case, a cross-ply stacking with a predominantly 90° fibre orientation relative to the load axis is studied. With increasing load, the occurrence of transverse matrix cracks (inter-fibre cracks) is observed, see Figure 5. In addition, fibre breakage is observed to occur in the 0° plies. From SRCT observations, no growth of delamination between the 0° and 90° plies was observed. Figure 6 shows the acoustic emission results of one specimen. Based on the pattern recognition results, cumulative hits for both signal classes are superimposed on the load-time curves. Each cycle with occurrence of acoustic emission additionally holds the corresponding Felicity ratios for each signal class. For this cross-ply stacking, all Felicity ratios were > 0.99, rendering it impossible to discuss the origin of acoustic emission signals at Felicity ratios << 1.00. However, there is a first indication, that Felicity ratios of fibre breakage related signals are typically larger than those of matrix cracking / interfacial failure related signals. This is in accordance with observations on macroscopic specimens [17].

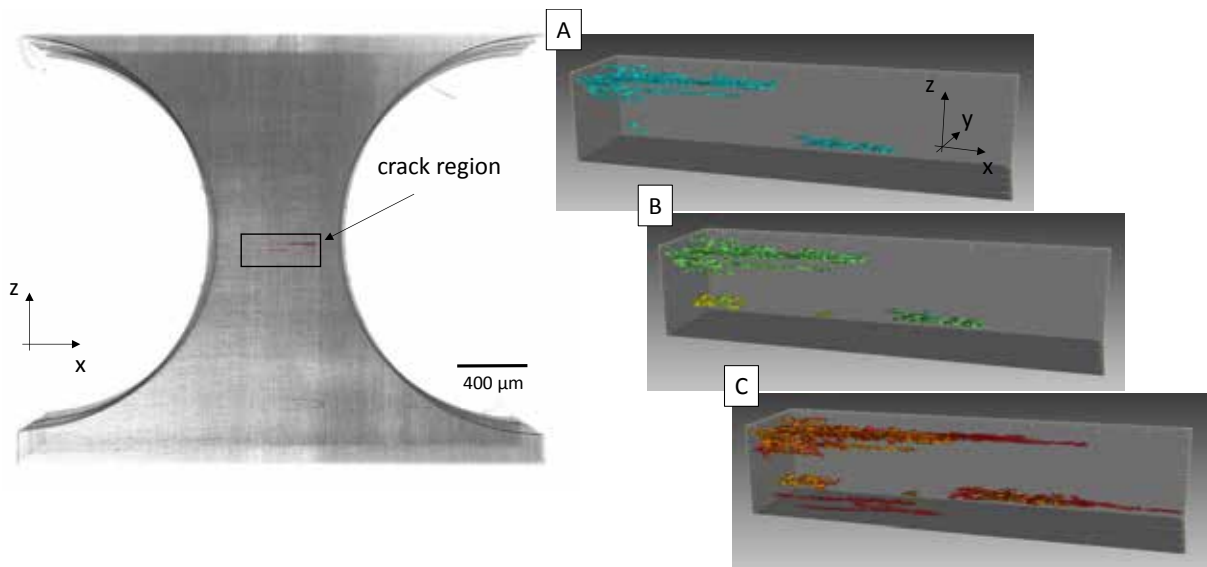


Figure 5. Visualization of inter-fibre crack and volumetric evaluation at three load levels (A-C) as noted in Figure 6.

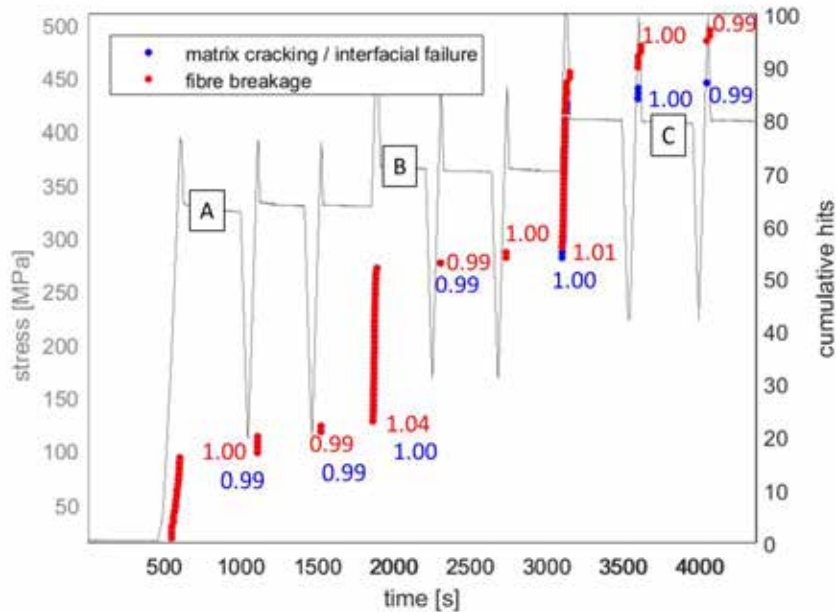


Figure 6. Example of layup $[0\ 90_3\ 0]$ including Felicity Ratios evaluated for fibre breakage signals (red) and matrix cracking / interfacial failure related signals (blue).

3.2. Layup $[\pm 45\ 0\ \pm 45]$

As second case study, a $\pm 45^\circ$ dominated stacking sequence was investigated. In the evaluation of acoustic emission signals, two cycles result in Felicity ratios significantly lower than unity (i.e. $FR = 0.85$ and $FR = 0.84$). Until reaching a load level of 57% ultimate tensile strength, in SRCT the only significant damaged region is observed close to the notch positions. As seen in the SRCT slice example for load level A in Figure 7, part of this damage is already present in the beginning of the experiment (centre break, bright zone on right). Accordingly, it is likely, that this damage is a residue of the drilling process used to introduce the notches. At increased load levels (example at load level B) the number of cracks appears to grow. However, in all cases inspected, indications of the presence of these cracks is already found in the first (unloaded) SRCT scan. With applied load, the cracks are seen much better than in the unloaded case due to crack opening, resulting in the appearance of crack growth. However, the potential occurrence of additional damage growth in this area cannot be excluded. This is likely causing the numerous acoustic emission signals recorded in the experiment. Unfortunately, with no other evidence of crack growth from SRCT inspection, this does not allow a dedicated interpretation of the recorded Felicity ratios for this stacking sequence.

3.3. Layup $[90\ 0_3\ 90]$

As third case, a cross-ply stacking sequence with predominant fibre orientation in 0° was tested. Other than the test case of Section 3.1, this apparently results in less acoustic emission activity as seen in Figure 8. However, the Felicity ratios for this case are also consistently > 0.99 , resulting in the same difficulty of interpretation of early onset acoustic emission signals. Similar to the previous cases, fibre breakage related signals apparently tend to result in slightly higher Felicity ratio values. In SRCT scans, we observed the occurrence of multiple fibre breaks. In the example shown in Figure 8, fibre breaks are visible at load level B located in

close proximity to a high-density inclusion (probably a dust particle introduced during specimen manufacture). Apart from that, no matrix cracks or delamination are visible in the SRCT scans.

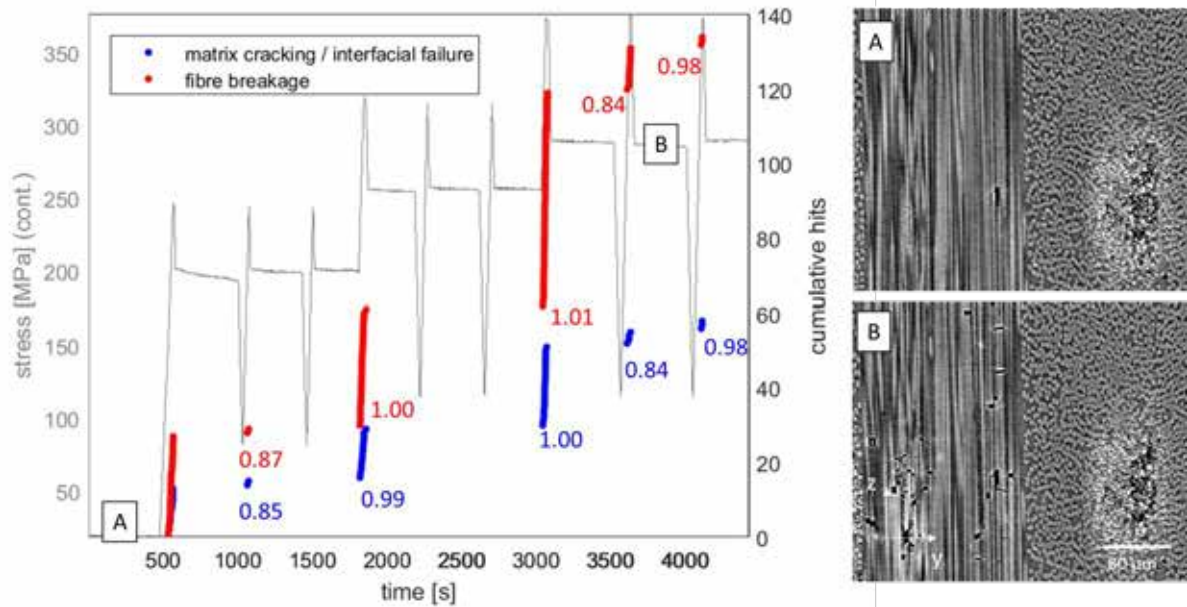


Figure 7. Example of layup $[\pm 45 \ 0 \ \pm 45]$ including Felicity Ratios evaluated for fibre breakage signals (red) and matrix cracking / interfacial failure related signals (blue) and SRCT slices at two load levels (A-B).

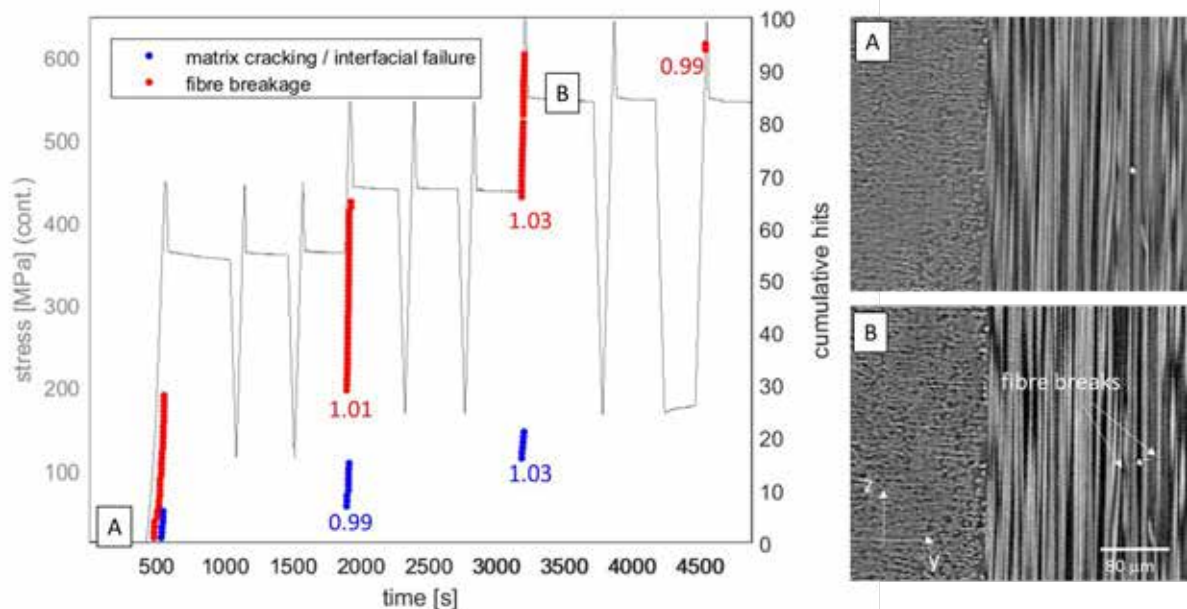


Figure 8. Example of layup $[90 \ 0_3 \ 90]$ including Felicity Ratios evaluated for fibre breakage signals (red) and matrix cracking / interfacial failure related signals (blue) and SRCT slices at two load levels (A-B).

4. Conclusion

The combination of high-resolution SRCT and acoustic emission measurements has been successfully carried out during step-wise cyclic loading of fibre-reinforced materials. The overall experimental approach appears promising to reveal the origin of the Felicity effect in fibre-reinforced materials. However, in the present test campaign the vast majority of cases results in Felicity ratios ~ 1.0 . Based on the tensile load and the layup used in these experiments, the fracture surfaces observed in SRCT are mode I dominated. No fracture surfaces were generated that are expected to undergo high tribological load during load/unload cycles. The only cases with Felicity ratios significantly below zero were the $[\pm 45\ 0\ \pm 45]$ samples. Based on this layup, the expectation is a delamination damage growth between plies, resulting in mixed mode loading. However, the SRCT observation do not indicate such delamination growth in the experiments. Accordingly, the present data basis does not allow a final judgement on the true origin of the Felicity effect. However, a general trend of fibre breakage Felicity ratios being larger than for matrix cracking and interfacial failure related signals has been observed. This potentially indicates a difference in the origin of signal onset in these failure modes. Accordingly, future test campaigns should take into account different load concepts and layups to force the occurrence of shear loaded fracture surfaces. This might result in a higher number of test cases with low Felicity ratios.

Acknowledgments

The authors would like to acknowledge the European Synchrotron Radiation Facility for provision of synchrotron radiation facilities and would like to thank Dr. Lukas Helfen and Ms. Elodie Boller for assistance in using beamline ID19. The authors also gratefully acknowledge the μ -VIS X-Ray Imaging Centre at the University of Southampton for provision of tomographic imaging facilities, supported by EPSRC grant EP-H01506X.

References:

- [1] T. J. Fowler, "Acoustic Emission Testing of Fiber Reinforced Plastics," *Proc. Pap. J. Tech. Counc. ASCE*, vol. 105(TC2), pp. 281–289, 1977.
- [2] J. Kaiser, "Untersuchungen über das Auftreten von Geräuschen beim Zugversuch," Dissertation, Technische Hochschule München, 1950.
- [3] J. Awerbuch, M. R. Gorman, and M. Madhukar, "Monitoring Acoustic Emission During Quasi-static Loading-Unloading Cycles of Filament-wound Graphite-Epoxy Laminate Coupons," *Mater. Eval.*, vol. 43, no. 6, pp. 754–764, 1985.
- [4] K. S. Downs and M. A. Hamstad, "Acoustic Emission from Depressurization to Detect/Evaluate Significance of Impact Damage to Graphite/Epoxy Pressure Vessels," *J. Compos. Mater.*, vol. 32, no. 3, pp. 258–307, Feb. 1998.
- [5] W. Haselbach and B. Lauke, "Acoustic emission of debonding between fibre and matrix to evaluate local adhesion," *Compos. Sci. Technol.*, vol. 63, no. 15, pp. 2155–2162, Nov. 2003.
- [6] M. R. Gorman, "Acoustic Emission in 2-D Carbon-Carbon Coupons in Tension," *J. Compos. Mater.*, vol. 25, no. 6, pp. 703–714, Jun. 1991.
- [7] K. Ono, "Structural integrity evaluation using acoustic emission techniques," *J Acoust. Emiss.*, vol. 25, pp. 1–20, 2007.
- [8] K. Ono and A. Gallego, "Research and Applications of AE on Advanced Composites," *J Acoust. Emiss.*, vol. 30, pp. 180–229, 2012.
- [9] M. A. Hamstad, "A review: Acoustic emission, a tool for composite-materials studies," *Exp. Mech.*, vol. 26, no. 1, pp. 7–13, 1986.
- [10] M. A. Hamstad, "Thirty years of advances and some remaining challenges in the

- application of acoustic emission to composite materials,” in *Acoustic Emission Beyond the Millennium*, S. Y. T. Kishi, M. Ohtsu, Ed. Amsterdam: Elsevier Science, 2000, pp. 77–91.
- [11] P. Wright, X. Fu, I. Sinclair, and S. M. Spearing, “Ultra High Resolution Computed Tomography of Damage in Notched Carbon Fiber--Epoxy Composites,” *J. Compos. Mater.*, vol. 42, no. 19, pp. 1993–2002, Oct. 2008.
- [12] A. E. Scott, M. Mavrogordato, P. Wright, I. Sinclair, and S. M. Spearing, “In situ fibre fracture measurement in carbon-epoxy laminates using high resolution computed tomography,” *Compos. Sci. Technol.*, vol. 71, no. 12, pp. 1471–1477, Aug. 2011.
- [13] S. C. Garcea, M. N. Mavrogordato, A. E. Scott, I. Sinclair, and S. M. Spearing, “Fatigue micromechanism characterisation in carbon fibre reinforced polymers using synchrotron radiation computed tomography,” *Compos. Sci. Technol.*, vol. 99, pp. 23–30, Jul. 2014.
- [14] S. C. Garcea, I. Sinclair, and S. M. Spearing, “Fibre failure assessment in carbon fibre reinforced polymers under fatigue loading by synchrotron X-ray computed tomography,” *Compos. Sci. Technol.*, vol. 133, pp. 157–164, Sep. 2016.
- [15] P. Wright, A. Moffat, I. Sinclair, and S. M. Spearing, “High resolution tomographic imaging and modelling of notch tip damage in a laminated composite,” *Compos. Sci. Technol.*, vol. 70, no. 10, pp. 1444–1452, 2010.
- [16] H. Akaike, “Markovian representation of stochastic process and its application to the analysis of autoregressive moving average processes,” *Ann. Inst. Stat. Math.*, vol. 26, pp. 363–387, 1974.
- [17] M. G. R. Sause, *In Situ Monitoring of Fiber-Reinforced Composites*, vol. 242. Cham: Springer International Publishing, 2016.
- [18] M. G. R. Sause, A. Gribov, A. R. Unwin, and S. Horn, “Pattern recognition approach to identify natural clusters of acoustic emission signals,” *Pattern Recognit. Lett.*, vol. 33, no. 1, pp. 17–23, Jan. 2012.
- [19] P. Potstada, S. Rosini, M. Mavrogordato, I. Sinclair, M. Spearing, and M. G. R. Sause, “Cross-validation of single filament failure by acoustic emission and high-resolution synchrotron computed tomography,” in *ECCM18 - 18th European Conference on Composite Materials*, 2018, pp. 1–8.
- [20] M. G. R. Sause, T. Müller, A. Horoschenkoff, and S. Horn, “Quantification of failure mechanisms in mode-I loading of fiber reinforced plastics utilizing acoustic emission analysis,” *Compos. Sci. Technol.*, vol. 72, no. 2, pp. 167–174, Jan. 2012.
- [21] M. G. R. Sause and S. Richler, “Finite Element Modelling of Cracks as Acoustic Emission Sources,” *J. Nondestruct. Eval.*, vol. 34, no. 1, p. 4, Mar. 2015.
- [22] K. S. Downs and M. A. Hamstad, “Correlation of Acoustic Emission Felicity Ratios and Hold-Based Rate Moments with Burst Strengths of Spherical Graphite/Epoxy Pressure Vessels,” *J. Acoust. Emiss.*, vol. 13, no. 3/4, pp. 45–56, 1995.
- [23] M. G. R. Sause, S. Schmitt, and S. Kalafat, “Failure load prediction for fiber-reinforced composites based on acoustic emission,” *Compos. Sci. Technol.*, vol. 164, pp. 24–33, Aug. 2018.

48 - Structural Health Monitoring of composites structures by Acoustic Emission analysis

Lars Schubert¹, Eberhard Schulze¹, Robert Neubeck¹ *, Bianca Weihnacht¹

¹ Fraunhofer Institute for Ceramic Technologies and Systems, Dresden, Germany

Abstract:

Fiber reinforced composites are often used in actual light weight structures applications like structural components for automotive or rotor blades for wind turbine power applications. The reliability of those components are of great importance for safety relevant areas. The lifetime of the components are affected by damages like fibre cracking or delaminations which can lead to early failure of the overall structure. The acoustic emission testing is well accepted for static or dynamic testing of fiber composite components since fiber breaks and delamination processes cause high energetic acoustic emissions. The challenge lies in the application of the method during field measurement tests like filtering any indications caused by the noisy environment and the development of special condition monitoring hardware which allows the instrumentation of rotating wind turbines. Damage evaluation parameters like the weighted peak frequency were evaluated during tensile lab test and full-scale fatigue tests and subsequently transferred to real operation of wind turbines. Results from field operation of several systems on wind turbine power blades will be presented and discussed.

1. Introduction

Fibre composites as used for the construction of rotor blades are constructed based on the principle of material science especially continuum mechanics and the well-known material characteristics of the single components. Nevertheless, a pre-damage or an actively introduced failure during operation may shorten the life time significantly and question the original material design.

The non-destructive testing of these materials is challenging. Despite to the standard visual testing, the proposed technique of acoustic emission testing (AET) may also detect damages in the material which are not visible from the outside. Specific acoustic emission parameters may serve as early warning factors since especially fibre breakage and delamination course strong acoustic emissions.

The technique of AET is based on the fact, that dynamic dislocations in the nm range can be detected on the surface of loaded objects by highly sensible piezoelectric sensors in the frequency range of 10 kHz – 1 MHz. The dislocations on the surface are caused by acoustic waves by short time and very small material dislocations due to micro crack development, crack growth, friction, delamination, matrix cracking etc.

Sensors have to be adapted to the characteristics of the material. Delaminations can be commonly detected up to 150 kHz, fibre debonding or cracks show significant higher frequencies. Any noise has to be filtered by band pass filtering. To determine electromagnetic noise, several sensors have to be applied to the testing object to differentiate between the data signal and noise.

2. Description of work

Tensile bending test

The 14 probes were manufactured at the project partner cp.max Rotortechnik and refer to real materials from rotor blade manufacturers regarding the layer design. During the experiments, the analogue signals of the force were monitored continuously during the experiment. The probes were instrumented with sensors developed at the Fraunhofer IKTS KAR601S which are adapted to the needed frequency range. Four sensors were positioned at the upper and lower border of the probe (as shown in Figure 1) to get redundant information in order to exclude noise. Furthermore, during the experiments an in-house developed measurement system MAS (Multi-Channel-Acoustic-System) was used for the data acquisition. These experiments were conducted at the project partner IMA Dresden.



Figure 1: Tensile testing at the moment of failure - Probe CP01 [3]

Full scale rotor blade test

Beside the lab testing, also a full scale dynamic fatigue test took place. These experiments were conducted at the project partner IMA Dresden with an optical fibre measurement system (Teletronic Rossendorf) which can also be used at a rotating wind mill despite the lightning issues.

The rotor blade was instrumented with 24 acoustic sensors as shown in Figure 2.

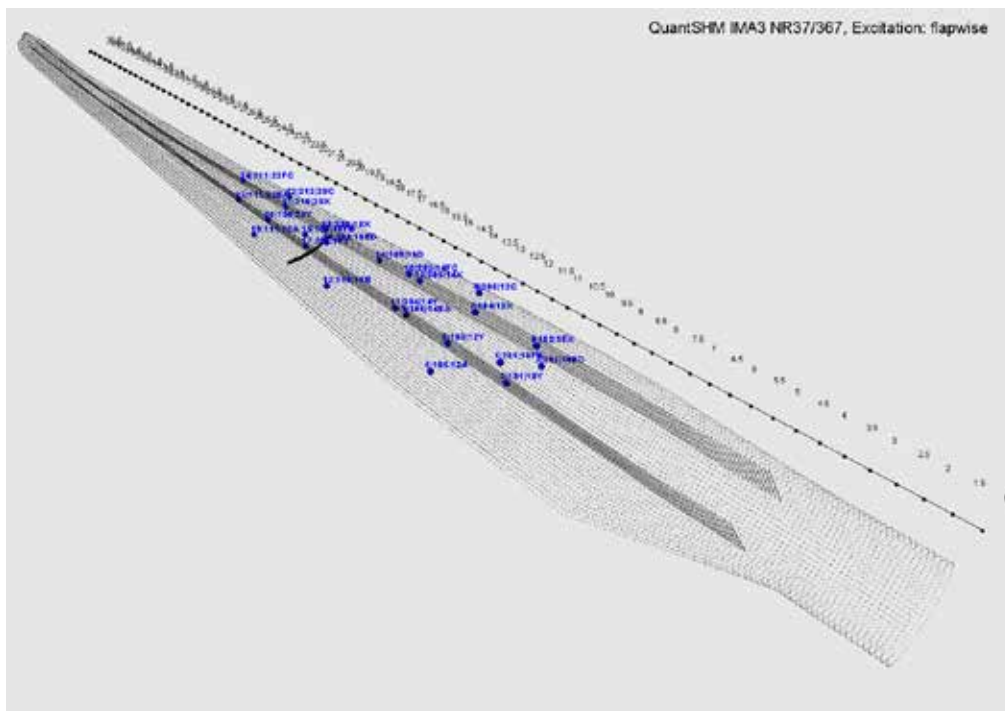


Figure 2: Spatial distribution of 24 acoustic sensors in the rotorblade

3. Discussion

Tensile tests

Figure 3 shows the characteristics of the location of the traverse during the experiment which increases due to weakening of the material. The size of the circles of the events in magenta is proportional to the energy of the burst signals. The diagram also shows the curves of the cumulated number of events in black and the cumulated burst energy in blue. The green curves allow for the estimation of the burst energy at the single experiment time intervals. As it can be seen, the experiment was stopped. During failure, the location of the traverse and also the burst energy increase significantly.

Figure 4 shows a summary of all measured probes which allows a clustering and therefore an evaluation of the damage mechanisms. The clusters in the parameter space of weighted peak frequency and partial power (150-300 kHz) display various source mechanisms and failure types. Low values of WPF <150 kHz are mainly caused by matrix failure / delaminations /

friction processes, whereas high values of WPF >150 kHz are mainly caused by fibre matrix failure and fibre breakage [1,2].

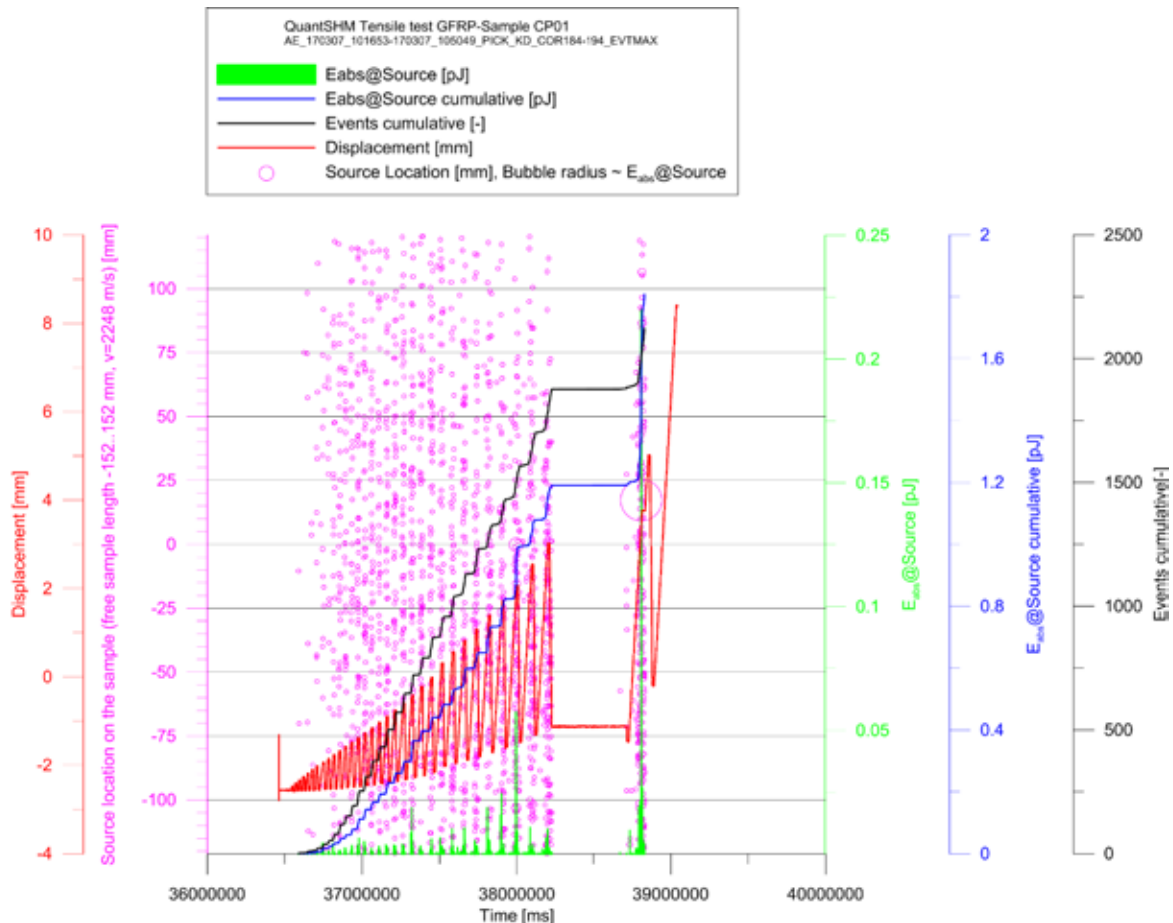


Figure 3: Results for the Probe CP01 - Displacement (red), Source location (magenta) [3]

Full scale rotor blade test

During the fatigue test, the rotor blade failed completely due to a transversal crack at R=18m Figure 5. The located events are shown in Figure 6. At the location of failure, little activity is shown. Therefore, clear indications are presented on both sides of the crack (diagonal structures). They indicate that those areas have to compensate the missing load bearing capacity in the failure area and loaded beyond the load they are designed for. To give a better insight, the following diagrams (Figure 7, Figure 8) show all events and the absolute power occurring at certain radii. It can be seen, that in the crack area which is marked with a vertical red line, no indications are shown. Nevertheless, at the radii of the diagonal failure zones, clear indications are found. Looking at the time scale, the failure can be determined at about 34000 cycles since the energy increases there significantly.

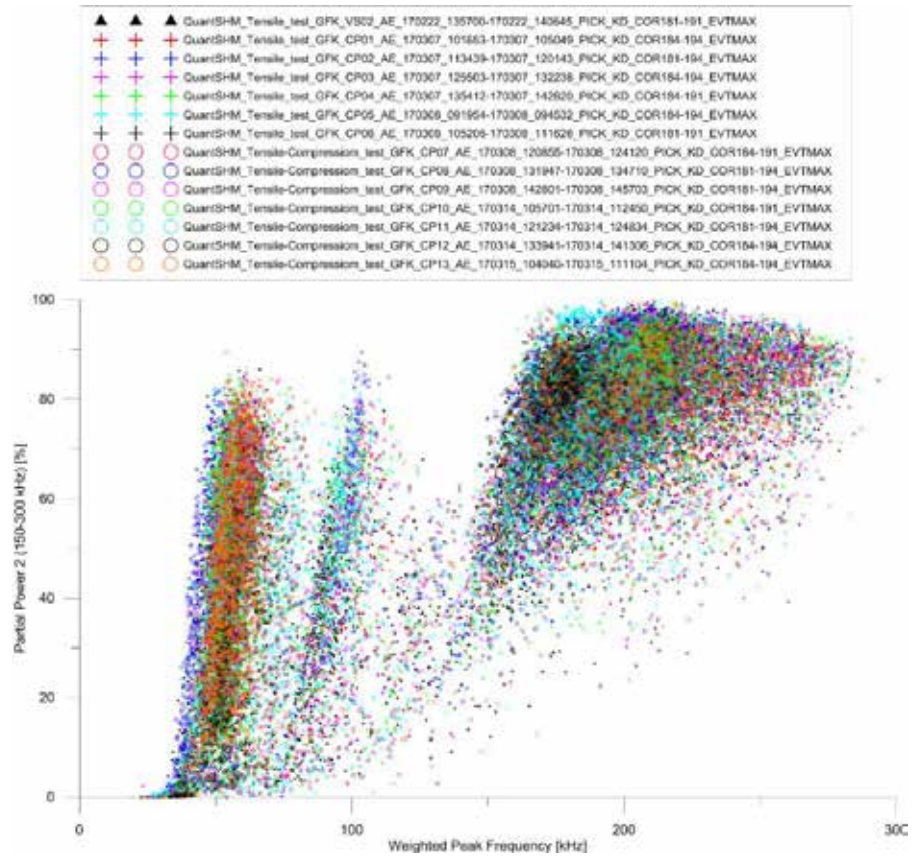


Figure 4: Partial power of the burst signals against their the weighted peak frequency (WPF)[3]



Figure 5: Medium chamber: transverse crack and failure of both spar caps at R=18,1 m

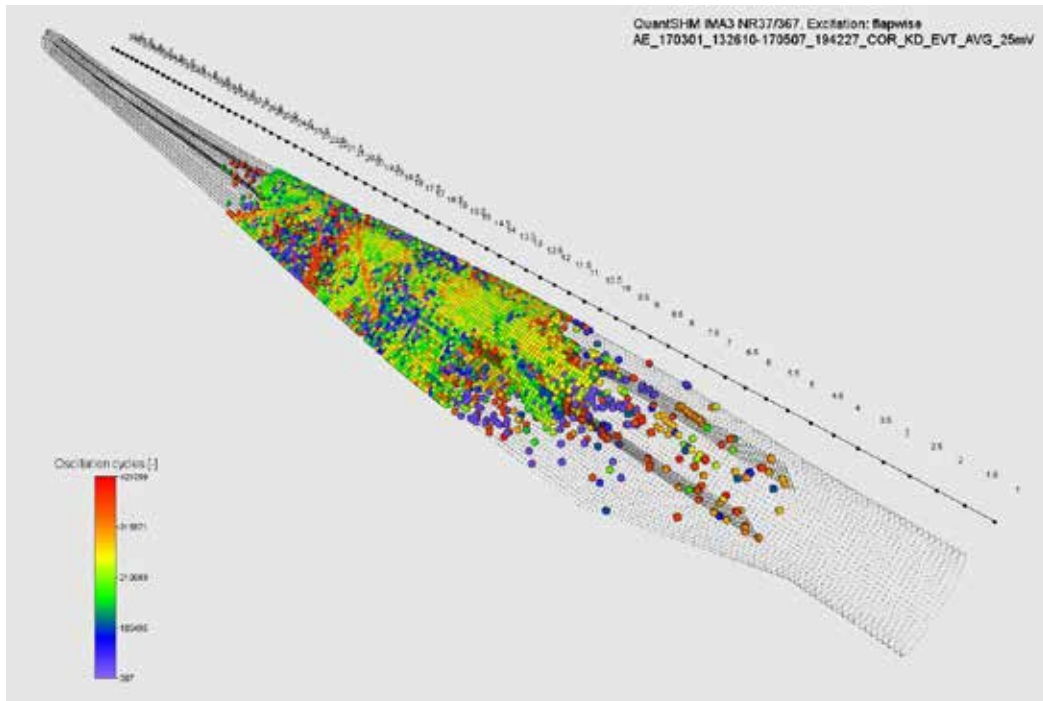


Figure 6: Overall view of the rotor blade with the cumulated event distribution depending on the load cycles (purple: early, red: late during the experiment)

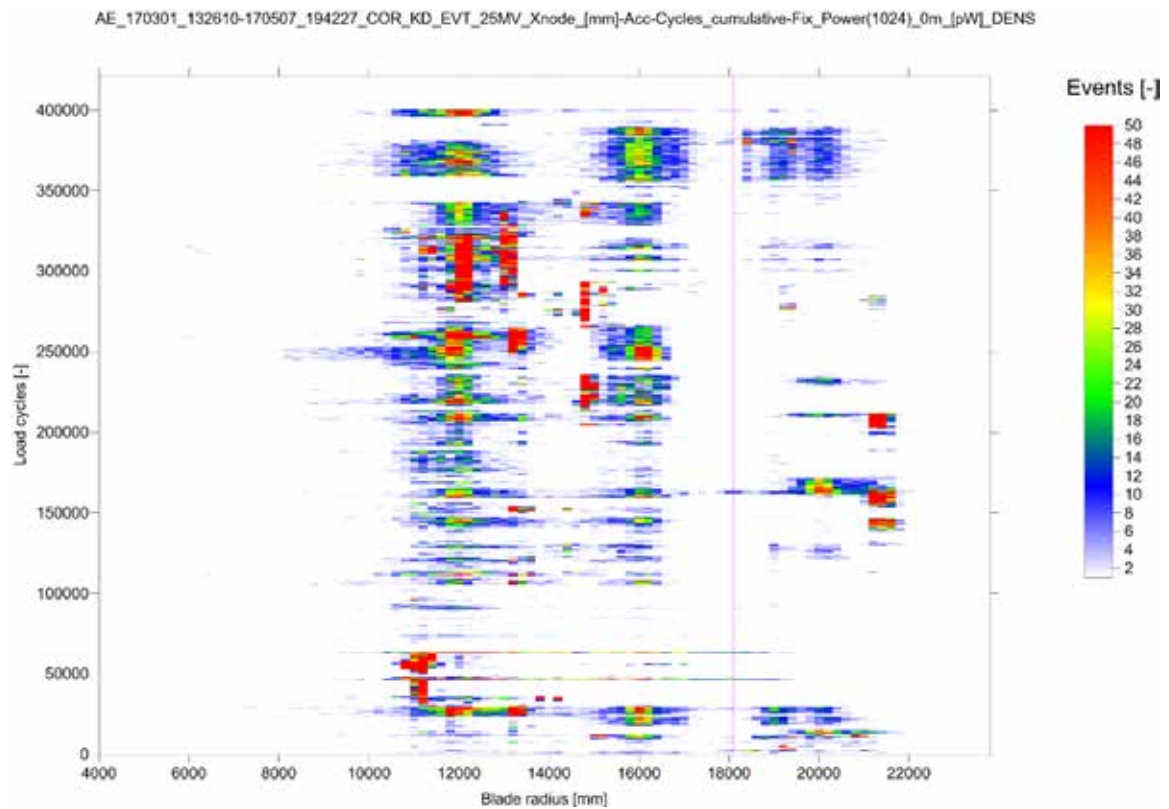


Figure 7: Events located over the radius and the load cycles

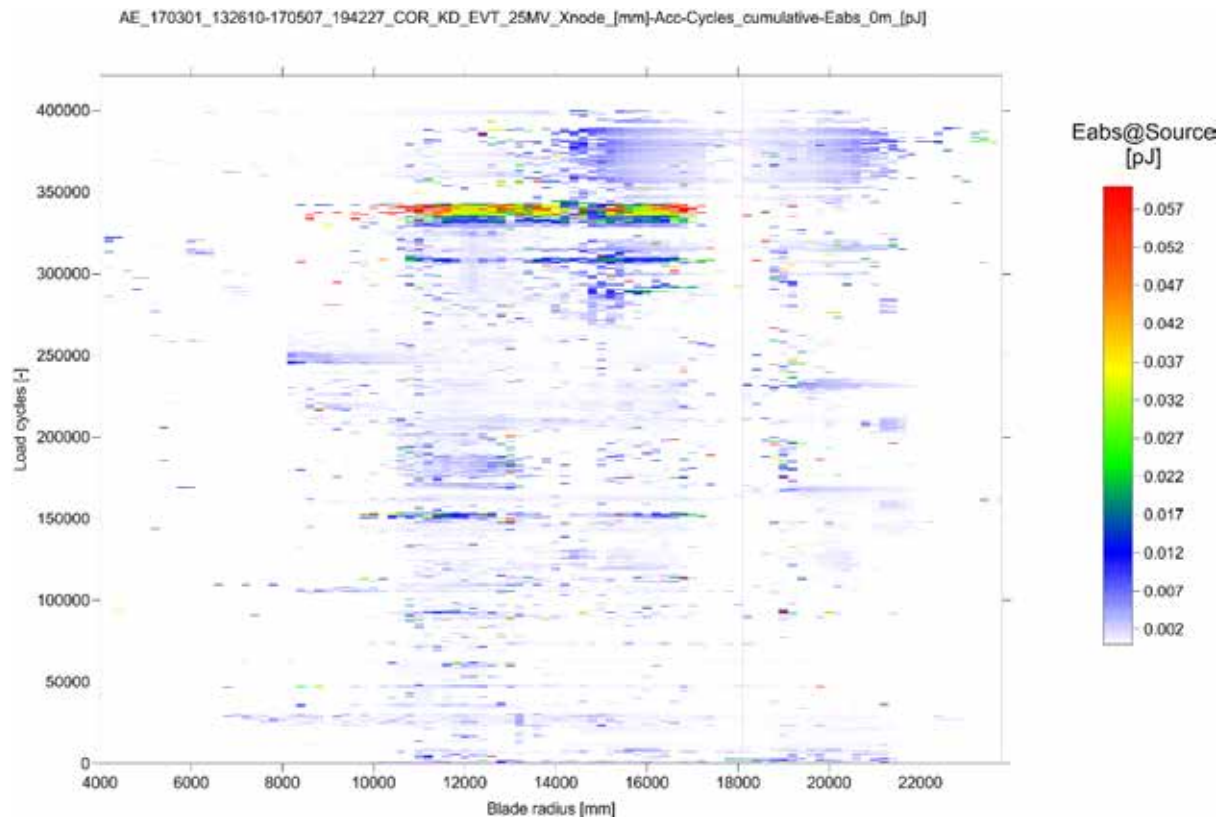


Figure 8: Absolut energy located over the radius and the load cycles

4. Conclusions

The paper deals with investigations on GFRP structures like rotor blade materials. Tensile tests have been carried out on 14 tensile probes. The results give the possibility to differentiate various failure types. Only a medium cluster cannot be clearly correlated.

Furthermore, a full size dynamic fatigue test has been carried out on a 37,5 m rotor blade which failed during the experiment. The results help to understand the failure mechanisms. It can be seen, that there are hardly any AE indications in the damaged area but in the areas which have to compensate the failure regarding the load.

These experiments help to understand the complicated failure mechanism in GFRP structures. They open the possibility for an online monitoring and may give clear indications of the single acoustic emissions. Nevertheless, more data is needed to develop a standard procedure for standardized rotor blade monitoring.

5. Acknowledgments

The presented investigations were funded by the Sächsische Aufbaubank in the project QuantSHM (Nr. 100207022). The authors thank the project partners cp.max Rotortechnik and IMA Dresden for very good cooperation.

References:

- [1] Hönig, U., Holder, U., Pietzsch, A., Schulze, E., Frankenstein, B., Schubert, L.: Definition of requirements for reference experiments to determine and evaluate various damage mechanisms in fibre composites by acoustic emission, 19th World Conference on Non Destructive Testing, München, Paper, 2016
- [2] Holder, U., Schreiber, C., Schulze, E., Schubert, L.: Zuordnung von Schallemissionsparametern zu spezifischen Schadensarten in CFK-Werkstoffen, Fulda, 21. Schallemissionskolloquium 2017
- [3] Weihnacht, B., Schulze, E., Pietzsch, A., Schubert, L., Vandenbrande, A., Cerbe, B., Borchers, K.-W.: Schallemissionsmessungen während der Durchführung von Zugversuchen an GFK-Proben, Leipzig, DGZfP Jahrestagung 2018

68 - Structural Health Monitoring of composite aerospace structures with Acoustic Emission

Martin Lehmann, Andreas Bueter, Oliver Schwarzaupt, Conchin Contell Asins

Fraunhofer LBF, Darmstadt Germany

Abstract:

While composite materials have many advantages due to their lightweight potential impact events or Foreign Object Damage (FOD) is critical for composite and many other lightweight and thin aerospace structures. FOD can lead to unscheduled maintenance in the cases of hail damage, tool drop, ramp rash or even loss in the cases of tire debris (Concorde Accident July 25th, 2000) or insulation debris (Columbia Space Shuttle Feb. 1st, 2003). Impact damage reduces the static load capability and the fatigue life of a structure. The cost of an aircraft on ground is about 40 k\$ per hour. Thus a decision on unscheduled inspection and repair or a return to flight must be taken fast and responsibly. Non-destructive inspection combined with numerical analysis is the state of the art. A detailed numerical analysis of predamaged parts may take several days or weeks. Novel fast Structural Health Monitoring (SHM) and predictive maintenance tools can support the necessary decision making process.

Impact damage generates characteristic acoustic signals that can be detected and analyzed by acoustic emission systems during the event. This was investigated in the Clean Sky Program in the Green RegionI (GRA) platform* by Fraunhofer LBF (Laboratory for "Betriebsfestigkeit" – structural durability). A fast but simple analytical model was developed that can analyze certain extracted acoustic features. This model was trained with 50 composite plates clamped to simulate a stringer bay each. The specimen were subjected to different impact energies and locations and corresponding Acoustic Emission (AE) features, damage sizes as well as the compression load after impact were derived from these tests. After this training the system could analyze impact events in near-real-time and present estimations on impact energy levels, location, damage size, mechanical properties, delamination growth as well as the remaining fatigue life under a given load level.

The project closed the loop from data acquisition with a commercial AE system, via the assessment of the structural properties based on sensor records to the prognosis of this structural health and its presentation in near real-time after impact events. Unfortunately the high scatter of results regarding impact testing as well as of the extracted acoustic signals affects the reliability of the system so far but with approaches from big data methods AE may become an interesting sensor type for predictive maintenance of sporadic failure types.



*Research leading to these results has received funding from the European Union (FP7/2007-2013) for the Clean Sky Joint Technology Initiative, rel. grant agreement.

1. Introduction

Two famous accidents in aerospace resulted after impact events. The loss of a Concorde after tyre parts damaged the tank marked the end of this type. The Space Shuttle Columbia was lost on re-entry after the leading edge had been damaged during the launch by rather lightweight foam-insulation debris. While a Structural-Health-Monitoring (SHM)-system would not have saved the Concorde, it may have given the crew of the Columbia an early warning of the damage of their vehicle. That is why NASA investigated SHM technologies for applications in the remaining Shuttle-Fleet after the accident.

In the search for the source of the damage to the leading edge, impact tests were made with foam segments on a spare Reinforced Carbon-Carbon (RCC) leading-edge. During the tests acoustic emission sensors could detect the impact of the foam segment and it was possible to locate the damage with these sensors. [1,2,3]

Different SHM-approaches were investigated in the Clean Sky program and a similar approach was investigated on aircraft structures in the work package described here. An impact event on composite structures results in impact induced damage (e.g. delaminations) and thus affects the structures compressive strength after impact (see figure1). Also possible is the delamination growth depending on the kinetic energy level of the impact event and the design of the structure. The primary reason for preliminary compressive failure of an impacted specimen is the lower buckling stiffness in the impact induced delamination area. The structural performance is investigated in compression strength after impact tests (CAI). The possible growth of delamination is investigated in compression after impact and fatigue (CAIF) tests. Potential delamination growth depends on the impact energy, the load level and of course the design and mechanical properties of the structure.

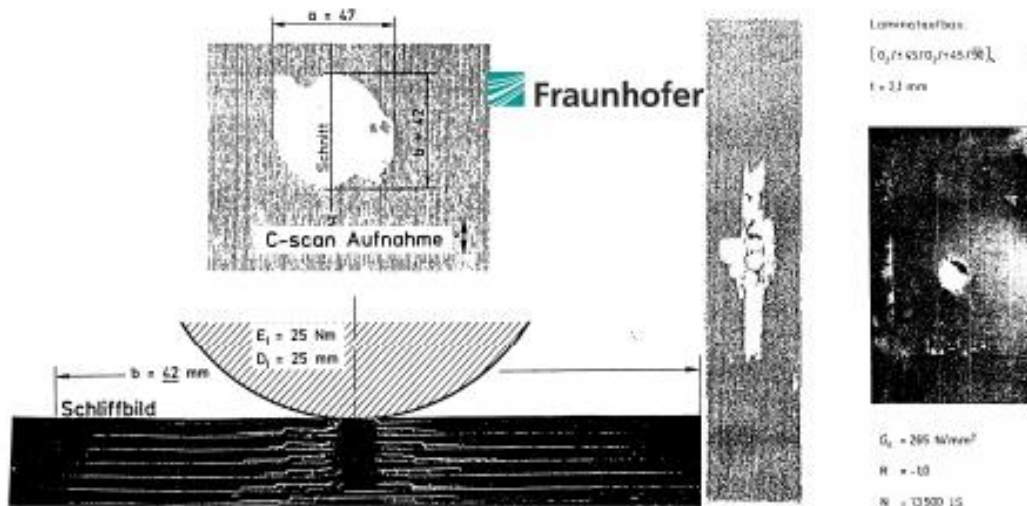


Figure 1: Impact induced delamination in composites and delamination growth by fatigue while barely visible (right) (Fraunhofer LBF)

The result of impact events can be divided in different levels based on certain energy levels and resulting structural damage.

The first threshold is when the impact damage has no detectable influence on the global compression strength of the composite.

The next threshold is the Barely Visible Impact Damage (BVID) upon which the dent of the impact damage becomes just visible. Unfortunately this does not necessarily correlate with the delaminated area as this depends e.g. on the material (matrix- and fiber type and layup) and its thickness. In figure 1 the very small contact area (much smaller than the diameter of the ball of 25 mm) led to a delamination of about 47 mm x 42 mm. Those delaminations can grow under further loading depending on boundary conditions.

The next threshold is the penetration level after which the effect of the impact induced damage on the compression strength remains nearly constant as the diameter of the resulting hole remains constant.

The following figure 2 shows the typical curve of the remaining compressive strength over the damage size with a certain "Allowable Damage Limits ADL", "Critical Damage Threshold CDT" in relation to the Design Limit (LL) respectively the Design Ultimate Load (UL).

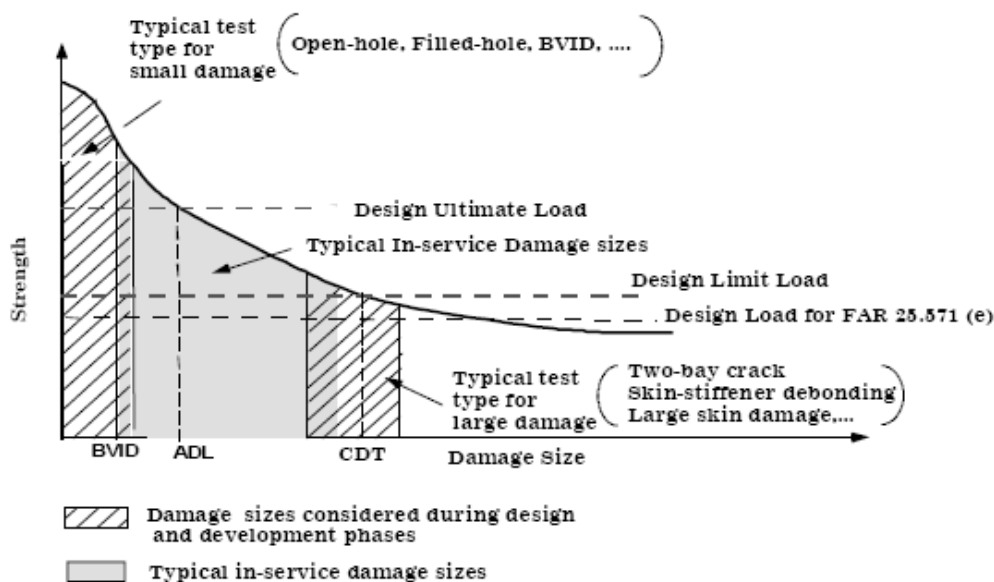


Figure 2: Residual Strength versus damage size Relationship [4]

The following diagram shows the need for a fast assessment of impact induced damages based on these remaining load capabilities of the part.

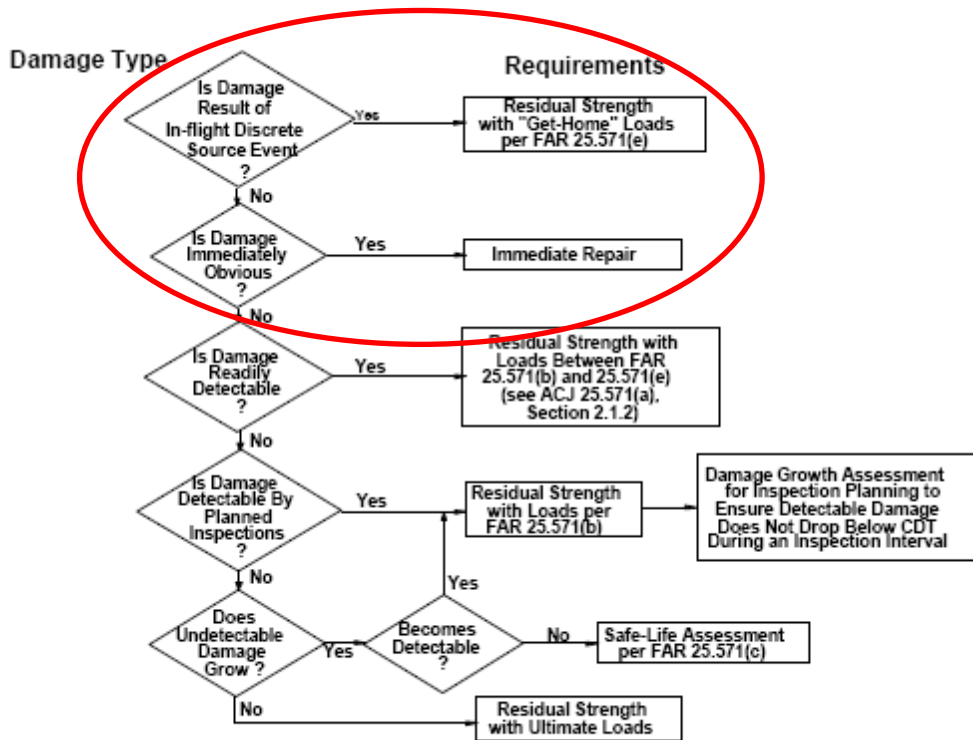


Figure 3: Levels of Damage Tolerance Assessments [4]

The diagram shows the need for a system that can assist to detect and classify impact events and assess their effects on the structure rapidly. In simplified terms the effect of impact induced damages can either lead to a grounded aircraft for immediate unscheduled repairs (very expensive) or the damaged plane may continue flying until a repair can be scheduled with upcoming maintenance cycles and prepared by detailed simulation. The type of approach depends on the extent of damage and if this can be expected to grow.

There are several possible monitoring systems that can be used to detect impact events and damages. One famous example for active systems is the Stanford Multi Actuator Receiver Transduction (SMART)-layer [5]. Here only passive systems based on AE-systems are investigated. Similar activities have been published [6], [7].

A future system for acoustic impact monitoring based on current Acoustic Emission technology combined with a structural analysis needs to fulfil the following requirements:

- detect impact events in-flight above a certain threshold using a very high sampling rate
- locate the position of the impact event
- categorize the impact event intensity and correlate a predicted impact induced damage magnitude (see above) based on the acoustic signature of the impact events and the calibration of the system with experimental tests. It will not be necessary to calculate an actual impact energy in Joule.
- estimate and predict the residual strength of the monitored part immediately after the impact event.

-support the prognosis of the remaining lifetime and damage growth of the predamaged structure under further loading (for a calculation of the repair urgency). A more detailed numerical analysis can be done later if the damage allows a later repair.

In order to achieve these requirements mature equipment in the AE-field was used. Speaking in the SHM terms of preprocessing, feature extraction and classification based on sensor signals, these elements of the monitoring system are processed mainly by a modified mature system. The corresponding hardware and software are combined with fast numerical tools for a quick structural analysis of sensor data.

The following flow chart (figure 4) shows the approach for SHM of composite aerospace structures with AE. An impact event results in an electrical sensor signal which is analysed using Acoustic Emission hardware and software with minor modifications only. The estimated position and magnitude information of the impact event is then analysed in a special software using information about geometry and material data of the structure.

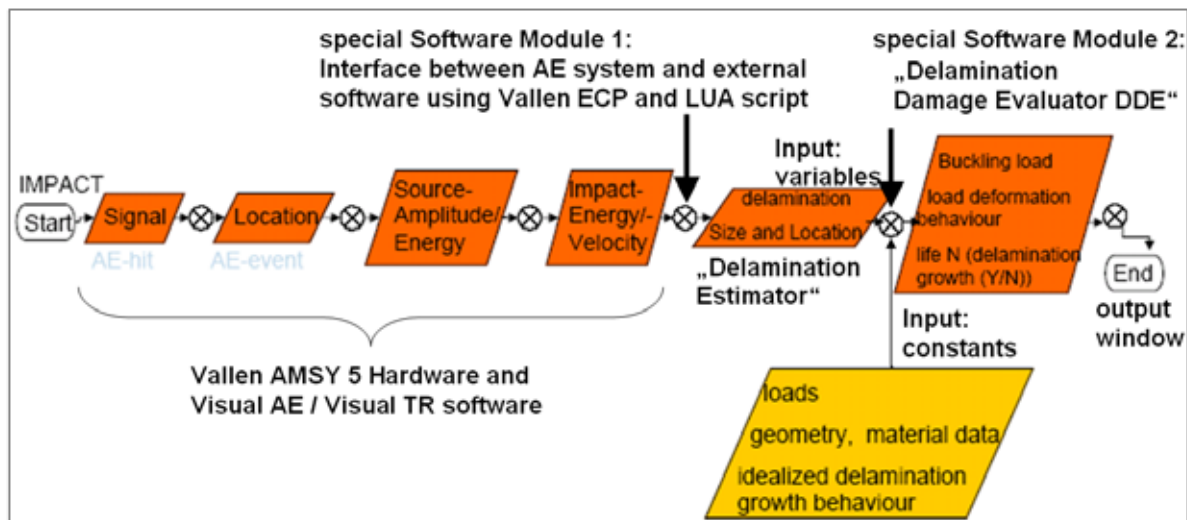


Figure 4: Flow chart of the approach for Structural Health Monitoring (SHM) of composite aerospace structures with Acoustic Emission (source: Fraunhofer LBF)

The optimization of sensor placement, the characterisation of the acoustic behaviour by impact (correlation of impact energy and resulting electrical signal) as well as the structural behaviour by impact (correlation of the impact energy and the resulting damage size) is done in empirical test campaigns for the necessary database.

2. Description of work

Test Campaign

For the localisation of impact events several sensors are used to triangulate the origin of acoustic emissions excited by the impact event and/ or impact induced damages to the composite structure. The sensors need to be placed at strategically optimal loactions to cope with different sound velocities and the certain attenuation behaviour of composites. At the time of the project there was no

compensation for the special effects of composite material on acoustic waves included in the system yet.

The sound velocities in composite materials depend on the fiber orientation and differ by the stiffness differences in matrix and fiber dominated directions. That is why an empirical approach was used to identify all sound velocities first. In Acoustic Emission testing the Hsu-Nielsen Pencil Lead Break test (PLB) is used to calibrate systems with reproducible acoustic events. In this case the velocity is higher by a factor of roughly 2 for 0° (predominate fiber direction) compared to the 90° direction. No detailed information on the material data can be given here unfortunately.

The solution to compensate for this effect was to modify the position of real sensor positions on the part to virtual ones in the software in order to be able to calculate the correct location. To compensate for the lower velocity 90° to the fiber direction the real position of the sensors is multiplied by the factor two in that direction in the software while the position in 0° direction (used as sound velocity) was not changed. By this way the system exports correct x,y coordinates on the part with a calculated level of uncertainty (LUCY) of 0.2-3 mm for panels of 300 mm x 200 mm in repeated tests. The LUCY value is the standard deviation of the calculated sensor distances to the source position and the distance according to the measured arrival time difference.

As the system showed good results for localising impact events, the next step for the identification of the impact energy was tested with a great number of clamped panels with symmetrical "mid-bay" impacts only to get the maximum number of results.

The effect of potentially different amplitude levels at the position of the sensors due to an excentric impact can be compensated by considering the mean value of the signal of the four sensors as the feature for the identification of the impact energy. This is one reason why this feature was investigated mostly for the identification of the impact energy.

A number of different tests were necessary for the identification chain

The results of the test campaign are discussed briefly only. Altogether 50 Carbon Fiber Reinforce Plastic (CFRP) panels of roughly 300 mm x 200 mm were tested in 50 impact tests accompanied by AE measurements. Afterwards the panels were cut down to 150 mm x 100 mm for standardized mechanical compression after impact (CAI) testing. The tests are discussed next very briefly.



Figure 5: Overview of the panels for CAI (left) and the original size for Impact tests (right)

Impact testing: The impact energy is preset with the drop height but the panels absorb only a part of this energy depending on the clamping conditions and energy level. The absorbed impact energy is calculated by the Impact Testing Machine Instron Dynatup 9250 HV. While the initial impact energy may be 10 J as one example only 6 J are absorbed. The difference is the elastic energy which reflects the impactor back to a secondary drop height which is measured but a second drop is prevented. According to the general point of view only the absorbed energy causes damage. The effects of different rates of elastic and absorbed energy on acoustic emissions are much less understood. Only the absorbed energy was considered in further examinations.

AE-Recording: The Vallen AMSY 5 System recorded acoustic signals in realtime during the 50 impact tests (see figure 6). Certain features were analysed afterwards. Only two results are discussed here. Other features may deliver better results in other cases. The development of more elaborate advanced signal analysis and filtering methods was not the intention of this work package so the AE-features "acoustic energy" and "counts" were used for correlating the electrical signals to the damage size.



Figure 6: Overview of the test rig with the Impact Test rig in the back and the Vallen AE-system in the front

Damage Analysis: The correlation of damage size to impact energy levels was done with a Lock-In-Thermography system for NDT and a special scanner system for detecting the delamination size. Water based ultrasonic test methods are unfavourable as these may influence the result of the subsequent compression after impact investigation. An observation grid printed on a special transparent film enabled an investigation of the damaged area in the relevant thermographic image with the highest visible area. A special scanner software was used to calculate the damaged area in square millimetres for each impact. Figures 7 and 8 show some images of delaminations of the panels.

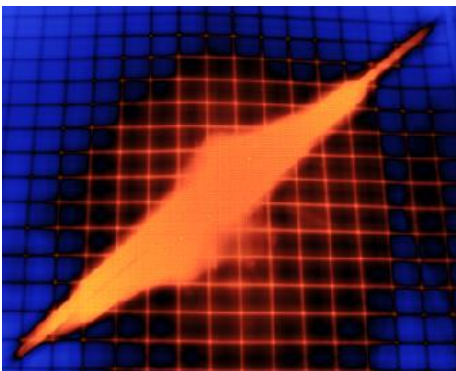


Figure 7: Lock-In-Thermography System and Screenshots with some delmainations under different Energy levels

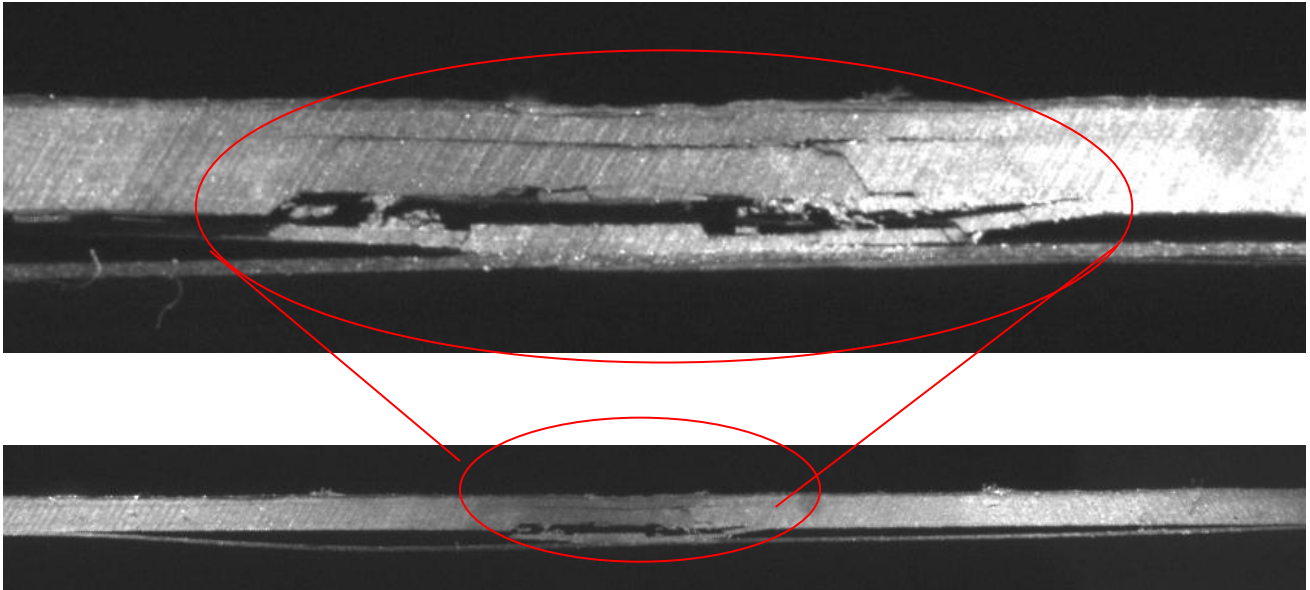


Figure 8: Microscopic analysis of delaminations.

The results of the tests are shown in the next figure

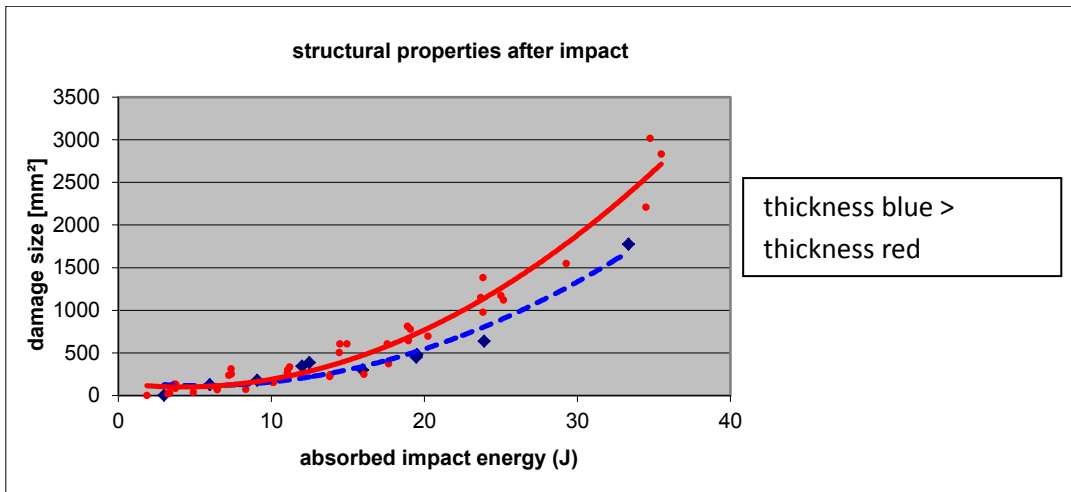


Figure 9: Damage Size over absorbed impact energy

Mechanical Analysis: Compression strength after impact testing of the panels to get results for the structural behaviour after impact for the simulation model. The result is shown next.

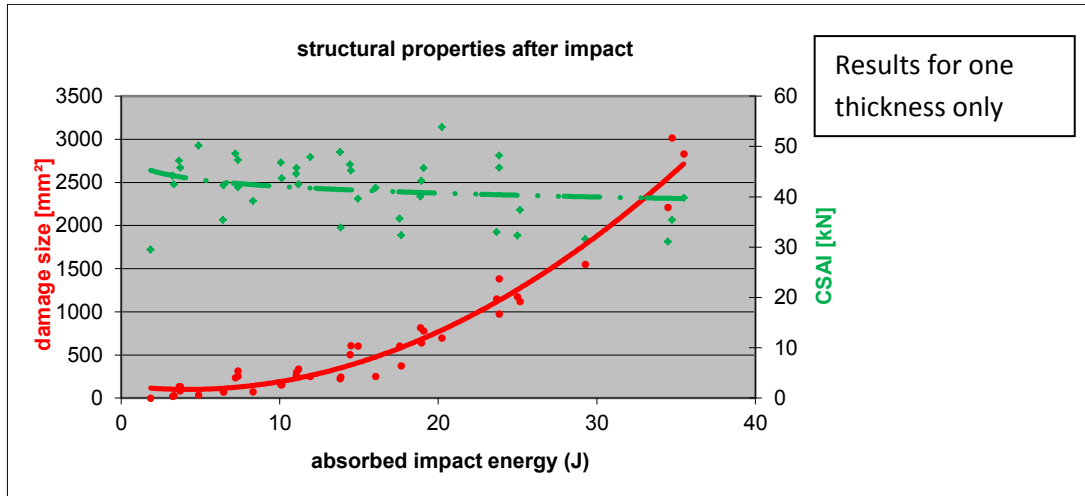


Figure 10: Compressive strength after impact and damage size over absorbed impact energy

Finally a correlation of the acoustic signal with the resulting delamination size and other values is possible by linking all the results (see figures 11-13). It was decided to use the calculated acoustic signal strength which is calculated as the Root Mean Square (RMS) result by integrating the absolute value of the electrical signal as a mean AE-signal. This value is given in energy units (eu) and measured in nVs (1eu = 1 nVs).

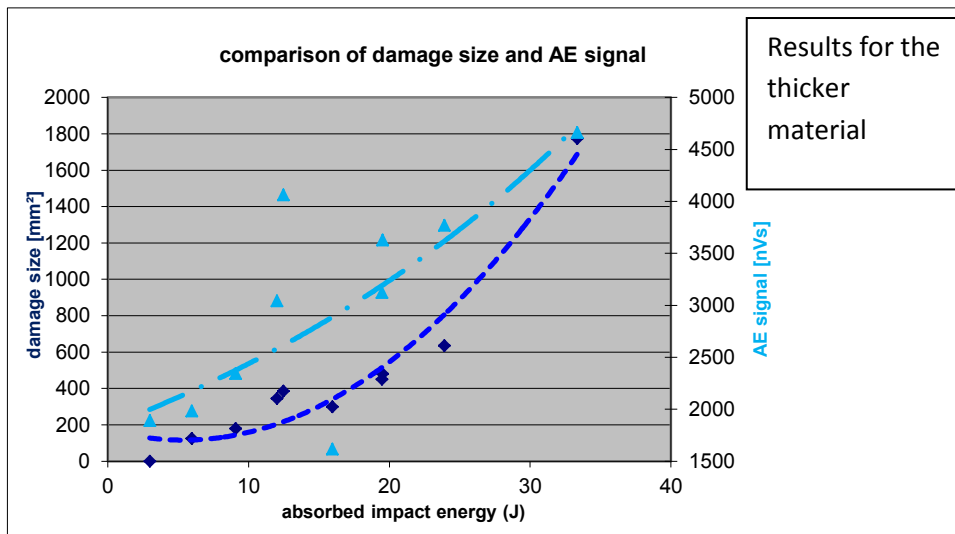


Figure 11: Comparison of damage size and AE signal over the absorbed impact energy for the thicker panel

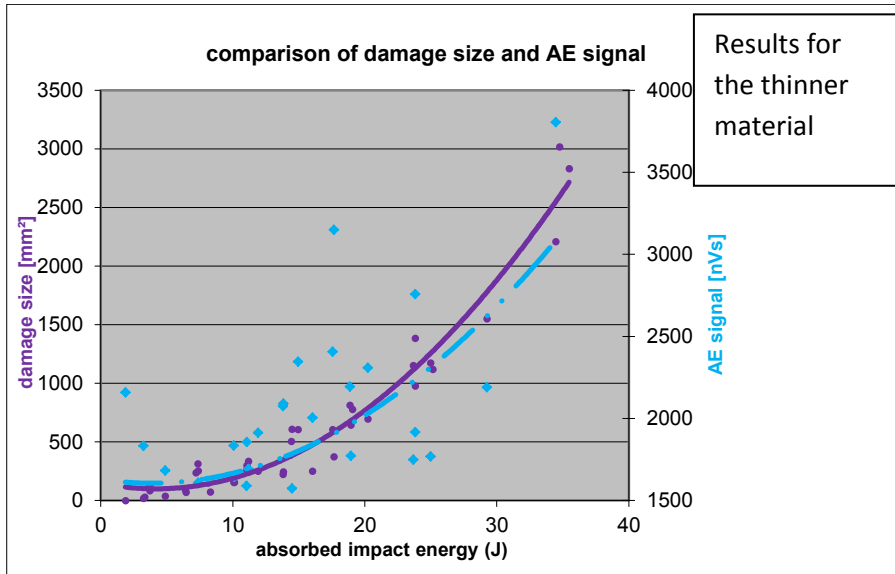


Figure 12: Comparison of damage size and AE signal over the absorbed impact energy for the thinner material. The following figure shows the correlation of damage size and the AE signal.

The most important result of the experimental test campaign that contained 50 sensorized impact tests and subsequent NDT evaluations on the reference material was the following correlation between the acoustic signal and the impact induced delamination size. It was decided to use a simple linear approach instead of a neural network as the scatter of results does not justify a better mathematical interpretation of the results. Though not very reliable due to the high scatter of results the simple linear equation y (damage size in mm^2) = $0.5274 \times$ (AE energy in nVs) - 484.11 was used here for the thinner material. For a higher reliability of such a system based on AE much more tests and a more systematic analysis of factors leading to scatter would be necessary.

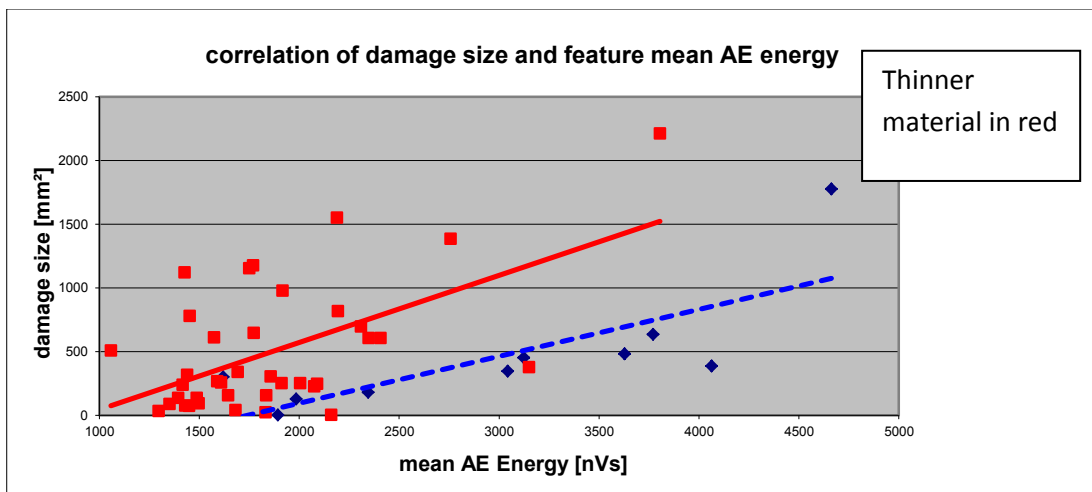


Figure 13: Correlation of damage size and acoustic mean energy (AE signal) delivered by the AE.

At best these results make it possible to correlate acoustic signals in this case in an area of about 10 J to 25 J. The penetration threshold was at around 35 J leading to high acoustic emissions and an override and errors in measurement at higher impact energies with this feature.

It is clear by looking at the scatter of results that it will be very hard to interpret the sensor signal and correlate a damage size with a high degree of certainty using this feature alone.

An alternative feature that may be used for detecting higher impact energies is the number of counts (see the following figure 14). The following figure shows a screenshot of a test series. While there is no relevant difference between the Amplitudes in the top left picture the number of counts rises rapidly in the big screen when the area of impact penetration is reached. This may make it possible to detect critical impacts with an additional feature where the feature acoustic energy becomes unreliable due to a sensor override.

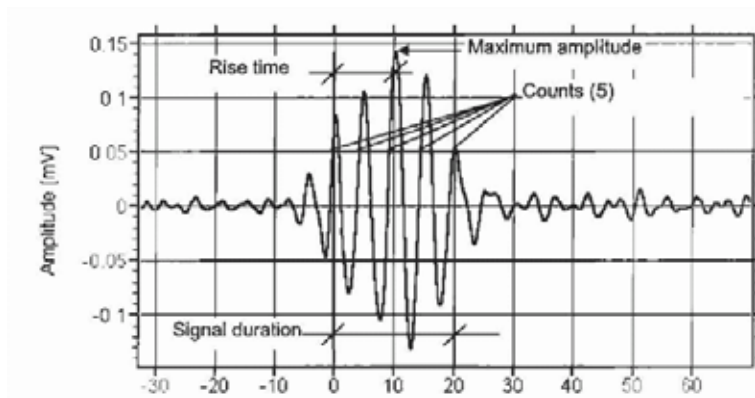


Figure 14: Possible features of acoustic signals [2]

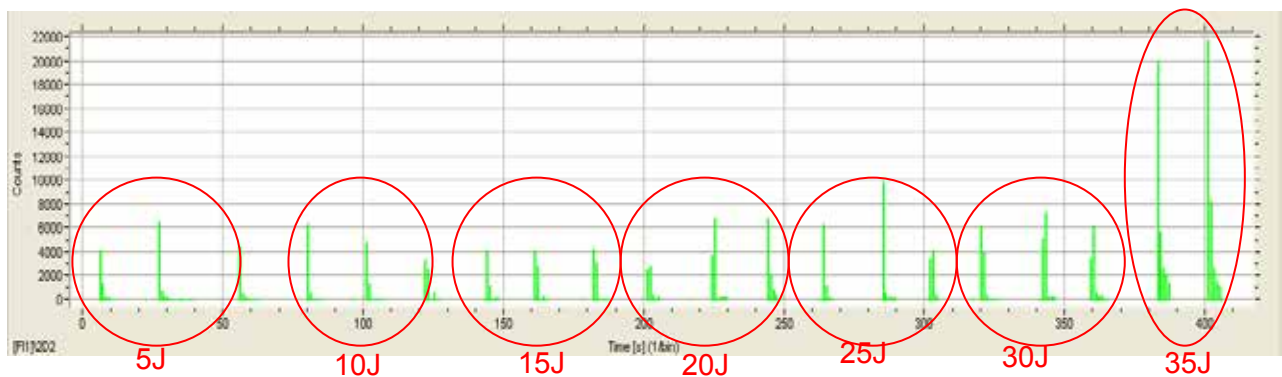


Figure 15: comparison of "counts" for different impact energy levels

The mean AE energy and location coordinates are the only variables to be exported by the AE-system for subsequent analysis of the post impact behaviour in the next step.

The interface-software is using the Vallen "Embedded Code Processor" Software (ECP) which is installed together with the Vallen "Visual AE and TR software" on the same laptop as the subsequent MATLAB software "Delamination Damage Evaluator" (DDE).

The interface software module is using a fast Lua script that generates and exports a file containing location and acoustic energy data as soon as an impact event is registered by the AE-system. The output of the Vallen "AE/TR software" are the location coordinates and a mean acoustic energy level calculated using four acoustic sensors.

The Calculation Tool for Delamination Damage Evaluation (DDE)

The software tool is used for a fast, simple calculation of damage caused by an impact event. A growth of damage could be measured by AE as well via e.g. the felicity-effect or Kaiser-effect but this is not considered here yet.

The numerical models of the DDE are based on previous research done by de Jonge at Fraunhofer LBF [8-38] but there is also the opportunity to add new or modify calculation models.

In the model, the plate is divided in sub-areas. Each of the sublaminates, created by a delamination, is such an area as well. The model idealizes the damage and starts from the assumption that the sublaminates are rectangular and in the middle of the plate (see Figure 16a). Then the load deformation behaviour of each of the areas is represented by a spring. In this manner, the whole plate is described by a system of parallel and in-series springs (see Figure 16b).

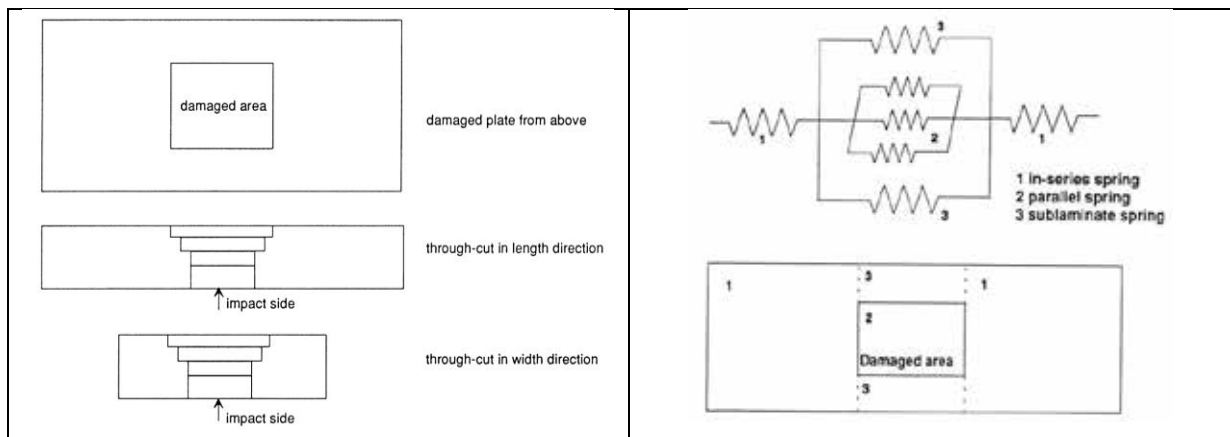


Figure 16: a) Idealization of the characteristic state of damage after impact. b) Areas representing springs in one-dimensional spring model (source: Fraunhofer LBF)

Once the load on a sublaminates has exceeded its buckling load, it will not behave like a normal spring anymore. The load a sublaminates can take after buckling equals the buckling load of the sublaminates. In this way, the load-deformation curve for a plate with certain damage can be calculated. By determining the released energy between two subsequent damage configurations from these curves, the expected life can be calculated with methods from fracture mechanics (see Figure 17).

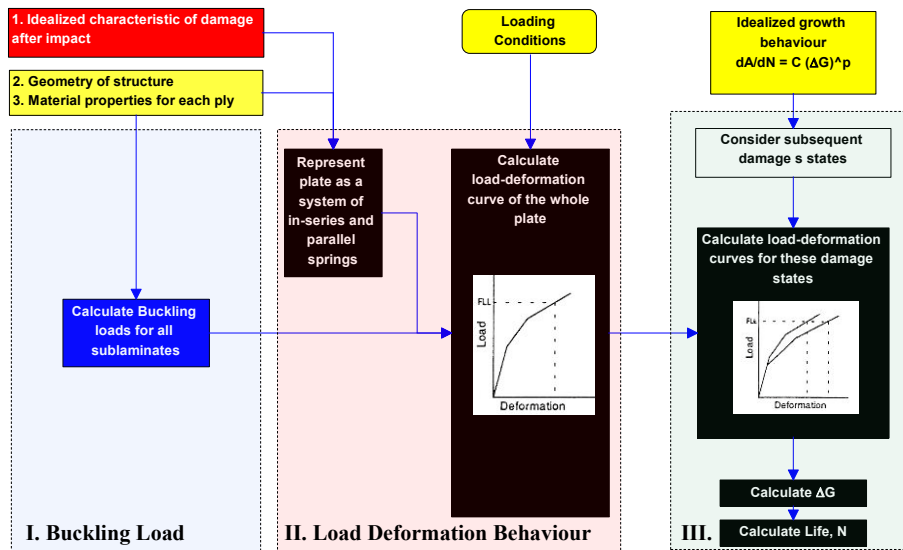


Figure 17: Schematical representation of the theoretical model that predicts damage growth (source: Fraunhofer LBF)

The prediction model uses fracture mechanics to describe the damage growth. For this, it is necessary to calculate the Strain Energy Release Rate (SERR), between two subsequent states of damage, before and after growth. The quantities needed for the calculation of SERR from the analysis of the load-deformation behaviour are the potential energy and the deformation at a Fatigue Load Level (FLL). The load-deformation curve for a damaged plate is calculated by representing different areas of the plate as a system of parallel and in-series springs, which will be referred to as a 'spring-model'. If a plate is loaded the sublaminates will start to buckle one after the other. Every time a sublaminate buckles, the stiffness of the plate changes a little and the load-deformation curve will show a change in slope.

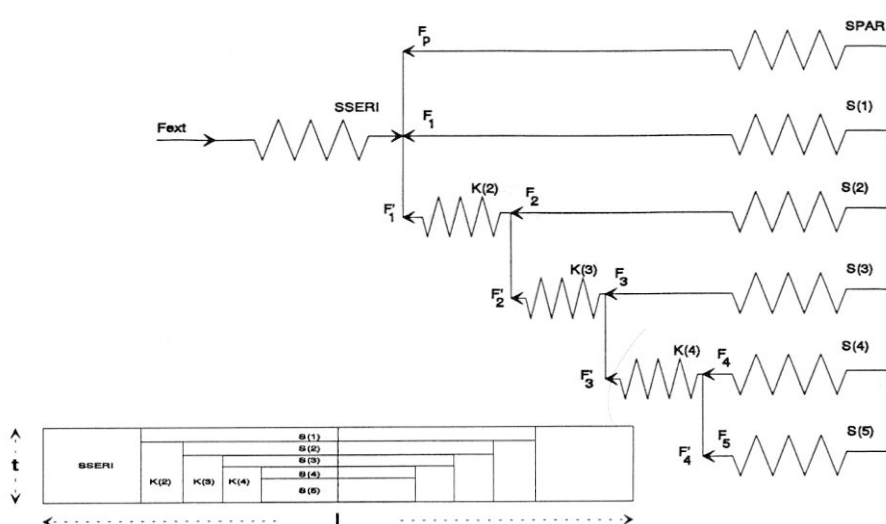


Figure 18: Spring Model (one half of the plate) (source: Fraunhofer LBF)

Performing this procedure iteratively and keeping in mind that the curve ends when the strain in the parallel spring is the critical (fracture) strain, gives the load-deformation curve for a plate with a certain

damage. As described above, the important parameters needed for the next part of the prediction method are the deformation at Fatigue Load level (FLL) and the potential energy of the overall plate at FLL.

The DDE is divided in three parts of calculation:

- I: buckling loads
- II load deformation behaviour
- III fracture mechanics

The computer program, based on the model, is able to make the calculations for each of the three parts. The first “off-line” part focused on modifications of material data by test results while the fast online tool to be developed is optimized on rapid calculation. (figure 19)

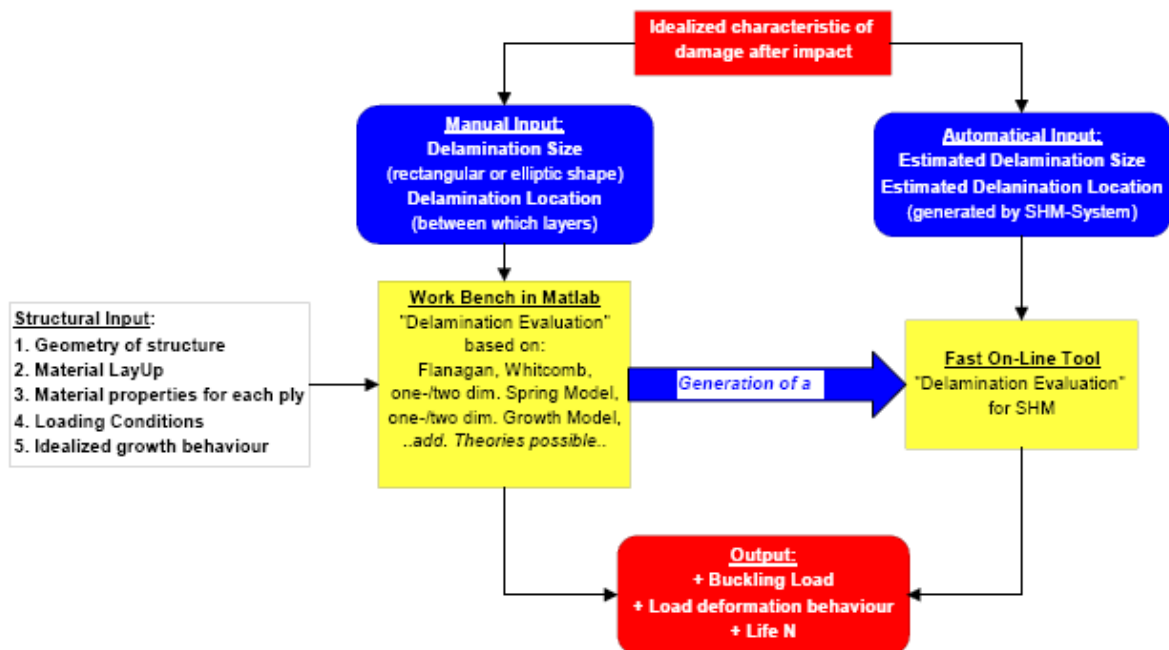


Figure 19: Two-Dimensional Spring Model (one half of the plate) (source: Fraunhofer LBF)

The “off-line” software was used for testing and optimised using experimental compression after impact results (see figure20).

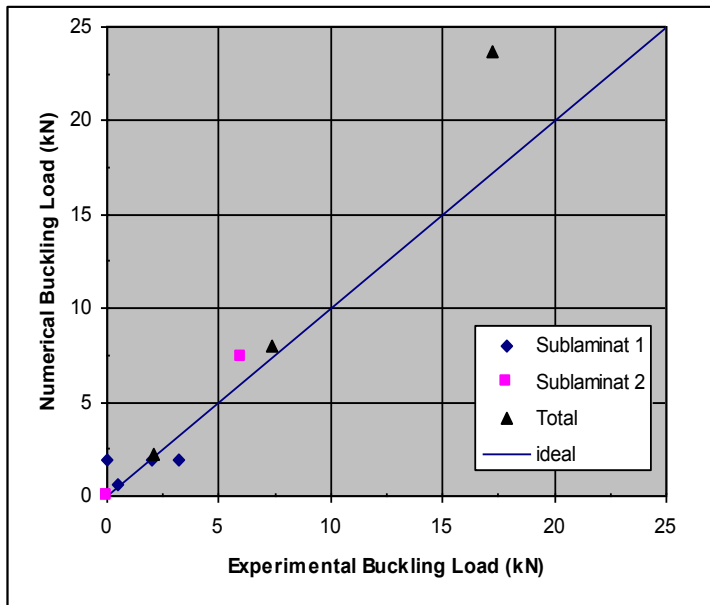


Figure 20: Buckling Loads Total and Sublaminat Buckling (source: Fraunhofer LBF)

The resulting online software is triggered automatically when the file with the variables is generated by the AE system via the fast Lua-script. Constants like material properties for the laminate, layup and dimensions, loads, mechanical and calculation parameters are defined beforehand.

The next figure 21 shows a flowchart of the DDE software. If, depending on the Delamination Size, Fatigue Load Level and material constants, a delamination growth is calculated 50-500 loops with gradually increasing delamination sizes resulting in gradually decreasing buckling loads are used to generate a graphical output of the Damage size over load cycles and Buckling loads over load cycles respectively.

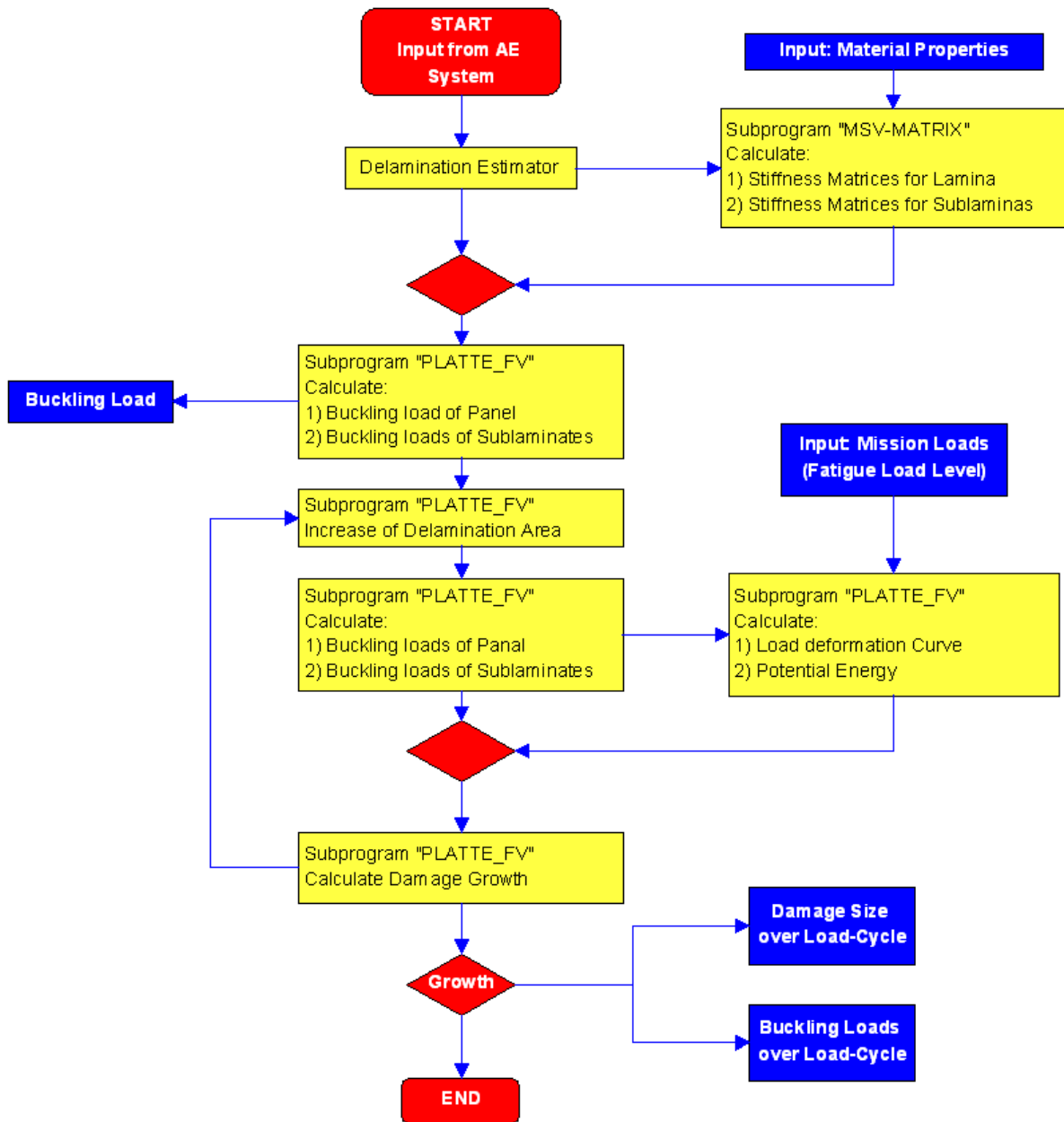


Figure 21: Flowchart of the DDE software

7. Discussion

Several blind tests were done with the system after the software was optimized to demonstrate the fast calculation on the different impact levels. As mentioned the reliability of the system is affected by the high scatter of signals.

Depending on the Impact Energy level and thus the estimated delamination size there are four possible warning levels (Figures 22-24) and context sensitive outputs the software creates when the calculation is completed about one second after the impact event as a pop up.

- a) uncritical damage when no damage is estimated as the mean AE energy level is below the critical threshold that was established by experiments



Fig 22: Output Window for Impact Events when no damage is estimated based on the mean acoustic energy level

- b) critical damage “Impact detected” when no delamination growth is estimated by the DDE-software tool. Here the damage size and the Estimated Remaining Buckling loads are presented (Fig. 19) so that they can be compared to maximum or minimum allowables (Allowable Damage Limits (ADL), Maximum Design Damage (MDD), Critical Damage Thresholds (CDT), Design LL, Design UL etc.).



Fig. 23: Output Window for Impact Events when delamination damage is estimated based on the mean acoustic energy level and a delamination size is estimated based on the correlation of these properties. A remaining buckling load is calculated by the DDE software in this case.

- c) critical damage “Impact detected” where delamination growth is estimated by the DDE-software tool. Additionally the estimated trends of the delamination growth and the static compression strength of sublaminates and laminates over the remaining lifetime is calculated in a way that a residual lifetime can be read until minimum or maximum allowables (see above) will probably be reached under the preset Fatigue Load level (Fig. 20). The chosen Paris constants needed for the calculation of damage growth could not be determined with experiments using the Cytac material but have been estimated based on earlier tests. Any

new material chosen for the monitoring with this system would require a certain minimum number of tests to gather realistic data on material constants.

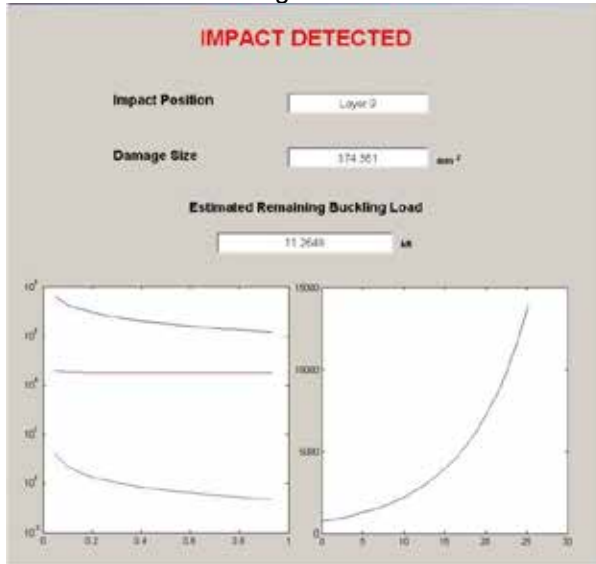


Fig. 24: Output Window for Impact Events when delamination damage is estimated based on the mean acoustic energy level and a delamination size is estimated based on the correlation of these properties. A remaining buckling load and a trend for sublaminates and laminate buckling loads (left) is calculated by the DDE software and the delamination growth (right) is calculated in this case.

- d) Penetration level impact where the impact energy was so high that a penetration of the panel is estimated. A different acoustic feature may be needed to detect penetration level impact events without doubt. Due to the high scatter of acoustic signals using the current acoustic feature “mean acoustic energy” there is a limitation to discriminate penetration levels from other strong impacts. This would have to be implemented in the future by putting in a “second path acoustic feature” in the Delamination Estimator.

3. Conclusion

In the scope of this WP in Clean Sky Fraunhofer LBF was able to close the loop from hardware to software and from data acquisition to presentation of the remaining structural health of a simplified composite part after impact events in near realtime.

The different hard- and software elements were successfully linked together with the specially developed DDE software and the monitoring system was tested in impact tests.

The calculation time was measured with about one second. There are impact induced damages where a fast evaluation of the incident is needed and preferable to a more sophisticated but more time consuming FE analysis (see figure 4). For some situations an onboard and online system may be beneficial to quickly differentiate between the severities of foreign object damages and advise the appropriate action. Some progress was made with the presented approach but future projects including a larger number of tests to account for the scatter would be necessary.

Contact :

martin.lehmann@lbf.fraunhofer.de , andreas.bueter@lbf.fraunhofer.de , www.lbf.Leichtbau.de

4. References

[1] COLUMBIA ACCIDENT INVESTIGATION BOARD Report

https://www.nasa.gov/columbia/home/CAIB_Vol1.html

[2] W.H. Prosser¹, S. G. Allison , S.E. Woodard, R. A. Wincheski¹, E.G. Cooper, D.C. Price,

M. Hedley, M. Prokopenko, D. A. Scott, A. Tessler and J. L. Spangler

STRUCTURAL HEALTH MANAGEMENT FOR FUTURE AEROSPACE VEHICLES

http://www.prokopenko.net/Publications/Agents/Australasian_SHM_Prosser.pdf

[3] Eric I. Madaras, William P. Winfree, William H. Prosser, Russell A. Wincheski, and K. Elliot Cramer, Nondestructive Evaluation for the Space Shuttle's Wing Leading Edge, NASA Langley Research Center, Hampton, VA 23681, 41st AIAA/ASME/SAE/ASEE Joint Propulsion Conference & Exhibit 10 - 13 July 2005, Tucson, Arizona

[4] H. Razi and S. Ward, PRINCIPLES FOR ACHIEVING DAMAGE TOLERANT PRIMARY COMPOSITE AIRCRAFT STRUCTURES, The Boeing Company Boeing Commercial Airplane Group Seattle, Washington, 11th DoD/FAA/NASA Conf. On Fibrous Composites in Structural Design Page Fort Worth, TX, August 1996

[5] Simone Mancini, Giorgio Tumino and Paolo Gaudenzi, Structural Health Monitoring for Future Space Vehicles, ,Journal of Intelligent Material Systems and DOI:

10.1177/1045389X06059077, Journal of Intelligent Material Systems and Structures 2006; 17;

577, <http://jim.sagepub.com/cgi/content/abstract/17/7/577>

[6] Cheng-Shung Wang, Yi Zhao and Tuan-Khoi D. Nguyen, Prediction of After-Impact Compressive Strength for Laminated Composites

http://www.sciencedirect.com/science?_ob=MIimg&_imagekey=B6TWT-3VRYHW4-J-1&_cdi=5571&_user=843885&_orig=search&_coverDate=12%2F31%2F1996&_sk=999439993&_view=c&_wchp=dGLbVzW-zSkWA&_md5=a4db394f84ef3d7e4de0127c1312d90b&_ie=/sdarticle.pdf

[7] D. Tsamtsakis, M. Wevers, P. de Meester, Acoustic Emission from CFRP Laminates during fatigue loading, Journal of Reinforced Plastics and Composites 1998; 17; 1185

[8] Gerharz, J.J. and Idelberger, H.: A method to predict residual strength and fatigue life of Impact damaged carbon epoxy laminates, Proceedings of the International colloquium of durability of polymer based composite systems for structural applications, held in Brussels, Belgium, 27.-31.8.1990, ed. by A. H. Cardon and G. Vercery, Elsevier Science Publisher, London (1990), pp. 445 – 454

[9] Gerharz, J. J.; Idelberger, H. and Gumnior, P., Impact-Damage Tolerance Untersuchungen an ebenen Faserverbundplatten-Konstruktionen, LBF-Report 6202, July, 1990

[10] Whitehead, R.S., Certification of Primary Composite Aircraft Structures in: New Materials and Fatigue Resistant Aircraft Design, ed. David L. Simpson, Proceedings of the 14th Symposium of the ICAF, June 1987, Ottawa Canada

- [11] Clark, G., Modeling of impact damage in composite laminates, *Composites* Vol. 20, Number 3, May 1989
- [12] Robert M. Bader, An, Post-Impact Composite Compression Strength Prediction, in *Review of Research on Aeronautical Fatigue in the United States, 1987-1989*, ICAF Meeting June 1989 in Jerusalem Israel
- [13] Shivakumar, K.N. and Whiteomb, J.D.: Buckling of a Sublaminate in a quasi-Isotropic Composite Laminate, *J. of C. Mat.*, Vol. 19, 1985, pp. 2-18
- [14] Whiteomb, John D.: Three-Dimensional Analysis of a Postbuckled Embedded Delamination, *J. of C. Mat.*, Vol. 23, 1989, pp. 862-889
- [15] Whiteomb, John D.: Mechanics of Instability-Related Delamination Growth, *ASTM STP 1059*, 1990, pp. 215-230
- [16] Chai, H., Babeock, C.D., and Knauss, W.G.: One-Dimensional Modelling of Failure in Laminated Plates by Delamination Buckling, *Int. J. Solids Structures*, Vol. 17, 1981, pp. 1069-1083
- [17] Chai, H. and Babeock, C.C.: Two-Dimensional Modelling of Compressive Failure in Delaminated Laminates, *J. of C. Mat.*, Vol. 19, 1985, pp. 67-97
- [18] Chai, H.: Buckling and Post-Buckling Behavior of Elliptical Plates: Part I - Analysis
J. of Appl. Mech., Vol. 57, 1990, pp. 981-988
- [19] Chai, H.: Buckling and Post-Buckling Behavior of Elliptical Plates: Part II - Results
J. of Appl. Mech., Vol. 57, 1990, pp. 989-994
- [20] Flanagan, G.: Two-Dimensional Delamination Growth in Composite Laminates Under Compression Loading, *ASTM STP 972*, pp. 180-190
- [21] Peck, S.O. and Springer, G.: The Behavior of Delaminations in Composite Plates - Analytical and Experimental Results, *J. of C. Mat.*, Vol. 25, 1991, pp. 907-929
- [22] Lagace, Paul A. and Jensen, David W., and Fineh, Douglas C.: Buckling of Unsymmetric Composite Laminates, *Composite Structures* 5, 1986, pp. 101-123
- [23] Lagace, P.A., and Vizzini, A.J., The Sandwich Column as a Compressive Characterization Specimen for Thin Laminates, *ASTM STP 972*, 1988, pp. 143-160
- [24] Vizzini, A.J., and Lagace, P.A.: The Buckling of a Delaminated Sublaminate on an Elastic Foundation, *J. of C. Mat.*, Vol. 21, 1987, pp. 1106-1117
- [25] Jensen, D.W., and Lagace, P.A.: Influence of Mechanical Couplings on the Buckling and Postbuckling of Anisotropic Plates, *AIAA Journal*, Vol. 26, 1988, pp. 1269-1277
- [26] Vizzini, A.J., and Lagace, P.A.: The Buckling of a Delaminated Sublaminate on an Elastic Foundation, *J. of C. Mat.*, Vol. 21, 1987, pp. 1106-1117
- [27] Yin, Wan-Lee: The Effects of Laminated Structure on Delamination Buckling and Growth, *J. of C. Mat.*, Vol. 22, 1988, pp. 502-517

- [28] Rohwer, K.: Einfluss der Biege-Torsionskopplung auf die Beullasten symmetrisch geschichteter Platten, Vortrag DGLR-Symposium, Berlin, 14-15 mai 1987
- [29] Rohwer, K.: Nachbeulverhalten von Platten und Schalenfeldern aus Faserverbundwerkstoff, ZFW 10, 1986, Heft 4, pp. 228-232
- [30] Davidson, B. D.: Delamination Buckling: Theory and Experiment, J. of C. Mat., Vol. 25, 1991, pp. 1351-1378
- [31] Rothschilds, R.J., and Gillespie, J.W., and Carlsson, L.A.: Instability-Related Delamination Growth in Thermoset and Thermoplastic Composites, ASTM STP 972, 1988, pp. 161-179
- [32] Ashton, J.E., and Whitney, J.M.: Theory of Laminated Plates Technomic, 1970
- [33] Luftfahrttechnisches Handbuch Struktur-Berechnung HSB, LTH Structural Analysis (IASB) working group <https://www.lth-online.de/en/working-groups/iasb-structural-analysis.html>
- [34] Timoshenko, and Gere: 'Theory of Elastic Stability' McGraw-Hill; New York (1961)
- [35] Little, G.H.: An efficient computer program for the large deflection analysis of rectangular orthotropic plates, Comp. & Struct., Vol. 27, 1987, No.4, pp. 467-482
- [36] Little, G.H.: Large deflections of orthotropic plates: some extensions to the computer program 'Eldarop', Comp. & Struct., Vol. 37, 1990, No.4. pp. 621-624
- [37] Popp, P. : Experimentelle Studienarbeit zur dreidimensionalen Erfassung und Darstellung von Impactschaden in Faserverbundplatten, Institut für Werkstoffkunde der Technische Hochschule Darmstadt und Fraunhofer-Institut für Betriebsfestigkeit (LBF), Darmstadt, 1990
- [38] Hackbusch, D.: Einsatz von Faserverbundwerkstoffen bei Knickstäben als Federelemente Diplomarbeit FH und Fraunhofer-Institut für Betriebsfestigkeit (LBF), Darmstadt

53 - Mechanical and Acoustic Emission characterization of lime-based masonry constituents

Naveen Shetty¹, Georgios Livitsanos³, Dimitrios G. Aggelis³, Danny Van Hemelrijck³,
Martine Wevers², Els Verstrynghe¹

¹ Building Materials and Building Technology Division, Department of Civil
Engineering, KU Leuven, Kasteelpark Arenberg 40, box 2448, 3001 Heverlee,
Belgium
e-mail: naveen.shetty@kuleuven.be

² Department of Materials Engineering, KU Leuven, Kasteelpark Arenberg 44, box
2450, 3001 Heverlee, Belgium

³ Department of Mechanics of Materials and Constructions, Vrije Universiteit Brussel,
Pleinlaan 2, 1050 Elsene, Brussels, Belgium

Abstract:

This paper deals with an improved representation of the progression of damage in lime-based masonry under cyclic loads using the Acoustic Emission (AE) technique. Stress-strain relations are a familiar concept in engineering which detail the elastic-plastic behaviour of the material. During AE monitoring, AE activates with the increase of stress and initiation of micro fracture due to local changes in the material structure. The population of AE events registered at an increasing stress levels provides information on the structure's integrity. In the present study, masonry couplets and walls were built with clay bricks in combination with two different mortar types: hybrid lime-cement (LC) and lime hydrate mortar (LH). One set of experiments focuses on masonry couplets and another set of experiments focuses on masonry walls, both under compression. The AE-based damage quantification is validated by a comparative analysis with strain measurements from Linear Variable Differential Transformers (LVDTs). In conclusion, results indicated that at initial stages the AE trend was closely related to axial strain for LC specimens and lateral strain for LH specimens. Regardless of size effects with respect to masonry couplets and walls, there was no significant difference in damage progress.

1. Introduction

Over many centuries, the traditional binder in historical monuments is found to be lime. Even today, lime mortar is primarily used in most repair and restoration work of historic buildings [1-3]. Lately, the combination of lime with cement is used because it is quick to set and has high compressive strength. Mortars are bound with the bricks to form masonry and behave in a complex manner. Mechanical properties are well documented for lime-based masonry in literature [4-6] but there continues to be a gap in understanding the behaviour of masonry under compression more precisely. This leads to a search for a non-destructive technique (NDT) to monitor the structure in real-time analysis.

Acoustic emission (AE) is an NDT which detects the release of high frequency elastic waves from a localized source generated by a crack within a material [7]. AE has been recognized for its ability in monitoring the damage progression in materials [8-10] and masonry structures [11,12]. Quantification of damage in lime-based masonry due to time-dependent progressive deterioration has been addressed in [13].

This paper contributes to the understanding of the mechanical behaviour of lime-cement and lime hydrate masonry under cyclic compressive loads using AE technique. From the literature [14], it is important to know whether the effect of size has an impact on the mechanical behaviour and progression of damage in masonry. Hence, in this study, we analyze the size effects of masonry couplets (combination of two bricks and one mortar layer) and masonry walls (seven bricks in height with running bond). This study shows how the degradation process in lime-based masonry will effectively be assessed by strain measurements and by AE data.

2. Methods and materials

2.1 Materials

Red clay bricks were used with dimensions 188x88x63 mm³ having an average compressive strength of 11.8 N/mm² (Standard deviation SD = 2.41 N/mm²) and average Young's modulus of 1238 N/mm² (SD = 208 N/mm²). Two different types of mortar were chosen, the composition of the mortar is as shown in Table 1.

Table 1. Mortar composition in mass percentage.

	Lime-cement ¹	Lime hydrate ²
Sand	70 %	74 %
Binder	15 %	9 %
Water	15 %	17 %

The binder for the preparation of:

¹ hybrid lime-cement mortar is a mixture of 66.7 mass-% of calcic lime [CL90S] and 33.3 mass-% of cement [CEM1 42.5R]

² lime hydrate mortar is calcic lime, CL90S

2.2 Methods and equipment

Two types of masonry specimens (couplets and walls) were tested under cyclic compressive loads to investigate the progressive damage by means of AE. Couplets were built out of two stacked bricks with overall dimensions 188x88x138 mm³, see Figure 1(a). Walls were built with seven courses in height with overall dimensions 388x88x515 mm³, see Figure 1(b). In all the specimens, an average mortar joint thickness of 12 mm was maintained. Two samples for each type of masonry were tested at the age of 28 days. The lime hydrate (LH) specimens were too 'young' at the time of testing as hardening relies solely on carbonation.

Cyclic compression tests were performed on the specimens using a hydraulic press testing machine 'Instron' with a capacity of 2,500 kN. The loading rate was 0.25 kN/sec. A thin layer of gypsum was applied on top and bottom of the specimens and slightly pressed under the platens of the hydraulic press to make it a flat surface for an equal distribution of load. Up to

7-9 loading and unloading cycles were done. In every new loading phase, a higher peak load value was reached. The peak load was maintained by 1.5 minutes and the successive cycles were separated by a time of approximately 1.5 minutes. In the final loading step, the load was increased until the ultimate failure of the specimen. Linear Variable Differential Transformers (LVDT) were used to measure the deformations. For masonry walls, the displacement was recorded across two mortar joints in vertical direction at three locations (3A-3B; 4A-4B; 2A-2B) and one mortar joint in horizontal direction (1A-1B). For masonry couplets, the displacement was recorded across only one mortar joint in vertical direction (1A-1B).

For masonry walls, AE data was recorded by a Vallen AMSY-6 system with six channels in a ASIP-2 board connected to a PC, with a sampling rate of 10 MHz. For masonry couplets, AE data was recorded by a Vallen AMSY-4 system with four channels. In both cases, piezoelectric sensors with a frequency bandwidth 100-450 kHz were attached to the specimens by means of a hot-melt glue. The set-up of the sensors was symmetrical with respect to the mid-section of the specimens as shown in Figure 1. The built-in band pass filter had a frequency range from 50-850 kHz for signal processing. Pre-amplifiers AEP5 with 34 dB gain were used. A threshold of 38.5 dB was set to eliminate the background noise.

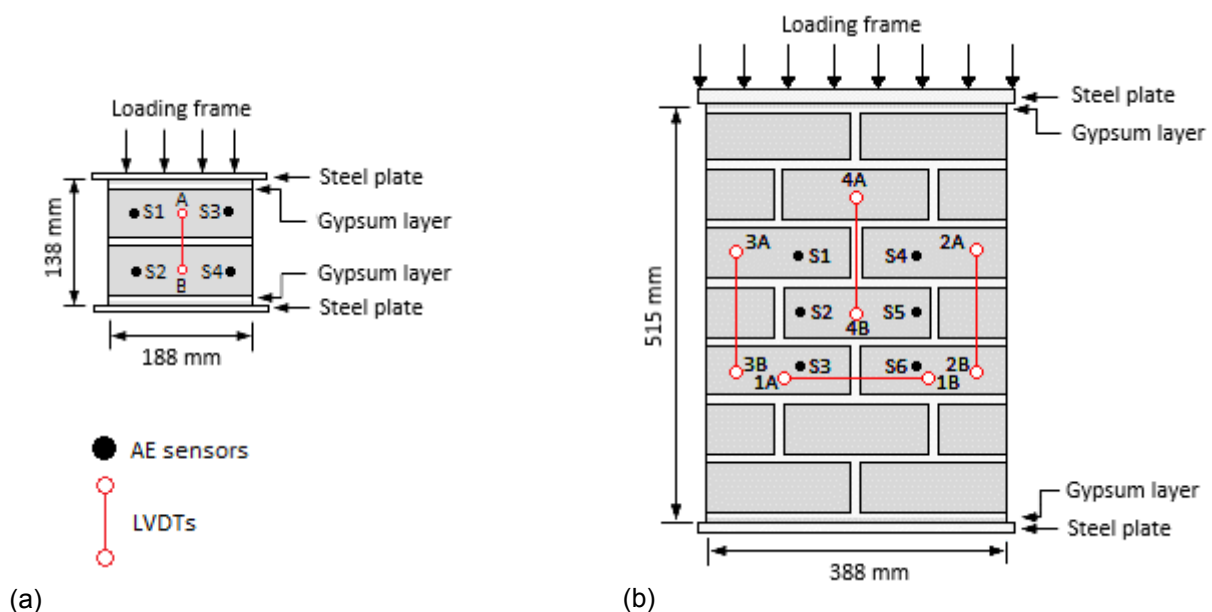


Figure 1. Test setup for compression test on masonry (a) couplet and (b) wall.

During the fracture process, AE hits exceeding the threshold are registered and subsequently grouped into AE events. For progressive damage evaluation in masonry, the Japanese Society for Non-Destructive Inspection proposed two AE indices in order to estimate the critical damage levels [15,16]. The first parameter is called the 'Load ratio'. It is calculated as the ratio between the load at the onset of AE activity in the subsequent loading step to the maximal load reached at the previous cycle. When the Load ratio is above 1, Kaiser effect is present, which indicates 'stress' memory in a material for the previously applied maximum load level. When the Load ratio is below 1, Felicity effect is present, which evidences the occurrence of micro-structural damage before previous maximum load. In this study, to calculate the Load ratio, the onset of AE activity is determined by the occurrence of at least 10 events in a time interval of 10 seconds. The second parameter is called the 'Calm ratio'. It is calculated as the ratio of AE

events registered during unloading to the AE events registered during the whole loading-unloading cycle.

3. Results and discussion

3.1 Stress-strain

Figure 2 shows representative stress-strain curves from the compression tests on masonry couplets and masonry walls. Two interesting observations can be made by comparing the type and size of masonry. Firstly, the lime-cement masonry has higher compressive strength than the lime hydrate masonry. Secondly, masonry couplets present a higher compressive strength compared to masonry walls.

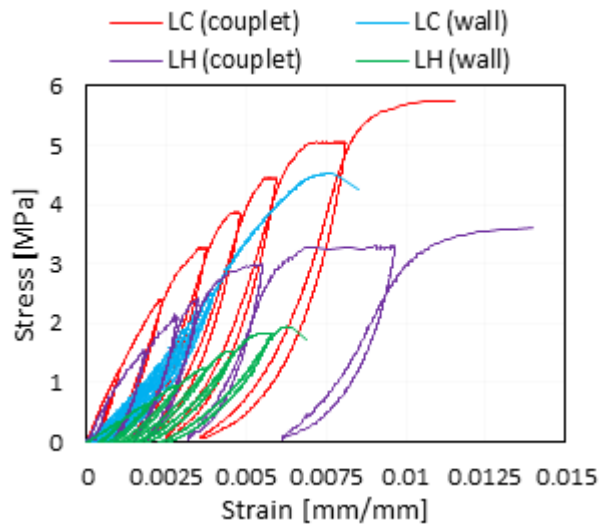


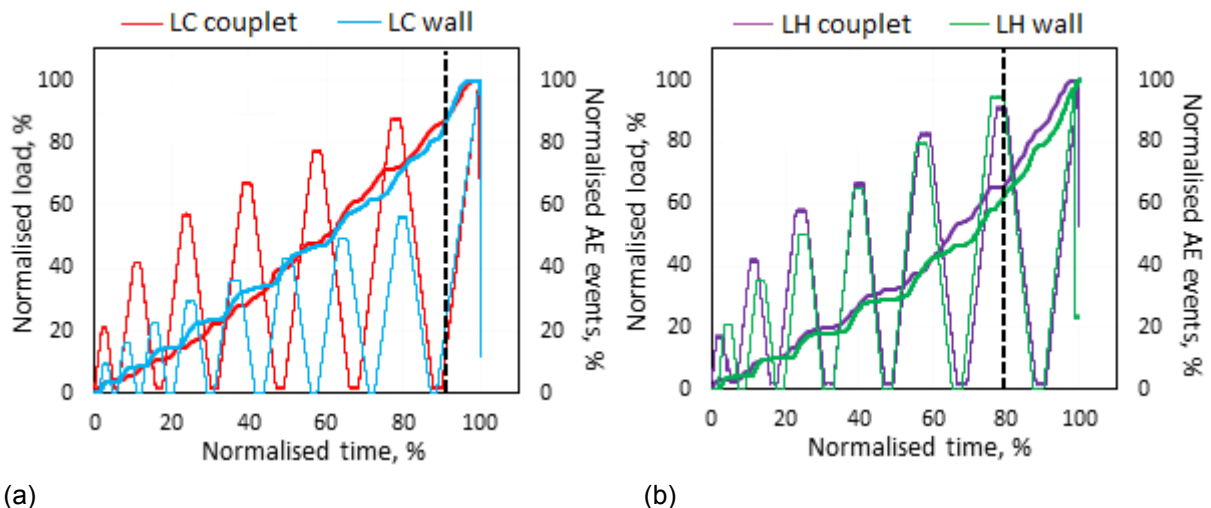
Figure 2. Stress-strain curves for compression tests on masonry couplets and walls.

3.2 Mechanical behaviour and AE trends

AE data obtained for cyclic compressive tests on both masonry types with different size (couplet and wall) are analysed. For this analysis, AE events generated in each cycle and localized all over the specimen were considered. The normalised cumulative AE events in relation to the normalised load and time is shown in Figure 3(a) and (b). The cumulative AE events is the total number of AE events received from the beginning of the test to a certain moment.

In Figure 3(a), the load levels for the LC wall are very low compared to the LC couplet, which results from an underestimation of the strength of the LC walls prior to testing. In Figure 3(b), for the LH couplet and wall, a good agreement between the load levels can be observed. In general, AE events registered for LC specimen are much higher than LH specimen. The reason for such a behaviour in AE activity is due to two reasons. Firstly, the LH specimen has lower mechanical strength and less brittle nature of cracking compared to LC specimen. Secondly, at higher load levels the formation of micro fracture in LH specimen largely increases AE attenuation. As can be seen in Figure 3(a) and (b), the AE activity increased progressively for successive load cycles. In both cases, irrespective of size effects, the cumulative AE events

remain similar apart from some scatter in the trend. Vertical dotted lines in Figure 3(a) and (b) are drawn at those moments when the macro-crack was visually observed.



(a) (b)
Figure 3. Results of a cyclic test with AE monitoring on a representative sample of (a) lime-cement masonry and (b) lime hydrate masonry.

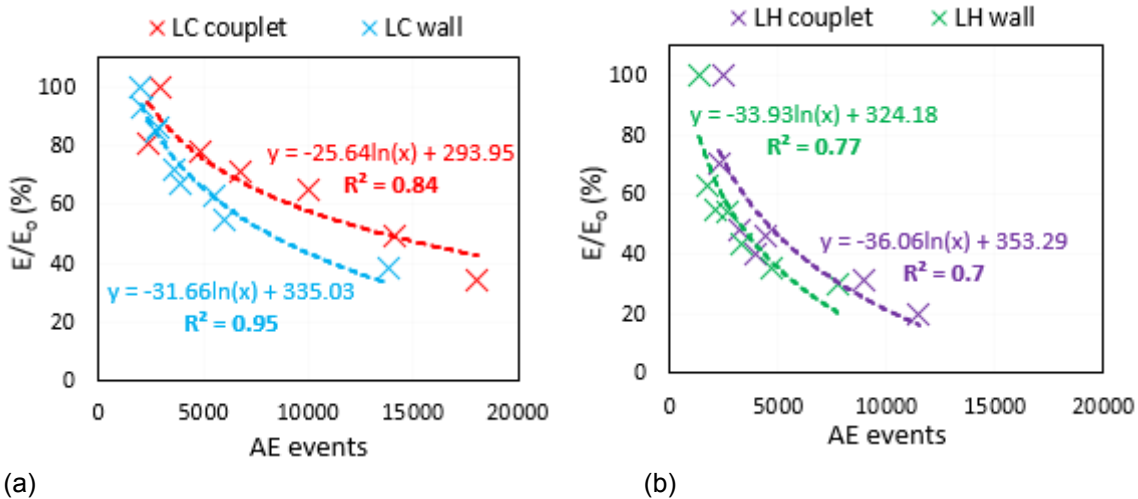
In Figure 4(a) and (b), the measured stiffness (E) for each load cycle normalised by the initial stiffness (E_0) of the first load cycle vs. the number of AE events is shown. The stiffness reduction with the increase in AE events for the successive load steps is observed. In this study, the elastic modulus (E) was calculated at the stress level in a current cycle that exceeds the previously applied maximum stress, and corresponding AE events were considered. For the correlation, a logarithmic fitting function is used.

In Figure 4(a), for the first load cycles, the number of AE events is less than 5,000. In the last load cycles, the number of AE events is reaching almost 15,000 to 20,000 for the LC wall and couplet with the stiffness modulus decreasing by approximately 30 to 40%. Similarly, in Figure 4(b), the number of AE events is reaching almost 8,000 to 11,000 for the LH wall and couplet with the stiffness modulus decreasing by approximately 20 to 30%. In both cases, as the stress approaches the ultimate strength of the masonry, an increase in AE activity at the cycle (norm. load = 80%) prior to failure is observed. This is due to the signals registered from spalling of the mortar. In the last loading cycle (norm. load = 95%), the macro-cracks followed by crushing of masonry leads to a huge drop in stiffness and an increased number of AE events.

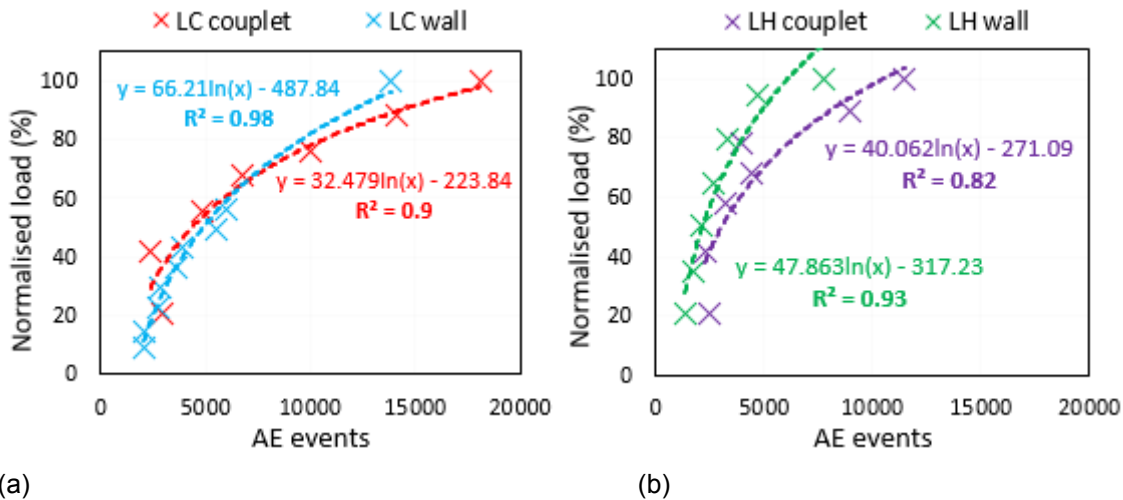
In general, as observed from these results for couplets and walls, LH specimen quickly deteriorates compared to LC specimen, which is dependent on the stiffness characteristics of the masonry constituents. However, in recent studies [17,18] this hypothesis has been highly investigated in different combinations of lime-based masonry. From the stress-strain graph (see Figure 2), LH specimen has low stiffness and large deformability compared to LC specimen. As can be seen in Figure 4, LC specimen has a better correlation between the stiffness and AE events compared to LH specimen. Another observation indicates that the couplet have high stiffness and large number of AE events compared to the walls. However, the masonry couplets and walls of the same mortar type have the same shape of trend irrespective of size effect.

In Figure 5(a) and (b), the normalised load vs. the number of AE events is shown. The increasing load values leads to higher AE activity which is due to more damage induced by

crack initiation and propagation. These trends illustrate that the correlation between the normalised load and number of AE events is slightly better than the correlation between the stiffness loss and the AE events.



(a) (b)
Figure 4. Stiffness modulus vs. number of AE events for (a) lime-cement masonry and (b) lime hydrate masonry.

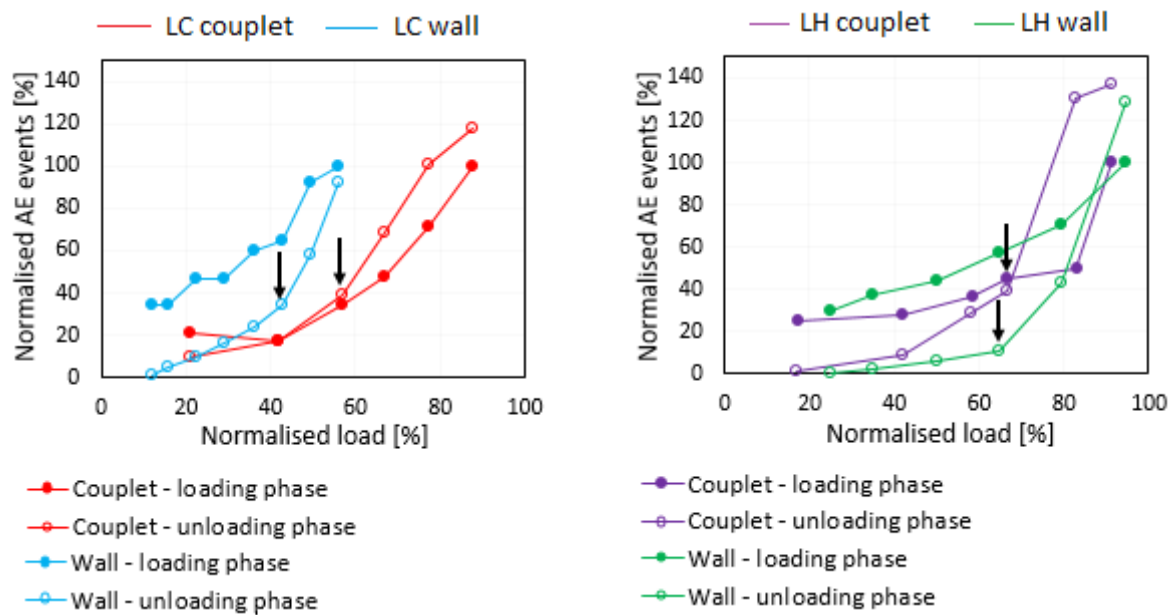


(a) (b)
Figure 5. Normalised load vs. number of AE events for (a) lime-cement masonry and (b) lime hydrate masonry.

3.3 AE activity during cyclic loading

In Figure 6(a) and (b), the trend represents the AE events accumulated during the loading and unloading phase of each loading cycle. The number of AE events is shown with respect to the normalised load during each loading step. Here, AE activities are grouped into two categories namely 'primary AE activity' and 'secondary AE activity'. As can be seen from the results, AE events were registered during the loading phase of subsequent loading cycles due to crack formation under compressive loading referred to as primary AE activity. Similarly, AE events were registered during the unloading phase of subsequent loading cycles due to friction between the existing crack surfaces referred to as secondary AE activity.

For LC specimen and LH specimen, the loading phase of the first cycles has higher AE activity which indicates the nucleation phases of micro-cracking in masonry. Upon continuing of the test, a sudden increase in secondary AE activity is observed by the change of slope in the trend (arrows in Figure 6). On approaching the ultimate strength of the masonry, the secondary AE activity is found to be dominant as a consequence of deterioration of the material's microstructure. Hence, the AE activity during the unloading phase appears to be an interesting characteristic to further investigate the fracture growth.



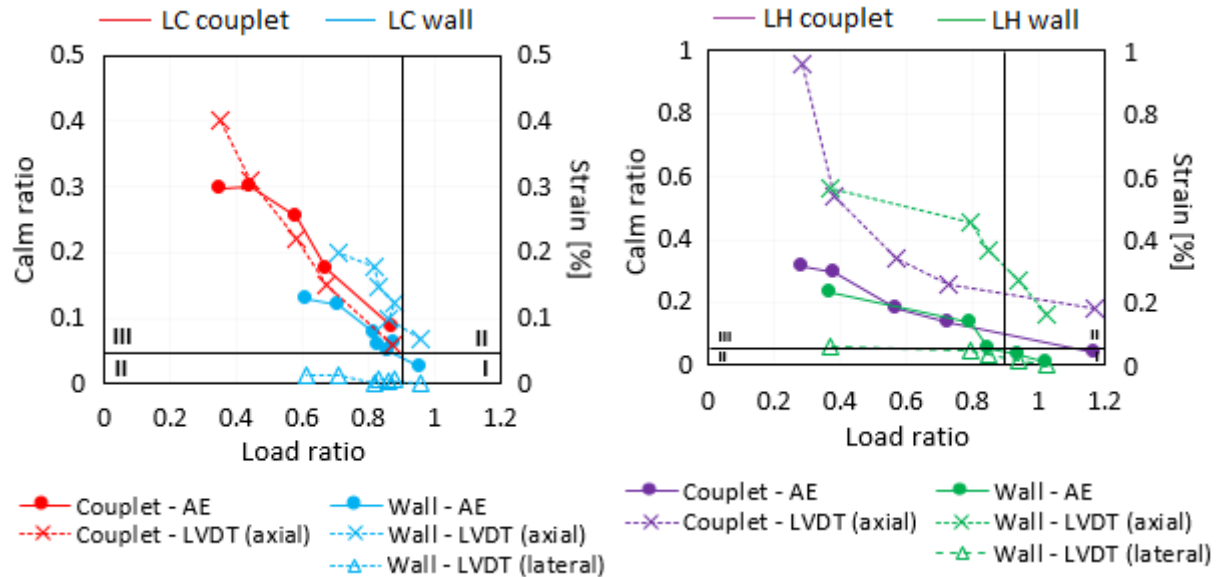
(a) (b)
Figure 6. AE activity during loading and unloading phase for (a) lime-cement masonry and (b) lime hydrate masonry.

3.4 AE and strain-based damage quantification

Load ratio and Calm ratio are applied to quantify the damage progress in masonry under cyclic compressive loading. Load ratio characterizes the damage based on the stress level at the onset of AE activity. Calm ratio is applied to assess the damage during unloading due to crack closure and rubbing. As previously explained, these two AE indices are important as they characterize the progression of damage during the loading and unloading phases. By combining both AE indices, Load and Calm ratio, this scheme classifies the damage into three zones: minor, intermediate and heavy damage [15,16]. The damage quantification limits for Load ratio (0.9) and Calm ratio (0.05) were developed from AE evaluation criterion in bending load for RC beams [16]. However, the same limits are used here to investigate their applicability for identifying the progress of damage from sub critical to critical stage in masonry under compression.

In this study, two different research questions are addressed. Firstly, the accuracy of AE-based damage quantification has to be validated. Secondly, most recorded AE signals during unloading are attributed to the damage development. These questions are addressed by comparing AE-based damage quantification with deformation measurements. A comparative analysis was performed with the measured deformation from LVDTs in terms of strain values with the Calm ratios, as shown in Figure 7(a) and (b). The axial strains are obtained from one

LVDT in couplets and the average of three LVDTs in walls. The lateral strains are obtained from one LVDT in walls. Results from AE and LVDTs present a clear trend representing the damage progress. Irrespective of masonry type and size effects, the trend shifts from the sound zone (phase I) to the heavy damage zone (phase III) with little or no accumulation at the intermediate damage zone (phase II). There is no major difference observed in the trajectories to reach the heavy damage region.



(a) (b)
Figure 7. AE and strain-based damage quantification for (a) lime-cement masonry and (b) lime hydrate masonry.

From the comparative analysis of the results of the lime-cement masonry, following observations are made, see Figure 7(a):

- For the LC couplet, AE is in good correlation with the axial strain throughout the experiment, except the last load cycle.
- For the LC wall, in the initial stage, AE is in good correlation with the axial strain. As the test continues, AE shifts apart from the axial strain. Nevertheless, AE is more close to axial strain rather than lateral strain.

For lime hydrate masonry, following observations are made, see Figure 7(b):

- For the LH couplet, from the initial to final stage, the AE-based trend line remains lower than the axial strain.
- For the LH wall, in the initial stage, AE is in good correlation with the lateral strain. In the last two load cycles, AE shifts apart from the lateral strain. Nevertheless, AE is in between lateral and axial strain.

The horizontal LVDTs were not installed in the couplets and therefore AE was not compared with lateral strains. In general, the interesting observation from these results is the shifting behaviour of AE in different masonry types. It can be seen that the AE trend either follows the axial strain or lateral strain or remains intermediate. Such behaviour is likely to be related with the AE activity in connection to the mode of cracking in the specimen. Usually, tensile type of cracks (mode I) are generated during the nucleation of cracks upon stress increase. Upon approaching the failure, the frictional activities in the crack surfaces generate shear type of AE

signals (mode II). The shifting behaviour of AE may be related to the change in the fracture mode of cracking from the tensile type to shear type of fracture. However, a further analysis is needed to confirm this hypothesis. On the other hand, the damage quantification limits seem to be too low and overestimate the damage grade for masonry under axial compression. Hence, in future, the Load-Calm ratio critical limits have to be calibrated with other NDT techniques. In this way, it provides the basis for damage quantification in masonry for laboratory and on-site applications.

4. Conclusion

In this study, the mechanical and acoustic emission behaviour of two different types of masonry with lime-based mortar is examined under cyclic compression. Walls as well as couplets are studied to investigate size effects. Firstly, the study focuses on comparing the AE and mechanical trends for lime-cement and lime hydrate masonry types. AE activity is strongly related to successive load levels, and a good correlation to the stiffness degradation of the material is observed. Secondly, the study focuses on the AE activity during cyclic loading. The presence of secondary activity has been indicated by the registered AE events during the unloading phase of a loading cycle.

Furthermore, the Load-Calm ratio in relation to strain values from LVDTs are applied to quantify damage. Irrespective of masonry type and size effects, the trend indicates similar trajectories to reach the heavy damage state. Comparison with strain measurements indicates that the damage quantification limits are to be revised. The trends of Load-Calm ratio from AE were in a reasonable agreement with the strain values from LVDTs. In general, AE is closely related to axial strain for LC specimens and lateral strain for LH specimens. Results demonstrate some interesting findings and raise questions about the mode of cracking for the two different types of masonry. A detailed study of the crack classification using the RA value and average frequency is a part of further work to investigate this hypothesis. Lastly, for masonry couplets and walls with respect to size effects, there was no significant difference in AE damage progress, apart from the registered number of AE events.

ACKNOWLEDGEMENTS

The Research Fund - Flanders (FWO) is acknowledged for funding the FWO project "AE-FracMasS: advanced Acoustic Emission analysis for Fracture mode identification in Masonry Structures" (G.0C38.15)

References:

- [1] RILEM TC 203-RHM : Repair mortars for historic masonry: Performance requirements for renders and plasters. *Materials and Structures*, Vol. 45, 2012, pp. 1277-1285.
- [2] M.R. Veiga, A. Fragata, A.L. Velosa, A.C. Magalhães, M.G. Margalha (2010). Lime-based mortars: Viability for use as substitution renders in historical buildings. *International Journal of Architectural Heritage*, April-June 2010, Vol. 4(2), pp. 177-195. ISSN 1558-3058.
- [3] L. Schueremans, Ö. Cizer, E. Janssens, G. Serré, K. Van Balen (2011). Characterization of repair mortars for the assessment of their compatibility in restoration projects: Research and practice. *Construction and Building Materials*, December 2011, Vol. 25(12), pp. 4338-4350.

- [4] A. Costigan, S. Pavía, O. Kinnane (2015). An experimental evaluation of prediction models for the mechanical behaviour of unreinforced, lime-mortar masonry under compression. *Journal of Building Engineering*, December 2015, Vol. 4, pp. 283-294.
- [5] A. Drougkas, P. Roca, C. Molins (2016). Compressive strength and elasticity of pure lime mortar masonry. *Materials and Structures*, March 2016; Vol. 49(3), pp. 983-999.
- [6] R. Hayen, K. Van Balen, D. Van Gemert (2004). The mechanical behaviour of mortars in triaxial compression. *Arch Bridges ARCH'04*. P. Roca, E. Oñate (Eds.), © CIMNE, Barcelona.
- [7] C.U. Grosse, M. Ohtsu (Eds.) (2008). *Acoustic emission testing - basics for research - applications in civil engineering*. Springer, Berlin.
- [8] D.G. Aggelis, N.-M. Barkoula, T.E. Matikas, A.S. Paipetis (2013). Acoustic emission as a tool for damage identification and characterization in glass reinforced cross ply laminates. *Applied Composite Materials*, August 2013, Vol. 20(4), pp. 489-503.
- [9] E. Eberhardt, D. Stead, B. Stimpson (1999). Quantifying progressive pre-peak brittle fracture damage in rock during uniaxial compression. *International Journal of Rock Mechanics and Mining Sciences*, January 1999, Vol. 36, pp. 361-380.
- [10] K. Andreev, N. Shetty, E. Verstrynge (2018). Acoustic emission based damage limits and their correlation with fatigue resistance of refractory materials. *Construction and Building Materials*, March 2018, Vol. 165, pp. 639-646. DOI: 10.1016/j.conbuildmat.2018.01.062
- [11] A. Carpinteri, S. Invernizzi, G. Lacidogna (2007). Structural assessment of a 17th-century masonry vault with acoustic emissions and numerical techniques. *International Journal of Architectural Heritage: Conservation, Analysis and Restoration*, Feb 2007, Vol. 1(2), pp. 214-226. ISSN: 1558-3058. DOI: 10.1080/15583050701287649
- [12] S. De Santis, A.K. Tomor (2013). Laboratory and field studies on the use of acoustic emission for masonry bridges, *NDT&E International*, January 2013, Vol. 55, pp. 64-74.
- [13] E. Verstrynge, L. Schueremans, D. Van Gemert, M. Wevers (2009). Monitoring and predicting masonry's creep failure with the acoustic emission technique. *NDT&E International*, September 2009, Vol. 42(6), pp. 518-523. DOI: 10.1016/j.ndteint.2009.03.001
- [14] K.S. Gumaste, K.S. Nanjunda Rao, B.V. Venkatarama Reddy, K.S. Jagadish (2007). Strength and elasticity of brick masonry prisms and wallettes under compression. *Materials and Structures*, March 2007, Vol. 40(2), pp. 241-253. DOI: 10.1617/s11527-006-9141-9
- [15] NDIS 2421 (2000). *Recommended practice for in-situ monitoring of concrete structures by AE*. Japanese Society for Non-destructive Inspection, 2000.
- [16] M. Ohtsu (2006). Quantitative AE techniques standardized for concrete structures. *Advanced Materials Research*, Feb 2006, Vol. 13-14, pp. 183-192.
- [17] N. Shetty, G. Livitsanos, D. Aggelis, D. Van Hemelrijck, M. Wevers, K. Van Balen, E. Verstrynge (2018). Visualization of crack propagation in brick masonry couplets under compression. In G. Milani, A. Taliervo, S. Garrity (Eds.), *10th International Masonry Conference*, July 9-11, 2018; Milan, Italy.
- [18] G. Livitsanos, N. Shetty, D. Hündgen, E. Verstrynge, M. Wevers, D. Van Hemelrijck, D.G. Aggelis (2018). Acoustic emission characteristics of fracture modes in masonry materials. *Construction & Building Materials*, Feb 2018; Vol.162, pp. 914-922.

22 - Characterization of particle impacts using Acoustic Emission

Lorenzo CARRILLO¹, Eric SERRIS¹

¹ Mines Saint-Etienne, SPIN EMSE, CNRS UMR 5307, LGF, CS 62362, F-42023 St Etienne, France

Abstract:

Acoustic emission has been successfully applied for monitoring a large variety of solids elaboration processes. In order to know the applicability of this technique in an industrial process such as grinding, mixing or also fluidized bed, we need to initially study the impacts of particles on different material surfaces. Namely, these will aim to simulate the industrial vessel walls. A wide range of powders and impact surfaces has been examined and the Hertz law has been applied to characterize the impact of particles. By considering only elastic deformations, the law has been simplified obtaining several parameters, such as the total displacement or the total load applied, which describe the impact. The influence on the acoustic emission of particle size and speed has also been explored in this study. A quasi-linear correlation has been found between these variables with a slope, which depends from material properties. Relevant differences have been observed within impact surfaces, especially in energy, caused by a different attenuation capacity in surface's material. These differences are evident in waveforms obtained during experimental phase. Regarding other parameters such as amplitude a correlation has been found with elastic properties of particles and surfaces. In particular, sugar particles have produced higher amplitudes caused by plastic deformations. Finally, centroids frequencies have shown values completely different, allowing understanding the composition of the surface. In conclusion, surface's properties influence frequency and energy fields, on the contrary particles elastic properties seem to affect amplitude values.

1. Introduction

Acoustic emissions have found several applications regarding material integrity and in a wide range of industrial processes. This technique must allow the monitoring of different process conditions. The main advantage is its non-intrusive applicability to sensor longer life processes. Several problems are linked to the interpretation of the transmitted signal and the big large amount of collected data. Different studies show that it is possible to elaborate prediction models using a statistical or physical interpretation of obtained parameters with data processing [1,2]. Numerous constraints are also related to the physical explanation of the impact between the particle and the surface. A characterization of this phenomenon could be given with the elastic impact theory and the Hertz law. Assuming a circular or elliptical impact surface, Hertz equations could be used to predict forces and interactions between particles and surfaces [3]. Several examples of this interesting application could be found in literature. Namely, fluidized bed reactors show issues related to the time of residence that could cause undesirable events like sintering or particles agglomeration [4]. This kind of phenomena can be prevented studying particles speed and bed level using acoustic emission [5]. Acoustic emissions could also be used to evaluate distribution of particles in cyclones in order to prevent problems as surging. Predictive models concerning

the particle size and the speed can be developed [6]. A good example of correlation between acoustic parameters and Hertz equations could be seen in Pecorari work [7]. Partial power could be related with the force generated by the impact. Hertz theory shows that the total load applied generated by the impact depends on elastic properties such as Young's modulus and Poisson coefficient. The dependence between amplitude of the waveform and particle's speed is widely demonstrated. In particular, it is proportional to the particle's speed, in the low frequency range, for example, when wavelength is greater than the body of impact thickness. Even increasing impact speed and incurring in plastic deformation, which means greater energy dispersion, amplitude continue to increase. However, in the last case a shift of amplitude distribution could be seen through higher frequencies. In conclusion, low-velocity impacts produce signal with little extensional mode and large flexural mode. On the contrary, extensional mode becomes larger and flexural mode becomes shorter in high-velocity impacts, due to the penetration of the particle in the surface of impact (plastic deformation) [8]. In this study, several correlations have been found between particles' speed and acoustic parameters. Furthermore amplitudes, energies and frequency centroid show certain dependence from surface elastic properties. This dependency could be seen in recorded waveform allowing a better explanation of acoustic wave transmission and attenuation phenomena.

2. Theoretical Model

When two solids with different geometry collide, they initially touch in a single point causing a deformation in its proximity. This causes a contact between the two areas, which depends on the collision force between the two bodies, their geometry and the material properties such as the Poisson ratio, and the Young's modulus. Regarding two solids of general shape, for convenience, a Cartesian coordinate system is placed in the point of contact. The collision causes a normal compressive load into the two solids, which is considered as all applied in the contact point. Hertz introduced some simplification to contact mechanics. He considered an elliptical contact surface and he also considered the two bodies as two half-spaces. This means that stresses in the two surfaces could be studied separately.

However, the contact area has to be really small compared with bodies' surface and with radii of curvature. Finally, Hertz assumed that two bodies are frictionless and their surfaces are perfectly smooth. The most notable case considers two solids of revolution with curvature radii R . Under these simplifications Hertz theory allows to define some interesting parameter, such as the contact area a and the total displacement δ [3]:

$$a = \sqrt[3]{\left(\frac{3PR}{4E^*}\right)} \quad (1a)$$

$$\delta = \sqrt[3]{\left(\frac{9P^2}{16RE^{*2}}\right)} \quad (1b)$$

with $\frac{1}{E^*} = \frac{1-\nu_1^2}{E_1} + \frac{1-\nu_2^2}{E_2}$, a mechanical constant that considers the Poisson ratios and the Young's moduli of the two bodies (1 for the particle, 2 for the surface) and P the applied load.

If the particle is falling under the gravitational force, from the energy balance the applied load could be expressed as:

$$F = F_o + 2F_S + 2[F_o F_S + F_S^2]^{\frac{1}{2}} \quad (2)$$

Where F_o is the gravitational force due to the mass particle and F_S are the surface forces, expressed by

$$F_S = 2\Delta\gamma\pi r_t^3 \left(\frac{1}{F_m E^*}\right) \quad (3)$$

$\Delta\gamma$ is the adhesion surface energy per m^2 , r_t is the total projected radius and F_m is the total mechanical force. For r_t and F_m , it is possible to define two contributions according to the elastic and plastic deformation. [9]. However, considering the particle falling on a perfectly flat surface and assuming the impact as perfectly elastic, the applied load (2) could be simplified as follows [7], with ρ the density of the falling particle and v the velocity of the particle:

$$F_{el} = [8,23\pi^3 \rho^3 v^6]^{1/5} R^2 E^{*2/5} \quad (4)$$

3. Materials and Methods

During the experimental phase, three kinds of particles of different nature are used. Silicon particles are provided by Elkem Silicones, the sugar powder is provided by Seppic and the glass bead are provided by Prolabo. Their properties are resumed in Table 1 (E Young's modulus, ν Poisson ratio, ρ density).

	Diameter [μm]	E [GPa]	ν	ρ [Kg/m ³]
Sugar	1100 - 305	4,5	0,3	1600
Silicon	1090 - 325	160	0,27	2330
Glass	995 - 354	70	0,22	2600

Table 1- Particles' properties

To characterize the impact, particles have been dropped in free-fall from four different heights. (Table 2) on three different surfaces (Table 3). A simple model neglecting the effect of air viscosity was used to calculate the speed.

Height [cm]	Speed [m/s]
2	0,63
10	1,40
50	3,13
90	4,20

Table 2 - Fall speeds

	Width [mm]	E [GPa]	v	ρ [Kg/m ³]
PMMA	10	3	0,33	1150
Steel	20	200	0,26	7850
Ceramic	5	87	0,17	2300

Table 3 - Surfaces' properties

Once particle drops on the surface, signals are recorded by using two piezoelectric sensors F-15 α (pass band 100 - 450 kHz) and WD (pass band 50 - 350 kHz). Signals were also amplified with 2 preamplifiers model 2/4/6-Mistras and digitalized with 2 channels acquisition card AEDSP. Finally, data streaming and acquisition were possible by using the software AEWIN. Mistras Group provided all the equipment.

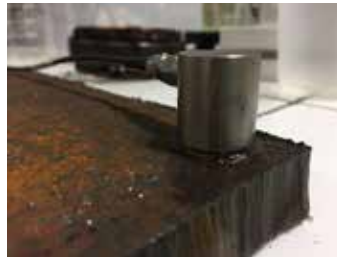


Figure 1 - Sensor F-15 α on steel surface. Coupling is insured with silicon grease.

The test was performed 10 times in order to a good quantity of data. The sensor F-15 α was placed at about 9 cm from the region where impacts occurred. The distance between the 2 sensors was about 39 cm. A 30-dB filter was used to screen background noise. Besides, the proper functioning of the sensor was assured with the Hsu – Nielsen Test.

4. Results

AEWIN software splits the signal in bursts every time it passes a threshold value. Thus, amplitudes in every burst have a similar size. Bursts are characterized by duration, amplitude, energy, average frequency, etc. The most interesting variables analysed are the energies, the amplitudes and the centroids frequencies.

Energies as function of particle's speed are resumed in figures 2 and 3.

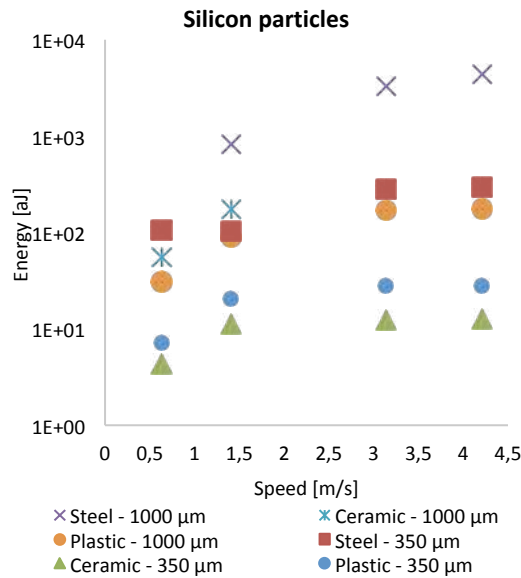


Figure 2 - Energy as function of particle's speed for silicon particles

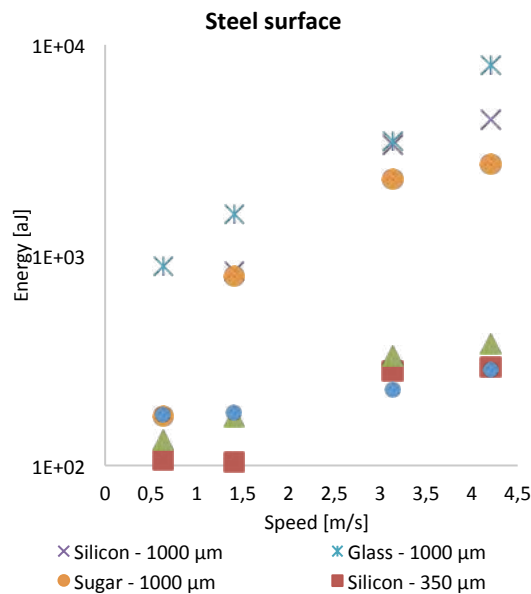


Figure 3- Energy as function of particle's speed for steel surface

Each point represents the average energy for a fixed speed. The graphics have been obtained by considering a single type of particle and a single type of surface. Anyway, same results could be observed by using all the other particles and the other surfaces. A linear trend between energy and particle's speed could be observed for each kind of particle

Regarding amplitudes, they could be represented as well as function of particles' speed, as shown in figures 4.

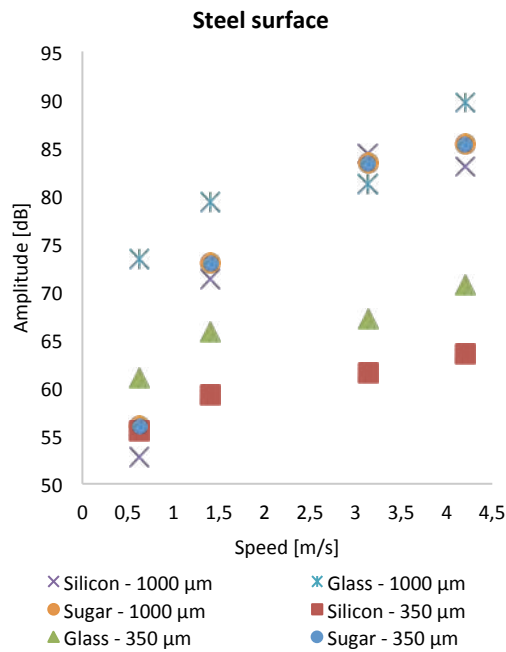


Figure 4 - Amplitude as function of particle's speed for steel surface.

Once again, an essentially linear relationship could be seen between amplitude and particle's speed. In this case the amplitude highest values may appear to correspond to those of the glass particles. However, the sugar ones presents high amplitudes as well probably because of plastic deformation, which causes exceeding dispersion energy.

By fixing the particle's speed at 3,13 m/s, Hertz theory of contacts' parameters could be correlated with acoustic variables. Glass and silicon particles have the same behaviour. However, the sugar shows a trend completely different. These differences could be observed by plotting the energy as function of total displacement δ and of E^* . Furthermore, sugar particles show a bigger total displacement because of their smaller stiffness. These particles are supposed to incur in plastic deformation, even if their energies are weaker than the others.

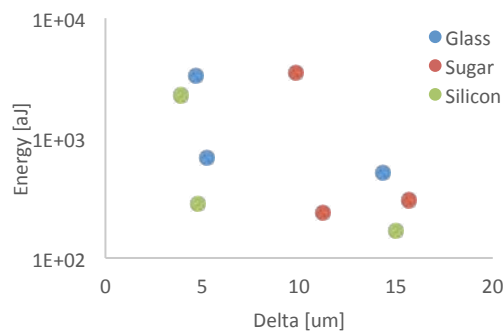


Figure 5 - Energy as function of total displacement. The 3 points for each series represent the 3 surfaces (steel, ceramic and plastic).

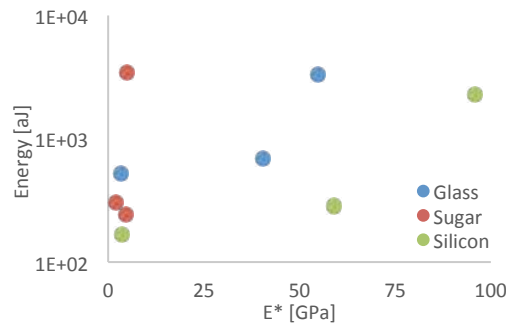


Figure 6 - Energy as function of E*. The 3 points of each series represent the 3 surfaces (steel, ceramic and plastic).

At the end, centroid frequencies have been analysed. For each surface, there is a limited range, except for glass particles, as shown in table 4.

Centroid frequencies [kHz]			
	Steel	Ceramic	Plastic
Glass	205	210	42
Silicon	102	190	39
Sugar	135	210	54
Average	147	203	45

Table 4 - Average centroid frequencies

In the last part, Hertz theory's parameters δ and E^* have been correlated with the energies. Figures 5 and 6 show the same tendencies for silicon and glass particles. In particular, for high values of δ , energies get weaker. δ shows the displacement caused by elastic and plastic deformations. Thus, it seems that plastic deformation reduces the energy collected by the sensors. In fact, in this case a part of particle's kinetic energy should be dissipated as energy necessary to plastic deformation.

In figure 6 a direct relationship could be observed. E^* increases energy collected for each kind of particle. However, it must take in account surfaces attenuation capacity.

It would be interesting to evaluate plastic deformations, in order to understand the ratio between the two contributions to energy and amplitude. This was not possible in this study. Attenuation coefficient and propagation's velocity of the acoustic wave have also to be considered.

5. Discussion

This study shows some correlations existing between acoustic emissions and mechanics contacts. How it has been observed, a quasi-linear relationship exists between energy (and amplitudes) and particles velocity.

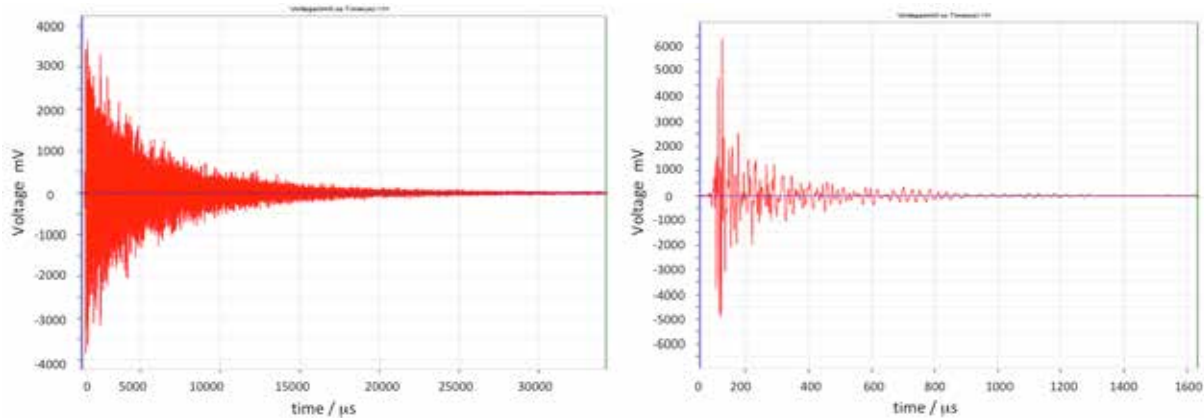


Figure 7 - Waveforms for steel surface (left) and plastic surface (right). Silicon particles were used and their speed was fixed to 3,13 m/s. The different attenuation of the signal could be easily observed.

It could be noticed that the steel surface produce higher energies if compared to the others. Through the examination of signals streaming, this phenomenon could be better understood. The plastic surface and the steel surface have been compared in figure 7. For the first one higher amplitudes could be observed even if the signal seems to get weaker in a short period. On the contrary, the steel surface shows amplitudes smaller but at the same time a greater number of oscillations in the unit of time. Furthermore, the duration of the signal is longer and it leads to exceeding energies. Thus, a key role in acoustic emission is played by the attenuation coefficient, which differs in each material.

Regarding particles, the main differences are caused by the diameter. Generally, a smaller diameter causes lower energies. Collected amplitudes always show high values, according to Prosser et al [8].

Glass particles produce the highest energies and the highest amplitudes. The impact seems to be independent of particles' density. However, by calculating the stiffness of particles and surfaces an inverse relationship could be observed. Stiffness is the resistance of an elastic body to deflection or deformation by an applied force and it is calculated as the ratio between the elastic force F_{el} and the total displacement δ .

	Ceramic	Steel	Plastic
	Stiffness [N/m]		
Sugar	2,76E+06	3,52E+06	3,74E+05
Silicon	4,03E+06	5,94E+06	4,13E+05
Glass	4,89E+05	5,01E+05	2,52E+05

Table 5 - Stiffness calculated for each particle impacting with the different surfaces. Particles velocity was fixed to 3,13 m/s.

In conclusion, the amplitudes and the energies are linked to the elastic contribution and a plastic contribution. The first one depends on the stiffness, which takes in account Young's moduli of the surface and the particle, but also their geometric properties. Thus, glass particles allow higher elastic deformations than the others.

6. Conclusion

A simple model proposed by Hertz was used to characterize mechanical impact. A spherical particle was launched under free fall on a smooth plane. The impact was considered as totally elastic. Thanks to these simplifications, energies and amplitudes have been evaluated. Essentially, linear correlations with particle's speed have been found in every case.

Furthermore, attenuation coefficient plays an important role in the characterization of these impacts. Energies are strongly linked to this parameter and waveforms could help us to better characterize this phenomenon.

On the other hand, particles produce high energetic acoustic emissions when they have a great stiffness. Thus, greater energy values could be observed when particles deform elastically more than plastically. However, amplitude seems to have an inverse correlation. This aspect should be better explored in order to understand how plastic deformation affect the mechanic of the contact.

References:

- [1] Vahaviolos S: Acoustic Emission: Standards and Technology Update [Internet], 100 Barr Harbor Drive, PO Box C700, West Conshohocken, PA 19428-2959, ASTM International, 1999. DOI: 10.1520/STP1353-EB
- [2] Boyd JWR, Varley J: The uses of passive measurement of acoustic emissions from chemical engineering processes. *Chem Eng Sci* 2001;56:1749–1767.
- [3] Johnson KL: Contact Mechanics [Internet], Cambridge, Cambridge University Press, 1985. DOI: 10.1017/CBO9781139171731
- [4] Jiang XJ, Wang JD, Jiang BB, Yang Y, Hou LX: Study of the power spectrum of acoustic emission (AE) by accelerometers in fluidized beds. *Ind Eng Chem Res* 2007;46:6904–6909.
- [5] Jingdai W, Congjing R, Yongrong Y: Characterization of flow regime transition and particle motion using acoustic emission measurement in a gas-solid fluidized bed. *AIChE J* 2010;56:1173–1183.
- [6] Spencer SJ: Monitoring of dense medium cyclone performance and condition by acoustic emission 2004

[7] Pecorari C: Characterizing particle flow by acoustic emission. *J Nondestruct Eval* 2013;32:104–111.

[8] Prosser WH, Gorman MR, Humes DH: Acoustic emission signals in thin plates produced by impact damage. *J Acoust Emiss* 1999;17:29–36.

[9] Wall S, John W, Wang HC, Goren SL: Measurements of kinetic energy loss for particles impacting surfaces. *Aerosol Sci Technol* 1990;12:926–946.

32 - The sound of metal: Acoustic Emission during the deformation of commercially pure titanium

Nick Goossens¹, Marc Seefeldt¹, Martine Wevers¹

¹ Department of Materials Engineering, KU Leuven, Kasteelpark Arenberg 44, 3001 Leuven, Belgium

Abstract:

Acoustic emission (AE) was monitored in situ during in-plane tensile deformation of a commercially pure titanium plate. Different load orientations were considered: parallel to the rolling direction (RD), transversal direction (TD) and under an angle of 45 degrees (45D) with RD. The AE event rate, peak amplitude, signal duration, rise time and ring-down counts were monitored during deformation. Orientation dependent mechanical behavior, AE signal characteristics and microstructural evolution was observed and correlated to the difference in texture and twinning phenomena. The intensity and characteristics of AE signals in RD and 45D do not change considerably during deformation, which was attributed to the continuous nucleation and growth of compression twins. Anomalous AE behavior in TD was observed, showing two distinct peaks. All signal parameters show significantly decreased values during a first peak, which was correlated to massive nucleation of small tensile twins. These tensile twins disappear with increasing strain, indicating the end of the first peak. The second peak is comparable to the plateau behavior in RD and 45D and occurs during necking. Compression twinning is dominant, but limited to the necking zone. An unfavorable textural effect in TD has been identified, which hinders the formation of compression twins during the homogeneous deformation, as opposed to RD and 45D, resulting in anomalous AE behavior. The acoustic emission technique proves to be a complementary technique to electron diffraction as it allows monitoring and identifying the twinning modes of commercially pure titanium in situ.

1. Introduction

Commercially pure titanium (CP-Ti) and titanium alloys have excellent engineering properties such as a good corrosion resistance, high specific strength and stiffness and a good biocompatibility. Therefore, titanium is extensively used in cutting-edge applications in the fields of aerospace, automotive and medicine, for instance for engine applications and medical implants. In all these applications, the material is loaded and the mechanical response has to be known precisely. For this purpose, a complete understanding on the deformation behavior of titanium is desired. However, titanium is a hexagonal metal and therefore has only access to three main slip systems: basal, prismatic and pyramidal. The von Mises criterion states that the activation of five independent slip systems is required to plastically deform polycrystals [1]. The prismatic $\langle a \rangle$, pyramidal $\langle a \rangle$, basal $\langle a \rangle$ and pyramidal $\langle a+c \rangle$ are the most common slip systems in titanium. However, $\langle a \rangle$ slip systems are unable to allow strain in the direction of the c -axis and the critical resolved shear stress of pyramidal $\langle a+c \rangle$ slip systems is high at room temperature. Therefore, twinning mechanisms have to complement dislocation slip to fulfill the von Mises criterion and allow plasticity [2,3]. The strong orientation-dependency of the activation of basal slip and particular twinning modes complicate the explanation of the entire deformation process of titanium.

Acoustic emissions (AE) are transient elastic waves that are formed by the relaxation of internal stresses, which are instantaneously imbalanced by a sudden change in the microstructure of a material [4]. AE carries information of the dynamic processes, from which they originated and which lead to plastic deformation. Twinning and the initiation of dislocation slip are known to be the principal sources of AE in titanium. AE can be measured *in situ* during the deformation of a material and therefore allows the extraction of dynamic information concerning the deformation mechanism. Because of this AE provides a dynamic complement to the classical static Electron Backscatter Diffraction (EBSD) technique, which has already been used to investigate the deformation mechanisms in magnesium alloys [5,6].

2. Description of work

A plate of hot-rolled commercially pure titanium grade 2 (0.30 wt.% Fe, 0.25 wt.% O, 0.1 wt.% C, 0.03 wt.% N, 0.015 wt.% H) having a thickness of 1 mm was used. The microstructure consists of equiaxed grains with a mean grain size of 52 μm and standard deviation of 20 μm . Two sets of three types of tensile specimens (fig. 1) were prepared with the load direction parallel to the rolling direction ("RD"), the transversal direction ("TD") and under an angle of 45° with respect to the rolling direction ("45D"). One set was used to carry out *in situ* AE measurements, whereas the other set was used for EBSD measurements. The tensile tests were performed on an Instron 4505 tensile machine (Instron, United States) equipped with a 100 kN load cell and a constant displacement rate of 0.5 mm min⁻¹ at room temperature. The specimens were strained until failure occurred.

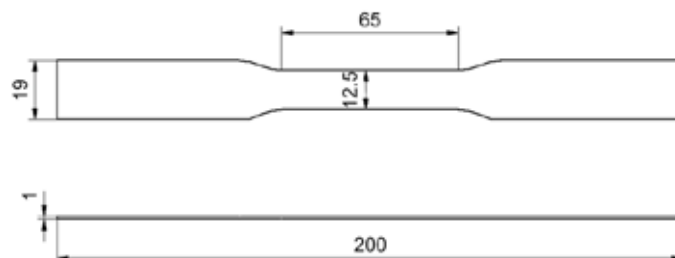


Fig. 1. Dimensions of the tensile specimens in mm.

AE was simultaneously monitored using the AMSY-5 system (Vallen Systeme, Germany). Two B1025 broadband transducers with a flat frequency response between 50 and 2000 kHz were symmetrically attached on the tensile specimens. The distance between both sensors was 100 mm. A signal threshold level of 30 dB was set just above the general noise level. Signals that were not generated in the area between both transducers, such as signals from the grips, were considered as noise and discarded by a location filter.

The microstructural evolution up to several different strain levels was investigated with automated EBSD scans using a scanning electron microscope (Nova 600 Nanolab, Thermo Fisher Scientific, United States) and TSL OIM Analyze v.8 (EDAX, United States) data acquisition and analysis software. An acceleration voltage of 20 kV and a step size of 2 μm were used. The final strain levels were chosen based on the observed AE behavior. All specimens were cut and mechanically polished after straining. In the last polishing step, a

colloidal silica suspension containing 30 vol.% H₂O₂ was used. All specimens were finally polished using a VibroMet (Buehler, United States) vibratory polishing apparatus for 2 hours.

3. Results

The true stress-strain curves for the three different specimens are shown in fig. 2. Fig. 3 shows the engineering stress-strain curves together with the corresponding AE event rates (number of events per time interval). Plastic anisotropy is evidenced by a slightly larger yield stress in TD compared to RD and 45D. The elongation to failure and the rate of strain hardening (slope of the stress-strain curves) are both the largest in RD and the smallest in TD, suggesting that the plasticity is the highest in RD and the lowest in TD. Anisotropic stress-strain behavior is well-known for commercially pure titanium and attributed to the texture, resulting in the activation of different twinning systems [7-10]. Different fracture types were finally observed: the TD specimen failed by a cup-cone type fracture, while the RD and 45D specimens failed by a shear-type fracture.

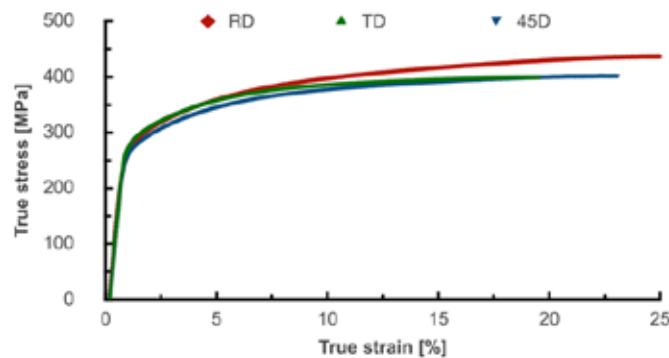


Fig. 2. True stress-strain curves of commercially pure titanium at room temperature parallel to the rolling direction (RD), transversal direction (TD) and under an angle of 45° with the rolling direction (45D).

The AE event rate curves are determined by burst-type emission, which is likely due to fast and discontinuous deformation phenomena such as twinning. An example of a typical AE burst signal is given in fig. 4. The AE response in TD differs from the RD and 45D and can be called anisotropic as well, corresponding to the mechanical behavior. The amount of detected acoustic events increases sharply at the onset of plastic deformation. In TD (fig. 3b) two maxima can now be distinguished: a first maximum around 9% strain when the ultimate tensile strength (UTS) is reached and a maximum peak around 26% strain, which coincides with the macroscopic necking of the tensile specimen. The AE response in RD (fig. 3a) and 45D (fig. 3c) is much less strain-dependent. The AE event rate increases fast to reach a plateau value, which remains nearly constant until the specimen fractures. The start of this plateau occurs when the UTS of the material is reached. Besides the shape of the curves, the magnitude of the AE event rate is remarkably different as well. It is the largest in RD, which corresponds to the outspoken strain hardening behavior. A plateau value of $81 \pm 9 \text{ s}^{-1}$ is obtained. In contrast, the lower strain hardening in TD is visible by a reduced AE event rate. At the first maximum, an event rate of $34 \pm 6 \text{ s}^{-1}$ is obtained, which is increased to $68 \pm 8 \text{ s}^{-1}$ at the second maximum. In 45D an in-between event rate of $60 \pm 7 \text{ s}^{-1}$ is obtained at the plateau.

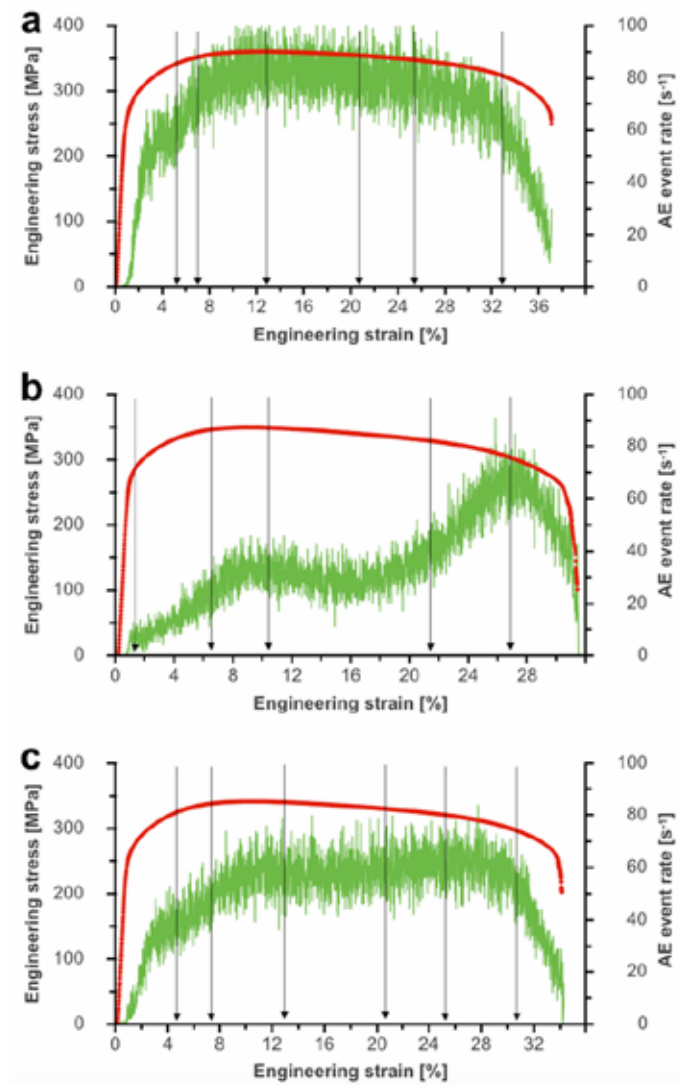


Fig. 3. Engineering stress-strain curves and corresponding acoustic emission event rate of commercially pure titanium at room temperature in a direction parallel to (a) RD (b) TD and (c) 45D. The arrows denote the strain levels at which the microstructure is investigated with EBSD.

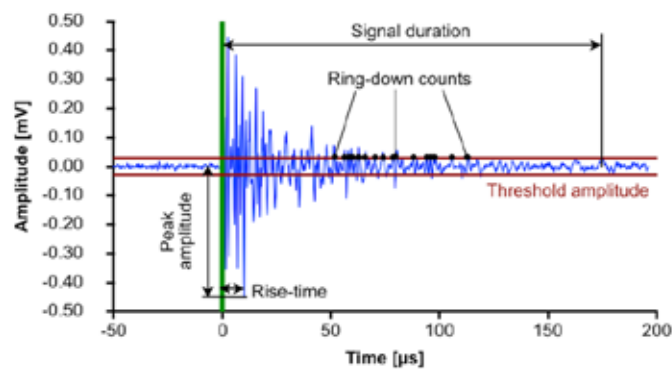


Fig. 4. Typical AE burst signal. Peak amplitude, signal duration, signal rise-time and ring-down counts are indicated. The threshold amplitude corresponds to 30 dB.

Whether the different AE response in TD translates into a different active deformation mechanism needs further investigation. Indeed, a different deformation mechanism would cause sound waves with different properties and characteristics. Therefore, the evolution of four signal parameters was monitored as a function of the strain (fig. 5) for the three different specimen orientations. Peak amplitude, signal duration, signal rise-time and the ring-down counts were considered.

A physical interpretation of these parameters is shown in fig. 4. The evolution of these parameters as a function of strain has a similar anisotropy. No outspoken change in the AE parameters occurs in RD and 45D with increased strain. Only the ring-down count has a tendency to decrease during the stage of inhomogeneous plastic deformation. Moreover, the distribution of the different signal parameters is quantitatively similar in RD and 45D. The values of the 50th and 80th percentile of the peak amplitude, signal duration, signal rise-time and the ring-down count distributions are given in table 1 for RD, 45D and TD.

Percentile	RD		45D		TD	
	50th	90th	50th	90th	50th	90th
Peak amplitude (dB)	40.0	48.7	40.0	48.5	39.9	48.4
Signal duration (μ s)	53	267	50	223	43	207
Signal rise-time (μ s)	5.0	13.6	5.4	11.3	7.0	13.4
Ring-down counts	12	36	11	33	10	27

Table 1. 50th and 90th percentile values of the distribution of the peak amplitude, signal duration, signal rise-time and ring-down counts of the acoustic emission measured with the load direction parallel to the rolling direction (RD), under an angle of 45° with the rolling direction (45D) and parallel to the transversal direction (TD)

The numbers for RD and 45D show that although the maximal values of all parameters in fig. 5a and fig. 5c seem to differ and appear to show large scatter, the vast majority of all the signals considered have considerably lower parameter values, which are comparable in both RD and 45D. The scatter in the values of these parameters is caused by a very small percentage of signals, which could be used to distinguish the two orientations: a larger part of the AE in RD can reach larger parameter values than the respective AE in 45D can.

The shapes of the parameter distributions obtained from AE during straining in TD are again different and show two maxima. The time (or strain) at which these maxima occur, is similar to the time (or strain) at which the maxima in the AE event rate curve (fig. 3b) occur. The maxima in the parameter distributions are less pronounced though. A similar quantitative approach is followed to compare the distributions of the AE signal parameters in TD with the earlier described distributions in the other directions (table 1). Except for the signal rise-time, all the values are lower than the respective values in the other directions. Again, the scatter in the parameter distribution is predominantly caused by a minority of the signals. To summarize, the majority of AE signals in TD have the lowest value of peak amplitude, ring-down counts and signal duration and the highest value of signal rise-time compared to the signals in RD and 45D. The same holds for the ring-down counts and signal rise-time of the minority signals. However, the highest percentile of these minority signals can achieve the largest values for the peak amplitude and the smallest values for signal rise-time. This

anomaly in the parameter distribution can be better illustrated using crossplots (fig. 6), in which two independent signal parameters are plotted against each other. In this case, the ring-down counts and peak amplitude of the signals are plotted against each other.

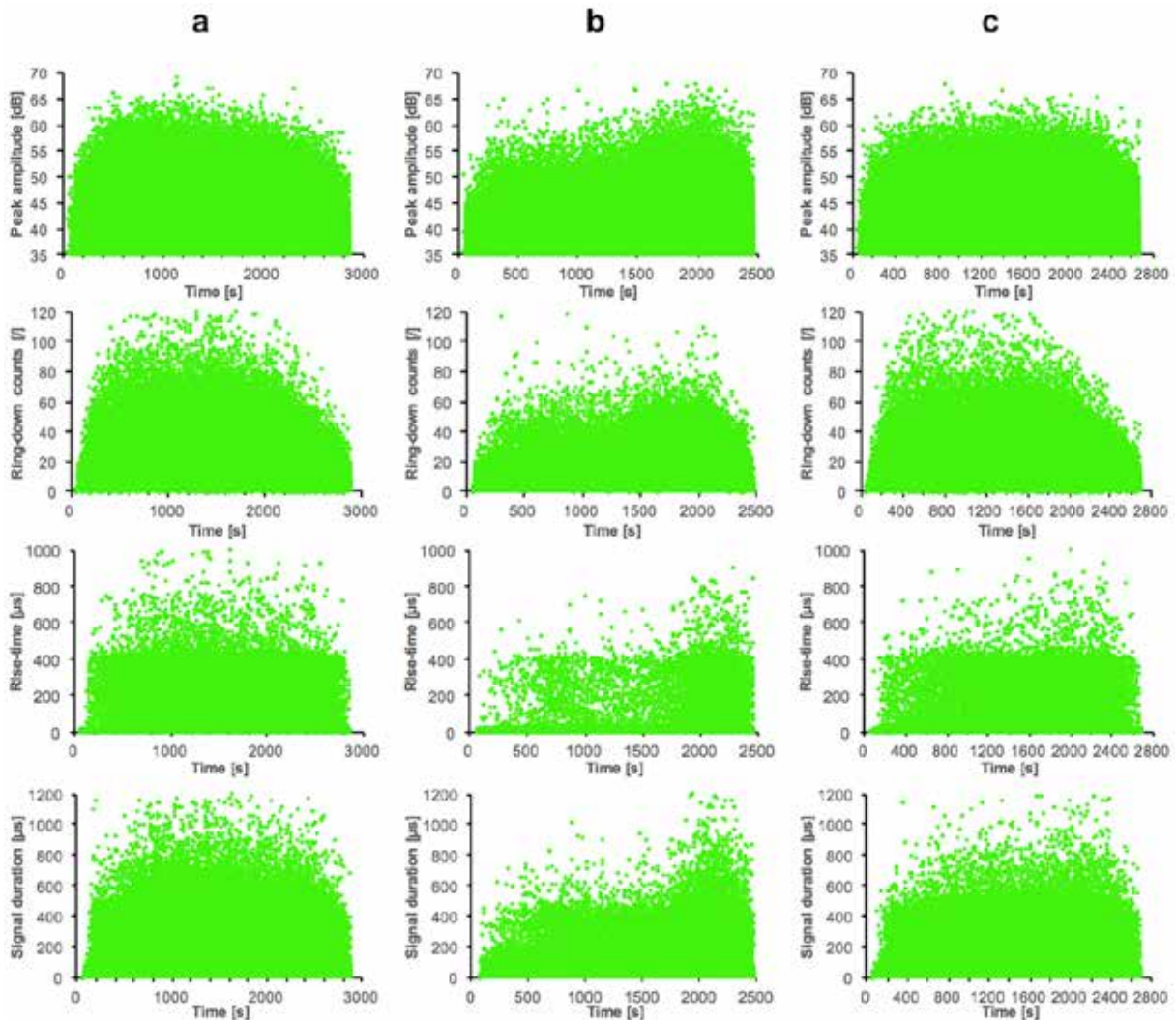


Fig. 5. Distributions of the peak amplitude, ring-down counts, signal rise-time and signal duration of the AE signals in function of time. The AE signals are received upon tensile deformation of commercially pure titanium at room temperature in a direction parallel to (a) RD (b) TD and (c) 45D.

The color code is related to the three 'deformation stages' that determine the mechanical behavior of the tensile specimens and were seen to influence the AE behavior in an anisotropic way. The blue data points correspond to the onset of plastic deformation. The green data points correspond to the moment when the UTS of the material is reached. Finally, the red datapoints correspond to the period during which macroscopic necking is observed. While the green and red region almost completely overlap for RD (fig. 6a) and 45D (fig. 6c) specimens, the red region is clearly stretched out more towards larger peak amplitudes than the green region for TD (fig. 6b) specimens. This essentially confirms the time (thus strain) indifference of the parameters in RD and 45D and the large similarities between those two orientations.

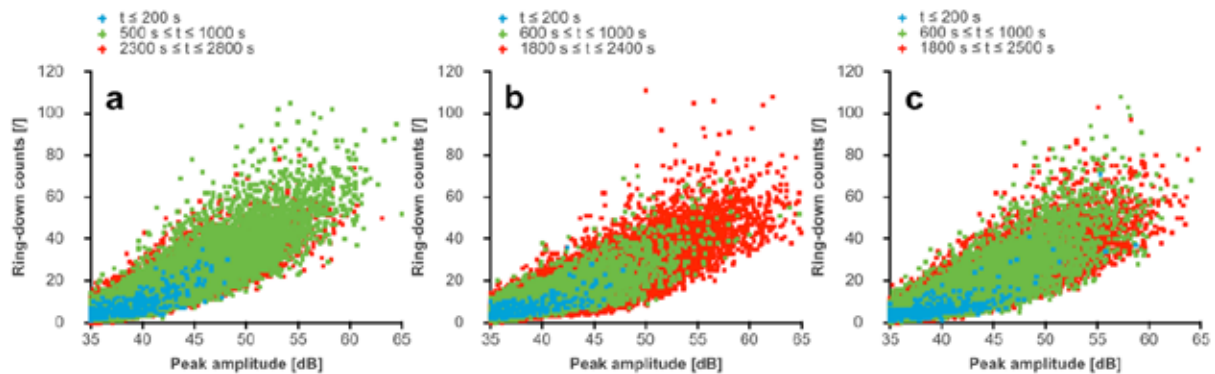


Fig. 6. Peak amplitude versus ring-down counts cross-plots of the AE during tensile deformation of commercially pure titanium at room temperature parallel to the (a) RD (b) TD and (c) 45D. The colors correspond to different time intervals during the deformation and are linked to mechanical deformation events. The blue points correspond to the onset of plastic deformation. The green points correspond to the time interval during which the UTS is reached. The red points correspond to the appearance of macroscopic necking.

In particular, 88.7% of these signals that have a peak amplitude larger than 50 dB are 'red' signals, meaning they originate during macroscopic necking. The 'red' signals also make up 92.3% of all signals with a peak amplitude larger than 55 dB. Signal localization revealed that the origin of nearly all 'red' signals is found in a zone that is about 2 cm long, which demonstrates that the 'red' signals are localized in the necking zone and can indeed be linked to the macroscopic necking of the tensile specimen. This necking has caused a specific AE response in TD as seen in the second peak of fig. 3b and the anomalous behavior of the minority signal parameters in fig. 5b. However, in the other directions no such different AE response, nor difference in signal parameters was observed. This anisotropy can be explained by a deformation mechanism that is only activated during the macroscopic necking in the TD, which does not yet occur during uniform plastic deformation. Based solely on the AE results, no such change in deformation mechanism would be expected in RD and 45D. This also implies that the activity of the deformation mechanisms and in particular their evolution with increasing strain in TD, must be orientation-dependent.

AE cannot reveal what these deformation mechanisms exactly are. In order to couple these observations to the microstructural deformation mechanisms, a second set of tensile tests was carried out to different maximal strain levels. The microstructure at these strain levels is investigated with EBSD. These levels are marked with vertical arrows in fig. 3. For the TD specimens, these strains are chosen to be immediately before and after the expected peak maxima (fig. 3b) and just before the strain to failure. For the other specimens, the strain levels were chosen before and after the beginning and the end of the plateaus (fig. 3a and 3c) and one strain level in the middle of the plateau. Fig. 7 shows image quality maps of the deformed tensile specimens in RD, TD and 45D respectively. The twin boundaries are marked with colored lines.

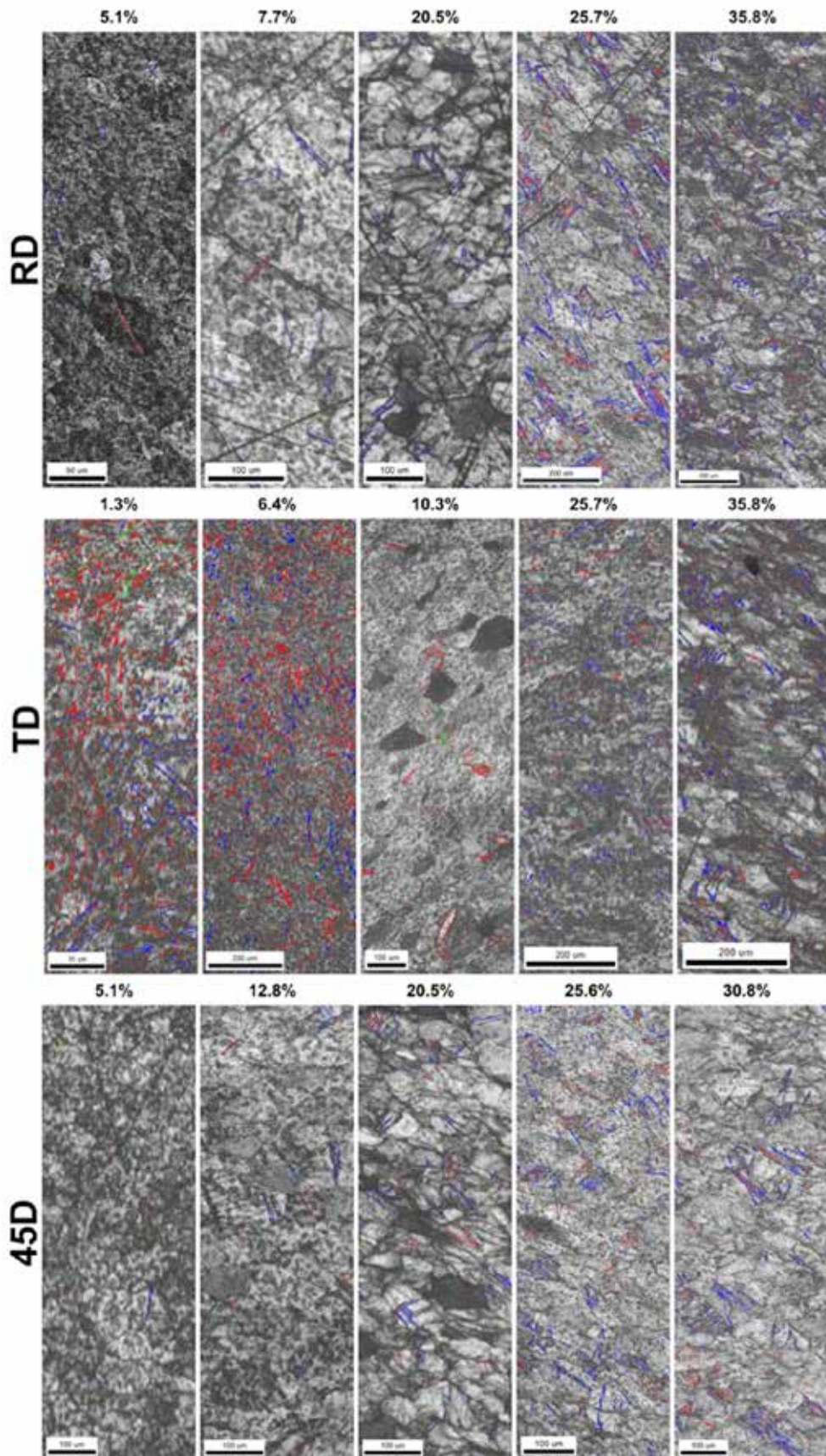


Fig. 7. EBSD image quality maps of tensile specimens deformed at room temperature until different strains with the load direction parallel to the rolling direction (RD), transversal direction (TD) and under an angle of 45° with the rolling direction in the rolling plane (45D). Twin grain boundaries are colored: tensile twins in red, compression twins in blue and compression twins in green. Deviations up to 5° from the theoretical K1 twinning planes and theoretical misorientations according to [3] are allowed.

4. Discussion

Partridge [3] reported that deformation twinning in titanium mainly occurs in the $\{10\bar{1}2\}$, $\{11\bar{2}1\}$ and $\{11\bar{2}2\}$ twinning planes. The magnitude of the twinning shear in these planes are 0.167, 0.638 and 0.225 respectively. These twins have already been observed in different studies [10-15]. Here, mainly $\{10\bar{1}2\}$ tensile twins with a misorientation of 90° and $\{11\bar{2}2\}$ compression twins with a misorientation of 65° are observed, in agreement with the theoretical values (94°52' and 63°58' respectively) [3]. Small deviations up to 5° from the theoretical twinning plane and theoretical misorientations are allowed. These deviations can be attributed to the relative rotation of the twins and other grains during further deformation. The twinning characteristics seem to be orientation-dependent. In RD and 45D twinning is dominated $\{11\bar{2}2\}$ by compression twins, while in TD twinning is dominated by $\{10\bar{1}2\}$ tensile twins. This observation is in accordance with other EBSD measurements [10,15,16] and crystal plasticity simulations [17].

The twinning activity appears to be low in RD and 45D until large strains (> 25%) are reached. Few twins are observed at a time in the microstructure. The twins are exclusively $\{11\bar{2}2\}$ twins in RD, but a combination of $\{11\bar{2}2\}$ twins and $\{10\bar{1}2\}$ twins appears in 45D, although $\{11\bar{2}2\}$ twins are the dominant type. Due to the generally low number of twins in RD and 45D the number of twins in consecutive scans and specimens shows a significant relative variability. Despite the large relative variations in the twin activity, the absolute number of twins remains low in general. This statement is backed by the AE data and fits the observation of the plateaus in fig. 3a and fig. 3c. The slightly larger width of $\{11\bar{2}2\}$ twins in RD, compared to 45D and the larger twinning shear of $\{11\bar{2}2\}$ twins compared to $\{10\bar{1}2\}$ twins [11] could explain the higher AE event rate and larger amplitudes in RD. For large strains (> 25%) the specimens showed macroscopic necking and the microstructure inside this necking zone was investigated. The microstructure inside the necking zone is composed of elongated grains which show a larger twinning activity. In both RD and 45D more $\{10\bar{1}2\}$ twins are present. However, in the AE no change in event rate or signal parameters is observed in the whole specimen, indicating that the increased $\{10\bar{1}2\}$ twinning is only happening locally in the necking zone.

The twinning evolution in TD is significantly different. Even at small deformations (1.3% strain) extensive twinning is observed. Besides $\{11\bar{2}2\}$ compression twins, a large fraction of $\{10\bar{1}2\}$ tensile twins is present. A small fraction of $\{11\bar{2}1\}$ compression twins is also distinguished. The twins are smaller in size than the twins in RD and 45D. Because the $\{10\bar{1}2\}$ twins result in less shear, their contribution to the deformation and, therefore, their associated deformation energy is smaller than $\{11\bar{2}2\}$ twins. The resulting AE signals in TD have a reduced energy and therefore lower amplitude for the same signal duration as compared to the signals in RD and 45D (fig. 5). It is likely that a larger fraction of those signals cannot exceed the threshold set for the amplitude and are blocked by the noise filter, resulting in a reduced AE event rate, as seen in fig. 3b. The twinning activity has decreased significantly at an intermediate strain of 10.3%, which coincides with the first AE peak in fig.

3b. A transformation has occurred during which the many narrow $\{10\bar{1}2\}$ twins have been replaced by a relative low amount of wider $\{10\bar{1}2\}$ twins. It is unclear whether the disappearance of certain twins and growth of other twins is coupled (e.g. twin merging) or not. Detwinning phenomena have been observed in pure titanium under reversed loading conditions during which $\{10\bar{1}2\}$ twins were replaced by $\{11\bar{2}2\}$ twins and vice versa [14,15]. The nucleation of twins requires more shear stress than the subsequent growth [18] and the resulting AE signal amplitude will be larger for twin nucleation than twin growth [19]. An in-situ study of detwinning in an AZ31 magnesium alloy showed that the initiation of detwinning results in higher AE amplitudes when compared to twin shrinkage [20]. However, no reversed loading has been applied during the tensile tests, which renders this option highly unlikely. The exact mechanism behind the change in twinning conditions remains unknown. At large strains (>20%) when macroscopic necking occurs, the microstructure inside the necking zone is dominated by $\{11\bar{2}2\}$ compression twins and the AE behavior becomes similar to the behavior observed in RD and 45D, as shown in fig. 6. The change in twinning mode also appears to be strongly localized inside the necking zone. It is suggested that the initial texture in the TD is unfavorable to the nucleation and growth of $\{11\bar{2}2\}$ twins. The $\{11\bar{2}2\}$ twins dominate the microstructure in RD and 45D suggesting that the unfavorable textural effect is only present when the loading direction is close to the TD. If the angle between the loading direction and the TD is increased, the unfavorable textural effect seems to disappear fast. When this angle reaches 45°, which is the case for the 45D specimens, the textural effect has already disappeared. The appearance of a majority fraction $\{11\bar{2}2\}$ twins in the TD in the necking zone can be attributed to the complex triaxial stress state present in the necking zone. The inhomogeneous deformation causes the local stress state to deviate significantly from the homogeneous uniaxial stress state. Therefore, the unfavorably oriented grains, which initially have low Schmid factors in the uniaxial stress state, can locally have higher Schmid factors in the triaxial stress state and can accommodate $\{11\bar{2}2\}$ twinning. Outside the necking zone the uniaxial stress state and consequently low Schmid factors are preserved. Therefore $\{11\bar{2}2\}$ twinning is not observed at all.

The low activity of $\{11\bar{2}2\}$ twins in RD and 45D corresponds to increased strain hardening and a large failure strain values, whereas the high activity of $\{10\bar{1}2\}$ twins in the TD corresponds to decreased strain hardening and smaller failure strain values in agreement to other experimental work. However, besides the twinning modes, the influence of the anisotropy on the dislocation motion and slip systems [3,8,17] must also be taken into account to correctly explain the full stress-strain behavior. The crystal-plasticity finite element simulation of Hama et al. [17] assumes a strong basal texture in which the c-axes of the grains are tilted between 20° and 40° from the plate normal direction to the TD and simulates the relative activity of various dislocation gliding mechanisms, $\{10\bar{1}2\}$ twinning and $\{11\bar{2}2\}$ twinning in RD and TD until a true strain of 9% is reached. In RD the relative activity of $\{10\bar{1}2\}$ twinning is nearly zero during the entire deformation, while the relative activity of $\{11\bar{2}2\}$ increases to 0.15 at 2% true strain and remains nearly constant during the subsequent deformation. In TD the relative activity of $\{10\bar{1}2\}$ increases fast to 0.20 at under 1% true strain, but is seen to decrease with increasing strain. At 6% true strain the relative activity has dropped under 0.10. The relative activity of $\{11\bar{2}2\}$ is small but non-zero and is seen to continuously increase, albeit slowly. These simulation results are in agreement with our data in the simulated strain range, highlighting the dependence of twinning on the texture.

5. Conclusion

The deformation mechanisms of commercially pure titanium subjected to uniaxial tensile load were investigated by combining in-situ AE measurements with EBSD investigations. The following conclusions could be drawn:

- (i) A simple plateau-shaped AE response is observed when the tensile load is applied in RD and 45D. The signal characteristics and intensity remain relatively constant during the deformation. The deformation microstructure is dominated by $\{11\bar{2}2\}$ compression twins.
- (ii) Different AE response and twinning mechanisms were observed when the tensile load is applied in the TD, compared to RD and 45D. Both the AE event rate and signal parameters follow a continuous upward trend exhibiting two distinct maxima. The first peak is associated with the transformation of many thin $\{10\bar{1}2\}$ tensile twins into a few broad $\{10\bar{1}2\}$ twins, while the second peak is associated with the appearance of $\{11\bar{2}2\}$ twins in the necking zone.
- (iii) The difference in twinning mechanisms and the resulting AE responses are closely related to the texture and stress state. $\{11\bar{2}2\}$ twinning is unfavorable in the TD as the texture is unfavorably aligned towards the uniaxial stress state and $\{10\bar{1}2\}$ twinning is initiated. Once the loading direction is rotated away from the TD, the $\{11\bar{2}2\}$ twinning becomes increasingly dominant. The comparable AE and twinning behavior in the RD and 45D suggest that a small angle between the load direction and the TD is already sufficient to allow $\{11\bar{2}2\}$ twinning. Additionally, during macroscopic necking, the stress state inside the necking zone becomes complex and triaxial and the disadvantageous texture alignment disappears. Extensive $\{11\bar{2}2\}$ twinning is then observed as well in the necking zone, regardless of the (in-plane) loading direction.

References:

- [1] von Mises R., *Mechanik der plastischen Formänderung von Kristallen*, Z. Angew. Math. Me., Vol. 8, 1928, 161-185
- [2] Yoo M.H., Slip, twinning, and fracture in hexagonal close-packed metals, *Metall. Trans. A*, Vol. 12, 1981, 409-418
- [3] Partridge P.G., The crystallography and deformation modes of hexagonal close-packed metals, *Int. Mater. Rev.*, Vol. 118, 1967, 169-194
- [4] Wevers M., Listening to the sound of materials: Acoustic emission for the analysis of material behaviour, *NDT & E Int.*, Vol. 30, 1997, 99-106
- [5] Máthis K., Chmelík F., Janeček M., Hadzima B., Trojanová Z., Lukáč P., Investigating deformation processes in AM60 magnesium alloy using the acoustic emission technique, *Acta Mater.*, Vol. 54, 2006, 5361-5366
- [6] Meza-García E., Dobroň P., Bohlen J., Letzig D., Chmelík F., Lukáč P., Kainer K.U., Deformation mechanisms in an AZ31 cast magnesium alloy as investigated by the acoustic

emission technique, *Mat. Sci. Eng. A-Struct.*, Vol. 462, 2007 297-301

[7] Roth A., Lebyodkin M.A., Lebedkina T.A., Lecomte J.S., Richeton T., Amouzou K.E.K., Mechanisms of anisotropy of mechanical properties of α -titanium in tension conditions, *Mat. Sci. Eng. A-Struct.*, Vol. 596, 2014, 236-243

[8] Nixon M.E., Cazacu O., Lebensohn R.A., Anisotropic response of high-purity α -titanium: Experimental characterization and constitutive modeling, *Int. J. Plasticity*, Vol. 26, 2010, 516-532

[9] Murasawa G., Morimoto T., Yoneyama S., Nucleation and Growth Behavior of Twin Region Around Yield Point of Polycrystalline Pure Ti, *Exp. Mech.*, Vol. 52, 2012, 503-512

[10] Wronski S., Jedrychowski M., Tarasiuk J., Bacroix B., Microstructure evolution of titanium after tensile and recrystallisation, *Mat. Sci. Eng. A-Struct.*, Vol. 692, 2017, 113-126

[11] Nemat-Nasser S., Guo W.G., Cheng J.Y., Mechanical properties and deformation mechanisms of a commercially pure titanium, *Acta Mater.*, Vol. 47, 1999, 3705-3720

[12] Salem A.A., Kalidindi S.R., Doherty R.D., Strain hardening of titanium: role of deformation twinning, *Acta Mater.*, Vol. 51, 2003, 4225-4237

[13] Tirry W., Bouvier S., Benmhenni N., Hammami W., Habraken A.M., Coghe F., Schryvers D., Rabet L., Twinning in pure Ti subjected to monotonic simple shear deformation, *Mater. Charact.*, Vol. 72, 2012, 24-36

[14] Chun Y.B., Yu S.H., Semiatin S.L., Hwang S.K., Effect of deformation twinning on microstructure and texture evolution during cold rolling of CP-titanium, *Mat. Sci. Eng. A-Struct.*, Vol. 398, 2005, 209-219

[15] Hama T., Nagao H., Kobuki A., Fujimoto H., Takuda H., Work-hardening and twinning behaviors in a commercially pure titanium sheet under various loading paths, *Mat. Sci. Eng. A-Struct.*, Vol. 620, 2015, 390-398

[16] Yi N., Hama T., Kobuki A., Fujimoto H., Takuda H., Anisotropic deformation behavior under various strain paths in commercially pure titanium Grade 1 and Grade 2 sheets, *Mat. Sci. Eng. A-Struct.*, Vol. 655, 2016, 70-85

[17] Hama T., Kobuki A., Takuda H., Crystal-plasticity finite-element analysis of anisotropic deformation behavior in a commercially pure titanium Grade 1 sheet, *Int. J. Plasticity*, Vol. 91, 2017, 77-108

[18] Pirouz P., Lawlor B.F., Geipel T., Bilde-Sørensen J.B., Heuer A.H., Lagerlo K.P.D., On Basal slip and basal twinning in sapphire (α -Al₂O₃)—II. A new model of basal twinning, *Acta Mater.*, Vol. 44, 1996, 2153-2164

[19] Li Y., Enoki M., Evaluation of the Twinning Behavior of Polycrystalline Magnesium at Room Temperature by Acoustic Emission, *Mater. Trans.*, Vol. 48, 2007, 1215-1220

[20] Yasutomi T., Enoki M., In-situ evaluation of detwinning behavior in extruded AZ31 Mg alloy by AE, Mater. Trans., Vol. 53, 2012, 1611-1616

38 - Analysis of kinking and twinning behavior in mg alloys by AE clustering method

Manabu Enoki ¹, Kengo Tamura ¹, Takayuki Shiraiwa ¹

¹ Department of Materials Engineering, The University of Tokyo, 7-3-1 Hongo,
Bunkyo-ku, Tokyo 113-8656, Japan

Abstract:

LPSO (Long Period Stacking Ordered Structure)-Mg alloy has both low density and high strength, and it is expected to be applied to transport equipment. However, it is necessary to evaluate the deformation and fracture behavior for usage as structural materials. Acoustic emission (AE) signals were analyzed and classified using several machine learning methods to evaluate the deformation mechanism of various LPSO-Mg alloys. It is difficult to identify AE signals due to each deformation mechanism in extruded materials consisting of two phases, α -Mg phase and LPSO phase. In this study, the high-speed camera was used to directly observe the kink deformation in LPSO phase and the twinning deformation in α -Mg phase. Compression tests were carried out, and AE signals during tests from sensors attached to the jig were continuously measured and recorded using Continuous Wave Memory (CWM) developed in our laboratory. Surface motion of specimens was captured by a high-speed camera using the AE signal as a trigger. Based on the recorded AE signals corresponding to kink deformation and twinning, AE behaviors of different extruded LPSO-Mg alloys were successfully classified into the kinking and twinning by machine learning methods.

1. Introduction

Recently, Mg alloy having a long period stacking ordered (LPSO) structure has been developed and lightweight application such as transportation equipment is expected because of its high strength [1-4]. It is necessary to evaluate the deformation/fracture behavior to use the LPSO-Mg alloy as structural materials. We have evaluated the deformation mechanism of LPSO-Mg alloy in both the directionally solidified (DS) specimen and the cast specimen using the microstructure observation and the clustering analysis of Acoustic Emission (AE) signals during the mechanical test [5-12]. there are also some researches on AE of Mg alloys [13-16]. However, in-situ deformation behaviors of extruded materials consisting of two phases of α -Mg phase and LPSO phase which are expected as practical materials have not yet been elucidated. Therefore, in this study we focus on the twinning deformation and kink deformation as the main deformation mechanism in the α -Mg phase and LPSO phase, respectively, and associate each deformation mechanism with the AE signal during the compression test of the model material. The dynamic deformation/fracture mechanism of extruded LPSO-Mg alloy containing two phases was evaluated by classifying of AE signals using the machine learning method with AE of model material as learning data.

2. Experiment and analysis method

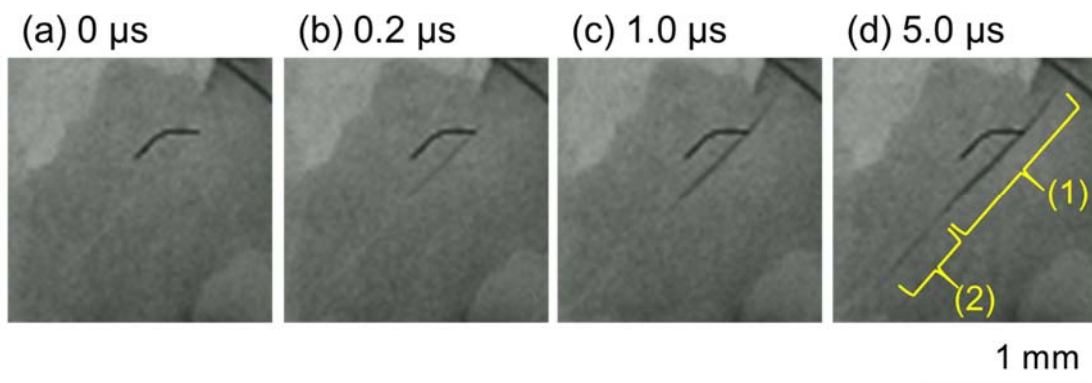


Fig. 1 Observation of twinning in pure Mg by high-speed camera.

Pure polycrystalline extruded Mg alloy (model material for twinning deformation), $Mg_{97}Zn_1Y_2$ extruded material (B3 material, LPSO phase volume ratio of 25%) and $Mg_{89}Zn_4Y_7$ extrusions (B4 Material, LPSO phase volume ratio 85%) with two-phase structure of α -Mg phase and LPSO were used. In all the extruded materials, the bottom texture is oriented in a direction parallel to the extrusion direction.

A cubic specimen of 5×5×5 mm was prepared from pure Mg and heat treatment was performed to increase the particle diameter, and then one side of the specimen was polished. Using this specimen, a compression test was conducted in a direction in which twin deformation is likely to occur, that is, a load was applied in the extrusion direction. During the test, the AE signal was measured by the AE sensor attached to the upper and lower jigs, and simultaneously the polished side surface was observed using a video microscope. By operating the high-speed camera with the AE signal as a trigger, in-situ observation was done at the instant of deformation occurred at a photographing speed of 5,000,000 fps or 10,000,000 fps. A cubic specimen of 5×5×5 mm was also prepared for B3 material and B4 material, and a compression test was conducted. The compression direction was a direction tilted by 0° and 45° with respect to the extrusion direction. The AE signal under test was measured in the same manner as pure Mg. Structural observation was carried out using SEM at each stress.

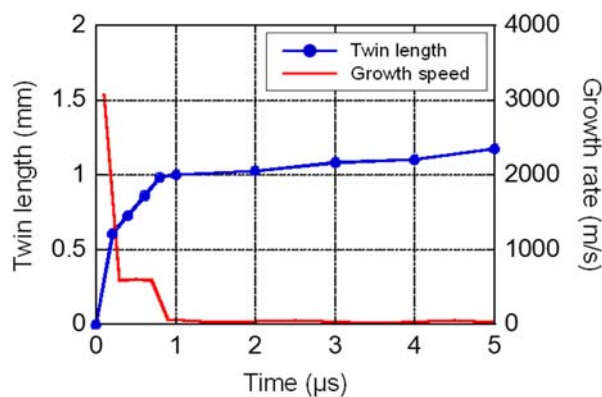


Fig.2 Evolution of length and growth speed of twin.

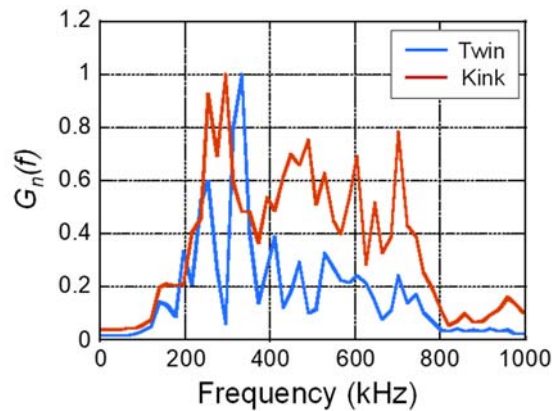


Fig. 3 Normalized average energy spectra of twin and kink for learning data.

AE events were extracted by setting a threshold value from continuous AE waveform, and energy spectrum of frequency was calculated [17]. In this study, we classified AE events using two kinds of machine learning methods. One is conventional clustering, which is an unsupervised learning method (hereinafter referred to as learning A). All generated AE events during one test were used as data and classified into two clusters by k-means method. The other is classification by supervised learning which uses AE waveform corresponding to in-situ observation as learning data (hereinafter referred to as learning B). Twin deformation observed with pure Mg corresponding to AE waveform and kink deformation observed in LPSO-Mg alloy of DS material [12] were prepared, and the machine learning was performed using these signals as learning data. After that, the AE event of B3 material and B4 material was classified as twinning or kinking as test data. Linear support vector machine (linear SVM) was used for learning algorithm.

3. Results

AE features due to twin generation were investigated. The characteristics of the AE waveform corresponding to the high-speed camera observations have the peak frequency majority of 200 ~ 400 kHz, and those were mainly generated in the initial stage of deformation. After the timing was adjusted by considering the propagation of the waveform and the time lag in the camera, the generation times of twin nucleus were consistent with AE waveform arrival times for almost all the events. Therefore, it was demonstrated that the AE acquired in this experiment was corresponding to twin nucleus generation.

Twinning was observed in crystal grains in pure Mg. Figure 1 shows an example of twin generation captured by a high-speed camera. A deformation zone of a certain length was generated within 0.2 μ s of Fig. 1(a) - (b), and then it grew and became as shown in Fig. 1(c). As shown in Fig. 1(d), another deformation zone was formed at the lower left with a slight delay in the first deformation zone. Figure 2 shows the evolution of the length of the first deformation zone and the growth rate. There was a region where the growth rate became constant between about 1 μ s immediately after generation and the growth rate at this time was 610 m/s. Similar growth rates were measured for other twin crystals, and it was distributed in the range of 300 to 1000 m/s.

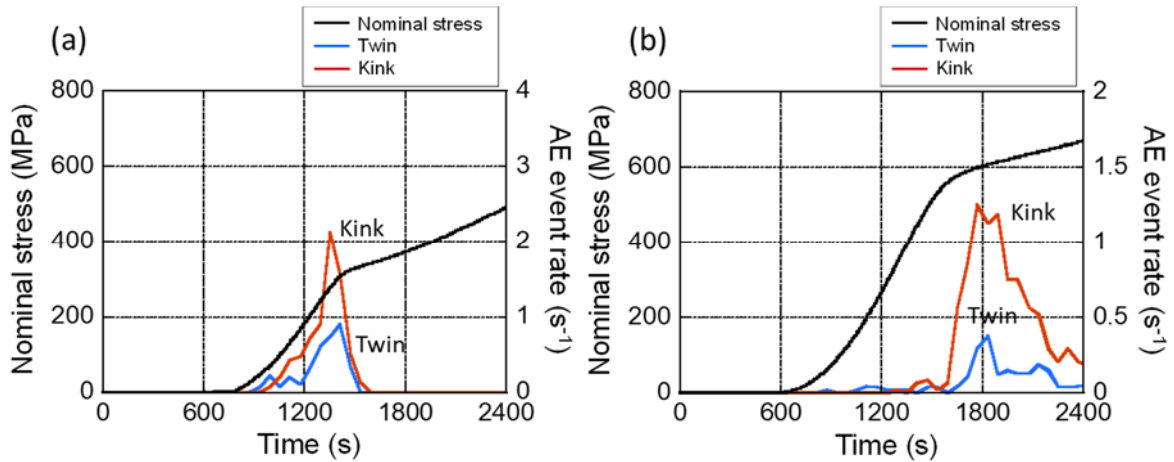


Fig. 4 AE event rate of twinning and kinking in (a) $Mg_{97}Zn_1Y_2$ and (b) $Mg_{89}Zn_4Y_7$.

Deformation behavior of extruded LPSO-Mg Alloy was also evaluated. First, the AE events of the extruded LPSO-Mg alloy were classified by learning A. In this case, the number of events of two clusters showing high energy on the low frequency side and the high frequency side were almost the same number of events. Next, classification was done by learning B. Figure 3 shows the energy spectra calculated for the twin/kink AE waveforms used for learning and they were normalized after averaging of the energy spectra. The twin showed the prominent peak in the low frequency band around 300 kHz with high energy, and the kink showed relatively high energy in the wide range from 200 to 800 kHz. Machine learning was performed using this learning data, and the AE events generated during the 0° direction compression test (B3-0, B4-0, respectively) of B3 material and B4 material were classified. Figure 4 shows the evolution of the twin and kink AE events. Overall, the ratio of kink tends to be larger in B4-0, which is considered to reflect that the ratio of LPSO phase is higher. Comparing learning A learning B, different criteria for each material is necessary to classify the phenomena in learning A and manually associate the clusters and phenomena. It results in the difficulty in the comparison between a plurality of materials. In learning B, the same classification model can be used for any material and the correspondence to kink or twin is automatically made. It is concluded that quantitative evaluation and comparison of deformation behavior are possible.

4. Conclusion

(1) Compression test was performed on pure Mg, and the instant of twin generation was observed by high-speed camera observation with the AE signal triggered. It directly indicates that the source of AE is twin nucleation. We could clarify the formation and growth rate at the time of twin generation from observation results.

(2) The AE waveforms by twinning deformation were extracted by making each twin responsive to AE waveform and the AE waveforms for kink deformation were also prepared. Finally, we prepared the twin and kink classification models by machine learning. By classifying the AE of the extruded LPSO-Mg alloy by using these data, the time change of deformation mechanism and the ratio of twin / kink to ratio of two phases were evaluated.

(3) Using the machine learning based on the results of in-situ observation by a high-speed camera, it is possible to classify AE more effectively than the conventional method and to evaluate and compare the deformation behavior quantitatively.

References:

- [1] Y. Kawamura, K. Hayashi, A. Inoue, T. Masumoto, Rapidly solidified powder metallurgy $Mg_{97}Zn_1Y_2$ Alloys with excellent tensile yield strength above 600 MPa, *Mater. Trans.* (2001) 1172–1176.
- [2] A. Inoue, M. Matsushita, Y. Kawamura, K. Amiya, K. Hayashi, J. Koike, Novel hexagonal structure of ultra-high strength magnesium-based alloys, *Mater. Trans.* 43 (2002) 580–584.
- [3] T. Itoi, T. Seimiya, Y. Kawamura, M. Hirohashi, Long period stacking structures observed in $Mg_{97}Zn_1Y_2$ alloy, *Scr. Mater.* 51 (2004) 107–111.
- [4] X.H. Shao, Z.Q. Yang, X.L. Ma, Strengthening and toughening mechanisms in Mg-Zn-Y alloy with a long period stacking ordered structure, *Acta Mater.* 58 (2010) 4760–4771.
- [5] Y. Li, M. Enoki, Deformation and anelastic recovery of pure magnesium and AZ31B alloy investigated by AE, *Mater. Trans.* 48 (2007) 2343–2348.
- [6] Y. Li, M. Enoki, Evaluation of the twinning behavior of polycrystalline magnesium at room temperature by acoustic emission, *Mater. Trans.* 48 (2007) 1215–1220.
- [7] Y. Li, M. Enoki, Recovery behaviour of pure magnesium in cyclic compression–quick unloading–recovery process at room temperature investigated by AE, *Mater. Trans.* 49 (2008) 1800–1805.
- [8] Y. Li, M. Enoki, Twinning behavior of pure magnesium quantitatively investigated by acoustic emission, *Mater. Sci. Eng. A* 536 (2012) 8–13.
- [9] Y. Muto, K. Matsumoto, T. Shiraiwa, M. Enoki, Detection of Crack Propagation by AE and Evaluation of Fracture Toughness in Various Mg Alloys, *J. Jpn. Inst. Met. Mater.* 78 (2014), 381-387.
- [10] T. Yasutomi, M. Enoki, In-situ evaluation of detwinning behavior in extruded AZ31 Mg alloy by AE, *Mater. Trans.* 53 (2012) 1611–1616.
- [11] Y. Muto, T. Shiraiwa, M. Enoki, A.E. Analysis, of compression test with different loading direction of unidirectional solidification LPSO-Mg alloys, *J. Jpn. Inst. Met. Mater.* 80 (2016) 697–701.
- [12] Y. Muto, T. Shiraiwa and M. Enoki, Evaluation of the deformation behavior in directionally solidified Mg-Y-Zn alloys containing LPSO phases by AE analysis, *Mater. Sci. Eng. A.* 689 (2017) 157-165.

- [13] E. Pomponi, A. Vinogradov, A real-time approach to acoustic emission clustering, *Mech. Syst. Signal Process.* 40 (2013) 791–804.
- [14] A. Vinogradov, D. Orlov, A. Danyuk, Y. Estrin, Deformation mechanisms underlying tension-compression asymmetry in magnesium alloy ZK60 revealed by acoustic emission monitoring, *Mater. Sci. Eng. A* 621 (2015) 243–251.
- [15] J. Čapek, K. Máthis, B. Clausen, J. Stráská, P. Beran, P. Lukáš, Study of the loading mode dependence of the twinning in random textured cast magnesium by acoustic emission and neutron diffraction methods, *Mater. Sci. Eng. A* 602 (2014) 25–32.
- [16] D. Drozdenko, J. Bohlen, F. Chmelík, P. Lukáč, P. Dobroň, Acoustic emission study on the activity of slip and twin mechanisms during compression testing of magnesium single crystals, *Mater. Sci. Eng. A* 650 (2016) 20–27.
- [17] K. Ito, M. Enoki, Acquisition and analysis of continuous acoustic emission waveform for classification of damage sources in ceramic fiber mat, *Mater. Trans.* 48 (2007) 1221–1226.

39 - Non-threshold Acoustic Emission analysis of damage evolution in pipe segments of steel S355J2H under bending load

Franziska Baensch, Wolfram Baer, Peter Wossidlo, Abdelkarim Habib

Bundesanstalt für Materialforschung und -prüfung (BAM), Unter den Eichen 87,
12205 Berlin, Germany

Abstract:

Four-point bending tests were carried out to analyze the acoustic characteristics of damage development in pipe segments made of steel, grade S355J2H, being 2.5 m long with an outer diameter of 168 mm and 16 mm wall thickness. To induce stable crack growth, the pipe segments were pre-damaged by a 90° circumferential notch in the middle of the pipe length. While the pipe was quasi-statically loaded, microscopic damage and plastic deformation accumulated to form a macroscopic crack that grew through the pipe wall until leakage. For acoustic emission (AE) monitoring, four broadband sensors of type VS 900 M were mounted close to the notch. Continuous AE signal detection was performed by the non-threshold method. Advantages and disadvantages of the non-threshold AE monitoring compared to a commonly employed method analyzing only signals exceeding a predefined threshold are discussed. The results of AE analysis are compared to additional information on the crack growth detected by the direct current potential drop (DCPD) technique. These studies were carried out in the course of the interdisciplinary research project AGIFAMOR, Ageing infrastructures - distributed acoustic monitoring of pipes at BAM.

1. Introduction

In the course of an interdisciplinary research project at BAM (AGIFAMOR, Ageing Infrastructures – Application of distributed acoustic and fibre optic sensors for continuous monitoring of pipes, 2015-2018), the potential of distributed acoustic fibre optic sensing methods (DAS) in terms of a condition monitoring system for pipelines has been investigated. Therefore, besides studies on the sensitivity of the DAS to noise caused by leakage [1] or to pressure shocks causing dynamic circumferential changes of the pipe, also the sensitivity of the DAS to acoustic emission (AE) caused by crack formation in a pipe wall is investigated. The latter scenario, object of this contribution, was realized by four-point bending tests carried

out on steel pipe segments. Originally, a similar experimental setup was designed at BAM in the 1990's to study crack initiation and growth on large steel pipes by means of the direct current potential drop (DCPD) and the AE method [2]. To validate the DAS sensitivity, the test is accompanied by accelerometers and AE measurements. The AE during initial tests was monitored using threshold-based approach with threshold settings above 56 dB_{AE} [3]. Analysis of the continuous data recorded by DAS and accelerometers compared to the AE dataset recorded using threshold-based approach turned out to be insufficient to characterize test progress at the test object as well as to assign sudden deviations and possibly technical artefacts due to the employed extensive monitoring instrumentation. Thus, another test was performed with continuous monitoring by AE, DAS, and accelerometers. First results of AE analysis in comparison to the detection by the DCPD method are presented in the following.

2. Description of work

To investigate the crack initiation and stable growth of a macroscopic crack, a four-point bending test was carried out on a pipe segment made of steel grade S355J2H. The pipe segment was 2.5 m long, had a wall thickness of 16 mm and an outer diameter of 168 mm. Centered at 1.25 m length, a 90° circumferential notch was shaped into the pipe wall by a CNC machine. The notch had an opening angle of 90°, a notch root radius of 0.2 mm and a ratio of wall thicknesses of 0.5. For deflection measurements, six angles were glued to the pipe at the 3 o'clock and 9 o'clock positions as technical aid for the displacement sensors. The bending test was performed with a 4 MN universal testing machine that operates hydraulically. Test was driven displacement controlled with a test speed of 0.25 mm min⁻¹.

The test was monitored by non-threshold acoustic emission (AE) measurement as well as by the method of the Direct Current Potential Drop (DCPD), DAS and accelerometers (Fig.1). Herein, exclusively the results of the AE and the DCPD measurements are focused on. For DCPD, a DC of 300A was injected and the potential drop was measured at five positions close to the notch. The measured potential U is normalized with its output value U_0 and plotted as a function of the deflection (Fig. 2). Then, the potential data are approximated with a fifth degree polynomial in a deflection interval from zero to a freely selectable value between maximum load and load of leakage growth. By doing so, the stable crack growth process is taken into consideration. Based on the first order derivation of the polynomial fit, information on the characteristic development of damage accumulation, crack initiation and stable crack growth are obtained.

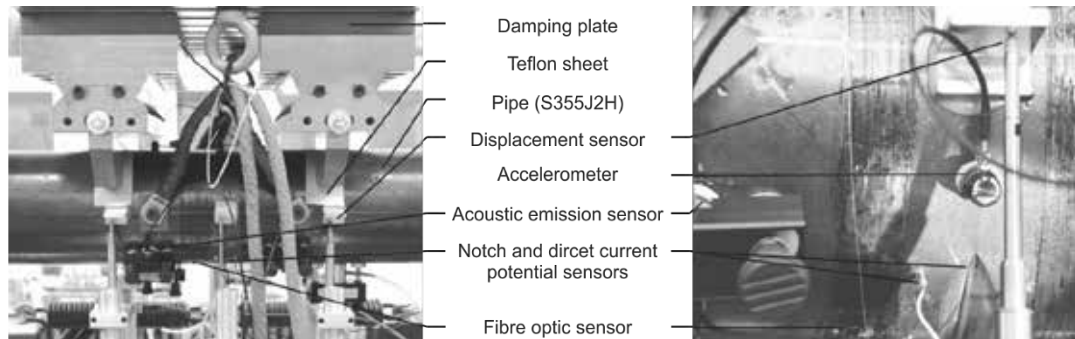


Figure 1. Experimental setup for monitoring of a four-point bending test of a 2.5 m long pipe segment by means of DCPD measurement, acoustic emission, accelerometers and fiber optical sensors.

The non-threshold AE monitoring was performed with the digital AE equipment AMSY-6 in continuous mode with a sampling rate of 3333333 Hz. Four broadband sensors, sensitive in the range from 100 kHz up to 900 kHz (type VS900-M), were used to ensure the monitoring of crack events. The response of the sensors is characterized by two peaks at 190 kHz and 350 kHz accompanied by two anti-resonances at 200 kHz and 400 kHz. The AE sensors were mounted with magnetic holders. Coupling agent was a reusable adhesive (Bostik Prestik made in South Africa). The four sensors were arranged in a square around the notch with approximately 100 mm distance to the notch. To enable good coupling of all sensors, the corrosion layers were removed by grinding surface at the appropriate areas along the pipe. Teflon sheets were inserted in between the pipe wall and the load bearings. Furthermore, PVC damping plates were assembled into the bearing elements (Fig.1). By this, the acoustic noise was reduced by approximately -10 dB. For AE analysis the near field behavior of the sensors with an attenuation of 9...17 dB must be considered. For the in-plane AE wave propagation a velocity of 5225 m s^{-1} was estimated.

First step in processing the AE data is to reduce the noise by applying a high pass filter at 150 kHz. For AE hit detection, the moving standard deviation of the measured amplitude values (mV) is calculated with a moving window size of 512 samples. To level low deviations relative to higher ones, the logarithm of the moved standard deviation is employed. Since the noise level increased with increasing load, the AE hits are detected by means of a moving threshold applied to the logarithm from the moved standard deviation of the measured amplitude values. Only AE events detected by all four sensors are evaluated. To determine the time shifts of one signal detected by the four sensors, the cross-correlation algorithm is applied to a time window of 2000 samples comprising the signal's arrival and its peak amplitude. According to the coordinates of the notch (AE source localization) and the AE sensors, the shift of a signal detected in all four sensors must not exceed $2.7E05 \text{ s}$ (90 samples) to be assigned to crack events at the notch.

3. Results

The quasi-static bending test of the pipe segment took about 75 minutes (Fig.2). After approximately 2500 s test duration, the piston movement was stopped in order to carry out corrective actions and checks to the setup. In total, a maximum load of 696 kN at deflection of 11.43 mm was yielded (Tab.1). The initial phase of bending test, the pipe segment undergoes an elastic deformation and its cross-section becomes ovalized. With progressive loading, mechanisms of plastic deformation set on; a macroscopic crack initiates and grows in a stable manner in the direction of pipe wall thickness. This is characterized by initial blunting and cross-section necking at the notch, increasing dislocation density as well as by accumulating ductile damage in the metal microstructure. After reaching its maximum, load decreases while the crack finally reaches the state of leakage. With progressing testing time, the leakage opens in a stable manner and the crack continues to grow in circumferential direction of the pipe wall on a low level. At this stage, the load curve stagnates due to equilibrium of strain hardening and crack growth, whereby the deflection increases further.

During the elastic deformation, the DPCD is approximately constant. The significant increase in potential drop indicating the initiation of stable macroscopic crack growth was found at 90% of maximum load (630 kN) and 56% of maximum deflection (6.5 mm). During the leakage grows in circumferential direction of the pipe wall, the potential drop increases with lower slope.

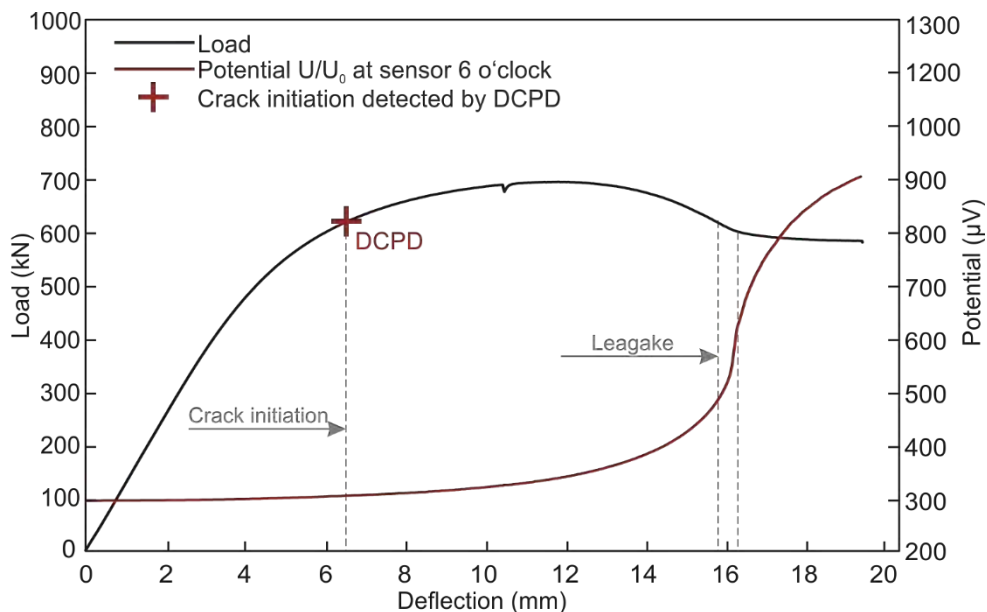


Figure 2. Load-deflection graph of the bending loaded pipe segment of steel (S355J2H). By means of the direct current potential drop (DCPD), the onset of macro cracking at the notch is detected. Leakage usually arises at the marked stage after maximum load.

AE data analysis revealed 1042 AE events (EV) detected by all four sensors, 185 of which are localized (LEV, located event) close to the notch. First LEV is detected within the elastic range at 150 kN after 334 s test duration (Fig. 3). 35 EV and 5 LEV occurred, randomly spread over time, until a significant AE set on. After approximately 1600 s of test duration, the cumulative curves of peak amplitudes significantly increase (Fig.4). Particularly, the increase in cumulative peak amplitude of LEV indicates the accumulation and formation of significant crack events at the notch. The occurrence of distinct AE signals correlates with the crack initiation determined by the DCPD method (Tab. 1). The development of macro-crack and its growth through the pipe wall thickness generates AE with corrected peak amplitudes up to 90 dB_{AE}. However, the LEV with the corrected maximum peak amplitude (95 dB_{AE}) was not detected close to the maximum load, but shortly before the load stagnated at 585 kN (3500 s) in the course of leakage growth. The formation of the leakage results in a steep increase in cumulated peak amplitude (Fig. 4). The subsequent crack growth in circumferential direction generated AE activity, since the four AE sensors detect approximately 150 EV. However, localization of the EV and, hence, the definite identification of AE source events close to the notch failed.

Table 1. Characteristic values from the DCPD and the AE monitoring of the four-point bending test. Mechanical properties at load peak and deflection peak.

	Crack initiation estimated by		Maximum load	Maximum deflection
	DCPD (6 o'clock position)	AE		
Load (kN)	630	626	696	575
Deflection (mm)	6.5	6.5	11.59	19.09

4. Discussion on AE results

During the test progress, the amplitude of noise in AE data rise with increasing load. This has a main impact on the sensitivity and accuracy of the AE method using “fictive” constant or moving threshold during post-processing of streaming signals, because only AE exceeding are detectable and, furthermore, the estimation of the AE arrival time is affected, too. Noisy signals range up to approximately 150 kHz in frequency. Furthermore, tracking damage processes particularly focuses on AE with higher frequency contents. Thus, setting a high pass at 150 kHz improves the data evaluation. When omitting the de-noising, only 33 LEV with peak amplitudes >60 dB_{AE} were identified, which is less than 20% of the herein presented 185 LEV.

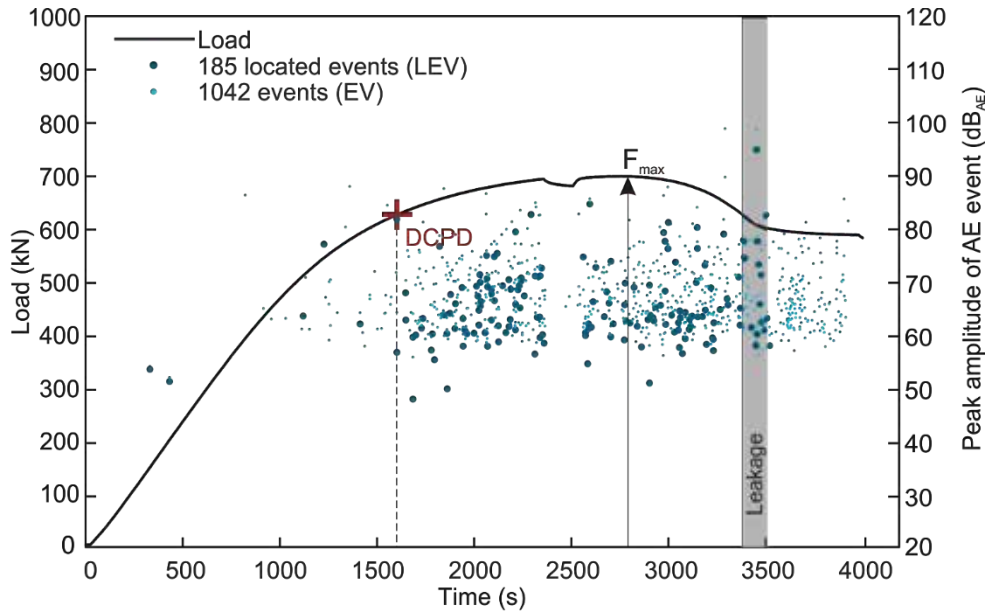


Figure 3. Load and corrected peak amplitudes of all detected AE events (1042 EV and 185 LEV) plotted vs. duration of the bending test of a pipe segment of steel. Highlighted characteristic states in the test progress are the crack initiation determined by DCPD, maximum load of 699 kN and leakage formation.

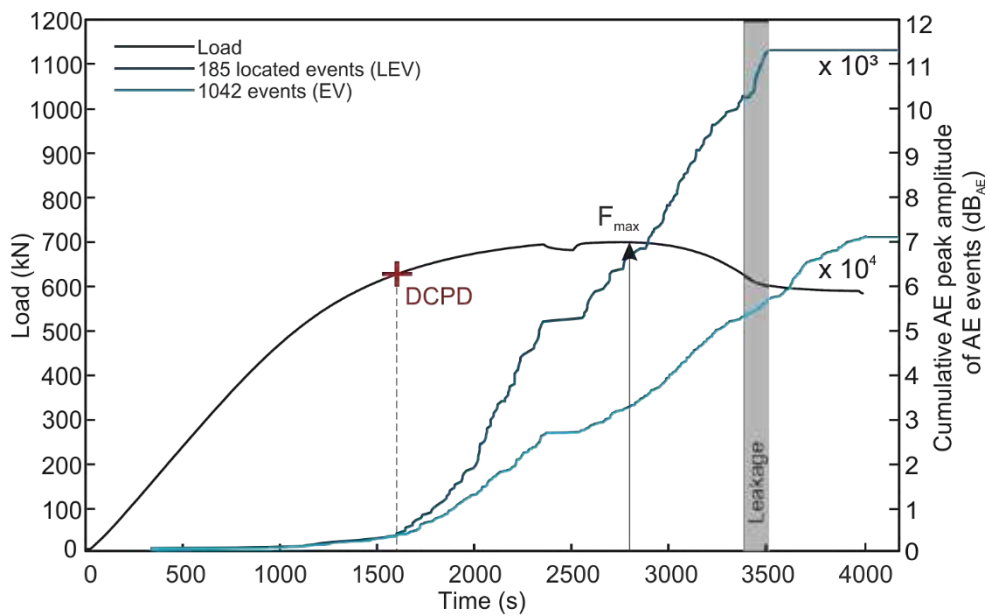


Figure 4. Load and cumulative corrected peak amplitudes of all detected AE events (1042 EV and 185 LEV) plotted vs. duration of the bending test of a pipe segment of steel. Highlighted characteristic states in the test progress are the crack initiation determined by DCPD, maximum load of 699 kN and leakage formation.

By post-processing the non-threshold streamed AE data, the sensitivity of the measurement system was improved. By applying a moving threshold-based on the standard deviation of signal amplitude, LEV with peak amplitudes $>30 \text{ dB}_{\text{AE}}$ are identified, even early LEV at low loading levels. The localization of EV of the subsequent crack growth in circumferential direction failed due to the limited AE sensors, their arrangement and the AE wave propagation interrupted by the leakage in the pipe wall.

Determination of the crack initiation by DPCD correlates well with results of the AE analysis. Analogous to the steep increase in DCPD, while crack finally breaks through the wall (leakage reached), also the cumulated AE peak amplitude increases even with a steeper slope. To improve the accuracy in EV localization, more sensors, at least six would be needed. Three sensors are needed on each side of the notch until leakage. Afterwards, as soon as the crack grows in circumferential direction, three sensors should be positioned close to both crack tips in radial direction.

5. Conclusion

AE monitoring by means of non-threshold recording enables true-to-the original replica of the test procedure. This might be particularly beneficial in the case of elaborate experiments, for example, to identify sudden deviations that occurred during the test progress and to clarify technical artefacts and possibly other phenomena retrospectively. The aim of the presented experiment is to investigate the sensitivity of the DAS. Since DAS and accelerometers record the acoustic information continuously during the tests, for comparison purpose, the non-threshold AE monitoring mode provides a sufficient database.

Transient recording with non-threshold mode provides limited information on AE activity in real-time analysis during the test due to the lack of arrival time estimation. The size of recorded datasets essentially depends on number of sensors, sampling rate and test duration. However, compared to the conventional threshold-based recording mode, large data volumes are produced. For example, the monitoring of a single bending test (75 min duration, 4 AE sensors, 3 MHz sampling rate in AE) produces a dataset of 110 GB, but only 10 % include relevant information on AE events due to damage mechanisms. The handling of large data volumes and the time-consuming post-processing data analysis are not insignificant. However, most important advantage of the non-threshold AE recording is that almost no information is omitted by digital threshold and frequency filter settings during the active measurement and the measuring system captures and stores the data with its maximum technical performance.

Acknowledgements

Pavol Stajanca and Sebastian Chruscicki are acknowledged for the measurements with the distributed acoustic fibre optic sensing system (DAS), Jens Prager and Tobias Homann for the measurements with the accelerometers, Margit Weltschev and Dirk Schmidt for the exchange of experiences in the field of damage to pipelines.

References:

- [1] Stajanca, P. et. al, Monitoring of pipes by distributed acoustic fibre optic sensors - A large scale test on a pipeline under realistic operation condition, Proceedings of the 13th Pipeline Technology Conference, Berlin, Germany, 2018.
- [2] Aurich, D. et. al, Methoden zur Extrapolation von JR-Kurven für die Vorhersage der Rissöffnungsgeometrie unter postulierten Belastungen, Teilprojekt 2 des BMFT-Vorhabens Analyse und Weiterentwicklung bruchmechanischer Versagenskonzepte Schwerpunkt: Anwendung fortgeschrittener zähbruchmechanischer Konzepte; Bruchübergang, Förderkennzeichen 1500 970, BAM-Forschungsbericht 232, ISBN 0938-5533, Berlin, Germany, 1999.
- [3] Baensch, F., et al.: BAM-Projekt AGIFAMOR – Zustandsüberwachung von Rohrleitungen, 21. Schallemissionskolloquium Fulda, Deutsche Gesellschaft für Zerstörungsfreie Prüfung (DGZfP), Fulda, Germany, 2017

71 - Galling detection by Acoustic Emission (AE) according to ASTM G98

Abdelkrim SAIDOUN¹, Catherine HERVE¹, Yan Ming CHEN¹, Thibault LESAGE²,
Salima BOUVIER²

¹ CETIM Senlis

² Université de Technologie de Compiègne

Abstract

For many mechanical companies, galling detection remains an important issue because it can occur in many mechanisms (bearings, transmissions ...) and thus lead to serious failures with consequences both in terms of production and in terms of people and machines safety. The diagnosis and identification of galling are made through facies observations and profilometry analysis (according to ASTM G98). When contact surfaces are not visible or easily accessible, it is not possible to actually know the state of galling. It is therefore important to have a method capable of performing a reliable diagnosis without having to stop or disassemble considered machines. Acoustic emission is a monitoring method for detecting the start of this physical phenomenon between two surfaces and also to follow its evolution.

Feasibility tests with CETIM tribology team have demonstrated the potential of this method and also assess possibilities to develop a detection criterion based on AE features. Experimental principle consists of applying a load on a pin which is slowly rotate to a fixed plate (360°). The galling threshold is determined from the pressure at which there is a first material transfer on friction surfaces.

The obtained results show the potential of the AE for the detection of the galling threshold. Furthermore, the correlation of AE measurements with the EBSD method (graphically showing grain orientation and size of grains before and after testing) revealed two types of galling: catastrophic and tolerant galling.

Key words: galling, acoustic emission, ASTM G98, EBSD, catastrophic and tolerant galling.

¹ EBSD (Electron Backscattered Diffraction) in a scanning electron microscope has recently become a widely used technique, especially in metallurgy for the simultaneous characterization of the local microstructure and crystallographic texture of polycrystalline materials. It provides access not only to orientation cartographies but also to phase cartographies. In addition, it allows for assessing elastic and plastic deformations, as well as the energy stored in the grains during deformation

1. AIMS AND SCOPE

One of the objectives is to understand the impact and relevance of different heat treatments on galling phenomenon in the case of stainless steels and to study their impact on the microstructure and the phases involved. Thanks to EBSD method (graphically showing grain orientation and size of grains before and after testing), two types of galling were characterized: catastrophic and tolerant galling. Acoustic emission must make it possible to quantify the rate of galling in a first time and then to differentiate these two types of galling.

This article explains how AE has been used to:

- Detect galling from AE data using a frequency analysis.
- Determine a criterion associated to galling phenomenon beginning. Thanks to this criterion, an alarm is generated to communicate and stop the tension compression machine when galling is detected.
- Quantify the galling severity (catastrophic and tolerant)
- Distinguish catastrophic and tolerant galling

This paper uses EBSD results of the thesis work carried out by T.Lesage in the context of GRIPAC's thesis: "GRIPpage of stainless steel and its consequences on the degradation of friction components in the agri-food and pharmaceutical industry".

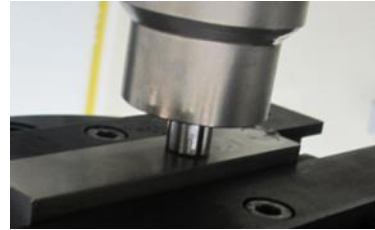
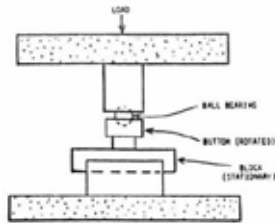
2. PRESENTATION OF STANDARD ASTM G98

The objective of this standard is to determine the susceptibility to galling of a couple of materials.

2.1 Principle

The test principle is a pin-on-disc type of test in which an Ø12.7 mm pin is placed on a flat surface (figure 1). The principle is to apply a load on a pin which is slowly rotated (Velocity= 10rotations/minute) one revolution 360° relative to a fixed plate. Both the flat surface and the pin are checked for galling. The criterion for either galling occurs or not is the appearance of specimens based on unassisted visual examination. The first selected load applied is 350MPa and then decreased progressively. The load program will depend to contact materials. If there is no galling of either surface, then the load is decreased and the test repeated. Then the average of the highest non-galled load and the lowest galled load is calculated (figure 2). This is the "galling threshold" at which the paired materials begin to show signs of galling (first material transfer on friction surfaces).

Nota: 5 pins are required per block for galling threshold determination.



- Tension compression Instron machine (capacity 250kN) "TTKMH3450 250KN"
- Load cell: A212-201 model 2511-320 250KN
- HBM torque sensor model TB2.
- HBM conditioner model: MGC and AB22A with ML10B and BL01 cards.
- SEW geared motor brand equipped with a brushless technology
- An acquisition station model YOKOGAWA « DL750 » with 8 channels: tension 0-10V and sampling frequency 100 kHz.

Figure 1. Galling machine presentation

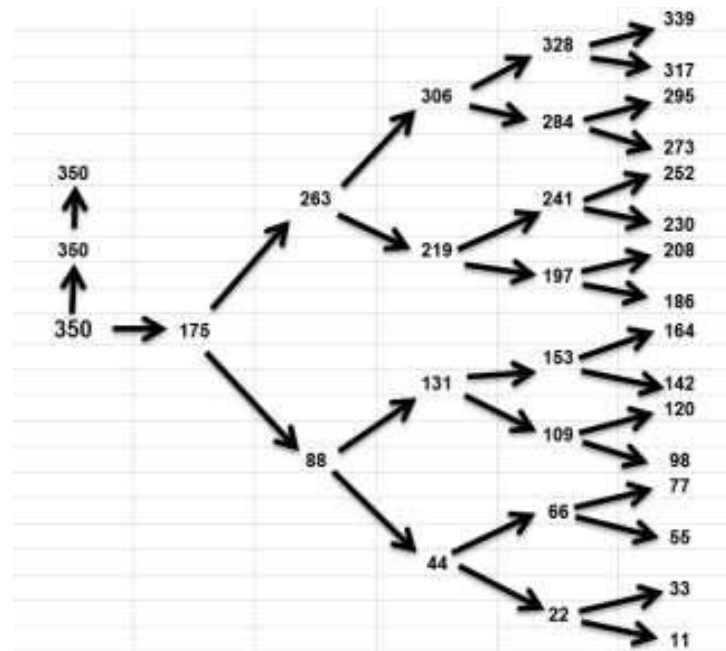


Figure 2. Experimental designs suggested by ASTM G98

2.2 Weaknesses of ASTM G98

The current method used to detect galling and to define the galling threshold between two materials presents two main disadvantages:

- For some cases, raking light is needed to rule if galling occurred or not. The same sample is presented below. Picture on the right was taken under raking light. If raking light is not used in this case, it would have been impossible to detect galling according to ASTM G98
- ASTM G98 is not able to quantify galling which is occurring during the test.

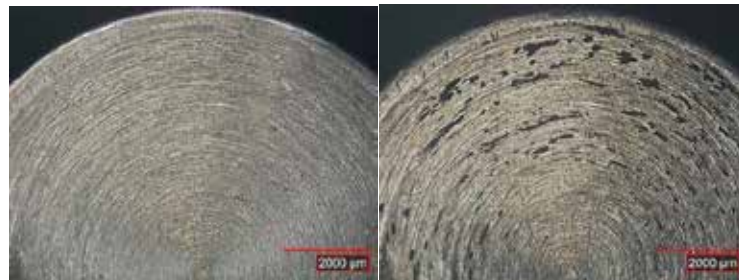


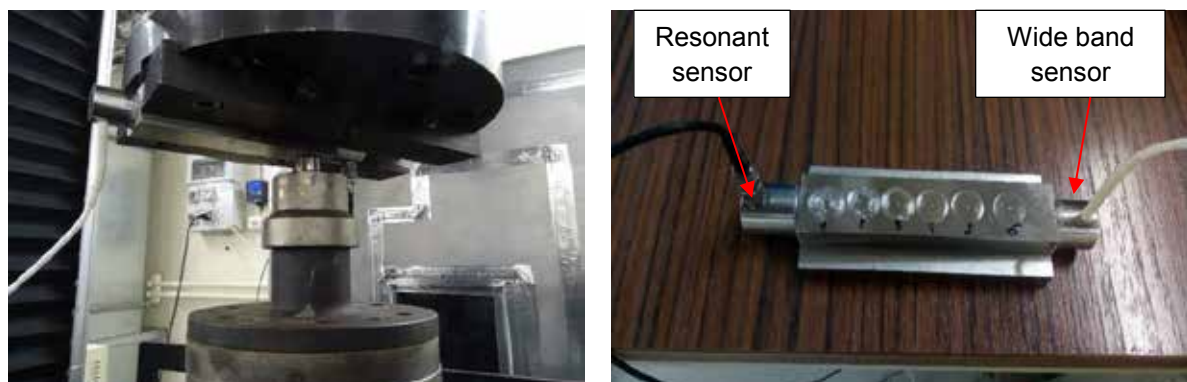
Figure 3. Galling, not galling?

Acoustic emission could be an effective method to improve ASTM G98 by instrumenting the test machine.

3. ACOUSTIC EMISSION: AN EFFECTIVE METHOD TO UNDERSTAND GALLING PHENOMENON

3.1 Experimental description

The experimental setup is shown in figure4. AE activity is recorded by two different kind of sensors:



Resonant AE sensor (MISTRAS)	Wide Band AE sensor (MISTRAS)
Resonance frequency: 150 kHz	Range frequency: [100; 900 kHz]
Number: 1	Number: 1
Preamplifier: AEP3H (Gain 34 dBea)	Preamplifier AEP3H (Gain 34 dBea)

Figure 4. Implementation of the AE sensors on the disc

Many different physical phenomenons are occurring during the ASTM G98 test (plastication, friction, galling, ...). The previous study [1] showed that the galling phenomenon occurs only in the rotation phase during the test. For this purpose, we focus in our analysis only on the acoustic emission data recorded during the rotation phase.

The previous study showed also that the frequency analysis of the AE signals is well adapted for the early detection of the galling phenomenon and possibly to characterize it (catastrophic and tolerant galling). That is why a large band sensor is used. The resonant AE sensor allows acquiring AE activity linked to galling with a higher sensibility than the wideband sensor.

A large number of tests were carried out on a variety shades of steel. in this paper, three representative examples are presented with respect to the resulting galling nature (no galling, tolerant galling and catastrophic galling) as shown in table 1.

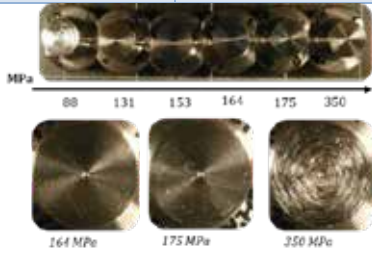
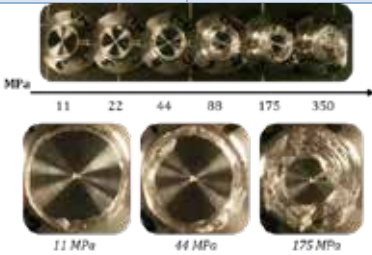
No galling		Tolerant galling			Catastrophic galling		
Pin: 316L (K33*)	Disc: 316L	Pin: Nit60	Disc: 316L		Pin: 17-4PH	Disc: 316L	
 <p>350 MPa</p>		 <p>MPa 08 131 153 164 175 350</p> <p>164 MPa 175 MPa 350 MPa</p>			 <p>MPa 11 22 44 88 175 350</p> <p>11 MPa 44 MPa 175 MPa</p>		
<p>K33: is a surface thermo-chemical treatments for a beter resistance to galling</p>							

Table 1. Summary of studied galling (tolerant galling, catastrophic galling)

In the next step on this paper, the metallographic characterization of the galling will be presented in order to explain the difference between the two types of galling (tolerant and catastrophic). Then the results of the AE analysis relative to the detection of galling will be presented. Finally, a correlation between the results of AE and those of tribological observations will be presented in order to discuss the possibility of galling characterization by AE.

3.2 Characterization of tolerant and catastrophic galling by the metallographic examination

One can see easily on the table 2 that for the similar load of 175Mpa, the galling occurring with Nitronic 60 is less severe than that occurring with the 17-4PH, so it is called ' tolerant' galling contrary to 'catastrophic' galling that will cause a blockage of the components

Nitronic 60	17-4PH
 <p data-bbox="416 663 517 689">175 MPa</p>	 <p data-bbox="1038 663 1139 689">175 MPa</p>

Table 2. Two types of galling are generated on Nitronic60 and 17-4PH under the same load 175MPa (tolerant galling, catastrophic galling)

In order to further the analysis of the two cases of galling, the thesis team performed EBSD scan as shown in the figure below.

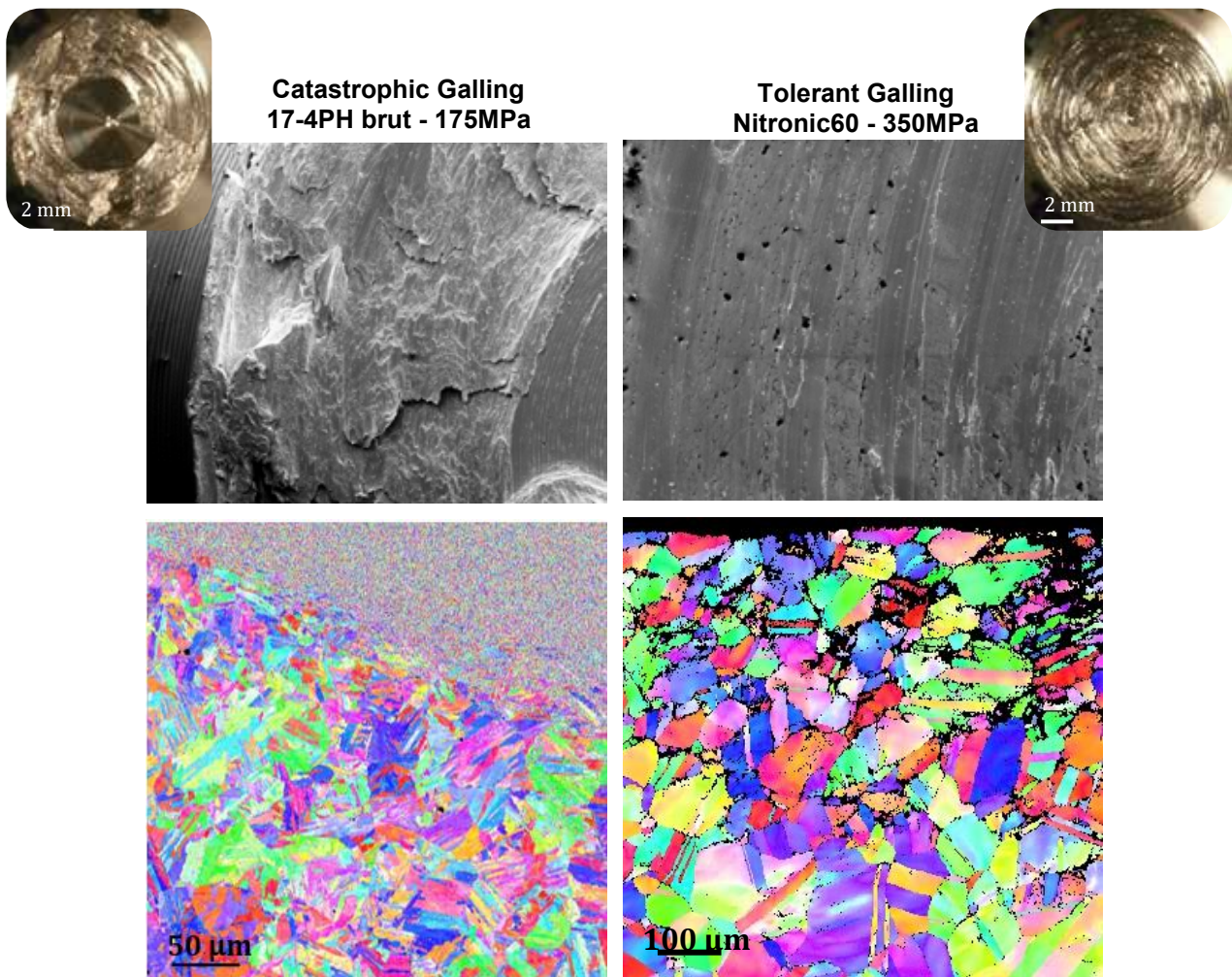


Figure 5. EBSD results (Nitronic60 (tolerant galling) and 17-4PH (catastrophic galling))

EBSD method is used to characterize the microstructure of the samples before and after testing. After galling, grain size is greatly reduced for all samples (in the case of catastrophic galling) apart from Nitronic 60 (tolerant galling, resulting in localized disorientation at the grain boundaries).

3.3 Detection and characterization of galling by AE

In order to study the detection of galling by AE, a frequency analysis of AE signals has been performed.

Firstly, the no-galling case is analyzed in order to determine the maximum limit of the frequency content of the signals recorded in this step. Figure 6.a shows the distribution of the frequency center (of signals recorded by the wide band sensor) as function of the time test for the couple 316LN/316L treated by K33 under a load of 350 MPa. As previously stated, this study focuses on the rotation zone to analyze galling. From this representation we can see that the recorded frequencies do not exceed 320 KHz. This result is true for other no-galling tests as shown in figure 6.b.

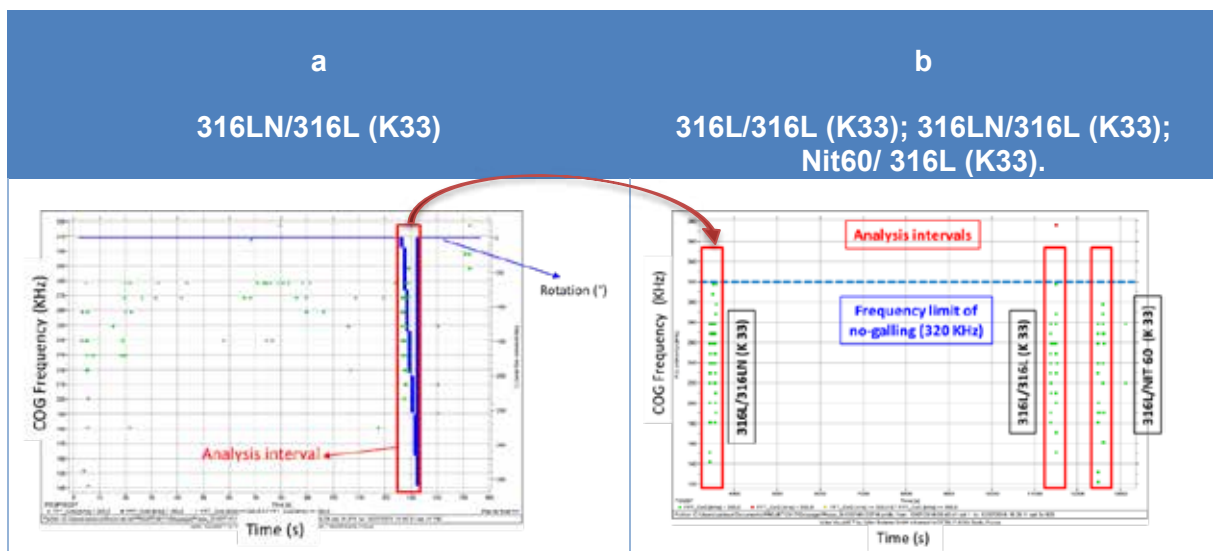


Figure 6.a. Distribution of the centroid frequency as function of the time test under a load of 350 MPa. **a.** for non-galling test 316LN/316L (K33). **b.** for other no-galling tests (316L/316L (K33); 316LN/316L (K33); 316L/Nit60 (K33))

In a second step, the case of catastrophic galling is considered. AE data of the couple 17-4PH/316L are analyzed. Figure 7 shows a comparison between the results obtained by the two used sensors (wide band sensor and resonant sensor).

Unlike the result obtained previously, for both sensors the frequencies obtained for the forces greater than 11 MPa exceed the limit of 320 KHz.

The wide band sensor has a slower dynamic compared to the resonant one, so the number of recorded signals is lower. On the other hand, as its spectrum is wider, the recorded frequency range is wider compared to the resonant sensor. In this study the wide band sensor is preferred over the frequency analysis.

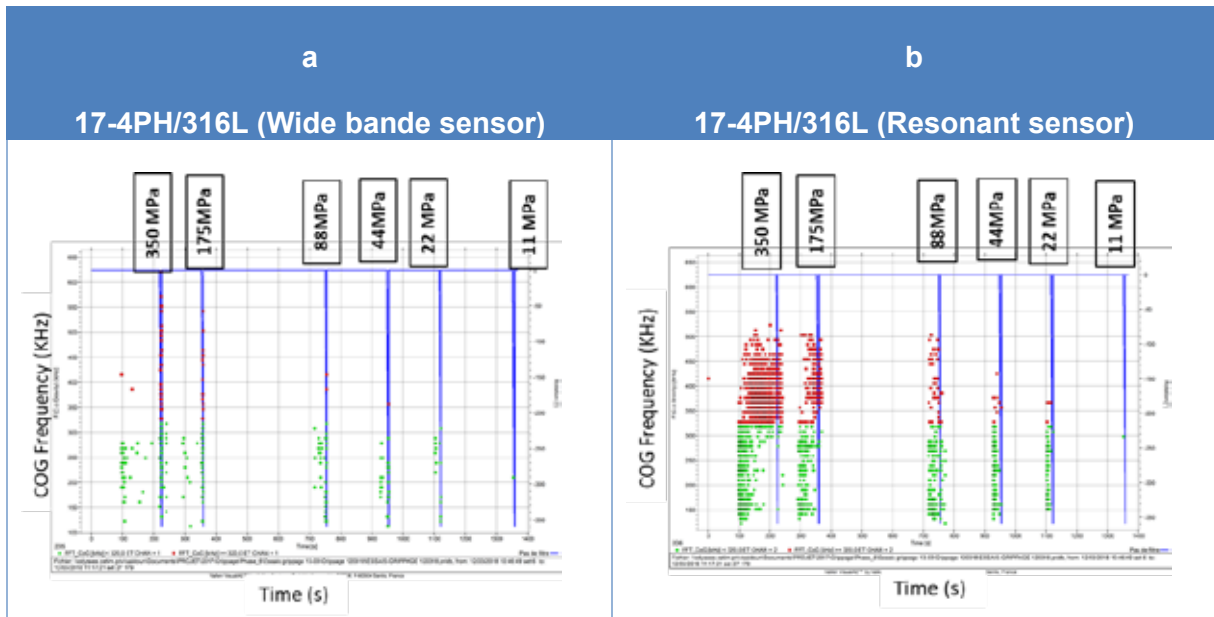


Figure 7. Distribution of the centroid frequency as function of the time test under different loads (green points represent frequency < 320 KHz; red ones represent frequency > 320 KHz).
a. AE recorded by a wide band sensor. **b.** AE recorded by a resonant sensor.

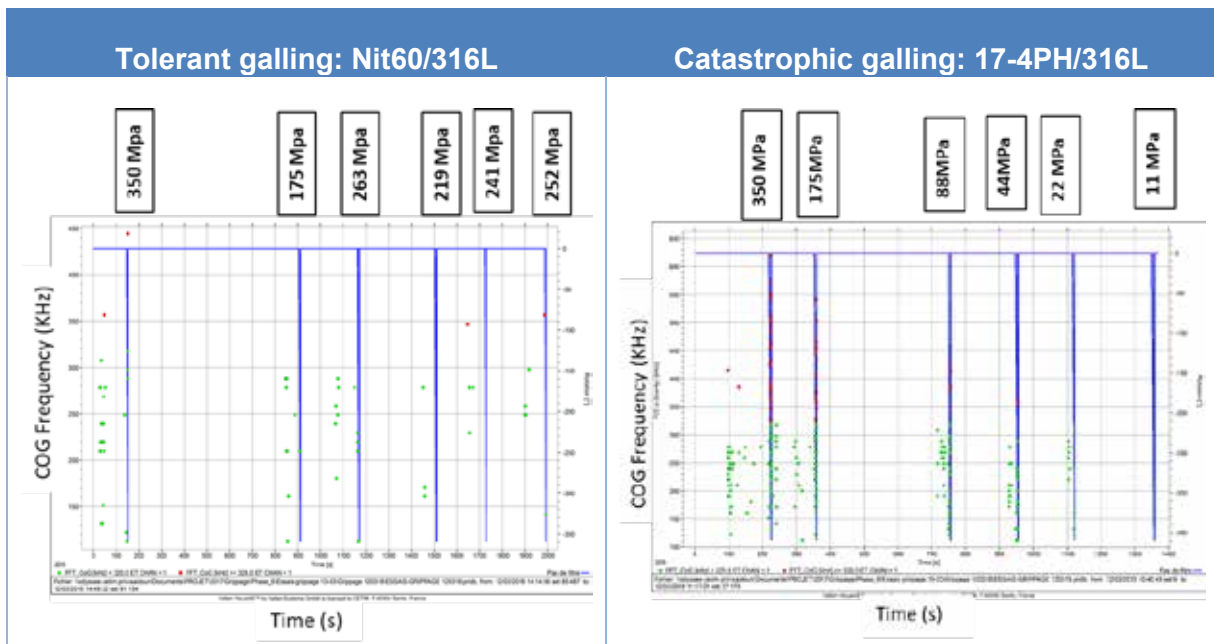


Figure 8. Comparison between tolerant galling and catastrophic one “distribution of the centroid frequency as function of the time test under different loads (green points represent frequency < 320 KHz; red ones represent frequency > 320 KHz)

The final step of this paper concerns the case of tolerant galling. AE data of the couple Nitronic60/316L are analyzed. Figure 8 shows a comparison between tolerant galling and catastrophic one, we notice that:

- The common result between the two types of galling is that the frequencies exceed 320 KHz. This result confirms that this frequency represents the threshold of galling phenomenon.
- On the other hand, it is noted that in the case of tolerant galling the number of signals is less compared to the catastrophic galling. In addition, the frequencies obtained during the tolerant galling (<450 KHz) remain lower than those obtained in the case of catastrophic galling.

4. Conclusion

In this study the AE technique was used on ASTM G98 tests. The first objective is to test the early detection of galling on stainless steel specimens with or without heat treatment. The second objective is to differentiate AE signals as function of galling severity (tolerant or catastrophic) in order to complete and clarify the existing standard.

The realized analysis of AE data shows that the frequency parameter is very sensitive to galling phenomenon.

- The results show that the AE technique is able to detect early the galling phenomenon by setting a frequency threshold (320 KHz).
- Thanks to the work thesis carried out by T.Lesage, two types of galling have been distinguished: tolerant galling (which is not critical) and the catastrophic galling (which can generate appalling effects). Using the EBSD method, it has been shown that tolerant galling does not change grain size (only disorientation at the joints), while catastrophic galling, leads to grain breakage until 40 micrometers.
- The first results show that acoustic emission seems to be able to distinguish these two types of galling, notably by using the centroid frequency of the acoustic emission bursts. If centroid frequency of a burst is less than 450 kHz, this burst is associated to tolerant galling

The results presented in this article are therefore encouraging. On the samples analyzed, it was possible, by acoustic emission, to quantify galling, and to distinguish between the two types of galling, catastrophic and tolerant. New test campaigns are planned to confirm these results.

References:

- [1] Friedrich, P et al., Galling detection by acoustic emission (AE) according to ASTM G98, Metallic Materials and processes: Industrial challenges, 25-27 October 2017, France.

11 - AE monitoring and three-dimensional observation of stress corrosion cracking from corrosion pits

Kaige Wu¹, Kaita Ito², Ippei Shinozaki³, Manabu Enoki¹

¹ Department of Materials Engineering, The University of Tokyo, 7-3-1 Hongo,
Bunkyo-ku, Tokyo 113-8656, Japan

² National Institute for Materials Science, Tsukuba 305-0047, Japan

³ Research Laboratory, IHI Corporation, Yokohama 235-8501, Japan

Phone: +81 3 5841 7129; fax: +81 3 5841 7181;

E-mail: kaigewu@rme.mm.t.u-tokyo.ac.jp

Abstract:

Stress corrosion cracking (SCC) is a complicated three-dimensional (3D) process involving both electrochemical and mechanical phenomena. The source mechanism of acoustic emission (AE) behavior during SCC development is still not well understood. In this work, AE monitoring combined with 3D characterization using X-ray computed tomography (X-ray CT) were proposed to investigate the SCC of an initially smooth sample of SUS420J2 stainless steel exposed to both a 0.6% constant strain and a neutral sodium chloride droplet at room temperature. Cracks were observed to originate from corrosion pits. Further 3D observation of the inner geometry of cracks indicated that cracks preferentially attacked the mouth, rather than the bottom, of the corrosion pit. It was also observed that by the path of crack propagation existed several interior corrosion pits which may play a critical role in crack growth. AE signals were detected during SCC evolution and characteristics of AE events were associated with crack initiation and propagation. K-means clustering analysis grouped the AE events into three clusters. With in-situ surface observation and 3D images of cracks, hydrogen bubble evolution, plastic deformation around the crack tip, and the crack propagation were considered as the possible AE source mechanisms during the SCC.

Keywords: stress corrosion cracking; corrosion pit; clustering; acoustic emission; X-ray CT

1. Introduction

Structural materials, especially stainless steels, are critical for developing and maintaining infrastructures. However, it can undergo stress corrosion cracking (SCC) by slow, environmentally induced crack initiation and propagation. The SCC process is concurrent by both electrochemical and mechanical phenomena that are the results of the synergistic effect of stress and corrosive environment on materials [1]. In many applications, corrosion pit serves the primary precursor to crack initiation and the general stages of SCC are therefore recognized as pitting corrosion, pit-to-crack transition and subsequent crack growth [2]. Regarding the crack initiation from corrosion pits, there still exist different arguments. Conventional viewpoint argues that SCC preferentially initiates at the base of a pit because the pit base not only serves the local stress-strain concentrator but also retains an aggressive environment [2-3]. Comparatively, another new perspective, based on the three dimensional (3D) observations with X-ray computed tomography (X-ray CT, or XCT), is put forward recently that cracks are not necessarily initiated at the pit base during the pit-to-crack

transition [4]. It suggests that cracks nucleate on the pit walls in relation to the dynamic strain provided by the growing pit. Subsequently, cracks grow around the pit and finally coalesce to form a complete through-crack. The inconsistency implies further research work is needed on the pit-to-crack transition during the early stage of SCC.

On the other hand, developing in-situ methodologies is important in understanding the cracking mechanism and evaluation of the health condition of metallic structure and components. Acoustic emission (AE) is an in-situ nondestructive evaluation (NDE) method that bases on the detection of elastic waves generated by the fast energy release during an irreversible change within materials and solids. AE method holds great potential in monitoring the progression of materials degradation and steel corrosion [5-10]. AE method has long been applied to study the crack initiation and propagation during SCC. In the literature, different damage mechanisms during SCC, including the rupture of pit cover [10], fracture of metallic ligaments [11-12], plastic deformation around the crack tip [11, 13-18], ductile fracture [14], hydrogen bubble evolution [10, 16-21], falling off of the surface grain [20-21], rupture of corrosion products [20-22], and the cracking process [11-24] have been correlated with AE signals. However, the interpretation of the source mechanisms in current reports was mainly based on speculation of AE evolution coupled with *post mortem* microstructural analysis. Therefore, an irrefutable elucidation of the source mechanisms of the detected AE signals requires more investigation of in-situ visualized linkage. Moreover, the SCC testing proposed in literature [13-14, 18] is difficult to directly correlate the detected AE signals to one single step of cracking evolution since multiple-pits and cracks may be initiated to develop at different steps when the samples were immersed in the corrosive solution.

In order to better understand the crack initiation, we developed an experimental methodology to study the evolution of one single crack under a NaCl solution micro-droplet. Simultaneously, AE monitoring accommodated with an in-situ surface observation was proposed to perform with the SCC testing. XCT was also used to give a 3D morphological observation of the crack and corrosion pit.

2. Experimental procedures

2.1 SCC testing and AE measurements

The material used here is SUS420J2 (C: 0.32 mass%, Si: 0.45 mass%, Mn: 0.54 mass%, Cr: 13.39 mass%, Ni:0.09 mass%, P: 0.031 mass%, S: 0.005 mass%, Fe : bal.). Three kinds of samples were prepared with different heat treatment sequences as follows. (Sample A): 600°C/1h → 800°C/1h → 1010°C/2.75h → gas cooling → 180°C/3h; (Sample B): 600°C/1h → 800°C/1h → 1010°C/2h45m → gas cooling; (Sample C): 950°C/2h → gas cooling. The Vicker's hardness of sample A, B, and C were HV 593, 611, and 511. Then they were polished to a mirror-like finish. The SCC samples were fixed in a jig with a curvature of R125 to apply a constant strain of 0.6% to the sample surface. A micro-droplet of 1.0 mass% NaCl solution of 1 μ L was set in the center of the surface of samples placed inside a thermostatic bath (298K, 99-100%). The bath was capped with a transparent glass cover to accommodate an in-situ surface observation with a digital microscope (VHX-5000, Keyence Corp., Japan). Two high-sensitivity R-CAST sensor systems of 200 kHz resonant (M204A, Fuji Ceramics, Japan) were respectively placed 10 mm and 30 mm away from the droplet site to filter out the noise outside the corrosion region by source location method. A continuous acquisition mode named "Continuous Wave Memory" (CWM) which was developed by our group [25] was used to record and analyze the AE signals. The sampling rate and threshold were 5

MHz and 20 mV, respectively. The experimental arrangements are schematically shown in Fig. 1. Finally, the extracted AE data were analyzed by k-means clustering algorithm [26].

2.2 3D observation of crack morphology

After testing, the SCC samples were both inspected by SEM and XCT. The SCC samples were polished and cut to a small size of XCT sample, schematically shown in Fig. 2(a), to meet the requirement of lab XCT scanning. A 3D XCT Scanner (TDM1000-IS, Yamato Scientific Co., Ltd., Japan) was used for scanning the internal structural information of cracks. The X-ray computed tomographic process is schematically shown in Fig. 2(b). The XCT sample was fixed on a rotational stage. A rotation step of 0.24 degree and 25 mins per full rotation was set for high-resolution scanning. The X-ray tube voltage was set to 100 kV and

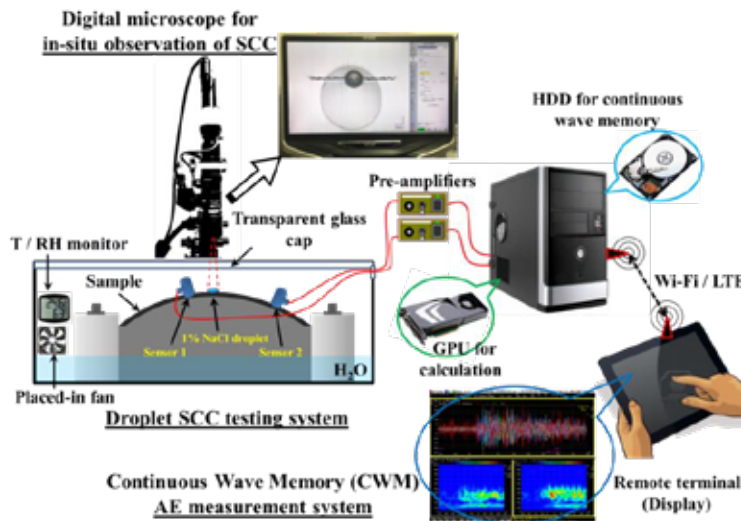


Fig. 1 Schematic of the AE measurements and SCC test incorporated with an in-situ digital microscope system.

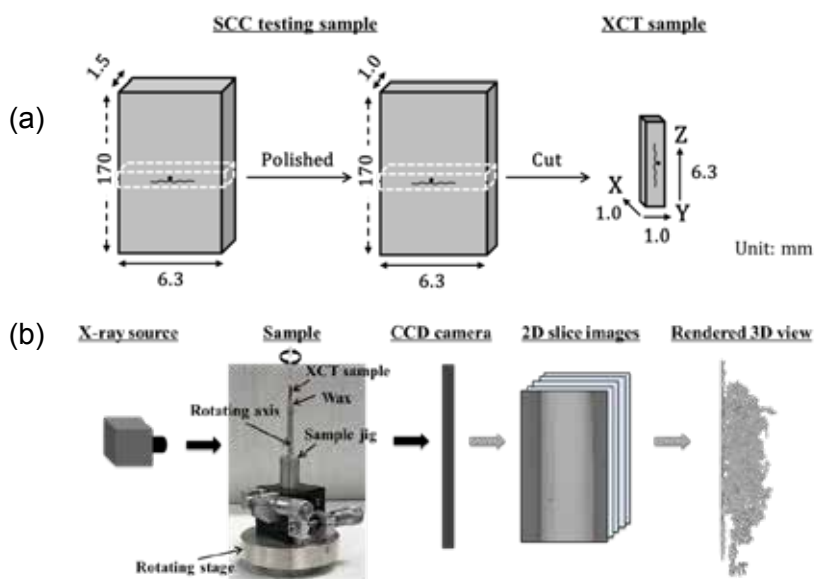


Fig. 2 (a) Schematic of the preparation of XCT sample, (b) 3D X-ray computed tomographic process of internal view of cracks.

X-ray tube current was set to 30 μ A~54 μ A in dependence of crack size. 2D-slice images were reconstructed using the image processing unit of the X-ray CT system. Finally, the volumetric image visualization and segmentation of the crack morphology were implemented using VoTracer software package (Riken, Japan).

3. Results

3.1 Surface and 3D observation of cracks

Fig. 3 shows the surface morphologies of cracks in three samples. First, one single crack was initiated under the micro-droplet. Regardless of the heat-treatment exposures, the cracks of all samples were observed to stem from the corrosion pits. In detail, the cracks developed preferentially at the place next to the pit mouth on the sample surface, rather than the general perspective that cracks develop preferentially and coalesce at the pit base [2-3].

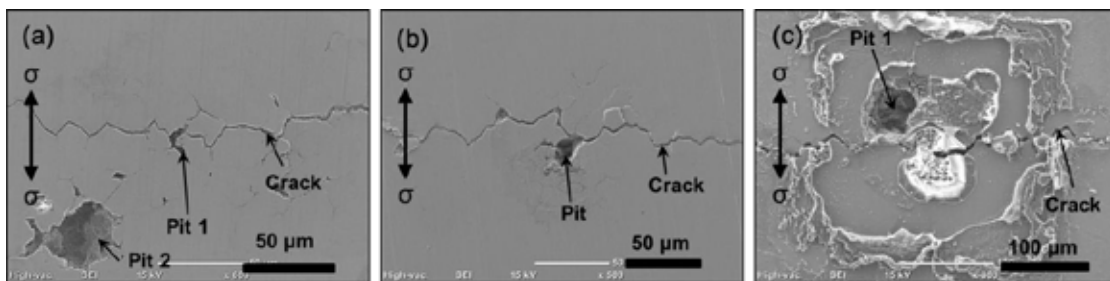


Fig. 3 SEM observations of the crack morphologies of samples (a) A, (b) B, and (c) C.

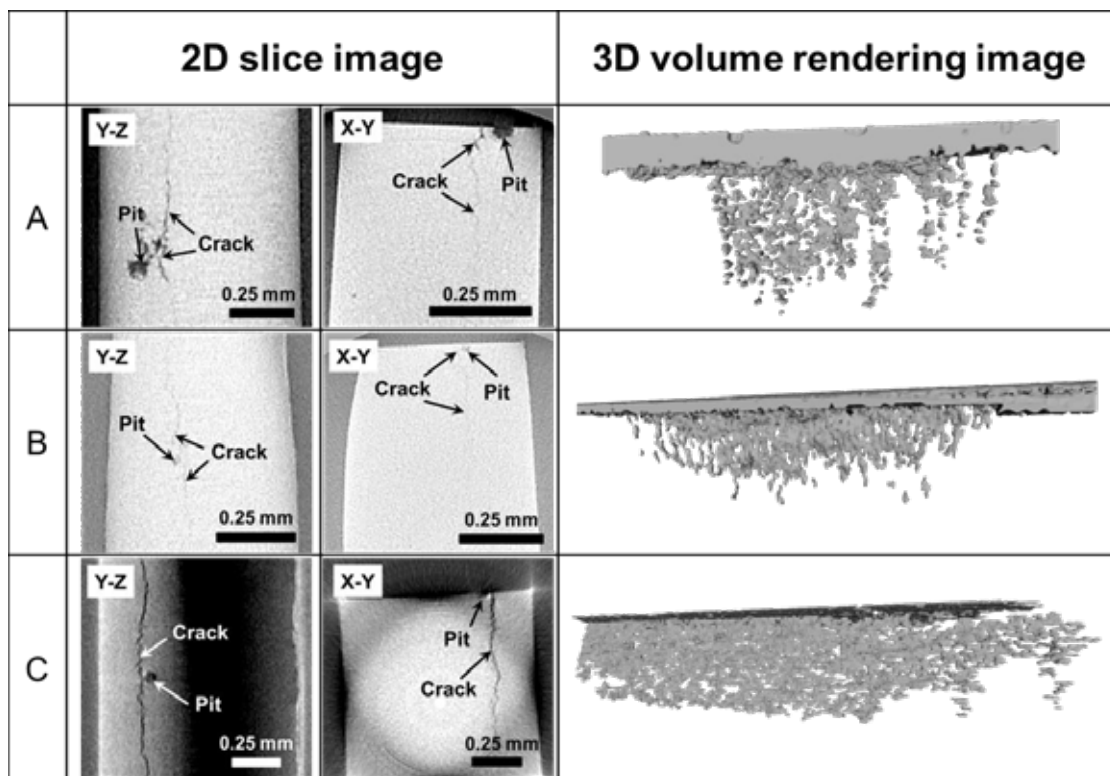


Fig. 4 Reconstructed tomographic 2D slices and 3D volume rendering images of cracks morphologies of sample A, B, and C.

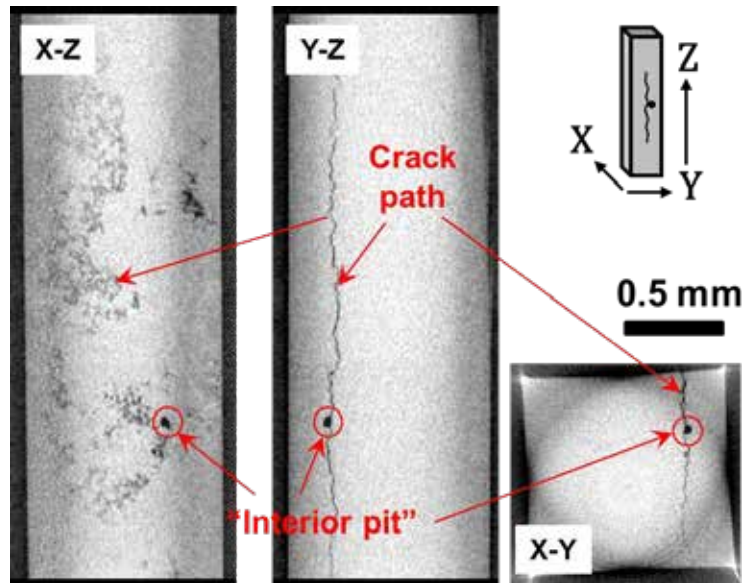


Fig. 5 Reconstructed tomographic slices showing an “interior pit” along the crack path of the sample C. The inserted schematic indicates the planes.

Fig. 4 shows the reconstructed slices and volume rendering images. The internal views provide a direct illustration of the relative position of the crack and corrosion pit, i.e., the crack is next to but does not cross through the corrosion pit. This observation is close to the recently-proposed viewpoint that the cracks primarily attack the mouth, rather than the bottom, of the corrosion pits [4]. But the different point is that the crack does not finally cross or combine the pit, unlike the formation of through-crack after crack growth rate exceeds the pit growth rate [2-4]. This may elucidate a different role of corrosion pits in the crack initiation in high strength steels. The volume rendering images indicate that the crack morphologies are not continuous in spatial distribution. The discreteness may imply a competition among different advancing crack tips which probably depended on the local inhomogeneity of the heat treated material. Furthermore, several interior cavities (named here “interior pit”) were observed to situate by the path of the crack propagation. One is shown in Fig. 5 by the reconstructed tomographic 2D slices. The interior pit is apparently an included local that may play a critical role in the crack growth.

3.2 AE signals and damage identification

Fig. 6 shows the evolution of AE signals obtained during SCC process of three samples. According to the increase trend and amplitude distribution, the data could be divided into four stages. Combined with the in-situ observational SCC evolution, the four-stage AE signals are associated with pitting corrosion, pit-to-crack transition, small crack growth and long crack propagation. Such observation is consistent with the fundamental steps of overall SCC development [1]. In stage I, chloride ions locally destroy the passive film surface of stainless steel sample, exposing the bare metal to the electrolyte and allowing the activation of localized corrosion. Later, local acidification by the hydrolysis of dissolving metal cations within pit lowers the pH value and generates the hydrogen bubbling which was captured in this work. A sharp increase in AE events in stage III reflects the transition from pit to crack. Stage II is a quiescence phase for sample A and B, but sharp increase for sample C. This stage seems to be microstructure dependent and will be further investigated in future work. Stage IV with the relatively low number of AE events is corresponding with crack propagation.

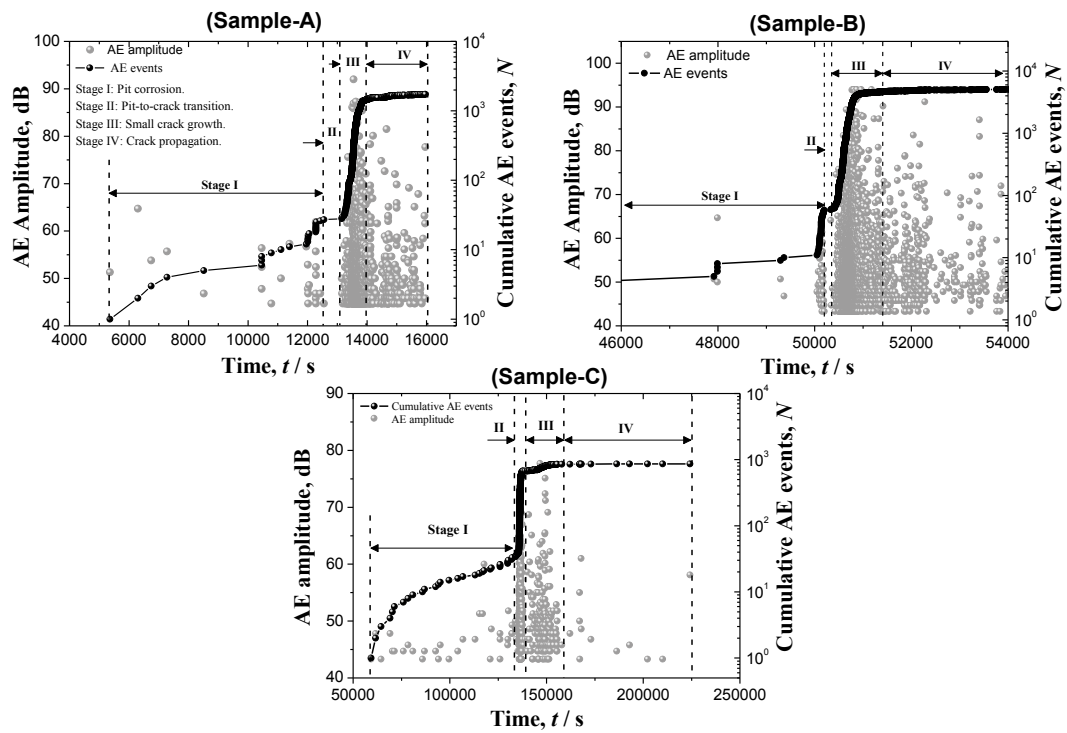


Fig. 6 Evolution of cumulative events and amplitude of AE signals obtained during SCC evolution of samples A, B, and C.

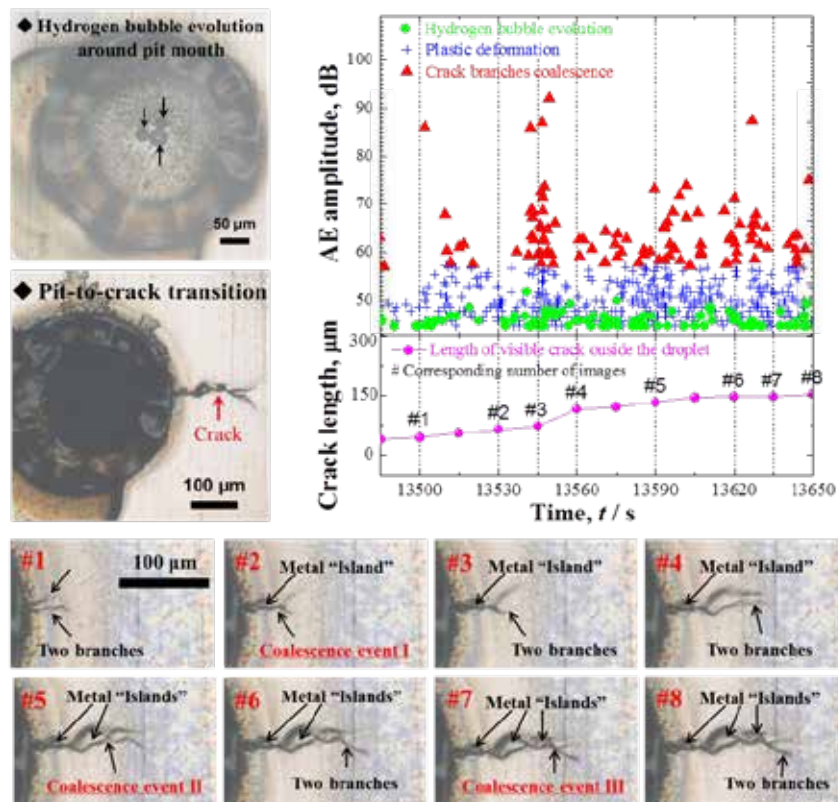


Fig. 7 Identification of AE source mechanisms during SCC from in-situ surface observation of the crack evolution (sample A).

To identify the damage mechanism for AE signals, k-means clustering algorithm was used to analyze the AE data. According to the similarity of AE data, three different AE clusters were obtained. From in-situ linkage analysis, three AE clusters were associated with hydrogen bubble evolution, plastic deformation and the cracking process. Fig. 7 shows the partial data of distribution of three AE clusters and the corresponding observation of a periodic coalescence phenomenon of two crack branches during crack propagation. Interestingly, high-amplitude signals were highly correlated with the occurrence of coalescence events of two branches. Therefore, the cluster 3 (red) is further attributed to the crack-branches coalescence. Suggestively, the plastic deformation and hydrogen bubble evolution dominate the detected AE signals during the crack growth. The cracking itself seems to be “silent” until the coalescence events occur with the concurrent high-amplitude signals. Moreover, the high-amplitude signals are not continuous in time series. This may be a response to the discrete morphologies of cracks shown in Fig. 4.

4. Discussion

The direct optic capture of the hydrogen bubble evolution approaching the point of crack initiation suggests that the hydrogen embrittlement mechanism may dominate the crack initiation of the high-strength steels in the present work. First, it is well known that any process producing hydrogen at a metal surface will induce considerable atomic hydrogen absorption and rapid diffusion into the metal lattice even at normal temperature [27]. The hydrogen diffusion phenomenon is more preferable in high-strength steels and enhanced by the applied tensile stress. The observed surface- and interior-pits can serve the source of hydrogen through the “local acidity” by hydrolysis of the dissolved metal ions [28]. Also, a previous report explained the SCC with hydrogen embrittlement mechanism accompanied by AEs in 13% Cr martensitic stainless steel exposed to 3% NaCl solution [29]. Furthermore, considering the observed zigzag-feature, the crack presents the intergranular type. Hydrogen is but one element that can segregate to grain- or interphase boundaries and its solubility in a metal depends on the applied tensile stress level [30]. This may account for that the cracks primarily attacked the pit/grain boundary interface on the sample surface, rather than the pit bottom. As the surface of bent sample suffered the highest stress level, which may cause the site near surface being the preferential crack nuclei. Furthermore, the final cracks did not cross through or combine with the corrosion pits, suggesting that the critical role of corrosion pits may be the source of hydrogen in the pit-to-crack transition in high-strength steels.

On the other hand, the distribution of high-amplitude cracking events with the plastic deformation events can be explained by the Hydrogen-Enhanced Localized Plasticity (HELP) mechanism [31]. The cracking was followed by the generation and accumulation of dislocation by the combination of hydrogen atoms and stress. Therefore, the plastic deformation dominated the AE signals of medium amplitude until the occurrence of crack-branches coalescence events which produced the strongest AE signals. This is consistent with the conclusions of previous reports [16-17] that the crack extending along the grain boundaries cannot generate detectable AE signals. Further work is required to give a reliable validation of this explanation.

5. Conclusion

The behavior of one single stress corrosion crack of 13Cr martensitic stainless steel was controlled and investigated by AE monitoring and 3D XCT observation. The crack was

observed to primarily originate from the mouth of a corrosion pit. The hydrogen embrittlement is supposed to account for the mechanism of crack initiation of SUS420J2. The corrosion pit may serve a critical role of providing the hydrogen in pit-to-crack transition. The evolution of AE signals were stage-by-stage associated with the crack initiation and propagation. By direct linkage with in-situ surface observations, the AE signals were attributed to the hydrogen bubble evolution, plastic deformation, and the coalescence events of crack-branches. However, a valid interpretation of the AE signals requires in-situ 3D visualizations of the crack evolution and quantitative evaluations of the crack behavior with AE data.

Acknowledgements

This work was supported by Council for Science, Technology and Innovation (CSTI), Cross-ministerial Strategic Innovation Promotion Program (SIP), "Structural Materials for Innovation" (Funding agency: JST). The authors acknowledge the great helps from Prof. Jun Takahashi, Dr. Mizuki Ohta, Dr. Pornthep Chivavibul, Dr. Takayuki Shiraiwa in X-ray CT scanning and image processing.

References:

- [1] Parkins, R.N., Stress corrosion spectrum, *British Corrosion Journal*, Vol. 7, 1972, pp. 15-28.
- [2] Turnbull, A., Zhou, S., Orkney, L., McCormick, N., Visualization of stress corrosion cracks emerging from pits, *Corrosion*, Vol. 62, 2006, pp. 555-558.
- [3] Parkins, R.N., Singh, P.M., Stress corrosion crack coalescence, *Corrosion*, Vol. 46, 1990, pp. 485-499.
- [4] Horner, D.A., Connolly, B.J., Zhou, S., Crocker, L., Turnbull, A., Novel images of the evolution of stress corrosion cracks from corrosion pits, *Corrosion Science*, Vol. 53, 2011, pp. 3466-3485.
- [5] Ono, K., Acoustic Emission in Materials Research – A Review, *Journal of Acoustic Emission*, Vol. 29, 2011, pp. 284-308.
- [6] Huang, M., Jiang, L., Liaw, P.K., Brooks, C.R., Seeley, R., Klarstrom, D.L., Using acoustic emission in fatigue and fracture materials research., *JOM*, Vol. 50, 1998, pp. 1-14.
- [7] Wu, K.G., Choe, C.Y., Lee, S.M., Yoo, J., Hyun, C.Y., Hong, D.P., Byeon, J.W., Real-time Monitoring of Degradation of Zirconia Ceramic by Acoustic Emission, *Applied Mechanics and Materials*, Vol. 433, 2013, pp. 816-820.
- [8] Wu, K., Jung, W.S., Byeon, J.W., Evaluation of corrosion critical variables of 304 stainless steel by delay time of acoustic emission, *Materials Transactions*, Vol. 56, 2015, pp. 398-403.
- [9] Wu, K., Jung, W.S., Byeon, J.W., Acoustic emission of hydrogen bubbles on the counter electrode during pitting corrosion of 304 stainless steel, *Materials Transactions*, Vol. 56, 2015, pp. 587-592.

- [10] Wu, K., Jung, W.S., Byeon, J.W., In-situ monitoring of pitting corrosion on vertically positioned 304 stainless steel by analyzing acoustic-emission energy parameter, *Corrosion Science*, Vol. 105, 2016, pp. 8-16.
- [11] Sung, K.Y., Kim, I.S., Yoon, Y.K., Characteristics of acoustic emission during stress corrosion cracking of inconel 600 alloy, *Scripta materialia*, Vol. 37, 1997, pp. 1255-1262.
- [12] Alvarez, M.G., Lapitz, P., Ruzzante, J., AE response of type 304 stainless steel during stress corrosion crack propagation, *Corrosion Science*, Vol. 50, 2008, pp. 3382-3388.
- [13] Kovač, J., Leban, M., Legat, A., Detection of SCC on prestressing steel wire by the simultaneous use of electrochemical noise and acoustic emission measurements, *Electrochimica Acta*, Vol. 52, 2007, pp. 7607-7616.
- [14] Kovac, J., Alaux, C., Marrow, T.J., Govekar, E., Legat, A., Correlations of electrochemical noise, acoustic emission and complementary monitoring techniques during intergranular stress-corrosion cracking of austenitic stainless steel, *Corrosion Science*, Vol. 52, 2010, pp. 2015-2025.
- [15] Shaikh, H., Amirthalingam, R., Anita, T., Sivaibharasi, N., Jaykumar, T., Manohar, P., Khatak, H.S., Evaluation of stress corrosion cracking phenomenon in an AISI type 316LN stainless steel using acoustic emission technique, *Corrosion Science*, Vol. 49, 2007, pp. 740-765.
- [16] Xu, J., Han, E.H., Wu, X., Acoustic emission response of 304 stainless steel during constant load test in high temperature aqueous environment, *Corrosion Science*, Vol. 63, 2012, pp. 91-99.
- [17] Xu, J., Wu, X., Han, E.H., Acoustic emission response of sensitized 304 stainless steel during intergranular corrosion and stress corrosion cracking, *Corrosion Science*, Vol. 73, 2013, pp. 262-273.
- [18] Calabrese, L., Bonaccorsi, L., Galeano, M., Proverbio, E., Di Pietro, D., Cappuccini, F., Identification of damage evolution during SCC on 17-4 PH stainless steel by combining electrochemical noise and acoustic emission techniques, *Corrosion Science*, Vol. 98, 2015, pp. 573-584.
- [19] Du, G., Li, J., Wang, W.K., Jiang, C., Song, S.Z., Detection and characterization of stress-corrosion cracking on 304 stainless steel by electrochemical noise and acoustic emission techniques, *Corrosion Science*, Vol. 53, 2011, pp. 2918-2926.
- [20] Yonezu, A., Cho, H., Ogawa, T., Takemoto, M., Simultaneous monitoring of acoustic emission and corrosion potential fluctuation for mechanistic study of chloride stress corrosion cracking, *Key Engineering Materials*, Vol. 321, 2006, pp. 254-259.
- [21] Yonezu, A., Cho, H., Takemoto, M., Monitoring of stress corrosion cracking in stainless steel weldments by acoustic and electrochemical measurements, *Measurement Science and Technology*, Vol. 17, 2006, pp. 2447-2454.

- [22] Shiwa, M., Masuda, H., Yamawaki, H., Ito, K., Enoki, M., In-Situ Observation and Acoustic Emission Analysis for SCC of MgCl₂ Droplet in SUS304 Stainless Steel, *Materials Transactions*, Vol. 55, 2014, pp. 285-289.
- [23] Shiwa, M., Yamawaki, H., Masuda, H., Ito, K., Enoki, M., AE signals analysis during chloride droplet SCC on thin plate of SUS304 steel, *Strength, Fracture and Complexity*, Vol. 5, 2009, pp. 109-116.
- [24] Ito, K., Yamawaki, H., Masuda, H., Shiwa, M., Enoki, M., SCC monitoring of chloride droplets on thin SUS304 plate specimens by analysis of continuous recorded AE waveform, *Materials transactions*, Vol. 51, 2010, pp. 1409-1413.
- [25] Ito, K., Enoki, M., Acquisition and analysis of continuous acoustic emission waveform for classification of damage sources in ceramic fiber mat, *Materials transactions*, Vol. 48, 2007, pp. 1221-1226.
- [26] Muto, Y., Shiraiwa, T., Enoki, M., Evaluation of the deformation behavior in directionally solidified Mg–Y–Zn alloys containing LPSO phases by AE analysis, *Materials Science and Engineering: A*, Vol. 689, 2017, pp. 157-165.
- [27] Rogers, H.C., Hydrogen Embrittlement of Metals: Atomic hydrogen from a variety of sources reduces the ductility of many metals, *Science*, Vol. 159, 1968, pp. 1057-1064.
- [28] Ryan, M.P., Williams, D.E., Chater, R.J., Hutton, B.M., McPhail, D.S., Why stainless steel corrodes, *Nature*, Vol. 415, 2002, pp. 770-774.
- [29] Okada, H., Yukawa, K.I., Tamura, H., Application of acoustic emission technique to the study of stress corrosion cracking in distinguishing between active path corrosion and hydrogen embrittlement, *Corrosion*, Vol. 30, 1974, pp. 253-255.
- [30] Courtney, T.H., Embrittlement, in: Courtney, T.H. (Eds.), *Mechanical Behavior of Materials*, Second ed., McGraw-Hill International Editions, Singapore, 2000, pp. 630-685.
- [31] Robertson, I.M., Sofronis, P., Nagao, A., Martin, M.L., Wang, S., Gross, D.W., Nygren, K.E., Hydrogen embrittlement understood, *Metallurgical and Materials Transactions A*, Vol. 46, 2015, pp. 2323-2341.

18 - Application of Acoustic Emission measurements to monitor the initiation and the propagation of single or multiple Stress Corrosion Cracks (SCC)

Omar Al Haj¹, José Bolivar², Alain Proust¹, Marion Frégonèse²

¹ MISTRAS GROUP S.A.S, Instrumentation, Research and Development,
F-94370 Sucy en Brie

² Univ Lyon, INSA de Lyon, MATEIS UMR 5510 , F-69621 Villeurbanne cedex

Abstract:

The aim of this study is to monitor the initiation and the propagation of single or a colony of intergranular SCC cracks using the acoustic emission technique. The main goal is a better understanding of the behavior and the propagation of multiple cracks for a better evaluation of the influence of cracks interactions on the failure process. For nuclear applications, the final aim is to propose new integrity criteria.

Several experimental tests were performed using mill annealed and sensitized samples of alloy 600, which were immersed in a 0.01 M of potassium tetrathionate solution acidified at pH 3.0 or 5.3. The experiments were also monitored by in-situ digital image correlation (DIC) and electrochemical noise (EN) measurements.

Three stages were identified in the propagation and the growth of both a single crack and a colony of cracks. During stage I, no crack was detected and the main acoustic emission signals were related to intergranular corrosion and/or anodic dissolution.

Stage II was characterized by surface crack propagation, mostly induced by anodic dissolution. The acoustic emission signals recorded during this phase were generated by intergranular corrosion processes.

During stage III, the interactions between the cracks became more and more intense (crack coalescences) with an important implication of plastic strain (macro cracking, plastic deformation,...). Such processes were identified as the source of the important acoustic emission activity detected during this last stage.

Finally, the implementation of acoustic emission technique coupled with DIC and EN measurements contributed to the understanding of the mechanisms involved in short stress corrosion cracks interactions which was determinant for the modeling of the colony behavior.

1. Introduction

Stress Corrosion Cracking (SCC) is one of the significant ageing degradation processes in industries operating under extreme conditions, especially in nuclear power plants (pressurized and boiling water reactors). SCC leads to a premature degradation process of metals and alloys generated by the synergistic effect of static tensile mechanical loading and environmental factors [1]. In that context, a better understanding and evaluation of the SCC process is considered as an important technical issue for the safety and maintenance of these ageing nuclear power plants (NPP) which are reaching a mean operating age of 30 years [2-3]. A streamlined approach to SCC risk evaluation involves the stage of initiation and the period of interaction between several cracks (e.g. shielding effects, coalescence and irregular propagation) [4-8]. For this purpose, acoustic emission technique (AE) represents an efficient non-invasive and non-destructive evaluation technique allowing the detection and localization of stress corrosion cracks [9-15]. Literature review about the use of AE technique for studying corrosion processes, confirms that several types of corrosion can be detected and monitored

by the mean of AE. Pitting, crevice, corrosion-abrasion in addition to stress corrosion cracking have been studied and found to be correlated with AE [16-22].

Yuyama [23] actually reported that several processes could liberate acoustic emission signals during SCC. These processes involve metal dissolution, hydrogen gas evolution, the breakdown of thick oxide films, fracture or decohesion of precipitate and inclusions, plastic deformation, martensitic transformation and micro/macro cracking (see Figure 1). Nevertheless these processes didn't release the same amount of energy and didn't present the same probability of being detected by piezoelectric sensors. Metal dissolution and film formation are the less energetic processes, in contrast the rupture of thick film, gas release, plastic deformation and cracks propagation represent the most energetic processes and can be easily detected.

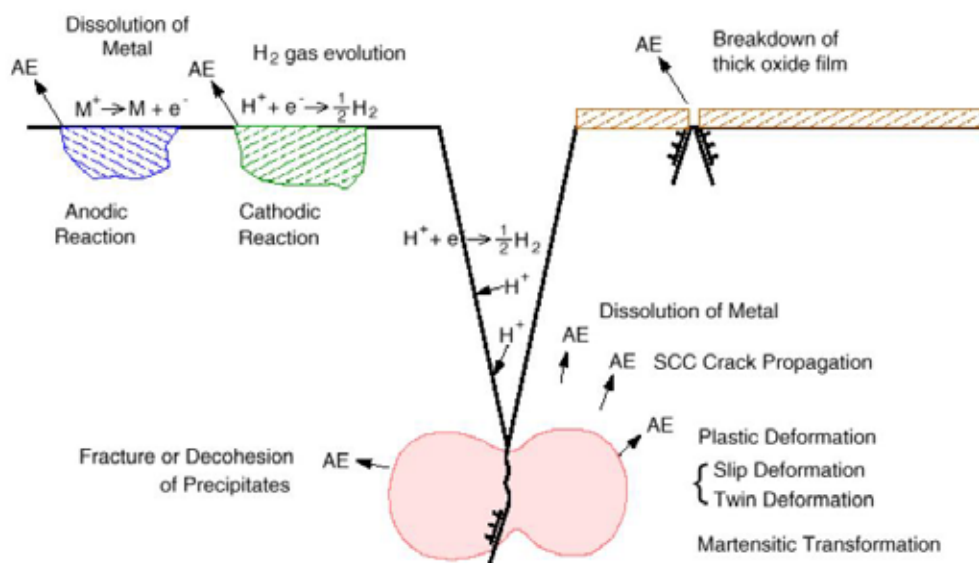


Figure 1: Sources of acoustic emission in SCC [23]

The main goal of this work is a better understanding of the behavior and the propagation of multiple cracks for a better evaluation of the influence of cracks interactions on the failure process. The correlation of different techniques: AE (Acoustic Emission), EN (Electrochemical Noise) and DIC (Digital Image Correlation) allow a better characterization of the behavior of a SCC colony considering the individual evolution of each crack. The use of these three techniques will enable the identification of the different stages of the crack colony evolution and on the mechanisms involved in each stage.

2. Description of work

All the experiments mentioned below have been conducted and performed during the PhD thesis of Bolivar, J. [24] which was a part of the ANR ECCOFIC project. This project aimed at studying the behavior of colonies of environmentally assisted short cracks. In the present work we focus particularly on the AE acquisition and the contribution of this technique in determining the characteristics of intergranular SCC defects. Otherwise Bolivar [24-26] has reported in details the technical aspects and results of the two other techniques mentioned in this paper (EN and DIC).

The experiments were performed on a 2 mm thick plate of Alloy 600. The chemical composition can be found in Table 1. The specimens were machined out by Electrical Discharge Machining, then heat-treated during 30 h at 600°C and air-cooled.

The specimens were partially covered with a silicon rubber in order to limit the exposed area. Only the middle section of the samples was exposed to the electrolyte, with an exposed area of 120 mm² on each side (15 X 8 mm). The test solution consisted in 0.01 M potassium tetrathionate acidified at pH 3 or 5.3 by H₂SO₄ addition.

Table 1. Composition of the tested Inconel 600 alloy

Element	Ni	Fe	Cr	Mn	Cu	Co	Ti + Al	C	S
Wt. %	bal.	9,25	15,52	0,12	0,1	0,1	0,25	0,03	0,002

Samples were immersed in the test solution at least 60 minutes before loading starts. Loading tests were performed after the immersion step at 80% of the yield stress ($\sigma_y = 263$ MPa) using an electromechanical tensile machine (LLOYD LR30K Plus).

Figure 2 shows the experimental device used during the tests and allowing the use of DIC, AE and EN simultaneously.

AE data acquisition was performed using MISTRAS *PC/2* acquisition system. The sample rate was set at 2 MHz, offering a good compromise between measurement accuracy and data file size. Two piezoelectric sensors (*R15D*) were used because of their good immunity against the EMI (Electromagnetic Interference), and allowing the conversion of transitory elastic waves resulting from corrosion processes into an electrical voltage. The sensors were fixed on the top and at the bottom of the stressed specimen (working electrode). These piezoelectric sensors present an operating frequency range between 50 – 400 kHz with a resonant frequency centered on 150 kHz.

Table 2 gathers the characteristics of the AE acquisition devices. Two 2/4/6 preamplifiers, with a selected gain of 60 dB_{AE}, were used. Furthermore, a band-pass filter was set-up between 100 kHz and 400 kHz, in order to minimize the environmental noise. The threshold was set to 23 dB_{AE}, intended first to get an appropriate sensitivity and then to separate effective signals from insignificant events.

Table 2. Main Characteristics of AE acquisition devices.

Instrumentation	Characteristics
Sensors	R15D
Threshold (dB _{AE})	23
System Filter (kHz)	100-400
Preamplifier – gain (dB)	2/4/6 – gain: 60 dB
PDT-HDT-HLT (μs)	300-600-1000
Waveform Sample Rate (MSPS)	2
Waveform Pre-Trigger	50 pts
Waveform Length	1K [512 ms]

The acquisition chain was computed using MISTRAS AWin™ software and results were analyzed using MISTRAS Noesis™ software. The normalized Hsu–Nielsen test [EN 1330-9] was carried out to verify the sensor coupling and the whole setup of the AE system.

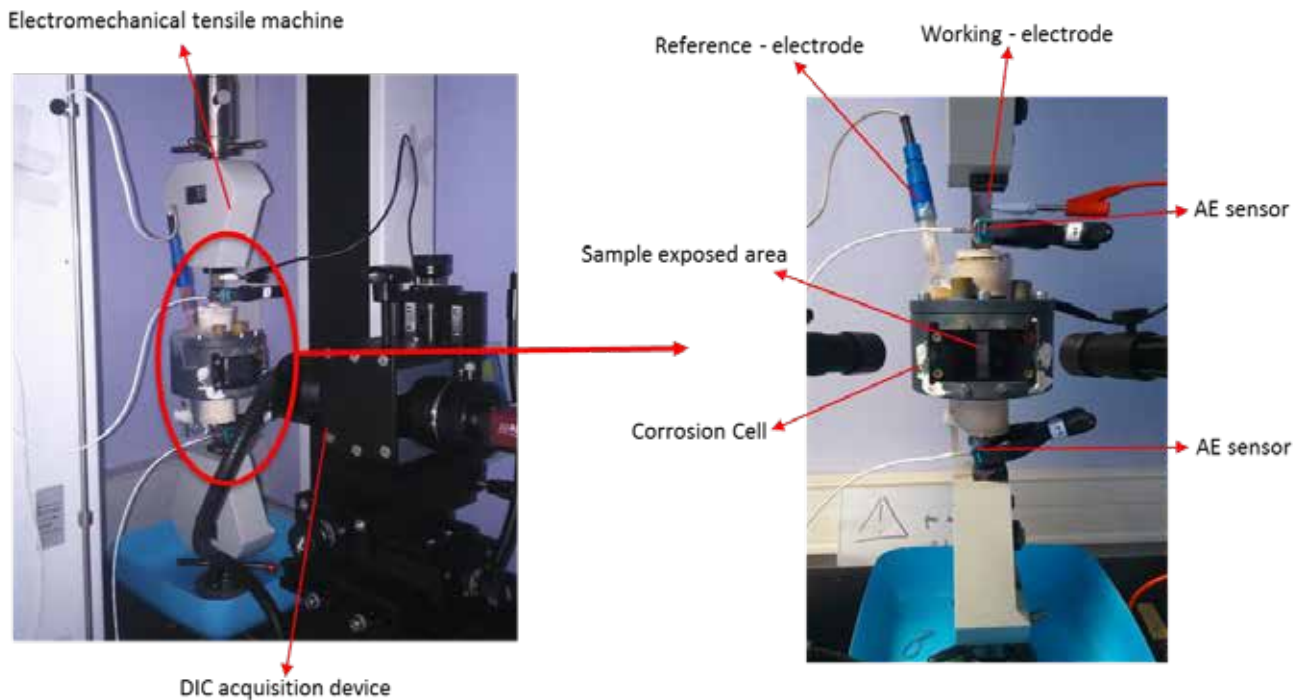


Figure 2: Experimental device used during the experiments

3. Results

Four room temperature SCC constant load tests were performed in a 10 mM $K_2S_4O_6$ (acidified to pH 3 or pH 5.3) solution and loaded until 80 % of the yield stress (tests name: CC-02-15, CC-03-15, CC-04-15, CC-07-15). One test has been conducted without loading, only under immersion condition (CI-01-15). Table 3 gathers the details of these different tests.

The experiments CC-02-15, CC-03-15 and CC-07-15 were performed under conditions where a dense crack colony propagated. Test CC-04-15 was conducted at higher pH (5.3) and a single IG-SCC defect was detected. It must be highlighted that the test CC-07-15 is different in comparison to other tests, as this test was not monitored by EN measurements.

Based on the correlation between DIC and EN results, Bolivar [24-26] has reported that the crack colony evolution could be split into 3 main stages (see Figure 3). Stage I' is representative of the lapse of time comprised from the moment when the loading started (t_0) until the detection of the first cracks by DIC (t_a). No cracks were detected by DIC throughout this initial stage, and the EN measurements reveals an intergranular attack signature (intergranular corrosion and/or anodic dissolution).

Stage II' was defined as the lapse of time between the end of the stage I' (t_a) and the moment where the crack density was maximal (t_b). This stage is mainly characterized by the detection

of superficial cracks which propagate mostly in surface. The propagation mechanism is mainly induced by the anodic dissolution of grain boundaries.

Finally, the stage III was comprised from t_b until the end of the test. Macro-cracks were observed during this stage after an increase of the cracks interaction (coalescences and shielding). Plastic mechanisms present an important implication throughout this stage (macro cracking, plastic deformation, rupture).

For AE data analysis, it was chosen to represent separately the data between $(t_0 - t_a)$, $(t_a - t_b)$ and $(t_b - \text{end of test})$. These time values were determined, based on DIC and EN results (t_a equal to 24000 seconds and t_b equal to 48000 seconds).

Table 3. Experimental characteristics of the different conducted tests (CC-02-15, CC-03-15, CC-04-15, CC-07-15 & CI-01-15).

ID test	Experimental conditions	pH	Immersion time before loading (h)	Test duration (h)
CC-02-15	MAS Alloy 600, Solution 0.01 M $K_2S_4O_6$ Loading ($0.8 \sigma_y$)	3	4	24
CC-03-15		3	1	23
CC-04-15		5.3	4	100
CC-07-15		3	1	25
CI-01-15	MAS Alloy 600, Solution 0.01 M $K_2S_4O_6$	3	No loading	113

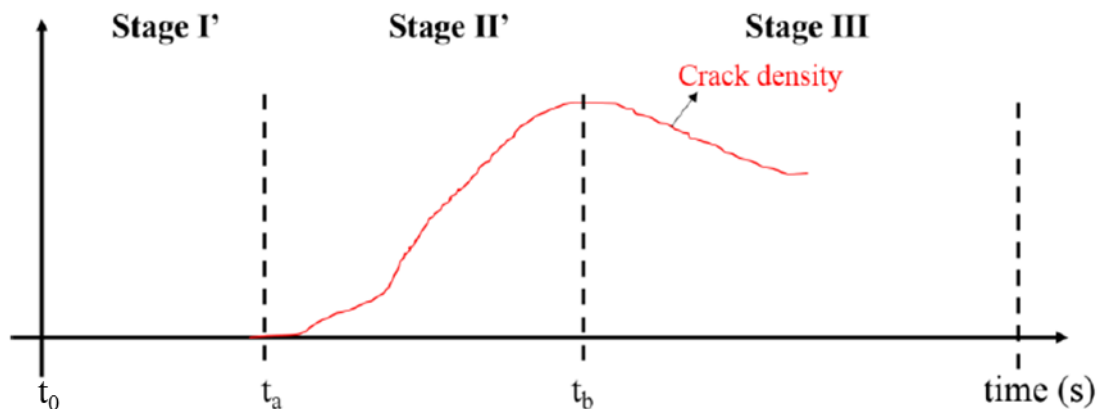


Figure 3: Representation of the different times and stages of crack colony evolution according to DIC & EN measurements [24]

The first step of the AE data processing was based on the discrimination between noise and significant signals. Table 4 presents the characteristics of noise signals (electromagnetic, high frequencies and mechanical). AE hits related to noise are mainly characterized by a hits amplitude lower than 27 dB_{AE} and a low number of counts per hit (1 count/hit). These signals were filtered from the AE analysis for the rest of the study.

Table 4. Characteristics of AE hits recorded during the different stages of crack colony evolution.

Class ID	Amplitude (dB _{AE})	Absolute Energy (aJ)	Counts	Frequency centroid (kHz)
Noise	23-26	< 0,1	1	220-320
Stage I'	24-40	0,1-10	1-20	240-300
Stage II'	24-50	<100	1-100	200-300
Stage III	24-50	<150	1-100	190-310

3.1 Stage I' (0 – 24000 seconds):

For this stage, AE data processing was performed based on following experiments: (CC-02-15, CC-03-15 and CC-03-15). These tests were carried out in similar experimental conditions.

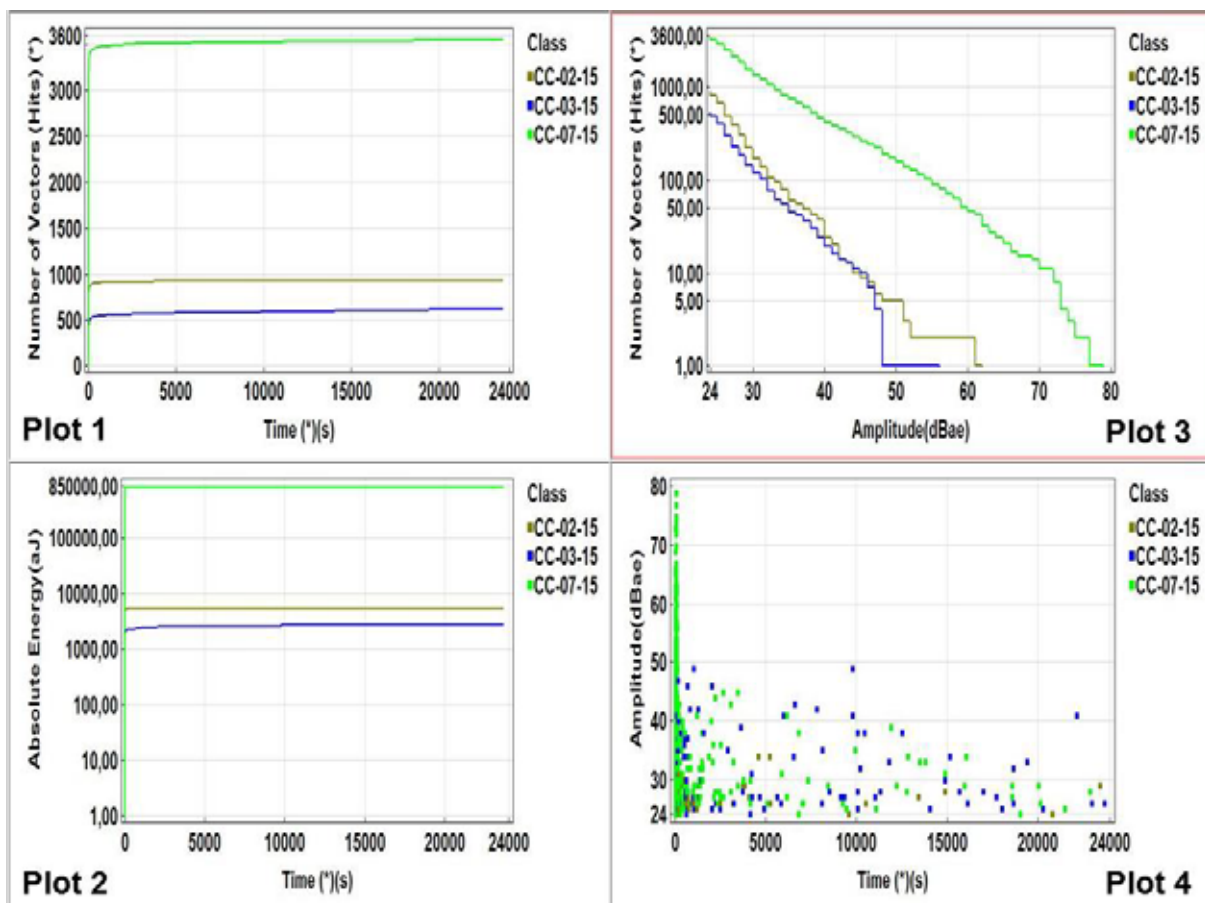


Figure 4: Filtered AE results recorded during the following tests (Stage I' [0 s - 24000 s]: CC-02-15, CC-03-15 & CC-07-15)

Plot 1: Cumulated Activity of AE hits as a function of time, Plot 2: Cumulated Intensity of AE hits as a function of time, Plot 3: AE hits number as a function of their amplitude, Plot 4: AE hits amplitude as a function of time.

Figure 4 recapitulates the AE filtered results obtained during the first stage of a crack colony evolution (stage I'). It shows the presence of an important AE activity at the beginning of the tests, which corresponds to the loading time (80% σ_y). The main part of these AE signals were induced by plastic deformation which occurred locally in the material, eventually in grain boundaries (dissolved zone after the immersion phase). The AE activity tends to decrease after the loading step, indicating a viscoplastic mechanical behavior of loaded specimens. Based on Figure 4, the test CC-07-15 presents a higher activity and intensity in comparison to the other tests CC-02-15 and CC-03-15.

3.2 Stage II' (24000 – 48000 seconds):

For this stage, AE data processing was performed based on following experiments: CC-02-15, CC-03-15 and CC-03-15 in addition to the immersion test carried out without loading (CI-01-15).

AE hits detected throughout this second stage are characterized by low and medium amplitude (24 dB_{AE} - 50 dB_{AE}). The main part of these hits presents an absolute energy lower than 10 aJ. AE activity remains constant during this stage and comparable to the AE signals detected during the constant load part of the first stage (see Figure 5).

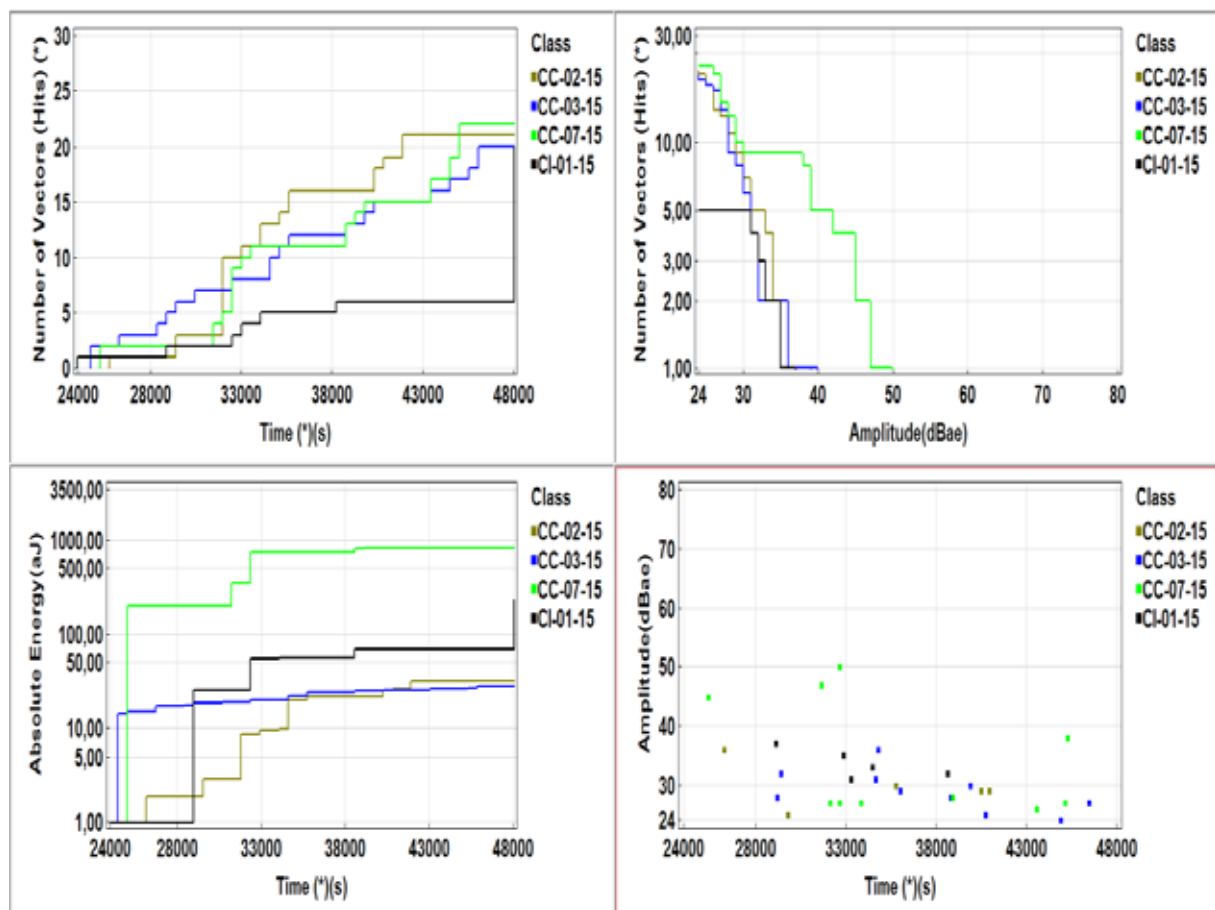


Figure 5: Filtered AE results recorded during the following tests (Stage II' [24000 s - 48000 s]: CC-02-15, CC-03-15, CC-07-15 & CI-01-15)

Plot 1: Cumulated Activity of AE hits as a function of time, Plot 2: Cumulated Intensity of AE hits as a function of time, Plot 3: AE hits number as a function of their amplitude, Plot 4: AE hits amplitude as a function of time.

These signals were compared to the signals detected during the immersion test (CI-01-15) in order to identify the source of these AE signals. A low AE emissivity was detected during the immersion test, otherwise this emissivity remains similar to the emissivity recorded during the three constant load tests (CC-02-15, CC-03-15 & CC-07-15). AE hits characterized by a low and medium amplitude were detected during these different tests (immersion and constant load tests) (see Table 4 & Figure 5).

The correlation of DIC, EN and AE results indicates that intergranular corrosion and superficial crack propagation are the emissive mechanisms of this stage with low energy hits.

3.3 Stage III (t>48000 seconds):

For this stage, we first compared the AE results obtained during the following experiments: CC-02-15 & CC-07-15, these experiments were interrupted before rupture. AE results indicate a significant increase of the AE activity and intensity, 57000 seconds after the beginning of the tests (see Figure 6). The correlation between DIC, EN and AE results indicates that this increase is induced by cracks coalescence and propagation.

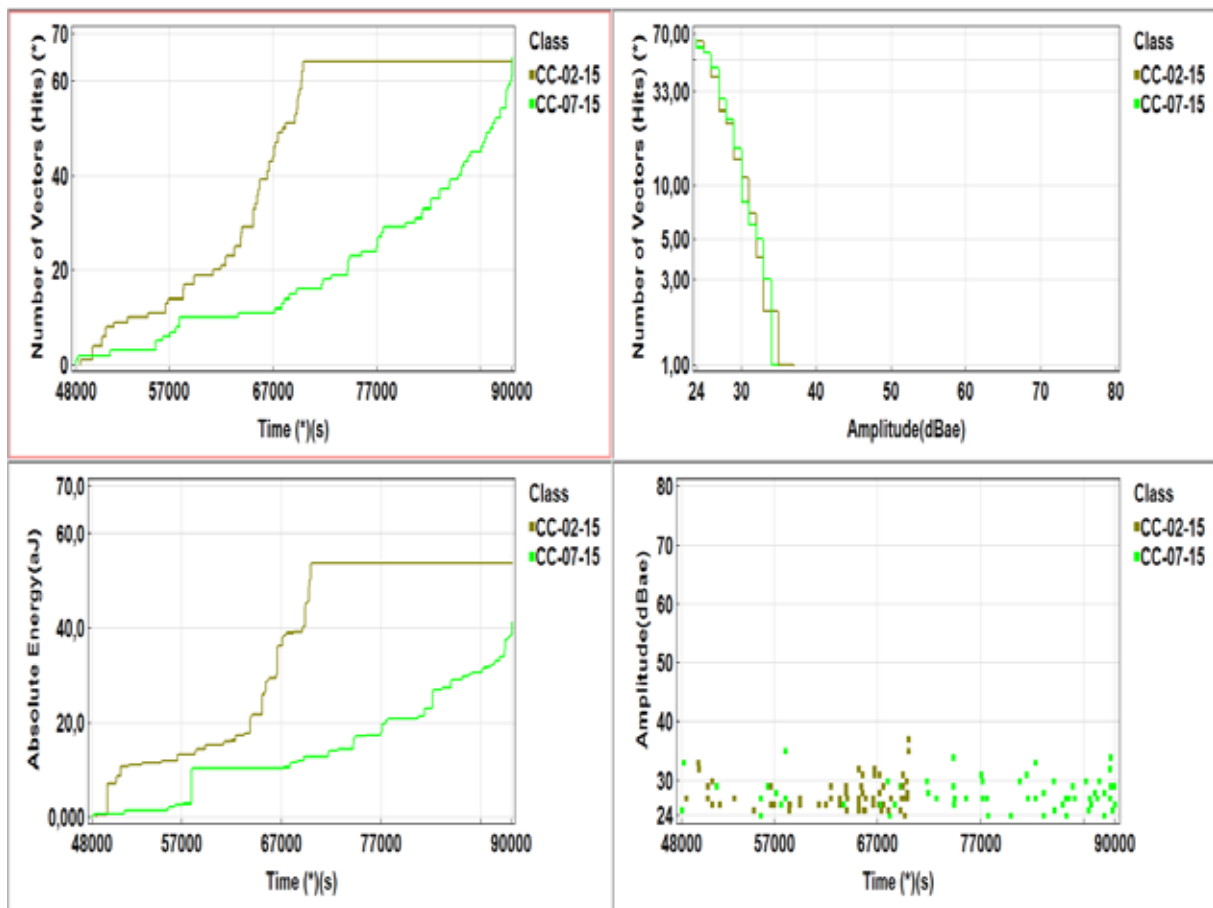


Figure 6: Filtered AE results recorded during the following tests (Stage III [t>48000 s]: CC-02-15 & CC-07-15)

Plot 1: Cumulated Activity of AE hits as a function of time, Plot 2: Cumulated Intensity of AE hits as a function of time, Plot 3: AE hits number as a function of their amplitude, Plot 4: AE hits amplitude as a function of time.

The test CC-03-15, was performed until rupture; the AE results obtained during this test are presented in Figure 7. These results indicate an AE activity increasing after 57000 seconds; this increase becomes more and more significant after 68000 seconds.

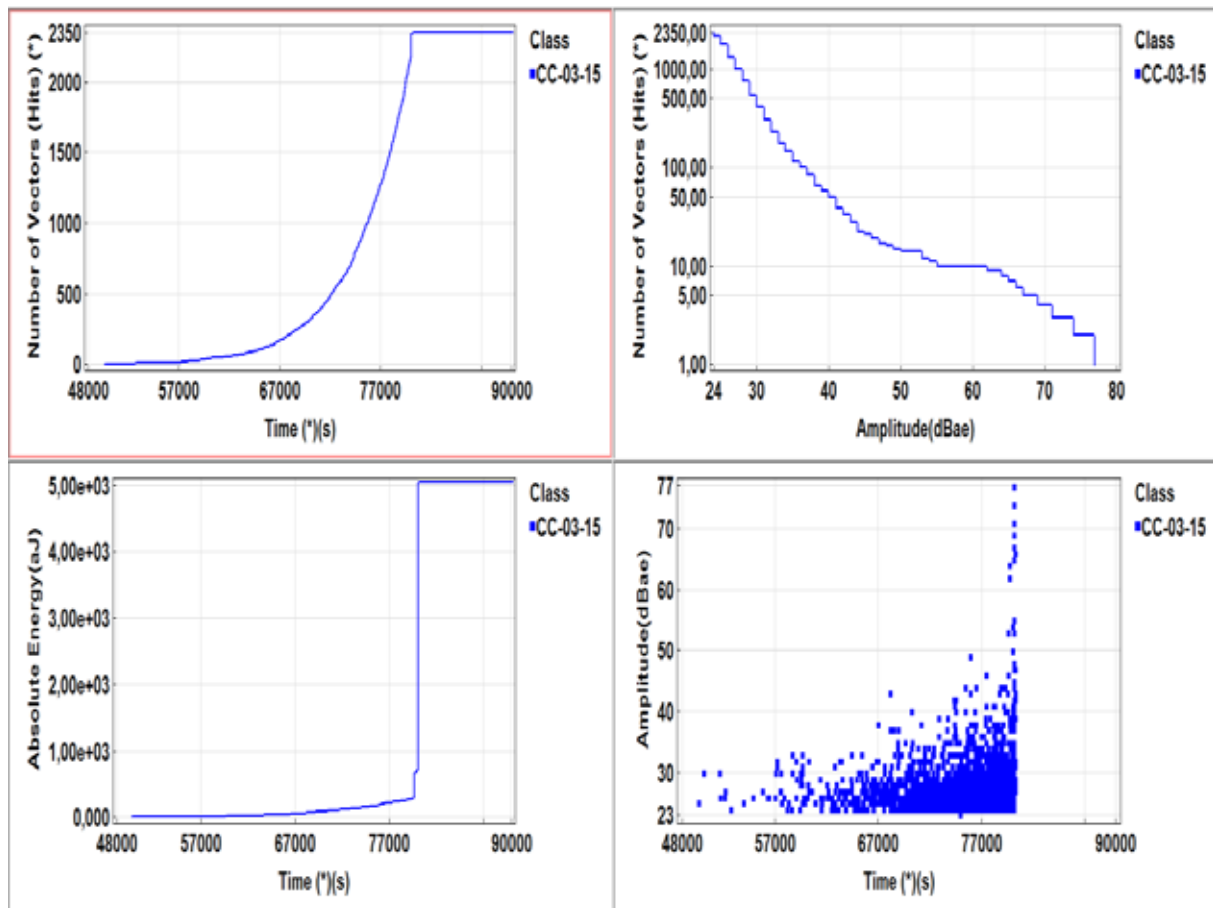


Figure 7: Filtered AE results recorded during the following tests (Stage III [$t > 48000$ s]: CC-03-15), Plot 1: Cumulated Activity of AE hits as a function of time, Plot 2: Cumulated Intensity of AE hits as a function of time, Plot 3: AE hits number as a function of their amplitude, Plot 4: AE hits amplitude as a function of time.

4. Discussion

The correlation of three different techniques (AE, EN and DIC) allows the identification of the different stages of cracks colony evolution and of the mechanisms involved in each stage. This correlation indicates that the stage I' of the crack colony evolution is mainly driven by the intergranular corrosion.

The AE activity detected during this stage is mostly induced by plastic deformation which occurred during the initial loading part. Mechanical tests monitored by AE technique of Inconel and austenitic alloys, show similar results indicating an important AE activity due to local plastic strain [14, 17]. Furthermore it must be noticed that AE activity decreases during the constant load phase without any full stabilization of AE, revealing a change in the emissive mechanism. Once the effect of the load is fully stabilized, AE activity is released by intergranular corrosion.

Multiparametric pattern recognition analysis of AE signals recorded during Stage II', indicates that these signals were closely similar to the signals recorded during the immersion test (see Figure 8). These hits were characterized by low and medium amplitude varying between 24 and 50 dB_{AE}. The hits were not very energetic and presented a frequency centroid band centered on 250 kHz (see Figure 8).

AE analysis was correlated with DIC and EN results, indicating the detection of superficial cracks during this second stage. Intergranular corrosion and superficial cracks propagation represent the active and emissive processes during this second stage ($t_a < \text{time} < t_b$).

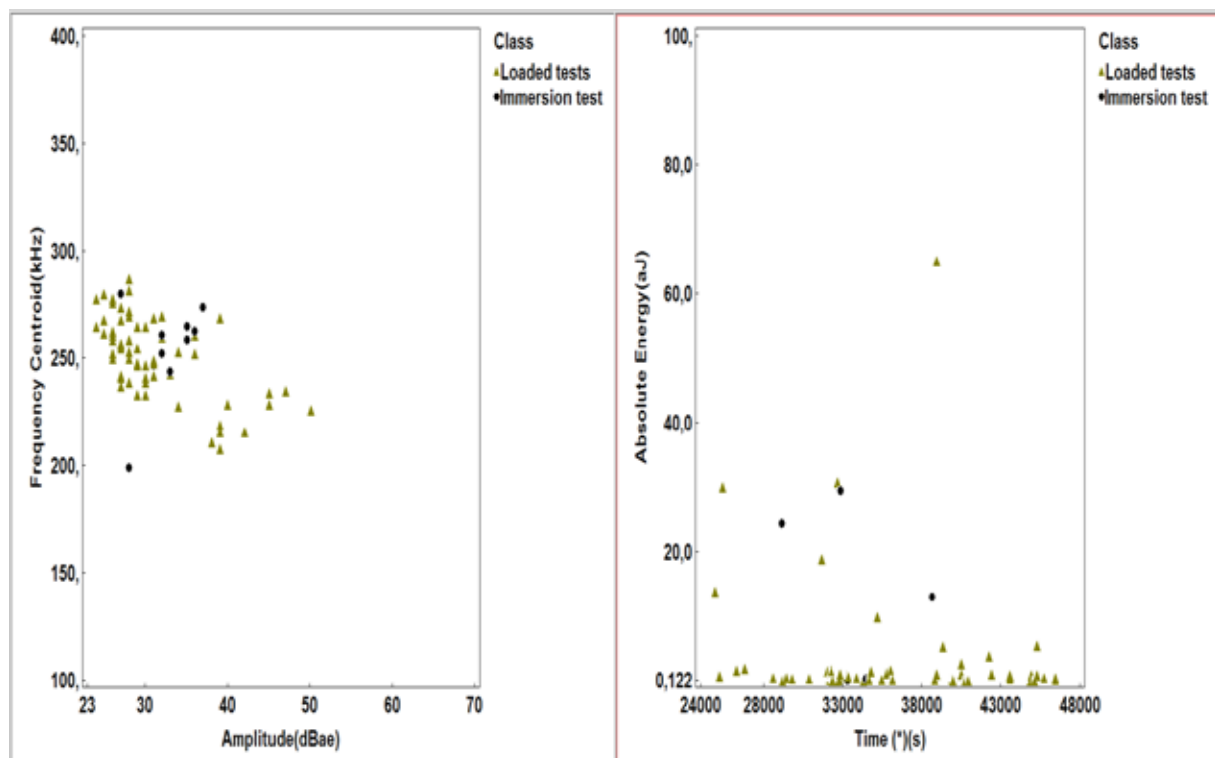


Figure 8: Frequency centroid of AE hits as function of their amplitude; Absolute energy of AE hits versus time (Stage II [24000 s - 48000 s]: Loaded tests CC-02-15, CC-03-15 & CC-07-15 – Immersion test CI-01-15).

The third stage of the crack colony evolution process is the most emissive stage and it is characterized by a significant increase of the AE activity and intensity. This AE emissivity is mainly induced by cracks propagation which results from local plastic deformation. These results confirm the interest and the sensitivity of AE technique on crack propagation detection.

In order to confirm the AE signature of plastic deformation and macro-cracking, AE results obtained during the test CC-03-15 (test conducted until rupture with an important colony of macro-cracks) and the test CC-04-15 (test with single crack due to an increase of pH) were compared. Figure 9 shows the single macro-crack observed at the end of the test CC-04-15.

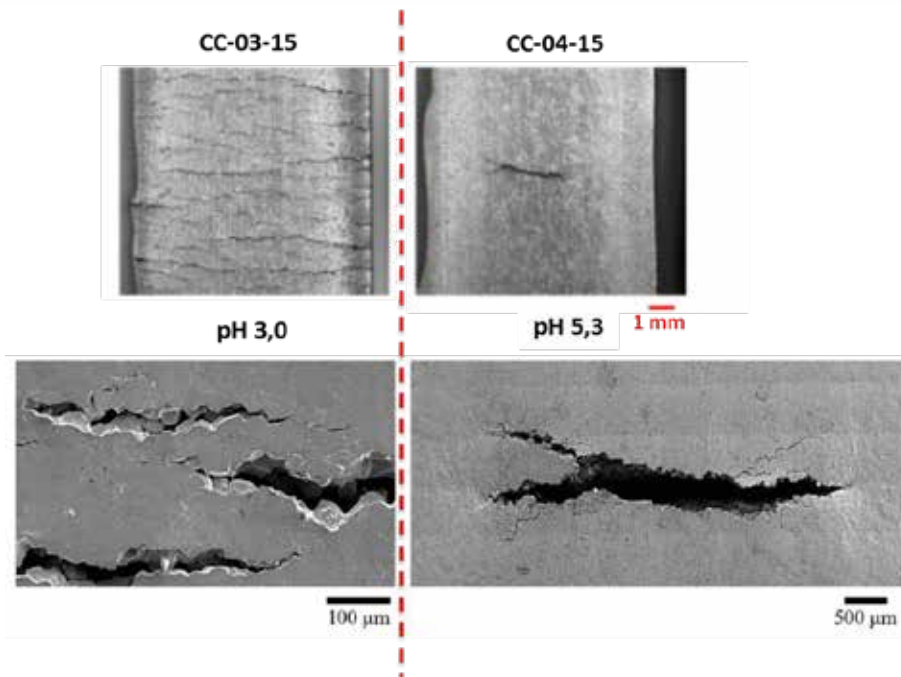


Figure 9: Optical observations and SEM images of sample surface after SCC tests under Constant Load ($0.8 \sigma_y$) of a MAS Alloy 600 sample in a 0.01 M tetrathionate solution at different pH.

The comparison of AE results recorded during these two tests (CC-03-15 & CC-04-15), is represented in Figure 10, allowing distinguishing macro-cracking signals from plastic deformation signals. For the single macro-cracking test (CC-04-15), the main part of AE signals was induced by plastic deformation mechanisms; only a few number of highly energetic AE signals were related to the macro-cracking propagation. It is notable that these high energy hits were more detected during the macro-cracking test CC-03-15, where an important colony of macro-cracks was observed.

Furthermore, it must be noticed that the AE signals recorded during the single-crack sample were closely similar to the AE signals recorded before the rupture of the multi-cracks sample (signals recorded between 57000 seconds and 80000 seconds). This indicates that these signals were released by the same mechanism (plastic deformation).

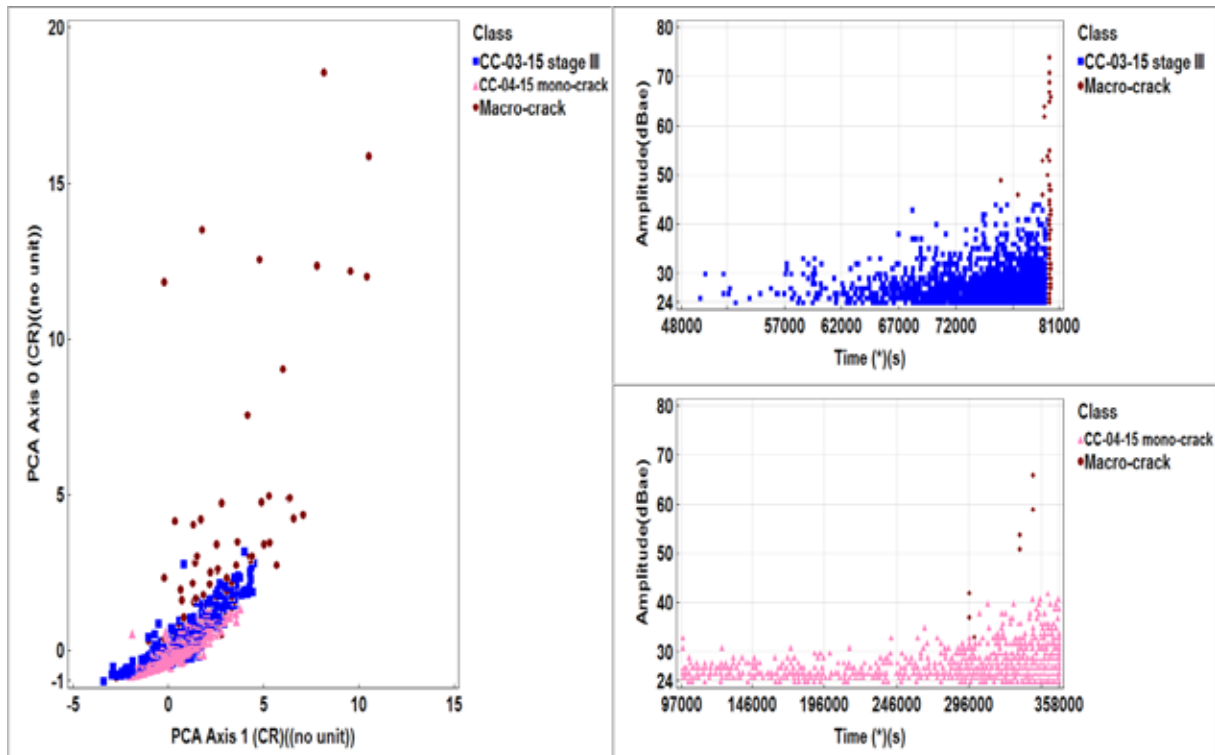


Figure 10: Multiparametric analysis and PCA (Principal Component Analysis) of AE filtered hits recorded during the tests CC-03-15 (multi-cracks) & CC-04-15 (single-crack).

5. Conclusion

Correlations between DIC, EN and AE results allowed characterizing the crack colony propagation into three different stages.

The first stage was characterized by a low acoustic emission activity and high levels of current (DC part). This result evidences active dissolution and lack of re-passivation during this stage; grain boundary dissolution affects only the surface.

In the second stage, AE activity remains constant with low energy signals. Anodic dissolution and intergranular corrosion remain the main mechanisms of this stage, in addition to some interactions between superficial cracks.

Finally, the last stage is the most emissive part of the crack colony evolution process. High energetic AE signals were detected during this stage resulting from local plastic deformation and cracks propagation and coalescence.

Associated to complementary techniques, AE is therefore a powerful tool to study and identify the different propagation steps of SCC, involving either a single crack or a colony.

Acknowledgements

The authors would like to acknowledge the National French Research Agency (ANR) for its financial support under contract MATETPRO ANR-12-RMNP-0020 (ECCOFIC project). The authors would also like to thank the different partners of this project: Institut de la Corrosion, AREVA, ANDRA and Pierre Combrade for the fruitful discussions and participations.

References:

- [1] Marcus, P., Corrosion mechanisms in theory and practice. Boca Raton; Florence: C R C Press LLC Taylor & Francis Group [Distributor], 2002.
- [2] Bataille, C. and Birraux, C., "La durée de vie des centrales nucléaires et les nouveaux types de réacteurs, Assemblée Nationale n°832, Mai 2003.
- [3] Mohanty, S., Majumdar, S. and Natesan, K., A Review of Stress Corrosion Cracking/Fatigue Modeling for Light Water Reactor Cooling System Components, Argome National laboratory, June 2012.
- [4] Leek, T. H. and Howard, I. C., An examination of methods of assessing interacting surface cracks by comparison with experimental data, *Int. J. Press. Vessels Pip.*, Vol. 68 (2), 1996, pp. 181–201.
- [5] Kamaya, M. and Haruna, T., Crack initiation model for sensitized 304 stainless steel in high temperature water, *Corros. Sci.*, vol. 48 (9), 2006, pp. 2442–2456.
- [6] Wang, Y.-Z., Ebtehaj, K., Hardie, D. and Parkins, R. N., The behaviour of multiple stress corrosion cracks in a Mn-Cr and a Ni-Cr-Mo-V steel: Metallography, *Corros. Sci.*, vol. 37 (11), 1995, pp. 1651–1675.
- [7] Leek, T. H. and Howard, I. C., Rules for the assessment of interacting surface cracks under mode I load, *Int. J. Press. Vessels Pip.*, vol. 60 (3), 1994, pp. 323–339.
- [8] Leek, T. H. and Howard, I.C., Estimating the elastic interaction factors of two coplanar surface cracks under mode I load, *Int. J. Press. Vessels Pip.*, vol. 60 (3), 1994, pp. 307–321.
- [9] Pugh, E.N., Progress toward understanding the stress corrosion problem, *CORROSION*, Vol. 41 (9), 1985, pp. 517-526.
- [10] Eitzen, D.G. and Wadley, H.N.G., Acoustic emission: establishing the fundamentals, *NBS Journal of research*, Vol. 89 (1), 1984, pp. 75-100.
- [11] Yuyama, S., Kishi, T. and Hisamatsu, Y., AE analysis during corrosion and corrosion fatigue process, *Journal of AE*, Vol. 2 (1/2), 1983, pp. 71-93.
- [12] Pollock, A.A., Acoustic emission capabilities and applications in monitoring corrosion, *Corrosion Monitoring in Indu*, ASTM-STP Public.908 Philadelphia, 1986, pp. 30-42.
- [13] Cassagne, T., Caron, D., Daret, J., Proust, A., Mazille, H., Turluer, G. and Boulanger, D., Initial results on the stress corrosion cracking monitoring of alloy 600 in high temperature water using acoustic emission, *Ninth Intl. Conf. on Environmental Degradation of Materials in Nuclear Power Systems-Water Reactors*. Newport Beach, CA., 1999, pp. 225-234.

- [14] Proust, A., Mazille, H., Fleischmann, P. and Rothea, R., Characterization by AE technique of emissive phenomena during stress corrosion cracking of stainless steels, *Journal of AE*, Vol.18-19, 2001, pp. 19229-19240.
- [15] Frégonèse, M., Idrissi, H., Mazille, H., Renaud, L. and Cetre, Y., Initiation and propagation steps in pitting corrosion of austenitic stainless steels: monitoring by acoustic emission, *Corrosion Science*, Vol. 43, 2001, pp. 627-641.
- [16] Cakir, A., Tuncell, S. and Aydin, A., AE response of 316L SS during SSR test underpotentiostatic control, *Corrosion Science*, Vol. 41(6), 1999, pp. 1175-1183.
- [17] Proust, A., Mazille, H., Fleischmann, P. and Rothea, R., Intl. Conf. Corrosion Deformation-Interactions, Fontainebleau, 1992, pp. 829 – 839.
- [18] Ferrer, F., Idrissi, H., Mazille, H., Fleischmann, P. and Labeeuw, P., On the potential of acoustic emission for the characterization and understanding of mechanical Damaging during abrasion–corrosion processes, *Wear*, Vol. 231(1), June 1999, pp. 108-115.
- [19] Ferrer, F., Idrissi, H., Mazille, H., Fleischmann and P., Labeeuw, P., A study of abrasion – corrosion of AISI 304L austenitic stainless steel in saline solution using acoustic emission technique, *NDT & E International*, Vol. 33 (6), September 2000, pp. 363-371.
- [20] Mansfield, F. and Stocker, P.J., Acoustic Emission from Corroding Electrodes, *Corrosion Engineers*, Vol. 35(12), 1979, pp. 541-544.
- [21] Saenkhum, N., Prateepasen A. and Kaewtrakulpong P., Classification of Corrosion detected by AE signal, IMECE 2003, Washington, D.C., Nov., 2003.
- [22] Prateepasen, A., Pitting corrosion using Acoustic Emission, Pitting corrosion Nasr Bensalah (Ed.), InTech, March 2012, pp. 43-60.
- [23] Yuyama, S., Fundamental Aspects of Acoustic Emission Applications to the Problems caused by corrosion, presented at the Corrosion Monitoring in Industrial Plants Using Nondestructive Testing and Electrochemical Methods, Philadelphia, vol. ASTMSTP 908, 1986, pp. 43–74.
- [24] Bolivar, J., Experimental study of the behavior of colonies of environmentally-assisted short cracks by Digital Image Correlation, Acoustic Emission and Electrochemical Noise, INSA de Lyon, MATEIS laboratory - Université de Lyon, Thesis defended in July 2017.
- [25] Bolivar, J., Nguyen, T. T., Shi, Y., Frégonèse, M., Réthoré, J., Adrien, J. King, A., Buffiere, J.Y. and Huin, N., Multiple cracks interactions in Stress Corrosion Cracking: in-situ observation by Digital Image Correlation and Phase Field Modeling, Proceedings of the 18th International Conference on Environmental Degradation of Materials in Nuclear Power Systems – Water Reactors, EDM 2017.
- [26] Bolivar, J., Frégonèse, M., Réthoré, J., Duret-Thual, C. and Combrade, P., Evaluation of multiple stress corrosion crack interactions by in-situ Digital Image Correlation, *Corrosion Science*, Vol. 128, 2017, pp. 120-129.

64 - Acoustic Emission from gas bubble nucleation and breaking away from a flat surface

Volodymyr KIETOV¹, Marcel MANDEL¹, Lutz KRÜGER¹, Alexei VINOGRADOV²

¹*Institute of Materials Engineering, TU Bergakademie Freiberg
Gustav-Zeuner str. 5, D-09599, Freiberg, Germany*

²*Departement of Mechanical and Industrial Engineering, Norwegian University of Science
and Technology - NTNU
Richard Birkelandsvei 2B, N-7491, Trondheim, Norway*

E-mail of corresponding author Volodymyr.Kietov@iwt.tu-freiberg.de

Abstract:

Gas evolution is an important source of acoustic emissions (AE) in many chemical and electrochemical reactions. Specifically, AE accompanies gas evolution during uniform and pitting corrosion of metals. Therefore, monitoring of gas evolution provides valuable information on degradation processes and their rates during corrosion. In the present work, gas evolution on a steel surface was investigated in detail to get the deeper insight into the properties of AE sources. The polished surface of the plane steel sample was used as an electrode for water electrolysis. Evolution of hydrogen and oxygen bubbles was filmed via a long-distance microscope with the high-speed-camera operating at a frame rate up to 100 000 fps. The processes of bubbles nucleation, merging and breaking away from the surface were observed and analysed frame by frame. The possible sources for acoustic emissions are associated with merging and breaking away of gas bubbles. The characteristic futures of the AE generated by gas evolution were estimated.

1. Introduction

Gas evolution is an important source of acoustic emissions (AE) in many chemical and electrochemical reactions. Specifically, AE accompanies gas evolution during uniform and pitting corrosion of metals. The acoustic emissions connected with the corrosion processes have been studied in many works. As a main result, the correlation has been established between the AE rate and the corrosion rate [1–6]. However, the details of relations between the AE parameters due to gas evolution are still missing and are of great interest. In several attempts, AE from gas bubbles formation was characterized by means of various parameters such as rise time, amplitude and duration [7–10]. Two types of acoustic signals associated with gas evolution were found: the low-amplitude resonant signals with the long duration and rise time and burst-type transients having the short rise time and duration and greater energy. The first type signals were attributed to the hydrogen formation inside the pits in case of localized corrosion [7–9], while the second category of signals was linked to the gas formation in case of the uniform corrosion [7,10]. A more elaborated approach implements the analysis of AE spectral features. It was noticed that evolution of the hydrogen bubbles during pitting corrosion was accompanied by discrete AE signals with the frequency peak in the range 100 – 120 kHz [11,12]. The resonant signals with the frequency of about 150 kHz were observed

in [13] in relation to the same process. On the other hand, in [14] the frequency maximum was used for discrimination of the AE sources during corrosion of the austenitic stainless steel. Acoustic emission produced by hydrogen bubbles formation during pitting corrosion was observed in the frequency range of 120 – 350 kHz whereas the signals with peak frequencies in the 120 – 450 kHz range were recorded during uniform corrosion. Similarly, on the basis of the frequency peak position the discrimination between different corrosion processes in aluminum was performed in [15,16]. Hydrogen formation was claimed to produce the AE signals in the range of 200 – 300 kHz. Both hydrogen and oxygen formation in the course of potentiodynamic polarization of the stainless steel generated the AE signals with the peak frequency of 100 – 300 kHz [10]. In [17] the AE signals from corrosion pitting of stainless steel were divided into 4 categories with respect to their waveforms. Some waveforms were similar to those described above but none was related to gas formation. As a resume, understanding of phenomenology of acoustic emission caused by gas evolution in corrosion processes is incomplete as yet. To get a deeper insight into this phenomenon, gas bubbles formation on the metal surface has to be investigated in more details.

The self-resonant frequency ν of the gas bubble inside the liquid was calculated in [18] for the first time and then was frequently used in relevant publications [12,14,19,20] in the following form:

$$\nu = \left(\frac{1}{\pi D_0}\right) \left(\frac{3KP_0}{\rho}\right)^{1/2} \quad (1)$$

where D_0 is the bubble equilibrium diameter, P_0 is a static pressure, ρ is the density of the liquid and K is the so-called polytropic index, which takes values between unity and the ratio of heat capacities at constant pressure and volume, i.e. is $K = 1.4$ at room temperature and atmospheric pressure.

The resonant frequencies calculated for bubble diameters ranging from 10 μm up to 1 mm, which are commonly observed in corrosion studies, are shown in Fig. 1.

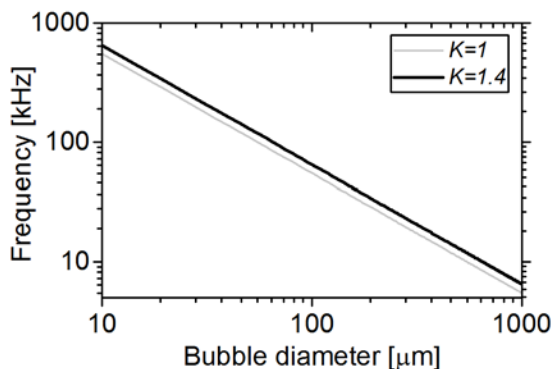


Fig. 1. Resonance frequencies of the hydrogen bubbles according to Eq.(1)

It is evident that the calculated self-frequency range corresponds to the frequency response of the most common acoustic transducers. The gas bubbles with the diameters smaller than 30 μm are rare. Thus, the upper frequency limit of ca. 400 kHz found in literature can be reasonably explained. The lower frequency of the common AE transducers is often limited to 20 kHz. Therefore, according to the calculation given above, the bubbles with the diameter greater than ca. 400 μm should not produce AE detectable by conventional transducers.

2. Description of work

Hydrogen bubbles formation occurs on the metal surface during the electrolysis of water. The austenitic steel plate with the thickness of 3 mm was ground and polished up to surface roughness of 1 μ m. The specimen's surface was covered with the isolating tape so that only a small area was exposed to the electrolyte. This ensured that all processes occurred within the view field of the high-speed camera used for direct observations of gas production. The schematics of the measurement unit is represented in Fig. 2.

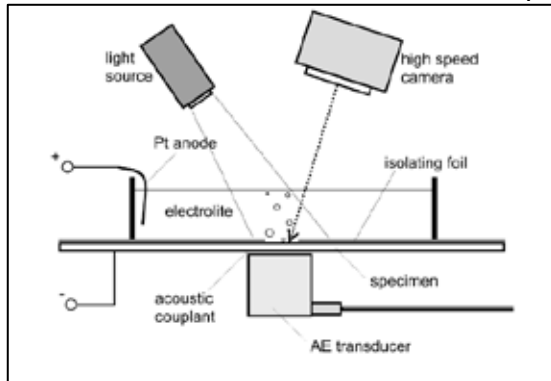


Fig. 2. Schematics of the measurement unit

Acoustic emissions were acquired using the PCI-2 system by Physical Acoustic Corporation (PAC, USA). The continuous waveform recording mode was implemented with the sampling frequency of 2 MHz. Two different transducers - WD from PAC, and 1045D from Fujicera - were connected to the preamplifier PAC 2/4/6 operated at 60 dB gain. The measurements with different transducers were performed separately.

The high-speed camera (Photron Fastcam SA-Z) operated at the shutter speed of 80000 frames per second with the resolution of 384 x 256 pixels and 108,667 pixel per millimeter. The field of view was calibrated using the stage micrometer to provide the measurement of the observed bubbles diameter. Using this way of measurement, the accuracy of bubble dimension measurements was $\pm 10 \mu$ m. The camera's TTL trigger output was used to synchronize the acoustic stream with the camera record. When the camera started recording, the TTL output sent the triggering signal to the PCI-2 board and the waveform streaming acquisition started simultaneously.

3. Results

During the experiments the metal surface was usually covered with gas bubbles. Direct observations revealed that the predominant process controlling the generation of acoustic emissions was the merging of bubbles. The breaking away of a gas bubble without preliminary merging with the other bubble was observed rarely. This event generated the waveform similar that observed during the bubble merging. Furthermore, it was noticed that the nucleation of the new bubble on the surface did not produce any detectable AE signal. An example of merging of two hydrogen bubbles is shown in Fig. 3a, and the corresponding acoustic signal in Fig. 3b.

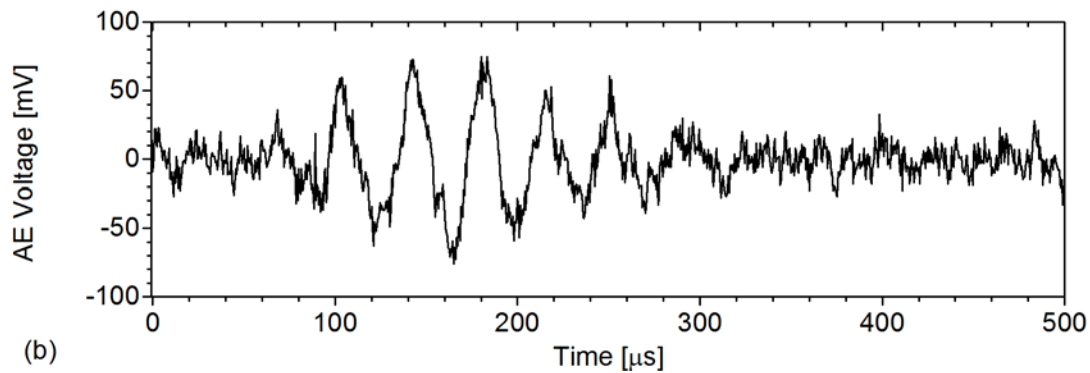
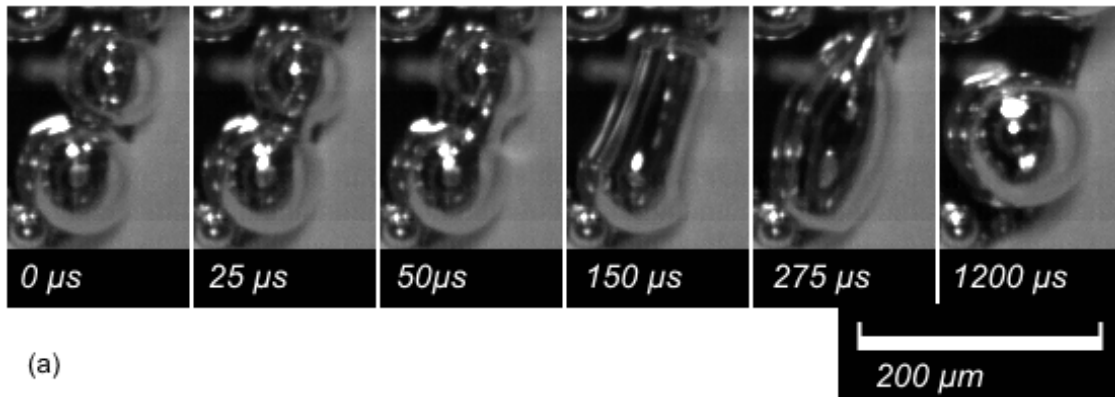


Fig. 3. Merging two hydrogen bubbles (a), and the corresponding acoustic signal (b), transducer Fujicera 1045D.

AE signals produced by the bubble merging process had relatively low amplitudes. Importantly is that the correlation between the amplitude of the signal and the final size of the merged bubble was not evidently observed, see Fig. 4, for example.

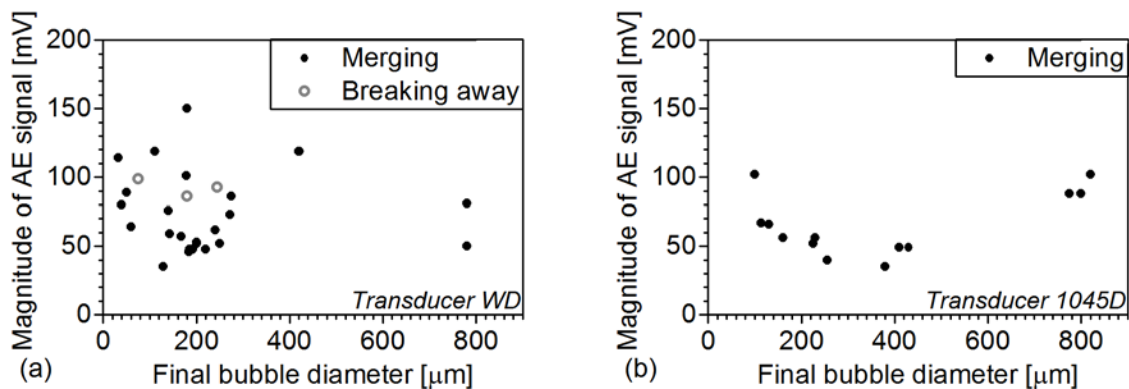


Fig. 4. Amplitude of the acoustic signals and the final size of the merged bubbles: (a) transducer WD by PAC; (b) transducer 1045 by Fujicera.

4. Discussion

In order to identify the AE parameters resulting from gas evolution, the collected AE signals were analyzed by means of their spectral characteristics. At first, the peak frequency - the frequency corresponding to maximum magnitude in the FFT- spectrum, was found. At second, the median frequency, f_m , of the Fourier power spectrum $G(f)$ was computed by definition as:

$$\int_0^{f_m} G(f)df = \int_{f_m}^{\infty} G(f)df \quad (2)$$

where f is frequency.

The dependence of the median frequency and the peak frequency on the final diameter of the merged bubbles was hardly to found when AE was acquired by the WD transducer, Fig. 5. Most of the AE events concentrated in two frequency bands, from 100 to 200 kHz and from 20 to of 70 kHz. The frequencies higher than 200 kHz were unlikely to observe. Most of the values were markedly higher than it could be expected from Eq. (1). It was evident, that the spectral characteristics of the used transducer affected the results of the measurements quite substantially.

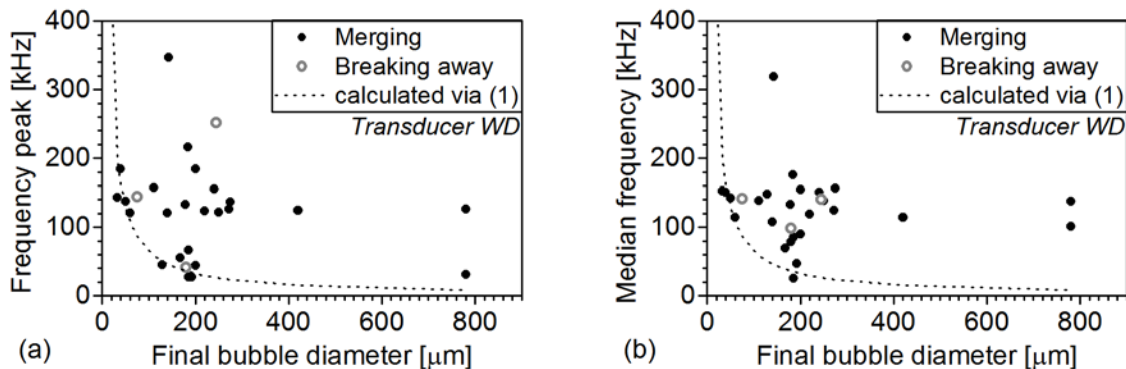


Fig. 5. (a) frequency peak and (b) median frequency of the signals collected by the transducer PAC WD.

When the measurements were repeated under similar conditions, but using the Fujicera broadband 1045D transducer, unlike the above results, the frequency peak and median frequency appeared to be lower for AE signals produced by larger bubbles, Fig. 6. This effect was more pronounced for the peak frequency than for the median frequency.

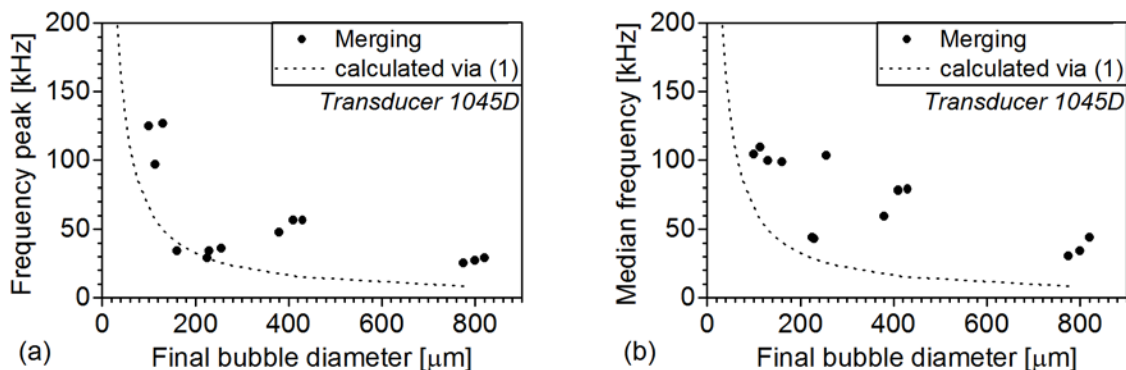


Fig. 6. (a) frequency peak and (b) median frequency of the signals collected by the transducer Fujicera 1045D.

Nevertheless, the observed characteristic frequencies were markedly higher than those expected from calculations by Eq. (1). This could be explained by the fact that Eq. (1) describes the vibrations of the ideal spherical bubble. During merging, the bubbles deform heavily, as illustrated in Fig. 3. Thus, Eq. (1) provides only a rough approximation of the expected frequency. On the other hand, the non-flat multiresonant frequency response of AE transducers has to be taken into account when experimental data are compared with calculations.

5. Conclusion

The conducted in situ rapid video observations synchronized with AE measurements allowed to clarify the AE features related to the gas bubbles evolution on the metal surface. Main AE sources were associated with gas bubble merging and breaking away from the surface. No AE signals corresponding to the nucleation of a gas bubble were observed in the present work.

The size of the gas bubbles cannot be simply correlated with the AE amplitude. However, the correlation does exist between the AE characteristic frequency and the size of bubbles. The larger bubbles tend to produce the AE signal with the lower peak frequency in the power spectrum. A strong distortion of the spherical form of bubbles during merging made the exact prediction of the characteristic frequency impossible. This frequency can be only approximately estimated from the bubble diameter. The nonlinearity of the transducer frequency response significantly affects the results of measurements, and therefore the judicious choice of sensor is of key importance if any quantitative characterization of the gas bubble evolution is aimed.

Acknowledgement

The authors gratefully acknowledge for the financial support of this study by the German Research Foundation as part of the Collaboration Research Centre 799 "TRIP-Matrix Composites", subproject B6.

6. References

- [1] Kasai N, Utatsu K, Park S, Kitsukawa S, Sekine K. Correlation between corrosion rate and AE signal in an acidic environment for mild steel. *Corrosion Science* 2009;51(8):1679–84.
- [2] Jones RH, Friesel MA. Acoustic Emission During Pitting and Transgranular Crack Initiation in Type 304 Stainless Steel. *Corrosion* 1992;48(9):751–8.
- [3] Skal's'kyi VR, Nazarchuk ZT, Dolins'ka IY, Yarema RY, Selivonchyk TV. Acoustic-Emission Diagnostics of Corrosion Defects in Materials (a Survey). Part. 1. Detection of Electrochemical Corrosion and Corrosion Fatigue. *Mater Sci* 2017;53(3):295–305.
- [4] Kim Y, Fregonese M, Mazille H, Féron D, Santarini G. Ability of acoustic emission technique for detection and monitoring of crevice corrosion on 304L austenitic stainless steel. *NDT & E International* 2003;36(8):553–62.
- [5] Rettig TW, Felsen MJ. Acoustic Emission Method for Monitoring Corrosion Reactions. *Corrosion* 1976;32(4):121–6.

- [6] Seah K, Lim KB, Chew CH, Teoh SH. The correlation of acoustic emission with rate of corrosion. *Corrosion Science* 1993;34(10):1707–13.
- [7] Fregonese M, Idrissi H, Mazille H, Renaud L, Cetre Y. Initiation and propagation steps in pitting corrosion of austenitic stainless steels: Monitoring by acoustic emission. *Corrosion Science* 2001;43(4):627–41.
- [8] Fregonese M, Idrissi H, Mazille H, Renaud L, Cetre Y. Monitoring pitting corrosion of AISI 316L austenitic stainless steel by acoustic emission technique: Choice of representative acoustic parameters. *Journal of Materials Science* 2001;36(3):557–63.
- [9] Xu J, Wu X, Han E-H. Acoustic emission during pitting corrosion of 304 stainless steel. *Corrosion Science* 2011;53(4):1537–46.
- [10] Mandel M, Kietov V, Dubberstein T, Krüger L. The Potentiodynamic Polarisation of a High-Alloy Steel—An Analysis by Acoustic Emission Testing and Long-Distance Microscopy. *Electrochimica Acta* 2017;240:350–60.
- [11] Calabrese L, Galeano M, Proverbio E, Di Pietro D, Cappuccini F, Donato A. Monitoring of 13% Cr martensitic stainless steel corrosion in chloride solution in presence of thiosulphate by acoustic emission technique. *Corrosion Science* 2016;111:151–61.
- [12] Wu K, Jung W-S, Byeon J-W. Acoustic Emission of Hydrogen Bubbles on the Counter Electrode during Pitting Corrosion of 304 Stainless Steel. *Mater. Trans.* 2015;56 :587–92.
- [13] Wu K, Jung W-S, Byeon J-W. In-situ monitoring of pitting corrosion on vertically positioned 304 stainless steel by analyzing acoustic-emission energy parameter. *Corrosion Science* 2016;105:8–16.
- [14] Jirarungsatian C, Prateepasen A. Pitting and uniform corrosion source recognition using acoustic emission parameters. *Corrosion Science* 2010;52:187–97.
- [15] Bernard J, Boinet M, Chatenet M, Dalard F. Contribution of the Acoustic Emission Technique to Study Aluminum Behavior in Aqueous Alkaline Solution. *Electrochem. Solid-State Lett.* 2005;8:E53.
- [16] Boinet M, Bernard J, Chatenet M, Dalard F, Maximovitch S. Understanding aluminum behaviour in aqueous alkaline solution using coupled techniques. *Electrochimica Acta* 2010;55(10):3454–63.
- [17] Shiwa M, Masuda H, Yamawaki H, Ito K, Enoki M. *In-Situ* Observation and Acoustic Emission Analysis for Corrosion Pitting of MgCl₂ Droplet in SUS304 Stainless Steel. *Mater. Trans.* 2012;53(6):1069–74.
- [18] Minnaert M. XVI. On musical air-bubbles and the sounds of running water. *The London, Edinburgh, and Dublin Philosophical Magazine and Journal of Science* 2009;16(104):235–48.
- [19] Leighton TG, Fagan KJ, Field JE. Acoustic and photographic studies of injected bubbles. *Eur. J. Phys.* 1991;12(2):77–85.
- [20] Leighton TG, Lingard RJ, Walton AJ, Field JE. Acoustic bubble sizing by combination of subharmonic emissions with imaging frequency. *Ultrasonics* 1991;29(4):319–23.

69 - Application of AE technique and thermography for assessment of sludge volume inside crude oil storage tanks

Ireneusz Baran ¹, Tomasz Dunaj ¹, Marek Nowak ¹

¹ Office of Technical Inspection (UDT), ul. Szczesliwicka 34, 02-353 Warsaw, Poland
Central Laboratory of Technical Inspection (CLDT)

Abstract:

When crude oil is stored in large tanks, invariably high-molecular-weight organic sediments (paraffin) are deposited but the resulting sediments contains also solid particles (sand, silt, corrosion products, etc.) and also water. After some period of in-service of tank, these deposits build up to form a sludge, which causes a reduction in the storage capacity. These high in hydrocarbons a valuable raw material could be proper recovered and recycled back to the refining process. Therefore, it is significant to know the sludge characteristics shape and volume to define the best form of treatment (maintenance of tank for control of level of sludge) and removal method (in case of out of service and opening of tank). The knowledge about volume and shape of such sludge inside tanks is important for user of tank farm due to a reasons such as:

- maintenance of storage tanks and control/monitoring of level of sludge inside them,
- when conventional treatments are used to remove crude oil sludge, there is a potential for high environmental impact, so the choose of the method of cleaning is very essential,
- most of design of tanks is with floating roofs, what in case when inside tank is high level of sludge could cause problems and/or damage of roof for low level stored product.

In this paper are presented AE and thermography techniques for assess of level, volume and shape of sludge inside storage tank. Thermography method is used to assess the level of sludge (heights) along the storage tank shell. AE technique is used in this case in different way than normally purposes. There is used specific layout of sensors on the wall and roof of the tank. The sensors generate of AE pulses according to established algorithm, which allows to record AE signals were caused the waves propagation and waves reflection (including from sludge) in storage product between sensors. Under measured differences in time of wave propagation are evaluated heights of sludge in various points inside on the bottom of tank.

In 2017 Office of Technical Inspection (UDT) opened the project to develop a system for assessing of the level, volume and shape of sludge inside crude oil storage tanks, using AE technique and thermography. As part of the project, UDT has started cooperation with company PERN S.A. the national and regional leader in oil logistics.

keywords: aboveground storage tank, sludge, crude oil, acoustic emission technique, thermography

1. Introduction

When crude oil is stored in large tanks, invariably high-molecular-weight organic sediments (paraffin) are deposited but the resulting sediments contains also solid particles (sand, silt, corrosion products, etc.) and also water. After some period of in-service of tank, these deposits build up to form a sludge, which causes a reduction in

the storage capacity. These high in hydrocarbons a valuable raw material could be proper recovered and recycled back to the refining process. Therefore, it is significant to know the sludge characteristics shape and volume to define the best form of treatment (maintenance of tank for control of level of sludge) and removal method (in case of out of service and opening of tank). The knowledge about volume and shape of such sludge inside tanks is important for user of tank farm due to a reasons such as:

- maintenance of storage tanks and control/monitoring of level of sludge inside them,
- when conventional treatments are used to remove crude oil sludge, there is a potential for high environmental impact, so the choose of the method of cleaning is very essential,
- most of design of tanks is with floating roofs, what in case when inside tank is high level of sludge could cause problems and/or damage of roof for low level stored product.

In this paper are presented AE and thermography techniques for assess of level, volume and shape of sludge inside storage tank.

2. Project of the system for assess of the sludge inside storage tanks

The origin and the reasons of the work are based on the following needs:

- expectations from users/owners of tank farms (fuel bases with crude oil) – storage tanks with crude oil require monitoring and good maintenance practice to keep sludge from becoming the problem,
- AE testing agency/laboratory need to have knowledge about level of sludge inside storage tank – necessity to assess the level of sludge before starting AE testing of storage tank bottom according to procedures and standards.

In 2017 Office of Technical Inspection (UDT) opened the project to develop a system for assessing of the level, volume and shape of sludge inside crude oil storage tanks, using AE technique and thermography. As part of the project, UDT has started cooperation with company PERN S.A. the national and regional leader in oil logistics. The goal of the project is to build up a concept and prototype system to assess the level and volume of sludge at the bottom of an crude oil storage tank. In principle, the system will use several research methods:

- acoustic emission in various measurement methods,
- evaluation of temperature field using thermography method and temperature measurement by non-contact method.

So far in frame of the project, a number of measurement procedures have been developed, i.e. tests using combined measurement methods: acoustic emission methods and thermographic methods together with contactless temperature measurement. The purpose of the tests carried out according to these procedures is to collect measurement data of heights of sludge at points along the wall and on the bottom inside the tank. Collected data in the form of a measurement database allow

next for spatial visualization (map of sediments) and assessment of the level and volume of sludge on the bottom of the storage tank.

3. Thermography and temperature measurement for evaluation of sludge level

The use of thermography to assess the level of sludge along the storage tank shell is already a known method and described many times in various publications. Temperature differences are caused of differences in the density of mediums and, as a result, their thermal properties, which allows to determine the transition line from liquid crude oil to solidified sediments on the bottom. It should be noted that it is not always possible to use thermographic tests to determine the sludge line. For example, in the case of double-shell tanks, due to the specific thermal conditions in the interstitial space, it is sometimes necessary to use conventional methods of wall temperature measurement (eg, contactless method), combined with the appropriate method of evaluation of the temperature field. As part of the project, a series of thermographic and temperature measurements were carried out to determine the sludge line along the storage tank's wall. In fig. 1 below is presented the example of thermal image of tank with sludge on the bottom.

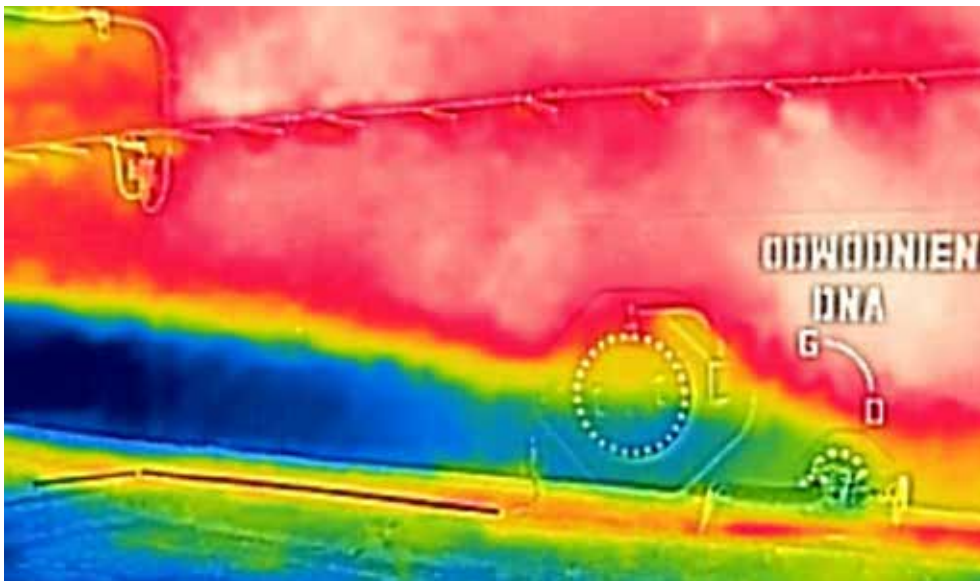


Fig 1. Thermal image of tank wall with visible sludge line

The measurement of the level of sludge along the wall on the circumference of the tank consists in assessing the temperature field every 3-5 m, as well as in the places where equipment (mainly pipelines and mixers) are present on the wall. After determining the heights of sediments at the specified points, a profile of sludge along the wall is drawn as shown in figure 2. Obtained measurement data of sludge heights are collected in the measurement database.

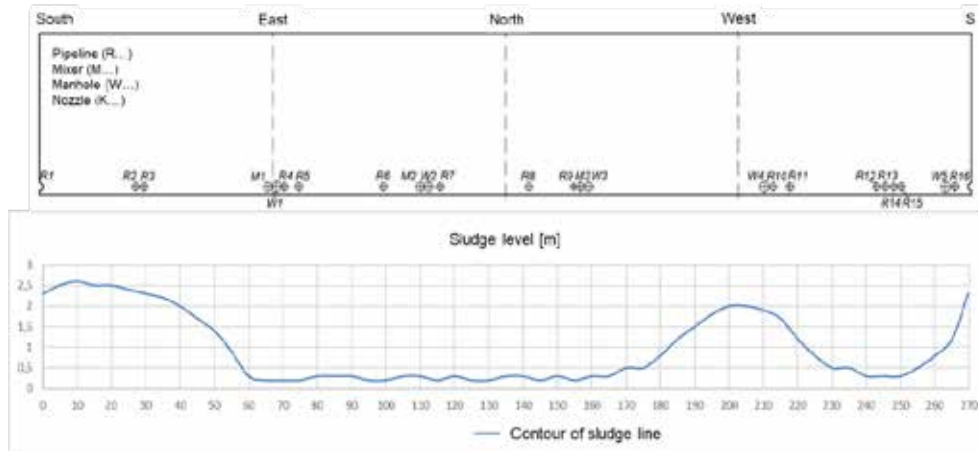


Fig 2. The line contour of sludge along circumference tank wall

4. AE technique for evaluation of sludge level

AE technique is used in this case in different way than normal purposes. There is used specific layout of sensors on the wall and roof of the tank (fig.3). The sensors generate of AE pulses according to established algorithm, which allows to record AE signals were caused the waves propagation and waves reflection (including from sludge – fig.4) in storage product between sensors. Under measured differences in time of wave propagation are evaluated heights of sludge in various points inside on the bottom of tank (fig.5). Obtained measurement data of sludge heights are collected in the measurement database. Fig. 3 shows an example of the layout of AE sensors when using AE technique for sludget heights measurement. Fig. 4 shows a waveform of the AE signal with echoes of waves from the bottom and roof of the tank. Fig. 5 presents the spatial visualization of the measurement data of sludge heights at specific points on the bottom of the storage tank.

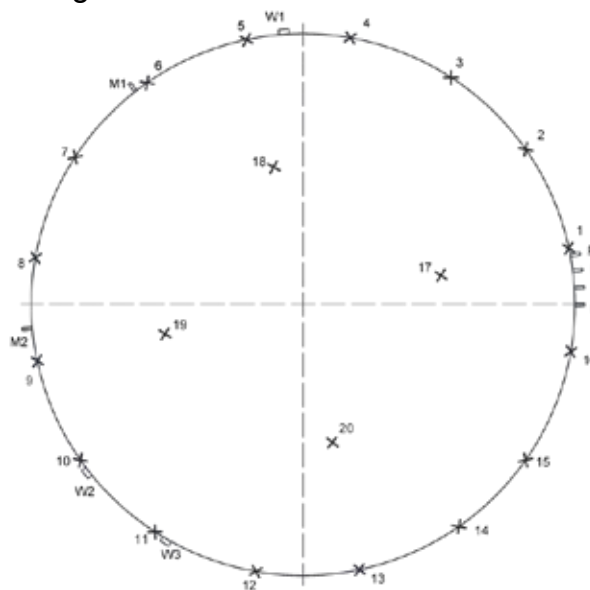


Fig 3. An example of the layout of AE sensors on the tested storage tank

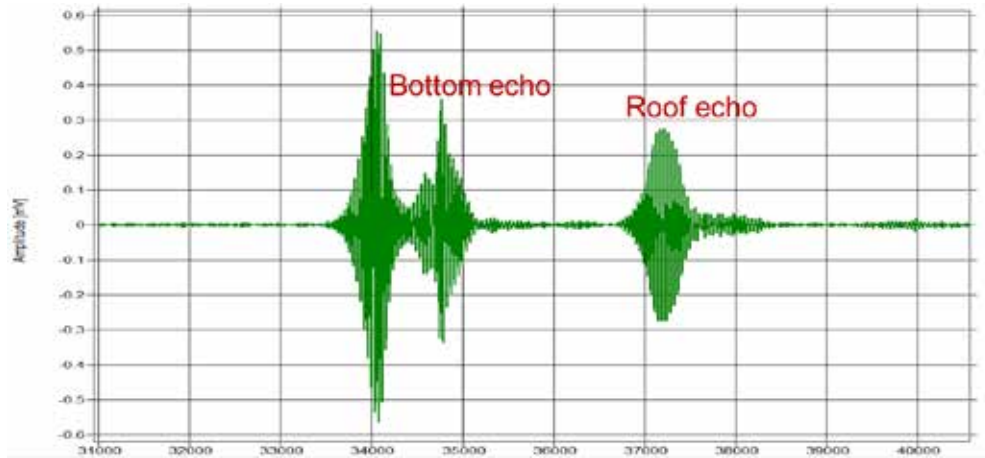


Fig 4. The wave propagation and wave reflection in storage product between AE sensors

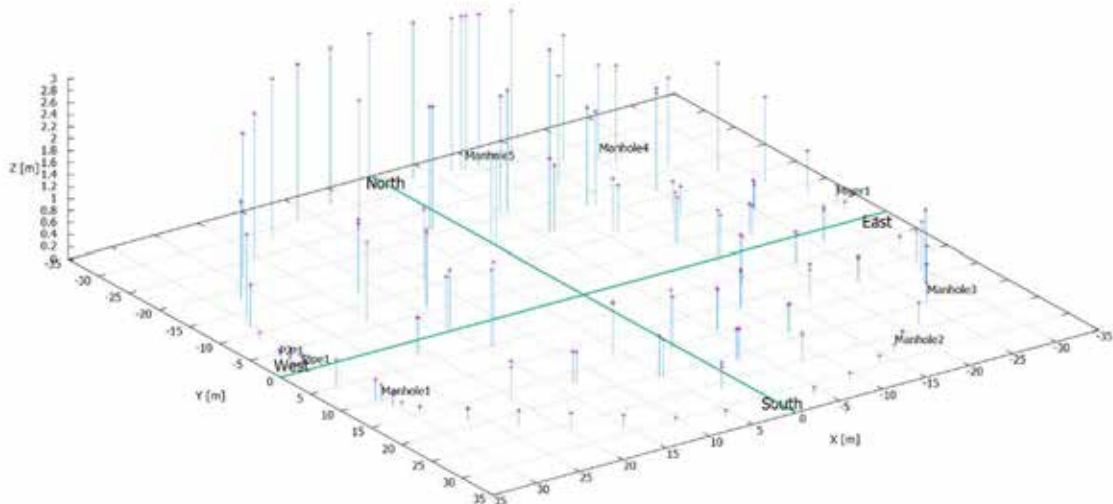


Fig 5. Spatial visualization of the sludge heights at the measurement points on the bottom of the tank

5. Determination the volume of sludge on the bottom of the tank

All measurement data of heights of sludge in many points, both on the wall and inside the tank are undergone mathematical polynomial interpolation, what finally give graph of shape of sludge (fig.6). Determination of the volume of sludge on the bottom of the tank, is carried out by the mesh of division into defined unit elements (fig.6) of the obtained spatial shape of the sludge and numerical counting (numerical integration using the rectangles method) volume of individual elements according to their heights. The result of the assessment of the sludge on the bottom of the storage tank is the volume of sludge in cube meters and spatial visualization of sludge.

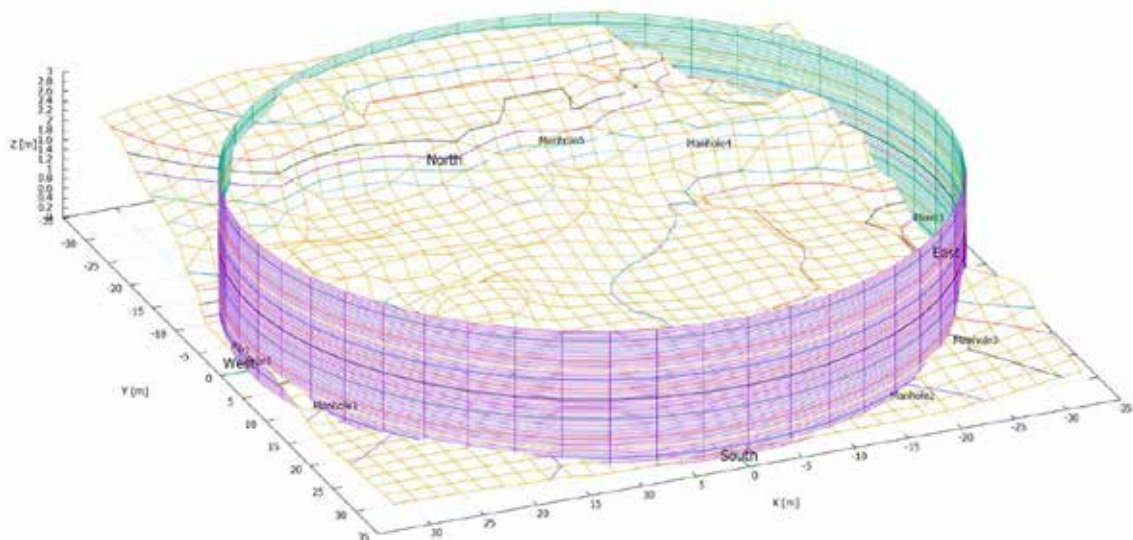


Fig 6. Spatial visualization of the sludge shape on the bottom of the tank with division into defined unit elements

6. Conclusion

The procedures and measurement methodologies developed at this stage of the project, as well as computational algorithms allow us to visualize the shape of sludge on the bottom of the tested storage tank and to determine the volume of sludge. The use of both AE technique and thermography method proved to be an effective tool for determining the heights of sludge at specific points inside the tested storage tank.

References:

1. M.Monteiro, V.Svet, D.Sandilands, S.Tsysar: Experimental Investigations of Various Methods of Sludge Measurements in Storage Oil Tanks, *Advances in Remote Sensing*, Vol. 4, 2015;
2. H.Hooyberghs: "Pictures" the Emissions of Storage Tanks with the Use of Infrared Cameras. 6th Annual Aboveground Storage Tank Conference & Trade Show Houston, Houston, 2013;
3. I.Baran, G. Lackner: Analysis of Corrosion Processes and Leaks in Aboveground Storage Tanks with AE Monitoring, EWGAE 2012;
4. NDT Handbook - Third Edition Vol.6 - Acoustic Emission Testing, Editors: R.K.Miller, E.v.K.Hill and P.O.Moor, ASNT 2005.
5. PN-EN 1330-9:2017-09 „Non-destructive testing - Terminology - Part 9: Terms used in acoustic emission testing”.
6. PN-EN 13554:2011 „Non-destructive testing - Acoustic emission testing - General principles”.
7. PN-EN 15856:2010 „Non-destructive testing - Acoustic emission - General principles of AE testing for the detection of corrosion within metallic surrounding filled with liquid”.
8. PN-EN ISO 18081:2016-08 “Non-destructive testing - Acoustic emission testing (AT) - Leak detection by means of acoustic emission”.

75 - New edition of GEA guideline for Acoustic Emission Testing of pressure equipments

C.DIGIULIO¹/C. HERVE²

¹Air Liquide France Industrie 152, avenue Aristide Briand 92227 BAGNEUX CEDEX

²CETIM 52 avenue Félix Louat 60304 SENLIS Cedex

Abstract:

To master over time the integrity of the equipment and ensure operational safety, in service inspections are carried out periodically in compliance with regulatory requirements and / or professional rules of supervision.

Acoustic emission now performed industrially for more than thirty years, is currently the only technique which, when applied in a suitable methodology enables to control an equipment in a global way regardless of the nature of damage that could be identified.

The AFIAP, only national entity bringing together the main parties involved in the pressure equipment: administration, manufacturers, users, technical centers, notified bodies, NDT provider organizations, mandated to a working group called "Acoustic Emission Group " the development of a " good Practice Guide for the acoustic emission.

This guide, which is officially recognized by the French administration, incorporates the requirements of the available standards and the experience gained by the professionals of this method.

It consists of general basis and annexes, each relating to a family of equipment. It is applicable in the context of the French legislation for the in-service monitoring of pressure equipment.

Previous editions of this guide were published in 2004 and 2009 with an enlargement to new annexes.

This new edition which is the subject of this presentation, takes into account the feedback over all these years of use and integrates new additional annexes, allowing extending the scope of this requalification method.

1. Introduction

Acoustic emission is a test technique that, when practiced according to a controlled and appropriate methodology, makes it possible to control globally an equipment regardless of its dimensions and its location. It is practiced now for more than thirty years and has been used on thousands of pressurized equipment of the oil, chemical, energy, ... The experience gained allows to have a great confidence in the information provided.

AFIAP - the only national entity including the five parties involved in pressure equipment: administration, manufacturers, users (represented in particular by UFIP and UIC), technical centers, non-destructive testing organizations - has developed, with the support of the French Administration, and maintains a "Guide to Good Practices for Acoustic Emission" (GBP).

The AFIAP Board of Directors has entrusted the preparation of this guide to a drafting committee called "Acoustic Emission Group" - GEA - composed of representatives of the five parties mentioned above.

This guide is approved by the Ministry of Environment, Energy and the Sea before it can be applied. Its ambition is to facilitate the practice of acoustic emission during requalifications of specific equipment by allowing to replace certain hydraulic tests by hydrostatic or pneumatic pressure tests, in order to avoid the opening of the equipment and the hydraulic re-proof test.

2. The practice of acoustic emission on pressure equipment

For more than 30 years acoustic emission tests have been performed on pressure vessels. They were first selected as a global control method during hydraulic tests and then, on a case-by-case basis, in the context of derogations, during pneumatic tests carried out in substitution of hydraulic re-proof test.

In the past, the requests made to the administration were made most often when a re-hydraulic proof test leads to heavy constraints on the equipment or when the test was impossible (structures not designed to take over the overloads induced by the hydro proof test, equipment apparatus that cannot be drained and dried completely, etc.) or when the overall cost induced by a re-test was industrially, economically excessive. The results obtained were quickly encouraging for several reasons: the test, as previously reported, makes it possible to obtain information on the globality of a structure,- the sensitivity of the test is great, - the test can be carried out during a "simple" process or pneumatic fluid pressurization, the overload being limited to 10% of the maximum pressure seen by the equipment during the last 6 to 12 months of operation, - the test requires the immobilization of the equipment only a limited time most often to one or a few days depending on the complexity of the equipment and that of the implementation of the test.

However, the practice of acoustic emission has been limited by:

- the need for expensive test equipment,
- few operators on the market, although now more and more providers are entering the field of activity,
- the limited experience of his practice a few years ago,
- The absence of implementation benchmarks recognized by the professions and the administration,
- the imposition of passage of applications for exemptions in Central Commission of Pressure Devices (CCAP).

The oil, gas, chemical and energy industries wished to develop (but not generalize) the application of this test method, particularly because of the openness offered by the new pressure equipment regulations relating to the operations to be carried out within the framework of the requalifications: decree of 15 March 2000, title V, article 23 § 7 and 8 "*Decisions taken after opinion of the CCAP, may provide that the hydraulic test be replaced by another test resistance under pressure ... that the periodic requalification be replaced by any other method which guarantees an equivalent level of safety.*"

2.1 Position of the administration

In order to be able to give confidence in the practice of testing the pressure equipment, the administration wished that a frame of reference covering all the stages that mark its implementation be drawn up by the actors concerned: Bureau of Risk and Network Equipment (BSERR), manufacturers, users, service providers, technical centers. This led to the creation of the Acoustic Emission Group (GEA) presented in § 1 and the drafting of the "Good Practice Guide for Acoustic Emission" (GBP) within AFIAP.

The GEA has produced a first version of the guide to the rules of good practice for acoustic emission in July 2001 (2001 edition) which was the subject of Ministerial Decisions DM-T / PN 32255 of 26 September 2002 and DM-T / PN 32460 of 1 April 2003.

A second version of the guide has been produced (May 2004 edition); it was the subject of Ministerial Decision DM-T / P N ° 32970 of May 28, 2004. This edition has been translated into English.

The revised Annex 4, relating to liquefied petroleum gas storage tanks (LPG) called "small bulk" was approved by the BSEI 05-442 of 23 December 2005. The annex 8 relating to the reactors (vessels in which occur chemical reactions) was approved by BSEI decision n ° 07-107 of April 13, 2007.

A third edition of the GBP took place in 2009. It was the subject of the BSEI decision N° 09102 of June 29, 2009 (modified by the BSEI n ° 11110 of October 5, 2011). Since then, annex 10 concerning stainless steel equipment has been validated by the BSEI decision N°13-009 of 17/01/2013 as well as appendix 7 on the equipment in composite materials by the decision BSEI N ° 14079 of 4 July 2014 and Annex 11 on exchangers by BSEI decision N°14110 of 31 October 2014.

This edition 2009 has been translated in English with the name "Guideline for acoustic emission testing of pressure equipment". [1]

Recently a new edition has being published in 2016 and released from the beginning of 2018 in computer form. It was validated by the BSERR decision N°16-034 of February 23, 2016.

Thus, any application, filed by an industrialist, to the requalification requirements, such as the replacement of a hydraulic re-proof test by a pneumatic test with acoustic emission monitoring in accordance with the requirements of the GBP and its annexes, may be treated at the level of the Authorized Organizations without passing through the DREAL or at the level of the CCAP.

3. The guide to Good Practices for Acoustic Emission

3.1 Constitution of the guide

The guide consists of a general part, applicable to all acoustic emission tests performed on ESPs, called "body of the guide", then appendices, each applicable to a family of equipment that defines the specificities of the Acoustic Emission attached to the family, including criteria and thresholds for interpretation of recorded data.

The body of the guide contains the chapters indicated in appendix 1.

3.2 Working methodology for guide development

The GEA is a group of about 30 representatives from the five entities involved: BSERR, manufacturers, users, service providers, technical centers. This group gives instructions for the work to be done and validates the documents. It is led by a user representative and its secretariat is provided by a technical center.

3.3 The body of the guide

It had been written by two "colleges".

- The "college 1" composed of representatives of the administration, the manufacturers, the users and the CETIM wrote the general chapters and those concerning the service provider / principal / inspection links,

- The "college 2" composed of representatives of the service providers, the technical centers wrote the chapters concerning the practice of the test and the interpretations of the recordings

3.4 Annexes

The first two appendices are general:

1. Standards, codes, regulatory texts,
2. Examples of equipment controlled by acoustic emission

Each of the following appendices is applicable to a family of equipment. They complete the body of the guide as to the modalities of the test and the interpretation of the results.

The available annexes concern respectively:

- 3 Methodology to be used for the elaboration of a procedure applicable to spheres
- 4 Methodology to be used to develop a procedure for underground "small bulk" LPG tanks
- 6 Methodology to be used to develop a procedure for cylindrical ESPs
- 7 Methodology to be used for the development of a procedure for composite material equipment
- 8 Methodology for the development of a reactor procedure
- 9 Methodology to be used to develop a procedure for autoclaves
- 10 Methodology for developing a procedure for stainless steel equipment
- 11 Methodology to be used for the development of a procedure for exchangers

The summary of these appendices is based on that of the guide body.

3.5 Working methodology for the preparation of an Annex

For a new family of equipment concerned, a first file must have been approved in CCAP. Two other files made on the same basis must also have been approved by the administration. These tests are the subject of a feedback analysis.

The decision to create a new annex is made by the GEA in plenary session. For each new annex, a working group of experts composed of representatives of service providers and users having practiced this type of acoustic emission tests on the family of equipment concerned is constituted.

Other appendices applicable to new families of equipment may be commissioned by industrial or professional unions.

The working group, led by a user, develops a draft annex. The convenor of the working group informs the GEA in plenary session of the progress of work. In the event of a blockage or technical difficulty, the assistance of a third-party expert can be requested from the GEA.

The project is then forwarded to the members of the GEA, accompanied with the Acoustic Emission Guide modification sheet and all supporting documents for approval of this annex.

The GEA plenary examines this project and decides to approve it after incorporating any minor adjustments or to return it to a working group for finalization.

Once approved by the GEA, the project, the modification sheet and the supporting documents are forwarded to the BSERR by the AFIAP President, for instruction and transmission to the CCAP for approval.

Between the various editions of the guide of intermediate evolutions (body of the guide, new appendix or revision of an existing appendix) can be subject to validation by the GEA and recognition by the Administration. As soon as they are recognized, these changes are made available to the users of the guide.

3.6 New Annexes available

Three new annexes have been included in the new edition of the 2016 guide.

- Annex 7: Methodology to be used for the development of a procedure for composite equipment

Composite ESPs are generally composed of a strong structure made from resin impregnated fibers, deposited around a sealing liner.

These structures are intrinsically heterogeneous, and their degree of anisotropy depends on the orientation of the fibers and the stacking of the various layers constituting the composite structure. This anisotropy will have an influence on the propagation of acoustic emission waves.

The acoustic emission produced by a composite material structure depends on many factors such as material components, laminate composition, manufacturing process, geometry and ambient conditions during the test. The interpretation of acoustic emission results will therefore depend on the knowledge and consideration of these various factors.

With this observation, it appeared that for a composite materials ESP, the performance of the pressurization tests and the data processing must be adapted to the specificities of the composite materials while following the practical recommendations described in the Guide of Good Practices for the control by Acoustic Emission, 2nd edition 2009 (GBPEA). Specific criteria were developed based on the experience gained by the members of the working group.

Working Group 7 of the GEA has therefore focused its work on the drafting of a specific annex for ESP in composite materials.

Initially it was planned to deal with two parts in the scope of the annex:

- Annex 7a concerning equipment operating at low pressure (<10 bar) and atmospheric tanks
- Annex 7b concerning pressure equipment.

Following the observation of the BSERR that the atmospheric tanks do not fall within the regulatory framework of the decree of March 15, 2000, the WG decided to devote first to the drafting of the section concerning pressure equipment.

Another point was raised in terms of "transportable" pressure equipment, which is covered by the amended decree of 29 May 2009 on the transport of dangerous goods by land (known as the TMD) which refers directly to the texts of international agreements on the transport of dangerous goods (RID / ADR / ADN). The ADR already provides the possibility to replace the hydraulic test of the periodic regulatory inspection by AE monitoring of a pneumatic test.

Despite the peculiarities of this fixed pressure equipment made of composite materials, this Annex 7 is as accurate and homogeneous as the other types of equipment already approved under GBPEA.

Annex 10: Methodology for the development of a procedure for stainless steel equipment

Tests and expertise show that stainless steels behave similarly to low-alloy steels with a lower emissivity and a generally higher attenuation.

This appendix for stainless steel equipment therefore proposes that:

- the carrying out of the pressurization tests follows the same treatment principle as for non-alloy steel equipment, i.e. the provisions with annexes already approved of the Guide to Good Practice for Acoustic Emission;

-some parameters are adapted to guarantee the objectives of the tests (thresholds and reference criteria).

The logic adopted by the GEA was therefore not to complete the existing annexes but to draft an annex common to all stainless steel ESPs.

For the development of a procedure for stainless steel ESPs, it is therefore appropriate to use Annexes 3, 6, 8 and 9 of the guide, respectively supplemented with the recommendations described in Annex 10.

- Annex 11: Methodology to be used to develop a procedure for interchanges

The exchangers are similar for the common parts (shells, bottoms, nozzles, etc.) to the other pressure equipment, the specific parts being the tube plates and the bundle. The tests and the expertise carried out show that the AE diagnosis is feasible on the tube plates; on the other hand, as far as the bundle is concerned, the state of the art so far does not completely cover this part even if information can be used on a case-by-case basis during the test.

As a result, the scope of this annex is limited to the parts covered by acoustic emission without bundle. In the context of the replacement of the periodic requalification hydraulic test, other measures shall be provided by the operator for parts not covered by AE, with the prior approval of the Administration. These measures are not described in this annex, which only concerns AE.

With these observations, it appeared that for a given exchanger, the implementation of the AE should follow for most common parts (shells, funds, nozzles ...), similar recommendations to those of Annex 8 "reactors" already approved of the Guide of Good Practices for the control by Acoustic Emission, 2nd edition 2009.

The drafting of this self-supporting appendix deals with the particularity of heat exchangers, especially for tube plates, and requires the AE test while the shutdown of the equipment.

This appendix is intended to be as accurate and homogeneous as those of the other types of equipment already approved and allows to frame the AE of the exchangers for the parts covered by the diagnosis.

4. Organization of feedback

Feedback is managed by Feedback Working Group and is carried out annually using two sheets to be completed by each user, a summary sheet and a detailed sheet that collects the essential characteristics of equipment controlled according to the GBP guide as well as the main results of the acoustic emission.

The objective is to identify the key points, the possible problems encountered, and the solutions chosen. Through the lessons learned from the experience described, these sheets can generate modification sheets of the guide.

These experience feedback sheets are then grouped by type of annexes concerned in order to develop a synthesis that is sent each year to the Administration.

Till now, more than 22,000 feedback sheets have been received since the implementation of the GEA guide. These sheets are distributed in the different annexes as follows:

Annex 3(spheres):	30
Annex 4(small bulks):	21 618
Annex 6(cylindrical vessels):	266
Annex 7(composites vessels):	2
Annex 8(reactors):	83
Annex 9(autoclaves):	341
Annex 10(inox vessels):	60
Annex 11(exchangers):	22

In parallel, 126 change sheets have been studied and integrated in the last edition of the guide.

5. Conclusion

The working group of the GEA is still active within AFIAP, it meets in plenary session twice a year to follow the application of the guide and to take into account the feedback. This work led to the new edition of the 2016 guide which will be available for the first time in electronic version.

An English version will be available soon.

Bibliography:

[1] Guideline for acoustic emission testing of pressure equipment - AFIAP - 2009 edition

15 - Use of Acoustic Emission for inspection of various composite pressure vessels subjected to mechanical impact

F. Dahmene¹, S. Yaacoubi¹, S. Bittendiebel¹, O. Bardoux², P. Blanc-Vannet², A. Maldachowska³, M. Barcikowski³, M. Panek³, N. Alexandre⁴, F. Nony⁴, K. Lasn⁵, A. Echtermeyer⁵, P. Sigurd Heggem⁶

¹ Institut de Soudure, Plateforme RDI CND, 57970 Yutz, France

² Air Liquide, Paris-Saclay-Research-Center, Jouy-en-Josas, France.

³ Wroclaw University of Technology, Poland.

⁴ CEA, DAM, Le Ripault, 37260 Monts, France.

⁵ Norwegian University of Science and Technology (NTNU), Trondheim, Norway.

⁶ Hexagon Composites, Raufoss, Norway

Abstract:

Motivated by the emerging hydrogen mobility uses, especially the need for storing a high amount of energy in a small and lightweight volume, type IV composite pressure vessels have become a state-of-the-art technology for high pressure hydrogen. They comprise a non load-bearing liner, generally made of plastic and assembled with metallic bosses, around which a carbon fibre-epoxy composite is wound. Though such vessels can already be operated safely, there is a lack of knowledge concerning their residual performance after a mechanical impact. There is a need for associated nondestructive examination (NDE) methods, able to assess whether a cylinder is still fit for service after impact. The FCH-JU funded pre-normative research project HYPACTOR was set up to investigate the damage created in type IV pressure vessels by mechanical impacts, and then the use of Acoustic Emission to build rejection criteria during inspection. The methodology was to combine several AE tests on healthy and impacted vessels and correlate the results with residual performances. The developed criteria were applied to a wide database of Type IV composite vessels with different sizes, design specifications and working pressures. The validation was carried out on 114 hydraulic tests on healthy and impacted vessels. Results have demonstrated a capacity to differentiate damaged cylinders from healthy ones, with some small influence of the number of pressure cycles between impact and inspection.

1. Introduction

Composite overwrapped pressure vessels (COPVs) are widely used for many applications. The combination of their light weight and high mechanical strength is a major benefit for transportation of large quantities of gas. Type IV composite pressure vessels have become a state-of-the-art technology for high pressure hydrogen (>350 bar), in transportable and on-board application. They comprise a non load-bearing liner, generally made of plastic and assembled with metallic bosses, around which a carbon fibre-epoxy composite is wound.

Though such vessels can already be operated safely, there is a lack of knowledge concerning their residual performance after a mechanical impact. There is a need for associated nondestructive examination (NDE) methods, able to assess whether a cylinder is still fit for service after impact.

Periodic inspection of transportable composite vessels is based on visual examination combined to hydraulic proof test [1]. This procedure, inherited from metallic vessels (type I) is not well adapted for composite structures assessment and leads to industrial drawbacks such as dismounting and handling steps, process disruption, need of drying process after hydraulic test... In this way, Acoustic Emission Testing, already used for some metallic vessels, may be a good candidate to perform a periodic inspection of COPVs.

The FCH-JU funded pre-normative research project HYPACTOR was set up to investigate the damage created in type IV pressure vessels by mechanical impacts, to assess the residual performances after impact in terms of burst (short-term performance) and cycling (long-term performance), and then the use of Acoustic Emission to build AE criteria. It has to be noted that an important work item of Hypactor was the construction of the relationship between impact, created damage and vessels residual performance to define rejection criteria for inspection purpose.

2. Description of work

The experimental trials were performed mainly on a certified 36L 70MPa type IV cylinders provided by Hexagon Composites. They are designed according to the on-board storage regulation EC79/EU406 [2] with a safety factor of 2.25. The liner is a polymeric and the composite shell is a carbon fibre reinforced polymer (CFRP) filament wound. Other larger cylinders 255L and 513L were also tested. One impact per vessel was chosen to assess residual performance at short term and long term (after further pressure loads in service). Different levels of impact energy were carried out in order to determine the burst pressure reduction curve. All impacts were performed using a hemispherical steel impactor in order to produce less damage to the composite than a sharper one and therefore make damage detection difficult or barely visible using visual inspection (less favorable situation for identification of damaged vessels by visual inspection and therefore assess acoustic emission ability). All impacts were carried out in the cylindrical part, using two different setups depending on the speed and energy required: a drop tower and a pneumatic canon, displayed in Figure 1.



Figure 1: The crash set-up used in this study. Left: Using drop tower. Right: Using pneumatic canon.

AE monitoring was performed using an advanced AMSY5/6 systems supplied by VALLEN, and eight resonant R15 α sensors. Six spring-loaded sensors were placed on the cylindrical part of the COPV by means of three belts, and acoustically coupled with vacuum grease. 2 Sensors were placed on bottoms. The eight sensors are distributed so that the COPV is fully covered. An example of sensors implementation is shown in Figure 2. The AE signals were amplified by a 34 dB fixed gain, using an AEP3N preamplifier. A relatively large pass-band [25-850] kHz hardware filter was used to detect a wideband of frequencies. A trigger threshold of 40 dB was selected, which was above the background noise level.



Figure 2: Distribution of the 8 used sensors on the COPV.

AE monitoring was performed for both healthy and impacted vessels at short and long term tests. For long term performance, vessels were monitored by AE after three cycling period in order to define pass-fail criteria enabling the identification of damaged vessel whatever the periodicity of control and in particular regardless the time between the occurrences of impact/damage to AE control. Vessels were then cycled between 0 and 875 bar which is the maximum pressure reached during hydrogen filling for a service pressure of 700 bar. Different cycling periods were carried out combined to AE monitoring: 50 cycles at 875 bar + AE at 1050 bar + 5000 cycles at 875 bar + AE at 1050 bar + 10000 cycles at 875 bar + AE at 1050 bar + burst.

For short term performance, AE test was carried out just after impact and then vessels were burst. The loading during AE test, should be gradually increased up to the maximum pressure (P_{max}), at least 110% of its nominal filling pressure (963 bar) and maximum equal to the test pressure 150% of its service pressure (1050 bar). In this study the test pressure was reached during AE test in order to collect more data related to damage propagation at high pressure. However, AE criteria were defined for a maximum pressure of 110% of the nominal filling pressure. The pressure sequence contains various bearings which allow to identify the

damage state and its evolution at each pressure level but also to avoid a sudden burst. To avoid too sudden stress relaxation, strain rate during depressurization was similar to that during pressurization (<5%Pmax) and regular as possible. An example of pressure sequence is given in Figure 3.

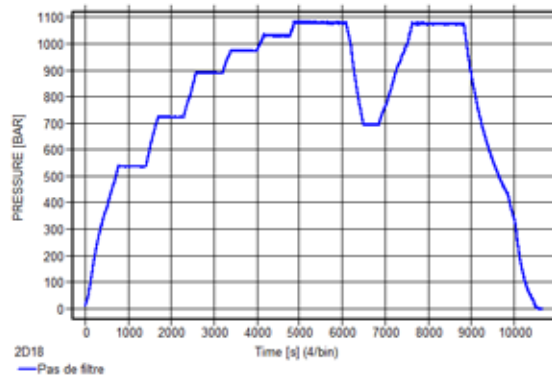


Figure 3: Pressure sequence for 36L vessels.

3. Results and discussions

In order to establish AE pass/fail criteria to be able to identify damaged vessel, the ideal approach is to record the AE signature of each vessel before and after impact. However, in practice, this proposal generates a complex pattern of vessel travel as well as a complex trials plan (since the impact trials and AE trials on short and long term performance were performed in different countries). To reduce and simplify trials, the solution proposed was to study the long term performance of 3 healthy vessels from different batches. These vessels were considered as a reference providing that AE dispersion is very low. These data were considered as a baseline of healthy vessels. In the case where scatterings would have been very high i.e the AE behaviour of vessels is different, AE tests would have to be performed for each vessel before and after impact.

As it can be seen in Figure 4, dispersion was evaluated at three conditions (after 100 cycles, after 5100 cycles and after 15100 cycles) by comparing the AE activity of the three vessels. The sum of events (first hit channel with Amplitude ≥ 50 dBae) detected by all channels per vessel was calculated for each holds. Results indicate a very low dispersion between vessels whatever the cycling period. These AE data can be considered as a baseline signature for all 36L COPV.

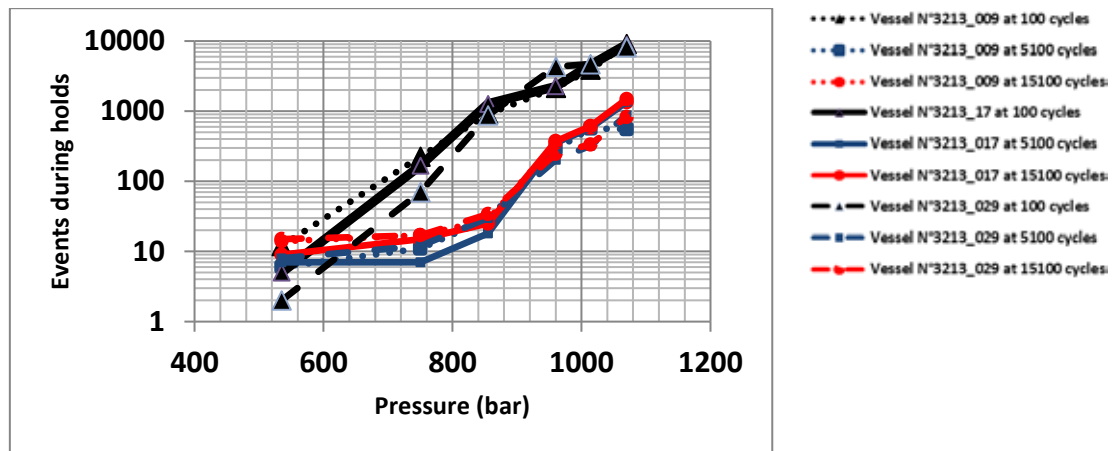


Figure 4 : AE activity dispersion evaluated for three vessels at three cycling periods.

The approach followed to define AE criteria is based on the appendix 7 of the French best practices guideline for Acoustic Emission, approved in 2014 by the French authority [3]. AE criteria are divided into two types, real-time shutdown criteria and post analysis criteria. The first one aims to detect and reject dangerous vessels in real time during the AE test, in case of vessels with high loss of performance to avoid a sudden burst. The second one aims to identify and remove from service vessels with a low loss of performance. Three categories are possible: for category 1 and 2: vessels are accepted while for category 3, vessels are rejected.

Parameters to take into account for real-time shutdown criteria and post analysis criteria are as follows:

- Setting: The evaluation threshold is set at 50 dBae and the reference threshold at 75 dBae.
- Activity and intensity evolution during the test. Activity (number of events and intensity energy) are assessed throughout the duration of the test.
- The number of counts N_a , determined by the number of counts generated by the break of fourteen 0.5mm 2H pencil leads at a distance from the sensor corresponding to an amplitude of 60 +/- 1 dBae, depending on the fibres direction (main or visible on the surface) and at 45° to this direction. The N_a value is equal to the mean of the number of counts obtained for each direction multiplied by 10 (value measured from the acquisition threshold).
- N2s: Events with Amplitude ≥ 75 dBae, calculated for the entire duration of the test
- N3s: Activity with Amplitude ≥ 50 dBae during holds
- Dm: Number of hits with duration higher than 5 ms
- FR: Felicity Ratio calculated during the unload/load ramp

More details about parameters thresholds are available on the appendix 7 [3]. The first step was the compliance assessment of criteria defined in this appendix to our vessels. It has been found that both criteria were conservative; most of healthy vessels (thus with no loss of performance) were systematically rejected. An example of zonal and planar analysis for a healthy vessel after 100 cycles at 875 bar is given in Table 1 and Figure 5. We can note that all parameters are classified in category 3 except the Felicity Ratio. For zonal analysis in particular when considering activity during holds, we talk about category 3 when the number of events exceeds 50 in the case of intermediate holds and 80 for final hold. This threshold is largely exceeded in our case. For planar localization, one red cluster appearance is sufficient to reject the vessel. A red cluster represents more than 50 located events in a very small area. This high activity could be related to the high thickness and high working pressure of on-board/transportable vessels. Indeed, the safety factor and design are different compared to stationary vessels. Although the appendix does not cover on-board and transportable vessels (the case of our study), the control protocol and the analysis methodology are still consistent and remain applicable via some modification.

Table 1 : Zonal analysis of a healthy vessel after 100 cycles at 875 bar.

	Act	Int.	Na	N2S	N3s/Zone (Blue color : 10min hold, analysed from [2 min; 10 min]; Red color : 20min holds analysed from [2 min; 20 min])									D>Dm	FR	Final Classe
activity	activity	Intensity	Na	A ≥ 75 dB	535 Bar	750 Bar	855 Bar	960 Bar	1050 Bar	750Bar	1050 Bar	Intermediate Classe	Hits Nb D>Dm	Felicity ratio		
1	3	3	3	3	0	13	162	996	1628	1	943	3	3	0,88	3	
2	3	3	3	3	0	10	113	416	853	0	255	3	3	0,99	3	
3	3	3	3	3	0	6	79	356	739	0	237	3	3	0,96	3	
4	3	3	3	3	0	11	165	745	1342	0	427	3	3	0,94	3	
5	3	3	3	3	0	13	142	631	1272	0	397	3	3	0,96	3	
6	3	3	3	3	0	3	102	507	973	0	326	3	3	0,97	3	
7	3	3	3	3	0	10	89	487	838	0	369	3	3	0,96	3	
8	3	3	3	3	2	4	25	180	557	0	243	3	3	0,97	3	

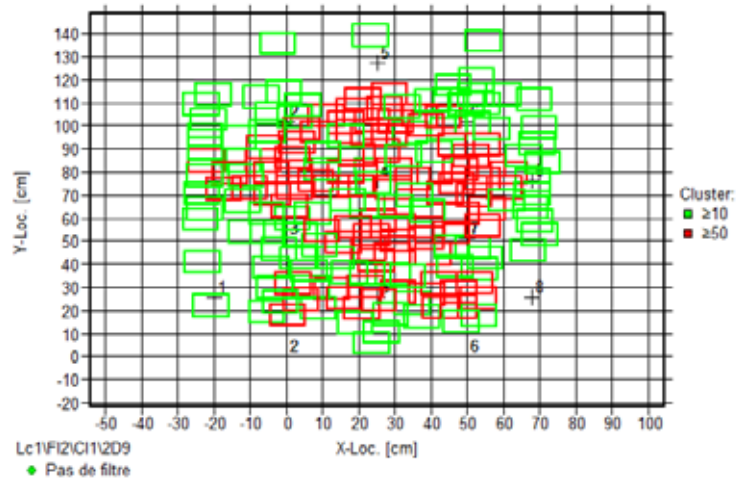


Figure 5 : Cluster localization of a healthy vessel after 100 cycles at 875 bar.

For confidentiality reasons, values of criteria thresholds are not communicated in this paper. However, the global approach followed to build and calibrate the AE pass-fail criteria is detailed hereafter.

Methodology is based on the construction of a burst pressure reduction curve, which give the measured burst pressure for several vessels with respect to impact energy (Figure).

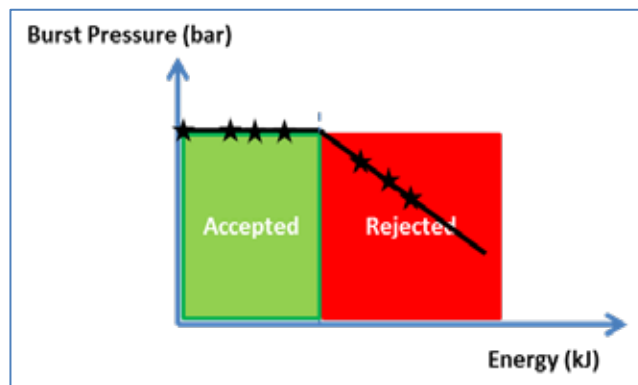


Figure 6 : Burst pressure reduction curve, with respect to impact energy.

It was demonstrated that the energy at which residual burst pressure starts to decrease is a relevant threshold to define a critical defect limit (from green to red area) where detection needs to be efficient [4, 5, 6].

As a recommendation, Hypactor project proposes to calibrate NDT method using this burst pressure reduction curve, giving the limit where NDT needs to detect a defect with a high reliability. It means that calibration of AE criteria should be performed for each vessel design, and connected to the burst pressure reduction curve, as well as visual inspection calibration.

AE test should be performed on “healthy vessels” (without and with impact but no loss of performance) located in the plateau of the curve of Figure 6 and also on impacted vessel at different energy levels with a loss of performance (red area).

In order to limit the number of destructive tests, a formula to estimate the threshold of critical energy (inflexion point of Figure 6) was given in [4, 5, 6] depending on vessels features.

$$E_{\text{abs}} / (P_{\text{burst}} * R_i) = 30.10^{-6} \text{ (units = S.I.)}$$

With:

E_{abs} = absorbed energy

E_{incident} = incident energy (impactor total energy)

P_{burst} = burst pressure of healthy vessel

R_i = inner vessel radius

By using $E_{\text{abs}} = 0.65 E_{\text{incident}}$ (proposal from [5]), the formula becomes:

$$E_{\text{incident}} = (P_{\text{burst}} * R_i) \cdot 30.10^{-6} / 0.65 \text{ (units = S.I.)}$$

In terms of damage induced by impacts, testing on empty vessels was found to be more conservative than on pressurized vessels. However, from the point of view of detection by AE, impacts on pressurized vessels is recommended because the propagation of damage will need an overpressure and criticality assessment is more difficult to predict by AE compared to empty condition. The calibration of thresholds of AE criteria is illustrated in the Figure . The methodology is to define the low limit and high limit for each AE parameter based on the burst pressure reduction curve (Figure). Thresholds will depend on vessels features (type, design, mechanical behavior, impact conditions...) and also on the safety factor to be adopted for the category 2. The extent of this category will depend on the safety factor adopted by the stakeholders which could be linked to vessel features and results scatterings.

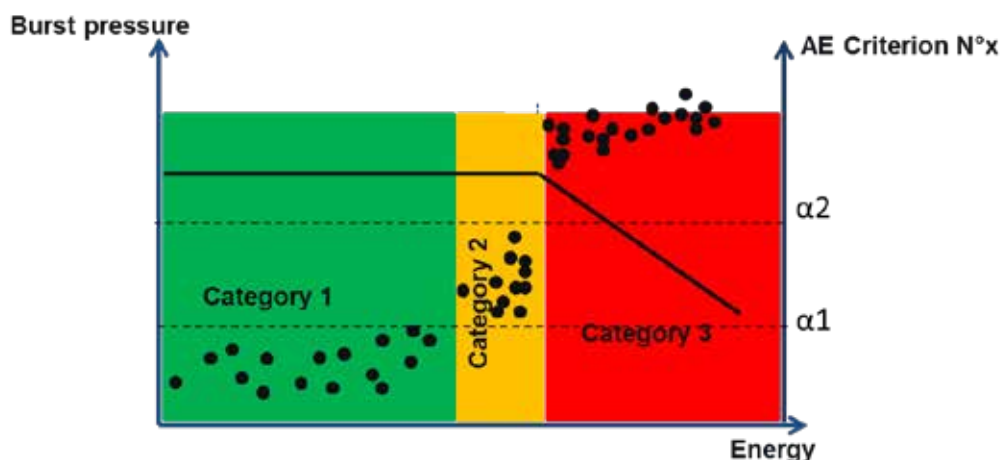


Figure 7: Burst pressure reduction curve and calibration of AE criteria protocol.

AE Criteria were first built in the framework of H2E project (Horizon Hydrogène Energie) [7] on transportable 143L vessels from Stelia Composites. Mechanical impacts have been carried out using a dedicated bench. The configuration of impact was in the dome area at 45°. The developed AE criteria have been used in Hypactor even if the design, impact configuration and operating pressure were different. The aim was to evaluate their application on 36L Hypactor vessels.

Refined criteria have shown satisfying results despite the high number of parameters (Table 1 & Figure 5). However, real time analysis requires a solid experience of the operator. The alternative proposed by the Institut de Soudure for real time criteria, is based only on two criteria, one zonal (N2s) and one using localization analysis (Clusters during holds). These criteria are very fast to analyze and simple to automate.

For healthy vessels, impacted vessels at 1kJ on empty condition and impacted vessels at 3kJ on 700 bar condition (all those vessels were without any loss of performance), only three vessels were stopped in real time during the AE test:

- 2 impacted vessels at 1kJ empty condition
- 1 impacted vessel at 3kJ 700 bar condition

After verification using visual inspection, it has been found that an external damage was located in the critical area identified by AE. Damage was induced by the rebound of the impactor after impact. A severe fiber cut was then identified.

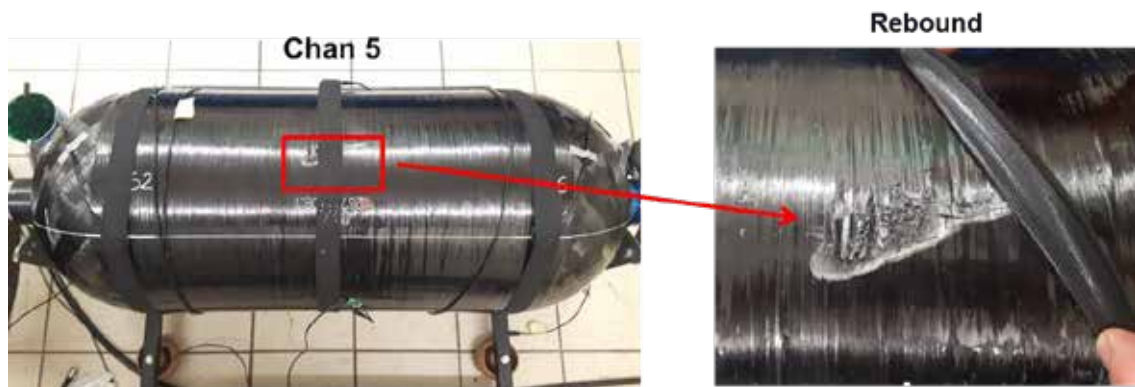
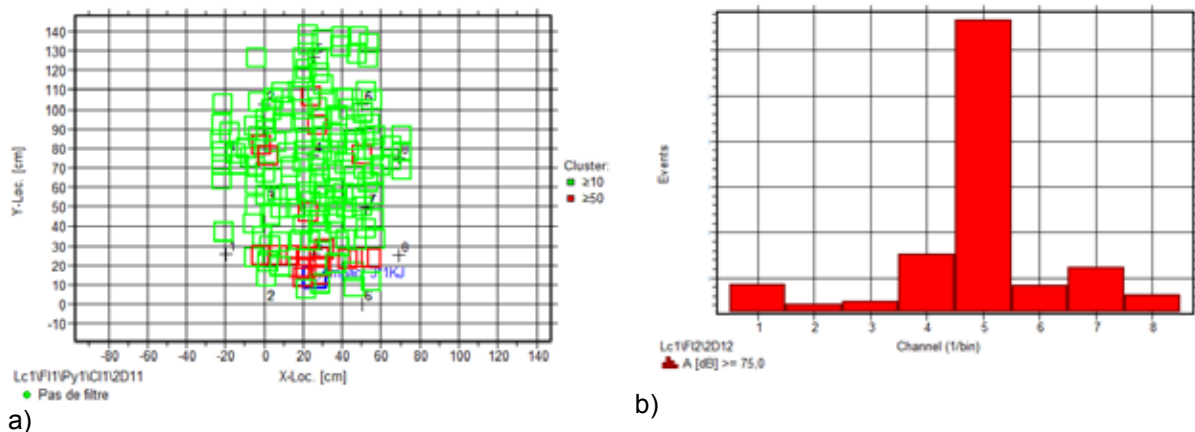


Figure 7 : Vessel impacted at 3kJ@700 bar. Rejection of vessel is due to a harsh surface damage induced by the projectile rebound. A) Localization of AE sources. B) Damage induced by the rebound.

All vessels impacted at high energy and presenting a loss of performance were also rejected by real time and post analysis criteria. An example of classification is given in the following tables (Table 2, Table 3).

Table 2 : Result of classification obtained by AE on impacted vessels at high energy at empty condition.

Impacted vessels at high energy @empty					
Number of vessels	Impact conditions	AE test condition	Burst pressure	AE Real time criteria	AE Post analysis Criteria
1	3 kJ@empty	After impact, after 50 cycles	decrease	Rejected	Rejected
1	4 kJ@empty	After impact, after 50 cycles	decrease	Rejected	Rejected
1	5 kJ@empty	After impact, after 50 cycles	decrease	Rejected	Rejected
1	7 kJ@empty	After impact	decrease	Rejected	Rejected

Table 3 : Result of classification obtained by AE on impacted vessels at high energy at 700 bar condition.

Impacted vessels at high energy @700 bar					
Number of vessels	Impact conditions	AE test condition	Burst pressure	AE Real time criteria	AE Post analysis Criteria
1	4 kJ@700b	After impact, after 50 cycles	decrease	Rejected	Rejected
1	5 kJ@700b	After impact, after 50 cycles	decrease	Rejected	Rejected
1	6 kJ@700b	After impact, after 50 cycles	decrease	Rejected	Rejected

The validation has been carried out on a large data base of 114 vessels from different type, dimensions, working pressure and manufacturer.

4. Conclusion

Currently there is no AE standards applicable for transportable COPVs. In FCH-JU Hypactor project, many AE test have been performed on type IV composite vessels in order to define AE rejection criteria for periodic inspection.

The methodology was to combine several AE tests on non-impacted and impacted vessels and correlate the results with vessels residual performances. The approach followed by ISA was to refine criteria thresholds from the appendix 7 of French Guide to good practice for acoustic emission testing [3] and adapt them for type IV vessels using zonal and cluster localization analysis. The use of both localization methods offers the possibility to obtain consistent result. This approach allows a calibration of AE criteria to accept or reject a vessel during pressurization. The developed criteria were applied to a wide database of Type IV composite vessels with different sizes, design specifications and working pressures.

Acoustic emission tests (AE) using developed ISA criteria have provided a good assessment of damage.

More details in www.hypactor.eu

Acknowledgment

The research leading to these results has received funding from the European Union's Seventh Framework Programme (FP7/2007-2013) for the Fuel Cells and Hydrogen Joint Technology Initiative under grant agreement n° 621194.

References:

-
- [1] ISO 11623 Gas cylinders - Composite construction - Periodic inspection and testing
 - [2] Regulation (EU) No 406/2010 implementing Regulation (EC) No 79/2009 on type-approval of hydrogen-powered motor vehicles
 - [3] Guide to good practice for acoustic emission testing of pressure equipment. 2nd ed. june 2009 [AFIAP] French association of pressure equipment engineers. edited by Sadave
 - [4] P. Blanc-Vannet, «Burst pressure reduction of various thermoset composite pressure vessels after impact on the cylindrical part,» Composite Structures, vol. 160, pp. 706-711, 2017
 - [5] P. Blanc-Vannet, «Residual performance of composite pressure vessels submitted to mechanical impacts» International Conference on Hydrogen Safety 2017
 - [6] FCH-JU HYPACTOR project "Pre-normative research on resistance to mechanical impact of composite overwrapped pressure vessels" – Final report
 - [7] <http://www.horizonhydrogeneenergie.com/programmehorizon-hydrogene-energie.html>, retrieved the 1st November 2015

30 - Detection and identification of low-amplitude Acoustic Emissions during plastic deformation under indentation and scratch testing

A. Danyuk¹, D. Merson¹, A. Vinogradov^{1,2}

¹ Laboratory of Physics of Strength of Materials and Intelligent Diagnostic Systems, Togliatti State University, Togliatti, Russia

² Department of Mechanical and Industrial Engineering, Norwegian University of Science and Technology – NTNU, Trondheim N-7491, Norway

Abstract

The acoustic emission (AE) technique is unique in that it enables real-time monitoring of processes of plastic deformation and fracture in materials by receiving signals originating from the entire volume of the testing. This capacity is hardly achievable by any other non-destructive methods aimed at continuous and/or in-situ monitoring of deformation processes. However, the price paid for the high sensitivity of the AE method is well known – the AE signal is buried into the electric noise: the higher the gain the higher the noise. This noise is a natural physical limit of the sensitivity of the method. In this paper, we overview the factors that interfere with the detection and identification of AE signals of very low amplitude. For probing these factors, the indentation and scratch testing were used as these testing methods are gaining popularity in modern laboratory and industrial practice. The low-amplitude AE arises in these tests from the sources caused by plastic deformation in small volumes loaded locally in the micrometre scale. Procedures for analysing and suppressing the external noise and the noise from testing equipment are proposed and discussed. Results of detection of AE events with low signal-to-noise ratio (SNR) during scratch testing of pure polycrystalline metals are presented. The efficiency of proposed algorithms for noise reduction and SNR improvement by AE digital signal processing is demonstrated on the examples of (1) wavelet-based “Phase Picker” signal detection algorithm, (2) spectrum noise gating procedure (Audacity), (3) spectral signal analysis. In this way, the AE technique has been proven to be a viable and versatile tool for investigations of local deformation mechanisms in situ.

Keywords: acoustic emission, scratch test, deformation mechanisms, signals detection, spectrum analysis.

1. Introduction

The acoustic emission method is highly sensitive to processes of local stress relaxation occurring in a crystal under external influence. These relaxation processes are associated with dynamic changes in the microstructure caused by phase transitions, fracture or plastic deformation. The latter is most often related to dislocation slip and/or twinning in crystals.

An estimate of the minimum sensitivity limit of the AE method is an interesting and challenging practical and theoretical task. An analysis of the theoretical sensitivity limit of the AE method is well presented in [1, 2] for various mechanisms. In particular, the theoretical sensitivity limit to dislocation motion has been explored in the continuum mechanics

approach within the Green's function formalism. The authors substantiate analytically that the elementary dislocation jump at a distance equal to the value of the Burgers vector forms an amplitude response on the surface at the AE sensor location of the order of the regular background noise level. However, the practical sensitivity threshold is significantly worse. The main factors complicating the registration of AEs from single dislocation glide events are related to signal attenuation during propagation and transformation, mechanical and electrical noise. Increasing the AE sensitivity to the elementary dislocation reactions in solids is a long standing fundamental and technical problem, the solution of which can bring the AE method to the foremost positions among other in-situ techniques used in modern material science.

We demonstrate a practical approach aiming at determining the actual level the AE method sensitivity to discrete dislocation events detecting during plastic deformation. The key points exploited in the present work are the controlled local deformation and the advanced signal processing algorithms for increasing the practical sensitivity of AE to low-amplitude events in in continuous time series with very low signal-to-noise ratio.

2. Experimental

To address these issues we have developed a versatile threshold-less AE signal recording and analysing procedure and applied it to the instrumented micro-scratching of copper polycrystals with the well-characterised initial microstructure.

Pure polycrystalline copper is a model material which deformation is mediated by dislocation glide at room temperature. Acoustic emission in pure single- or poly-crystalline copper appears as a powerful continuous wide-band signal under tension or compression [3-5]. Such a signal is formed by a huge number of gliding dislocation. It is not possible to separate an individual signal from a single dislocation slip source by amplitude, signal duration or any other AE parameter even if the low-noise equipment and high sensitivity resonant sensors are used.

The samples of 3N (99,9% Cu) polycrystalline copper with dimensions of $20 \times 20 \times 2 \text{ mm}^3$ were annealed in vacuum at 1170 K for 1 h and electrolytically polished to a mirror-like finish. The microstructure was investigated by electron backscattered diffraction (EBSD) measurements in a field-emission scanning electron microscope (SEM) ZEISS-SIGMA equipped with the EDAX/TSL EBSD detector.

To promote highly localised AE within individual grains, scratch tests were carried out using the Nanovea tester. The driver of the setup was previously examined by AE and configured to exclude mechanical noise. It is the noise level that limits the amount of loading and speed of the indenter's movement. To reduce the effect of interfacial friction between stylus and specimen [6, 7] the Berkovich diamond indenter in the edge-forward orientation was moved linearly at relatively high constant dragging speed $V_s = 12$ and 24 mm/min until the scratch reaches 2 mm length. The normal load F during the test was set constant at the minimum stable controllable value 1 N and 2 N.

The piezoelectric sensor AE-900S-WB (NF-Electronics, Japan) with a frequency band of 100–1000 kHz was attached to the samples through vacuum oil with a rubber band. The short distance between indenter to sensor was a few millimetres. The signals were amplified by 60 dB by the low-noise pre-amplifier and acquired by the 16-bit PCI-2 board (MISTRAS,

USA) operated in a continuous threshold-less mode at the sampling rate of 5 MSamples/s. The on-board filters were set in the widest possible range of 20 kHz to 2 MHz and the additional +6 dB gain was pre-set. The AE waveforms were continuously recorded and synchronised with the scratch path.

The stationarity of loading conditions and propagation of AE waves is the main advantage of indentation and scratch-testing in comparison to other mechanical testing modes. During the test, the shape of the sample does not change and the transfer function for AE waves propagation is constant. The indentation techniques allow for precise positioning and localisation of the deformation zone. However, the local strain rate and the deformed volume change considerably while the indentation test is in progress. In the present work we confine ourselves to the scratch test, in which the average strain rate remains constant and the stationarity of the deformation process is ensured. This feature of the scratch test makes it possible to control test duration within a comfortable range.

When a scratch test is performing, the indenter deforms serial crystals (grains) separated by boundaries. Generally, the crystal axes of grains have an arbitrary crystallographic orientation with respect to the test surface. Therefore, the spatial configuration of slip systems is different for each grain and is characterised by the Schmidt factor. This difference in dislocation glide activation in different grains should result in a distinct relaxation response of the AE signal. To identify the AE of dislocation, three different approaches to signal detection were tested:

- 1) The Wavelet-based “Phase Picker” signal detection algorithm proposed in [8]. This method demonstrates an excellent temporal localization of the picked phases even for the signals with the very low signal-to-noise ratio. This procedure detects the time of arrival of AE hits with high accuracy. Furthermore, it is efficient in the analysis of distributions of amplitudes and time intervals between the signals.
- 2) Spectrum noise gating procedure implemented in the Audacity software [9]. This is a nonlinear procedure for reducing noise spectral components and restoring the waveform by inverse FFT. It can reveal the nonstationary fluctuations inside streaming data, which are associated with dislocation line growth.
- 3) Analysis of the spectral parameters of the AE signal is Power and Median frequency coordinates calculated using a sliding time window technique applied to the continuous stream [10].

The AE signal processing workflow includes the following steps:

- A continuous raw stream was divided into successive frames of 8192 (1.6 ms) readings.
- For each frame, the forward FFT was applied, and two parameters were calculated in the frequency domain – the Power as the integral over the power spectral density and the Median frequency as the frequency which separates the low and high frequency spectral domains with equal power.
- The obtained time series of Power and Median frequency were smoothed by a low-pass Butterworth filtering procedure with the cut-off frequency, 19 Hz at present tests.

3. Results

The footprint of indenter tip and the initial AE stream are shown synchronously in figure 1. The footprint has the uneven width because of anisotropy of deformation in differently oriented grains in fcc crystals. The variation of crystallographic orientations in neighbouring grains is shown in figure 1 by the EBSD map.

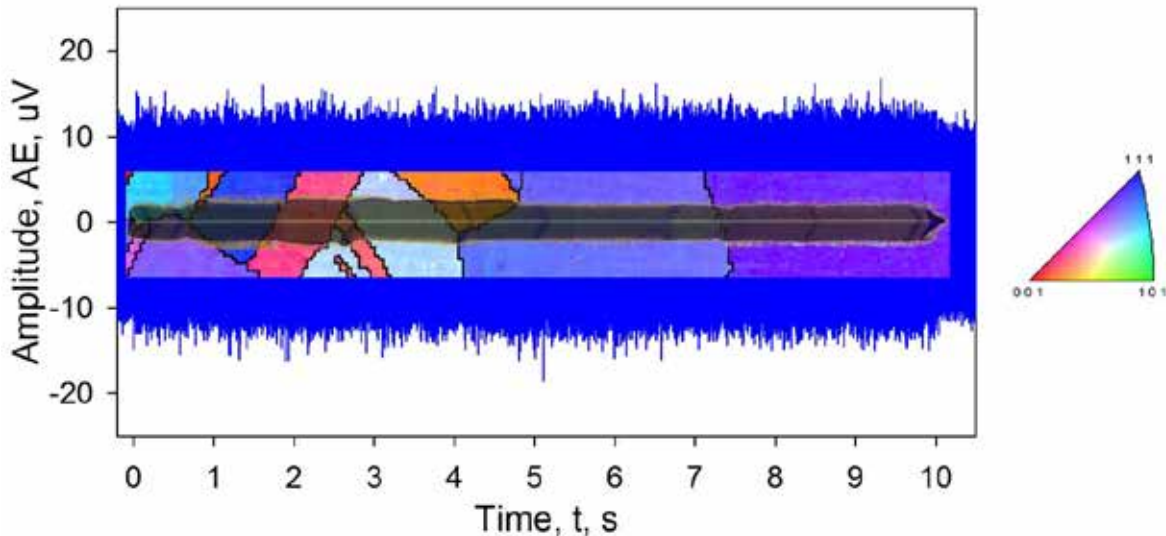


Figure 1 – Scratch test raw data, load force 1N and scratch velocity 12 mm/min: EBSD scan map of test surface superimposed with the continuous acoustic emission stream.

The test duration was of 10 seconds. The background noise was recorded before and after the test and this can be seen in Figure 1. An amplitude of AE signal does not exceed the amplitude of the noise signal significantly so that any amplitude-based threshold detection is impossible.

The Wavelet-based "Phase Picker" algorithm was applied to detect the signals with the low signal-to-noise ratio. At the output, one obtains a set of arrival times and signal durations. The distinct feature of the "Phase Picker" detector is a statistically determined distance $a \cdot \delta$ which is introduced in the algorithm a measure of the difference between the useful signal and pre-analysed noise. The parameter a is a scale coefficient, and δ is a variance of the noise statistics. For a low-amplitude signals detection $1 < a \leq 2$. The obtained data can be represented by distributions shown in figure 2. The AE amplitude increases in response to (1) the increasing indenter velocity and (2) increasing volume of the material deformed by the indenter tip. The longer intervals between the AE events were observed at slower indenter movement and lower load. As opposes to this, at higher loads (larger material's volume involved in the deformation process), the intervals between AE events are shorter.

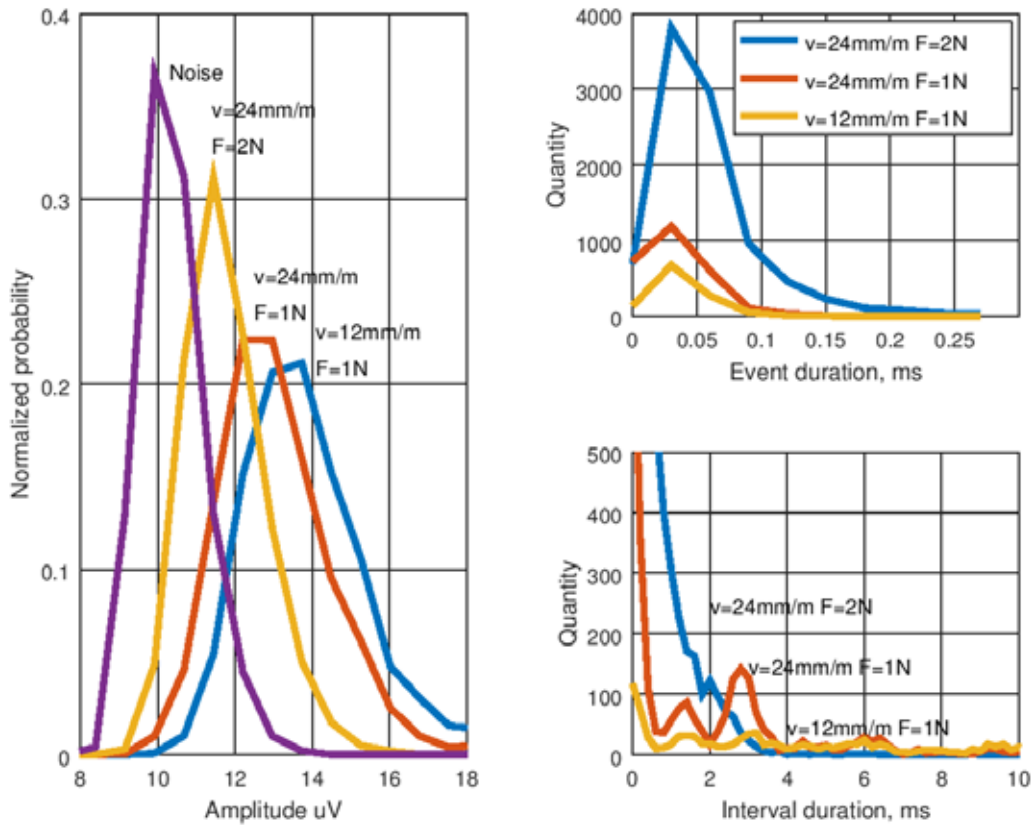


Figure 2 – Distributions of AE features during scratch test of a copper polycrystal. Amplitude distribution (left); Signal duration distribution (top right); Inter-arrival interval distribution (bottom right)

When a small load was applied during the scratch test, the relatively long duration of intervals between signals was detected. Duration of inter-event intervals was longer than a characteristic relaxation time of the applied sensor. The intervals between neighbouring signals are filled with the background noise. We tried to highlight it using the noise-reduction procedure implemented in the open-access Audacity software. The noise-reduction is based on the "Spectrum Noise-Gating" algorithm [9]. It consists of a few steps. At the first stage, the signal was amplified by +40dB. On the second stage, an average spectral characteristic of the noise signal was determined from the AE record immediately after the test completion. The final stage is the "Noise Subtraction" procedure was applied with the noise suppression of 60 dB. One should bear in a mind that the noise reduction procedure is substantially non-linear. As such, it strongly distorts the frequency spectrum of the original signal.

Figure 3 (inset) shows the signal after noise-reduction. Discrete signals and pauses between them are clearly visible. Figure 3 also illustrates a fragment of the surface area in front of the indenter tip. The correspondence of distances between the slip lines on sample surface and intervals between transients in the AE time series is evident. It should be noticed that the coarse and long slip lines correspond to the most powerful signals.

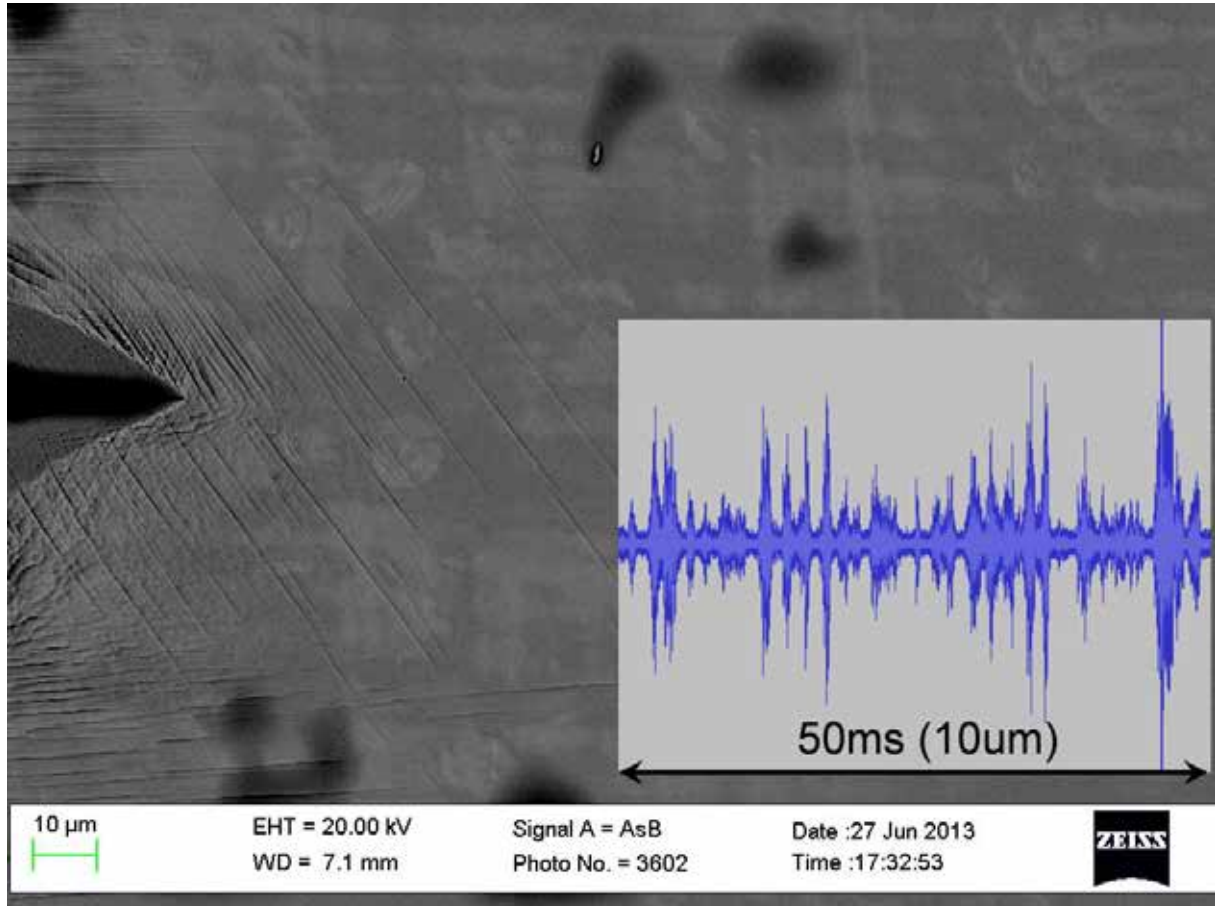


Figure 3 - Comparison between the surface topology in front of the indenter tip and the AE signal after noise reduction.

We assume that the sources of recovered AE transients are associated with long slip lines formed by dislocations escaping from the crystal lattice to a free surface. The “active” zone of a perfect crystal lattice, where plastic deformation initiates, is located in front of the indenter tip as shown on the EBSD map in figure 1. We should expect that all variations in the AE response stems from variations of the Schmid factor when the indenter passes through grain boundaries. However, the AE response should be stationary as long as the indenter moves within the grain and as long as the effect of grain boundaries is minimised. To verify this, we performed the analysis of major spectral parameters of raw AE data using a sliding window. The result of the behaviour of AE Power and spectral Median frequency (see definitions given, for example, in [3]) is shown in figure 4. This figure shows the bi-variate distribution of AE Power vs. Median frequency, where the colours correspond to those of inverse pole figure colours from the EBSD maps of respective grains. The grey dots indicate the transition stages when the indenter passed through the boundaries between the grains.

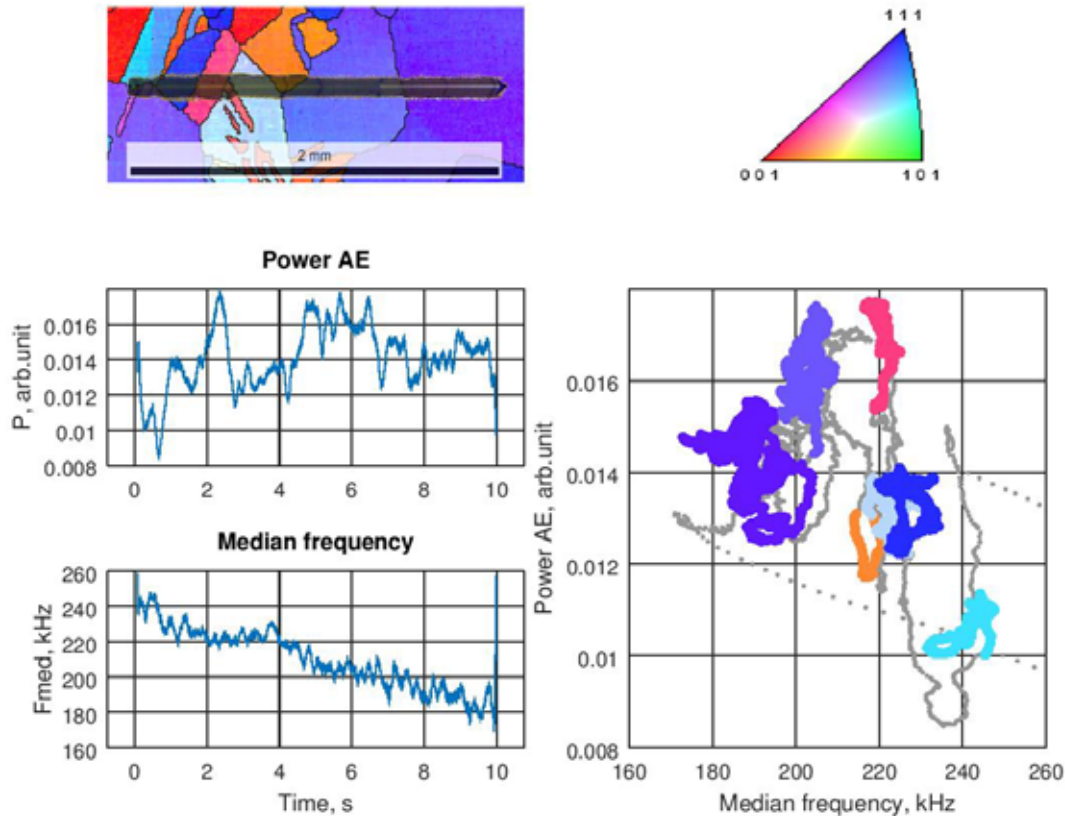


Figure 4 - Power and Median Frequency of Acoustic Emission for a Scratch Test (Copper, 12 mm / min, 1N)

4. Discussion

The acoustic emission method is a highly sensitive tool capable of analysing of crystal lattice dynamics on a very fine scale corresponding to individual slip lines. A sensitivity of the method to highly localised deformation of polycrystalline copper is shown in the present paper. The dislocation slip is a major mechanism of deformation in pure copper at room temperature. The AE Power and Median frequency exhibit a good response to different crystallographic orientations of grains. A similar effect was observed in [3, 5] in tensile testing of samples with different crystallographic orientations of loading axes.

During the scratch test, the crystal deforms locally, which allows detecting discrete events of dislocation glide in the AE signal if the appropriated nose cancelling procedure is used to rectify the signal and increase the signal-to-noise ratio. Admittedly, the largest fraction of elastic energy is released when a dislocation escapes to a free surface [11]. It is therefore plausible to suppose that the "loudest" events corresponding to dislocation annihilation at the surface on the early stage of strain hardening resent most of the AE signal. Plastic deformation commences in the local zone ahead of the indenter where the stress exceeds the critical resolves shear stress for dislocation nucleation and where long slip lines are formed resulting in the intermittent plastic flow such as that reported in [12] for nanoindentation tests. The slip lines in plastic zone ahead of the indenter are featured by a

reasonably larger height, of up to 50 nm (as has been confirmed by scanning white light interferometry) in a large grain. This roughly corresponds to 200 dislocation segments in the same slip line. This can be now seen as a reasonable lower bound estimate of the detectability threshold for the AE method.

Conclusions

The AE response during a scratch test is highly sensitive to the crystal orientation and the grain boundary properties. The thresholdless data acquisition technique and the noise-reduction signal processing methods demonstrate an outstanding capacity of the AE technique to reflect the collective dislocation behaviour within individual slip lines emerging to a free surface of a crystal in front of the moving indenter.

Financial support from the State Assignment of the Ministry of Science and Education of Russia according to the contract N 11.5281.2017/8.9 is gratefully appreciated

References:

- [1] Scruby, C.B. et al., Dynamic elastic displacements at the surface of an elastic half-space due to defect sources, *J. Phys. D. Appl. Phys.* 16 (6), 1983, pp. 1069–1083
- [2] Wadley, H.N.G. and Mehrabian, R., Acoustic emission for materials processing: a review, *Materials Science and Engineering*, 65 (2), 1984, pp. 245-263.
- [3] Vinogradov, A. et al., Acoustic Emission Spectrum and Its Orientation Dependence in Copper Single Crystals, *Mater. Trans. JIM.*, 36 (4), 1995, pp. 496–503.
- [4] Danyuk, A.V., et al., The effect of stacking fault energy on acoustic emission in pure metals with face-centered crystal lattice, *Letters on materials*, 7 (4), 2017, pp. 437-441
- [5] Vinogradov, A. et al., Correlation between Spectral Parameters of Acoustic Emission during Plastic Deformation of Cu and Cu-Al Single and Polycrystals, *Mater. Trans. JIM.*, 36 (3), 1995, pp. 426–431.
- [6] Challen, J.M., et al., Plastic Deformation of a Metal Surface in Sliding Contact with a Hard Wedge: Its Relation to Friction and Wear, *Proc. R. Soc. A Math. Phys. Eng. Sci.*, 394 (1806), 1984. pp. 161–181.
- [7] Hamid, R.C., et. al., The effect of Berkovich tip orientations on friction coefficient in nanoscratch testing of metals, *Tribology International*, 103, 2016, pp. 25-36.
- [8] Pomponi, E., et. al., Wavelet based approach to signal activity detection and phase picking: Application to acoustic emission, *Signal Processing*, 115, 2015, pp. 110–119.
- [9] How Audacity Noise Reduction Works, 2018, https://wiki.audacityteam.org/wiki/How_Audacity_Noise_Reduction_Works
- [10] Vinogradov, A. et al., Probing elementary dislocation mechanisms of local plastic deformation by the advanced acoustic emission technique, *Scripta Materialia*, 151, 2018, pp. 53–56.
- [11] Merson, D., et al., On the role of free surface in acoustic emission, *Mater. Sci. Eng. A*. 234-236, 1997, pp. 587–590.
- [12] Borc, J., et. al., Investigation of pop-in events and indentation size effect on the (001) and (100) faces of KDP crystals by nanoindentation deformation, *Materials Science and Engineering: A*, 708, 2017, pp. 1-10.

33 - When AE (Acoustic Emission) meets AI (Artificial Intelligence) II

Kilian WASMER¹, Fatemeh SAEIDI¹, Bastian MEYLAN¹, Quang Tri LE¹,
Sergey A. SHEVCHIK¹

¹Laboratory for Advanced Materials Processing, Empa - Swiss Federal Laboratories for Materials Science and Technology, Feuerwerkerstrasse 39, CH – 3602 Thun, Switzerland; Phone: +41 58 762 62 71; Email: kilian.wasmer@empa.ch

Abstract:

Acoustic emission (AE) is an effective method to monitor and control the quality in different technical processes, including tribology and fracture mechanics. However, in highly dynamic processes, the processing of AE signals is very burdensome. At the same time, artificial intelligence (AI) has been considered as a new and powerful tool to overcome both: the complexity of the large data processing with a reasonable computational time. In this contribution, we will present two examples from completely different process where AE techniques are combined with AI in order to make a significant step forward in process monitoring and quality control.

To start with, in additive manufacturing, which has been at the center of attention in recent years, we will demonstrate that the combination of AE with AI makes possible to detect several types of defects, including pores..

With the second example, we will prove that the combination of AE with AI is a very promising approach for in situ and real-time monitoring of electrical discharge inside natural rocks.

1. Introduction

Analysis of acoustic Emission (AE) takes its origin from the middle of the 20th Century and its progress has been closely related to the development of measuring devices [1]. AE based methods have numerous advantages such as high sensitivity, indifference to structural resonances and mechanical background noises, real-time capability of monitoring as well as early and robust detection of defects [2]. In addition, in recent years, the AE machine manufacturers have made a significant progress to simplify the usage of the hardware for data recording and storage. This makes AE now has become very much a mainstream. Consequently, AE techniques are considered by many as being one of the most effective monitoring methods, in particular for Nondestructive Testing (NDT), Nondestructive Inspection (NDI), and Nondestructive Evaluation (NDE) [3]. This technique has been successfully applied to a broad range of engineering applications, as well as investigations of a wide range of materials, material compositions and structures [1]. The industrial applications of AE also includes the tracking of dynamic processes, such as failure of brittle components [3] and, more recently, laser welding and/or additive manufacturing (AM) [4, 5].

Despite all the advantages of the AE, its major drawback is the interpretation of the AE signals. This is particularly true for complex and dynamic processes. The main reason is that the AE signals content is generally the result of mix of multiple background physical events, which take place inside a material at different time scales. Taking this into account, each specific application requires an exclusive understanding of the specifics of the AE generation, ideally relating those with the underlying fundamental physical phenomena. Unfortunately, in most real-life cases, the combinations of the physical phenomena that take place at the same time cannot be recovered with details. One typical example is the AE of laser-material interaction. The complexity of AE, in this case, is additionally complicated by the presence of noise that is a vital part of the real-life conditions and industrial environments. Under such circumstances, a new approach is necessary to bring a robust analysis of the AE signals into real-life applications. Artificial Intelligence (AI) may be a solution as it possesses numerous of advantages. AI allows bypassing the development of complex physical models for process understanding. It relies on statistics that can be easily collected in industrial applications. Also, AI allows using highly non-linear data transforms and automatically reduce the noises. To do so, AI builds complex empirical rules for intricate big data, thus correlating the acquired AE with the real events. The latest achievements in AI allow reducing the effect of the non-accuracies in preparations of training sets which results in reducing the preparation costs. These capabilities of AI were exploited for continuous crack propagation, laser welding and additive manufacturing [6]. The requirements for AI are sufficient AE data (input data) that corresponds to the desired outputs such as quality, quantification of defects, or some other process related phenomena of interest.

In fracture mechanics, the AE signals may have at least the five following origins (1) elastic interaction & impacts; (2) changes in stress-strain state of a local volume around the crack tip; (3) plastic deformation and damage at the crack tip; (4) generation, motion and interaction of dislocation; (5) energy liberation when two new surfaces are created due to crack initiation and propagation [2].

Additive manufacturing and laser welding are analogous in numerous aspects. Both processes have phenomena such as rapid heating, melting, solidification, and cooling. Consequently, the content of the AE signal seizes comprise material phase changes, dynamics inside the melted material and solidification processes. In addition, the AE signals are altered by the material and surface characteristics (e.g. chemical composition, phase transformation, optical properties, surface roughness, and environments), machine parameters (e.g. laser type, spot size, wavelength, pulse length, optical components) as well as the process parameters (laser power, scan speed, and scan line spacing). In addition, additive manufacturing is known to be prone to various defect types such as pores, balling, unfused materials, and cracking [7-10]. Under these circumstances, AE is of main interest in process monitoring. Obviously, even with the help of a fundamental physical understanding of the laser-material interaction, to correlate the AE signals with the real events is a challenge.

This contribution is an extension of our previous work [6]. Hence, we present two examples where acoustic emission (AE) was selected as a process monitoring method and the recorded data were analyzed by artificial intelligence (AI). The first case shows how AE system can be used for quality monitoring of additive manufacturing. The second is related to the monitoring of the pre-weakening of rocks during electric discharge.

2. Signal processing - Deep learning

In recent years, deep learning (DL) is actively introduced in many practical applications becoming an essential part of speech recognition, natural language processing, internet services and tele-communications [11, 12]. Originally inspired by the biological neuronal systems [11], today, this technique outperforms other traditional processing approaches in analysis of big arrays of data even in unsupervised way [11-13]. Such a rapid introduction from theory into practice in the past decade was possible thanks to the developments in optimization techniques that allowed involving a greater number of the basic computational units (neurons, decision trees etc.) into the DL architectures [11-13]. Consequently, this has given advantages in selection of more relevant information while suppressing the non-relevant one and made it possible to analyze more intricate data arrays [14]. At present, further developments in this field turn DL into a ready “on-shelf” tool. Thus, DL also starts to be involved into more complex scientific problems, for example description of dynamic systems [15], analysis of DNA [16] and computer vision tasks [11]. Such universality, combined with the computational power, makes DL attractive for industrial applications, and the first successful trials are seen in the literature. An interpretation of the acquired data for classification of the critical states in the same way was also shown in the field of fracture mechanics, laser welding and additive manufacturing [6]. The aforementioned applications are distinguished by the extreme operating rates. The complexity of those industrial problems is in the acquired data that take into account the dynamics of the underlying physical phenomena. Usually, in real-life, the latter is known for high non-linearity thus making interpretation in terms of existing physics extremely difficult, but still possible involving DL [6].

Today, DL incorporates a number of additional tools that increase the analytical efficiency when operating with real-life data and that can be involved to solve the industrial problems. Obviously, DL has become an attractive framework also for the monitoring of processes in real-life applications [6, 17-19] thus motivating us to investigate its applicability for various industrial problems. Under such circumstances, DL has many advantages in particular in extracting the relevant information [14]. As an example, belief propagation networks collect the relevant information in analogy with the renormalization that is widely used for the analysis of complex physical systems [15]. Convolution networks (CN) reach excellent results involving the convolutions over the given data that is followed by data compression [11]. The strong side of this technique is the recent extension for the adaptive and non-regular convolutions that allow operating on more complex data-grids [11]. Some other optimizations on simple feed forward networks also bring to better performance of those when analyzing complex data [11]. All this gives a rich instrumentation for development of new architectures and methods and adapt those to specific applications.

3. Examples

3.1 Example 1: AE meets AI in the field of AM quality monitoring

The first example shows that AE is strong instrument for monitoring in situ and in real-time the quality in additive manufacturing. Today the quality monitoring in additive manufacturing (and generally in all laser based processes) is mainly carried out either with temperature measurements of the melt pool or high resolution imaging of the process zone [7, 20]. Despite all the efforts to bring these technologies to the market, there is a consensus among scientists and industries that these monitoring techniques still do not provide acceptable rates in quality reproducibility during production [7, 20].

Wasmer, Shevchik et al. [17, 18] proposed an approach which combines AE with AI for in situ and real-time monitoring of AM. The results were obtained on real process.

An industrial 3D printer Concept M2 (Concept Laser GmbH, Germany) was used. It is a powder-bed technology, also known as a selective laser melting (SLM) process. The machine was equipped with a fiber laser operating in continuous mode at a wavelength of 1071 nm with a beam quality M2 = 1.02 and a spot size of 90 μm . The powder had a particle size distribution ranging from 10 to 45 μm and was made of CL20ES stainless steel (1.4404 / 316L). In addition, an opto-acoustic, a fiber Bragg grating (FBG), operated as an acoustic sensor. The FBG was mounted in the machine 20 cm away from the process zone.

A workpiece with dimension 10x10x20 mm³ was produced under N₂ atmosphere (See Fig. 1a). During the process, the laser power P was 125 W, the hatching distance h was 0.105 mm and the layer thickness t was 0.03 mm. Three laser velocities were selected to achieve three porosity contents that determined three different quality grades. The three colors visible in Fig. 1a correspond to the different process parameters, where 800 mm/s are bright regions, 500 mm/s are brown regions and 300 mm/s are dark/blueish regions. Typical light microscope images of the three qualities are shown in Fig. 1b-1d. The porosity concentration was 0.3 ± 0.18 % (medium quality; 300 mm/s; 132 J/mm³; Fig. 1b), 0.07 ± 0.02 % (high quality; 500 mm/s; 79 J/mm³; Fig. 1c), and 1.42 ± 0.85 % (poor quality; 800 mm/s; 50 J/mm³; Fig.1d). In Fig. 1, the insets show typical defects observed such as a) tubular, b) small lack-of-fusion and c) large lack-of-fusion defects. The z- and y-directions is based on Fig. 1a.

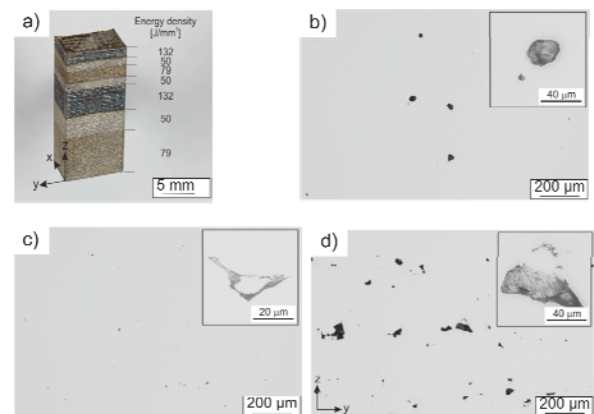


Figure 1: a) Test workpiece produced with three porosity contents; b) – d) Typical light microscope cross-section images of the regions produced with b) 300 mm/s (medium quality), c) 500 mm/s (high quality) and d) 800 mm/s (poor quality).

Reprinted by permission from Elsevier License: Elsevier, [18].

In terms of signal processing, the main techniques employed are based on Deep Learning (DL), in particular Convolution Neural Networks (CNN) [17] and Spectral Convolution Neural Networks (SCNN) [18]. In both cases, the search of distinct features is carried out in the time-frequency domain using wavelet spectrograms. Also, the intensity measurement of the AE components in spectrograms was taken as the relative energies of the narrow frequency bands which were the input features for the NN classifiers. The frequency bands were extracted using several wavelet families such as Daubechies, Symlets, and Coiflets as well as adaptive M -band wavelets.

The analysis of the acquired AE signals was performed using one or two running windows (RW) that scanned the signal. The choice of the time span for the RW is a compromise between the spatial resolution in defects detection and classification accuracy. On the one hand, a short running window increases the spatial resolution in the detection of possible defect areas within each layer. On the other hand, very short time spans are more affected by noise and thus are deteriorating the classification efficiency. Several time spans and using of two RW were investigated.

Obviously, to achieve the best classification accuracy, there are many decisions that have to be made. The choices included the selection of the NN (CNN or SCNN), the number of convolution layer, number of pooling layer, wavelet family, decomposition level, or type of adaptive wavelet, the number of running windows, their corresponding time spans, etc... Wasmer, Shevchik et al. [17, 18] defined that the best choice was provided by the NN and wavelet which showed the minimum approximation errors on the given AE signals. In terms of RW, the time span was selected after an exhaustive search in which the classification accuracy was evaluated after each retraining using RWs with different time spans.

A typical AE signal from one complete layer of medium quality (300 mm/s) is shown in Fig. 2a. Figure 2a contains two running windows that are delimited by the red and a green box. They represent a long (LRW – red box) and short running windows (SRW – green box) scanning the acquired signal. Figure 1b is the reconstructed spectrogram from the relative energies of the *M*-band wavelets from a pattern of the signal in Fig.2a that is bounded by the red box between 0.2 and 0.4 s [17].

In terms of NN used, Fig. 3 displays a scheme of the CNN used in Wasmer et al. [17]. In this figure, it is seen that the spectrograms build from the LRW and SRW pass through two different convolution layers from which a series of perception maps 1 are build. Then, the information is combined in the pooling layers 1 before the information from both flows is pushed into a common convolution layer 2 followed by a second pooling operation (see pooling 2 in Fig. 3). The final classification is carried out in fully connected layers. The classification result/accuracy is the output of the procedure which is often given in a table.

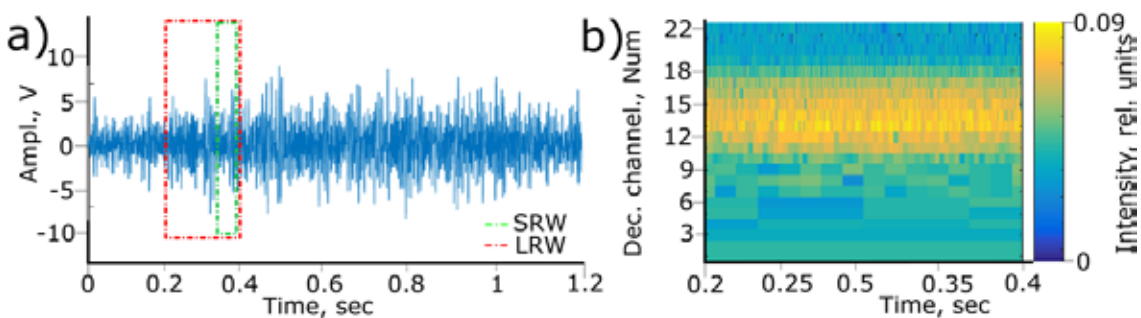


Figure 2: a) A typical AE signal from one complete layer of medium quality (300 mm/s). The red and green boxes are the long (LRW) and Short Running Windows (SRW) scanning the acquired signal; b) reconstructed spectrogram for the LRW time span bounded by red lines in Fig. 2, a).

Reprinted by permission from Springer Nature: Springer eBook, [17].

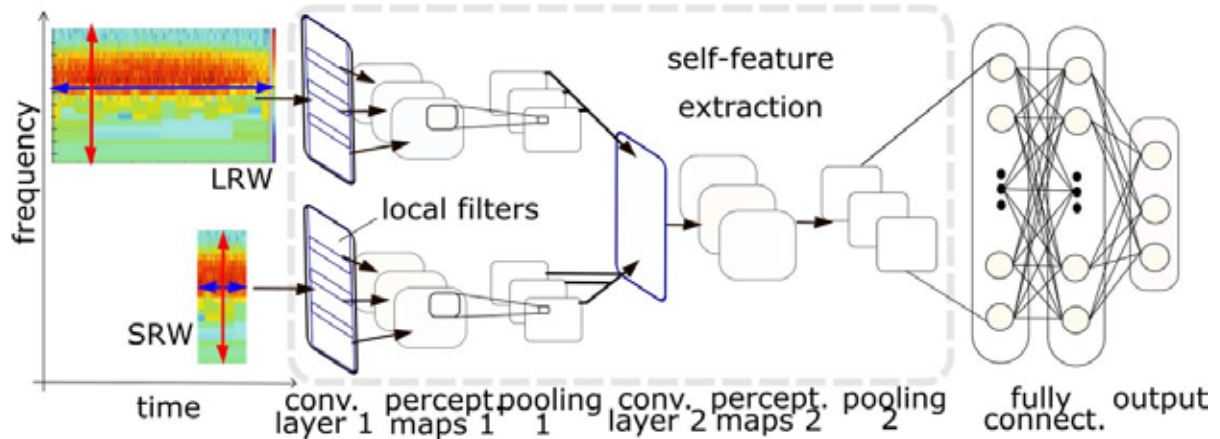


Figure 3: The structure of the CNN, where LRW and SRW denote the long rang window and short range window, respectively.

Reprinted by permission from Springer Nature: Springer eBook , [17].

The main results of these feasibility studies from Wasmer, Shevchik et al [17, 18] are summarize in Table 1. In this table, the numbers in bold and in italic are the lowest and highest classification accuracies found to date. The classification accuracies in the table are defined as the number of true positives divided by the total number of tests for each category. These values are given in the diagonal cells of the table (red cells). The classification errors are computed as the number of the true negatives divided by the total number of the tests for each category. These corresponding values are filled in non-diagonal row cells. For example, the highest accuracy rate for the poor quality was 89%. The classification error is more or less equal between the medium and high qualities, 4 and 7%, respectively.

It was found that, by and large, the lowest accuracy rate was found using the Daubechies wavelet with ten vanishing moments to reconstruct the spectrogram, one running window and the conventional CNN for classification. In contrast, the best results are mainly obtained using also the Daubechies wavelet with ten vanishing moments to reconstruct the spectrogram, one running window but with the spectral CNN (SCNN) for classification [18]. However, it is important to note that using *M*-band wavelets, two running windows and the conventional CNN, the classification accuracies are only slightly lower than the highest ones presented in Table 1. Therefore, it shows that there is still some potential improvement by using *M*-band wavelets, two running windows and the SCNN as a classifier.

To conclude this example, Wasmer, Shevchik et al [17, 18] could demonstrate that their innovative approach that is combining AE with AI has some potential for in situ and real-time monitoring of additive manufacturing (AM) processes.

Table 1: Classification accuracy test results in % for three categories of events*

Test \ Ground truth	Poor quality	Medium quality	High quality
Poor quality (1.42 ± 0.85 %, 800 mm/s)	62 - 89	19 - 4	19 - 7
Medium quality (0.3 ± 0.18 %, 300 mm/s)	25 - 5	53 - 85	22 - 10
High quality (0.07 ± 0.02 %, 500 mm/s)	18 - 8	21 - 9	61 - 83

Red and light red highlight the classification accuracies and errors, respectively

3.2 Example 2: AE meets AI in the field of fracture mechanics

Pre-weakening of solid materials using electric discharge is a new technique aiming at reducing the costs and energy consumption of raw materials processing in mining and recycling industries. However, the absence of an effective pre-weakening quality control prohibits its introduction into a wide practice. In our previous work [6], we showed the potential to use AE to monitor this process with transparent materials. The aim of this work is to show that this process can be applied to real mining materials.

Stones of different sizes were selected from a copper ore. The stones were separated by successive sieving in 4 size categories; (i) 25-31mm, (ii) 31-35mm, (iii) 35-40mm and (iv) 40-45mm. Each stone was then submitted to a single pulse using the same voltage generator as previously described [6, 23]. Each stone was placed individually on the metallic conveyor belt that acts as a counter electrode and aligned with the electrode as shown in Fig. 4. The gap between the electrode and counter electrode was fixed at 50 mm for all the tests and the belt was kept motionless.

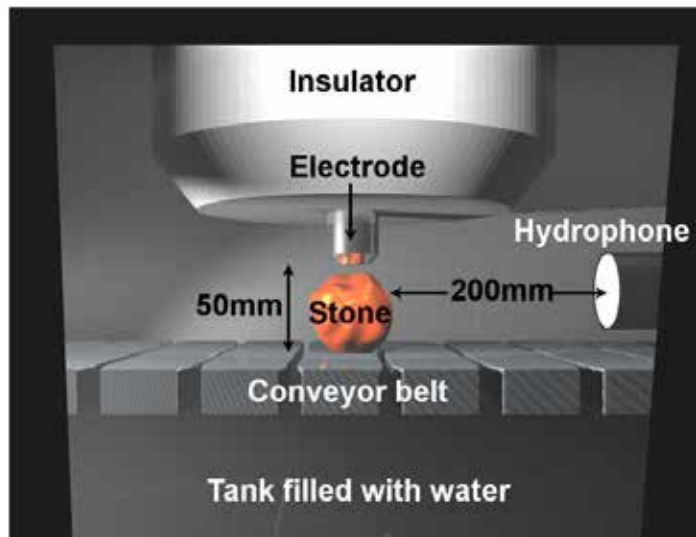


Figure 4: Schematic representation of the setup.

The stones were treated at 200kV and four different capacitance (10, 15, 22.5 and 37.5 nF), which correspond to energy of 200, 300, 450 and 750 J per pulse. For the two smaller sizes categories, 30 stones of each were tested at each energy level. For the two larger stone sizes, 20 stones of each were tested at each energy level. This gives a total of 400 stones tested.

For each electrical pulse, the corresponding AE signal was recorded simultaneously. The detection of the acoustic signals was made directly inside the water filled chamber using an acoustic hydrophone sensor R30UC. It was placed at a distance of 20 cm from the electrode gap (See Fig. 4). The AE signals were recorded with a 10 MHz sampling rate for 20 ms and the record was synchronized with the pulse start.

Contrary to our work with transparent samples, the categorization is not straightforward as the presence of cracks inside the sample cannot be directly observed. What can be characterized is the presence or absence of discharge and the eventual fragmentation of the stone in pieces. To quantify the fragmentation the weight of the stone before (W_{before}) treatment is measured and the weight of the larger remaining particle after discharge is measured (W_{after}). The weight loss is then calculated as $W_{loss} = (W_{before} - W_{after})/W_{before}$. Two examples of stones from the category 25-31 mm are given in Fig. 5. The two stones have a weight loss of 44 and 6%, respectively.



Figure 5: a) and b) Stones of the 25-31mm size category shown before discharge. c) and d) the same stones shown after discharge of 200kV and 37.5nF.

the corresponding AE signal shown in Fig. 6b. This category is often also considered as surface discharge as the path is mainly at the surface of the stone and entered the stone only in a small edge as shown in Fig. 5d.

In this work, we defined 5 categories based on the weight loss and presence or absence of discharge. The absence of discharge is easily recognizable due to the lack of discharge sound and lack of damage on the stone. The AE signal as shown in Fig. 6a is also very characteristic. The amplitude and duration of AE is much less than for other categories as presented in Fig. 6b and 6c. The next category is surface discharge or weight loss of 0-1%. In this category, the discharge occurred mainly in water or at the stone interface and did not fragment the stone. The next category is a weight loss between 1 and 10% as illustrated in Fig. 5d with the

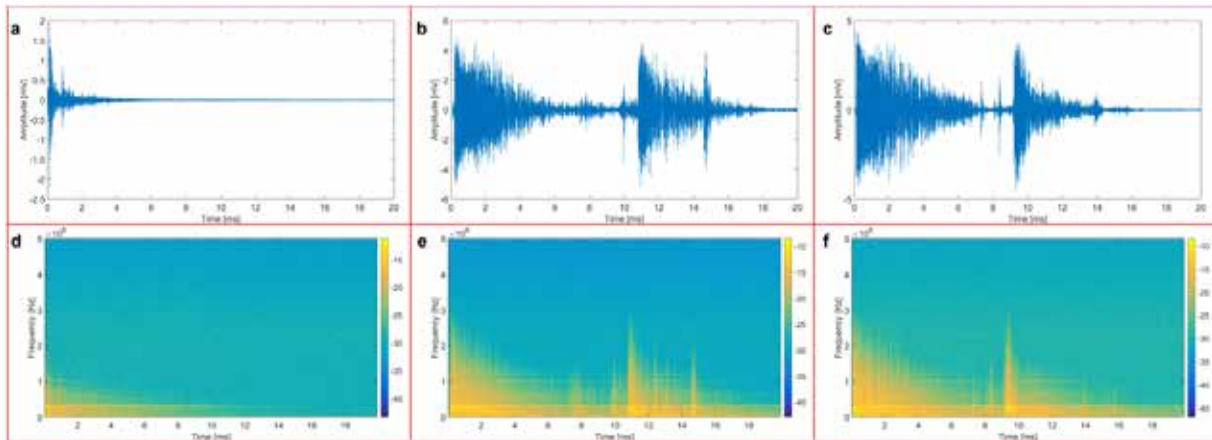


Figure 6: a) AE signal for a pulse without discharge, b) AE signal from the stone shown in Figure 2b and d, corresponding to 6% weight loss, c) Ae signal from the stone shown in Figure 2a and c, corresponding to a 44% weight loss. d), e) and f) are the corresponding sonogram.

The last two categories correspond to various degree of fragmentation, the first with a weight loss of 10-50% and the second with a weight loss of more than 50%. A stone with a weight loss of 44% is shown in Fig. 5c and the corresponding AE signal is in Fig. 6c.

The AE signals for the no discharge case are easily separated from the discharge case with both a lower intensity and shorter duration of the acoustic emission (see Fig. 6a and 6d). However, all the other signals where discharge occurred are showing similar characteristic and similar sonograms (see Fig. 6b, 6c, 6e and 6f). Indeed, the frequency with the highest response on the sonogram is around 300 kHz and corresponds with the highest sensitivity of the sensor. The amplitude and duration of the signals, as well as the frequencies are similar and advanced processing techniques are needed to separate the signals.

For this work, we used a similar approach to our previous work [6]. We used first wavelet decomposition in order to extract the features from the AE signals. In this work we used standard Daubechies wavelet with 10 vanishing moments to decompose the signals in time-frequency domains.

Before classification, only the most informative features are selected using the principal component analysis (PCA) [24]. The disposal of non-informative features decreases the noise and additionally reduces the computational complexity [24].

The classification was performed using support vector machine (SVM), a statistical learning technique proposed by Cortes and Vapnik [25].

The classification results are presented in Table 2. As expected the classification results of the no discharge category presents no difficulty to correctly separate. Good news is for the correct separation with a 90% accuracy of fragmentation with a weight loss of more than 50%. This category corresponds to discharge with the most damage created and means that the process is running correctly. It is important to recognize sample from this category. The category surface discharge is also relatively well separated with an accuracy of 70%. The categories in between suffer from a lower accuracy of 53 and 66%. This can come from the fact that the boundary between the category are just arbitrary selected and it is well possible that these categories have common features with neighboring categories as the process is not expected to physically vary between them. It is also well possible that a lot of invisible

cracks are created in the stones without the stone being fragmented, a process known as pre-weakening. In this case the acoustic signal is expected to be very similar to a complete fragmentation. This could explain why a lot of signals from low weight loss categories are classified in the more than 50% weight loss category.

Moreover, the process was not run in optimal conditions as the gap between the electrodes was kept constant at 50mm. This gap is good for big stones that fill most of the gap and thus limit that amount of discharge occurring in the water above the stone. For the small stones, a large portion of the discharge will occur anyway in the water which means that all the signals will have common water discharge features and not only the stone from the 0 - 1% weight loss category.

4. Conclusions

Following our first contribution “*When AE (Acoustic Emission) meets AI (Artificial Intelligence)*” presented at the 21. Kolloquium Schallemission – in Fulda, Germany, 2017 [6], we presented two new examples where AE meets AI. The first example is related to quality monitoring of additive manufacturing (AM) process. To do so, the approach is to use state-of-the-art opto-acoustic sensors as AE sensors and analyses the recorded AE data with Deep Learning (DL) techniques such as convolution neural networks (CNN) and spectral neural networks (SCNN). It was found that the classification accuracy between three close categories varies significantly depending on the selection of the NN (CNN or SCNN), the number of convolution layer, number of pooling layer, wavelet family, decomposition level, or type of adaptive wavelet, the number of running windows, their corresponding time spans, etc.... However, the best classification accuracies are higher than 83% even though the results are only based on two feasibility studies. This demonstrated the potential of this approach to be industrialized as in situ and real-time quality monitoring in AM processes.

A second example related to highly dynamic fracture mechanics, in particular for mine industries. We demonstrated that by combining AE with AI, it is possible to classify with acceptable accuracy the effect of electrical discharge in rocks in terms of weight loss (WL). This is also an important result as it may allow saving a significant amount of energy in the mine industry, especially for pre-weakening of rocks. This technology was patented [26].

Finally, based on the two examples presented, it can be concluded that by combining AE signals with a state-of-the-art signal processing, it is possible to address highly complex industrial processes. We demonstrated that, even in very noisy and dirty environments, we are able to achieve reliable classification of investigated events. This makes this methodology very effective for industrial applications even though it does not explain the nature of the AE signals, but this is planned as the future work.

Table 2: Classification accuracy test results in % for three categories of events*

Ground truth \ Test	No discharge	WL 0-1%	WL 1-10%	WL 10-50%	WL >50%
No discharge	100	-	-	-	-
WL 0-1%	-	70	-	3	27
WL 1-10%	-	7	53	2	38
WL 10-50%	-	8	-	66	26
WL >50%	-	5	-	5	90

*Red and light red highlight the classification accuracy with the ground truth and classification mistakes, respectively.

References:

- [1] Grosse, C., Ohtsu, M., Acoustic emission testing basics for research - applications in civil engineering, 1st ed., Springer, Berlin, Heidelberg, 2008, DOI: 10.1007/978-3-540-69972-9
- [2] Baranov, V., Kudryavtsev, E., Sarychev, G., Schaveli, V., Acoustic emission in friction, vol. Volume 53. Tribology and Interface Engineering Series. Elsevier, 2007.
- [3] The Japanese Society for Non-Destructive Inspection, Practical Acoustic Emission Testing, 2nd ed. Springer, Tokyo, Japan, 2016, DOI: 10.1007/978-4-431-55072-3
- [4] Huang, M., Jiang, L., Liaw, P.K., Brooks, C.R., Seeley, R., Klarstrom, D.L., Using acoustic emission in fatigue and fracture materials research, JOM, Vol. 50, 1998, pp. 1-12.
- [5] Gu, H., Duley, W.W., A statistical approach to acoustic monitoring of laser welding, Journal of Physics D: Applied Physics, Vol 39, 1996, pp. 556 – 560.
- [6] Wasmer, K., Saeidi, F., Meylan, B., Vakili-Farahani, F., Shevchik, S.A., When AE (Acoustic Emission) Meets AI (Artificial Intelligence)”, Presented at 21. Kolloquium Schallemission, Fulda, Germany, 9 – 10 March, 2017 and published in NDT.net Vol.22 Issue 010, October, 2017, ISSN 1435-4934.
- [7] Everton, S.K., Hirsch, M., Stravroulakis, P., Leach, R.K., Clare, A.T., Review of in-situ process monitoring and in-situ metrology for metal additive manufacturing, Materials and Design, Vol. 95, 2016, pp.431-445.
- [8] Zhang, L.C., Attar, H., Selective laser melting of titanium alloys and titanium matrix composites for biomedical applications: a review, Advance Engineering Materials, Vol. 18, 2016, pp. 463–475.
- [9] Khairallah, S.A., Anderson, A.T., Rubenchik, A., King, W.E., Spatter formation in powder-bed selective laser melting, Acta Materialia Vol. 108, 2016, pp. 36-45.
- [10] King, W.E., Barth, H.D., Castillo, V.M., Gallegos, G.F., Gibbs, J.W., Hahn, D.E., Kamath, C., Rubenchik, A.M., Observation of keyhole-mode laser melting in laser powder-bed fusion additive manufacturing, Journal of Materials Production Technology. Vol. 214, 2016, pp: 2915-2925.
- [11] Schmidhuber, J., Deep learning in neural networks: An overview, Technical Report IDSIA-03-14 / arXiv:1404.7828 v4 [cs.NE] (88 pages, 888 references)
- [12] LeCun, Y., Bengio, Y., Hinton, G., Deep learning: review, Nature, Vol. 521, 2015, pp. 436-444.
- [13] Voulodimos, A., Doulamis, N., Doulamis, A., Protopapadakis, E., Deep learning for computer vision: A brief review, Computational Intelligence and Neuroscience, Vol. 2018, Article ID 7068349, 13 pages, 2018.
- [14] Tishby N., Zaslavsky N., Deep Learning and the Information Bottleneck Principle, ITW 2015; 2015 IEEE Information Theory Workshop, arXiv:1503.02406
- [15] Mehta, P., Schwab, D.J., An exact mapping between the variational renormalization group and deep learning, 2012, arXiv:1410.3831
- [16] Deadwood, J., Bagirov, A., Kelarev, A.V., Machine learning algorithms for analysis of DNA data sets, Machine learning algorithms for problem solving in computational applications: intelligent techniques, IGI Global, 2012.

- [17] Wasmer, K., Kenel, C., Leinenbach, C., and Shevchik, S.A., In situ and real-time monitoring of powder-bed AM by combining acoustic emission and artificial intelligence, Proceedings of Additive Manufacturing in Products and Applications - AMPA2017 – Industrializing Additive Manufacturing, M. Meboldt and C. Klahn (eds.), Zürich, Switzerland, pp: 200-209, Springer, 2018, DOI: 10.1007/978-3-319-66866-6_20.
- [18] Shevchik, S.A., Kenel, C., Leinenbach, C., Wasmer, K., Acoustic emission for in situ quality monitoring in additive manufacturing using spectral convolutional neural networks, Additive Manufacturing, Vol. 21, pp: 598-604, 2018, DOI: 10.1016/j.addma.2017.11.012.
- [19] Wasmer, K., Le-Quang, T., Meylan, B., Vakili-Farahani, F., Olbinado, M.P., Rack, A., Shevchik, S.A., Laser processing quality monitoring by combining acoustic emission and machine learning: A high-speed X-ray imaging approach, accepted in Physics Procedia, LANE 2018 - 10th Conference on Photonic Technologies.
- [20] Grasso, M., Colosimo, B.M., Process defects and in situ monitoring methods in metal powder bed fusion: a review, Measurement Science and Technology, Vo. 28, 2017.
- [21] Lin, T., Xu, S., Shi, Q., Hao., P., An algebraic construction of orthonormal *M*-band wavelets with perfect reconstruction, Applied Mathematics and Computation, Vol. 172, 2006, pp. 717-730.
- [22] Tazebay, M.V., Akansu, A.N., Adaptive sub-band transforms in time-frequency excisers for DSSS communications systems, IEEE Transaction Signal Processing, Vol. 43, 1995, pp. 2776-2782.
- [23] Shevchik, S.A., Meylan, B., Mosaddeghi, A., Wasmer, K., Acoustic emission for in situ monitoring of solid materials pre-weakening by electric discharge: A machine learning approach”, submitted to IEEE Access.
- [24] Jolliffe, I.T., Principal Component Analysis, second edition (Springer), 2002.
- [25] Cortes, C., Vapnik, V., Support-vector networks, Machine Learning Vol. 20, 1995, pp. 273-295.
- [26] Vaucher, S., Violakis, G., Meylan, B., Shevchik, S.A., Wasmer, K., Mosaddeghi, A., Method of treating a solid material by means of high voltage discharges, Patent N° PCT/CH2016/000090.

65 - AE fracturing modes classification by means of shear tensile source model

Petruzalek¹, M., Lokajicek¹, T. Svitek¹, T., Jechumtalova², Z., Kolar², P., Adamova², P. and Sileny², J.

¹Institute of Geology of the Czech Academy of Sciences, Prague, Czech Republic

²Institute of Geophysics of the Czech Academy of Sciences, Prague, Czech Republic

Abstract:

A shear-tensile crack (STC) is presented as a suitable source model for acoustic emission (AE) events. The experimental data comes from an uniaxial compression test realized on the Westerly granite specimen using a 14 channel Vallen Amsy5 AE monitoring system. The advantage of the STC against the traditional MT is: (i) it is a physical source – contrary to MT, as STC describes straight the simple fracture modes anticipated inside the loaded sample, namely the shear-slip and both the opening and closing tensile crack, (ii) it is simpler, described by less parameters (5 instead of 6 for the unconstrained MT), which is essential in solving the inverse problem. Proposed STC procedure was tested on 38 AE events selected in the range of 50 – 98% of uniaxial compressive strength. Compare to the MT model, the STC model showed similar fit of the input data while providing by far smaller confidence regions. That means more certain determination of mechanism orientation but mainly the highly improved reliability of the decomposition components. Thus the use of STC model allow, besides other things, to better distinguish between tension and shear type of AE events, which may be a crucial in recognizing approaching failure. In this particular experiment, the application of STC model proved to be useful in recognizing threshold of unstable microcracking and indicative in determination of failure plain orientation. The AE crack length was found to be slightly above the range of the largest grains. The principle stresses orientation, inverted from the STC mechanisms, corresponded to the stress conditions of uniaxial compression test.

1. Introduction

Acoustic emission (AE) is a phenomenon that spans the generation and propagation of acoustic (elastic) waves caused by sudden irreversible changes in the internal structure of a type of material. In the case of rock, it is closely connected to the generation, growth, and interaction of microcracks and leads to a brittle failure [1]. As such, an AE event may be considered, on a very small scale, as an earthquake with a size on the order of millimeters in the case of laboratory experiments [2]. Considering phenomena similarity [3] and approximately 70 years of seismology, it is not surprising that most of the methods for quantitative AE analysis originally came from seismology [4].

From a rock mechanics point of view, an AE analysis contributes to recognizing microcracking thresholds [5]: the crack initiation threshold (CI) and the crack damage threshold (CD). The fracturing process becomes unstable when crossing the CD threshold and the transition from tension to shear microcracking [6]. While an AE analysis helps describe the spatio-temporal evolution of damage, studies of AE source mechanisms and their dependence on the current stress state of rock enables detailed insight into the microscale of the fracturing process.

A simple method that distinguishes between shear, tension, and collapse source types is based on average first arrival polarity [7]. Using first arrival polarity, [6] illustrated an increase in shearing in the expanse of tension type when specimens were approaching failure in triaxial tests. A more sophisticated approach for examining failure mechanisms is the application of the moment tensor (MT) model. [8] used the MT to determine crack type and crack orientation. Since introduction of the above studies, application of the MT analysis has helped us determine the fracturing process in all types of laboratory studies. Moment tensor analyses have revealed that shear cracks are dominant during uniaxial and triaxial loading experiments [7, 9, 10]. Shear faulting was also determined to be a dominant type of failure in a plane-strain compression test [11] and a three-point-bend fracture test [12]. Although the moment tensor has become a standard for describing seismic sources across all scales, it may not provide resolvable information for all data sets. For some applications, it may be useful to constrain the full MT with the aim of increasing resolution. A suitable alternative to the MT is the shear-tensile crack (STC) model, a model that possesses the capacity to discern shear vs. tensile dislocation and to yield a more robust inverse task. Additional details on this model are provided in the Methods chapter. Until now, applications of the STC have only been employed for earthquakes (e.g., Jechumtálová et al., 2014; Šílený et al., 2014). Here, we apply the STC in a laboratory acoustic emission experiment and demonstrate its usefulness as compared to the standard MT approach.

2. Experiment

The specimen of fine grained Westerly granite was uniaxially loaded up to the failure. A 14 channel AE apparatus was used for AE monitoring as well as for periodical ultrasonic sounding (US). More information about the experiment or the rock properties can be found in Petruzalek et al., (2017, 2018). The determined mechanical properties were: uniaxial compressive strength (UCS = 226.6 MPa), Young's modulus ($E = 51$ GPa), poisson ratio (0.26). Crack initiation threshold (CI = 45% of UCS, the stress level at which stable microcracking begins) and the crack damage threshold (CD = 72% of UCS, the stress level at which unstable microcracking begins) were determined in detail using three independent methods based on stress-strain data, AE activity, and ultrasonic attenuation [13]. AE events were localized by a grid search procedure with anisotropic velocity model. The accuracy was up to 2 mm [14]. Thirty-eight of the strongest AE events, with very low localization were used to make the input amplitudes as reliable as possible. Eleven of these AE events were located in the portion of stable microcracking and twenty-seven were located in the regime of unstable microcracking. The 38 selected AE events were further used as a data set for testing AE source mechanisms. Peak to peak first arrival amplitudes (AM), corrected for the particle velocity sensitivity (S) of used sensors and for AE sensor directional sensitivity ($\cos(\alpha)$, where α is the angle of incidence, served as an input (AC) for the source mechanism inversion: $A^C = SA^M \cos(\alpha)$.

3. Methods

We assessed the reliability of mechanisms for selected microearthquakes by estimating the error of the evaluation and by comparing the mechanisms retrieved using the two source models: MT and STC. The MT approach is routine across scales – from earthquake seismology ranging from mega-earthquakes, to strong and moderate events, to weak intraplate seismicity, to the rupturing of rock and other samples in the laboratory and the fracturing of materials in civil and mechanical engineering. The STC results from a special type of constraint applied to the MT, offering enhanced robustness for the retrieved mechanism.

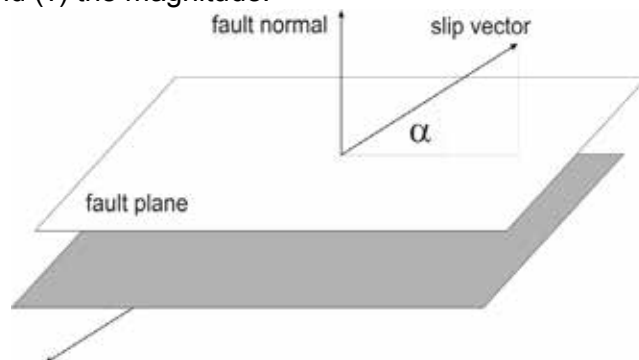
The Moment Tensor – MT

The unconstrained MT is the most comprehensive description of shear and non-shear sources and is the body force equivalent of a rupture that generates the same wave field in a continuous medium as an actual rupture. Thus, the MT is not a physical source but a substitute for real processes occurring within the focus. As a system of body forces, the MT is not a priori convenient for offering simple insight into processes within an earthquake focus. Therefore, it is generally decomposed into simple sources. The method of decomposition is not unique. The most common and widely used procedure is one that splits the general MT into isotropic and deviatoric portions (unique), and then splits the deviatoric portion into a double couple (DC) and a compensated linear vector dipole (CLVD) with a common major tension or pressure axis that is ambiguous (e.g., [15]). Thanks to its generality, the MT is relevant to the fracturing of a solid body, including all of the modes of fracturing recognized within fracture mechanics and their combinations. However, since the MT does not describe the rupture itself but rather body force equivalents of actual rupturing, it also includes mechanisms that do not generally represent realistic physical sources. In other words, sometime the MT is needlessly general. In addition to rupture mode I (tensile fracturing) and rupture modes II and III (plane and anti-plane shear slip), combinations of forces that do not correspond to a physically feasible rupturing are also present. Therefore, for the simple rupturing expected within the foci of tectonic or induced earthquakes, the MT is unnecessarily complex, leading to more parameters than those relevant to simple rupture models.

The Shear-Tensile Crack – STC

Among constrained MTs, a particularly convenient model is one that combines modes I and II/III of the fracturing, namely the shear slip and tensile crack. The model's design dates back to the 1980's to a manuscript by [16] and follows the applications of [17] and [18]. Later, a combination of shear fault with a tensile crack, leaving a fault tip at various angles, was studied by [15]. A special case of geometry amongst the superpositions of a shear fault with a tensile crack is the geometry that occurs when the tensile crack formally coincides with a shear fault and perpendicularly opens to a fault at the same time instant. The concept of shear slip and simultaneous opening of the same fault originated in [19], afterward appeared in [20], and was revisited by [21, 22]. Although the concept has been differently named by various authors, here, we refer to it as the Shear-Tensile Crack (STC). A big advantage in comparison to the MT is the fact that the STC is a physically based concept for the source mechanism. Simply stated, it is a slip along a fault that may open or close at the same time (i.e. it directly describes a seismoactive process in terms of the rupture occurring within the focus), Fig. 1. If we fix the values of the material constants, the STC is described by five parameters: (i) the dip of the fault; (ii) the strike of the fault; (iii) the rake angle specifying the shear component of the slip; (iv) the angle, α , referred to as the slope, which represents the off-plane component of the slip vector; and (v) the magnitude.

Fig. 1. The STC source model - a combination of shear-slip and tensile crack represented by the slip vector off the fault plane and the slope angle α ($\alpha = 0^\circ$ is a pure shear slip and $\alpha = 90^\circ$ is a pure tensile crack).



The number of parameters is the same as that for the deviatoric MT which is frequently applied in order to constrain the MT for the sake of increasing the stability of inversions of teleseismic and regional records for Global CMT and regional CMTs. On the other hand, the STC also has the capability for describing a change in volume within the focus. In fact, it is the simplest source model for incorporating a shear slip and a volume change. In this way, it combines a

desirable amount of generality with the maximum possible simplicity, ensuring robustness for the inverse task [23, 24].

Confidence zones

To assess the reliability of the STC solution obtained, we evaluated the confidence zones of source model parameters or their combinations. Confidence zones are objects within the model space that specify the volume in which the solution of the inverse task is contained in an a priori specified probability, taking into account errors in the data. In other words, confidence zones describe a distribution for model parameters that yield a good match to the data. The size and shape of the confidence zones indicates the uncertainty of the estimated parameters: large confidence zones indicate a poor solution while small confidence zones suggest a good solution. Both reliability for determining the orientation of the mechanism and its characteristics for the DC and non-DC content, should be estimated. To assess geometric reliability, we constructed confidence zones for the T, P, and N axes of the deviatoric portion of the MT solution corresponding to the retrieved STC, and confidence zones for decomposition of this type of MT in order to determine the characteristics for both the DC and non-DC content. For the latter, parallel information is the confidence zone for the slope angle. For the procedure, we scanned the model space within a regular grid and evaluated a match to the data and the probability density function (PDF) for the grid points. We then integrated the PDF across a trial volume within the model space and searched for a patch in which the cumulative probability acquired certain values, generally 0.9, 0.95, and 0.99 (details are provided in [25]). This type of visualization is also relevant if properties of the mechanism described by the unconstrained MT are studied.

A comparison of MT and STC

Solving the inverse task requires matching predicted amplitudes to observed data. The criterion is met by minimizing the quantity expressing the misfit. For this work, we minimized the root mean square of the differences normalized by the norm of the data, the quantity n_{rms} (Tab. 1). A perfect fit implies a value of 0 and values below 0.5 are considered acceptable. Only a few solutions were below 0.15. However, the bulk of solutions (70%) were below 0.3 and only a single event (event number 34) had the misfit worse than 0.5. Misfit values did not differ much for the MT and STC inversions, the latter being slightly larger based on the definition (six parameters in the MT model vs. five parameters for the STC). The Thanks to the 3-D configuration of the observations, coverage of the focal sphere by sensor projections was generally good. For events located deep inside the specimen, this feature was obvious. The benefit is illustrated on focal sphere coverage for events number 9, 5, and 24 (Fig. 2), which are analyzed in this paper in detail.

Figure 2. Examples of the quality of coverage for the focal sphere by observation site for event numbers 9, 5, and 24. Sensors located above the focus are displayed as triangles pointing down, while sensors below the focus are displayed as triangles pointing up. Color marks the polarity of the incoming P wave: blue – compression, red – dilatation. Equal-area projections of the lower focal hemisphere were applied.

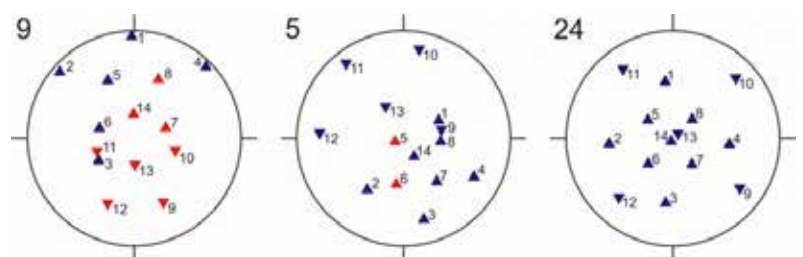


Table 1. Results of the MT and STC inversion of the 38 events selected from the laboratory experiment. Source type (STC determined) of AE event: T – tension, S – shear, ST – combined.

Event nr.	MT RMS	STC RMS	Kagan angle [°]	MT			STC				
				DC	V	CLVD	DC	V	CLVD	Constrained type	AE source type
				[%]	[%]	[%]	[%]	[%]	[%]		
1	0.297	0.306	5.6	34.9	44.5	20.6	27.8	40.1	32.1	3	T
2	0.12	0.19	5.2	64.2	2.5	-33.3	95.3	2.6	2.1	1	S
3	0.229	0.251	8.9	11.8	35.3	52.9	34.4	36.4	29.2	2	T
4	0.168	0.171	3.8	22.7	46.9	30.4	19.2	44.9	35.9	2	T
5	0.342	0.344	0.9	34.7	38.9	26.4	33.6	36.9	29.5	2	T
6	0.074	0.085	1.4	21.9	38.7	39.4	27.4	40.3	32.3	1	T
7	0.132	0.149	17.7	14.4	33.4	52.2	35.4	35.9	28.7	1	T
8	0.179	0.221	3.3	45.6	52.3	2.1	12	48.8	39.2	3	T
9	0.211	0.224	1.4	60.5	14.6	24.9	76.2	13.2	10.6	1	S
10	0.094	0.111	4.5	13.9	35.8	50.3	37.4	34.8	27.8	1	T
11	0.091	0.099	2.7	27.7	33.5	38.8	37.9	34.5	27.6	1	T
12	0.143	0.144	0.6	91.8	7.6	-0.6	87	7.2	5.8	1	S
13	0.252	0.267	3.4	27.9	24.2	47.9	53.1	26.1	20.8	1	ST
14	0.165	0.166	2.6	53.5	23.7	22.8	55.9	24.5	19.6	1	ST
15	0.159	0.165	2	82.8	-2.2	15	98.3	0.9	0.8	1	S
16	0.33	0.349	17.8	5.6	48	46.4	14.8	47.3	37.9	3	T
17	0.264	0.271	1.4	52.7	29.9	17.4	48	28.8	23.2	2	ST
18	0.201	0.238	11.1	14.7	29.7	55.6	46.3	29.8	23.9	3	ST
19	0.15	0.19	4	17.4	27.5	55.1	46.3	29.8	23.9	2	ST
20	0.128	0.162	11.3	21.2	33.5	45.3	36.4	35.4	28.2	2	T
21	0.065	0.099	1.4	27.3	35.6	37.1	34.5	36.4	29.1	1	T
22	0.217	0.223	1.9	73.5	17.7	-8.8	73	15	12	1	S
23	0.154	0.161	3.2	64.3	17.2	18.5	71.9	15.6	12.5	1	S
24	0.241	0.243	7.2	23.8	48.7	27.5	15.7	46.8	37.5	3	T
25	0.24	0.25	0.9	24.8	32.2	43	40.5	33.1	26.4	2	ST
26	0.209	0.235	1.4	77.6	-1.2	-21.2	96.9	-1.7	-1.4	1	S
27	0.151	0.152	4.1	73.1	15.1	-11.8	76.3	13.2	10.5	1	S
28	0.435	0.47	15.7	29.7	15.7	54.6	69.9	16.7	13.4	3	S
29	0.165	0.204	1.6	34.6	41.8	23.6	25	41.6	33.4	3	T
30	0.48	0.482	11.7	41.8	41.1	17.1	44.4	30.9	24.7	2	ST
31	0.155	0.16	8	19.5	38	42.5	29.4	39.2	31.4	2	T
32	0.223	0.228	1.6	25.7	29.2	45.1	48.8	28.4	22.8	1	ST
33	0.151	0.153	2.9	27.5	32.3	40.2	38.9	33.9	27.2	1	T
34	0.536	0.582	13.2	17.4	37.9	-44.7	32.6	37.4	30	4	T
35	0.283	0.297	1.8	76.6	0.1	-23.3	96.9	-1.7	-1.4	2	S
36	0.156	0.161	2.4	63.5	28.2	8.3	51.6	26.9	21.5	1	ST
37	0.209	0.218	1.8	15.5	39.8	44.7	27.4	40.3	32.3	2	T
38	0.251	0.257	0.4	92.2	1.2	6.6	97	1.7	1.3	1	S

The expectation of obtaining well-determined mechanisms in terms of both the MT and the STC, thanks to the distribution of sensors surrounding the foci, came true for most events from the treated set. MT and STC solutions were very similar for the bulk of treated data. The principal axis deviation angle (the Kagan angle) was determined for 75% of tested events below 5° and less than 20% of the data set had a Kagan angle of 10-18° (Tab. 1). The range of confidence zones was used for comparison of reliability of MT and STC mechanisms. As an illustration, three events are presented in Fig. 3: (1) a well-constrained mechanism for event number 9 (constrained Type 1 in Table 1), (2) an inferior solution in terms of the size of the confidence zones represented by event number 5 (constrained Type 2 in Table 1), and (3) event number 24, a poorly resolved mechanism for both orientation and DC vs. non-DC content (constrained Type 3 in Table 1). The size of a confidence region directly

depends on the constraint imposed on the source mechanism: the stronger the constraint, the smaller the confidence region, as is obvious and follows from the definition. From this viewpoint, the fact that confidence regions for the STC shrink as compared to those related to the MT is not surprising. The constrained mechanism displays an inferior fit to the data, as compared to the unconstrained mechanism, but yields a more “certain” solution: its confidence region shrinks. The point is that we only dealt with solutions that still fit the data well (i.e. further investigation was restricted to data that could be considered successful solutions of the inverse task). How the confidence region shrinks was also considered. It affects both the orientation of the mechanism and the decomposition. Concerning the former, the ambiguity for the principal axes position can be removed. Concerning the latter, it may allow us to determine shear vs. non-shear performance for an examined event. Describing the orientation, such a scenario was definitely the case for event 5 and, partially, for event 24. For event 5, the confidence regions for all of the principal axes in the MT solution were very large and, in fact, merged. The result indicates that the orientation of the MT was entirely uncertain. In contrast, within the STC solution they were markedly smaller: the confidence region of the T-axis was fairly compact, indicating that its direction was very well resolved.

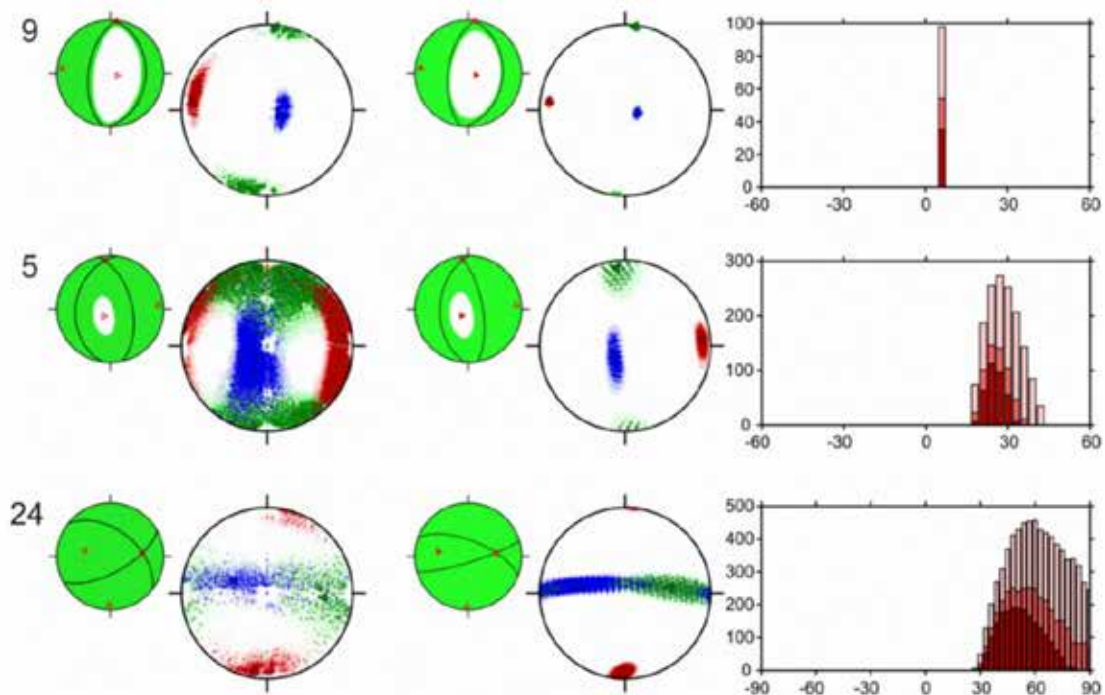


Fig. 3. The MT (left) vs. STC (right) mechanisms and estimates of their uncertainty for event number 9), 5 and 24. The MT panel: Column 1 – a traditional fault-plane solution plot (nodal lines, zones of compression for P-waves in green; principal axes, red triangles (T-axis, triangle up; P-axis, triangle right; N-axis, triangle left); Column 2 - the T (in red), P (blue), and N (green) axes and their confidence regions at the 90% (dark color), 95% (medium), and 99% (pale color) probability levels. The STC panel: Columns 1-2 – the fault-plane solution and the T, P, and N confidence zones similar to the MT solution. Column 3 – the confidence zone (in the form of a histogram) for the slope angle α .

For the P and N axes, they were stretched but remained mutually isolated (i.e. although less certain than the T-axis, the P and N axes were resolved one from the other, unlike the case of the MT solution). For event 24, a decrease in the confidence regions for all of the three

principal axes were observed when comparing the STC and MT solutions. When using the STC, the T-axis becomes well-resolved while the P and N axes remain ambiguous (they merge together and there even seems to be bimodality in the P-axis position, see the blue spots on the green background). They are, however, at this point, tightly constrained to the plane perpendicular to the well-determined T-axes.

The above discussion concerned orientation of the mechanism. Equally important is its decomposition, i.e. the content of individual “elementary mechanisms”, namely the DC, ISO, and CLVD components in mechanisms resolved using the MT and STC approaches. Obtaining the DC, ISO, and CLVD percentages in the MT approach is straightforward. For obtaining them using the STC approach, it is necessary to first evaluate the moment tensor corresponding to the current STC and to then decompose it in the standard way. Using this approach, it is possible to directly compare individual components and their percentages and the uncertainty of their retrieval expressed by their confidence regions. When inspecting histograms corresponding to the MT and STC solutions in Fig. 4, it is obvious that the latter are narrower than the former. Thus, percentages in the STC solution are better resolved than those within the MT solution. Such a result is logical, as previously indicated, because the STC is one of the constrained MTs. The benefit of using the constrained source model results from the fact that increased resolution may allow recognition of features within the mechanism decomposition that are lost during the unconstrained MT approach. This is the case for all three of the events in Fig. 4. Event number 9 is largely a DC event (Table 1) and confidence regions for non-DC portions of the MT approach are rather wide. Both the ISO and CLVD involve a value of zero. Therefore, by taking into account all of the involved errors, we can conclude that the ISO or CLVD components, although their best values are non-zero, are zero. However, for the STC solution this is not the case. The solution is even more DC than the MT solution (76 vs. 61 percent), although the non-DC components were significantly recovered because their confidence zones were very tight (the event belongs to Group 1 of the well constrained solutions, see Table 2) and remained well apart from the zero value. Event number 5 is a part of Group 2 with a bit less of a constrained orientation. Nevertheless, the same conclusion, as for the previous case, can be reached. The event was largely non-DC and the DC content was only around 34 percent. The non-DC components were even less certain than they were for the previous event. However, the confidence region of the ISO component remained markedly above zero. As a result, we concluded that the resolved ISO was significantly positive. The same cannot be said for the CLVD since its confidence region included zero and the component remained unresolved as for its sign. Similar to the previous event, the STC solution was markedly more constrained. Confidence regions for all of the three source components were fairly narrow. Both the ISO and CLVD yielded positive values far from zero. Therefore, they were significantly resolved as positive and the event may be classified as a slip with an extension. Worth noting here is that the histograms relevant to the STC inversion for data subjected to random noise contamination were markedly wider than histograms describing the confidence regions, and we, again, assumed this was due to the fact that the noise experiments were not entirely relevant to error estimates consisting of confidence region construction since they changed the data.

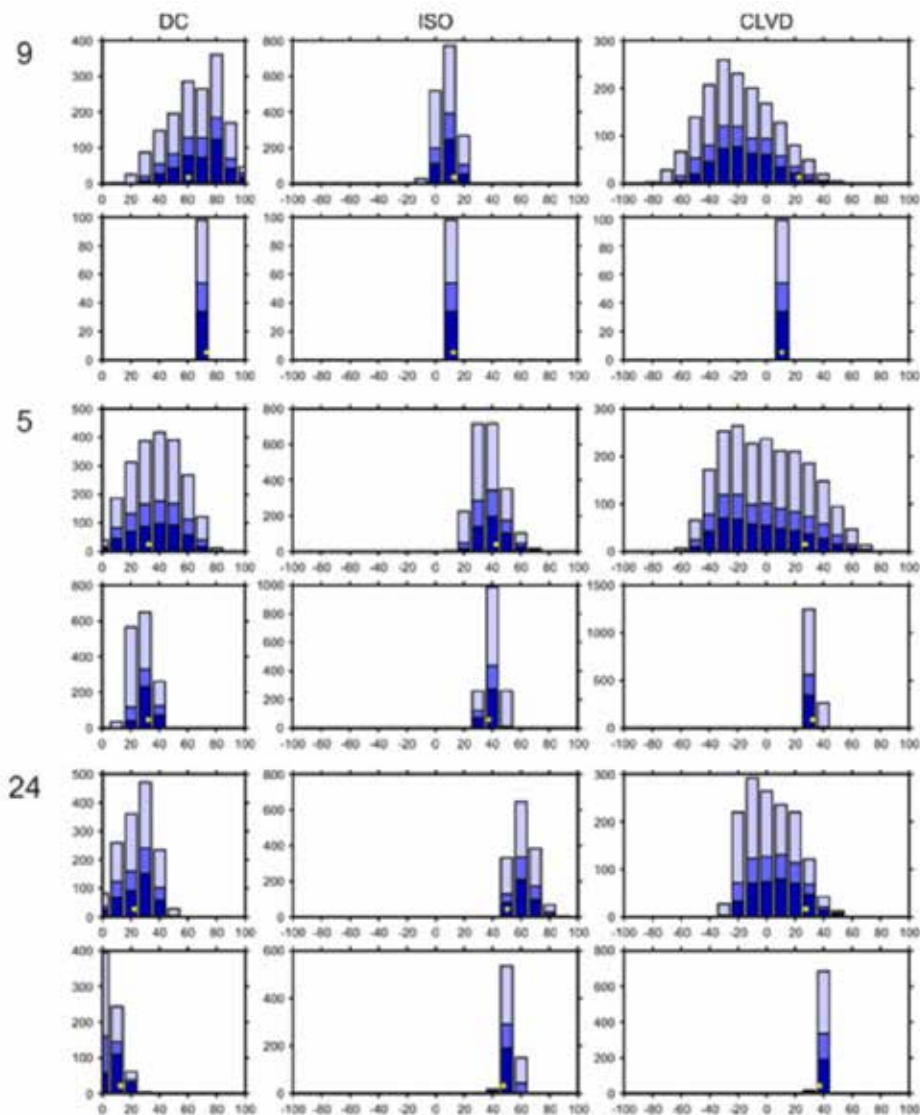


Fig. 4. Decomposition of the mechanisms for event number 9, 5 and 24. The top row in the panel corresponds to the full moment tensor (MT) solution. The bottom row corresponds to decomposition of the moment tensor corresponding to the shear-tensile crack (STC) solution. Histograms - confidence regions at the 90% (dark color), 95% (medium), and 99% (pale color) probability levels are shown.

The last example, event number 24, belonged to Group 3 events that were not very well constrained for orientation, see the large confidence zones of the principal axes in Fig. 6. Surprisingly, this property was not transformed into the decomposition and confidence zones for the source components were approximately the same size as those corresponding to events 5 and 9. A large quantity of the non-DC content was determined for the mechanism of event 24. However, the CLVD within the MT solution remained insignificant. In contrast, the ISO was significantly positive because its confidence region was entirely located within positive numbers. Similar to previous events, the STC, by far, yielded much more constrained source components and we concluded that the mechanism is significantly extensional. As previously mentioned, such behavior may contradict a common experience in which the decomposition is worse resolved than the orientation. However, uncertainty in determining the orientation here was not universal, and it, in fact, only involves the P and N axes while the T-axis was very well recovered (see Fig. 5 of the STC solution).

Event number 9, 5, and 24, representing examples of the mechanisms, were very well constrained (with respect to orientation), less well constrained, and rather poorly constrained, respectively. Considering the MT and STC solutions as two alternative source models, the latter was preferred because a similar fit was kept for the data but smaller confidence regions were obtained. The result not only indicates more certain solutions for orientation of the mechanism, but also whether or not the focus was simply shear, taking into account uncertainty in the mechanism determination or a non-shear mechanism (i.e. having either an extensional or a dilatational component). As a result, we processed the entire data set (all 38 events) in terms of the STC source model.

The STC mechanism in a rock mechanics context

The main goal of this work is not to present a detailed analysis of the fracturing process, but to test and present an STC approach for AE mechanism determination for a set of 38 selected AE events (from approximately 20,000 registered events). Despite limitations for the AE data set, discussing how STC obtained mechanisms fit the general idea of the fracturing process in compression tests is illustrative.

For the case of rock mechanic compression tests, the fracturing process can be divided into two phases, stable and subsequent unstable microcracking, with the CD threshold being the boundary between the two. Unstable microcracking indicates that after crossing the CD threshold the sample fails even without additional increased stress above the CD threshold. That is why CD stress, which is approximately 70-80% of the uniaxial compressive strength, may be used as an estimate of long term strength. Tension microcracking, with cracks parallel to the maximum compressive stress, is supposed to be dominant during stable microcracking. Shearing, on planes inclined to the maximum compressive stress at angles of 20-30°, plays a significant role throughout unstable microcracking. The mentioned suppositions were determined by considering the interpretation of stress strain behavior for the compression tests (e.g. [26, 27] and the microscopic analysis of thin sections obtained from loaded specimens [28]. The analysis of AE source types (the average first arrival polarity) corroborated different microcracking mechanisms for both microcracking stages [6].

Based on the STC model decomposition (Tab. 1), the source types of AE events were divided into three different categories: 1. Shear type (S), DC > 70%; 2. Tension type (T), DC < 40%, CLVD > 25%; and 3. Combined type (ST), DC: 40-56%, CLVD: 19-23%. Of the 38 analyzed AE events, the first 11 belonged to the stable microcracking stage and the remaining 27 to the unstable microcracking stage. Even with the limited AE data set, the source type distribution well-fit the general fracturing process idea (Fig. 5). Tension dominated stable microcracking (T: 82%, S: 18%, and ST: 0%). When the axial stress crossed the CD threshold, shearing began to play a significant role in the fracturing process (T: 33%, S: 33%, and ST: 33%). For comparison, a very similar source type distribution, determined using just the first arrival polarity, was also reported by [6]. While both of the source planes from a mathematical standpoint are equivalent, we chose the more probable plane (the red colored plane in Fig. 5) based on principal stresses orientation with respect to the source type mechanism. The more vertical plane was chosen for the tension source type. The plane with a closer declination to 60-70° (20-30° from σ_1) was chosen to represent a shear crack plane. Fig. 9a provides the orientation distribution of the poles for chosen crack planes. From the pole graph one can determine that the tension crack planes have an inclination of 65-85° and almost a random azimuthal distribution. Most of the cracks for the S and ST source types had an inclination in the interval of 55-65° (25-35° from σ_1). The S and ST poles displayed a slight preference for the azimuthal orientation (the two marked clusters in Fig. 6a).

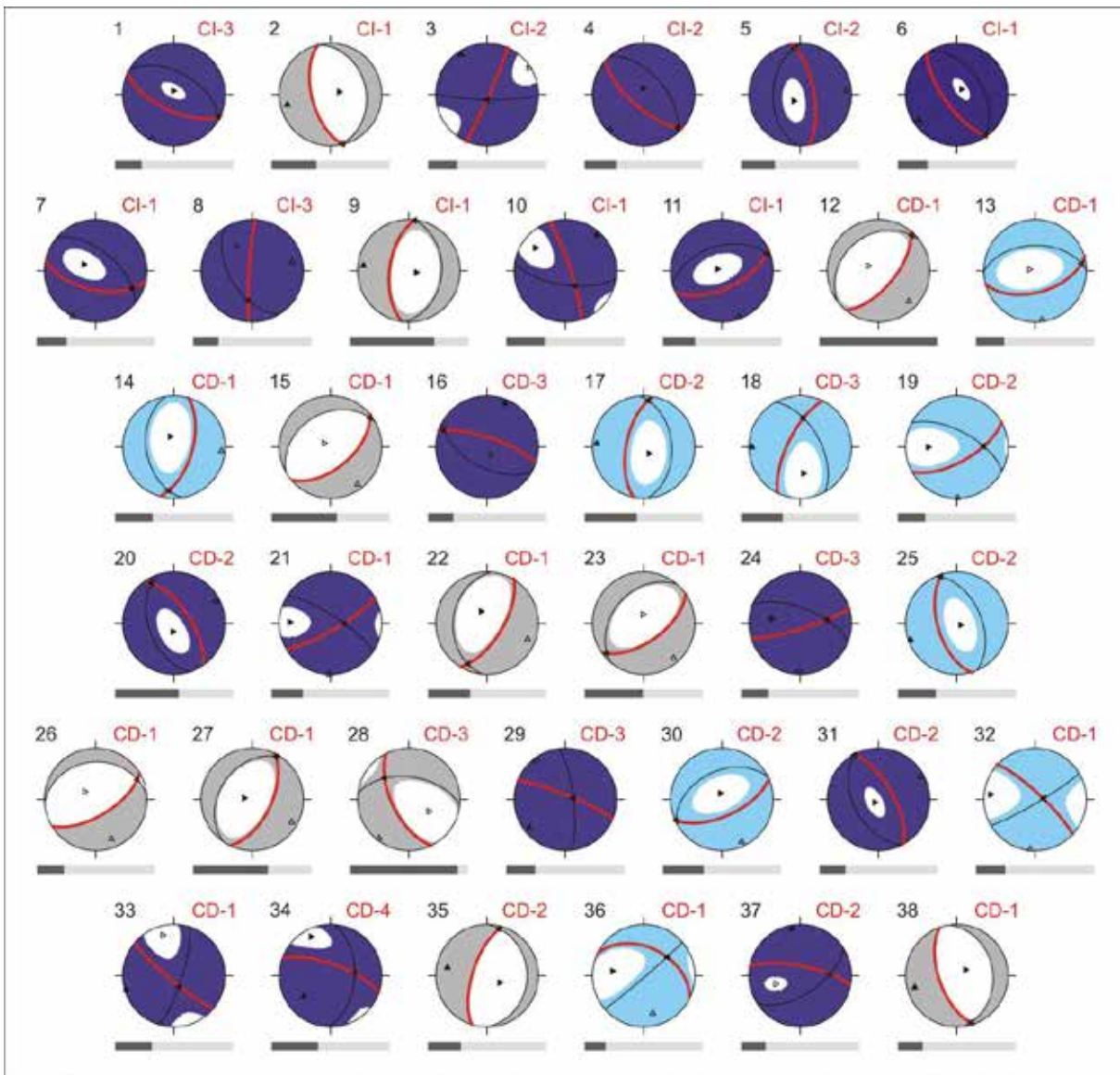


Fig. 5. STC mechanisms for the set of 38 selected events displayed using a traditional fault-plane solution plot (source lines and zones of compression for P-waves are shown in color; principal axes, triangles (T-axis, triangle up; P-axis, triangle right; N-axis, triangle left)). Colors represent different source types: T-dark blue, S-gray, and ST-light blue. Red labels mark the phase of the uniaxial loading test for CI-stable microcracking and CD-unstable microcracking; the numbers mark a constrained type. Bars correspond to the size of the event.

The strike/dip coordinates of the center points of the clusters (85/30 and 319/30) may represent the poles of macroscopic failure planes (175/60 and 47/60). The plane 175/60 (the red color in Fig. 6) corresponds rather well with its dip and azimuthal orientation to the only macrocrack (190/56) found on the surface of the tested specimen (Fig. 6b). However, the location of the 38 selected AE events did not display any preferential orientation (Fig. 6c).

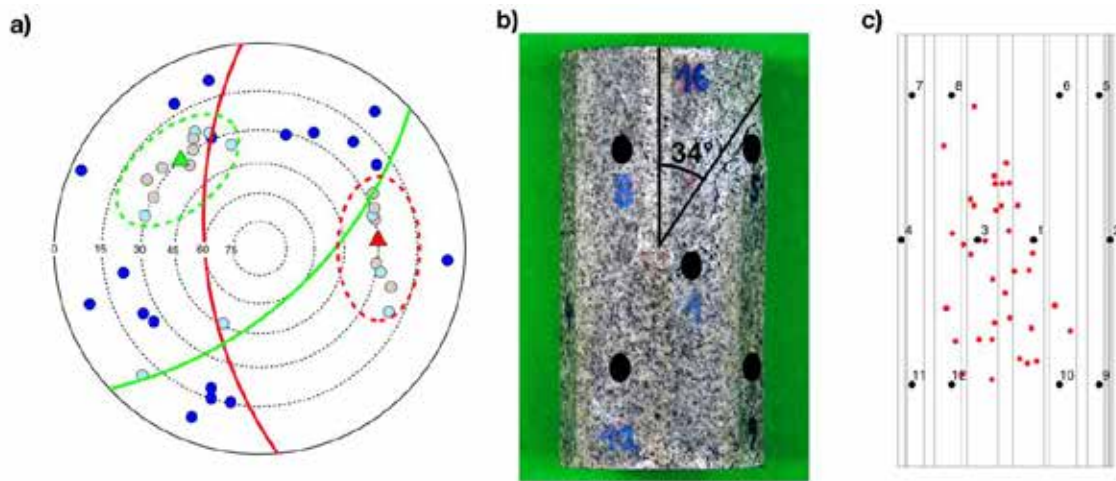


Fig. 6. . a) An equal area stereographic projection (lower hemisphere) of poles to the selected crack planes (red in Fig. 5). The set of 38 AE events and the STC determined mechanisms. Dark blue is the tension source type, gray is the shear source type, and light blue is the combined source type. Red and green triangles indicate poles and great circles for the two possible failure planes. b) The WG specimen after testing with its orientation of failure. c) The location of the 38 selected AE events.

4. Conclusions

As compared to the MT model, the STC model displayed a similar fit for input data while providing far smaller confidence regions.

The STC results indicate a more certain determination of source mechanism when compared to MT solution.

The use of STC solution leads to a highly improved the reliability of decomposition components.

Application of the STC model allowed, in addition to other things, better distinction between the tension and the shear type of AE events that may be crucial for recognizing an approaching failure.

Transition from tension to shear microcracking was recognized while crossing the CD threshold.

Preferential orientation of the shear cracks was determined to coincide with orientation of the failure plane.

Acknowledgement

This study was partially supported by the Czech Science Foundation research grants 16-03950S, 18-08826S and by the Czech Academy of Sciences project RVO 67985831.

References:

- [1] Paterson, M. S., & Wong, T. (2005). *Experimental rock deformation--the brittle field*. Springer.
- [2] Sellers, E. J., Kataka, M. O., & Linzer, L. M. (2003). Source parameters of acoustic emission events and scaling with mining-induced seismicity. *Journal of Geophysical Research: Solid Earth*, 108(B9).
- [3] Lockner, D. (1993). The role of acoustic emission in the study of rock fracture. *International Journal of Rock Mechanics and Mining Sciences & Geomechanics Abstracts*, 30(7), 883–899.
- [4] Grosse, C. U., & Ohtsu, M. (2008). *Acoustic emission testing : [basics for research, applications in civil engineering]*. Springer.
- [5] Eberhardt, E., Stead, D., Stimpson, B., & Read, R. S. (1998). Identifying crack initiation and propagation thresholds in brittle rock. *Canadian Geotechnical Journal*, 35(2), 222–233
- [6] Stanchits, S., Vinciguerra, S., & Dresen, G. (2006). Ultrasonic Velocities, Acoustic Emission Characteristics and Crack Damage of Basalt and Granite. *Pure and Applied Geophysics*, 163(5–6), 975–994.
- [7] Zang, A., Wagner, F. C., Stanchits, S., Dresen, G., Andresen, R., & Haidekker, M. A. (1998). Source analysis of acoustic emissions in Aue granite cores under symmetric and asymmetric compressive loads. *Geophysical Journal International*, 135, 1113–1130.
- [8] Ohtsu, M. (1991). Simplified moment tensor analysis and unified decomposition of acoustic emission source: Application to in situ hydrofracturing test. *Journal of Geophysical Research: Solid Earth*, 96(B4), 6211–6221.
- [9] Chang, S.-H., & Lee, C.-I. (2004). Estimation of cracking and damage mechanisms in rock under triaxial compression by moment tensor analysis of acoustic emission. *International Journal of Rock Mechanics and Mining Sciences*, 41(7), 1069–1086.
- [10] Shah, K. R., & Labuz, J. F. (1995). Damage mechanisms in stressed rock from acoustic emission. *Journal of Geophysical Research: Solid Earth*, 100(B8), 15527–15539.
- [11] Carvalho, F. C. S., & Labuz, J. F. (2002). Moment tensors of acoustic emissions in shear faulting under plane-strain compression. *Tectonophysics*, 356(1–3), 199–211.
- [12] Kao, C.-S., Carvalho, F. C. S., & Labuz, J. F. (2011). Micromechanisms of fracture from acoustic emission. *International Journal of Rock Mechanics and Mining Sciences*, 48(4), 666–673.
- [13] Petruzalek, M., Lokajicek, T., & Svitek, T. (2017). Ultrasonic Method for Estimation of Crack Initiation Stress. In *proceedings of the 51st US Rock Mechanics/Geomechanics Symposium, ARMA 2017, 25.-28. 7. 2017, San Francisco*
- [14] Petružálek, M., Vilhelm, J., Rudajev, V., Lokajíček, T., & Svitek, T. (2013). Determination of the anisotropy of elastic waves monitored by a sparse sensor network. *International Journal of Rock Mechanics and Mining Sciences*, 60, 208–216.
- [15] Julian, B. R., Miller, A. D., & Foulger, G. R. (1998). Non-double-couple earthquakes 1. Theory. *Reviews of Geophysics*, 36(4), 525–549.

- [16] Teisseyre, R. (1980). Some remarks on the source mechanism of rockbursts in mines and on the possible source extension. *Acta Montana*, 58, 7–13.
- [17] Rudajev, V., & Šílený, J. (1985). Seismic events with non-shear component: II. Rock bursts with implosive source component. *Pure and Applied Geophysics PAGEOPH*, 123(1), 17–25.
- [18] Kozák, J., & Šílený, J. (1985). Seismic events with non-shear component: I. Shallow earthquakes with a possible tensile source component. *Pure and Applied Geophysics PAGEOPH*, 123(1), 1–15.
- [19] Dufumier, H., & Rivera, L. (1997). On the resolution of the isotropic component in moment tensor inversion. *Geophysical Journal International*, 131(3), 595–606.
- [20] Minson, S. E., Dreger, D. S., Bürgmann, R., Kanamori, H., & Larson, K. M. (2007). Seismically and geodetically determined nondouble-couple source mechanisms from the 2000 Miyakejima volcanic earthquake swarm. *Journal of Geophysical Research: Solid Earth*, 112(10), 1–20.
- [21] Vavryčuk, V. (2001). Inversion for parameters of tensile earthquakes. *Journal of Geophysical Research: Solid Earth*, 106(B8), 16339–16355.
- [22] Vavryčuk, V. (2011). Tensile earthquakes: Theory, modeling, and inversion. *Journal of Geophysical Research: Solid Earth*, 116(12), 1–14.
- [23] Pesicek, J. D., Sileny, J., Prejean, S. G., & Thurber, C. H. (2012). Determination and uncertainty of moment tensors for microearthquakes at Okmok Volcano, Alaska. *Geophysical Journal International*, 190(3), 1689–1709.
- [24] Šílený, J. (2009). Resolution of non-double-couple mechanisms: Simulation of hypocenter mislocation and velocity structure mismodeling. *Bulletin of the Seismological Society of America*, 99(4), 2265–2272.
- [25] Šílený, J., Jechumtálová, Z., & Dorbath, C. (2014). Small Scale Earthquake Mechanisms Induced by Fluid Injection at the Enhanced Geothermal System Reservoir Soultz (Alsace) in 2003 using Alternative Source Models. *Pure and Applied Geophysics*, 171(10), 2783–2804.
- [26] Bieniawski, Z. T. (1967). Mechanism of brittle fracture of rock: Part II—experimental studies. *International Journal of Rock Mechanics and Mining Sciences & Geomechanics Abstracts*, 4(4), 407–423.
- [27] Brace, W. F., Paulding, B. W., & Scholz, C. (1966). Dilatancy in the fracture of crystalline rocks. *Journal of Geophysical Research*, 71(16), 3939–3953.
- [28] Tapponnier, P., & Brace, W. . (1976). Development of stress-induced microcracks in Westerly Granite. *International Journal of Rock Mechanics and Mining Sciences & Geomechanics Abstracts*, 13(4), 103–112.

21 - AE sensor sensitivity verification using a stimulated motion verified by laser-vibrometry

Hartmut VALLEN¹,

¹Vallen Systeme GmbH, Germany, www.vallen.de

Abstract

This presentation describes work in progress towards a practicable procedure for obtaining the receiving sensitivity spectra of an AE sensor under test (SUT) using a face-to-face (F2F) setup. Sensitivity is expressed as the SUT's output in units of volt per unit of particle motion input, which can be nanometer of particle displacement or millimeter per second of particle velocity. The motion was stimulated by a commercially available transmitter. The transmitter's surface motion was measured in absolute units of velocity, by using a scanning laser vibrometer, at 16 positions per ring over 10 rings covering an active diameter of 25,4 mm. Two transmitter units of same type were used alternatively with the expectation that both will lead to almost identical spectra of a SUT's receiving sensitivity. Differences in the obtained sensitivities have been obtained and some explained by differences in the uniformity of motion distribution over the transmitter face.

1. Introduction

An easy-to-use, economic and reproduceable method for sensor sensitivity verification has been a top desire of many users of acoustic emission phenomena for many years. AE sensor calibration has been reviewed by Hill and Breckenridge [1,2] and the face to face (F2F) method was described [1]. Dunegan published no details of his method, which were recorded by Ono's interview, reported in [3, 5]. Ono [5] made a systematic study of AE sensor calibration methods and updated the F2F method using laser interferometry, instead of hydrophone calibration used by Dunegan. The principle of the F2F setup and the sensitivity reference to "V/ μ bar" originated from the hydrophone calibration of a standard transducer used in a F2F verification by Harold Dunegan in 1968. However, no systematic study of the F2F method was published until Burks' and Hamstad's paper in 2015 [4] and Ono's paper in 2016 [5]. Ono clarified the correlation between reference scales of V/ μ bar, V/(m/s) and V/nm, so any one of them is workable. However, a reference to particle velocity or displacement is preferred for AE sensors as these are mounted to solid surfaces where particle motion is the appropriate input of the sensor.

2. Description of work

2.1 Block diagram of face-to-face setup

Fig. 2-1 shows the block diagram of the face-to-face setup. The arbitrary function generator (AFG, Keysight 33500) delivers a voltage pulse U_T (blue curve in Fig. 2-5) to the transmitter, causing a transient motion in normal direction (90°), which is converted by the sensor under test (SUT) to the output voltage U_{SUT} . Both, U_{SUT} and U_T , are measured by a transient recorder (Picoscope 5442, set to: 2 chan, 20 MHz BW, 8 MHz low-pass, 15 bit, 50 μ s/div, 64 kS, for 8ns sampling interval, later interpolated to 25 ns). The AFG amplitude was set to 4,9 Vpp. Due to the high impedance of the transmitter, a maximum voltage of 9,8V was measured for U_T . See

Fig. 2-5. A mechanical tool centered transmitter and SUT without touching the active transmitter face. A coupling agent warranted reproducible acoustic coupling. The SUT was pressed down onto the transmitter face by a 9 N cylindric weight.

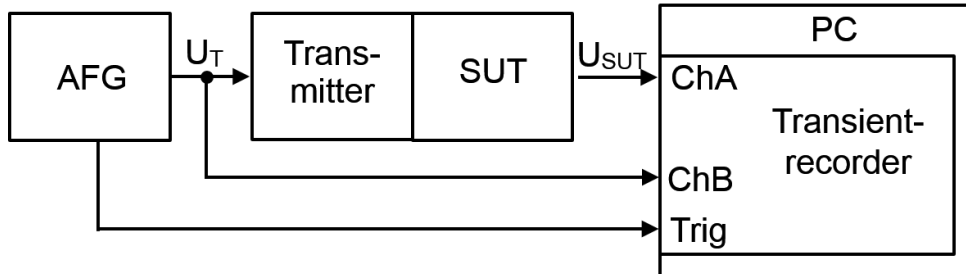


Fig. 2-1 Block diagram of face-to-face setup

As transmitter the ultrasonic probe model Olympus V104 was used. The element diameter is 25,4 mm, the frequency at maximum amplitude 2,25 MHz. We changed from model V103 with 12,7 mm diameter element to the larger one to achieve a more uniform motion distribution. Two transmitter units (A and B) were used alternatively with the expectation that both will lead to almost identical spectra of a SUT's receiving sensitivity.

2.2 LVM Measurements and signal averaging

The velocity of the particle motion normal (90°) to the transmitter's face was measured by using a scanning laser vibrometer (Polytec PSV 400), hereafter called "LVM". Fig. 2-2 shows the positions of 161 measured points: 10 rings of 16 points each, plus one in the center. The outermost ring covered a circular area of 25,4 mm diameter. For improved signal-to-noise ratio 200 measurements per position were averaged to one signal "velocity vs time".

Sixteen time-series signals from sixteen positions per ring were averaged to one time-series signal per ring. From center point (ring 0) outwards up to the ring number of interest (1 to 9), the ring signals were averaged considering the proper weight per ring. Data of the outermost ring 10 was not used, due to reduced signal-to-noise ratio. Analyzing data over a varied center distance shall reveal, if so, a non-uniform motion distribution. For sensitivity verification, the ring numbers averaged shall be adopted to the size of the sensitive area of the SUT.

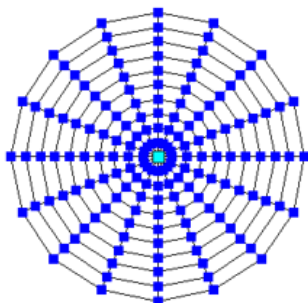


Fig. 2-2 161 Measurement positions

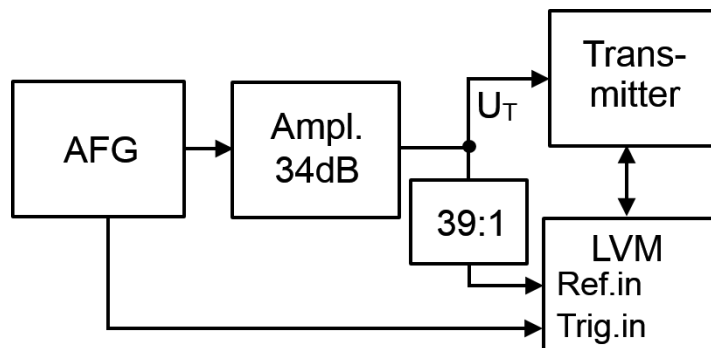


Fig. 2-3 Block diagram of LVM setup

Fig. 2-3 shows the block diagram of the LVM setup. The arbitrary function generator (AFG) delivers the same stimulation signal as used with the F2F setup, but the amplitude set to 2 Vpp, triggered in burst mode in 10 ms time interval. A 34 dB post-amplifier (Falco Systems WMA-300) was used to supply up to 100 V and up to 300 mA peak over the amplifier internal 50 Ω impedance to the transmitter. The transmitter voltage was measured over a 39 to 1 voltage divider by the LVM's reference input.

The LVM filter was set to 10 kHz high-pass of “middle quality”, the average count to 200, trigger to 10% of 200 μs recording time. The distance LVM head to transmitter face was 300 mm.

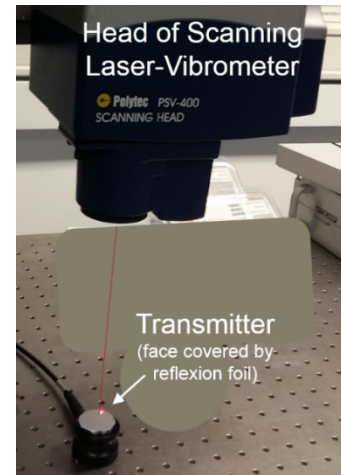


Fig. 2-4 LVM scanning the transmitter surface

Fig. 2-4 shows the vibrometer while it scans a transmitter's face.

2.3 Stimulation signal

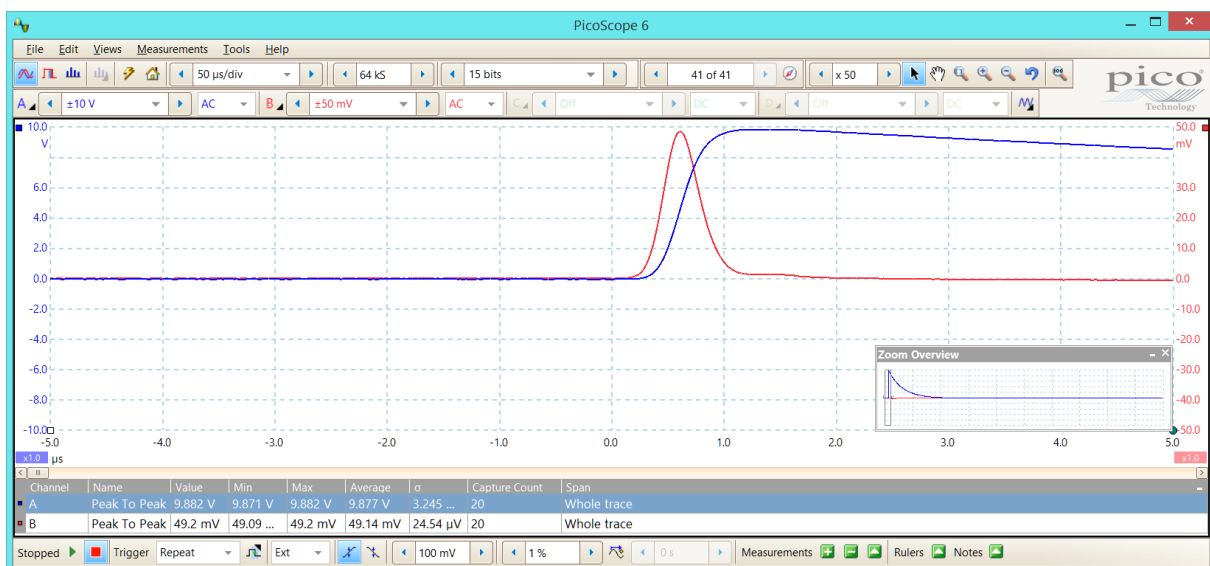


Fig. 2-5 Transmitter voltage (blue) and current (red), measured by Picoscope

In the F2F setup the transmitter was stimulated by the signal shown in Fig. 2-5 in blue. The signal rise was shaped to cause a short unipolar Gaussian current pulse (red curve in Fig. 2-5, 1 mV corresponds to 1 mA) through the transmitter. The shorter this pulse the higher the probability that a non-uniform motion over the transmitter's face, e.g. due to transmitter internal reflections, can be revealed.

After the fast rise at $t=1,2 \mu\text{s}$ in Fig. 2-5 the amplitude decays exponentially by 50 % per 18 μs. Neither the peak current nor the spectrum of the current through the transmitter of the used model changed measurably, whether the transmitter is used in free air or coupled to a solid material.

2.4 Signal interpolation

The LVM model used delivered 2,56 Msamples per second (MS/s) only. Hence, meaningful LVM data can be expected up to about 1 MHz. For the calculation of a smooth time-series signal, the 2,56 MS/s data from LVM was interpolated to 40 MS/s by using the “sinc” function (available with Matlab). Fig. 2-6 shows the samples from LVM as blue circles and the interpolated curve as green line. All graphs shown in this work were produced from 40 MS/s data. All FFT calculations used a FFT buffer of 32K zero padded samples, resulting in a FFT-resolution of 1,2207 kHz (40 000 / 32 768).

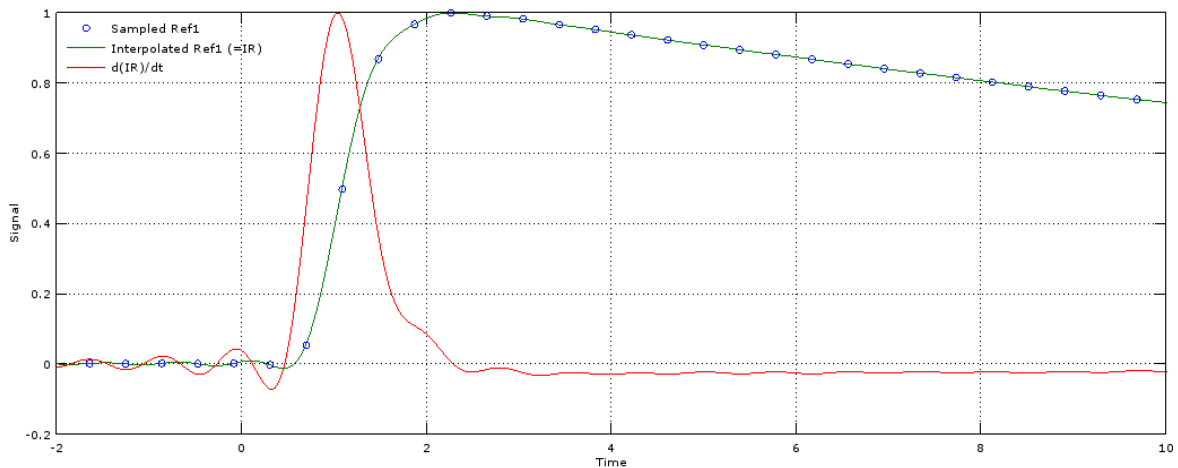


Fig. 2-6 Transmitter voltage (normalized) from LVM data (blue circles) and 40 MS/s interpolated signal (green line) and its 1st derivation du/dt (red line) that represents T -current

2.5 Windowing

Behind the averaging process a FFT windowing takes place for the optional removal of signal parts before and behind the first main arrival.

Table 2-1 defines seven window signals identified by “W2” to “W8”, Fig. 2-7 shows the window signal W2 with a flat range from $-0,5 \mu\text{s}$ (pre-peak time) to $+1 \mu\text{s}$ (post-peak time).

The meanings of the table header:

- Up (0-1): the number of microseconds the window signal takes for the sine-squared up-ramp from 0 to 1 before the pre-peak phase begins.
- Pre-peak: the number of microseconds the window signal stays at 1 before the positive or negative maximum occurs.
- Post-peak: the number of μs the window signal stays at 1 after the positive or negative maximum.
- Down (1-0): The number of μs the window signal takes for the sine-squared down-ramp from 1 to 0.

Windowing takes place by multiplication of the input signal with the selected window signal.

Id	Up (0-1)	Pre-peak	Post-peak	Down (1-0)
μs	μs	μs	μs	2
W2	2	0.5	1	2
W3	2	0.5	1.5	2
W4	2	1	2.5	2
W5	2	1	4	2
W6	2	1	11	5
W7	2	1	50	10
W8	2	2	100	5

Table 2-1 Window definitions

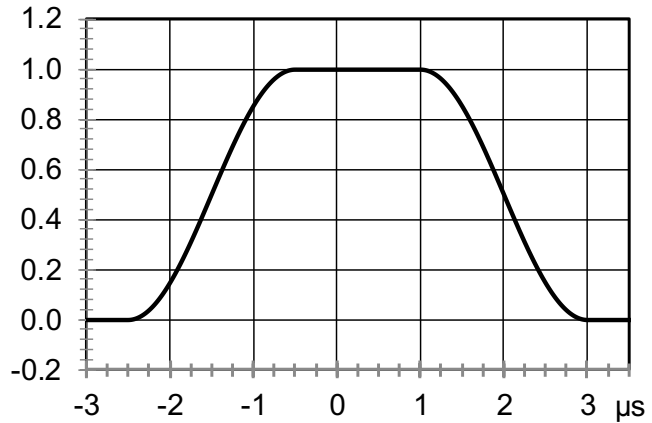


Fig. 2-7 Window signal W2, maximum at $t=0$

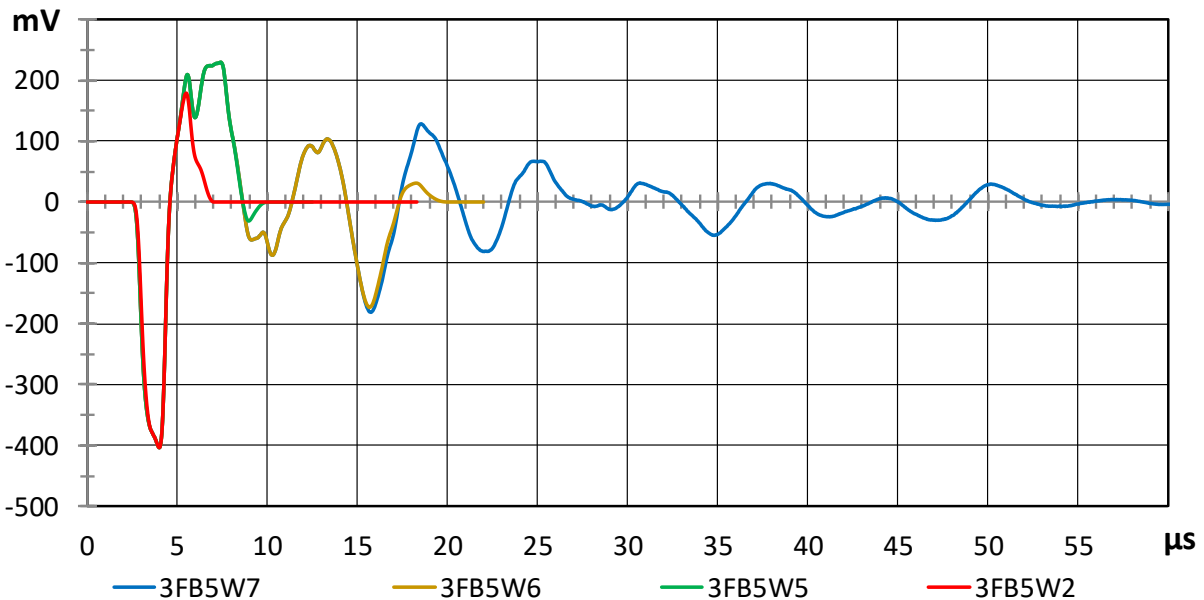


Fig. 2-8 Application of 4 FFT windows (W7, W6, W5, and W2, see last two characters in the legend) on the response of a resonant 150 kHz sensor.

Fig. 2-8 shows the response of a resonant 150 kHz sensor. Four window signals were applied: W7 (blue), W6 (brown), W5 (green), W2 (red), with the shorter window signals in foreground. The maximum amplitude of all windowed signal arrives at $t = 4 \mu\text{s}$. The return to zero for the W2 signal is 3 μs later.

Fig. 2-9 shows for each signal in Fig. 2-8 the obtained displacement receiving sensitivity. The shortest window (red) leads to the smoothest FFT. The longest window W7 (blue) leads to the highest resonance at about 160 kHz, about 10 dB above the red FFT curve. It should be well understood: The 10 dB higher maximum of the blue FFT curve does not indicate that the maximum response amplitude is larger. The resonance peak of the blue curve in Fig. 2-9 at 160 kHz stems from the larger duration of low-amplitude reverberations fed into the FFT, as seen in Fig. 2-8.

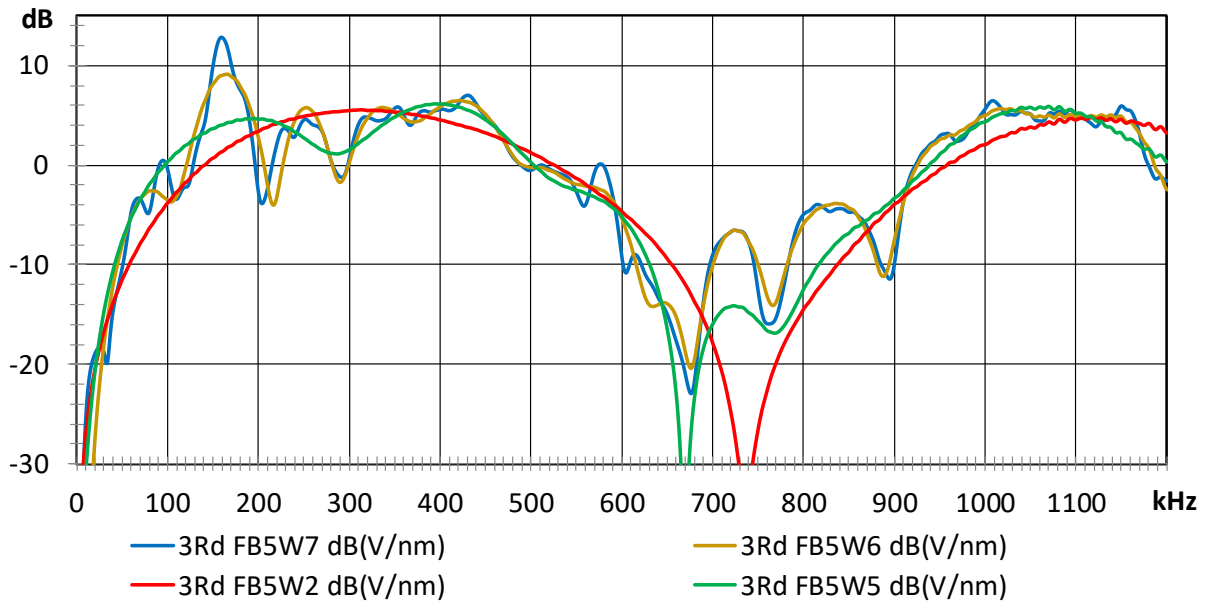


Fig. 2-9: Displacement receiving sensitivities derived from the time-series signals in Fig. 2-8.

3. Results

3.1 Glossary of signal names

SUT output signals having passed the windowing process are identified by a designation like: “1FA5W2” with the following meaning:

- “1” stands for a character of [1...6] identifying the concerned SUT type. In this work, only data of SUT type 1 (V103) and SUT type 3 (VS150) are shown.
- “F” stands for a character of [F, N, D] identifying the coupling configuration. In this work, only data from coupling configuration F are shown.
- “A” stands for a character of [A, B] identifying the transmitter involved
- “5” stands for a character of [0...9] identifying the highest ring no included in the averaging process. It shall match the radius of sensitive area of the SUT.
- “W2” stands for the applied FFT window.

Velocity signals from LVM having passed the interpolation, averaging and windowing processes are identified by a sequence of characters, beginning with “V” and followed by e.g. “FA5W2” (same meaning as with SUT output signal 1FA5W2).

3.2 Comparing velocity signals of different ring nos in configuration F

Fig 3-1 top shows velocity signals from transmitter A, rings 9 to 0, with window W6 applied, in time domain. The legend shows the ring no to which the average is processed and the radius belonging to. The lower ring number curves are drawn last and overlay the previous drawn curves.

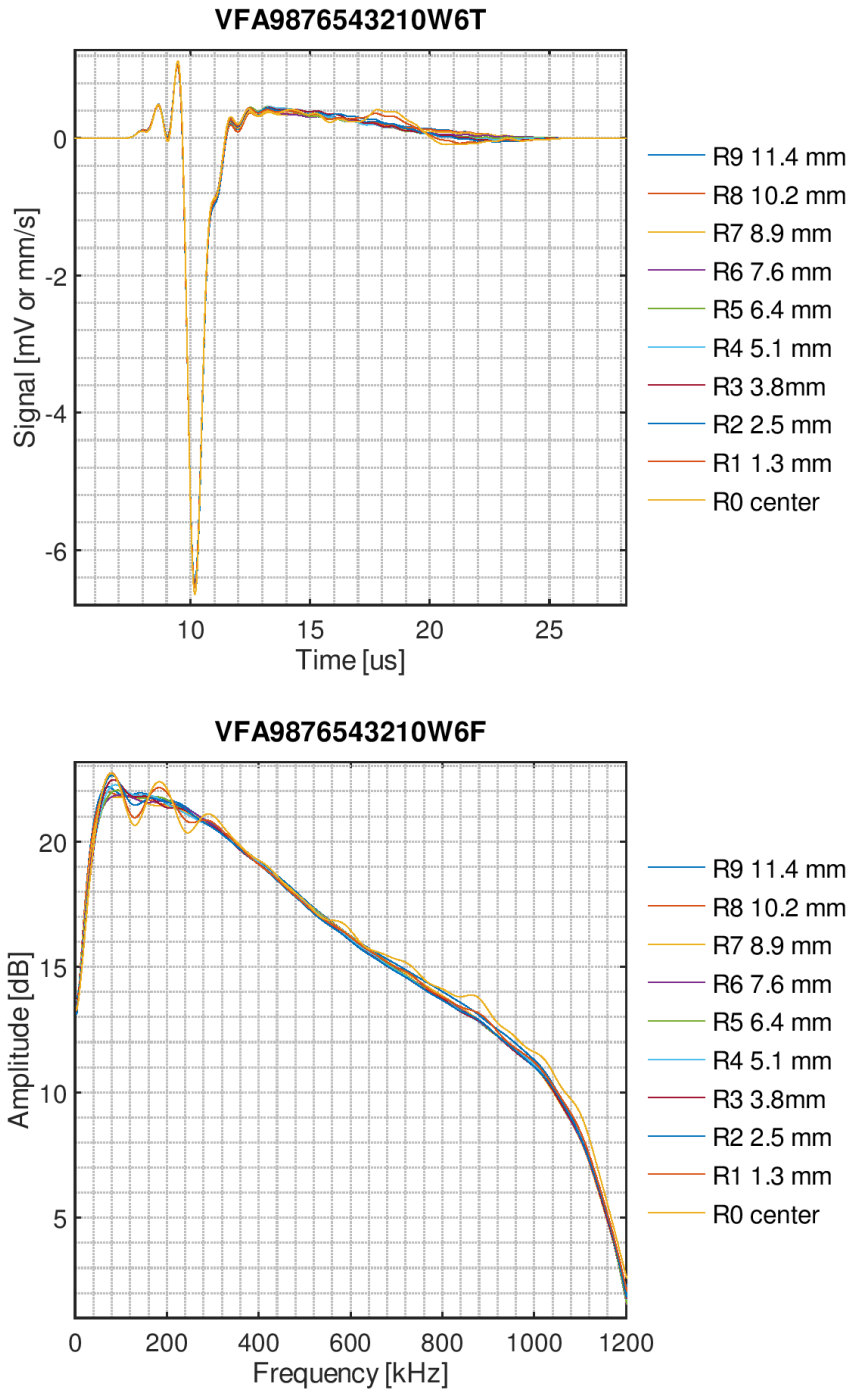


Fig 3-1 top: Velocity signals from transmitter A, rings 9 to 0, window W6 in time domain.
Bottom: the FFTs of the time domain signals in top graph

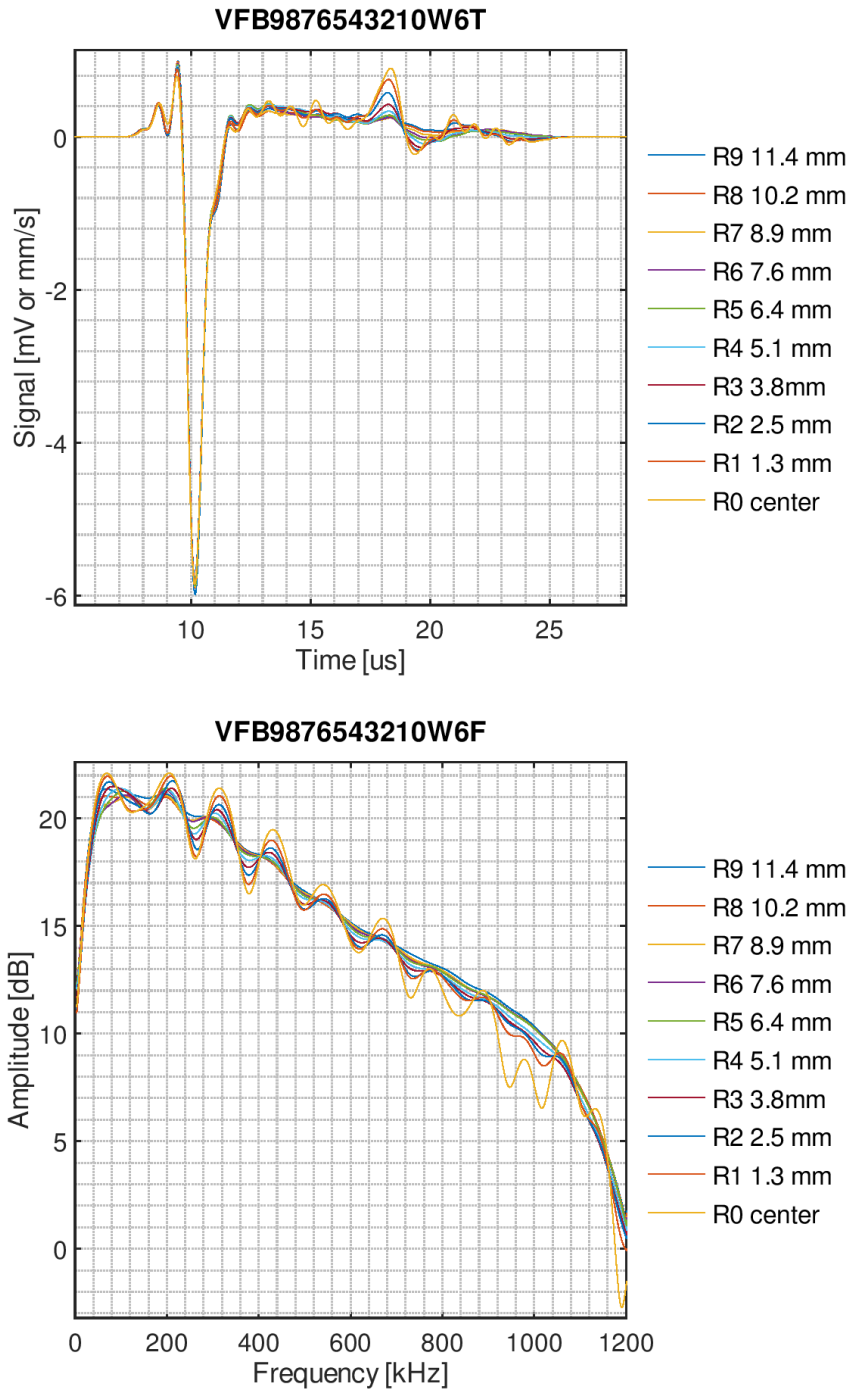


Fig 3-2 like Fig. 3-1 but from transmitter B.

Fig. 3-2 shows the same as Fig 3-1 but the data are from transmitter B. It shows on top at $t = 18 \mu\text{s}$, $8 \mu\text{s}$ after the main pulse, an additional spike with a maximum amplitude of 1 mm/s (pp, 14 % of main pulse amplitude). The spike causes in the FFT (bottom) ripples of up to 5 dB (pp). The amplitude of the spike varies with center distance. It is highest in the center, curve R0 yellow. That spike clearly indicates for transmitter B a less uniform motion distribution compared to A.

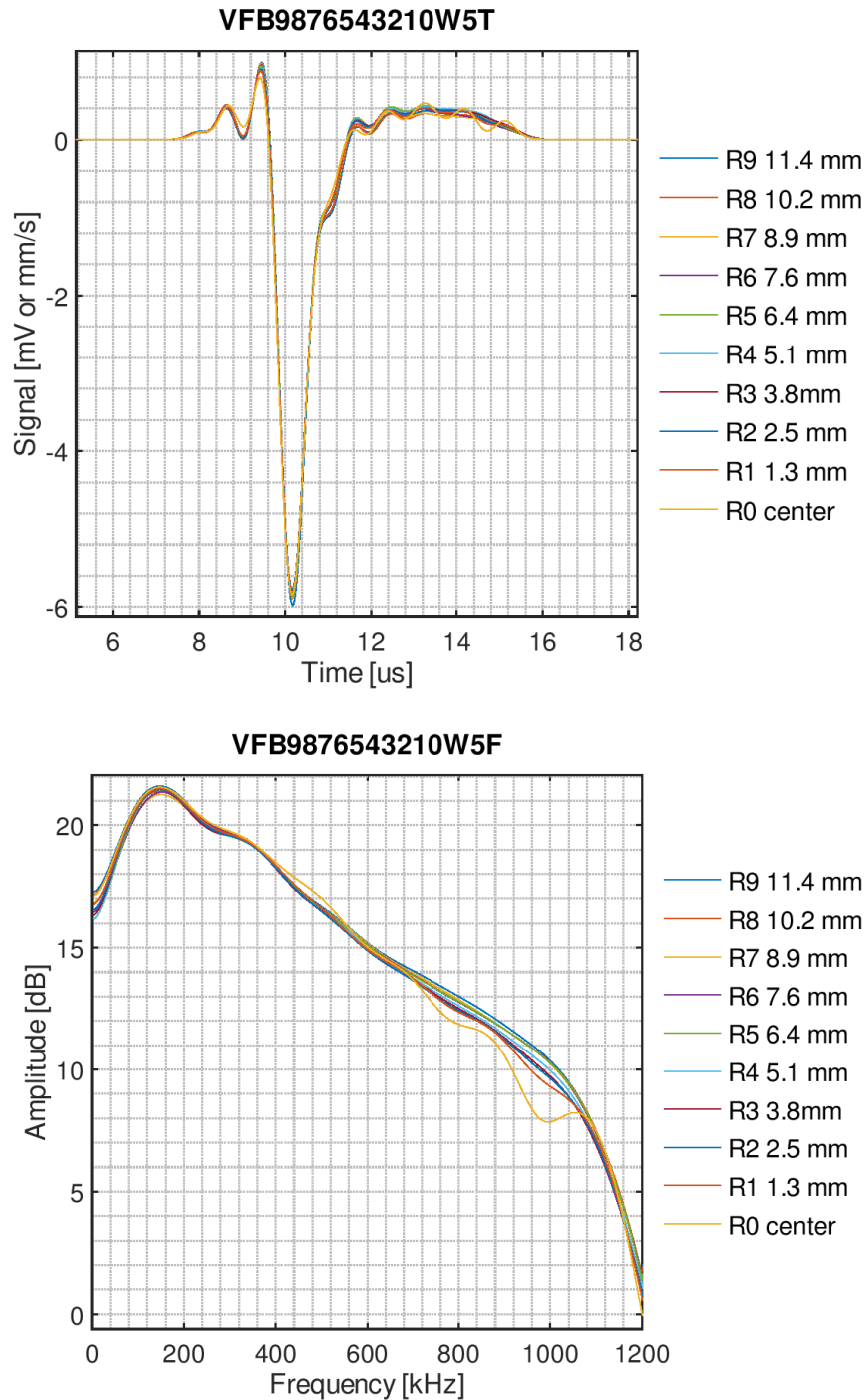


Fig 3-3 like Fig. 3-2 but window size shortened from W6 to W5.

Fig. 3-3 shows the application of the shorter window W5 compared to W6 in Fig. 3-2. The spike is now eliminated from the velocity diagram because the window signal zeros it. However, the spike is still active and will cause a SUT to respond. Hence, a short window must also be applied to the SUT signal, if the receiving sensitivity from transmitter B shall match that of A.

3.3 Obtaining the receiving sensitivity of a SUT in Vs/m and V/nm

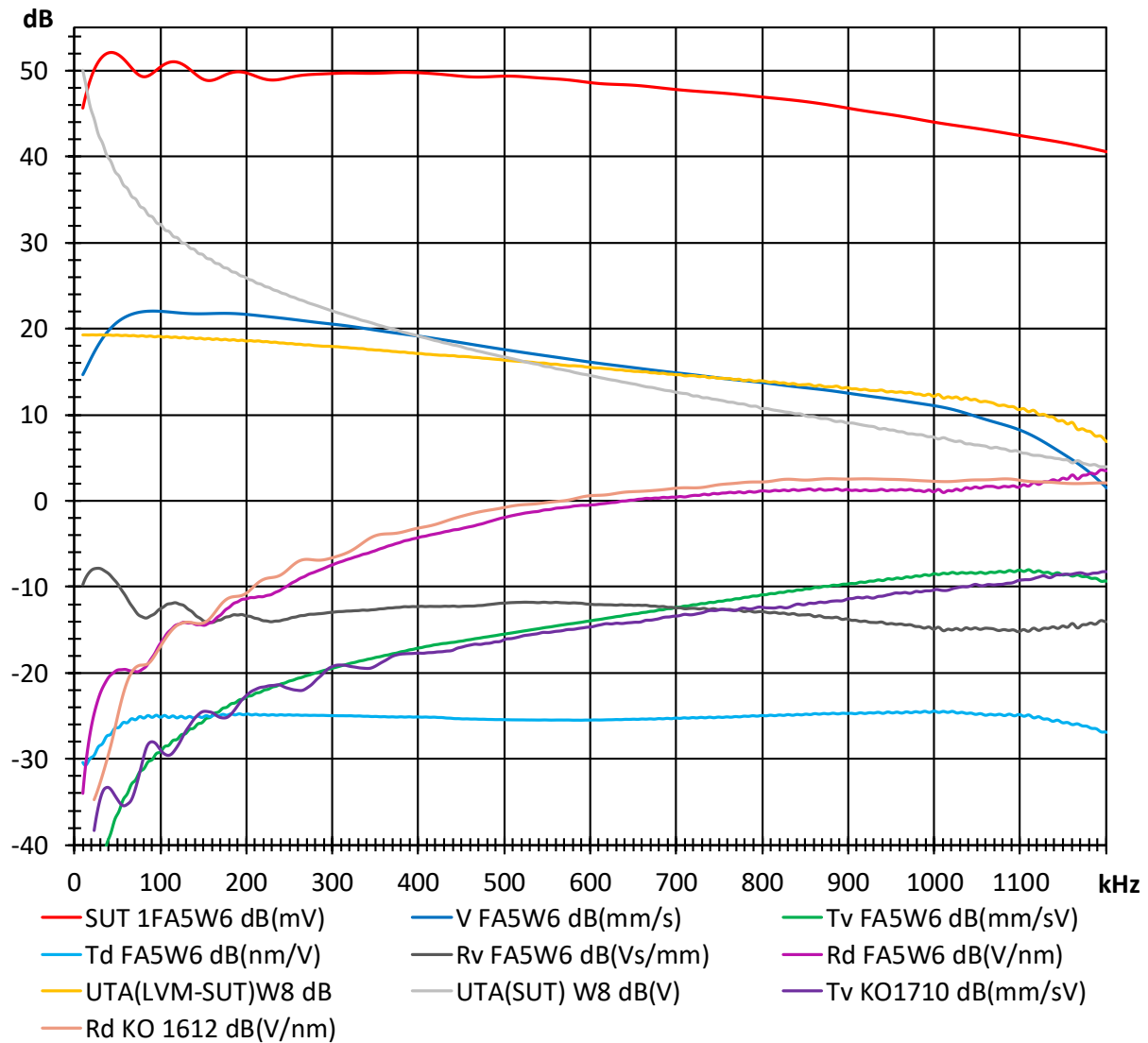


Fig. 3-4 Relevant FFT curves for sensitivity determination.

The ten signals shown above in Fig. 3-4 are hereafter described from top to down (at 100 kHz line) with reference to their legend below the graph. Lines in {...} are alternatives but not shown in Fig. 3-4.

SUT 1FA5W6 (red) SUT response in dB referred to 1 mV.
 Meaning of the code "1FA5W6":
 1: SUT 1 (V103 wideband UT probe, SNo -64),
 {3: SUT 3 (VS150 resonant sensor SNo -6379)}
 FA: laser scanned free surface of transmitter A (V104-55),
 {FB: dito transmitter B (V104-09)}
 5: area of rings 0 to 5 were averaged,
 W6: FFT window W6 was applied.

UTA(SUT) (light gray) Voltage spectra at transmitter A during SUT measurement in dB referred to 1V

- V FA5W6** (dark blue) Velocity at free face of transmitter, scanned by laser vibrometer, 81 points averaged over rings 0 to 5 (6,3 mm radius), in dB referred to 1 mm/s.
- UTA(LVM-SUT)** (orange) Transmitter voltage “UTA during LVM measurement” minus “UTA during SUT measurement” in dB.
- Rv FA5W6** (dark gray) Velocity receiving sensitivity in dB referred to 1 Vs/mm.
 $Rv = SUT\ 1FA5W6 - V\ FA5W6 + UTA(LVM-SUT) - 60$
 (-60 adjusts dB(mV) of SUT to dB(V)).
- Rd FA5W6** (light purple) Displacement receiving sensitivity in dB referred to 1 V/nm.
 $Rd = Rv + 20 \cdot \log_{10}(2 \cdot \pi \cdot f\ [Hz]) - 120$.
 (-120 dB adjusts mm to nm)
- Rd KO1612** (thin pink) Displacement receiving sensitivity in dB referred to 1 V/nm from the setup described in [5] for same SUT 1, provided by Prof. Kanji Ono, for comparison.
- Td FA5W6** (light blue) Displacement transmitting sensitivity (of transmitter A) in dB referred to 1 nm/V. **$Td = Tv - 20 \cdot \log_{10}(2 \cdot \pi \cdot f\ [Hz]) - 120$** .
 (-120 dB adjusts mm to nm)
- Tv FA5W6** (green) Velocity transmitting sensitivity (of transmitter A) in dB referred to 1 mm/Vs. **$Tv = V\ FA5W6 / UTA(LVM)$** .
 UTA(LVM) is the transmitter voltage during LVM measurement (not shown in graph). UTA(LVM) = UTA(SUT) + UTA (LVM-SUT), both are shown in graph.
- Tv KO1710** (dark purple) Velocity transmitting sensitivity shown in [5] Fig. 5, provided by Prof. Kanji Ono. This curve shows the transmitting sensitivity curve of another V104 sample for comparison. Small deviations between the curves are normal.

3.4 Obtaining sensitivity differences when using transmitter B instead of A

For Fig. 3-5 data of velocity was taken from V FB5W6 (not shown) and for SUT from SUT 1FB5W6 (not shown), using transmitter **B** instead of **A**.

The “velocity receiving sensitivity difference” is shown as thin red curve (signal “Rv **FB-A5W6** * 10”, see the legend of Fig.3-5, where “* 10” means the difference is multiplied by 10). It shows three maxima: 2,2 dB difference at 250 kHz, 1,3 dB difference at 180 kHz and 1 dB difference at 80 kHz. The difference stays below 1 dB above 300 kHz.

The “displacement transmitting sensitivity difference”, signal “Td **FB-A5W6** * 10”, is the thin blue curve in Fig. 3-5 that shows a minimum of -1.5 dB at 250 kHz, several other minima of -1 dB, and several maxima that are all below zero.

One reason for the Td difference was already seen in the additional peak of the time-series signal at 18 μs in Fig. 3-2. Improvement seems possible when the transmitters are selected for minimum difference in Tv or Td.

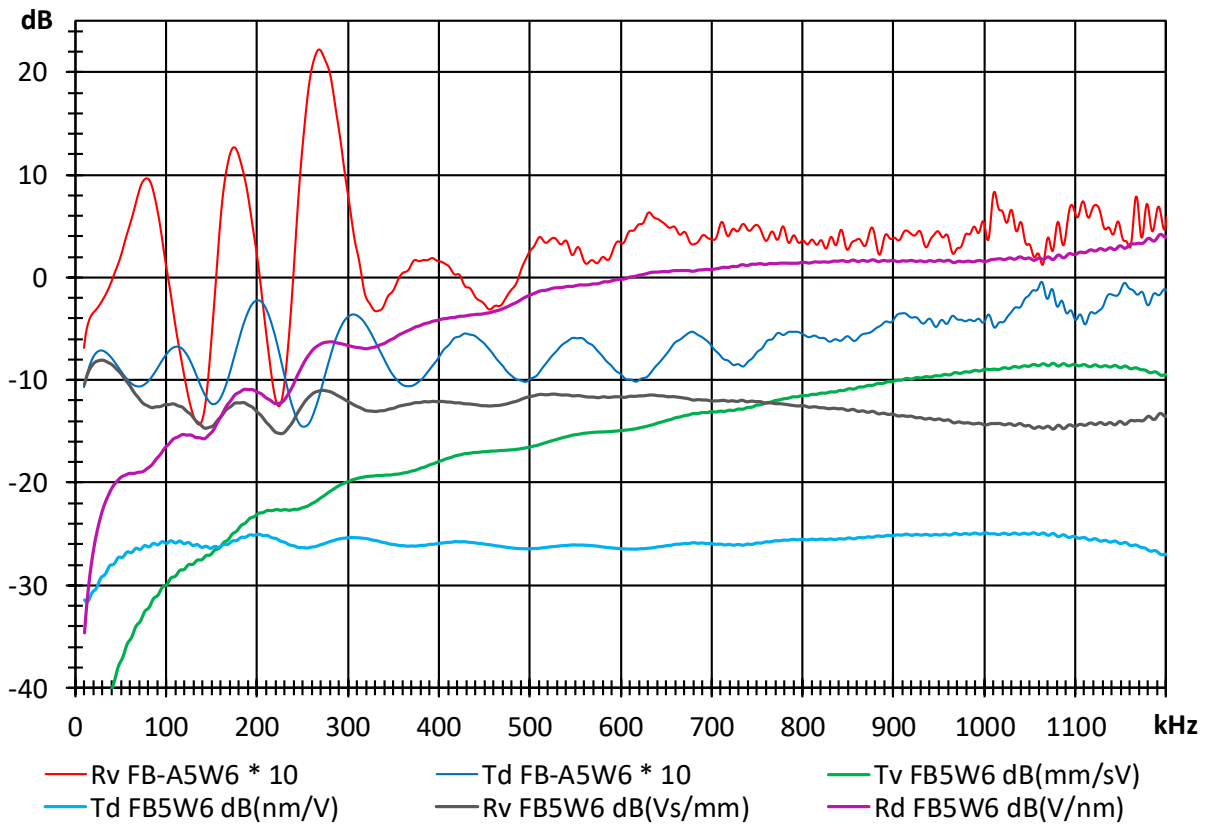


Fig. 3-5 Transmitting and receiving sensitivities using transmitter B and deviation to

3.5 Differences in receiving sensitivity of a resonant SUT

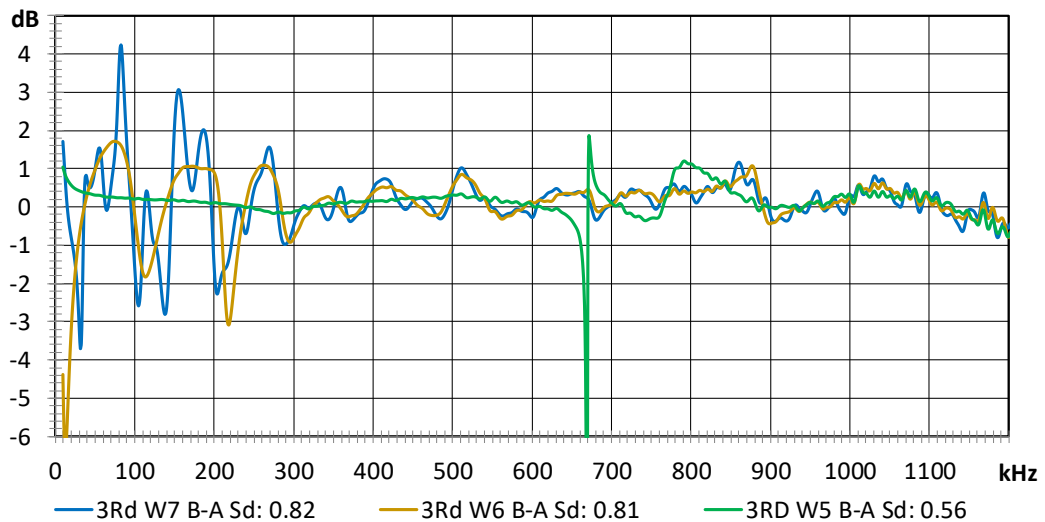


Fig. 3-6: Differences of R-sensitivity of a 150 kHz sensor, obtained by using transmitters A and B with windows signals W5 to W7.

Fig. 2-8 and Fig. 2-9 (page 5) show data from a 150 kHz sensor using FFT windows W7, W6, W5, and W2. Fig. 2-8 shows the time-series signals that exhibits reverberations initiated by the

main pulse. The peak sensitivity for the main pulse is that shown in red in Fig. 2-9. The peak sensitivities shown in brown and blue stem from the lower amplitude reverberations.

Fig. 3-6 shows the differences in displacement receiving sensitivity, when using different transmitters (A and B) and different windows (W5 to W7). With W7 we see differences of up to 4 dB in the interesting range of 50 to 300 kHz. With W5 we see only one substantial difference at the strong resonance dip, outside of the interesting frequency range 50 to 500 kHz.

4. Discussion

4.1 Windowing

Windowing is a tool to separate a SUT's sensitivity on the short main pulse motion against the sensitivity on the full response comprising main pulse plus reverberations and reflections.

Example: Compare red curve 3Rd FB5W2 in Fig. 2-9, at 160 kHz (+1,4 dB), with light purple curve Rd FA5W6 in Fig. 3-4 (-14 dB). One would correctly expect that VS150 delivers a maximum amplitude that is about 15 dB above that of V103. If one would compare with VS150 sensitivity 3Rd FB5W7, which is about 11 dB higher than W2 sensitivity, he would overestimate the expected amplitude from VS150, compared to V103, by $11+15 = 26$ dB!

Other purposes to separate the pure main pulse response from the full response:

- to extract that part of information that is not influenced by any kind of post pulse motion,
- to eliminate the effect of disturbing spikes, e.g. from non-uniform motion distribution (Fig. 3-2).
- to obtain the true sensitivity of a resonant sensor for the detection of a short main pulse, (the example mentioned above)!
- to allow for measurement of cancellation effects, e.g. the aperture effect, e.g. when using a small transfer block, (not treated in this work).
- To visualize the spectrum that initiates reverberations versus the spectrum that includes initiation and post pulse motion.

4.2 Motion reference

A laser vibrometer measures normal (90°) motion on a free surface. When a sensor is mounted to that surface, the motion between sensor and surface will be modified by the sensor's mechanical load. This raises the question, whether a SUT's sensitivity shall be scaled to the motion of the free surface or to the real motion at the SUT's surface, when it is mounted to the test block. The most recent standard on primary sensor calibration [6] deals with this topic and states:

“Since AE sensors are used to monitor motion at a free surface of a structure and interactive effects between sensor and structure are generally of no interest, the free surface motion is the appropriate input variable. It is, therefore, recommended that the units of calibration should be voltage per unit of free motion; for example, volts per meter.”

This justifies to scale the sensor sensitivity to the free motion measured by LVM even though the motion at the sensor-loaded surface differs.

5. Conclusion

The velocity measurement by using a scanning laser vibrometer allows for obtaining an absolute and trustworthy sensitivity to the normal (90°) motion of the free surface of a transmitter. Sensitivity is expressed in absolute units of volts per nanometer particle displacement, or volts per meter per second particle velocity scaled to the free surface motion.

The uniformity of motion distribution over the transmitters' active face differs between unit A and B of same transmitter model, what can cause differences of several dB in the obtained sensitivity of a SUT. Fig.3-5 reports differences of a wideband SUT (V103) of up to 3,5 dB (peak peak), when using window W6, Fig. 3-6 reports differences for a resonant sensor (VS150) of up to 4,6 dB (peak peak), when using window W6. We think for getting wide acceptance, these differences need to be reduced, e.g. by using better matching transmitter units.

Main points treated in this work:

A layout for LVM measurement positions for laser vibrometry has been designed, for an optimal averaging of the motion over a circular array of variable diameter.

A shape of stimulation pulse has been designed, causing an extremely short main response comprising frequencies down to less than 10 kHz.

Problems with the LVM digitizer rate of only 2,56 MS/s have been solved by an interpolation process to 40 MS/s.

The signal windowing can process windows of a few μ s up to 100 μ s length meaningfully and reproducibly.

The obtained receiving and transmitting sensitivities have been compared with absolute curves, kindly provided by Prof. K. Ono, and match these.

This reports the current (1807) status of our work towards a practical sensor verification method.

Acknowledgement

We are thankful to Professor Kanji Ono for his excellent advise and for providing us two curves included in Fig. 3-4 for comparison with our results, identified in the legend by "Tv KO1612" and "Rd KO1710".

References:

- [1] R. Hill, "Reciprocity and Other Acoustic Emission Transducer Calibration Techniques," JAE 1-73 (1982)

- [2] F. R. Breckenridge, "Acoustic Emission Transducer Calibration by Means of the Seismic Surface Pulse," JAE 1-87 (1982)
- [3] K. Ono, H. Cho, T. Matsuo, "Experimental Transfer Functions of Acoustic Emission Sensors," JAE 26-72 (2008)
- [4] B. Burks, M. A. Hamstad, "An Experimental-numerical Investigation of the Face-to-face Sensor Characterization Technique." Mat Eval. 2015, 73, 414-423.
- [5] K. Ono, "Calibration methods of acoustic emission sensors," Materials, 2016, 9, 508.
- [6] ASTM E1106-12 (2017), "Standard Method for Primary Calibration of Acoustic Emission Sensors," ASTM International, West Conshohocken, PA, USA, 2016; 12p

(This paper was revised on February 6, 2019.)

76 - Method for assessing the likelihood of fatigue crack detecting

V.A. Barat¹, D.V. Chernov¹, S.V. Elizarov²

¹NATIONAL RESEARCH UNIVERSITY "MPEI", MOSCOW, RUSSIAN
FEDERATION

² LLC «INTERUNIS-IT», MOSCOW, RUSSIAN FEDERATION INTERUNIS-IT LLC,
ENTUZIASTOV SHOSSE 20B, MOSCOW, 111024, PO 140, RUSSIA

Abstract:

An estimation of the probability of defect detection (POD) is an actual task of acoustic emission (AE) testing. Despite the fact that AE testing is the most sensitive method of NDT, the POD is difficult to estimate. The probability depends on a set of random factors also not directly related to the size of the defect. The probability of detecting defects is currently being studied by many researchers, but the proposed approaches are not yet applied in practice.

In the frame of this work, the method allowing to estimate the probability of fatigue crack with help of AE testing method was developed. This method allows to calculate the probability of fatigue defect detection taking into account the following factors: the stage of defect growing, the distance between AE source and sensor and the noise level.

1. Introduction

The great numbers of industrial facilities operate under mechanical or thermal cyclic loads. Long-term exploitation under cyclic loads leads to formation and accumulation of fatigue damages which degrade strength properties and working lifespan of facilities. A fatigue crack develops unevenly as it goes through initial, stable power growth and unstable growth stages. The last stage - unstable fatigue crack propagation - results in the rapid failure of the structure, so precise detection of fatigue crack is a very important task. During every stage a fatigue crack is a source of acoustic emission and could be efficiently detected by AE testing. AE of fatigue damages is investigated in many papers [1-5], generally development of diagnostic model, i.e. correlation between AE parameters and mechanical properties, as damage rate and crack growth rate, is considered.

The purpose of this paper is analysis of accuracy for fatigue cracks detection against noise. Experimental research of AE during cyclic loading of metal specimen till its destruction was conducted. Experimental investigation of AE during cyclic loading of metal samples before its destruction was carried out. Specimens made of alloyed low-carbon steel 09G2S were tested with an Instron Testing System. The amplitude of the loading cycle was varied from 50 to 70% of the yield point. This loading scheme in some approximation repeats the operational mode of the industrial structure.

The influence of maximal load in cycle, load rate and stress ratio on AE parameters was investigated. On the basis of experimental AE parameters was calculated and statistical model of AE – source was constructed.

Function of the propagation path was approximately evaluated by means of attenuation coefficient as a function of distance between the sensor and AE source. Attenuation coefficient was empirically estimated during calibration measurements on a gas pipeline.

The probability for crack detection on its different stages was calculated in the form of one and two-dimension POD-diagrams. The calculated POD – diagrams allow to estimate the probability of detection for fatigue damages on a various growth stages upon specific conditions of AE testing. It also make possible to choose the maximum distance between the sensors and threshold value to provide defined probability of fatigue crack detection.

2. Materials and Materials and methods of research

In order to solve the task, a series of laboratory tests on the fatigue strength of the notched specimen was carried out. Specimen were made from low-carbon steel 09G2S, which is used in the production of a wide range of industrial structures, for example, tanks, vessels and pipelines. The choice of the shape and geometric dimensions of the specimen was based on the recommendations described in the State Standard [6].



Fig. 1 The sample installed in the clamps of the testing machine

The thickness of the specimen was 3 mm, width 50 mm, and the length – 350 mm. Fatigue load was carried out on Instron 8801 servo-hydraulic testing machine. To reduce the noise of the test machine, metal pads with dimensions of 50x110x3 mm with 4 through-holes were used (Fig. 1). The specimen was loaded according to a specially developed loading scheme, the parameters of which are similar to the loads of industrial structures – pipelines, tanks and vessels. Fig. 2 shows the main stages of the loading scheme.

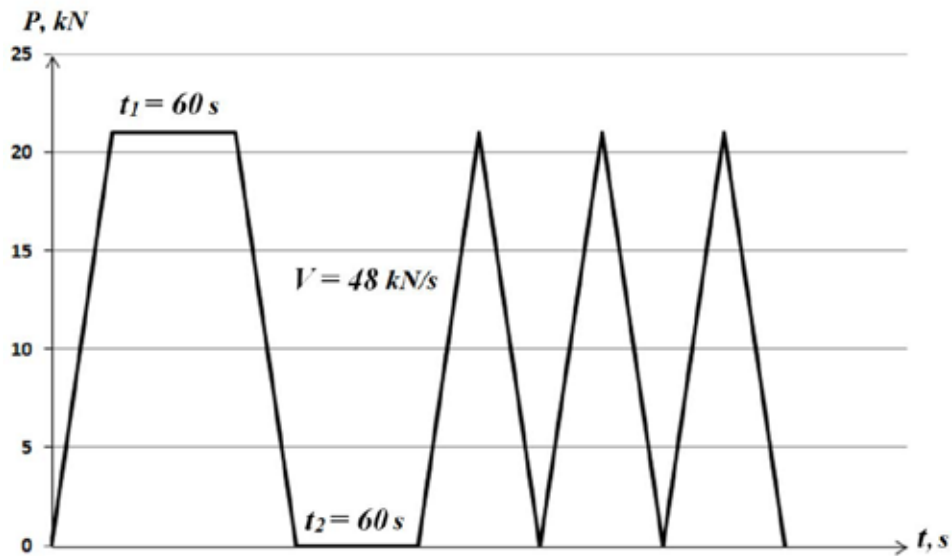


Fig. 2 Loading scheme

The first stage is a single cycle of a trapezoidal shape, including a load lifting and rejection section, as well as two holding sections of duration $t_1 = 60$ s and $t_2 = 60$ s at maximum (P_{max}) and zero load, respectively. A preliminary loading cycle is necessary to evaluate the acoustic activity of noise sources. It checks the efficiency of the measuring equipment, clarifies the level of mechanical noise that occurs when the electric drive of the loading installation is operated [7]. The second stage is a sequence of cycles of a triangular shape with a frequency from 0.5 to 2 Hz. The maximum load P_{max} is taken as it is in operating stresses arising during operation of main oil pipelines.

The value of P_{max} varies from 19 to 23 kN, and the R-ratio from 0 to 0.5. The measuring of AE was carried out by the industrial system A-Line 32D of «INTERUNIS-IT» LLC with the resonant sensors GT200 and preliminary amplifiers of the electrical signal PAEF-014 with a gain of 26 dB. Taking into account the noise of the loading machine the threshold value was chosen equal to 40 dB. To determine the length of the fatigue crack during the cyclic loading of metallic samples, an optical method was used. Using an endoscopic chamber, a photograph was taken at intervals of 5 seconds from one of the side surfaces of the sample, and the length of the fatigue crack was determined from the obtained photographs. Totally 45 fatigue experiments were conducted.

3. AE data analysis

In the results of laboratory tests, there is a considerable scatter of both the fatigue characteristics of the material and the values of standard AE parameters. Fig. 3 shows the dependence of the cracks size on the number of loading cycles.

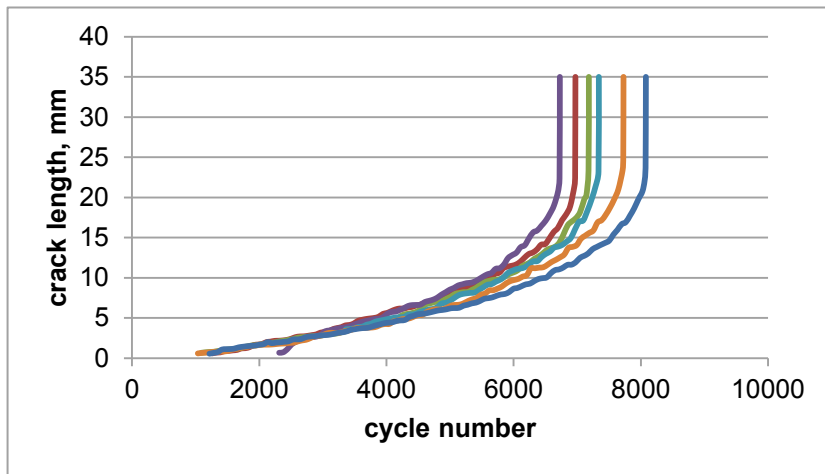


Fig. 3 Dependence of the cracks size on the number of loading cycle

As shown in Fig. 3, the destruction of a metallic sample under loading by the same scheme can occur for a different number of cycles from 6500 to 8100. Such a scatter could be caused by the structural heterogeneity of the material (the presence of internal defects, nonmetallic inclusions, etc.), leading to a change in the kinetics of fatigue crack.

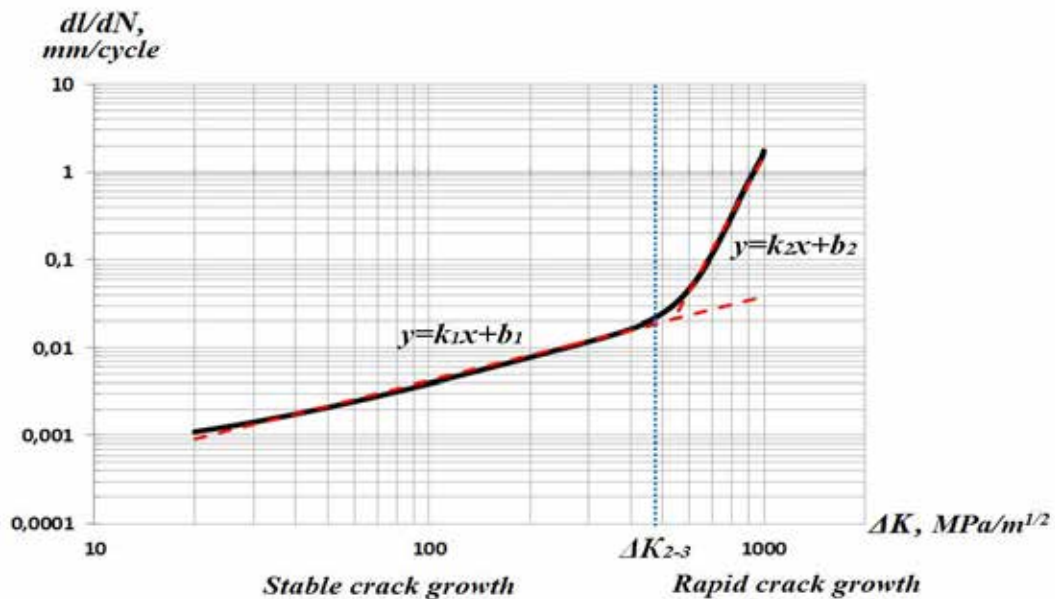


Fig. 4 Typical KDFF, registered during experiment: dl/dN – the crack length / change during N loading cycles; ΔK – stress intensity factor peak-to-peak range

The fatigue crack growth rate is described by the kinetic diagram of fatigue failure (KDFF) [8], the shape of which is shown in Fig. 4.

The two linear parts of the KDFF correspond to a stable and unstable stage of crack growth. Monitoring of the stage of crack initiation is impossible due to the limited sensitivity of optic and acoustic equipment.

At each stage of development, the fatigue crack is the source of acoustic emission. The sensitivity of the AE testing system made it possible to detect the impulses that arise during the development of the fatigue crack already at the stage of stable growth at a length of 300-500 μm and a growth rate of the order of 1 μm per cycle.

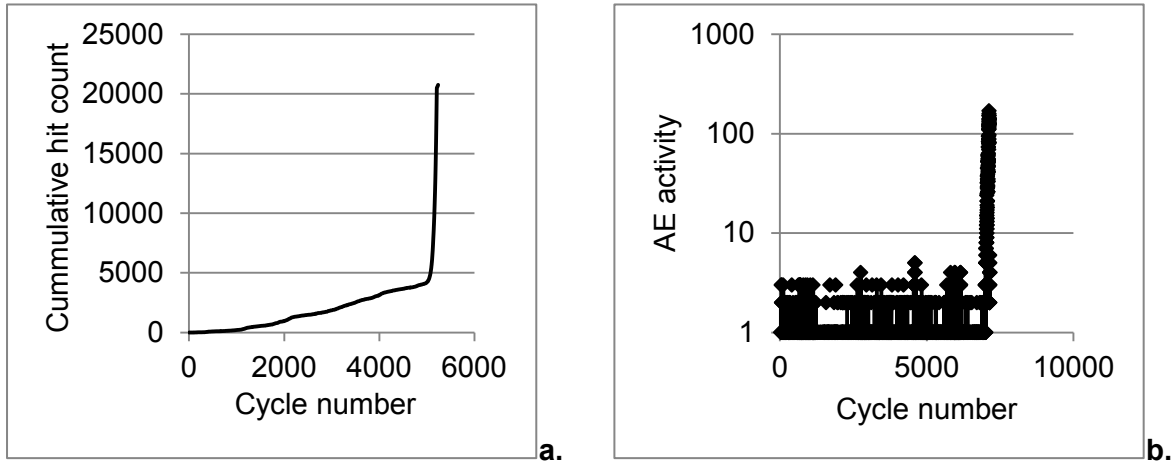


Fig. 5 Dependence of cumulative hit counts and AE activity vs. loading cycle number

Comparison of KDFE and the trends of AE parameters show the similar consistent patterns. At the stage of stable growth of the fatigue crack, the acoustic emission process is stationary and characterized by low activity of the order of 0.5-5 impulses per loading cycle, the accumulation of impulses occurs predominantly linearly. At the stage of the rapid growth, the number of AE impulses increases avalanche-like, the activity value reaches about 100 impulses per cycle. The dependences *cumulative hit count vs. cycle number* and *AE activity vs. cycle number* is shown on the Fig.5 a,b.

The distribution of the amplitudes of AE impulses is shown on Figs.6a, b. Fig 6a corresponds to the stable crack growth, Fig.6b to the rapid growth stage.

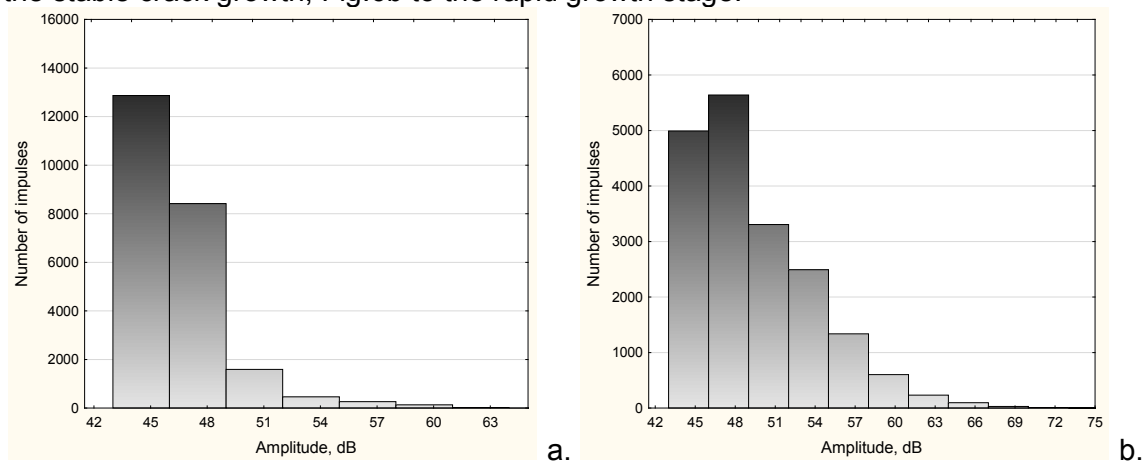


Fig.6 Histograms of amplitudes distribution at different stages of fatigue crack growth a. for stable stage b. for accelerated growth

A sufficiently low level of amplitudes is noted during the fatigue test for the most specimen - no more than 55 dB for the stage of stable growth, not more than 70 dB for the stage of accelerated growth.

It is noted that in all experiments the parameters of the AE are changed in accordance with the changing of the crack growing stage. At the stage of stable growth, comparatively low activity and low amplitudes of AE impulses are noted, with the propagation of the fatigue crack to the final stage of development, the number of impulses and their amplitudes substantially increase. The averaged AE parameters are given in Table 1

Table 1

Activity		Average amplitude, dB		Experimental conditions		
stable crack growth	rapid crack growth	stable crack growth	rapid crack growth	P _{max} , kN	f, Hz	R
1.4±0.8	55.3±6,3	45.8±3.4	56.5±9.4	23	1	0
1.2±0.9	56.5±8,5	46.4±2.4	58.6±5.6	23	2	0
0.9±1.1	61.5±5,5	45.2±3.6	55.6±7.8	23	0,5	0
0.8±1.2	60.8±9,5	46.0±3.2	57.6±10.4	21	1	0
1.0±1.4	57.4±4,6	44.9±2.5	61.2±6.8	19	1	0
1.1±1.5	52.4±6.5	47.5±2.3	59.9±8.6	21	1	0,25
0.9±0.8	62.3±7.8	44.7±1.8	58.4±8.7	21	1	0,5

Analysis of the results shows that the AE parameters have a significant variance in each series of experiments. While the maximum cyclic loading, loading frequency and the ratio R do not significantly affect the average values of the amplitudes and activity of the AE impulses. For example, the average activity value at the stage of stable crack growth for any loading parameters is approximately equal to one impulse per cycle. While, the variance of this parameter is significant and even exceeds the average value. The same trend is also observed for other parameters.

The variance of the AE data, which is observed in a number of experiments, may be explained by the influence of the metal microstructure. Fractographic analysis carried out within the framework of this study allows to suppose the presence of the secondary sources of AE, creating additional AE activity. Nonmetallic inclusions, microcracks present in the metal, lateral cracks and stratifications can be a secondary sources of AE impulses

When comparing the results of fractographic analysis and AE data, a number of regularities were established. In particular, it was noted that the presence of nonmetallic inclusions leads to a short-term, up to 5-10 cycles of loading, generation of high-amplitude AE impulses, with an amplitude reaching 80 dB. Fig.7b shows the dependence of the amplitudes of AE impulses vs. the number of the loading cycle. The moment of the occurrence of high-amplitude AE impulses during the 900th and 1100th loading cycles corresponds to the propagation of the crack front through the nonmetallic inclusion shown on the fractographic image.

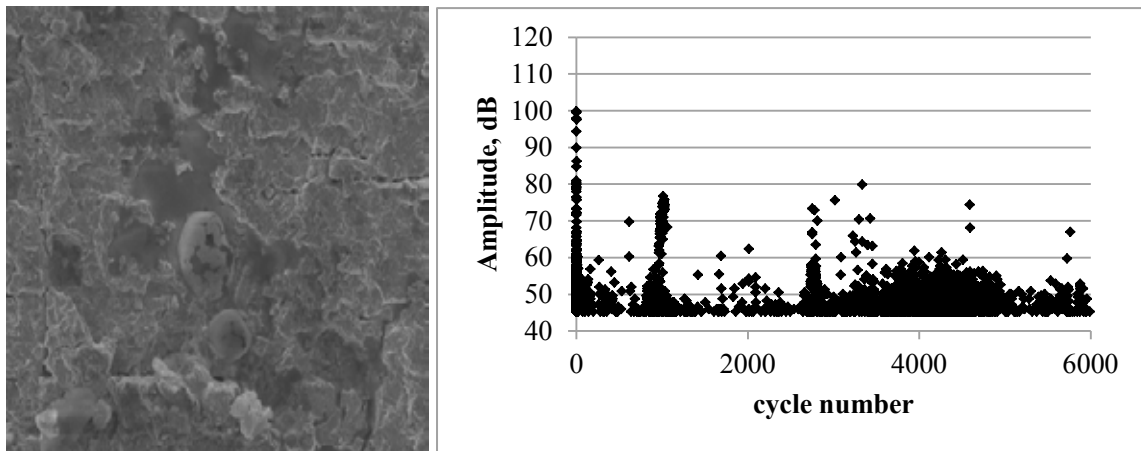


Fig. 7 a. Nonmetallic inclusions on the fractographic image; b. Dependence of AE impulse amplitudes vs. cycle number

In some experiments, activity during the stage of the stable crack growth increases in the several times and reaches 10 impulses per cycle. The fractographic and metallography evaluations of the specimen for which this phenomenon was observed show the presence of the additional cracks initiated presumably due to non-metallic inclusions. These cracks whose lengths do not exceed 300 μs are shown at the metallography image (Fig.8a), dependence *rate of AE impulses vs. time* with an anomaly increasing of AE activity at the stable stage of the crack growth is shown on the Fig.8b.

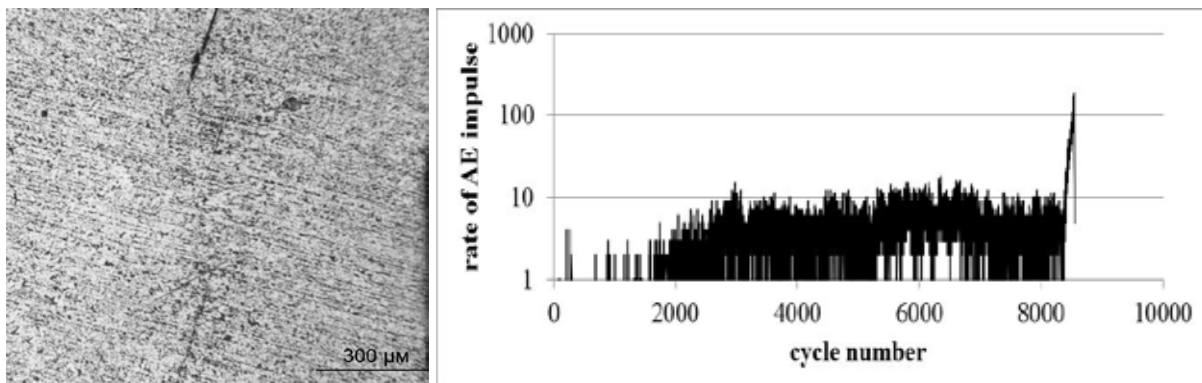


Fig. 8 a. Metallographic image of the additional fatigue crack b. increasing of AE activity vs cycle number due to the presence of additional defects

Another atypical case of the trend of changing AE parameters is the appearance of samples in the amplitude spectrum of AE impulses, which, firstly significantly exceed the averages level, and secondly, have practically constant values in a certain time interval. Illustration for this case is shown on Fig.9. The amplitudes of the part of AE impulses increase until 70 dB in the period from 1500 to 7000 loading cycle.

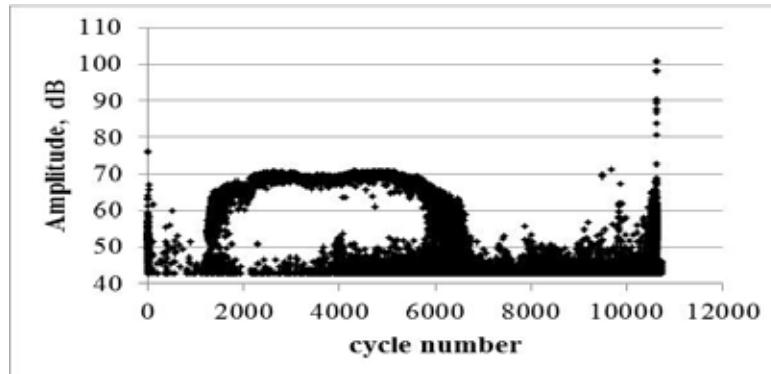


Fig. 9 The secondary AE process on the dependence of impulse *amplitude vs. time* with the secondary high amplitude AE process

This phenomenon was explained by the influence of the friction effects caused either by the Elber effect, or the crack face contact, or the effect caused by the falling of nonmetallic inclusions into the pores and stratifications that have arisen upon the destruction [11]. The above-described cases of atypical changes in the AE parameters, on the one hand, complicate the interpretation of the AE data and the classification of the AE source, but on the other hand, contribute to a more reliable identification of fatigue defects due to generation additional AE impulses.

4. Results

Based on the results of 45 experiments, it is possible to estimate the probability of detecting fatigue defects by the AE method. The probability of detection depends on multiple factors, in particular, on the stage of fatigue crack growth, the distance between the sensor and the defect, on the properties of the propagation path and the noise level.

For defect detection by AE method, it is necessary that the sensitivity of the AE testing system is sufficient to register the impulses emitted by a defect after the energy dissipation caused by the passage of AE signals through the propagation path [12].

$$s(t) = u_{source}(t) * h_{channel}(t) * h_{sensor}(t) \quad (1)$$

$$AE_data = Threshold(s(t), thr_level) \quad (2)$$

The AE signal that is detected by the sensor can be represented as a result of convolution of the AE source function $u_{source}(t)$ with the transfer function of the propagation path $h_{channel}(t)$ and the impulse response of the AE sensor $h_{sensor}(t)$ (1). Further, as a result of threshold processing, detected AE impulses are represented as a number of AE parameters (2).

Within the framework of the study, the assumption is made that a defect is detected if the AE system measures more than N impulses ($N = 10$). The probability of detecting a fatigue crack is equal to the percentage of defects for which the number of AE impulses will be greater than $N=10$ after taking into account attenuation factor and threshold level.

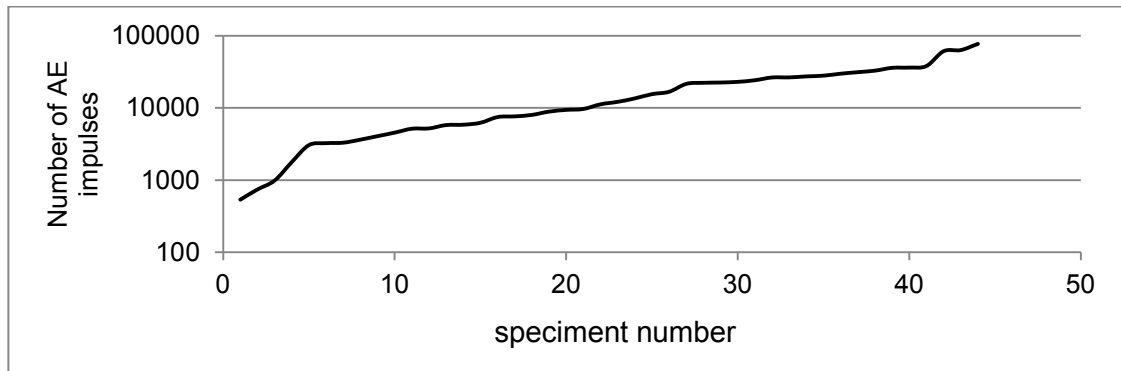


Fig.10 Number of AE impulses measured during the stable crack growth represented in the form of the ordered series

The function of AE source was estimated empirically on the basis of the results experiment. As was shown in the previous section, a fatigue crack in a low-carbon steel is the AE source with relatively low-amplitude impulses, 95% of impulses have an amplitude of less than 55 dB on a stable growing stage. The number of impulses registered during the stable growth stage is characterized by a significant spread of the values observed from the specimen to the specimen. The empirical distribution of the number of impulses for the stable stage of crack growth in the form of the ordered series is shown in Fig.10. The greatest AE activity is observed in the case of the presence of secondary AE sources lateral cracks, cracks face contact or the influence of the nonmetallic inclusions. The lowest AE activity is observed in more homogeneous materials. It should be noted that the influence of the sensor transfer function has already been taken into account as the AE data was obtained experimentally.

The transfer function of the acoustic channel was evaluated approximately using the attenuation function of the AE waves from the distance until 11 meters in the frequency band from 100 to 500 kHz.

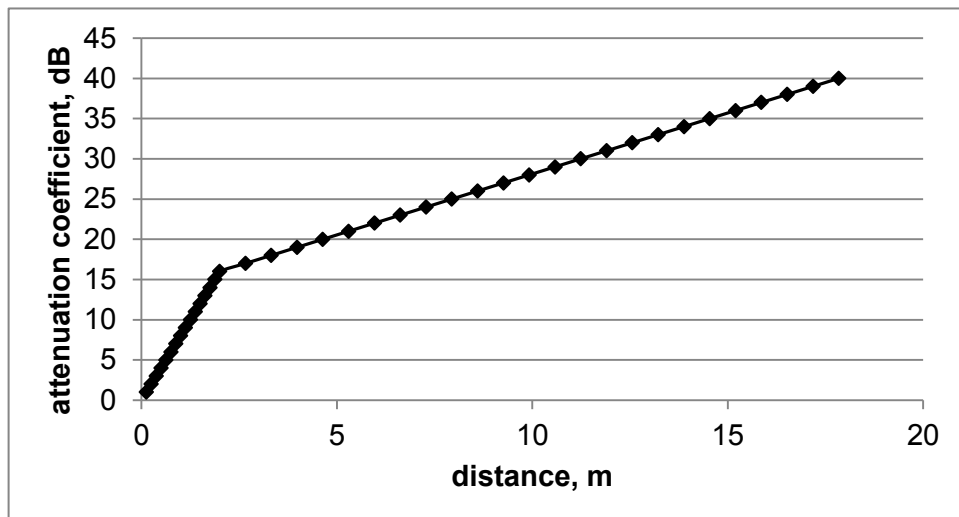


Fig.11 The attenuation coefficient depending on the distance between sensor and AE source

The dependence of the attenuation coefficient vs. distance is show on Fig.11. In the near field, the attenuation coefficient is 8 dB per meter, in the far field - 1.5 dB per meter.

The probability of a defect detection was calculated using the following algorithm. The amplitudes of the AE data obtained as a result of the experiment were recalculated to a certain distance, in accordance with the attenuation parameter of the propagation path (Fig.11). The influence of noise was taken into account by setting the threshold value. It was assumed that the noise level did not exceed the threshold value. All impulses which turned out to be below the threshold were excluded from consideration. The probability of detecting a defect was determined as the number of defects for which the detection criterion is met divided by the total number of defects.

The results of calculating the probability of defect detection at different stages of the crack growth are shown in Figs. 12 and 13. The dependence of Fig.12 shows the probability of a defect detection at different distances between the AE source and the sensor at different noise levels during the stage of stable growth of the fatigue defect. The same dependencies for the stage of accelerated growth of the fatigue defect are shown on Fig.13.

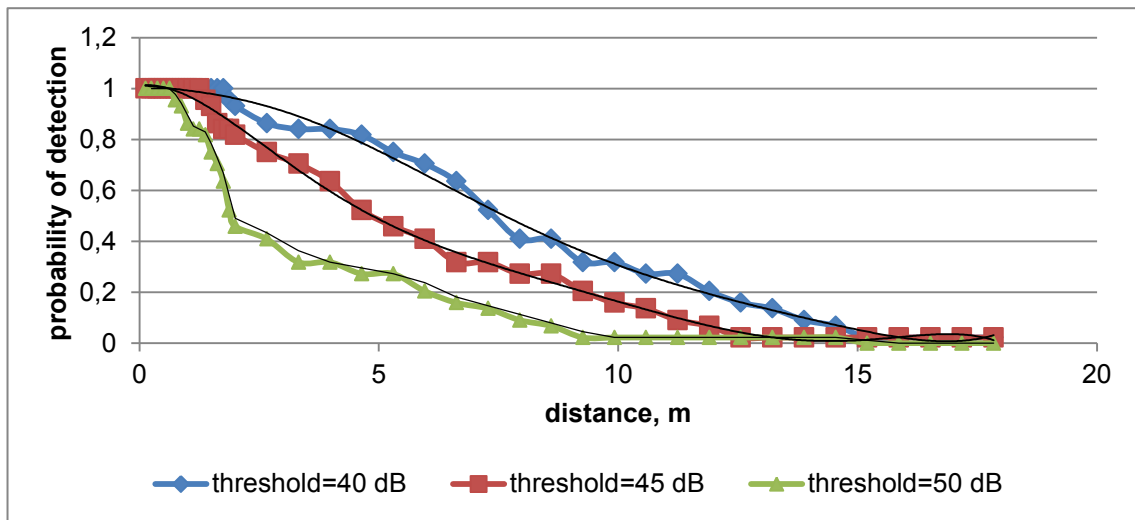


Fig.12 Probability of fatigue crack detection on the stable growing stage depending on the distance and threshold value

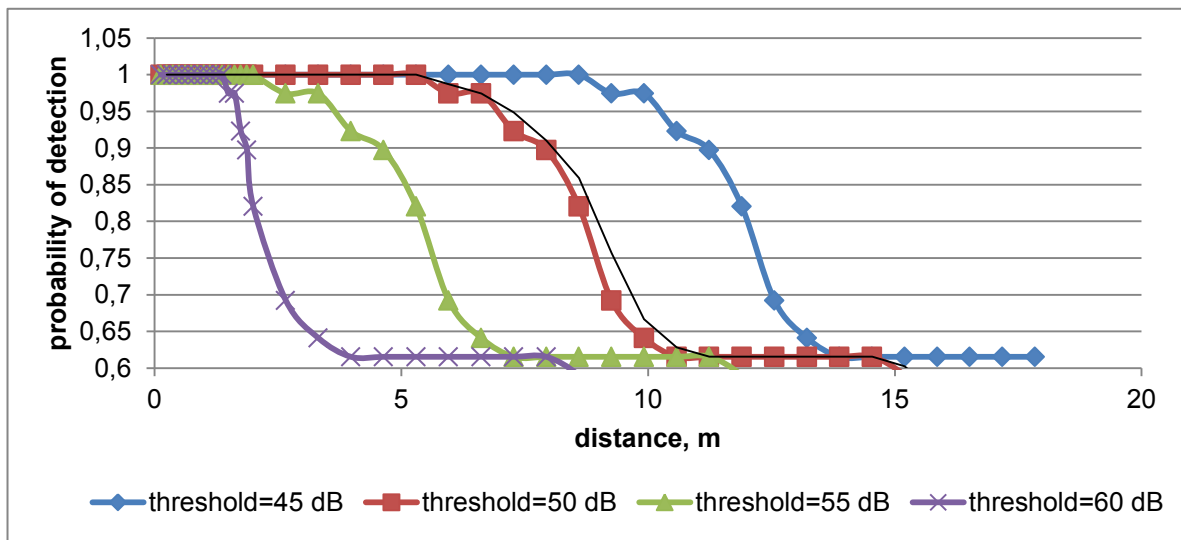
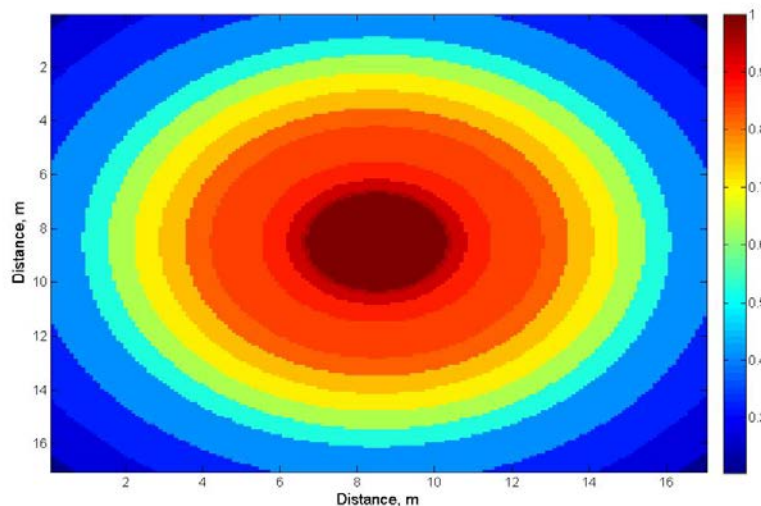


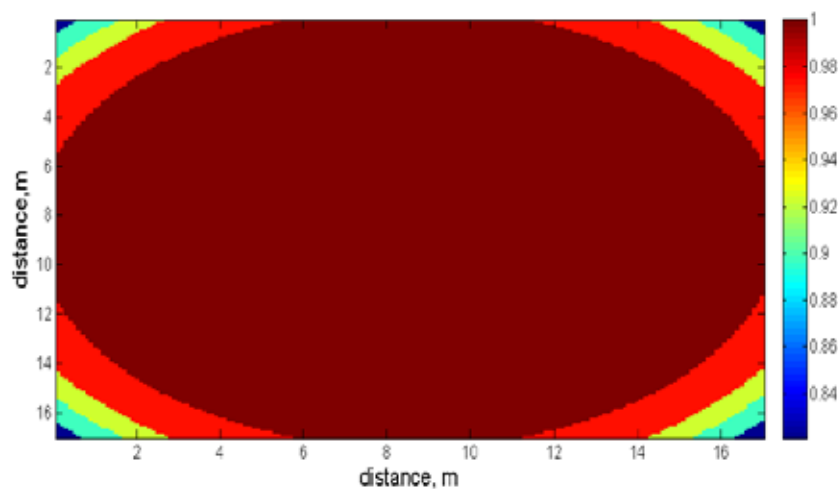
Fig.13 Probability of fatigue crack detection on the unstable growing stage depending on the distance and threshold value

As can be seen from the figures, reliable detection of the fatigue defect at the stage of its stable growth is possible only if the sensor is placed in the immediate vicinity of the source. With a probability of 90%, a fatigue defect in low-carbon steel can be detected at a noise level of 40 dB at a distance of 2.5 m from the source, if the noise level is 45 dB, then the distance corresponding to the 90% probability decreases to 1.5 m and with noise which does not exceeded 50 dB to 1 meter.

For the stage of the unstable defect growth, more optimistic results were obtained. At the final stage of destruction more high-amplitude signals are generated, so the distance of a reliable detection of the fatigue defect essentially increases. At a noise level of 45 dB, the fatigue defect is detected with a probability of 90% at a distance of 11 m, with a noise level of 50 and 55 dB at distances of 8 and 4.5 m correspondingly. Even with a noise level of 60 dB, the fatigue defect is reliably detected at a distance of not more than two meters from the source.



a.



b.

Fig.14 Two-dimensional representation of the POD diagrams (threshold level = 40 dB) a. POD for stable growing stage b. for the unstable growing stage

For practical use, the two-dimensional version of POD diagrams is more preferable. Fig. 14 shows the POD diagrams depending on the distances from the sensor located in the center of the diagram.

5. Conclusion

The method of calculating the probability of detection of fatigue defects in low-carbon steels by the AE testing method is considered in this paper. The probability estimation was conducted taking into account the empirical function of the AE source, the attenuation parameter of the propagation path, and the noise level.

Despite the fact that not all the influenced factors have been investigated in detail, the results obtained are of practical importance. The calculated POD – diagrams allow to estimate the probability of detection for fatigue damages on a various growth stages upon specific conditions of AE testing. It also make possible to choose the maximum distance between the sensors and threshold value to provide defined probability of fatigue crack detection.

Acknowledgment

Research work was carried out during the implementation of the State order project of the Ministry of Education and Science of Russian Federation in the field of scientific activity № 11.9879.2017/8.9.

References

- [1]. Ido N., Tagami M., Katou K., Tsuji T. Evaluation of fatigue crack propagation rate by acoustic emission method / 7th International conference on NDE in relation to structural integrity for nuclear and pressurized components.2009.
- [2]. Fady F. Barsoum, Jamil Suleman, Andrej Korcak, Eric V. K. Hill. Acoustic emission monitoring and fatigue life prediction in axially loaded notched steel specimens // Journal of acoustic emission. 2009. Vol. 27. P. 40-63.
- [3]. Dimitrios G. Aggelis, Evangelios Z. Kordatos, Theodore E. Matikas Monitoring of metal fatigue damage using acoustic emission and thermography // Journal of acoustic emission. 2011. Vol. 29. P.113-122.
- [4]. Claudia Barile, Caterina Casavola, Giovanni Pappalettera, Carmine Pappalettere Fatigue damage monitoring by means of acoustic emission and thermography in Ti grade 5 specimens // Procedia Engineering. Vol. 114(2015). P. 487-492.
- [5]. Zain M.S.M., Jamaludin N., Sajuri Z., Yusof M.F.M., Hanafi Z.H. Acoustic emission study of fatigue crack growth in rail track material // National Conference in Mechanical Engineering Research and Postgraduate Studies (2nd NCMER 2010) 3-4 December 2010, Faculty of Mechanical Engineering, UMP Pekan, Kuantan, Pahang, Malaysia; pp. 82-90.

- [6]. GOST 25.506-85. Methods of mechanical testing of metals. Determination of fracture toughness characteristics (fracture toughness) under static loading.
- [7]. Building norms and rules: SNiP 2.05.06-85. Trunk pipelines [Text]: normative and technical material. – Moscow, 1985. – 89 p.
- [8]. Matvienko Yu.G. Models and criteria for fracture mechanics. - M .. FIZMATLIT, 2006. – 328 p.
- [9]. Terentyev V.F., Korableva S.A. Fatigue of metals. Moscow: Nauka, 2015. - 479 p.
- [10]. Parton V.Z. Mechanics of destruction: From theory to practice. Ed. 3rd. Moscow: Publishing house LCI, 2010. - 240 p.
- [11]. Guohao S., Zhengxing W., Delian K., Mingqing B., Yang Zh., Fengjing Xu., Jiazhen P. Analysis on acoustic signal characteristics of the fatigue crack in anchor structure of cable stayed bridge stayed bridge tower. Russian Journal of Nondestructive testing, N12, 2012
- [12]. A. Pollock Probability of detection for acoustic emission./Journal of acoustic emission, V25, 2007, pp.231-237

78 - Statistical non-parametrical algorithm for Acoustic Emission impulses detection adapted on the basis of modal analysis approach

V.A. Barat¹, D.A. Terentyev¹, S.V. Elizarov¹

¹ INTERUNIS-IT LLC, Entuziastov shosse 20B, Moscow, 111024, PO 140, Russia.
E-mail: tyev@interunis-it.ru

Abstract:

This work is devoted to the study of a nonthreshold method for detecting acoustic emission impulses. As a method of impulse detection, a statistical ranking algorithm based on comparing the ranks of samples in two neighboring sliding windows is considered. To select the setting parameters of the algorithm and verify its reliability, the modal analysis method is used. The modal analysis is a mathematically exact method that leads to a closed integral equation for the elastic fields in the waveguide and which naturally includes the problem of the selectivity of the mode, offering an idea of the physics of waveguide behavior. The non-threshold algorithm developed in the framework of this paper was tested using 10000 model signals. The results of the research showed its high reliability and accuracy. A numerical experiment based on model signals showed that using the proposed nonparametric rank detection algorithm, in comparison with the threshold method, the location error has decreased by 1.5-2 times.

1. Introduction

Among many methods of nondestructive testing the acoustic emission (AE) is one of the most complicated in the field of data processing. The raw data volume could be as big as several terabytes whereas the noise part in it is generally about 90-99%. So the upgrading of AE impulse detection methods is a critical task. Threshold method is a convenient one, as it is simple for realization, but it has substantial drawbacks, such as inaccuracy of measured arrival time and other AE parameters. This method easily provides low level of false detections, i.e. type I statistical errors. But if the noise level is high then it leads to high level of type II statistical errors, i.e. undetected AE impulses.

Threshold-free algorithm, based on signal detection theory, would allow to substantially decrease the level of missed AE impulses as the level of false detections is set. Efficiency is provided by method intellectualization, as detection of AE impulses is based on its typical waveforms. Development of such an algorithm has a main problem in great variability of AE impulse parameters; it is induced in general by unknown acoustic propagation path.

2. Description of work

2.1. Non-parametric algorithm of AE impulse detection

A statistical non-parametric algorithm for the detection of AE impulses is proposed as an alternative to traditional threshold data recording. It allows to detect AE impulses in an automatic mode without setting a threshold value.

Nonparametric detection methods [1] are effective for detecting AE impulses whose shape and parameters are a priori unknown. The methods are based on comparing the parameters of the AE signals distribution in the time intervals which can be neighboring, overlapping or in intervals of different time scales. In this case, the difference in the distribution parameters is verified by means of a statistical hypothesis. If the difference in distributions is ascertained with a high probability, the AE impulse is recognized.

Nonparametric algorithms are widely used in the practice of AE data processing. An example of nonparametric analysis can be the use of LTA / STA technology, the Akaike criterion and the method of higher-order moments as hypothesis testing criteria [2-4]. As works devoted to non-parametric detection of AE pulses, we can also mention [5] and [6], in which the authors use the sequential probability ratio test and autoregressive analysis.

In this paper, we investigate a ranking impulse detection method, based on comparing the ranks of the sample values of the AE signal in neighboring shifting time intervals. With the correct choice of the observation interval, comparison of ranks is a sensitive method of detecting AE impulses, which are represented by short-time burst parameter changes in the long-time noise process.

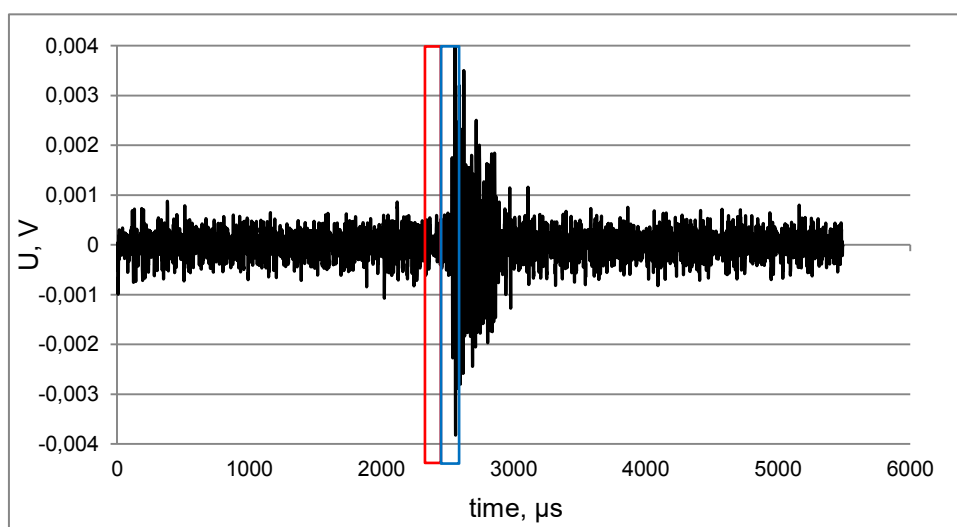


Fig.1. AE impulse against background noise, two time intervals are marked with color rectangles

In Fig.1 AE impulse with a characteristic waveform and corresponding to the growth of a fatigue defect is shown. The two time intervals allocated for comparing the distribution parameters are indicated by a red and blue rectangle, respectively. The left window contains noise samples. The onset of the impulse belongs to the right window. The samples of both windows are grouped together, sorted in ascending order and then samples taken from left window are replaced by zeros and samples taken from right window are replaced by ones. Fig. 2 shows the result of such operation.

corresponding to the defect do not differ in amplitude, but differ significantly in time observation scale. The AE impulses have a relative small RT and RA, while these parameters for friction noise process are substantially higher.

Fig. 4 represents a scatterplot with the quantitative analysis result. On the dependences RA vs RT the points corresponding the noise are marked with the red color, the AE impulses from the crack growth are marked in blue. As you can see, the parameters RA and RT are significantly different and do not overlap on the scatterplot.

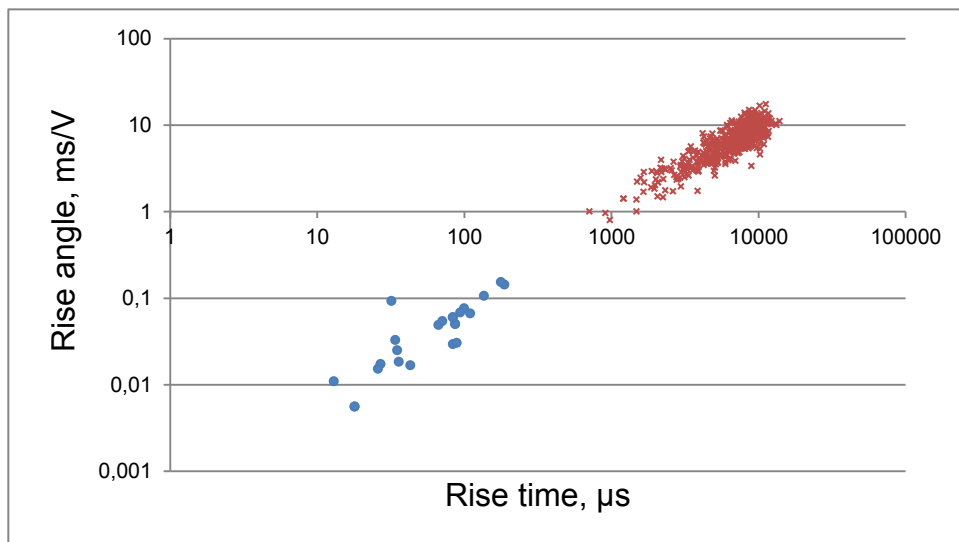


Fig.4. Scatterplot Rise angle vs Rise time for AE signal (blue points) and friction noise (red points)

Such a difference in parameters makes it possible to detect AE pulses against the friction noise due to the correct choice of the time interval T_{window} . Fig. 5 shows the result of applying a ranking algorithm to processing a friction noise signal. Since the process is completely noise, all detected pulses correspond to false detections. Fig. 5 represents the dependence of the number of false detections on the duration of the observation interval. If the T_{window} value is comparable with the RT of the noise signal, the number of false detections reaches hundreds. If T_{window} parameter decreases by an order in comparison with RT, the number of false detections also decreases by approximately an order.

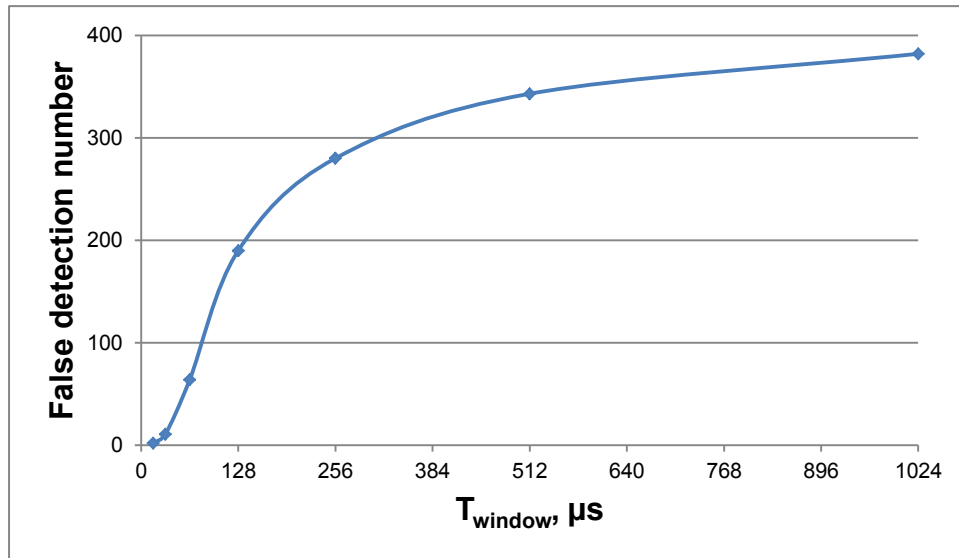


Fig.5 The number of false impulse detections depending on the duration of time interval

Effective detection of AE pulses against the friction noise is achieved, in this case, due to the intellectuality of the non-threshold ranking algorithm of AE impulse detection. This algorithm allows indirectly, due to the choice of the observation interval, to take into account the waveform of the impulse, and not only its amplitude.

However, the complexity of the algorithm has not only advantages, but also drawbacks. One of them is a greater number of specific settings parameters, which values should be precisely selected. For example, the correct operation of the ranking algorithm in the case under consideration is achieved if the value of the T_{window} interval, firstly, is compliant with the RT and RA parameters of typical AE impulses; second, its value should be as small as possible to ensure a minimum number of false detections.

It is well known that the propagation path of the testing structure has the greatest influence on the shape of the AE impulse [10]. The greater the distance from AE source to AE sensor, the greater RT and RA parameters of AE impulse. Therefore, in order to correctly select the parameters of the impulse detection algorithm, it is necessary to know the distribution of the AE impulse parameters that are expected at certain acoustic properties of the structure, the length of the propagation path, the presence or absence of isolation, etc. To study the influence of the propagation path, numerical simulation was used in this paper. The application of the modeling approach allows to study the main influencing factors, without resorting to a large number of experiments. As a result of the simulation, a numerous AE signals corresponding to all possible geometric and acoustic parameters of the testing structure were obtained.

2.2. Modal analysis approach

Modal analysis approach was used for acceleration of modelling because it is an effective analytical method based on the expansion of the forcing terms acting in the waveguide into the set of its proper modes. Modal analysis is a mathematically exact technique that leads to a closed form integral equation for the elastic fields in the waveguide, and which incorporates in a natural way the issue of mode selectivity, offering insight on the physics of waveguide behavior.

The PCDISP package proposed in [9] for analyzing the L-, F-, and T-modes in the waveguide in the framework of the Pochhammer-Chree model was used as the basis for the mathematical apparatus. This mathematical package was reworked for calculations related to Lamb waves in a plate. In general, the calculation of the model signal $u(z, t)$ is as follows:

$$u(z, t) = F^{-1}[U(z, \omega)], \quad (1)$$

where

$$U(z, \omega) = U(0, \omega)a_p(z, \omega); \quad (2)$$

$$U(z, -\omega) = U^*(z, \omega), \quad (3)$$

$U(0, \omega)$ contains information about the spectrum of the emitted signal, $a_p(z, \omega)$ contains both the frequency response of the AE sensor, and the effects caused by propagation of the signal in the form of normal waves. One of the main stages of calculations is the computation of phase velocities of normal waves for a certain set of frequencies.

The thickness and material of the plate, the distance between the source of the signal and the sensor, the emitted Lamb mode, as well as the time dependence of the emitted signal are used as model parameters.

The limitation of the method is as follows: an infinite plate is modeled without defects and inhomogeneities, damping is not taken into account. In addition, there is no possibility of studying the dependence of the energy ratio of different Lamb modes and the spectrum of the emitted signal on the type of defect, its depth and orientation [10-11].

Calculations were carried out for plate thickness values from 3 to 40 mm, at propagation paths from 0.5 to 12 m. Acoustic parameters of carbon steel were used: $c_L = 5900$ m/s, $c_T = 3100$ m/s.

Separately, signals that came in the form of S_0 or A_0 waves were modeled separately, then such signals were used individually or as a sum. The frequency of digitization of the simulated signal was 1 MHz. The duration of the simulated waveforms was from 4096 to 16384 μ s, while the typical calculation time on a computer with a processor with a clock speed of 3.5 GHz when using one core was from 0.04 to 0.16 s, respectively (without taking into account the time for recalculation of the dispersion curves required for each new thickness value or when changing material parameters).

At first, the Morlet wavelet was used as the emitted signal, which made it possible to obtain compactness both in the time and in the frequency domain. Model AE signals were obtained, possessing all the characteristic features of real AE signals relating to the shape of the envelope and frequency filling (Fig. 6). Both in model and real signals, the fastest, but at the same time low-frequency components of the S_0 -mode are observed in the initial part of the signal corresponding to velocities of about 5000 m/s. In the middle of the signal, as a rule, the maximum value of the instantaneous amplitude is observed, caused by the almost simultaneous arrival of many components of the S_0 and A_0 modes having different frequencies, but practically the same velocity of the order of 3000 m/s. In the final part of the signal, corresponding to velocities of the order of 1500-2000 m/s, acoustic beat can occur due to the interference of simultaneously arriving two components of the S_0 -mode having slightly different frequencies and the same velocities. On the spectrograms [10, 12] of the

model signals, the dispersion curves of Lamb waves were found, which lends evidence the correctness of the simulation (Fig. 7).

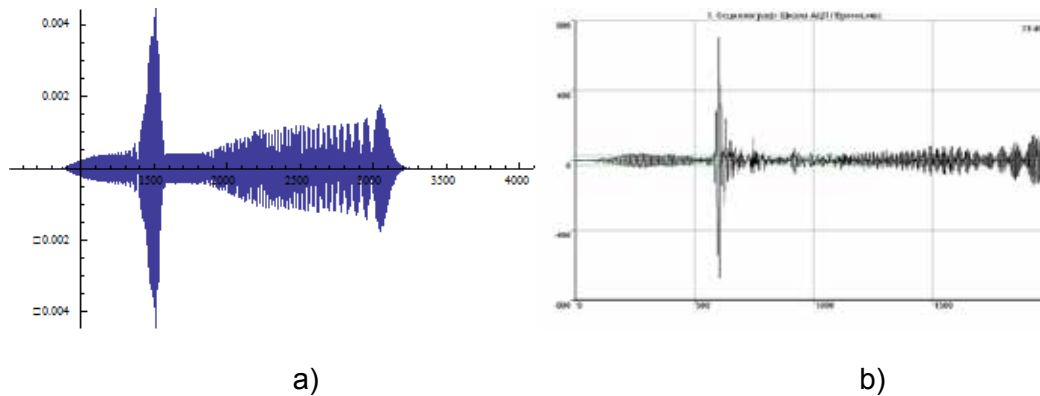


Fig. 6. a) Model signal for thickness of 17 mm and a distance of 5 m, created on the basis of the Morlet wavelet with a center frequency of 160 kHz; b) the actual signal received by the GT200 sensor on the 17 mm plate at a distance of 5 m from the source

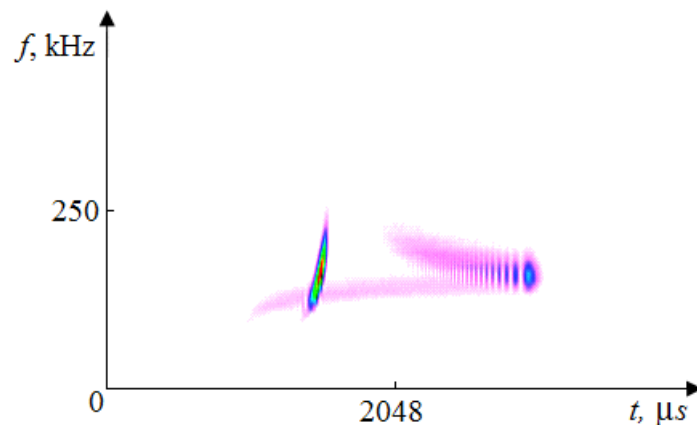


Fig. 7. Continuous wavelet transform of the model signal shown in Fig. 6a

Hereafter, waveforms of the real signals received by the GT200 sensors (130-200 kHz), which was located at a distance of 2 cm from a crack, were used as the emitted signals. This method made it possible to take into account in the calculations the spectrum of the AE source and the impulse response of the AE sensor.

Signals modelled in such a manner had a more complex envelope shape (Fig.8) than the signals modelled with the use of the Morlet wavelet. This circumstance is associated with a complicated form of the spectrum of real AE sensor, which affects the distribution of the amplitudes of different frequency components of the signal arriving at different times.

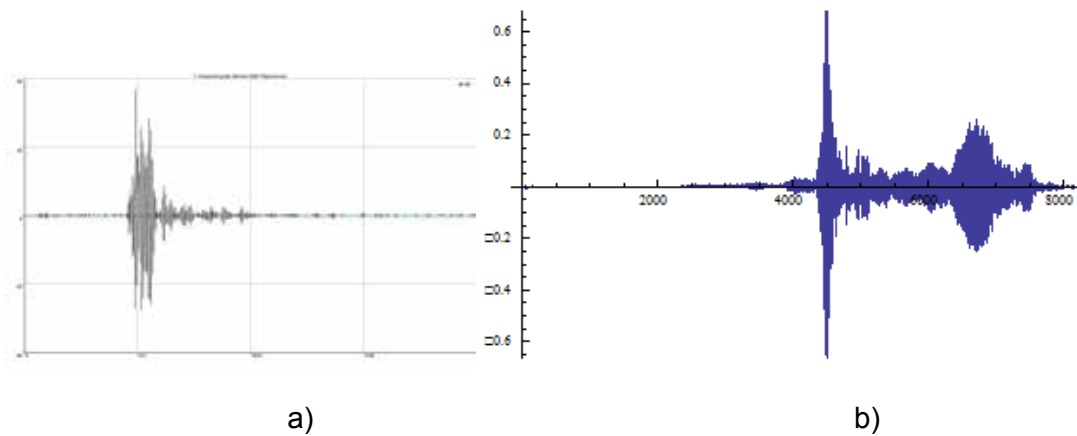


Fig. 8. a) Real signal detected by the GT200 sensor at a distance of 2 cm from a crack; b) modelled signal, which would be registered after passing 12 m along a plate with a thickness of 17 mm

It was found that with the same source signal and the absence of the attenuation, the envelope of modelled signals received at different distances is practically identical and differs in fact only by scaling along the time axis (Fig. 9).

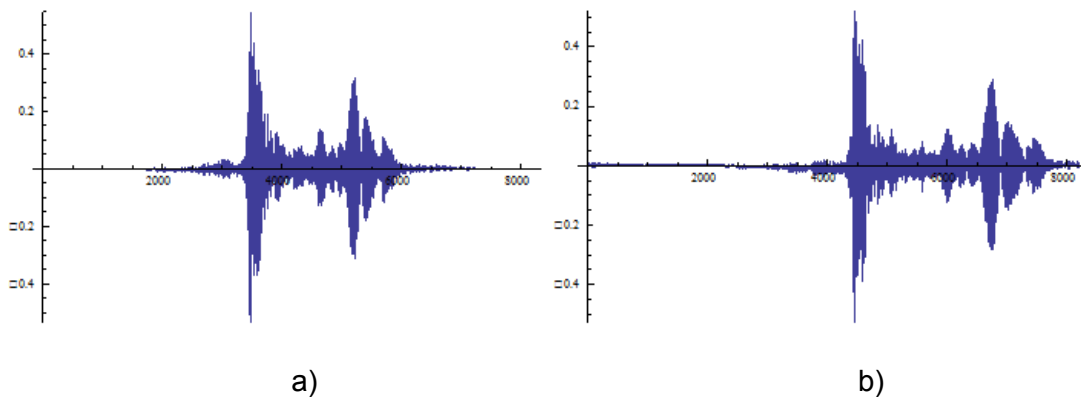


Fig. 9. Signals modelled on the basis of the same emitted signal, corresponding to the distances: a) 9 m, b) 12 m

Thus, the modal analysis method has appeared an effective analytical method, as a result of which it was used to model the order of 10^4 signals during the development of the algorithm for automatic threshold-free data recording based on the theory of signal detection.

2.3. The account of attenuation during propagation through an acoustic path

Since the PCDISP model does not include attenuation calculation, the attenuation of AE waves in the object was calculated using a special algorithm. The algorithm was implemented as follows, it was assumed that the amplitude of each frequency component of the signal decreases with the distance from the source in accordance with the power law, with the damping coefficient proportional to the frequency. Therefore, the simulation of attenuation of AE waves was carried out using a set of digital filters, with a transfer characteristic (4), of the form

$$H(f) = 10^{-\alpha f}, \quad (4)$$

where α – empirical coefficient, which depends on the acoustic properties of the tested object.

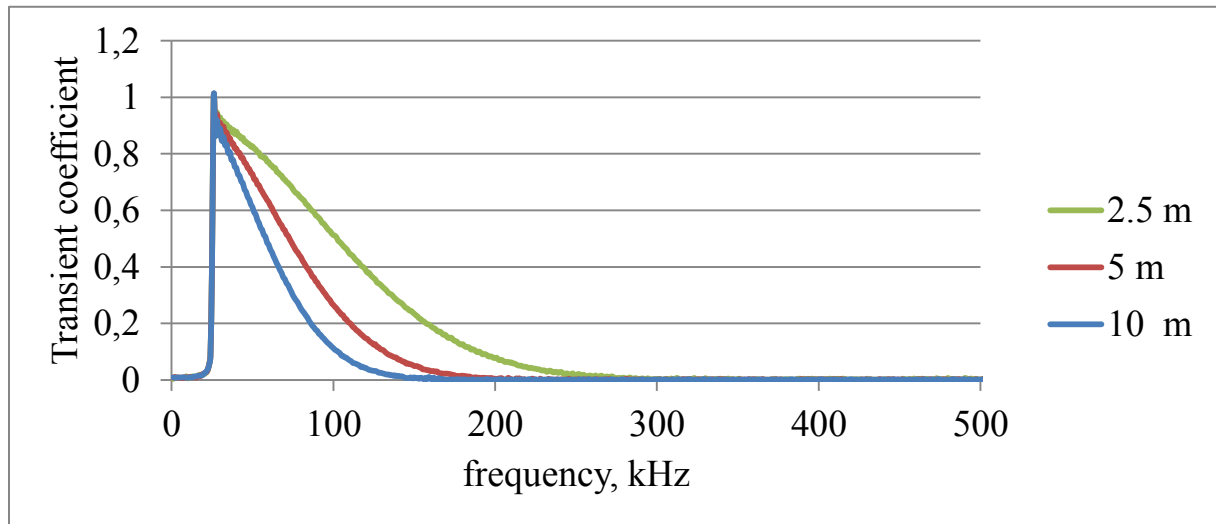


Fig. 10. The transfer function for the attenuation filters

The transfer characteristics of the filters are shown in Fig. 10. To match the filter with the frequency characteristics of the AE system, the filter (4) is combined with a high-pass filter with a cutoff frequency of 30 kHz.

3. Results and discussion

As a result of using the reworked PCDISP package and the attenuation algorithm, realistic models of AE pulses were obtained, with the help of which, without resorting to complex field experiments, it was possible to determine the correspondence between the numerical parameters of the AE pulses and the physical parameters of the monitored object. Gaussian noise level of 30 dB was added to all signals having amplitude 60 dB.

Fig. 11a, b shows the dependence of the mean values of the parameters RT and RA on the distance between the AE source and the sensor. As can be seen, the parameter RT increases linearly, with a speed of approximately 150 $\mu\text{s}/\text{m}$, RA parameter increases according to the $x \cdot \exp(x)$ law, increasing at a distance from 0.5 to 12 m by approximately two orders.

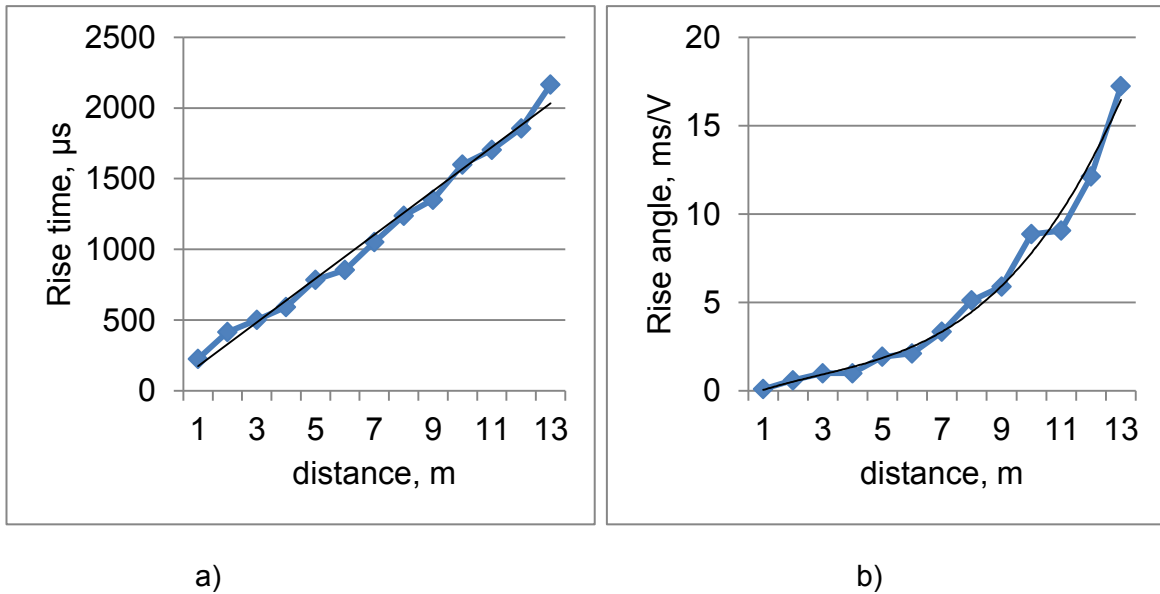


Fig.11 Rise time and rise angle parameters calculated for the modeling signals depending on the distance between the defect and sensor

Fig. 12 represents the correlation plane rise time vs. rise angle, which shows the parameters of pulses, the source of which according to the simulation is located at a distance of 1, 5 and 10 m from the sensor. As can be seen from fig.12 there is a significant variation in the parameters, which is explained by the fact that the modeling is based on AE data obtained from a real defect, having an original shape and spectrum. The spread of the parameters is the greater as the length of the acoustic path is longer.

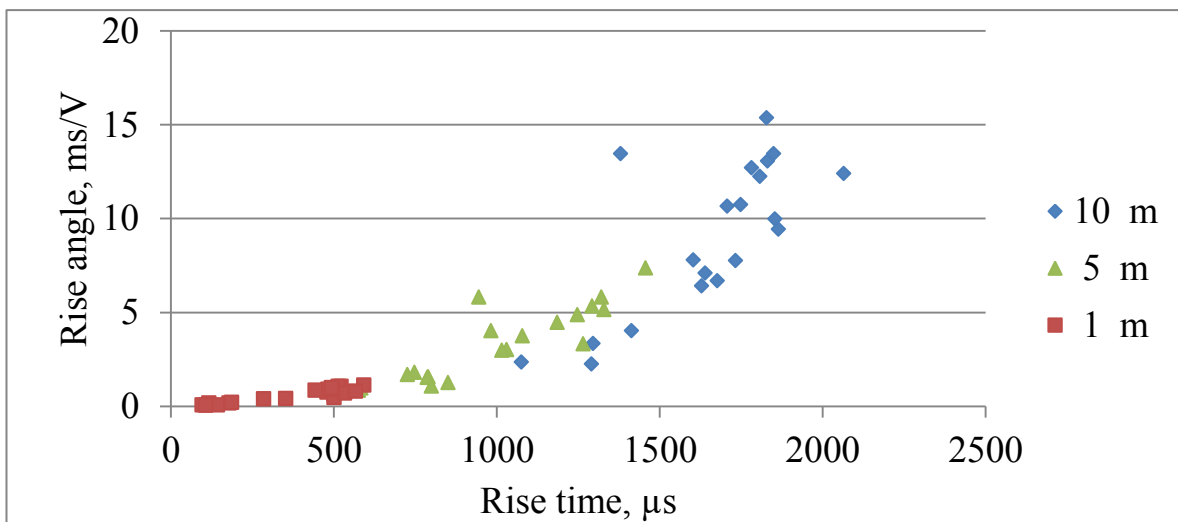


Fig.12. The scatterplot rise angle vs. rise time for the modelling signals

On the basis of the dependences obtained, it is possible to automatically adapt the parameters of the nonthreshold algorithm for AE impulses detecting. As mentioned above, the recommended value for the observation interval is a half of RT. For testing structure of a short extension up to 1 m, it is recommended to select the T_{window} parameter not exceeding

50-100 μ s, at long distances it can reach 1000 μ s. It is also recommended to use multi-scale processing algorithms for more reliable impulse detection in the case of large-scale testing structures.

Models of AE impulses were used for a comparative analysis of the efficiency of the traditional threshold algorithm and a nonthreshold ranking algorithm. The comparison was carried out as follows, for each pair of model AE impulses calculated for distances l_1 and l_2 , the arrival time was determined by the threshold ($t_{1\ thr}$ and $t_{2\ thr}$) and the nonthreshold automatic method ($t_{1\ smart}$ and $t_{2\ smart}$), then based on arrival time differences $\Delta t_{thr}=(t_{1\ thr} - t_{2\ thr})$ and $\Delta t_{smart}=(t_{1\ smart} - t_{2\ smart})$ the location of the AE source was conducted. When calculating the position of the AE source, it was assumed that the first sensor is located directly nearby the defect, and the coordinate of the second is $l_1 + l_2$. If the arrival time difference is correctly determined, the result of the location should be equal to l_1 . The threshold level was selected 36 dB which is two time higher than the noise level. The average location errors are shown in Table 1.

Table 1. Average location errors

Distance between sensors, m	Average location error, m									
	1	2	3	4	5	6	7	8	9	10
Threshold method	0.18	0.29	0.34	0.33	0.39	0.34	0.37	0.33	0.35	0.41
Ranking method	0.12	0.16	0.14	0.17	0.16	0.21	0.20	0.18	0.18	0.23

As follows from the Table 1, the error of location for the ranking algorithm is 1.5-2 times smaller than for threshold. This accuracy is explained by the fact that the ranking algorithm allows to determine the impulse arrival time with a significantly lower delay than the threshold algorithm.

Fig. 13 shows the result of processing the AE pulse models calculated for the same radiated impulse and different distances from 1 to 12 m. The arrival times calculated by the rank and threshold algorithm are shown in Fig. 13 as a function of distance.

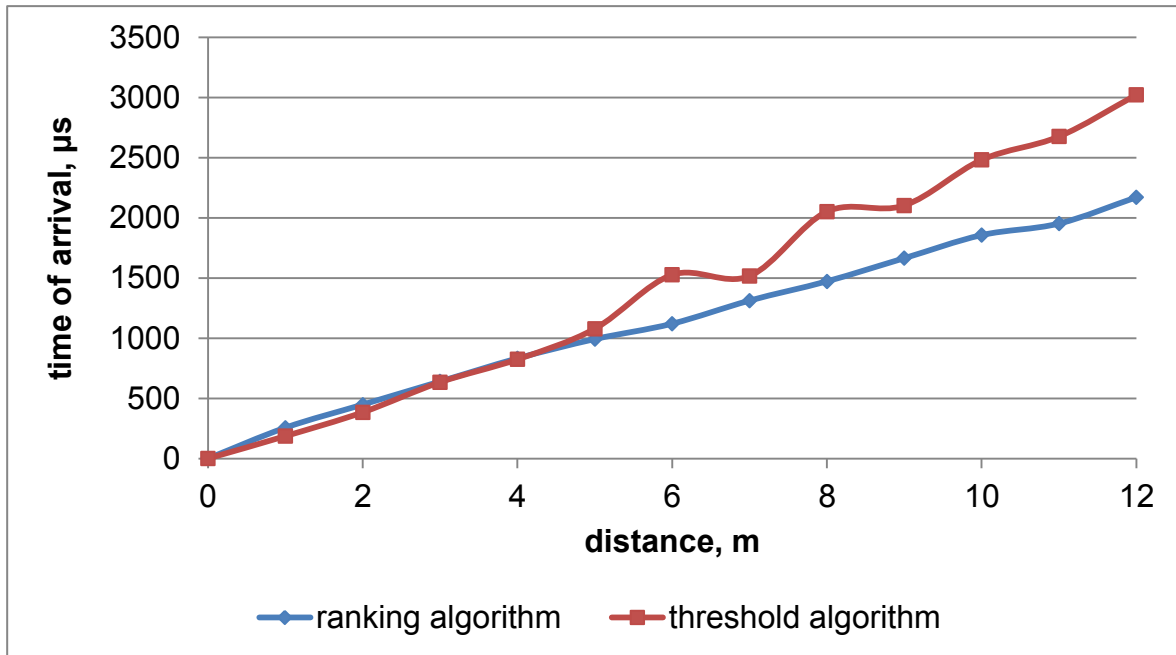


Fig.13. Time of arrival depending on the distance between the source and the sensor

The times of arrival obtained with the rank algorithm increase linearly depending on the distance, and therefore correspond to the same velocity of AE waves propagation equal to approximately 5400 m/s, which corresponds to the fastest component of the Lamb waves the low-frequency part of the S_0 wave. Times of arrival, calculated with the help of the threshold algorithm, depend on the propagation distance nonlinearly and consequently correspond to different components of the Lamb waves.

4. Conclusion

Modal analysis approach has appeared an effective analytical method for the modelling of waveforms of AE signals propagated in plates. It was used for the modelling of the order of 10^4 AE signals received by sensors mounted at different distances from AE sources.

As a result of the conducted researches, a threshold-free automated algorithm for detecting AE impulses is proposed, that uses the modal analysis approach for selecting setting parameters. A numerical experiment based on model signals showed that when using the proposed nonparametric rank detection algorithm, in comparison with the threshold method, the location error has decreased by 1.5-2 times.

A nonparametric rank detection algorithm for signals was implemented at the hardware level in the UNISCOPE portable system of the company INTERUNIS-IT LLC [13].

At present, the study of the nonthreshold algorithm for detection of AE impulses is in progress. It is planned to optimize the choice of rank criteria to minimize type I and type II errors. It is also planned to study the results of the algorithm in the case of various types of noise, and also to calculate the probability of defects detection using the procedure for modeling of the propagation path.

References:

1. Shakhtarin B.I. Signal detection. Gelios press (in Russian), 488 p.
2. Karen M Holford and Mark Eaton. Recent Advances in Acoustic Emission. Proceedings of World conference of Acoustic emission, 2011, Beijing, pp. 58-66.
3. P. Sedlak, Y. Hirose, S.A. Khan, M. Enoki and J. Sikula. New Automatic Localization Technique of Acoustic Emission Signals in Thin Plates. Ultrasonics, 49, 2009, pp. 254-262.
4. T. Lokajicek and K. Klima. A First Arrival Identification System of Acoustic Emission (AE) Signals by Means of a Higher-Order Statistics Approach. Measurement Science and Technology. 17, 2006, 2461-66.
5. G. Por, P. Berezcki, Z. Danko, P. Trampus. Detecting Acoustic Events during Thermal and Mechanical Loading. Proceedings of the 31st Conference of the European Working Group on Acoustic Emission, Dresden, 2014.
6. Rastegaev I.A., Danyuk A.V., Vinogradov A.Y., Merson D.L., Chugunov A.V. Location of noise-like sources of acoustic emissions using the spectral similarity method. Russian Journal of Nondestructive Testing. 2013. V. 49. № 10, pp. 553-561.
7. S. Elizarov, V. Barat, A. Shimansky. Nonthreshold Acoustic Emission Data Registration Principles. Proceedings of the 31st Conference of the European Working Group on Acoustic Emission, Dresden, 2014.
8. V. Barat, S. Elizarov, I. Bolokhova, E. Bolokhov Application of ICI Principle for AE Data Processing. J. Acoustic Emission. V. 30, 2012.
9. F. Seco and A.R. Jiménez, Modelling the generation and propagation of ultrasonic signals in cylindrical waveguides. In Ultrasonic waves, chapter 1, pp. 1-28, Intech Open Access Publisher, 2012. <http://www.car.upm-csic.es/lopsi/people/fernando.seco/pcdisp/>
10. Hamstad M. A., O'Gallagher A., J. Gary. A Wavelet Transform Applied to Acoustic Emission. J. Acoustic Emission, 20 (2002), pp. 39-82.
11. Gallego A., Martinez-Jequier J., Suárez E., Juanes F. J., Valea A. Real-time Algorithm to Classify AE Events of Lamb Waves in CFRP. Proceedings of the 31st Conference of the European Working Group on Acoustic Emission, Dresden, 2014.
12. Suzuki H., Kinjo T., Hayashi Y., Takemoto M., Ono K., Appendix by Hayashi Y. Wavelet Transform of Acoustic Emission Signals, J. Acoustic Emission, Vol. 14, No.2 (1996, April-June), pp. 69-84.
13. S. Elizarov, V. Barat, A. Shimansky. Intelligent Acoustic Emission System. Proceedings of the 31st Conference of the European Working Group on Acoustic Emission, Dresden, 2014.

09 - Acoustic Emission measurements during a tensile fatigue test in reinforced concrete

Gerd Manthei¹, Manuel Koob¹, Jens Minnert¹

¹THM · UNIVERSITY OF APPLIED SCIENCES, GIESSEN, GERMANY
Institute for Structural Engineering (IKT)

Abstract:

In a research project funded by the German Federal Ministry of Education and Research (BMBF) acoustic emission (AE) measurements were carried out during a tensile fatigue test on a plate-shaped reinforced concrete specimen to investigate the fatigue behaviour of an embedded steel anchor with a clothoid-shaped form in reinforced concrete. The results of AE measurements show that the AE activity begins immediately after starting dynamic loading. Due to the limited location accuracy, the located AE events are not identified on fracture planes, but are cloud-like distributed in zones of the high stresses on the left and right edges of the steel anchor. During the test 9,132 AE events could be located using the longitudinal (L wave) and transverse (T wave) wave onsets. The locations of the AE events let suggest that microcracks occur due to the form-closed connection between the concrete and the steel anchor under fatigue stress.

1 Introduction

Today, many constructions activities deal with repair of existing buildings and it will gain in importance in the future. In order to decide on the necessity the type and scope of a redevelopment measure, the knowledge about the conditions of the existing building is required. The current mapping of reinforced concrete structures extends to the visual inspection about damage of the structure surface without technical aids. This appraisal of the structure is necessary but not always sufficient. Damage inside the building remains hidden and can only be discovered with a delay.

The use of non-destructive testing methods can provide information on processes inside the structure. Acoustic emission (AE) testing is a non-destructive testing method, which is used to detect material damage. Due to the damage of structures like concrete components elastic waves emit during fracturing of materials under load. The AE signals are detected by AE sensors, which are mounted on the surface of the component, allowing the state of the material and the cause of the deformation to be traced.

The investigation of AE in reinforced concrete started very early. Rüsç (1959) examined in first tests on concrete pressure prisms (100 mm · 150 mm) the strength, the deformation behaviour and the AE activity under short-term and continuous load and under cyclic load [1]. He traces out that the so-called "Kaiser effect" on concrete is not valid. The "Kaiser effect" is defined as the absence of AE at stress level below the previously applied maximal stress [2]. In the 1960s and 1970s this was followed by many further investigations using AE analysis to detect crack formation in concrete. A good overview of literature provides the bibliography made by Drouillard (1986) [3]. Manthei (2016) gives an overview about the application of the AE in concrete in the last decades [4]. Further important works about AE in concrete are

published by Schechinger (2005), Shiotani et al. (2006) and Grosse & Ohtsu (2008) [5-7]. Pull-out tests of concrete reinforcing bars were examined by Finck (2005) with AE analysis. The focus of the study was the material behaviour of concrete under static load until failure [8].

At the THM (Germany), Koob et al. (2015) are developing an innovative hybrid framework with low material input in an ongoing research project [9]. The hybrid framework will serve as a supporting structure for the construction of wind turbines. Due to the rotation of the rotor blades, the building materials are exposed to high dynamic loads, whereby the fatigue limit of the used materials can be achieved. In this intention anchored concrete dowels are examined under dynamic tensile stress. The specimen is inspected for stress, marginal forces, cracking and fatigue behaviour. The damage to the transition zone between concrete and reinforcing bars is preceded by the formation of microcracks in the concrete matrix. AE is based on the appearance that elastic waves are emitted during deformation or cracking in a material. These elastic waves can be detected with sensitive AE sensors. The aim of the AE measurements is to directly measure microcracking and to locate the AE events. With the location of the cracks the progress of damage during dynamic loading is analysed. Changes in the velocity of the elastic waves are measured using transmission measurements with ultrasonic signals. These can also indicate cracking.

2 Testing programme

2.1 Description of the experimental specimen

With the help of pull-out experiments, a concrete dowel anchorage should be checked under dynamic conditions. Koob and Minnert (2018) investigated the pull-out resistance, the slip development and the failure mechanism of the dowel anchorage [10]. In the plate-shaped specimen of reinforced concrete with the dimension 146 cm · 45 cm · 16 cm a 61 cm long and 26 cm wide steel anchor with a thickness of 20 mm were embedded into the specimen. Figure 1 shows a front view (left) and a side view (right) of the specimen with the location of the embedded steel anchor with a clothoid-shaped form and the reinforcing bars. The arrows indicate the direction of the tensile load.

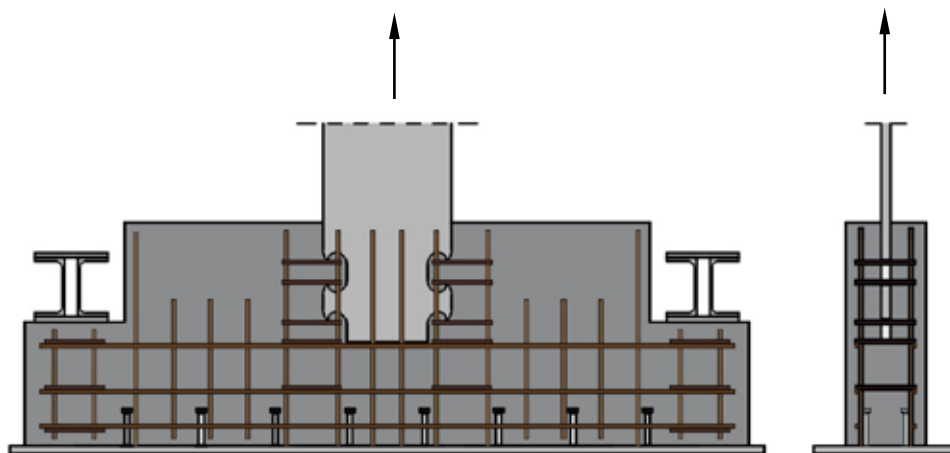


Fig. 1: Front view (left) and side view (right) of the specimen of reinforced concrete with position of the embedded steel anchor with a clothoid-shaped form and the vertical and horizontal reinforcing bars. The arrows indicate the direction of the tensile load.

The entire specimen mounted on a solid steel plate for attachment to the lower punch of the testing machine. To initiate the tensile force of the testing machine the concrete dowel protruded about 41 cm out of the specimen. In the concreted part of the concrete dowel recesses are cut out in clothoid-shape (Fig. 1). By encasing in concrete, the concrete hardens in the recesses and it forms a positive anchoring of the dowel in the concrete. In order to increase the bearing strength, additional reinforcing bars are laid through the recesses.

2.2 Experimental setup for AE measurement

In a previous research project, broadband AE sensors with a measurement frequency of up to 200 kHz were developed for the detection of microcracks especially for concrete. For the three-dimensional location of the AE sources, 16 of these AE sensors were attached to the surface of the plate-shaped specimen. The bottom of the sample was inaccessible because the steel plate for attaching the specimen was fixed of the testing machine. The arrangement of the AE sensors can be seen in Figure 2 (left).

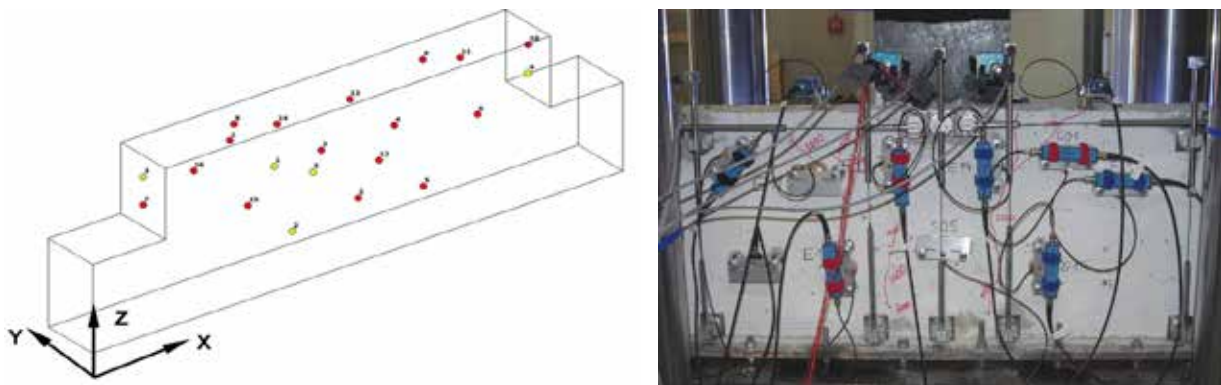


Fig. 2: Left: Perspective view of the contour of the specimen with the position of the AE sensors (red dots) and ultrasonic transmitters (yellow dots). Right: Installation situation of the specimen with the AE sensors and preamplifiers (blue boxes) and displacement sensors in vertical and axial direction.

Six AE sensors (red dots) were placed on the front side and back side, two sensors were placed on the top and one sensor on the left and right side of the sample. With the additional ultrasonic transmitters (yellow dots) ultrasonic measurements could be made in longitudinally and transversely direction at three points of the specimen. The sensors were mounted to the test specimen with screws. The couplant between the sensors and the surface of the specimen was a high-strength vacuum grease to improve the acoustic conductivity. A 16-channel system was used for AE and transmission measurement (manufacturer: GMuG). The measuring system digitized the signals in a very high frequency with a sampling frequency of 10 MHz and an amplitude resolution of 16 bit. The signals were pre-amplified by 40 dB (factor 100) and bandpass filtered. The lower and upper cut-off frequency of the bandpass was set to 20 kHz and 200 kHz, respectively. The transmission measurements were repeated at the beginning of the test and during stopping phase of the testing machine to measure the wave velocities used for AE location. During a single transmission measurement eight signals of different shape were transmitted serially through the specimen to the receiver. There were used a wide band signal (step function) with rise time of 1 μ s and seven signals with centre frequencies between 20 and 200 kHz. In order to improve the signal quality up to 256 stacking (i.e. repetitions with summation) were performed for each

measurement. A servo-hydraulic testing machine was used for the test, which was designed for tensile and compressive forces of up to 2,000 kN and dynamic load up to $\pm 1,600$ kN.

2.3 Experimental procedure

The load of the specimen was applied in three phases. After a static preload phase of 80 kN, the dynamic testing of the specimen was force-controlled carried out. Figure 3 shows the time course of the tensile load (black continues line) and the vertical displacement of the testing machine (red continues line). The cyclic load history at 8 Hz is shown in the inset in the upper left corner of Figure 3. During a periodic load cycle the applied load oscillates with ± 36 kN with a mean tensile force of 44 kN. Thus, the upper and lower tensile force is 80 kN and 8 kN, respectively. A total of 10 stress cycles were performed with 10,000 cycles each. After 100,000 load cycles, a residual carrying capacity of about 161 kN was measured. Furthermore, it can be seen that during the dynamic load the displacement of the testing machine remains nearly constant at approximately 1 mm. At the ultimate load, the displacement is about 3.0 mm and increases up to 30 mm until failure.

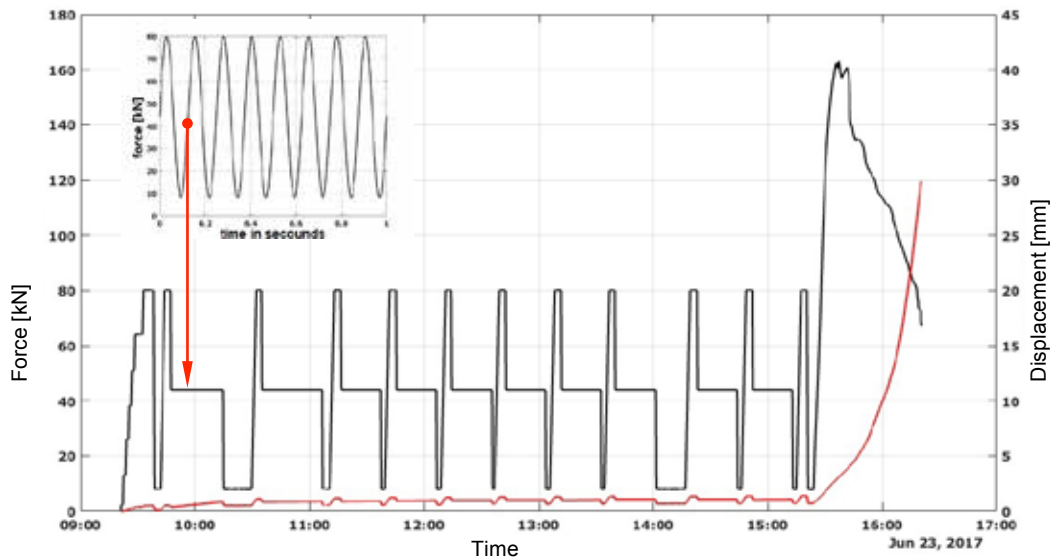


Fig. 3: Load (black continues line) and displacement behavior (red continues line) versus time. Upper left: Reduced representation of the dynamic tensile load with oscillation frequency of 8 Hz with a mean tensile force of 44 kN.

3 Results of AE measurement

The main part of the evaluation was the three-dimensional location of the AE sources for the analysis of the spatial distribution of the cracks in the specimen. For this purpose, an automatic location programme was used. The location method uses clear discernible onsets of L and T waves. A location is valid if the location error is below 5 cm and more than five L- and T-waves onsets are used for location. The location error is calculated using the travel-time residuals of the L and T waves. We assume that the real location error is two times greater. An event was rejected when these conditions are not fulfilled.

The waveforms for an event with 16 channels are shown in Figure 4. At the end of the signal trace the maximum of the amplitude is given in volts. The automatically determined L- and T-waves onsets used for location are marked above the signal by a vertical line. Dashed lines

below the signals mark the calculated arrival times of the L and T waves. The considered event was located using 10 and 2 L-waves and T-waves onsets, respectively. The measured L-wave velocity is 3.6 mm/ μ s and T-wave velocity is 2.1 mm/ μ s, which were used for location. The occurrence origin of the considered event is approximately in the middle of the front of the sample with coordinates $x = 61.1$ cm, $y = 2.8$ cm, and $z = 24.6$ cm. The calculated location error is about 2.7 cm. The good agreement between the measured and calculated onsets leads to the expectation that the real location error is in the range of the calculated error.

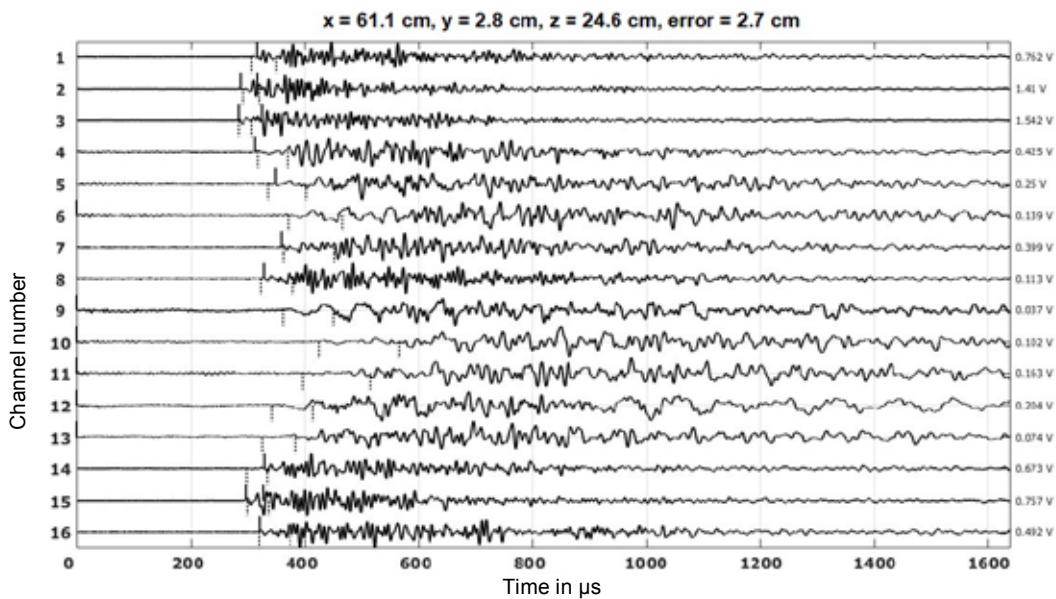


Fig. 4: Event originating from the middle of the front of specimen. The picked and calculated first (L wave) and second (T wave) arrivals are marked by vertical ticks above and below the signal traces, respectively.

Figure 5 shows the cumulated AE events versus time (red continues line) together with the tensile force of the testing machine (black continues line).

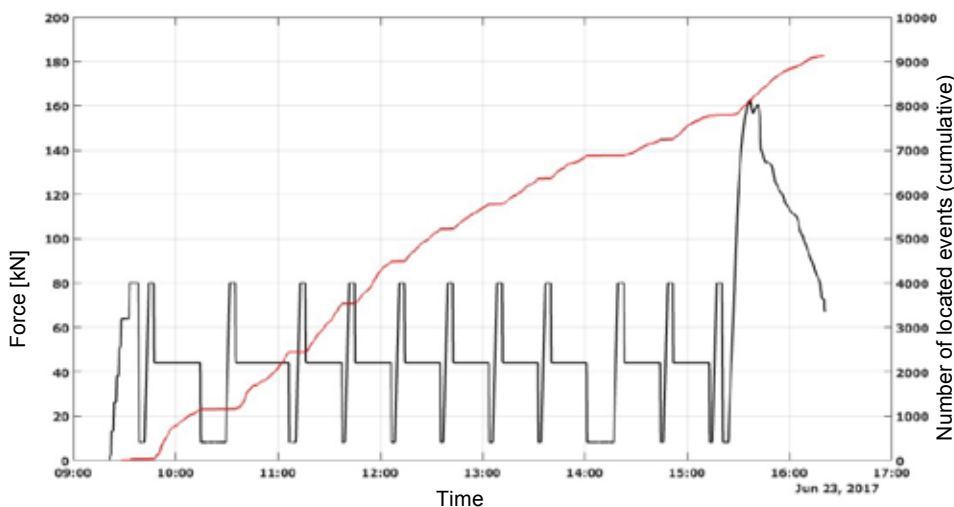


Fig. 5: Temporal course of cumulative number of localisations (red continues curve) and tensile force (black continues curve) during the test.

The AE activity starts immediately with the dynamic load and increases steadily during the test. At approximately 12:30 the number of AE events decreases slightly, which is certainly due to the fact that the damage to the sample has increased and open gaping cracks hinder the propagation of AE signals. However, a slight increase of the number of the AE events can be seen at the end of the test, when reaching the residual load capacity. Figure 6 shows all located events in a lateral view in projection onto the x-z-coordinate plane.

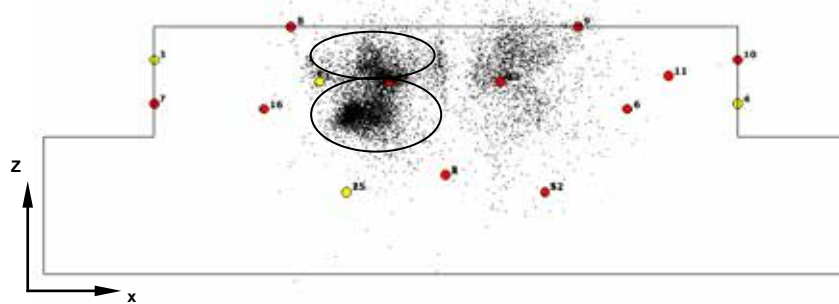


Fig. 6: Location of the 9,132 AE events in lateral view on the x-z coordinate plane.

A total of 9,132 events could be located over the test period of approximately 7 hours. Figure 6 shows that the events are preferentially distributed in some accumulations of event at the edge of the embedded concrete dowel. It is noticeable that about 6,700 events are distributed in two accumulations on the left edge (ovals in Fig. 6).

Figure 7 displays an enlarged part of the specimen together with the contour of the concrete dowel. This figure illustrates that the above-mentioned accumulations of events are clustered in zones, where the clothoid-shaped recesses of the concrete dowel influence the stress state.

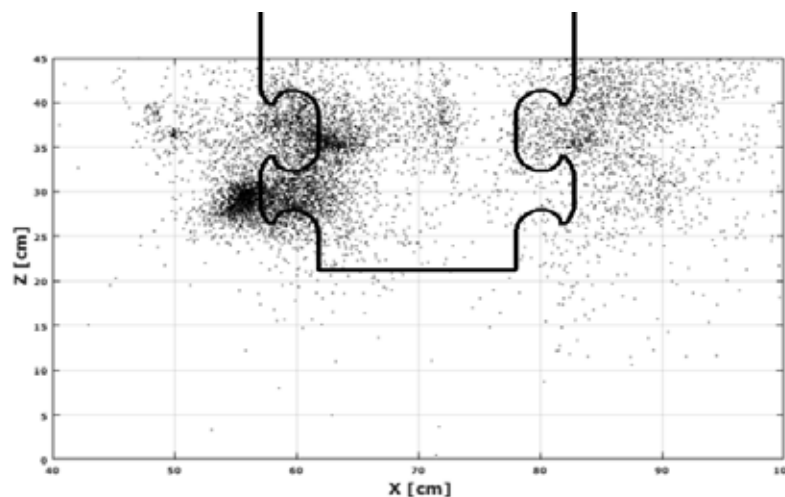


Fig. 7: Position of the located events in a projection onto the x-z-plane together with the contour of the concrete dowel in an enlarged view.

For further verification of the AE results, the located AE events were compared with the result of a non-linear finite-element calculation of the anchorage in the concrete. The remaining tensile strength of the concrete after the dynamic load is shown in Figure 8. The tensile strength is displayed in projection onto a vertical cross section in the middle of the concrete dowel anchorage in a perspective view. In this figure the red colour is indicating

areas of undisturbed concrete, whereas in the blue collared areas the bearing capacity of the concrete are significantly decreased. That means in this zones the concrete structure is damaged and no tensile force can be transmitted. In comparison with the results of the AE measurements the main part of the AE events occurred in the high damage, where the bearing capacity is very low (blue areas in Fig. 8). According to the results of the AE location, the damaged zone continues below the clothoid recess, approximately to the lower end of the concrete dowel.

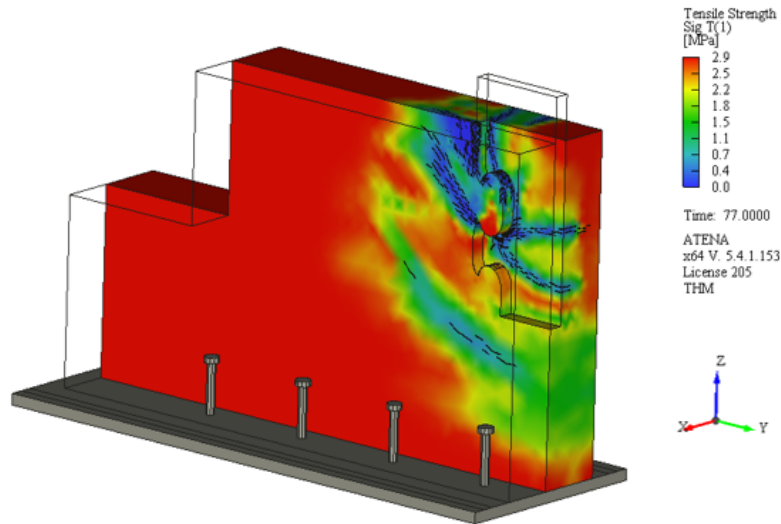


Fig. 8: Non-linear finite-element calculations of the tensile strength in projection onto a vertical cross section in the middle of the concrete dowel anchorage in a perspective view.

4 Conclusions

This work demonstrates, that AE is a non-destructive method for localisation of fracture processes in loaded concrete structures. During the execution of a cyclic pull-out test, the crack formation in the reinforced concrete specimen could be detected by AE measurement. The main task of this work was the location of cracks within the specimen. Because of the limited location accuracy of the AE sources, there is no direct proof that cracking indicated by AE occurs on planer microscopic cracks. The AE activity starts early in the loading immediately after beginning of the dynamic load. In the later stages of the test microcracking occurred in the vicinity of the concrete dowel. In these highly damaged zones, the ultimate failure occurs. In our experiment it was not possible to follow this development by AE source location because microscopic open tensile cracks lead to a high attenuation of wave propagation.

The aim of further investigations is to optimise the evaluation procedure and thus extend the AE analysis to the application for existing structures with high dynamic loads such as bridges or wind turbines.

Acknowledgment

The described research project in this paper is currently in development by the THM (University of Applied Sciences, Giessen, Germany) together with the precast company Oberhessisches Spannbetonwerk (Nidda, Germany). This project (FKZ / project-no. 13FH012IX4) is sponsored by the Federal Ministry of Education and Research, Germany.

References

- [1] Rüschi, H., Physikalische Fragen der Betonprüfung, Zement-Kalk-Gips, Vol. 12, No. 1, Bauverlag GmbH, Wiesbaden, 1959, pp. 1-9.
- [2] Kaiser, J., Untersuchungen über das Auftreten von Geräuschen bei Zugversuchen, Dissertation at the TU München, 1950, Germany
- [3] Drouillard, T.F., AE Literature – Concrete, JAE, Vol. 5, No. 2, 1986, pp. 103-109.
- [4] Manthei, G., Anwendung der Schallemissionsanalyse im Bauwesen, in: Minnert, J. (Hrsg.), 13. Giessener Bauforum, Shaker Verlag Aachen, 2016, pp. 19-38.
- [5] Finck, F., Untersuchung von Bruchprozessen in Beton mit Hilfe der Schallemissionsanalyse, Dissertation at the University of Stuttgart, 2005, Germany
- [6] Schechinger, B., Schallemissionsanalyse zur Überwachung der Schädigung von Stahlbeton, Dissertation at ETH Zurich, 2005, Switzerland.
- [7] Shiotani, T., Luo, X., Haya, H., Damage Diagnosis of Railway Concrete Structures by Means of One-Dimensional AE Sources, JAE, Vol. 24, 2006, pp. 205-214
- [8] Grosse, C., Ohtsu, M., Acoustic Emission Testing, Springer-Verlag Berlin Heidelberg, 2008.
- [9] Koob, M., Wolff, D., Minnert, J., Innovative Hybrid-Tower for Onshore Wind Energy Plants, CPI - Concrete Plant International, Edition 1/2015, pp 152-156.
- [10] Koob, M., Minnert, J., Untersuchungen einer Betondübelverankerung unter dynamischen Einwirkungen für den Einsatz bei Windenergieanlagen, Proceedings 21. DAST-Kolloquium, Kaiserslautern, Germany, 2018, pp 146-151.

77 - Test of bending reinforced concrete structures by means of Acoustic Emission method

Bardakov V.V.^{1,2}, Sagaidak A.I.³, Elizarov S.V.¹, Barat V.A.^{1,2}

¹ INTERUNIS-IT LLC, Moscow, Russian Federation, 111024, Shosse Entuziastov str., 20B

² National Research University Moscow Power Engineering Institute, Moscow, Russian Federation, 111250, Krasnokazarmennaya str., 14

³ JSC SIC Construction, Moscow, Russian Federation, 109428, 2nd Institute's str., 6

Abstract:

The paper presents the results of the conducted experimental studies on three-point bend testing of reinforced concrete beams with incremental cyclic load, up to destruction, using the acoustic emission method. Special attention is paid to the investigation of the relationship between destructive processes occurring during the testing of reinforced concrete beams and the evolution of acoustic emission data registered during the test. The analysis described in the article makes it possible, on the basis of acoustic emission data, recorded during the tests, to distinguish the stages corresponding to the different engineering status of reinforced concrete structures.

1. Introduction

Reliability and security of existing infrastructure facilities (bridges, stadiums, tunnels, etc.) has recently received more and more attention. This kind of objects is required to have increased security, as their destruction threatens human lives and significant financial damage. One of the key structural elements in these structures is reinforced concrete (RC) elements, which in general are subject to bending loads. RC is an indispensable material in modern construction due to its high strength, which is ensured by the joint work of concrete and reinforcement. At the same time, RC like any other material subjected to an external load needs examination of its integrity and engineering status.

Traditionally, the engineering status of reinforced concrete structures is estimated on the basis of periodic diagnostic results. As a rule, periodic testing of such objects is based on visual inspection, which allows fixing large size surface defects and deviations. To detect internal defects, the most widespread for periodic testing get ultrasonic method implemented, as a rule, for most critical parts of constructions by means of tomography. In addition, in some cases, periodic testing of RC elements is limited to measuring the strength of individual sections of construction by mechanical or ultrasonic methods of Non-Destructive Testing (NDT).

However, periodic testing does not allow detecting of sudden changes in the state of construction between inspections, is extremely time-consuming, and also has low reliability

[1]. In this regard, the actual task is to perform monitoring of such objects. Acoustic emission (AE) method is a promising one, which has proved itself for monitoring of the oil and gas industry objects due to its remoteness and high sensitivity.

AE testing is a method of NDT, it is based on the phenomenon of stress waves generation caused by sudden stress redistribution in the material structure. Traditionally, AE testing is carried out for metal objects. However, the development of AE method for concrete testing is gaining increasing popularity. AE testing of concrete is more difficult and less studied compared with metals. It is associated with complex structure of RC. The typical AE source in metal is a growing crack. In RC, due to its complex and heterogeneous structure, which consists of brittle concrete and plastic steel reinforcement, AE sources are more diverse. So, in addition to the crack formation as AE sources can be debonding and slipping between concrete and reinforcement and also reinforcement and cement stone deformation.

There are works in which authors proposed criteria that allow evaluate integrity and damage degree of RC structures based on criteria parameters determined on the basis of AE data recorded during the testing of RC beams [2-6].

The main purpose of this paper is identification of correlation between AE data recorded during destruction of RC beams and physical processes which characterized deferent structural state of construction. Determining of this correlation, in prospect, will allow estimate the damage degree of RC structural elements.

2. The destruction stages of RC beams in the bending test

Concrete is a brittle material with high compressive and low tensile strength. Low tensile strength of concrete doesn't allow its single using in critical building structures. This disadvantage is compensated by addition of steel reinforcement in concrete, which has a high plasticity. Using of two materials with different physical and mechanical properties make it possible compensate disadvantages which materials have individually. Therefore, an important aspect of RC structures reliability is to test joint operation of reinforcement with concrete during their deformation.

In accordance with modern views, when RC beams are tested with a consistently increasing load, up to destruction, three characteristic stages of their stress-strain state can be distinguished [7], each of which is characterized by different engineering status of the RC beam.

Stage I. Before the appearance of cracks in the concrete of the tension zone. At low loads on RC, the stress in concrete and reinforcement is small, the concrete deformations are mostly elastic. The stress in concrete is less than the tension strength and tensile forces are perceived by concrete and reinforcement together. With increasing load on the concrete of the tension zone, inelastic deformations begin to develop, stresses in concrete approach the tensile strength limit. This characterizes the end of stage I. With further increase in load, cracks are formed in the concrete of the tension zone. There comes a new qualitative state - stage II.

Stage II. The stage of permissible operation of RC. In that place of the tension zone where cracks were formed, the tensile force is perceived by the reinforcement and the concrete section above the crack. In the areas between the cracks, the adhesion of the reinforcement

to the concrete is not completely disturbed, and the concrete continues to work on stretching. With further increase in load, the fracture gap continues to grow, shortening the area of the concrete that is still stretching, the stress in the reinforcement and in the concrete of the compressed zone increases. The end of this stage is characterized by the onset of noticeable inelastic deformations in the reinforcement.

Stage III. Stage of destruction. If the load continues to increase, the stresses in the reinforcement reach a physical (conventional) point of yielding, the stresses in the concrete of the compressed zone reach the value of the compression break down point. The structure is destroyed.

The destruction of reinforced concrete beams during bending can occur according to two different schemes:

- For RC elements with a normal content of tension reinforcement, the fracture begins with the reinforcement of the tension zone and ends with the crushing of concrete in the compressed zone. Such destruction is plastic.
- For RC elements with excess content of tension reinforcement, the destruction occurs over the concrete of the compressed zone and is always brittle in the case of incomplete use of tension reinforcement. The transition from stage II to stage III occurs suddenly.

3. Description of experimental studies

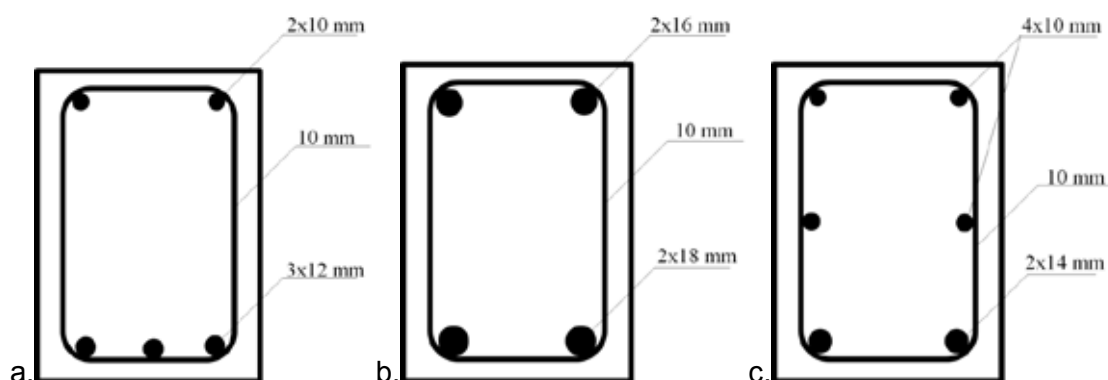
3.1. Experimental samples

The experimental samples of RC beams were made from concrete of 2 classes of compressive strength: M60 and M90. In total, 3 reinforced concrete beams were made from heavy concrete. Compositions of concrete for experimental samples are presented in Table 1.

Table 1. Compositions of concrete for experimental samples

№	Concrete grade	Cement, kg	Sand, kg	Crushed stone, kg	Water, l
1	M90	470	720	970	160
2	M60	350	840	970	170
3	M90	470	720	970	155

RC beams were reinforced with cages of various configurations (Fig. 1). Steel rods A500C of various diameters were used as reinforcement.



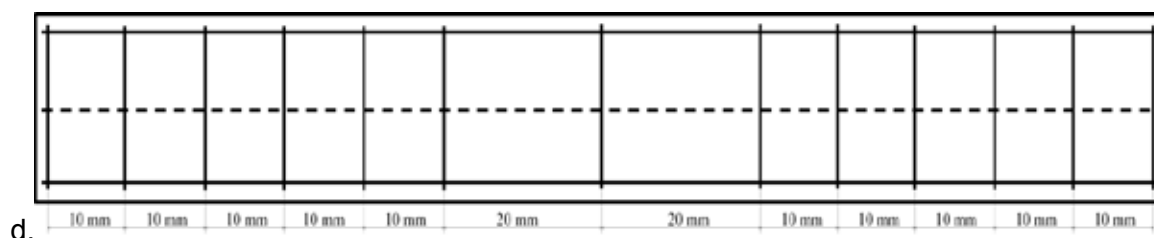


Fig. 1 – Reinforcement cages cross-section view (a) type1, (b) type 2, (c) type 3, (d) end

All the beams were overreinforced, as a result the destruction had a fragile character.

Weld plates (150x200 mm) were placed on the undersides of each frame, which were used as supports during testing. Concreting was carried out in metal molds with dimensions of 1500x200x150 mm, in which the reinforcing cage was pre-installed.

During the concreting, in addition to the beams, witness samples were prepared in the amount of 10 pcs. from compositions completely analogous to those used for beams. These samples were hardened under conditions similar to beams in plastic molds of 100x100x100 mm size, and were used to perform strength measurements under the press.

Generalized data on the beams participating in the experiments are presented in Table 2.

Table 2. Generalized data on the beams

No	Designation	Cage type	Compression strength, MPa	Beam load to failure, kgf
1	M90	2	101.3	10000
2	M60	3	80.3	13500
3	M90(2)	1	94.3	10500

At the expiration of the 28 days hardening period, the RC beam was tested for a three-point bending with incremental cyclic load, up to destruction.

3.2. Test Equipment

INSTRON 8802 system was used as a loading machine. The load was applied to the central part of the beam from one side. Felt pad was used to reduce the effect of the friction between loading device and the concrete surface. On the other side the beam was fixed by two supports, one of which was movable and the other was fixed (Fig. 2).



Fig. 2 – RC beam testing

The loading scheme was incremental cyclic load and consisted of the next stages - load, load exposure, unloading, and no-load exposure. The loading was carried out to the same value of the load for two cycles (), after which the load value was increased. Then the process was repeated until the sample was destroyed. As an example, Fig. 3 shows the loading scheme for RC beam M90(2). Loading schemes for other beams were similar and differed only in value of the destructive load. In addition to the load, the system also was recording the displacement of cross-beam.

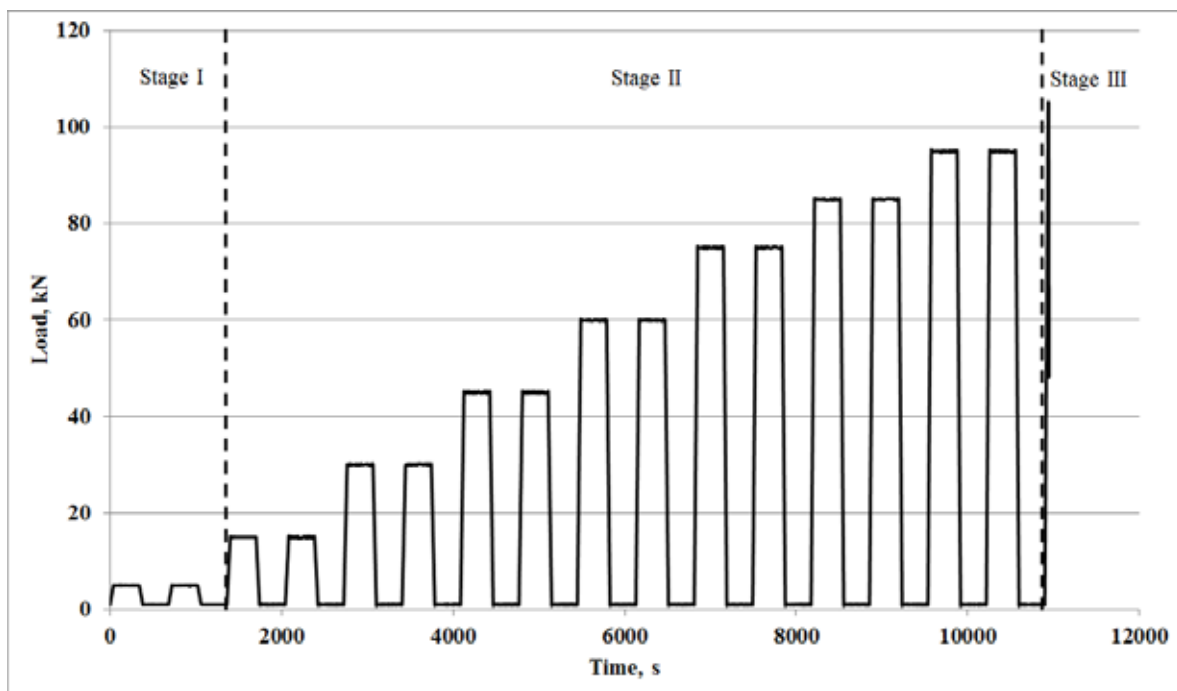


Fig. 3 – Loading scheme for RC beam M90(2)

As a fixed parameter of loading, the duration of each stage - loading / unloading and loading / unloading exposure - was the same. The duration of the loading / unloading intervals was 40 seconds, and the load / no-load exposure interval was 300 seconds. At the end of each stage of loading, cracks were observed on the surface of the beam, and the value of their opening was also recorded. The three-point bending tests were accomplished by AE control.

3.3. Data acquisition system

A-Line 32D DDM system with 10 channels was used as a data acquisition system. Band DIS 30-300 transducers with frequency band of 30-300 kHz were used as the acoustic emission sensors. Sensors were installed on the surface of a concrete sample through a contact fluid layer. Sensor fastening was carried out by means of magnetic holders, which were previously glued to the surface of the concrete sample with by epoxy glue. The arrangement of AE sensors is shown in Fig. 4.

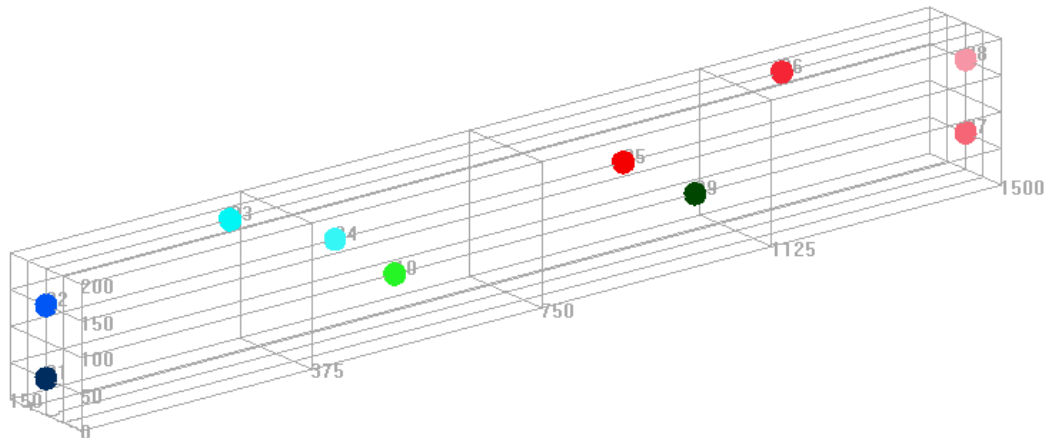


Fig. 4 – The arrangement of the sensors

The selected arrangement of the sensor made it possible to determine the location of AE sources using linear and 3D location algorithms.

4. AE data analysis

The AE method has a high sensitivity and allows detecting of destructive processes occurring in a material subjected to external loading on the basis of an estimation of AE parameters evolution. Fig. 5 depicts the cumulative hits for most active channel and the load for the RC beam M90(2) as functions of time.

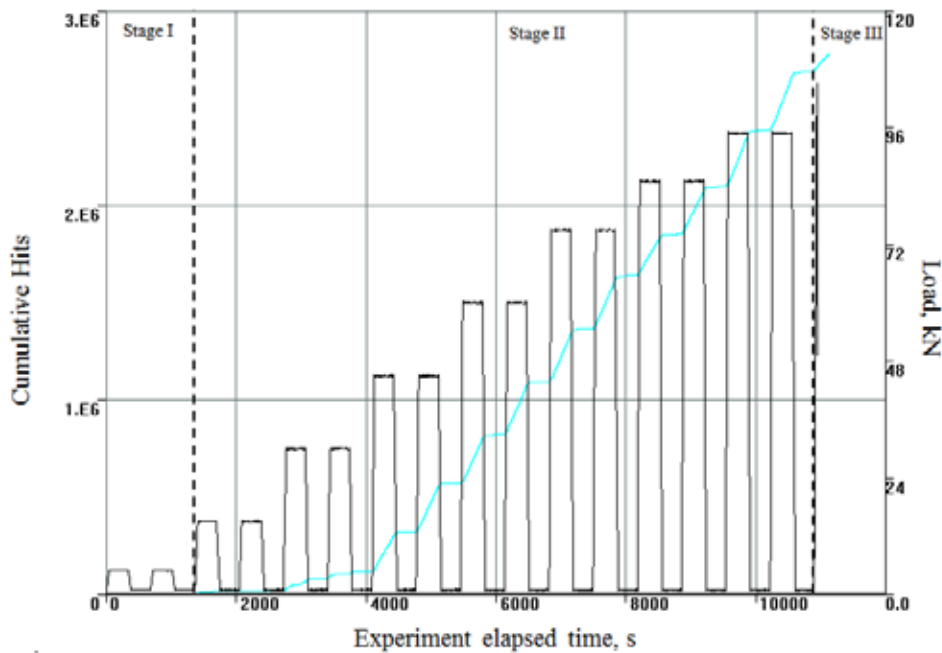


Fig. 5 – Cumulative hits and the load for the RC beam M90(2)

This dependence characterizes the process of damage accumulation in the RC beam with time. Based on the change in the AE parameters, it is possible to distinguish the stages characterizing the structural state of the facility, including the 3 stages of the stress-strain state described above. Let's consider each of the stages in more detail. Stage I, as already mentioned corresponds to low loads. AE activity at this stage is also not high (Fig. 6a) and does not exceed tens of hits per second.

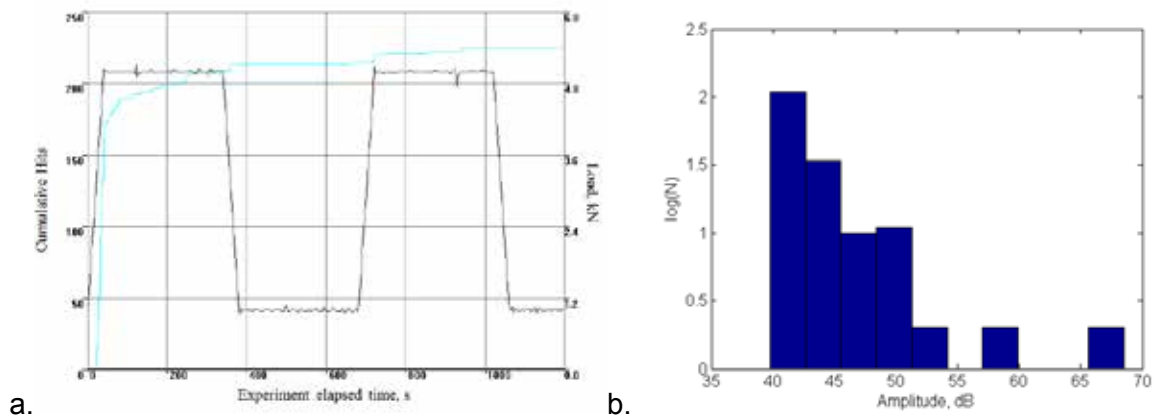


Fig. 6 – (a) Cumulative hits and the load for the RC beam, (b) Amplitude distribution for loading less than 5 kN (first loading step)

AE activity occurs at this stage mainly due to the presence of primary concentrators of internal stresses arising from the physical and chemical processes of cement stone hardening. Cumulative hits on the load is linear, jumpy in nature, the amplitudes of the detected signals are low, which is confirmed by the amplitude distribution data (Fig. 6b). At

the end of the first stage, there are no visible cracks on the surface of the beam. The appearance of the first visible cracks coincides with the beginning of stage II.

Stage II, in its turn, can be divided into 2 sub-stages (stage IIa and stage IIb), each of which corresponds to different levels of engineering status of the RC beam. Stage IIa occurs simultaneously with the moment of occurrence of the first cracks. Formation of the first cracks occurs in the tension zone (Fig. 7), and their position can be localized using a linear location algorithm even before they are visible visually.

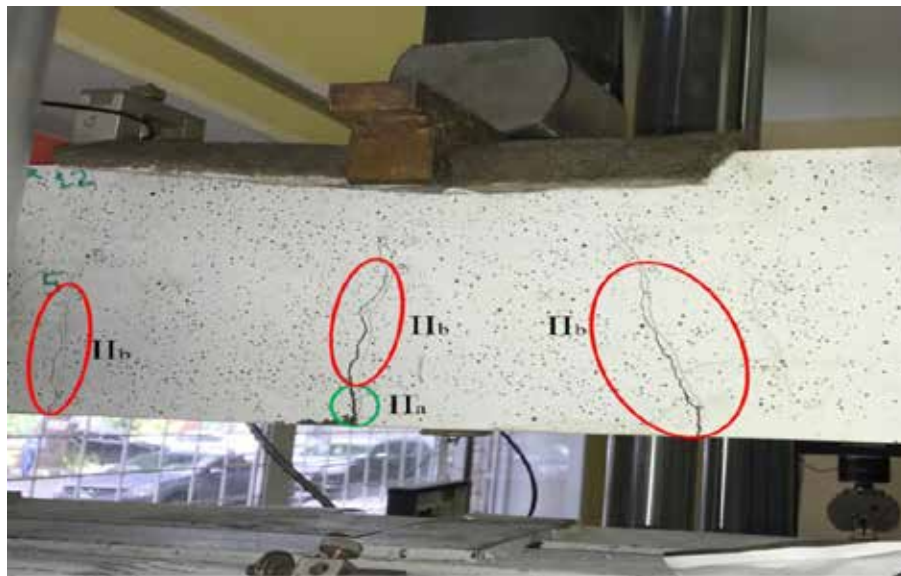


Fig. 7 – The central area of the RC beam M90(2) under the bending test

The beginning of the crack formation is accompanied by a sudden increase in AE activity (Fig. 8a).

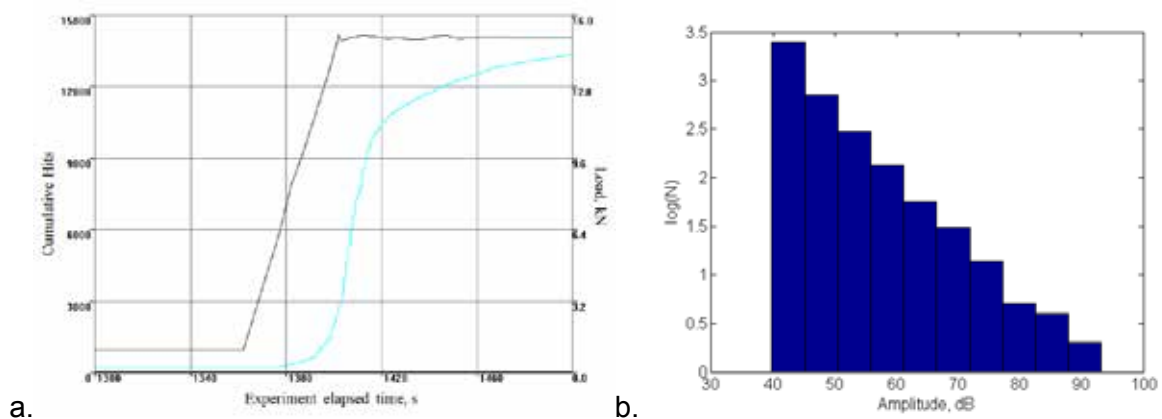


Fig. 8 – (a) Cumulative hits and the load for the RC beam, (b) Amplitude distribution for loading to 15 kN (first loading cycle of the second loading step)

The time dependence of the cumulative hits has a nonlinear (power-law) nature for a linearly varying load. This kind of dependence for metals characterizes them as defective [8]. Obviously, this statement is also true for complex structural materials, such as reinforced

concrete. In addition to AE activity increasing, the amplitudes of the detected signals also increase (Fig. 8b). However, the number of low-amplitude signals is still dominant.

At this stage, there is also a sudden increase in AE activity on exposure to the load. The onset of AE activity is associated with creep of concrete. The dependence of the cumulative hits has a logarithmic character of time characterizing the gradual attenuation of this process.

Stage IIa will continue until the crack has reached the reinforcement in the concrete. The beginning of stage IIb, conditionally, can be considered as the development of a crack in the tension zone above the reinforcement. From this moment, the joint work of concrete and reinforcement is disrupted, which is reflected in turn on the AE data (Fig. 9a).

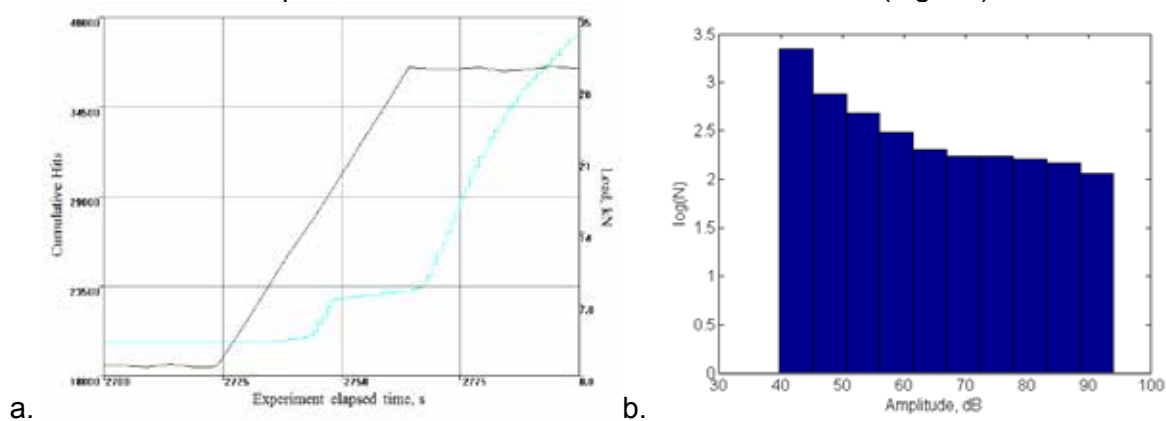


Fig. 9 – (a) Cumulative hits and the load for the RC beam, (b) Amplitude distribution for loading to 30 kN (first loading cycle of the third loading step)

The dependence shown in Fig. 9a can be divided into two sections: non-linear (power-law) dependence and linear dependence. The section of nonlinear dependence corresponds to the state of RC beam, in which the reinforcement has not yet begun to deform separately from the concrete (at the initial stage of stage IIb), or when the values of the previous deformation (under repeated loading) have not been exceeded. The section of linear dependence proposed corresponds to the state of the RC beam, in which the reinforcement begins to deform separately from the concrete. In this case, the slope of the cumulative hits is reduced. The decrease of the slope is associated with an increase in the durations of the recorded AE signals. The main sources of AE at this stage are friction and adhesion failure, as well as the formation of microcracks in the area of contact between concrete and steel reinforcement, which is most active, according to the location data, in the anchoring points of the reinforcement. In this case, high-amplitude AE signals are generated, which significantly change the shape of the amplitude distribution (Fig. 9b), in comparison with the previous stage (Fig. 8b).

At the moment of the inflection of the cumulative hits versus time, a similar inflection can also be observed on the dependence of the beam deflection versus time.

Stage IIb corresponds to the appearance of significant activity at the unloading of the sample, which corresponds to the friction between fractured surfaces, which at the moment are sufficiently large and in the no-load stage, which is associated with stress relaxation. Among other things, it should be noted that the transition from stage IIa to stage IIb approximately coincides with the moment of inclined cracks formation (Fig. 7). With a further

increase in the load, the nature of the dependencies is similar. In this case, the change of the non-linear character to linear, with decreasing slope, approximately corresponds to the moment when the amount of deflection (deformations) reached at the previous cycle is exceeded, during the loading stage (due to creep of the structure).

Dependencies view described above is similar for all RC beams used in experiment (fig. 10).

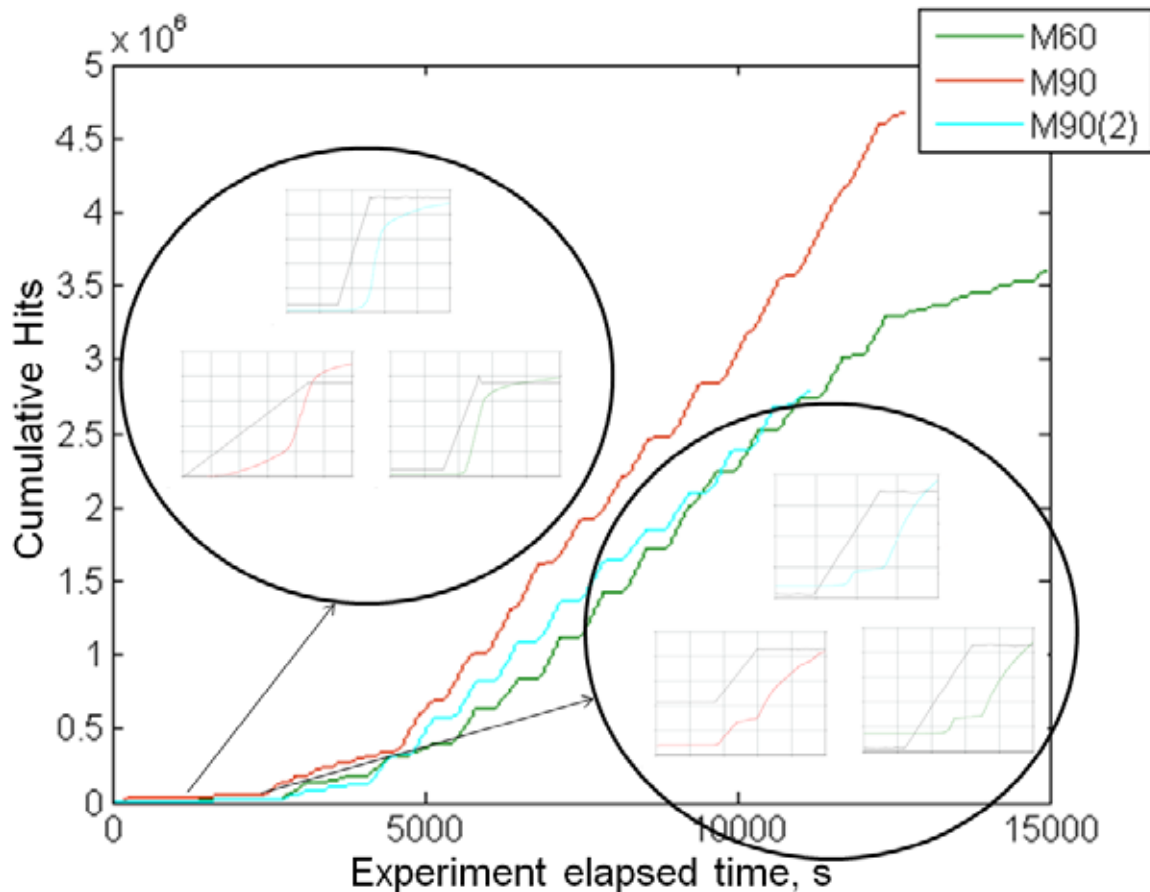


Fig. 10 – Dependences of cumulative hits on time for all RC beams

This kind of dependence of cumulative hits will persist until the collapse of the test specimen, as it in strongly reinforced structures comes suddenly (fragile destruction) and, at the time of destruction, the reinforcement has not yet used its resource. That fact was established previously by other authors [9]. In the case of normally reinforced structures, the destruction process accompanies a nonlinear increase of AE parameters.

5. Comparison of the results with NDIS-2421

Classification of the damage level according to the quantitative criterion NDIS-2421 [4] was carried out for AE data recorded during experiments. That criterion is based on the definition of two parameters:

$$\text{Load ratio} = \frac{\text{load on the onset of activity in the subsequent loading}}{\text{the previous maximum load}}$$

$$\text{Calm ratio} = \frac{\text{the number of cumulative AE activity under unloading}}{\text{total AE activity during the whole cycle}}$$

In our experiments Calm ratio was calculated as the number of cumulative AE activity under unloading divided into the number of cumulative AE activity under loading, to exclude AE activity on the load/no-load exposure intervals.

The use of these parameters makes it possible to classify damage levels into minor, intermediate and heavy for each loading cycle (Fig. 11a). An example of applying of this criterion for M90(2) beam is represented in Fig. 11b.

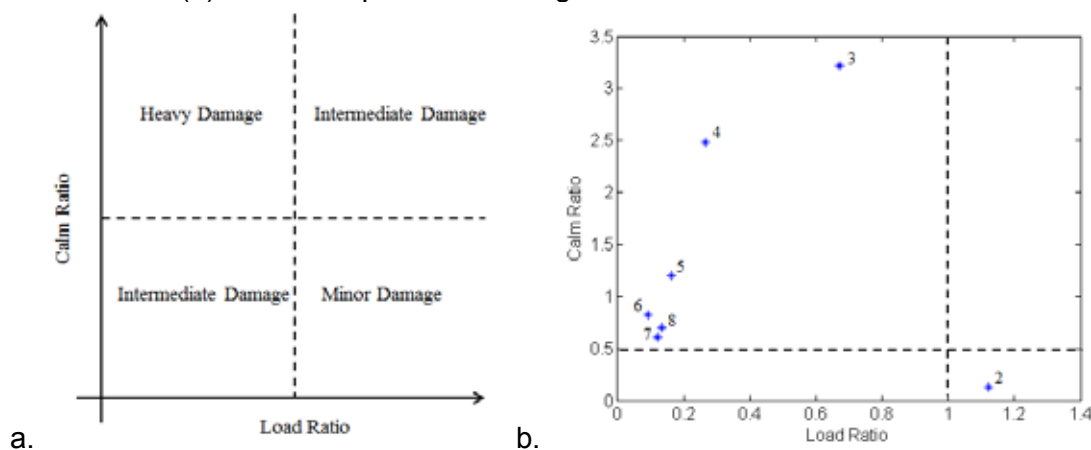


Fig. 11 – Classification of the damage levels (a) theory, (b) results

The number near the point in Fig.11b represents the number of loading step for the first of two loading cycles (Fig. 3) for the most active channel. The classification levels were determined as 0.5 for calm ratio (based on the beam deflections experiment results) and as 1 for load ratio (based on Kaiser effect).

According to the obtained diagram, damages are classified as heavy beginning with third loading step. This result corresponds to loading step for which joint operation between concrete and reinforcement was disturbed, and also corresponds to the transition from Stage IIa to Stage 2b. That moment was noted earlier based on the change of AE data (Fig. 9).

6. Conclusion

The investigation of RC beams destruction by three-point bending with AE data acquisition was carried out. The features of AE data which characterized different stages of stress-strain behavior were selected. Selected features can be used to develop criteria for destruction state estimation of RC beams.

7. Acknowledgements

These results are obtained during the execution of the State Assignment of the Ministry of Education and Science of the Russian Federation in the field of scientific activity (Project Code 11.9879.2017/8.9)

References:

- [1] V.V. Bardakov, V.A. Barat, D.A. Terentyev, D.V. Chernov, K.O. Osipov, Osobennosti primeneniya metoda akusticheskoy emissii pri monitoringe mostovykh konstrukcij, Testing. Diagnostics. 1(211) (2016) 32-39. (in Russian).
- [2] Recommendation of RILEM TC 212-ACD: acoustic emission and related NDE techniques for crack detection and damage evaluation in concrete. Test method for classification of active cracks in concrete structures by acoustic emission. 29 July 2010.
- [3] Recommendation of RILEM TC 212-ACD: acoustic emission and related NDE techniques for crack detection and damage evaluation in concrete. Test method for damage classification of reinforced concrete beams by acoustic emission. 29 July 2010.
- [4] NDIS 2421, Recommended Practice for In-Situ Monitoring of Concrete Structures by AE. 2000.
- [5] Michael C Forde, Sabrina Colombo et al, Predicting the Ultimate Load Capacity of Concrete Bridge Beams from the «Relaxation Ration» Analysis of AE Signals, Progress in Acoustic Emission XVIII. (2016) 359-364.
- [6] A.I. Sagaidak, S.V. Elizarov, Acoustic emission parameters correlated with fracture and deformation processes of concrete members, CONSTRUCTION AND BUILDING MATERIALS, 21(3) (2007) 477-482, <https://doi.org/10.1016/j.conbuildmat.2006.04.004>.
- [7] V.N. Baikov, Eh.E. Sigalov, Zhelezobetonnie konstrukcii: obshchij kurs, fifth ed., Stroyizdat, Moscow, 1991. (in Russian).
- [8] H.L. Dunegan, D.O. Harris, Acoustic Emission – A new Non-destructive Testing Tool, Ultrasonic. 7 (1969) 160-166.
- [9] C.U. Grosse, M. Ohtsu, Acoustic Emission Testing, Springer, Berlin, 2008.

81 - Assessment of infrastructures by rainy induced AE tomography with wave velocity and attenuation rate

Tomoki Shiotani¹, Katsufumi Hashimoto¹, Nobuhiro Okude¹, Kazuo Watabe^{2,3}
and Hidefumi Takamine^{2,3}

¹ Dept. Civil & Earth Resources Engineering, Kyoto University

² Toshiba Corporation Corporate Research and Development Center

³ NMEMS Technology Research Organization

Abstract:

As damage evaluation of infrastructures to establish an efficient non-destructive testing (NDT) is highly demanded, an acoustic emission (AE) tomography technique has been developed. It is very important nowadays to establish economic and appropriate management systems for ageing concrete infrastructures, in order to guarantee the performance and safety with identifying severe deterioration through their service life. The AE tomography estimates wave velocity distribution, which is supposed to be decreased as the damage progresses, inside the reinforced concrete. The AE tomography combines an iterative AE source location algorithm with travel-time tomography to produce a 3D visualization of the elastic wave velocity. However, since the computation for the elastic wave ray-trace algorithm considering all potential detours of elastic waves takes up much time, and in case that only a few AE signals are detected, AE tomography technique does not always work efficiently. In this paper, AE signals induced by rain droplets hit on surface of RC deck are utilized as elastic waves' excitations, and wave velocity and attenuation tomography assuming linear ray paths are performed in conjunction with AE source locations. Accordingly, rain-induced elastic waves lead to thousands of AE events after in-situ measurement for an hour. Consequently, the 3D tomography results show accurate and time-saving analysis, compared to the above-mentioned conventional AE tomography technique, for quantifying the damage in RC deck.

1. Introduction

It is generally recognized that preventive and proactive maintenance works are necessary for such infrastructure as bridges and tunnels to implement rational maintenance programs. For reinforced concrete (RC) members, essential issues include establishing a maintenance system with the appropriate measures prior to extensive damage and failure.

As a result of budgetary restrictions, preventive and proactive maintenance of infrastructure is desired, and inspections by non-destructive testing (NDT) methods must be applied. In terms of damage assessment and estimation of repair and retrofit recovery in concrete structures, in addition to current NDT, innovative methods must be established.

Tomography techniques have been studied based on elastic-wave and acoustic emission (AE) to visualize internal defects in concrete in three dimensions. The applicability of these techniques has already been reported as elastic-wave tomography [1][2] and AE tomography [3][4][5].

Through the tomography technique, internal distributions are obtained using elastic-wave parameters such as amplitudes and elastic-wave velocities. In this study, elastic-wave velocity and attenuation rate are used as the parameters. In elastic-wave tomography, both the location of the excitation and the excitation time should be known, whereas they are unknown for AEs induced by random excitations such as steel ball hammering and rain fall hits. Specifically, tomography can evaluate the elastic-wave velocity and attenuation rate in each set-element over the structure, which is supposed to be theoretically associated with the modulus of elasticity. Because of the presence of such internal defects as cracks and voids, the values would be exhibited as low-velocity and high-attenuation zones.

2. Attenuation rate and wave velocity tomography

2.1 Computation procedure for damage detection

An innovative non-destructive method for inspecting the interior of concrete has been introduced and applied to the RC slab of a bridge in service [6]. The method, referred to as single-side attenuation tomography, which is based on the principle that the elastic waves traveling through concrete are to impinge on the cracks. It could provide the tomogram on the attenuation rates inside the tested specimen. To summarize, single-side attenuation tomography must be understood as a very practical non-destructive testing method for identifying the parts of a reinforced concrete member which are very likely to present serious damage.

Assuming that the propagation path of P-wave is a straight line, the tomography analysis via the attenuation-rate and the wave-velocity distribution was carried out in order to identify the horizontal cracks in RC slab. Fig. 1 shows the flow chart to compute the attenuation-rate and the wave-velocity distribution. The data processing flow is followed so as extracting AE events. As summarized in the figure, first, the source locations of all AE events are used as input, where a constant wave velocity (m/s) and attenuation-rate (dB/m) across the tested member is assumed for calculation. Second, the amplitude and the excitation time at the source of the considered AE event is estimated on the basis of the arrival times and the amplitudes recorded by the sensors. Third, the attenuation rates and wave velocities along all straight ray-paths between the source and the receiving sensors are computed.

2.2 Source location algorithm

The algorithm for AE source location is based on the Inglada's method, which is used in seismic engineering for locating the epicentre of earthquakes. By assuming a constant wave velocity inside the tested specimen, the source location of an AE event is determined from the arrival times of their associated elastic waves at the locations of several sensors. In this paper, 3000 m/sec was set as the constant value in consideration of averaged speed in intact and deteriorated concrete.

2.3 Estimation of travel time and peak amplitude at AE source

For each AE event, the peak amplitude of the elastic wave at the source is unknown. Consequently, it can be approximated to calculate wave velocity and attenuation rate along the considered wave paths. First, the arrival time and the peak amplitude of the signal recorded by each sensor is plotted as a function of the distance between the source and the sensors. Second, a linear regression between the arrival time and the peak amplitude of the elastic

wave and the distance from the source is computed. The AE dispatched time and the peak amplitude at the source is referred to as equal to the value for the case that the distance is equal to zero. As shown in Fig. 2, the linear estimation on assumed logarithmic function for the recorded amplitude, $f(x)$, can be re-calculated for linear function, $F(x)$, in order to estimate the amplitude at AE source ($x=0$).

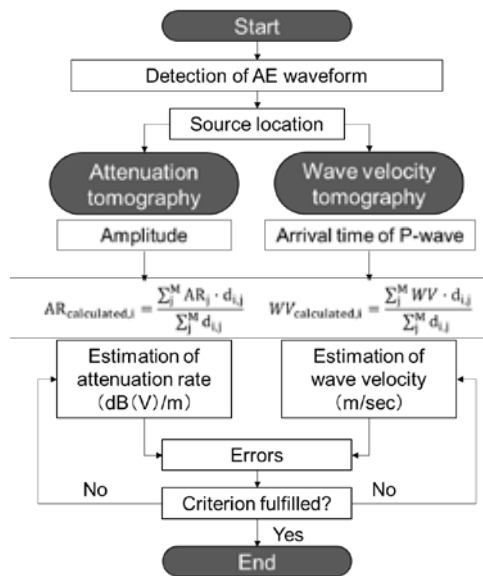


Fig.1 Flow chart to compute wave-velocity and attenuation-rate tomography

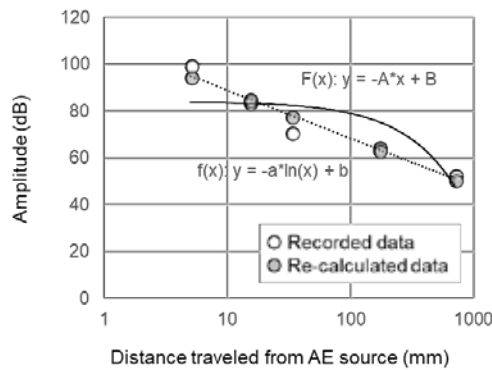


Fig. 2 Linear estimation on travel time amplitude from AE source to sensors

2.4 SIRT algorithm for tomography computation

Tomography computation is carried out based on elastic wave parameters with the velocity and the attenuation rate in this paper. In the tomography based on the attenuation, the area of interest and analysed must be divided into mesh elements characterized by their own wave velocities and attenuation rates. Then, a first estimation on distribution of the wave velocities and the attenuation rates is to be provided as input. By comparing those values along each wave path to its calculated value of the assumed distribution, the SIRT algorithm could lead to proper distribution of the wave velocities and the attenuation rates.

The measured travel time and attenuation rate along each ray path is estimated from eq. (1).

$$AR_{\text{measured},i} = \frac{A_{\text{source}} - A_{\text{sensor},i}}{\sum_j^{N_i} d_{i,j}} \quad (1)$$

Where: $AR_{\text{measured},i}$: measured average attenuation rate along the wave path from the source to the i^{th} sensor, A_{source} : estimated peak amplitude of the elastic wave associated to the considered AE event at its source, $A_{\text{receiver},i}$: peak amplitude of the elastic wave measured at the i^{th} sensor, N_i : mesh number of elements crossed by the wave path from the source to the i^{th} sensor, $d_{i,j}$: length of the wave path from the source to the i^{th} sensor in the j^{th} element

The attenuation rate along each wave path based on distribution of the attenuation rates in the mesh elements is computed by eq. (2).

$$AR_{\text{calculated},i} = \frac{\sum_j^M AR_j \cdot d_{i,j}}{\sum_j^M d_{i,j}} \quad (2)$$

Where: $AR_{\text{calculated},i}$: calculated average attenuation rate along the wave path from the source to the i^{th} sensor (dB/m), AR_j : attenuation rate in the j^{th} element (dB/m), M : mesh number of elements crossed by the ray path from the source to the i^{th} sensor, Afterwards, the difference between the measured and the calculated attenuation rates is calculated for each wave path by using eq. (3).

$$\Delta AR_i = AR_{\text{measured},i} - AR_{\text{estimated},i} \quad (3)$$

In a similar manner to Equation 1, the differences of the attenuation rates on all the wave paths are estimated by eq. (4).

$$\Delta AR_j = \frac{\sum_{i=1}^N \Delta AR_i \cdot d_{i,j}}{\sum_{i=1}^N d_{i,j}} \quad (4)$$

Where N is the number of wave paths crossing the j^{th} element. The attenuation rate in each element is then updated with eq. (5).

$$AR_{j,\text{updated}} = AR_j + \Delta AR_j \quad (5)$$

The procedure from eq. (2) through eq. (5) is repeated until the convergence is reached. As for wave velocity as the parameter of SIRT algorithm, the same manner as attenuation rate is applied for computing wave velocity distribution in the area of interest and analyzed.

3. Rain-induced AE detection at exiting RC bridge deck

A real RC bridge deck was selected as a study target which has deterioration such as rebar corrosion, breaking by salt damage, and deck fatigue. AE measurement was carried out in the RC bridge deck. 15 AE sensors are set on the bottom side of RC bridge decks. Resonant frequency of AE sensor is 30 kHz. AE sensors arrangement on the RC deck is shown as in Fig. 3. Thickness of both RC bridge decks is 235 mm. Large cracks with water leakage trace were confirmed. Threshold value of LUCY (location uncertainty) is set on 300 mm as half spacing of two adjacent sensors in this study. LUCY means source location accuracy and is

the root-mean-square of the difference between calculated and observed distances between the source and the sensor [7].

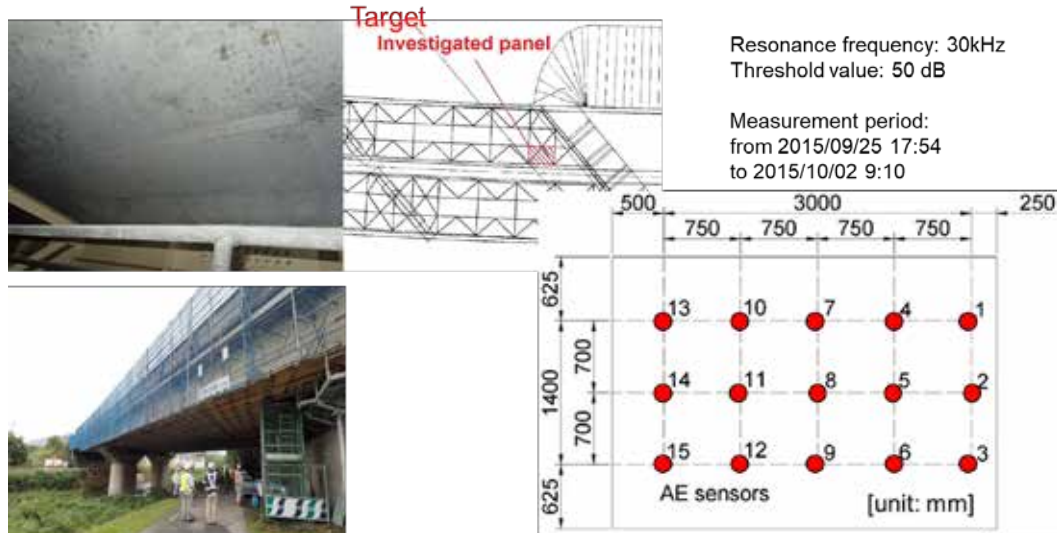


Fig. 3 Sensor arrangements for AE measurement on the real RC bridge decks

AE hits by one hour in the measurement period is shown as in Fig. 4. A lot of AE hits were acquired from 120 to 130 hours. A rain drop is known as factor of AE generation when it hits on a solid material [8]. After the consideration of AE activity in the panel between 120 to 130 hours shown in Fig. 4, AE hits can be regarded as hits induced by rain drops on the surface of RC deck.

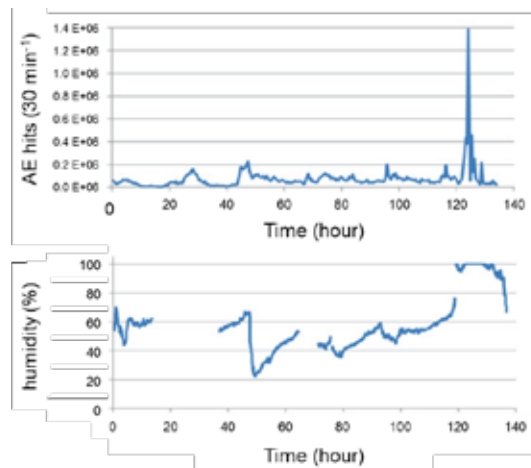


Fig. 4 AE activities and relative humidity during measurement

In Fig. 4, an extremely high AE activity is observed at around time 120 hours. Besides relative humidity at the bridge is also measured and shown in the bottom of Fig. 4 as well. Around 120 hours, the humidity also rises to 100%. In the weather record, precipitation and wind was also recorded at that period. Thus, the peak of AE activities is considered to be caused by heavy rainfall. It indicates that the impacts of raindrops on the road surface cause AE activity, and the AE reaches the sensors attached on the bottom of the deck are recorded. Those

concentrated AE activities are not correlated to the traffic load and not emitted from cracks inside the bridge decks. Therefore, those signals are considered not to reflect the deterioration of the deck and should be treated as noise. However, it was found that the rain-induced noise signals could be used to inspect the inside of the bridge decks.

The data was extracted during the rain peak and analyzed the source locations. Fig. 5 shows the AE source result of the measured panel. Source locations considered to have low reliability has been filtered. The extracted data for only 700 seconds indicated enough amounts of AE sources for analysis are identified. In the figures, relatively low-density areas surrounded by dashed lines can be seen in the panel. Red line shows the sensor arrayed area. This low-density area is suspected to be heavily deteriorated as in the following reason.

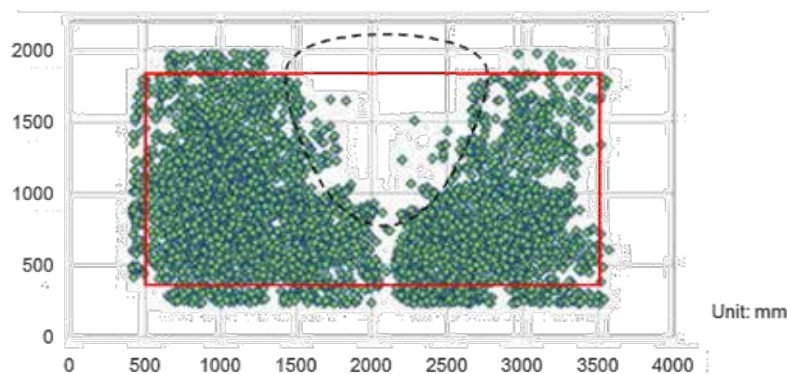


Fig. 5 Result of AE source location analysis

Since raindrops hit all over the road surface uniformly, the AE source locations should also show a uniform distribution in the case of the uniformly sound case. On the other hand, if severe damage like a large horizontal crack is partially existed inside the deck, as depicted in the figure, the AE generated at the road surface is attenuated, diffracted, or blocked by the crack. Consequently, AE sensors right under the crack receive fewer AE or don't receive rain-induced AE activity at all, and the source distribution under the crack would be sparse or vacant.

Therefore, by calculating the AE source locations, the density of the AE sources would reflect the damage condition inside the deck. Since all AE sources generated by raindrops are on the same plane namely the road surface, the 3D source locations can be readily estimated by fixing datum point in the depth direction. Additionally, heavy rain generates large amount of AE hits on the road in a short time so that it is realized that the inspections of serious damage inside the deck could be carried out with great efficiency.

4. Wave velocity and attenuation rate tomography for rain-induced AE activity

In order to guarantee the applicability of the proposed tomography technique it is necessary to quantitatively clarify that the tomography results are simulated with in-situ measurement condition. It is investigated in this paper if a measurement condition performs for an adequate resolution of tomography results, followed by AE measurement.

In the present study, using wave propagation simulation based on visco-elastic wave equation, the result of AE tomography is numerically investigated. A stand-alone computer software

package that generates solutions to practically any ultrasonic (elastic wave propagation) problem with simulating received waveforms, was used for wave propagation analysis to numerically identify the influence of ray path density followed by sensor arrangements (sensor-to-sensor distance) in the area of interest on the accuracy of tomography computation results. The specific acoustic equation that is simulated is given by eq. (6). Fig. 6 shows geometrical information and parametrical information provided into the simulation models in this study.

$$\rho \frac{\partial^2 w}{\partial t^2} = \left[\mu + \eta \frac{\partial}{\partial t} \right] \nabla^2 w + \left[\lambda + \mu + \phi \frac{\partial}{\partial t} + \frac{\eta}{3} \frac{\partial}{\partial t} \right] \nabla(\nabla \cdot w) \quad (6)$$

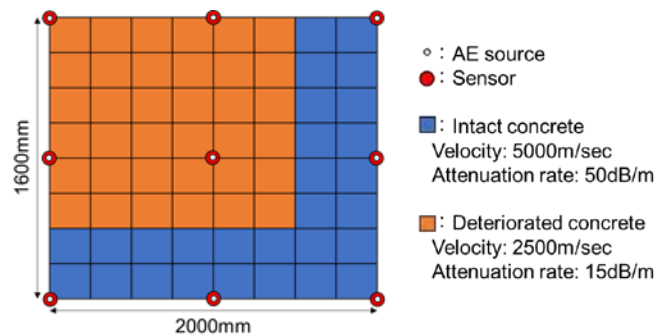


Fig. 6 Geometrical information and parametrical information for wave propagation analysis

The wave velocity and the attenuation rate distribution are shown as in Fig. 7. 2500 m/sec and 15 dB/m are the boundary between the intact and deterioration cases in the numerical results with any sensor distances, threshold value of wave velocity and attenuation rate for identifying the presence of horizontal crack are unknown in terms of inspection for existing structures.

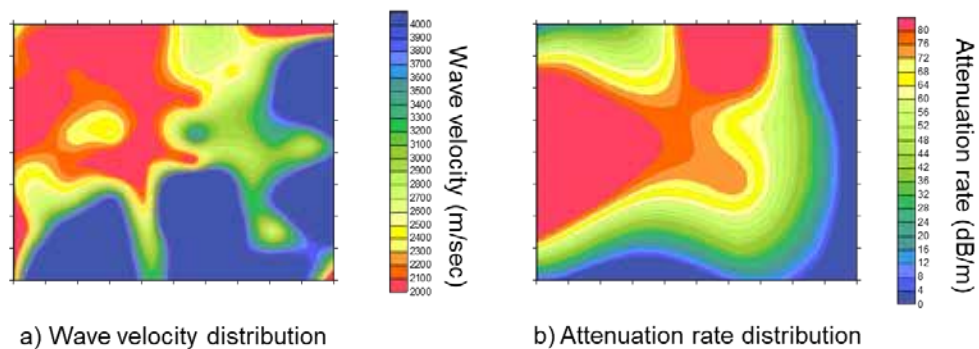


Fig. 7 Numerical analysis for tomography results on wave velocity and attenuation rate

As expected and afore-mentioned, a sufficient number of rain-induced AE events respecting the quality criteria has been found. The wave velocity distribution by means of AE tomography, as explained above, in this panel has been successfully computed from these data and the results are presented in Fig. 8 for wave velocity tomography, also they are described in Fig. 9 with a tentative classification for using pulse velocity as an indicator of quality known in Table 1 [9]. Accordingly, wave velocity distribution output provided from the proposed tomography technique is colored in red (poor < 3050m/sec) or blue (intact < 3050m/sec). Fig. 10 shows the results for attenuation rate tomography respectively, with core sampling results which were taken out from the deck to verify the results and visually observe the presence of horizontal

crack. Tomography results show top and bottom layer of 117.5mm each in the deck depth (235mm) since 3D computation was performed in this paper.

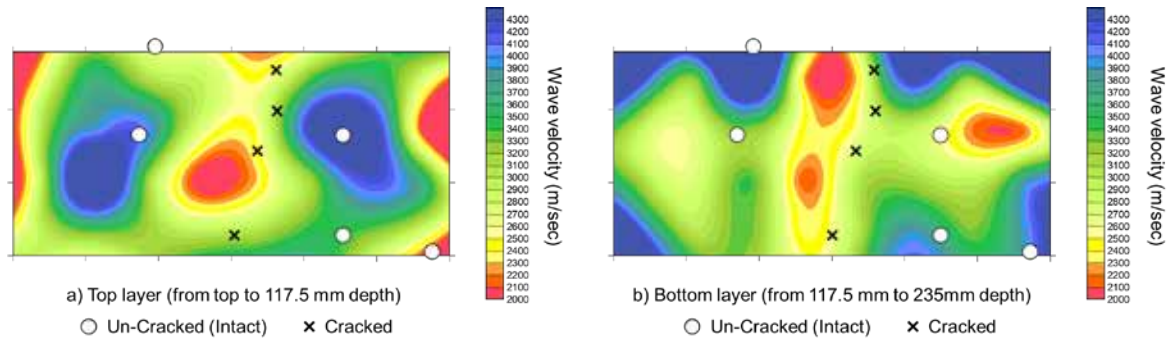


Fig. 8 Wave velocity distribution

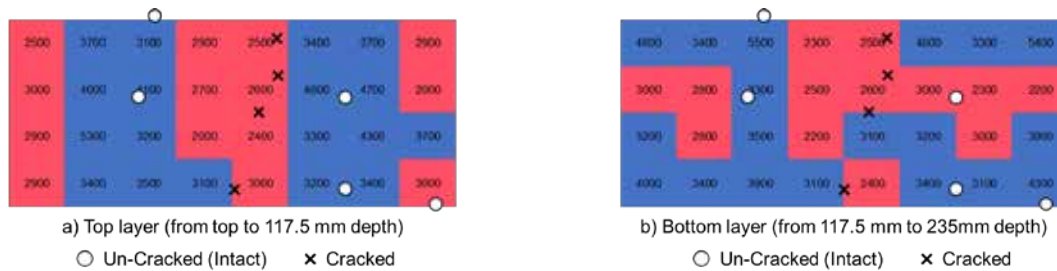


Fig. 9 Wave velocity distribution with quality classification

Table 1 Concrete quality and P-wave velocity

V_p (m/sec)	Condition
Above 4,570	Excellent
3,660-4,570	Good
3,050-3,660	Questionable
2,130-3,050	Poor
Below 2,130	Very poor

The relatively low-density AE source areas in the panel surrounded by dashed lines in Fig. 5 is supposed to be a largely extended horizontal crack [5]. The horizontal cracks were located at 150 mm or less from the surface of the deck (mostly in the top layer) by visual inspection of the cored samples. Therefore, it is reasonably understood that wave velocities and attenuation rate in top layer are lower than bottom layer. After all, in the tomography results, the soundness of concrete and the presence of horizontal crack roughly correspond to the wave velocity, and it is similarly seen observed for the attenuation rate distribution as well. The wave velocity and attenuation rate inside the core samples presenting large horizontal cracks are generally lower than 2400-3000 m/s and more than 15-20 dB/m at least over a certain part of their depth and the wave velocity inside the un-cracked core samples is generally higher than 3000m/s over their entire depth.

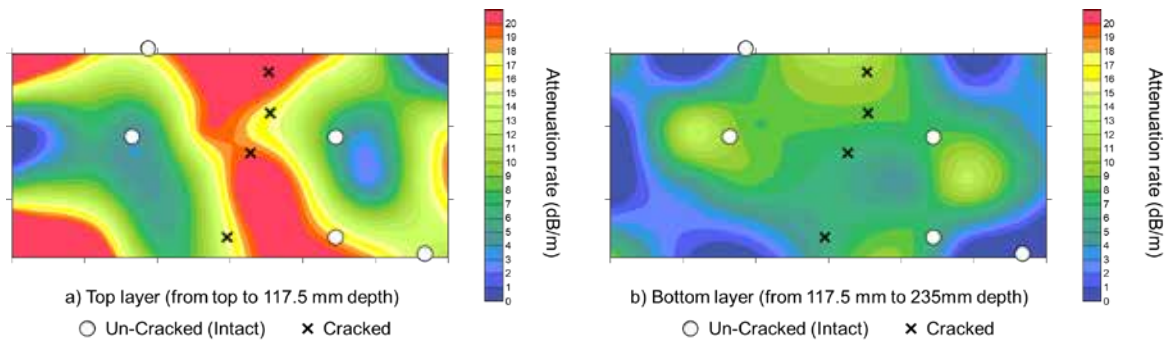


Fig. 10 Attenuation distribution

5. Conclusion

The elastic waves generated by the rain hitting the pavement surface can be recorded and used for reconstructing the wave velocity and the attenuation rate distribution inside RC slab. This method presents the advantage that a large number of AE events can be recorded in a very short period of time. Also, the computation technique assuming linear ray-paths enables to make the computation time drastically shorter than conventional ray-trace algorithm since the calculation process is undoubtedly simpler based on linear ray-paths without the detours. It is additionally believed that wave velocity and attenuation rate distribution can be calculated with hundreds or thousands of the rain-induced AE events more precisely than those results with using a few internal AE events such as secondary AE induced by traffic loading. Further investigation is needed to identify the appropriate sensor array and the threshold value of elastic wave parameters, wave velocity and attenuation rate, to judge the damage in targeted structure when the proposed tomography technique is applied. It is necessary to pay attention the AE measurement condition, such as sensor-space distance, when wave velocity is used as a parameter for acoustic emission tomography on the assumption with linear ray-paths of elastic wave travels to simplify the computation process.

References:

- [1] Y. Kobayashi, T. Shiotani and H. Shiojiri, Damage identification using seismic travel time tomography on the basis of evolutionary wave velocity distribution model, Structural Faults and Repair 2006 (CD-ROM), 2006.
- [2] Y. Kobayashi, T. Shiotani, D. G. Aggelis, H. Shiojiri.: Three-Dimensional Seismic Tomography for Existing Concrete Structures, Proceedings of Second International Operational Analysis Conference, Vol. 2, pp. 595-600, 2007.
- [3] Y. Kobayashi and T. Shiotani, Seismic tomography with estimation of source location for concrete structure, Structural Faults and Repair 2012, CD-ROM, 2012.
- [4] T. Shiotani, N. Okude, S. Momoki and Y. Kobayashi, Proposal of assessment method for infrastructures by AE tomography, Proceedings of 2011 National Conference on Acoustic Emission, 39-42, 2011 (in Japanese).

- [5] H. Asuae, T. Shiotani, T. Nishida, K. Watabe, H. Miyata, Applicability of AE Tomography for Accurate Damage Evaluation in Actual RC Bridge Deck, Structural Faults & Repair Conference, No.1743, 2016.
- [6] C. Granier, Shiotani, T., Hashimoto, K., and Nishida T., Visualization of internal damage in RC slab with single side access attenuation tomography, Proceedings of IAES-23, IIIAE2016 Kyoto and ICAE-8, pp. 383-387, 2016.
- [7] M.A. Hamstad, Acoustic emission source location in a thick steel plate using lamb modes, J. Acoustic Emission, Vol. 25, pp. 194-214, 2007.
- [8] T. Shiotani, Evaluation of rock slope stability by means of acoustic emission, NDT&E international, Vol.39, pp. 217-228, 2006.7
- [9] E. A. Whitehurst, Evaluation of Concrete Properties from Sonic Tests, ACI Monograph 2, American Concrete Institute, Detroit, MI, pp. 94, 1966.

34 - Contouring geodetically accurate Acoustic Emission sources via kernel density estimates

Ing. Petr Gális¹, Ing. Václav Kůs¹

¹ Department of mathematics, FNSPE, Czech Technical University in Prague, Trojanova 13, Prague 2, CZ (galispet@jfifi.cvut.cz, vaclav.kus@jfifi.cvut.cz)

Abstract:

We deal with numerical model of localization of acoustic emission (AE) sources on real complex solid bodies. Our approach is based on exact geodesic curves on 3D vessels composed of several parametrized surfaces. The numerical computations are provided via Finite difference, Newton–Raphson, and Fixed-point iteration methods applied to geodesic equations acquired from differential geometry theory. To speed up computations, some technical improvements and optimizations are proposed. The variable propagation velocity and also the case when the geodesic curve has to bypass a given obstacle there is also included into the model. These techniques are employed in the real experimental setup on bodies with higher geometrical complexity. The results (localization maps) of AE localization principle using length (ΔL) or time (ΔT) differences, obtained by means of geodesics, are then processed through the two-dimensional Kernel probability density estimates executed directly on the 3-D surfaces, which give us the most probable areas of the AE source positions on the main body. The placement of piezo-ceramic AE sensors is outside the central part of the vessel because it can be inaccessible due to possible high temperature or radioactivity, such as in the case of nuclear power station health monitoring. This outward position of all AE sensors can result in a dispersed AE wave detected, or attenuated because of welded intersections of different surfaces. Thus, the Change-point analysis of AE signals is also discussed in order to obtain the most precise arrival times of AE events, which is crucial for $\Delta T / \Delta L$ localization.

1. Introduction on geodesics

In our mathematical model of geodesic-based localization of acoustic emission sources we employ a posteriori evaluation of acquired localization maps. This is carried out by using the statistical kernel density estimates in 2D, which are applied either in parametric domain of the surface or directly on the 2D surface embedded in 3D. The resulting geodetic-kernel localization is applied to two experiments – the ionized iron watering can and steam reservoir. The method of geodesic localization itself is based on the well-known time differences localization principle. Measured time differences are compared (via certain functional F) with length differences that are computed using geodesic curves. These geodesic curves (geodesics) possess the property of the shortest length curves between two points and they are obtained from the following system of two non-linear ordinary differential equations [3] of the second order

$$\begin{aligned} \ddot{u} + \Gamma_{11}^1 \dot{u}^2 + 2\Gamma_{12}^1 \dot{u}\dot{v} + \Gamma_{22}^1 \dot{v}^2 &= 0, \\ \ddot{v} + \Gamma_{11}^2 \dot{u}^2 + 2\Gamma_{12}^2 \dot{u}\dot{v} + \Gamma_{22}^2 \dot{v}^2 &= 0, \end{aligned}$$

with a boundary conditions $u(a) = \alpha_1$, $u(b) = \alpha_2$ and $v(a) = \beta_1$, $v(b) = \beta_2$, where $u = u(t)$ and $v = v(t)$, $t \in (a, b)$, are coordinate functions of the geodesic in parametric domain of the surface with parametrization $\mathbf{x} = \mathbf{x}(x(u, v), y(u, v), z(u, v))$. The symbols Γ_{ij}^k are called Christoffel symbols and they describe a metric on the surface. We go through the each point

of a surface and numerically compute the geodesics to each sensor. Since many real bodies cannot be, in general, parametrized by a single parametrization, the algorithms obtaining a geodesic between two arbitrary points on the body are required [1, 2].

2. Numerical computation of geodesic curves

The above system of geodesic equations is solved via finite difference method, which leads to the system of algebraic non-linear equations [2], which is solved through the Newton-Raphson iterative method, given by the following principle

$$dF(\omega^k) \Delta \omega^k = -F(\omega^k), \quad \omega^{k+1} = \omega^k + \Delta \omega^k,$$

with initial root guess ω^0 as a straight line in parametric domain. To be able to compute geodesics on real bodies we need to decompose them to elementary surfaces so that we can describe each of them parametrically and easily obtain its Christoffel symbols. Then we compute the geodesics on the every sectional surface between start/end points by using a connection point lying at the intersection of two surface sections (Fig. 1 left). Then we iterate through each point of intersection and minimize the sum of lengths of partial geodesics. The computational cost can be very high, mostly when we have to iterate through many intersections.

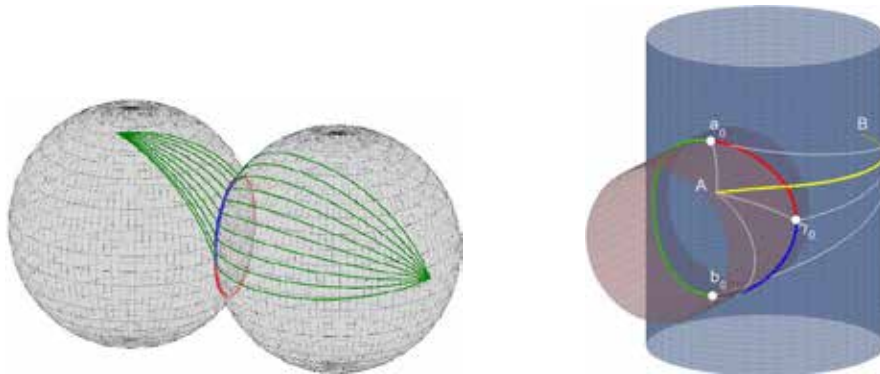


Figure 1: Computing geodesics through intersection on compound body.

To fasten the computation through intersections, the *Sequential Algorithm (SA)* is applied [1]. It is based on bisectional method and iterates through the points of intersection with minimal sum of length of geodesics (Fig. 1 right). Let $(a_0, b_0) \subset J$ be one part of parametric domain of the intersection curve. Set $\gamma_0 = (a_0 + b_0)/2$ and the step $\sigma_0 = |b_0 - a_0|$. Now we compute geodesics through the points $a_k, b_k, \gamma_k, k \geq 0$,

$$\begin{aligned}
 a_{k+1} &= \gamma_k + \sigma_{k+1}, & b_{k+1} &= \gamma_k - \sigma_{k+1}, & \sigma_{k+1} &= \frac{\sigma_k}{2} \\
 \gamma_{k+1} &= \operatorname{argmin}\{L_{a_{k+1}}, L_{b_{k+1}}, L_{\gamma_k}\},
 \end{aligned}$$

where L_i means the length of geodesic through the point i . This SA algorithm is very fast but there may be possible disadvantage that the points, through which the SA iterates, are not restricted to the interval (a_0, b_0) . Then a simple modification of the algorithm is needed.

There occurs one serious problem when solving geodesic system of equations. In short, the curve obtained need not be the shortest possible path between two points (Fig. 2). It happens in practical applications while working with solid vessels whose elementary parts form closed rotary surfaces. It means that at least one of coordinates u, v of its

parametrization domain takes values in $(0, 2\pi)$ or $(-\pi, +\pi)$. These intervals are mathematically equivalent apart from the discontinuity at $2\pi \leftrightarrow 0$ or $\pi \leftrightarrow -\pi$, which has an influence to the geodesic curve solution. Therefore, if $|u_A - u_B| > \pi$, we a priori change the computational parametric range of the angular coordinate, where u_A, u_B are angular coordinates of selected two surface points. The idea of this criterion comes from the observation that greater angle between two points results in longer arc and consequently greater length of geodesic curve.

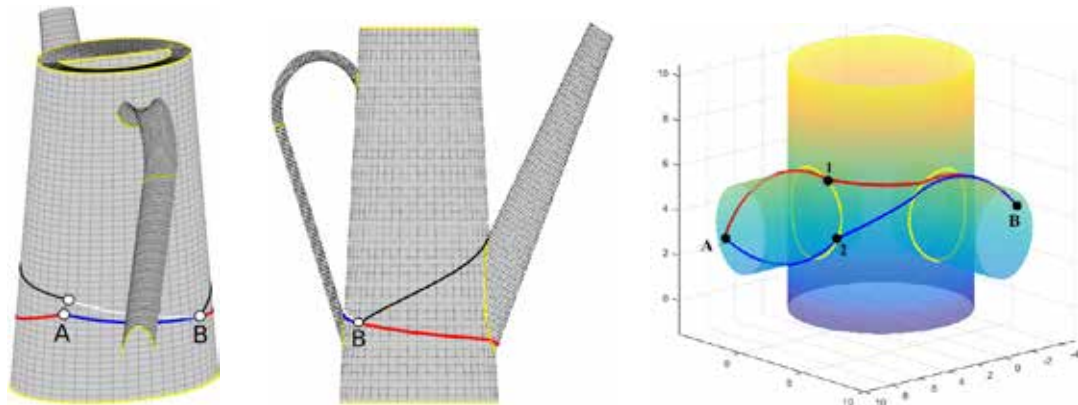


Figure 2: Conditional a priori reparametrization of $(0, 2\pi)$ to $(-\pi, +\pi)$.

We also have to deal with computations of geodesic curves around obstructions, e.g. see Figure 4. It is clear that the exact geodesic computations around obstacles can give more realistic signal paths and more exact AE source localization [2]. Thus, we have to find out sets of points for each obstruction through which we minimize the sum of length of all parts of geodesic (this may be tricky if we are dealing with multiple obstructions and advanced graphical methods are needed [4]). This algorithm is considerably time consuming because we are forced to compute very large number of geodesics in both reparametrizations.

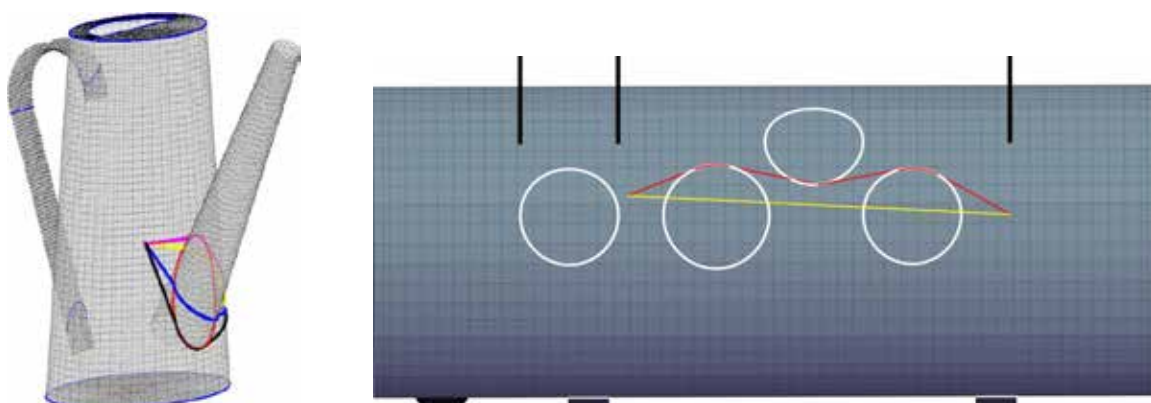


Figure 3: Geodesic curves in cases of path obstructions.

3. Localization of acoustic emission sources

In this part we present results from experiments with watering can and steam reservoir using the exact geodesic method mentioned above. First, SIC algorithm [5] is used to determine time arrivals of acoustic signals (produced by pentests) and then the common localization of

AE sources is carried out by means of either *length differences*: $F_L = \sum_{i < j} |c_{ij} \Delta t_{ij} - \Delta l_{ij}|$, or *time differences*: $F_T = \sum_{i < j} |\Delta t_{ij} - \Delta T_{ij}|$, where c_{ij} denotes the specific velocity between i-th and j-th component of the surface. There may occur the differences between resulting localization maps because the velocities c_{ij} are in general different from the velocities on each component itself (Figure 4 (right)).

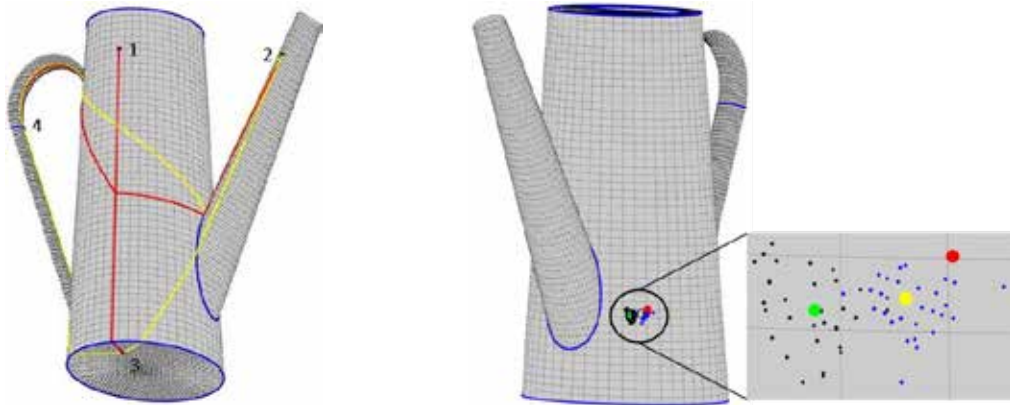


Figure 4: Sensor placement on the watering can (left) and an example of localization map using length (black+green) or time differences (blue+yellow), the source is red (right).

In the sequel, we use the time differences for our pentest experiments on steam reservoir, where the localization results are shown in Figure 5. As we can see, the precision of localization is quite high. This precision was mainly maintained due to incorporation of the variable velocity (non-constant on the whole surface) and also due to computing geodesics around obstacles (pouring ladle, welded pipes). We point out here that SIC criterion for obtaining the AE signal arrivals played a very important role in localization accuracy.

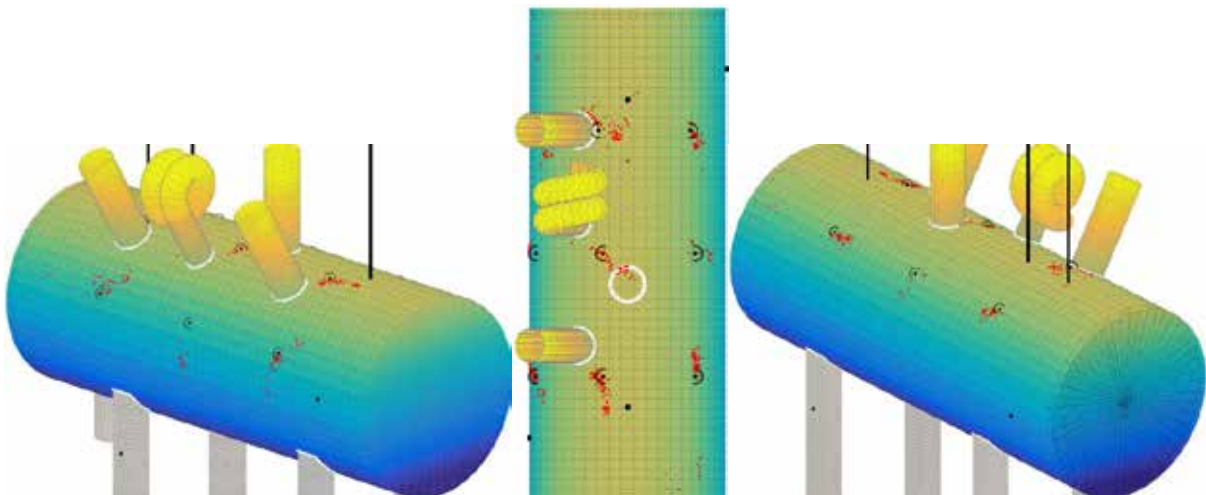


Figure 5: Localization maps on steam reservoir. Black dots with circles denotes pentest areas.

4. Kernel density estimates in 2D

The Kernel density estimate [6] of some unknown density f is defined by

$$\hat{f}(\mathbf{x}) = \frac{1}{n} \sum_{i=1}^n K_{\mathbf{H}}(\mathbf{x} - \mathbf{X}_i),$$

where $\mathbf{X}_i = [u_i, v_i] \in \mathbb{R}^2$ represents the i -th localized point in the parametric domain of the surface, $\mathbf{x} \in \mathbb{R}^2$, $\mathbf{H} = (h_{ij})_{i,j=1}^2 \in \mathbb{R}^{2,2}$ is a symmetric and positive definite *smoothing matrix* and $K_{\mathbf{H}}$ is determined through the *kernel function* K by the expression

$$K_{\mathbf{H}}(\mathbf{x}) = |\mathbf{H}|^{-1/2} K(\mathbf{H}^{-1/2} \mathbf{x}).$$

\mathbf{H} plays a similar role as the *window width* in one dimensional case. The essential thing about kernel density estimates is that it weakly depends on K , however it substantially depends on the smoothing matrix \mathbf{H} . We briefly present two algorithms which determine the matrix \mathbf{H} automatically.

Reference density method (RD): If we suppose that the unknown density f belongs to the family of normal densities, then the estimate of \mathbf{H} is $\hat{\mathbf{H}}_{RD} = n^{-1/3} \hat{\Sigma}$, where $\hat{\Sigma} = (s_{ij})_{i,j=1}^2$ stand for the estimate of covariance matrix obtained from measured data set.

Iterative method (IT): IT estimate of \mathbf{H} , based on the family of normal densities again, is

$$2h_{11} \sqrt{S(s_{ij})} \sum_{i,j=1, i \neq j}^n \Lambda_{\mathbf{H}}(\mathbf{X}_i - \mathbf{X}_j) = n V(K),$$

with $S(s_{ij}) = (s_{11}s_{22} - s_{12}^2)/s_{11}^2$, $V(K) = \int_{\mathbb{R}^2} K^2(\mathbf{x}) d\mathbf{x}$, and $\Lambda_{\mathbf{H}}(\mathbf{z}) = (K \star K \star K \star K - 2 K \star K \star K + K \star K \star K)(\mathbf{z})$, where \star denotes the convolution. The equation can be solved for example with Newton-Raphson method. The remaining h_{12}, h_{21}, h_{22} are then obtained from h_{11} as $h_{ij} = h_{11} s_{ij} / s_{11}$. Note that \mathbf{H} is symmetric and thus $h_{12} = h_{21}$.

5. Localization results using kernel density estimates

The localization map from Figure 5 is further processed through kernel density estimate which tells us the most probable location of AE sources. This kernel density estimate can be carried out either in parametric domain of the surface and then transformed onto the surface in 3D, or preferably, can be performed directly on the curved surface 2D object embedded in 3D.

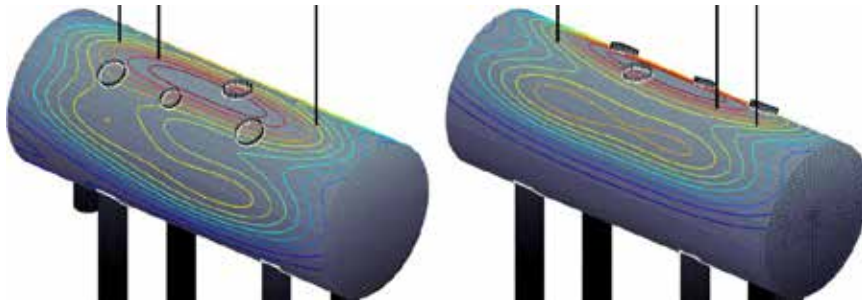


Figure 6: Kernel density estimates on the steam reservoir applying RD procedure.

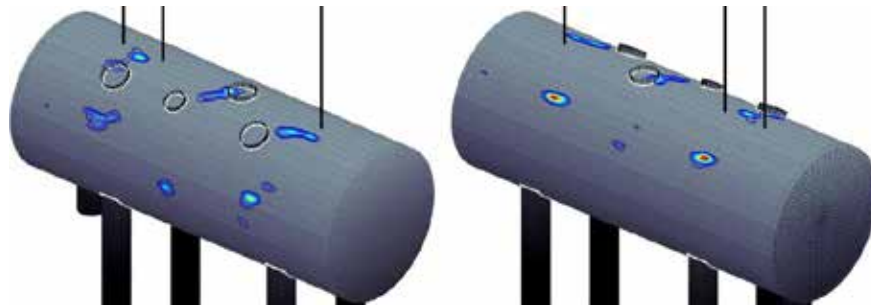


Figure 7: Kernel density estimates on the steam reservoir under IT procedure.

The former resulting kernel density estimates can be seen in Figures 6 and 7, where the significant difference between IT and RD methods can be observed. The outstretched RD kernel estimate is caused by its application on quite dispersed pentest data with big variance, consequently leading to unusable estimates. However, if we treat the data separately for each localization cluster then the RD method provides practicable estimates. Further, we found out that although the IT algorithm also depends on the covariance matrix Σ , this IT method does not suffer from the dispersed estimates.

The second approach based on direct kernel computations on the curved surface in 3D is presented in Figure 8. It was realized by means of generalized definition of the kernel estimator using geodesic metric ρ at the surface and restricted to the *window radius* h . This method offers wider variability of adjusting magnitude of the kernel window, unlike the methods for automatic estimate of smoothing matrices \mathbf{H} . For comparison purposes, the direct surface kernel estimates were also transformed back into the parametric domains of the surface, see Figure 8 (left).

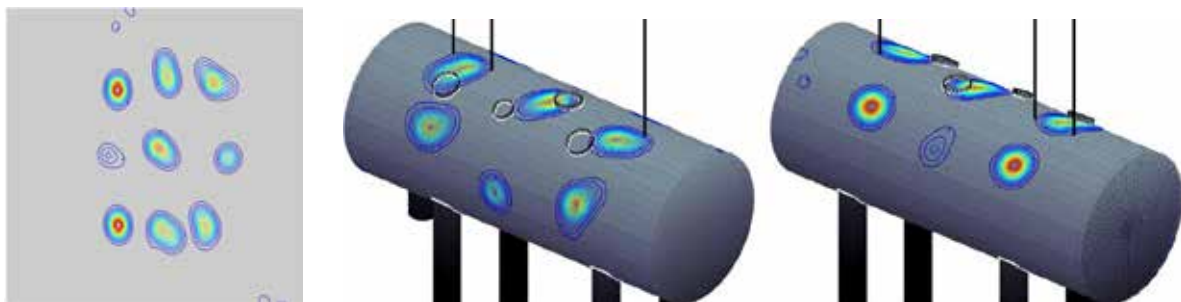


Figure 8: Kernel estimates computed directly on the steam reservoir with window radius 1 cm.

6. Conclusions

Mathematical model of sources of AE based on time differences principle expanded from plane to curved surfaces make use of geodesic curves obtained from geodesic equations. These equations are solved numerically via finite difference method and Newton-Raphson method. Both the variable propagating velocity of acoustic signal and the geodesics bypassing obstacles were incorporated into the model. This led, with other support techniques, to high accuracy of AE localization model. Computation is parallelized for the possibility of online localization. Resulting model was applied to laboratory experiments on ionized watering can and steam reservoir. The watering can represents higher geometric complexity, whereas the steam reservoir brings computations of geodesics bypassing multi-obstacles. Resulting localization maps were processed with 2D kernel density estimates

which provided most probable locations of AE sources. Based on our comparison we point out the possibility of computing the kernel estimates directly on the 2D surface in 3D, which can be very useful and more accurate. All the results can be found in [2] in details.

Acknowledgments: The experimental data on steam reservoir was measured by Ing. Milan Chlada, Ph.D., from the Institute of Thermomechanics, Academy of Sciences of the Czech Republic. We thank him very much for his considerable help with data handling. This work was supported by the grants LM2015068 (MYES) and SGS18/188/OHK4/3T/14 (CTU).

References:

- [1] Kůs, V., Záveský, M., Převorovský, Z., Acoustic Emission Defects Localized by Means of Geodetic Iterative Procedure - Algorithms, Tests, AE Experiment, In: Proceedings of the 30th European Conference on Acoustic Emission Testing & 7th International Conference on Acoustic Emission. Granada: Universidad de Granada, 2012. pp. 536-546.
- [2] Gális, P., Geodetic optimization and acoustic emission localization maps processing, Diploma thesis, Department of mathematics, FNSPE CTU in Prague, Prague, 2018.
- [3] Carmo, M.P., Differential Geometry of Curves and Surfaces, Prentice Hall, New Jersey, 1976.
- [4] Foley, J., Dam, A., Feiner, S., Hughes, J., Computer Graphics (3rd Edition), Addison-Wesley Professional, 2013.
- [5] Gupta, A.K., Chien, J., Parametric Statistical Change Point Analysis, Birkhäuser, Basel, 2000.
- [6] Silverman, B.W., Density Estimation for Statistics and Data Analysis, Chapman & Hall, New York, 1986.

41 - Analysis of AE source location precision for general sensor configurations

Milan CHLADA¹, Petr GALIS², Zdenek PREVOROVSKY¹

¹ NDT Laboratory, Institute of Thermomechanics AS CR, v.v.i.,
Prague, Czech Republic;

² Department of Mathematics, FNSPE,
Czech Technical University in Prague, Czech Republic.

Abstract:

Proper sensor placement is the crucial step and a premise for precise AE source location estimate. Optimal sensor configuration in cases of complex structure shapes is one of AE expert challenges. It leads to numerical analysis of relations between the signal arrival chronology and the coordinates of emission sources. Using the algorithm for finding the shortest ways in discretely defined bodies it is possible to design three parallel tools how to evaluate problematic areas, namely the location sensitivity, similarity and ambiguity maps, available even for non-continuous or anisotropic materials. Analogically to Global Positioning System, location of AE sources meets the geometrical dilution of precision (GDOP) phenomena. Similarly to GDOP parameter, recently introduced sensitivity map shows critical regions characterized by strong sensitivity of location results to signal arrival time changes or errors. Remaining two mentioned methods illustrate the topology of arrival time differences space and possible ambiguities of source location. To check the numerical forecast of location capabilities of given sensor configuration, theoretical results were reviewed with the data measured during real experiment.

1. Introduction

To ensure reliable AE source location results in particular structure part, it is needed to choose proper configuration of sensors, or, conversely, take into account only AE events coming from “stable” region defined by sensor placement. Improper positions of receivers towards the source can generally disable location methods using the signal arrival delays. Similar problem is solved also in the field of satellite navigation. In order to predict the accuracy of location results, the geometry of the setup (i.e. known position of satellites and the estimated position of GPS signal receiver) is exploited. The dimensionless parameter modelling expected location accuracy is called Geometric Dilution of Precision (GDOP) [1, 2]. The idea is to state how the measurement errors affect the final location estimation. If small changes in measured data (time delays) are not resulting in large location changes, the solution is not too sensitive to measurement errors.

$$GDOP = \frac{\Delta(\text{output location})}{\Delta(\text{measured data})} \quad (1)$$

In general the GDOP solely depends on the arrangement of sensors and the emitter position. GDOP serves as a measure of the location errors magnification derived from perturbations in arrival times. In areas of great GDOP values, especially outside the convex hull of the sensor array, it is not recommended to locate AE sources, due to expected high location uncertainty and errors.

Another indicator of expected location precision is the Location Uncertainty (LUCY) parameter [3]. It describes how well a calculated source position fits the measured arrival-time-differences and can be used as a filter criterion to separate the sources with poor location accuracy.

All above mentioned approaches are theoretically ready to be applied for general body shapes, however, their usage is mostly restricted by essential knowledge of shortest (direct) paths between the source and sensors. Following chapters deal with forecasting of location possibilities and precision by application of numerical analysis of particular sensor configurations. The methodology is formulated for discretely defined bodies and it is demonstrated for real complex structure, namely the steam storage vessel with embedded pressure and temperature sensors, waveguides and supporting legs (see photos in fig.1). The goal is to predict the accuracy of AE source location for selected group of sensors. The “numerical forecast” is then reviewed with nine sets of pencil-lead breaks (PLBs) realized in nine mesh points on the main body surface.



Fig.1: Experimental body.

2. Arrival-time chronology parametrization

The mostly applied approach to AE source location is the analysis of time chronology (delays), in which the elastic wave arrives at each sensor. However, the arrival-time information can be furthermore parametrized by various ways. Instead of commonly used time-differences, let's demonstrate advice methodology of location precision analysis for arrival-time profiles. For group of N sensors, the arrival-time profile (ATP) is a vector of numbers p_i defined as:

$$p_i = \frac{T_i - \frac{1}{N} \sum_{j=1}^N T_j}{T} = \frac{t_i - t_s - \frac{1}{N} \sum_{j=1}^N (t_j - t_s)}{T} = \frac{t_i - \frac{1}{N} \sum_{j=1}^N t_j}{T} \quad (2)$$

where T_i is arrival time period (signal propagation time from source to sensor i), t_s the AE source inception time, t_i signal arrival time and T is a normalization period representing the length of time interval which AE signal needs to pass between two appropriately selected points. Since no AE analyser measures the arrival time periods T_i before precise AE source location is done, the left part of equation (2) can be considered only when computing the database of typical arrival-time profiles in points sufficiently covering the body. Arrival-time

profiles are independent on elastic wave velocity and structure scale changes and these parameters can be calculated by real arrival times t_i or time periods T_i evaluated on a physical or numerical model. Normalization period T serves as a calibration time, which must be measured on the real structure and computed for corresponding points on the model body. Finally, arrival-time profile $P=(p_1, \dots, p_N)$ represents a kind of arrival-chronology relativizing (see fig.2).

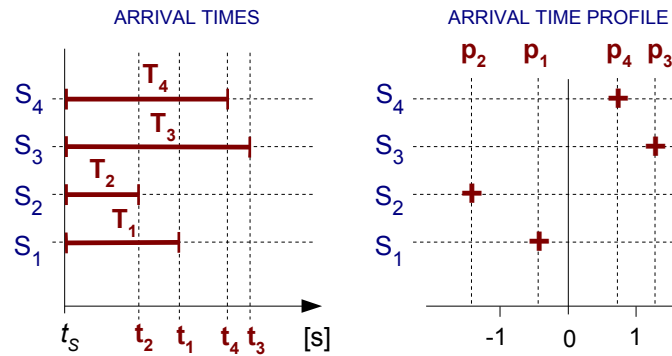


Fig.2: Relativisation of arrival-times by arrival-time profile.

For further computations let's consider the sensor configurations outgoing from a body shape and sensor placement illustrated in fig.3. Experimental setup includes also the positions of nine PLBs performed within the most complex part of steam storage vessel. All computations are done in 2D on unwrapped main body surface (see right part of fig.3).

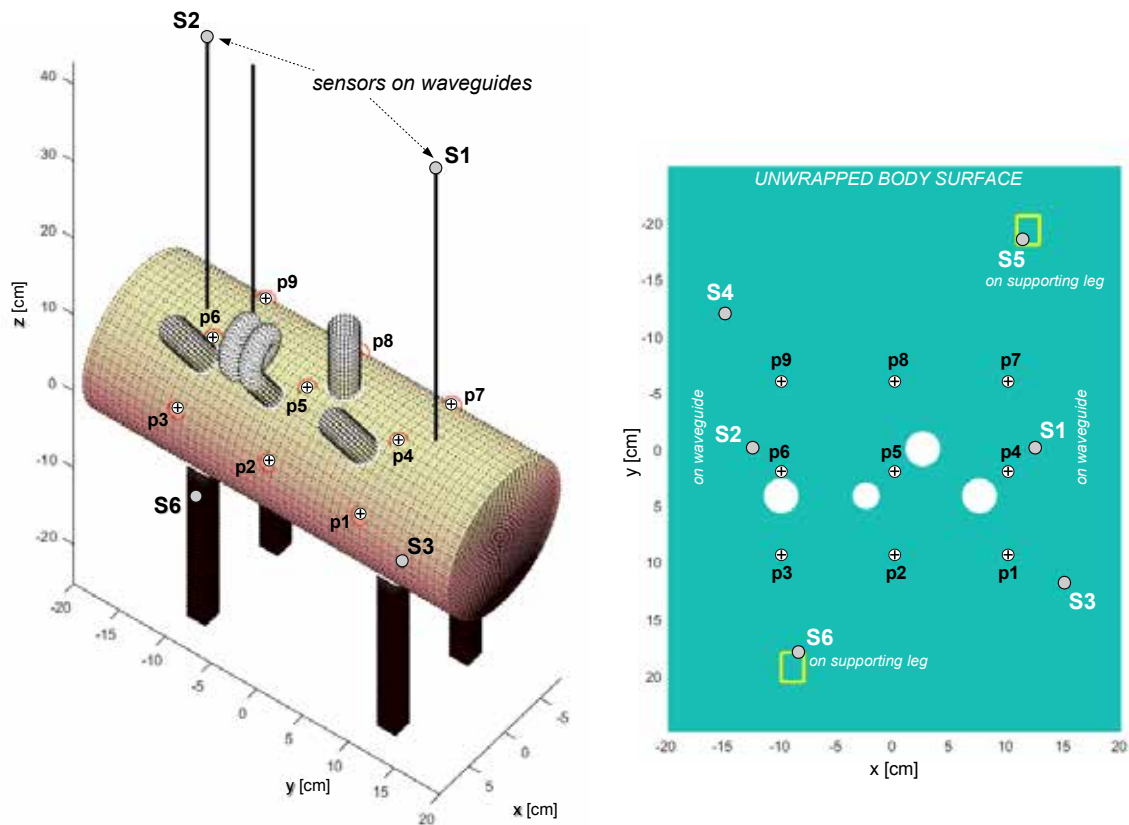


Fig.3: Experimental setup scheme.

3. Shortest ways finding in discrete bodies

For reliable results of AE source location it is needed to trace elastic wave while propagating from initiation point to sensor and estimate the distance between them. The choice of most suitable method for solving the problem depends largely on the kind or form of the body shape definition. It can be given as a photograph, as 2D or 3D computer sketch, otherwise as a mathematical model etc.

Due to its simple implementation and sufficient precision, the method of shortest ways finding similar to Dijkstra's [4] algorithm was considered as a basic model of the direction of wave propagation. It is suitable for discrete bodies derived from 2D or 3D bitmap pictures [5] and enables tracing of elastic waves propagating in structures of complicated shapes and also considering the anisotropy, without mathematical models of wave propagation. The method is inspired by Huygens' principle: each point on advancing wave front may be considered as a new point source generating spherical Huygens' wavelets. Such approach enables collecting of sufficient amount of representative data for AE source location algorithms based on database searching or artificial neural networks.

Having the tool for general finding the distances in incoherent bodies, it is possible to show the aspects of particular configurations of sensors in accordance with the sensitivity of location results to the changes of arrival-time profiles together with their possible variability and ambiguity (discussed in next chapters).

4. Sensitivity maps

Analogically to *GDOP*, let's define the location sensitivity parameter *SM* for any pixel X_A and its neighbourhood N_A in discretely defined body with N placed sensors. The scheme in the right part of the fig.4 shows the detail view of structure part:

$$SM(X_A) = \mathop{\text{mean}}_{X \in N_A} \left\{ \frac{d_E(P(X_A), P(X))}{d_E(X_A, X)} \right\} \quad (3)$$

where $P(X_A)$ is ATP for pixel X_A

$P(X)$ is ATP for pixel X

and $d_E(\dots, \dots)$ is Euclidean distance

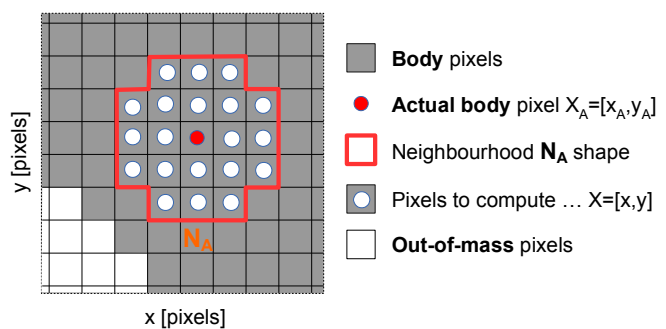


Fig.4: Definition of sensitivity parameter *SM*.

After computation of *SM* parameter for all body pixels, it is possible to show resulting sensitivity map. Higher values predict possible good location precision, while the poor is shown by small numbers caused by significantly higher variance of AE source coordinates compared to variance of corresponding arrival-time-profile. Following figure illustrates the case of two selected configurations of three sensors. Problematic areas in a sense of location precision can be expected in areas characterized by small levels of *SM* (dark regions) and close to the points with more steepest changes of this parameter (sharp lines in fig.5).

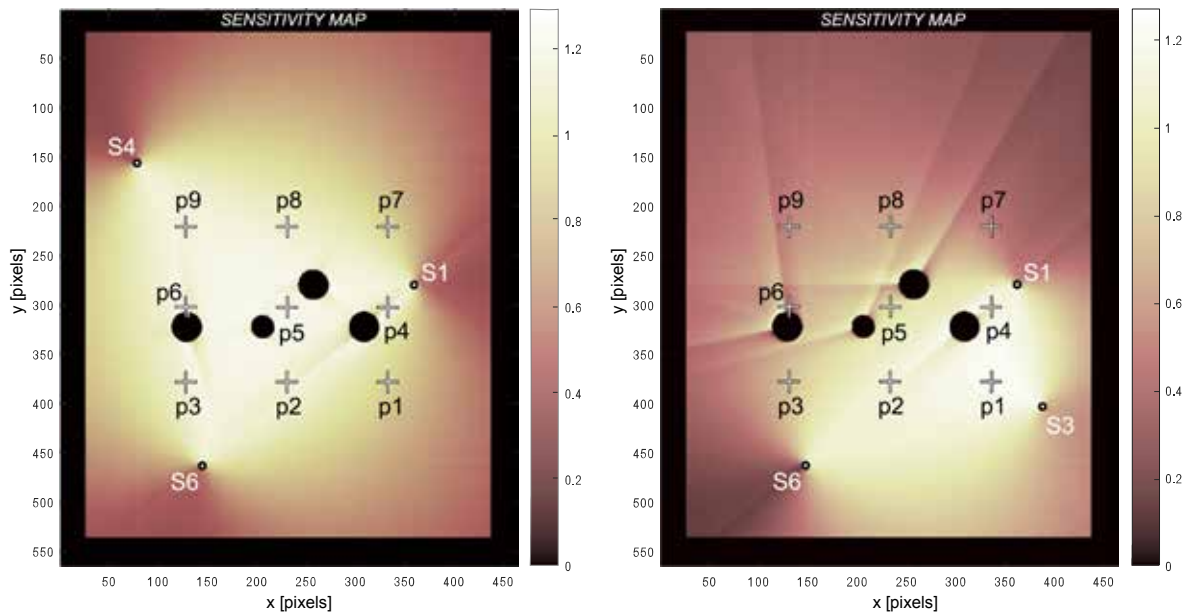


Fig.5: Sensitivity maps for two selected combinations of three sensors.

As expected, the best region for location should be in a convex hull of the three sensors. Some singularities or numerical stability problems can be caused by the holes in material.

5. Similarity of arrival-time profiles

To illustrate how the arrival-time profiles vary within the complicated body, the similarity map was assorted as well. Each colour distinguishes the regions having in some small tolerance similar chronology of signal arrivals to sensors. Large regions detect problematic areas and vice versa (see fig.6).

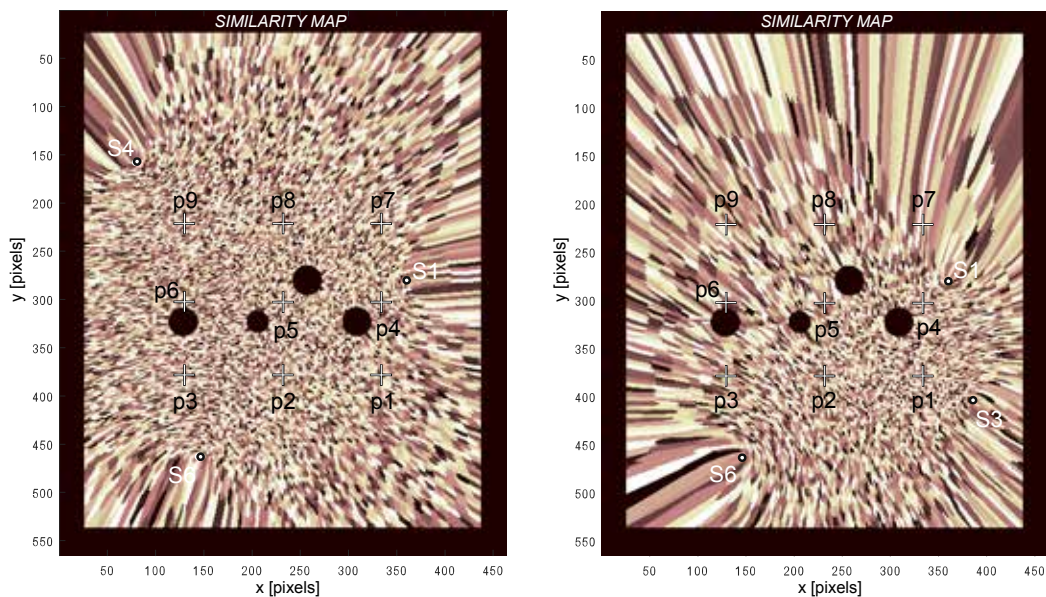


Fig.6: Similarity maps for two selected combinations of three sensors.

6. Location ambiguity measure

Another point of view to location problem aspects can be illustrated as finding a crossing of the two hyperboles in localization by time-differences. It is clear, that 2D location of AE sources using 3 transducers is not unambiguous [6]. Left part of fig.7 shows the problem of possible existing of two different source locations inducing the same time-differences. Naturally, the number of such coupled-points is not limited.

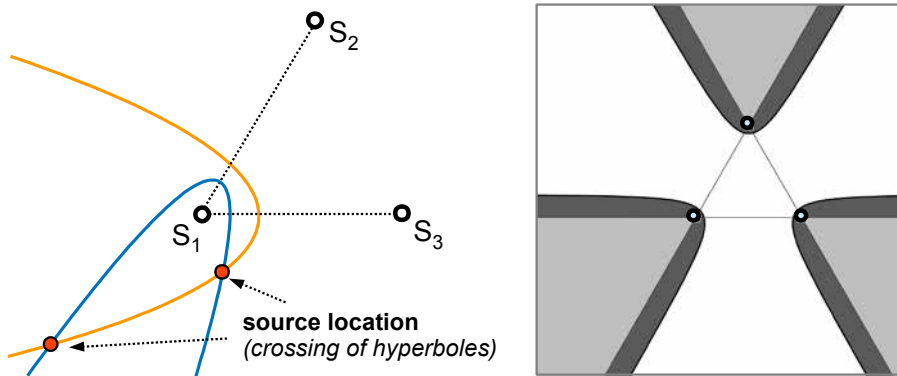


Fig.7: 2-D AE sources location ambiguity.

The right part of fig.7 shows the areas of unambiguous locations for this particular sensor configuration. Any AE source in dark grey area has the same time-differences as corresponding source in light grey area and vice versa. The problem is usually solved by adding the fourth sensor, while the area of unambiguous locations is theoretically reduced to insular points.

The location ambiguity is generally caused by the insufficient number of sensors and concerns with the arrival-time profiles as well. To detect distant pixels having very similar arrival-time chronology, so-called Location Ambiguity Map (*LAM*) is introduced. For every body pixel $X=(x,y)$ it is needed to find a set of other pixels X_i that are not direct neighbours indeed, but have very close arrival-time profile by Euclidean measure. It means that their distance is less than a small tolerance *tol*. For such pixels X_i the resulting number $LAM(X)$ is the mean ratio of distances in arrival-time profile and x-y-coordinate spaces:

$$LAM(X) = MEAN \left\{ \frac{d_E(P(X), P(X_i))}{d_E(X, X_i)} \mid d_E(P(X), P(X_i)) < tol. \right\} \quad (4)$$

An ambiguity map is the set of numbers $LAM(X)$ enumerated for all body pixels and can be considered as a useful tool for finding an adequate setup of sensors. Small numbers detect problematic areas of pixels for which somewhere exist points with nearly the same arrival-time chronology. Thus, the estimate of unique AE source location is unable in such areas.

After analysis by all above mentioned methods, both two sensor configurations (1-4-6 and 1-3-6) were tested by real measured arrival-times of AE signals. The goal was to compare numerical prediction of location precision with resulting locations of sets of PLBs (see fig. 8 and 9).

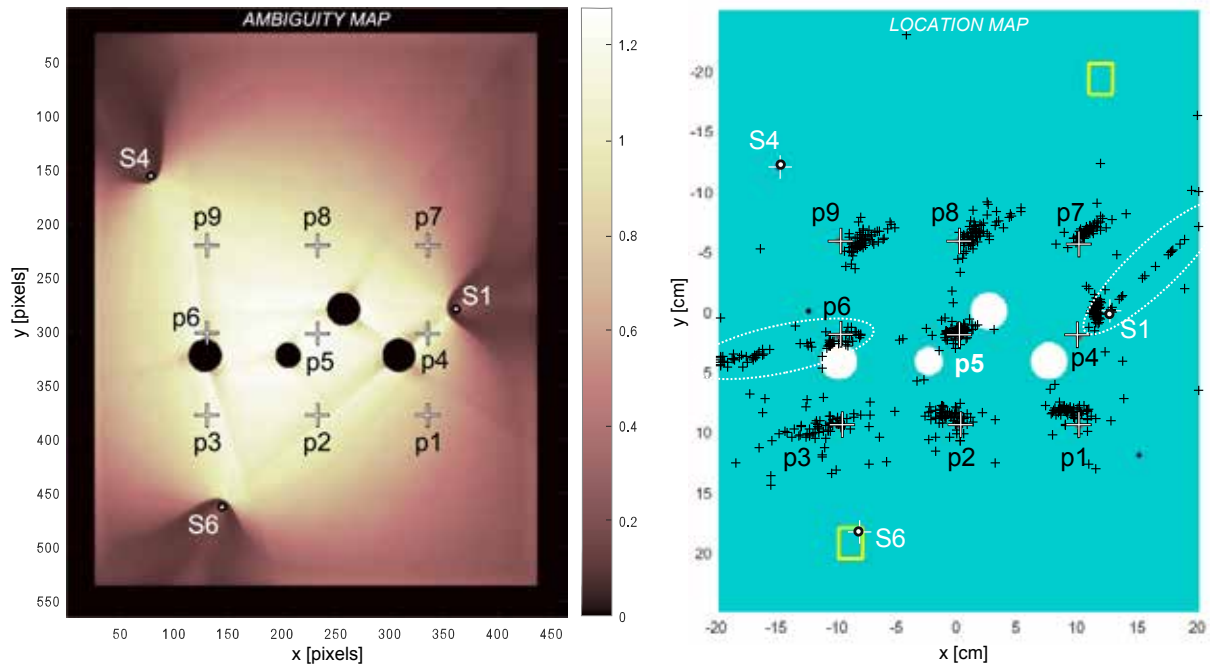


Fig.8: Location Ambiguity Map versus location results for sensor group 1-4-6.

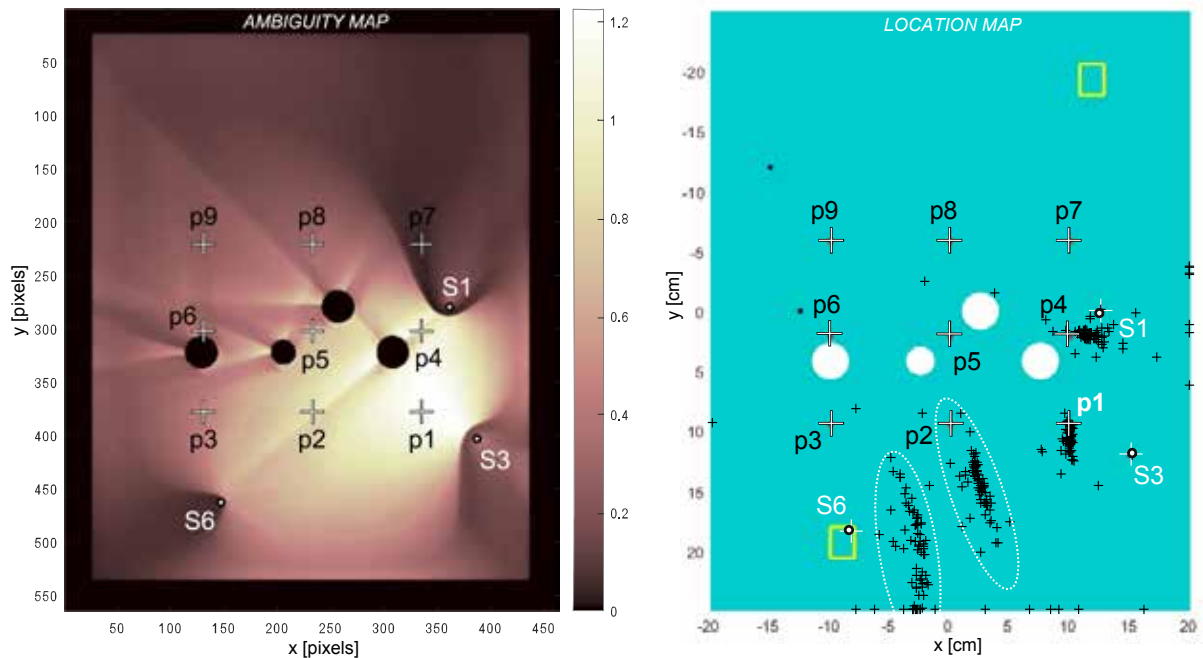


Fig.9: Location Ambiguity Map versus location results for sensor group 1-3-6.

7. Discussion of results

After recording of nine sets of approximately 50 PLBs by six AE channels, the crucial step for their location was to estimate the signal onsets. While testing the most stable and precise

approach, the expert signal edge detection method [7] approved as the best. Another problem was to fit the elastic wave velocities for each component of the testing structure with the numerical pixel model. The sensors were placed directly on the main body surface, on the waveguide, or the supporting leg, each part made from different materials. As a reference point for the best fitting, the position of PLB with the most stable location in the meaning of Location Ambiguity Map was selected (position 1 for sensor configuration 1-3-6 and pos. 5 for configuration 1-4-6). The optimal elastic wave velocities approximately measured and then corrected by gradual fitting proved best around 5 km/s. As the final location estimate of each AE event, the x-y coordinates of pixels with the closest numerically computed arrival-time profile were established.

Comparing the left and right sides of fig. 8 and 9 it is possible to conclude, that the reliability of AE source location can be illustrated very well by Location Ambiguity or Similarity Maps. Especially in the case of sensor group 1-3-6, the resulting variance and shift of estimated x-y AE source coordinates matches the envelope of LAM levels. The satisfactory precision was found for PLB position 1, while for positions 2 and 3 precision subsequently failed. Resulting small shift at position 4 seems to be caused by location sensitivity detected by certain edge coming through corresponding pixels of LAM. The results for remaining positions are not displayed, because of too high variance and shift. In conclusion, for particular configurations of sensors it is possible to analyse the location capability of the setup by means of sensitivity, similarity and ambiguity maps.

Acknowledgements

The work was supported by the Grant Agency of the Czech Republic under the grant no. GACR 17-22615S, and by Institutional support RVO: 61388998 (CR), which is gratefully acknowledged.

References:

- [5] Benneths, J.B., Organisation for Materials, NDT Journal Concept, Vol. 54, 2001, pp.
- [1] Zekavat, R., Buehrer R. M., Handbook of Position Location: Theory, Practice and Advances, Vol. 27. John Wiley & Sons, 2011.
- [2] Bar-Shalom, Y., Li, X. R, Kirubarajan, T., Estimation with Applications to Tracking and Navigation: Theory Algorithms and Software, John Wiley & Sons, 2004.
- [3] Thenikl, T., Altmann, D., Vallen, H., Quantifying Location Errors, Proc. of EWGAE 2016. Prague, Czech Society for Nondestructive Testing, ISBN 978-80- 214-5386-9, pp. 495-502.
- [4] Dijkstra, E. W., A note on two problems in connexion with graphs, (PDF). Numerische Mathematik 1: 269–271. doi:10.1007/BF01386390.
- [5] Chlada, M., Prevorovsky, Z., Shortest Ways Finding in Discrete Bodies, Proc. of NDT in Progress 2015. Prague, Czech Society for Nondestructive Testing, ISBN 978-80-214-5262-6, pp. 69-74.
- [6] Blahacek, M., Time Differences Uncertainty Influence on Acoustic Emission Source Location Accuracy, Proc. of NDT in Progress 2007. Prague, Czech Society for Nondestructive Testing, ISBN 978-80- 214-3505-6, pp. 15-22.
- [7] Chlada, M., Prevorovsky, Z., Expert AE signal arrival detection. International Journal of Microstructure and Materials Properties 6(3/4), pp. 191-205.

54 - Time reversal localization of continuous and burst AE sources under noise

Z. Prevorovsky¹, J. Krofta¹, J. Kober¹, M. Chlada¹, M. Mracko¹

¹Institute of Thermomechanics CAS, Prague, Czech Republic

Abstract:

Time reversal (TR) processing of acoustic and ultrasonic signals is effective tool for complicated problems solution in NDT /E and structural health monitoring. TR enables space-time focusing of elastic wave and thereby relatively easy location and partial reconstruction of both burst and continuous acoustic emission (AE) sources. AE source location problems come up in situations with high external noise, wave dispersion in thin-wall structures, and wave velocity changes in complex structures containing welds, flanges, branches, etc. Localization problems in such cases mostly require large sensor arrays and sophisticated signal processing and filtration. A new solution with using TR approach is suggested in this paper. This approach allows planar location of burst AE sources with only one transducer, and continuous AE sources with two transducers, both under high background noise from other sources. TR procedure is in this paper applied to long random noise (leakage) signals for the first time.

Suggested method was experimentally verified by simulated burst and continuous AE sources on a thick steel plate and thin Al-plate with various holes. Source location results certified high robustness of suggested approach. Need of detailed scanning of a region around a pre-localized source constitutes certain disadvantage of that method. Numerical simulations shown that scanning can be omitted by inserting experimental TR signals into the computer model of monitored structure ("digital twin") and perform the source location in the model. Localization accuracy of suggested procedure proved by LDV is about one mm, which is better than the wavelength and transducer aperture.

1. INTRODUCTION

Reliable and relatively precise location of Acoustic Emission (AE) sources is one of the most important inverse problems of AE monitoring in NDT and SHM of engineering structures and many industrial processes. A lot of different ways exists today how to determine the AE source position using one or more AE transducers. Classical algorithms of AE source location are mostly based on time differences of signal arrival (TDOA) between two or more transducers, which give satisfactory results only in relatively simple cases using classical triangulation method with the aid of reliable first arrival signal 'picker', like e.g. AIC (Akaike Information Criterion) [1] or expert signal detection [2]. Such localization can completely fail under situations when e.g. wave dispersion and/or high background noise occur. A lot of different procedures were already proposed to solve these problems [1,3]. Some years ago we contributed to that by fuzzy-probabilistic approach with extracted signal features [4] and artificial neural networks (ANN) [5]. In addition to more convenient, variously improved threshold signals arrival detection are widely used alternative approaches based e.g. on frequency analysis and filtration, cross-correlation functions (CCF) of two signals [6], etc. The dispersion and/or noise problems are easily solvable when we localize burst type AE sources.

2. CONTINUOUS AE SOURCE LOCATION

Location of random noise-like AE sources occurred during leaks, plastic deformation, friction and wear, etc. [7] is much more complicated than location of discrete AE sources under heavy conditions. Conventional triangulation techniques cannot be there used. The arrival times are not well defined, and only time differences between more channels acquired e.g. by CCF are available. The standard, but only rough AE method of leakage source location is based on signal strength defined as RMS or similar energy parameters [8,9]. If we omit manual searching with single transducer, larger array of transducers is necessary for linear location e.g. on a simple tube. Various specialized devices and methods for continuous AE monitoring and localization are mentioned in more US patents (e.g.[10]). The methods employ e.g. octave filters to determine characteristic frequencies, noise distribution histograms, floating threshold values to determine time offsets between signal spikes, time profile changes of AE parameters, etc. Authors [11] used spectral similarity of noise signals, authors of [12,13] developed intelligent AE locator employing general regression ANN with learning on prototype sources. They also discussed the use of correlation techniques, and stated that an optimal wave packet with approx. constant velocity along the structure must be found for dispersive waves. To solve the problem of separation signals from more mixed sources they used 'blind source separation' technique with independent component analysis (ICA). ANN for AE source location apart from structure size and velocity changes (portability of already learned ANN) we used with 'Arrival Time Profiles' (ATP) in [5], which is based on chronology of signal arrivals to sensor array, determined e.g. on precise structure drawings. For continuous AE location, proposed in the patent [14] were ATPs replaced by 'Positional Profiles' independent on structure attenuation. The method needs amplitude calibration of a virtual model for ANN learning. Wang et al. [15] recently proposed gas leak location algorithm using optimally spaced multi-array sensors subjected to correlation and the phase differences profiles. Xu Bian et al. [16] proposed time-space correlation method using AE sensor array for acquiring directional orientation of the leakage source, and Yong et al. [17] presented new technique for gas leaks location with low frequency AE sensors and signal analysis in both time and frequency domains with empirical mode decomposition and signal reconstruction to eliminate wave speed changes and attenuation along the pipeline. A comprehensive survey on gas leak detection and localization techniques published Murvay and Silea [18]. Most of the above techniques require optimally dispersed large arrays of sensors and their calibration, optimal signal filtrations, time-frequency decompositions, and knowledge of monitored structure properties (geometry, wave velocities, etc.). Most of them are based on TDOA acquired by CCF.

2.1 Time reversal source location

Some years ago we elaborated new concept of more precise AE source location and identification in arbitrary complex structures [19, 20, 21]. That concept is based on the Time Reversal(TR) signal processing broadly used in many fields (NDT/E and SHM, acoustics, seismology, telecommunications, medicine, etc.).The background noise is suppressed in TR operation when its sources are out of the localized source origin[22]. The TR robustness originates in the waves character and their space-time reciprocity (solution of wave equation is invariant with respect to TR operation).TR space reciprocity enables also reciprocal TR processing when the source position is used to rebroadcast TR signals received by the original receiver.TR experiments are accomplished in two steps: 1. forward propagation, when a source $s(t)$ excites the medium and response $u_j(t)$ is recorded by a set of j transducers at different locations; 2.back propagation, when the response signals are reversed in time and rebroadcast into the original structure. This results in wave energy focusing at the original

source location and in the (partial) reconstruction of the source function [22]. A partial reconstruction can be accomplished using only one receiving transducer but summation of TR responses from more receivers lead to better reconstruction results. Rebroadcast TR signal, monitored on the body surface, exhibit local peaks, and the largest one correctly reveals the source location. Smaller side lobe peaks result from reflections and incomplete coverage by small number of transducers. At the focal time, a strong maximum occurs at the source location corresponding to the original pulse source signal. After the focus, the incoming waves pass through each other, propagating outward.

AE signal $u(r, t)$ recorded by a transducer placed at the distance r outside the source at r_0 can be in forward propagation generally considered as a convolution of the source function $s(r_0, t_0)$ with the Green's function $G(r, r_0; t, t_0)$, which represents wave transfer between the source and a receiver:

$$u(r, t) = G(r, r_0; t, t_0) * s(r_0, t_0). \quad (1)$$

Another convolution with transfer functions of device and transmitting and receiving transducers is omitted in (1). TR operation is described as a transform $t \rightarrow T - t$, where T is duration of TR signal, and a new source function $w(t)$ can be expressed as proportional to the TR source [23]:

$$w(t) = G(t) * u(T - t) = G(t) * G(T - t) * s(T - t) \approx s(T - t), \quad (2)$$

where we suppose approximation $G(t) * G(T - t) \approx \delta(t)$ (Dirac's function) as both signal directions are equivalent. The fact that resulting signal represents time reversed reconstruction of the original source function in its position at focal time T is very important for AE source location and further analysis. So we can use TR as a robust procedure for localization also in a case with external noise created by other sources. Precise time alignment of TR signals returned from receivers randomly dispersed around a point-like pulse source can illustrate principle of TR-based source location [19]. If three signals are detected by various transducers in times t_1, t_2, t_3 , after their TR are rebroadcast to the source with delays $\Delta t_1, \Delta t_2, \Delta t_3$. As $\Delta t_1 + t_1 = t$, $\Delta t_2 + t_2 = t$, and $\Delta t_3 + t_3 = t$, all three TR signals are coming to the source synchronously with the same delay t , and any small deviation from the original source location or changes in the structure and/or receiver positions impairs their alignment [20, 24].

3. SOURCE LOCATION EXPERIMENTS

3.1 Simulated leakage noise on a steel plate

In a simpler case of burst AE (pulse) are synchronized signals maxima at the source position clearly detectable (visible) and only one receiving sensor may be used to source location with about 1 mm precision. Worse situation is in the case of continuous AE source like leakage noise, where TR localization was not yet studied as its reconstruction gives again random noise signal. Hence we performed further documented experiments showing that one sensor is not enough to reliably localize bounded noise sources and instead CCF of signals from two sensors should be used.

Source location experiments were performed on a steel plate 500x500x45 mm shown in Fig.1. Four relatively broadband small piezoelectric AE transducers DAKEL IDK 09 (9 mm diameter with 6mm contact ceramic wear plate) indicated in Fig.1 as T1 to T4 were glued to

the plate with cyanoacrylate glue. Their typical frequency response is shown right in Fig.1. On the plate are shown distances between receiving sensors and marked are also positions of artificial AE sources S1 and S2. In position S1 was placed another AE transducer as a source transmitting two different signals simulating a) continuous leakage noise, and b) pen-test AE burst. Original random noise signal (a) was recorded on a tube of diameter 160 mm and 4.5 mm wall thickness during compressed air (6 bar) leak through 0.8 mm orifice. 13ms long signal from leak detected by AE transducer was input to the arbitrary waveform generator (AWG) and emitted as a source signal at S1. Simulated leakage signal with its spectrum of approx. 200 kHz maximum is plotted in Fig.2. All signals were sampled with frequency 10 MHz by two Tie-Pie HS5 USB oscilloscopes with AWG.

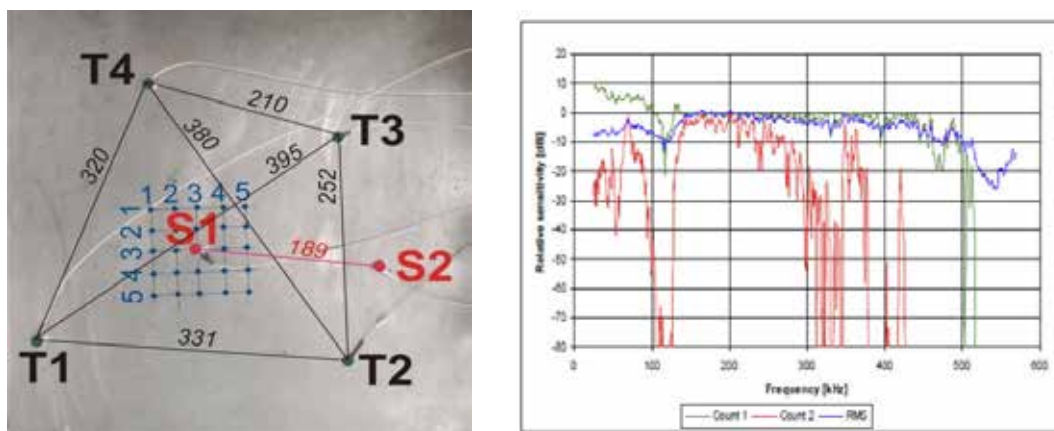


Fig. 1: Testing steel plate with marked placement of four AE transducers (T1 to T4) and artificial AE sources (S1, S2) – left. Right is frequency response of the IDK 09 transducers.

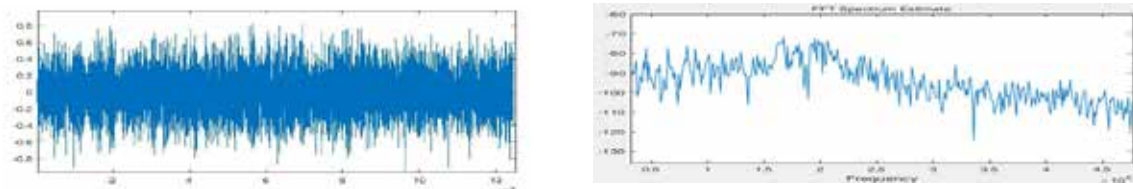


Fig. 2: Source signal of leakage noise $n(t)$ (left) and its frequency spectrum (right).

3.2 Simulated pulse location under leakage noise

Burst signal (b) simulating crack extension was recorded at pen-test on the tube surface. We don't know exactly its waveform, so as the burst AE source was used short sine-train pulse $p(t)$ of 40 μ s duration (simulated pen-test), which gives TR reconstruction similar to that of real pen-test. Simulated pen-test signal $p(t)$ was emitted by AWG as the burst source at position S1, and by synchronized second AWG was at position S2 simultaneously transmitted leakage noise $n(t)$ shown in Fig.2. Noise signal was before transmitting amplified up to four levels by power amplifier (max. amplitudes 5,10,15, and 20 V) while transmitted burst signal $p(t)$ was held on 1V max. amplitude. So the burst signal was -14 to -26 dB below the noise level. Signal mixtures were recorded by four transducers T1 to T4, then time reversed and repeatedly sent back from all transducers working in transmit mode. Transmitted TR signals were recorded by AE transducer DAKEL MDK 17 with magnetic wear plate (15 mm diameter) at 25 nodes on 25 mm mesh around the source S1 (see Fig.1) and quality of TR reconstructions was evaluated. The same position search 'scanning' was performed also in tests with localization of continuous noise source alone.

3.3 Location of two simultaneously emitting different leakage noise sources

Further localization experiments were performed with two different noises (continuous AE sources) simultaneously acting on the steel plate. The first noise $n_1(t) = n(t)$ was emitted at position S1, and other noise signal $n_2(t)$ also recorded from leakage with similar characteristics was emitted by transducer at position S2. The aim of this experiment was to verify the capability of TR procedure to localize 'leakage' AE source under extraneous random noise from other source, which is in real situations extremely difficult task. Both noise signals were emitted by two synchronized AWGs and their mixture was recorded by four transducers T1 to T4.

3.4 AE source localization on thin Al-plate with holes

Similar experiments as on the steel plate were realized also on an Al plate of dimensions 501x501x5 mm with randomly dispersed 10 circular holes of various diameters ($\varnothing 7$, $\varnothing 15$, $\varnothing 20$, and $\varnothing 30$ mm) shown in Fig. 3 (left). Both continuous and burst sources were tested. Ricker's pulse 220 kHz was used as a burst AE source, and continuous random noise $n(t)$ was applied for 'leakage' simulation. The goal of these tests was to prove real possibilities of suggested TR source location procedure on more complicated structure with highly dispersive behavior and many wave propagation obstacles. For more precise source location has been used detailed noncontact scanning with LDV (Laser Doppler Vibrometer) POLYTEC OFV-5000 with laser head OFV-505 mounted on 3D scanner STARMANS. Detailed scanning was performed on area 30x30 mm with 1.5 mm steps around the source. The experimental setup is shown right in Fig. 3. For synchronized signals generation and recording was used modular system NI-PXI and before TR operation were recorded signals amplified by power amplifier. Transmitting and receiving probes were switched by 8-channel multiplexer.

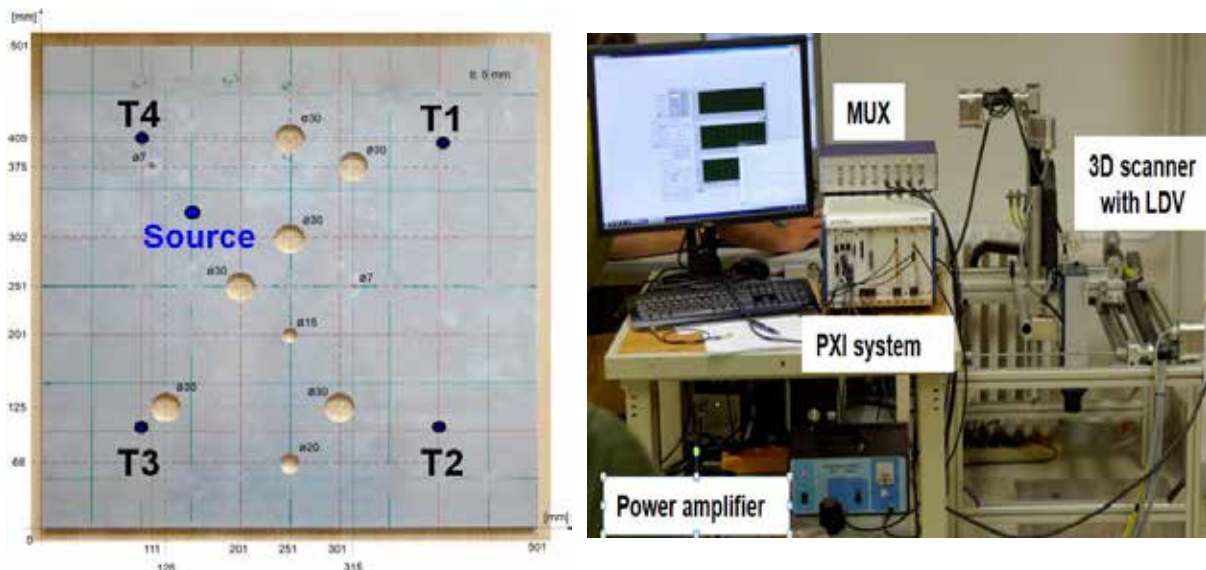


Fig.3: Left - 5 mm thin Al plate with circular holes and marked placement of four sensors T1 – T4 and Source transducer; right – experimental arrangement with scanning LDV.

4. DISCUSSION OF AE SOURCE LOCATION RESULTS

4.1 Localization of pulse buried in noise

TR localization of AE quasi-point burst signal sources always gives excellent results with precision better than wavelength and sensing transducer diameter (up to 1 mm) independently on dispersion and other influences [9]. The tests with simulated pen-tests buried in higher leakage noise originated outside the source position approved the same conclusions up to approx. -40 dB S/N ratios. Following results in Fig.4 illustrate source location capabilities of TR procedure in two cases: -14 dB and -26 dB S/N. Simulated Pen-test signals recorded by T1-T4 transducers are plotted left in part (a) of Fig. 4, mixtures of burst and noise signals (S/N = -14 dB) are in the middle, and their TR reconstructions at burst source S1 are in the right.

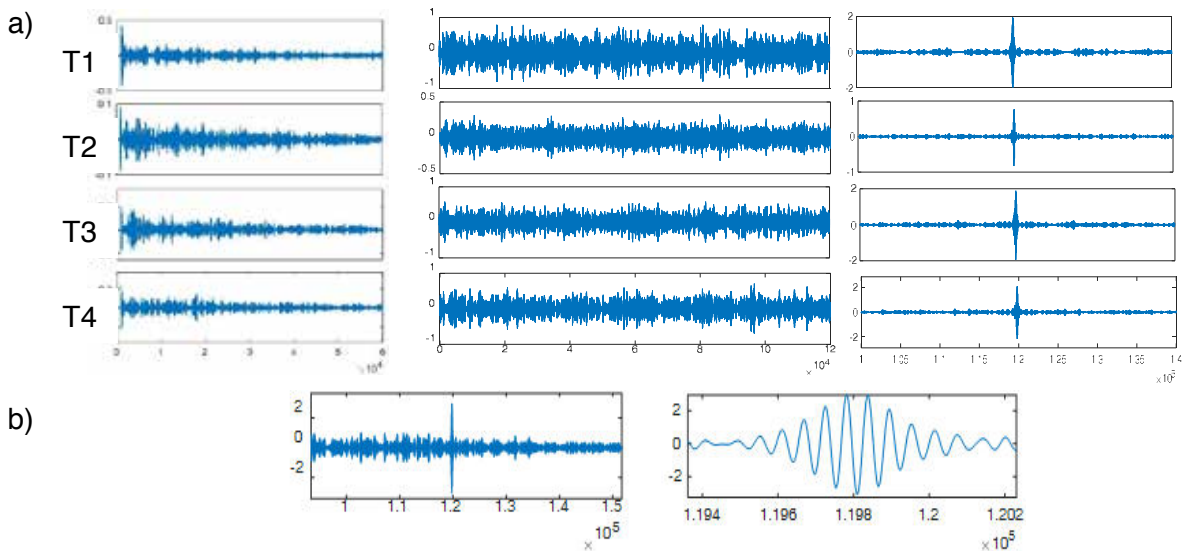


Fig 4: a). Direct burst signals of recorded 'pen-tests' by T1-T4 are plotted left, direct mixed signals under S/N = -14 dB condition are in the middle, and their TR reconstructions are right; b) Sum of reconstructions with its zoomed central part under S/N = -26 dB condition.

Part b) of Fig. 4 shows result of all four TR signals summation under S/N = -26 dB condition and the detail of the source reconstruction. TR signal reconstruction lies always just before the middle of transmitted TR data, which simplifies its search and source location over a large area. The source position is characterized by much higher absolute amplitude or RMS in the central part of recorded TR signal over other signal parts (the highest S/N). Length of the central part corresponds with double length of reconstructed source signal and can be tracked by sudden amplitude enhancement. In the first case of burst AE buried under noise by -14 dB is the TR amplitude +17 dB over noise maximum, which means +31 dB improvements due to TR operation in one channel. Further improvement by summation of all TR channels is of +1 to +3 dB better but eliminates possible faults in some channels (in our case weaker T2). TR reconstruction in the worst situation (S/N = -26 dB) resulted in +9 dB maximum at the source position over the rest, which represents +35 dB improvement, and the hidden source can be reliably located. Necessity of point-by-point searching is drawback of this method. Maximal point distance in searching grid is about 20-25 mm in our case [7] but the 'scanning' can be effectively solved as discussed later.

4.2 Precise location of continuous AE noise source on steel plate

Previous section illustrated simpler case with TR reconstruction of hidden burst AE where exactly synchronized maxima are distinctly visible and precise source location is possible using only one transducer. Location of continuous leakage source is more difficult. An estimate of source location can be accomplished by methods based on signal attenuation and/or other changes with distance from the source or by cross-correlation function (CCF) of signals from 2 or more sensors. The first approach gives only rough and unreliable data and simple CCF approach is also disputable. CCF $w(t)$ between two signals $u(t)$ and $v(t)$ is generally defined (for discrete signals) as:

$$w(n) = u(n) \star v(n) = \sum_{m=-\infty}^{\infty} u^*(m)v(n+m). \quad (3)$$

CCF is not commutative and associative as a convolution of two signals but sometimes is more convenient to compute CCF as a convolution, i.e. by multiplication of FFT spectra. Maximum of CCF indicates time delay (lag) between two similar signals. The lag for two identical signals is equal to zero and CCF maximum is used as a measure of signal waveforms similarity. Simple standardized use of CCF for determination time delays between more channels is not applicable on direct detected noise signals as it is shown in Fig. 5 for our experiments with leakage noise signal acting on the plate. Left in Fig.5 are four signals recorded by transducers T1 to T4 from the same leakage noise source $n(t)$ acting at position S1. There are 6 possibilities how to correlate 4 signals, which are denoted as C12 (CCF between signals from T1 and T2), C13, ..., C34, and to obtain 6 delays between transducers (only 3 are necessary to locate source on the plate). All CCFs are plotted in the middle of Fig. 5 (all time axes are in sample numbers, so divided by 10 gives time in ms). As all four detected signals originate from the same source, they should be similar, and CCFs maxima should indicate their time delays, redundant for standard source location. Nevertheless, when we computed corresponding lags, we got absolutely unrealistic results illustrating unreliability of standard procedures for random noise source location. Right in Fig. 5 are plotted zoomed central parts of CCFs with many peaks of slightly different amplitudes. CCF increases correspondingly to accidental peaks in recorded signals, and absolute CCF maxima are randomly distributed. The reason why recorded noise signals from the same source must not contain exactly similar segments is caused by their unknown time shift changes through the wave propagation and attenuation on the plate and also by different response characteristics of transducers.

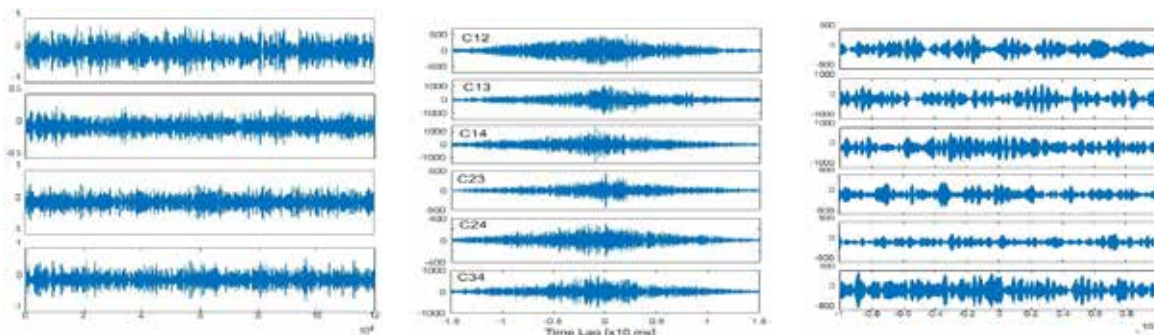


Fig.5: Direct signals from noise source at S1 detected by four transducers T1-T4 (left), six CCFs between all two-signal combinations C12, C13...C34 (middle), and their zoomed centers around zero lag (right).

The actual time delays, estimated from knowledge of transducer–source distances and measured wave propagation celerity (3.04 km/s) were very small (about 2 ms) due to small distance differences in each transducer pair (6 mm in average). In such situations are errors of source location using CCF for computing time delays inaccurate and extremely dependent on measurements precision. It is also the reason why various authors used optimized spacing of transducers. Up to now we didn't find references about TR properties in a case of long random noise signals (except TR noise suppression). Fig. 6 illustrates that one transducer TR source location in the case of continuous random noise is not applicable as there is no detectable maximum. By comparison three different TR source reconstruction positions in Fig.6 it follows that the right location of the source reconstructions cannot be easily determined neither by amplitudes nor by sharp rise near the signal middle, which occur e.g. in the TR signal coming from T3 in right part of Fig.6 at false location.

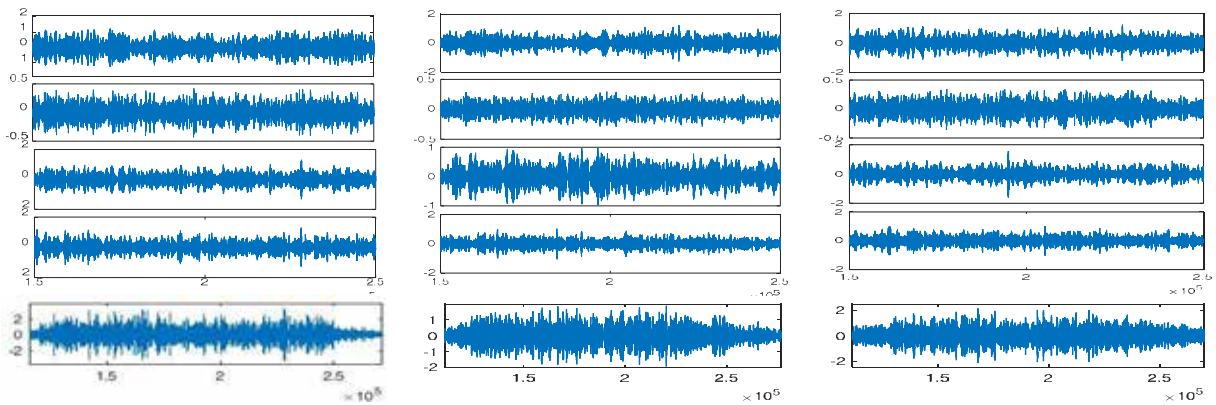


Fig.6: Comparison of TR leakage noise signals emitted by T1-T4 and reconstructed at the source position (left), at 25 mm (middle) and 50 mm (right) positions out of the source. In the bottom row are TR summations of all 4 channels.

The localizing inability of the simple TR procedure due to random character of reconstructed signals is clearly visible in Fig. 7 where are plotted TR reconstructions maxima, detected at all 25 nodal regions in the 5x5 matrix grid positions p_{ij} around the source (see Fig.1). Noise source is in 13th point (i,j=3,3) and its marked TR maxima from all emitting transducers T1-T4 are comparable or even lower than at other grid nodes. The same holds also for 'improving' TR summations plotted right in Fig.7.

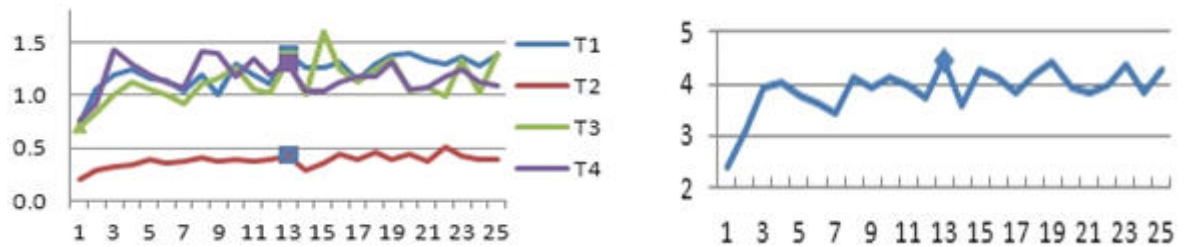


Fig. 8: Maxima of TR reconstructions at 25 nodal areas in the 5x5 mesh around the source position (13th point $p_{3,3}$). TR signals maxima emitted from T1-T4 are plotted left and maxima of their summations are plotted right.

To correct TR localization inability is suggested to use cross-correlation of TR signals from two transducers. Results for all six CCF combinations presented in Fig.8 confirm efficiency of this approach summations right.

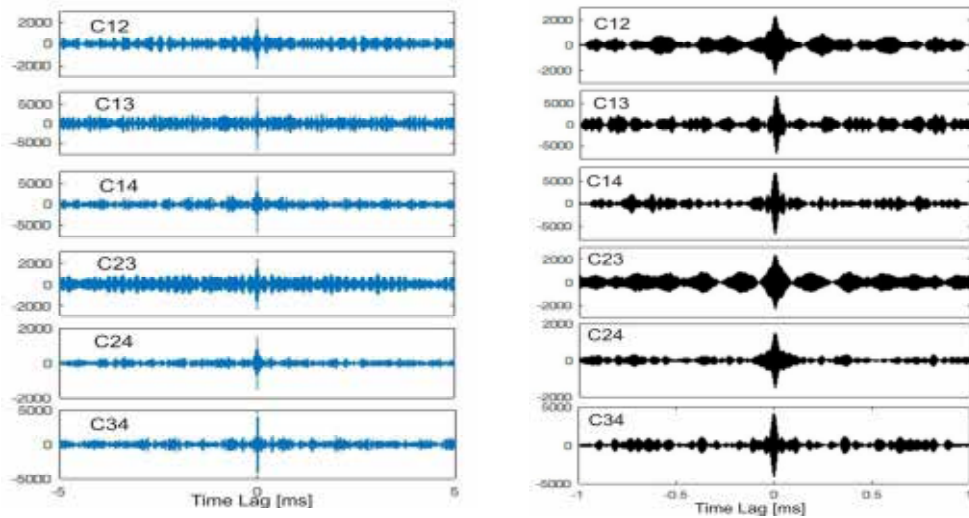


Fig. 8: Cross-correlations (CCF) of all TR signal pairs detected at the source point. Right are CCFs zoomed around zero lag.

Example results for all 25 mesh points around the source are presented in two tables:

Table 1: CCF maxima between TR signals emitted by T1 and T4 (C14_{ij}) and reconstructed at 25 nodal positions $p_{1,1}$ to $p_{5,5}$ in the 5x5 grid. Maximum at $p_{3,3}$ (noise source) is emphasized.

Table 2: Instead of maxima are similarly shown CCF34 lags (L34) representing time shifts (in 0.1 ms samples) between TR signals emitted by T3 and T4. Zero lag at the source position $p_{3,3}$ means that both TR signals are perfectly synchronized. Zero or very small lags (0.1 up to 3 ms) were determined in all CCF combinations at the source position. Lags at the source have always absolute minima compared to other mesh points and any positions out of the source. Results from Tab. 1 and 2 better surpass in 3D or color flat surface views in Fig. 9.

Table 1: C14 maxima at grid nodes.

C14	1	2	3	4	5
1	564	2196	2059	1934	2063
2	1837	2079	2050	1886	1767
3	1871	3354	6935	2800	3233
4	2360	2776	2006	2817	2605
5	1557	2031	1880	2627	2411

Table 2: C34 lags (L34) at nodal points (in 0.1 μs)

L34	1	2	3	4	5
1	18495	1246	12549	-18153	36233
2	-5367	7039	13753	6192	-25971
3	12603	27792	0	-23002	13907
4	-3058	17470	1063	12419	22331
5	-2349	8859	31094	-6203	29195

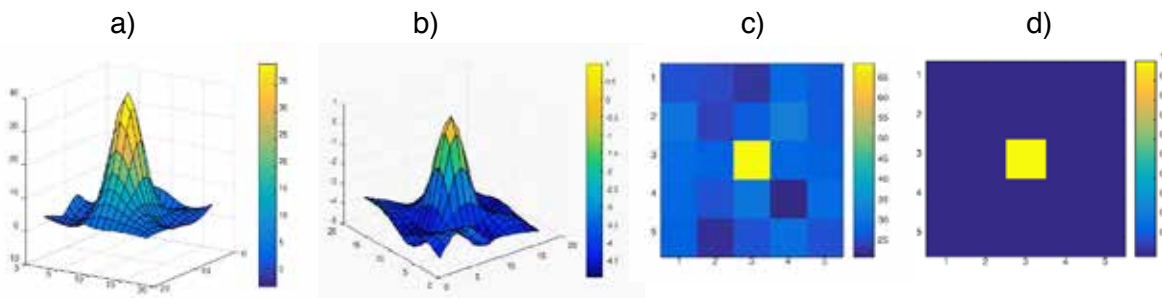
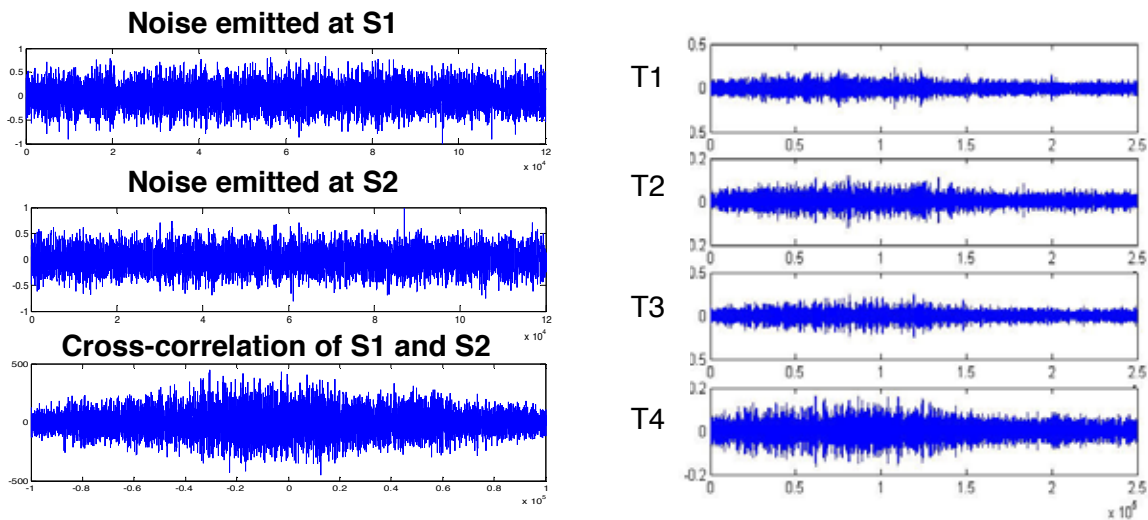


Fig. 9: 3D and flat surface mapping of resulting values detected in 5x5 mesh around the source location: a) C14 Cross Correlation Coefficients (in %), b) negative logarithms of L34 absolute lag values (both 3D pictures are 2nd order cubic interpolated), c) flat color map projections of C13 correlation coefficients without interpolation, d) L34 reciprocal time lag minima values.

Reliable source recognition better than CCF maxima in Table 1, and further enhanced S/N ratio over the rest of the plate enable normalized Pierson's cross-correlation coefficients plotted in % values in Fig.9 a). Fig. 9 b) shows interpolated 3D representation of negative absolute values of lag logarithms from Tab.2 ($-\log(\text{abs } L_{34})$). In part c) is a color map of Table 1 (without interpolation), and in part d) are reciprocal values of L_{34} lags from Tab.2 ($1/(\text{abs } L_{34})$). Zero lags at the source were replaced by one (i.e.100 ns). All six CCF combinations exhibit sharp maxima of CCFs and their coefficients at the source position (30% in average), which means average separation +20 dB, and +28 dB is average separation of reciprocal absolute minima lag values (max. 3 ms) overall other points on the plate. CCFs maxima with their lag minima together indicate the precise source location.

4.3 Location of two simultaneously emitting noise sources on the steel plate

Next example illustrates the ability of TR localization procedure to recognize and locate two independent uncorrelated 'leakage' noise sources simultaneously acting at different places on the steel plate. Fig. 10 left shows two noise signals emitted at sources S1 and S2 and their cross-correlation function. In the right part of Fig. 10 are mixtures of both signals recorded by transducers T1 to T4.



*Fig. 10: Left – noises emitted at S1 and S2, and their cross-correlation.
 Right – mixed signals recorded by transducers T1 to T4.*

Mixing of both signals may be also interpreted as 'leakage' signal buried in extraneous noise. TR reconstructions of mixed signals from both sources are plotted for all four transducers in Fig. 11. Left are TR reconstructions at the source S1, in the middle at the source S2, and right are plotted for a comparison TR reconstructions detected at the mesh node $p_{1,1}$ outside of both sources. From these plots is clear that the localization of sources based on TR signals reconstructions from only one transducer is not possible. In Fig.12 is documented TR separation of both signals located at their 189 mm distant sources with help of TR reconstruction cross-correlations (CCF) from two transducers. Left are six CCFs of reconstructions at the source S1, in the middle at the source S2, and right are CCFs out of sources. Resulting CCFs from two transducers show positions of both sources reliably by CCF maxima at near zero lags. More quickly can be results obtained by comparing maxima

of normalized cross-correlation functions, but it is less reliable when CCF maximum is not precisely at zero lag.

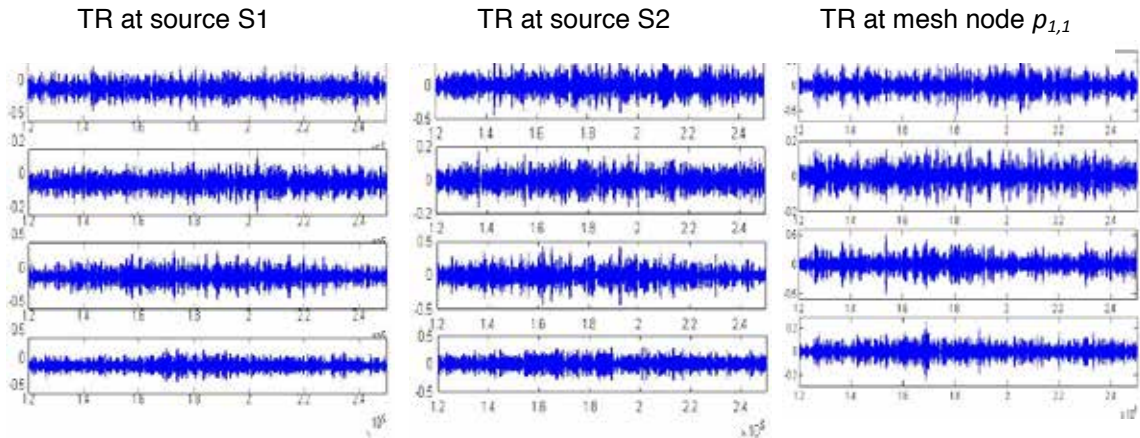


Fig. 11: TR reconstructions at the source S1, in the middle at the source S2, and right are plotted for a comparison TR reconstructions detected at the mesh node $p_{1,1}$ outside of both sources.

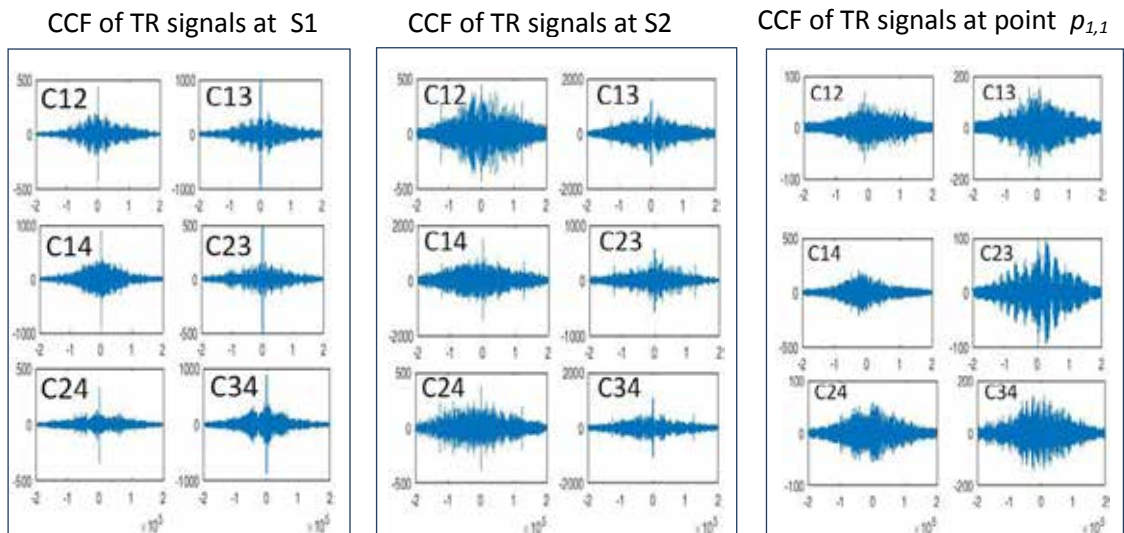


Fig. 12: Separation and localization of two noise sources at S1 and S2 using cross-correlation of TR reconstructions from 2 transducers.

4.4 AE source location on thin Al-plate with holes

The 5 mm thick Al sheet with ten circular holes of various diameters represents a more complicated structure for precise AE source location tasks than previously tested steel plate of similar planar dimensions. Two main reasons make those tasks difficult: 1. Strong wave dispersion effects and 2. Geometrical discontinuity substantially complicates wave-paths between the AE sources and sensing transducers, which holds also for TR backpropagation. It is well known that each wave reflecting obstacle can enhance TR reconstruction as virtual transducer [22], which supports the use of TR localization procedure. Nevertheless, there was a challenge to verify how precise will be source location under such conditions when standard localization methods are mostly unreliable. Both burst and continuous AE sources were tested on that plate. The Ricker's pulse 220 kHz was used as a burst, and simulated

leak $n(t)$ as a continuous source. As an example, Fig. 13 illustrates TR reconstruction capability of burst signal from T1 at the source (left) and at the plate corner (right).



Fig. 13: TR reconstruction of the burst signal from T1 at the source (left) and at the plate corner (right).

Maxima of TR reconstructions from all four transducers T1 to T4 in the region 30x30 mm around the source are shown in Fig. 14. Remarkable are concentric circles around the source representing lower maximal amplitudes of reconstruction, which are related to the wavelength distance. Fig.15 shows distribution of maximal amplitudes along horizontal sections of flat projections in Fig.14. Even more reliable localization results may be obtained using cross-correlations of TR reconstructions from two transducers how illustrates Fig. 16. They are also necessary for location of continuous AE sources.

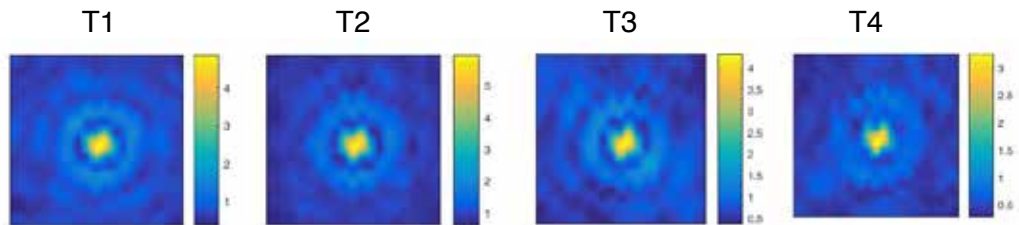


Fig.14: Distribution of TR reconstructions maxima from transducers T1 to T4 in the region 30x30 mm around the source (cubic interpolation).

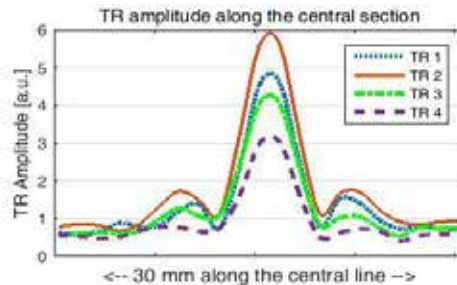


Fig. 15: Distribution of maximal amplitudes along horizontal sections of flat projections in Fig. 15.

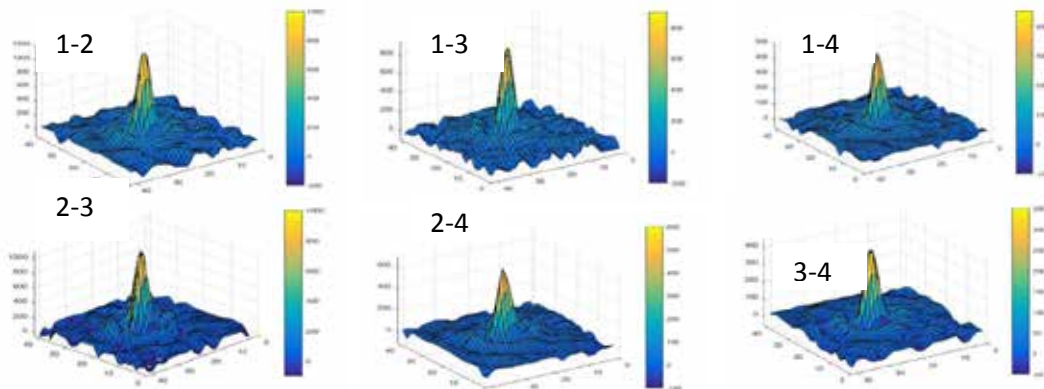


Fig. 16: Cross-correlations of TR reconstructions of burst signals from two transducers.

Similar results as in previous sections were obtained on Al plate with holes also for continuous AE source emitting signal $n(t)$. Fig. 17 shows distribution of TR reconstruction maxima of the noise source from individual transducers. It is evident from this figure that only one transducer cannot be used to random noise source location. Against that, cross-correlations of two TR reconstructions again allow its precise location, which illustrates Fig. 18. In the part a) are compared cross-correlation functions at the source (left) and at the plate corner (right). In the part b) are 6 distributions of CCFs maxima around the source.

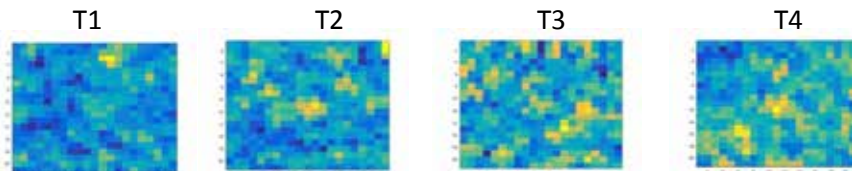


Fig. 17: Distribution of TR reconstructions maxima of the noise source from individual transducers.

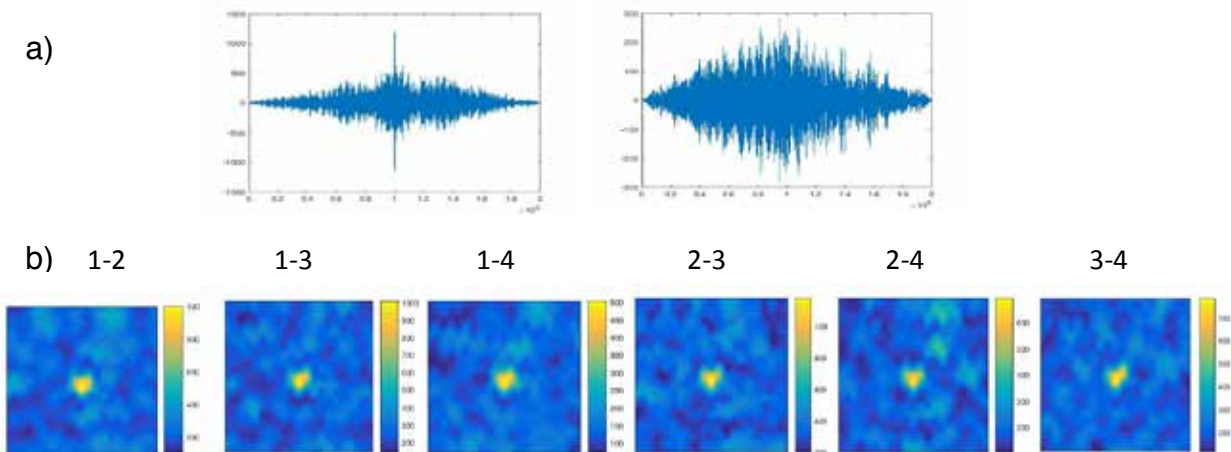


Fig. 18: a) Cross-correlations of 2 TR reconstructions at the source (left) and at the plate corner (right), b) Distributions of CCFs maxima at 30x30 mm region around the source.

CONCLUSIONS

AE source location procedures based on time reversal signal processing were tested on a steel plate using simulated burst and continuous AE sources. Compared to other techniques, the AE signal processing based on TR procedure can fetch the source location most precisely. Quasi-point sources can be reliably localized with up to 1 mm precision, which is less than the wavelength and transducer aperture. After TR, any arbitrary time segment of the signal returns to the source position, and therefore TR methods don't need any timing features. TR also eliminates problems with wave dispersion, attenuation, reflections, etc. in relatively simple way with no need of some huge computations and knowledge of structure geometry and wave celerity. Burst sources buried in out of source 'leakage' noise of higher amplitude is possible to detect and precisely localize by only one sensor up to -40 dB S/N ratio. Two sensors are necessary to localize continuous AE sources up to the same precision (about 1 mm) using cross correlation of two time-reversed signals. The same procedure can be used to separate and localize two simultaneously emitting continuous AE sources at different places. Tests with simulated both burst and continuous sources on the thin Al plate with randomly dispersed circular holes verified the same conclusions also for more complicated structures. Detailed scanning is required for localization in the region around roughly pre-localized source in the monitored structure of any geometry. Scanning can be

efficiently realized e.g. by scanning laser interferometer or by mechanical movement of air coupled transducers or other sensor arrays with the only requirements of partial covering frequency band of detected signals. Another possibility gives also reciprocal TR with structure excitation at scanning mesh points by TR signals using e.g. air coupled contactless instrument. The advantage is that the rebroadcast TR signals can be arbitrarily amplified to compensate attenuation or extraneous noise of other origin. The new potentiality has TR signals transfer from the real source onto its physical or reliable computer model, so called 'digital twin' [23] where the source is localized by numerical searching procedure, which is however limited by some restrictions more discussed in [25]. Such modelling with TR signal transfer from real structures is now performed in the frame of currently solved project.

Acknowledgement

This research was supported by the Czech Grant Agency under grant no. GACR 17-22615S, which is gratefully acknowledged.

References:

- [1] Grosse Ch. U., Ohtsu M.(eds): Acoustic Emission Testing. Basic for Research - Application in Civil Engineering, Springer-verlag, 2008.
- [2] Chlada M., Prevorovsky Z.: Expert AE Signal Arrival Detection. Int. J. Microstructure and Materials Properties, Vol. 6 (3/4), 2011, 191-205.
- [3] Kundu T.: Acoustic source localization. Ultrasonics, Vol. 54, 2014, 25–38.
- [4] Blahacek M., Chlada M., Prevorovsky Z.: Acoustic Emission Source Location Based on Signal Features. Advanced Materials Research, Vol. 13-14, 2006, 77-82.
- [5] Chlada M., Prevorovsky Z., Blahacek M.: Neural network AE source location apart from structure size and material. J. Acoustic Emission, Vol. 28(1), 2010, 99-108.
- [6] Miller R.K., ed.: NDT Handbook Vol.5: Acoustic Emission. ASNT 1987.
- [7] Ono K., Cho H., Takuma M.: The origin of continuous emissions. J. Acoustic Emission, Vol.23, 2005, 206-214.
- [8] ASTM E1211 / E1211M - 12 : Standard Practice for Leak Detection and Location Using Surface-Mounted Acoustic Emission Sensors. ASTM International, West Conshohocken, PA, 2012, www.astm.org.
- [9] ISO 18081 International Standard: Non-destructive testing - Acoustic emission testing (AT) - Leak detection by means of acoustic emission. First Edition 2016.
- [10] US patents No.: 4428236-1989; 4609994; 4858462; 8638226-2014.
- [11] Rastegaev I. A., Danyuk A. V., Vinogradov A. Yu., Merson D. L., Chugunov A. V.: Location of Noise-Like Sources of Acoustic Emissions Using the Spectral Similarity Method. Russian J. of Nondestructive Testing, Vol. 49 (10), 2013, 553–561.
- [12] Kosel T., Grabec I.: Intelligent location of two simultaneously active acoustic emission sources. Part I and II. arXiv: 07040050v1, April 2007.
- [13] Kosel T., Grabec I., Mužič P.: Location of acoustic emission sources generated by air flow. Ultrasonics 38, 2000, 824-526.
- [14] Chlada M. Prevorovsky Z.: Continuous Acoustic Emission Source Location in Material Objects. CZ Patent 305461 B6, 2015.
- [15] Wang Tao, Wang Dongying, Pei Yu, Fan Wei: Gas leak localization and detection method based on a multi-point ultrasonic sensor array with TDOA algorithm. Meas. Sci. Technol., Vol. 26, 2015, 095002, 10pp.
- [16] Xu Bian, Yu Zhang, Yibo Li, Xiaoyue Gong, Shijiu Jin: A New Method of Using Sensor Arrays for Gas Leakage Location Based on Correlation of the Time-Space Domain of Continuous Ultrasound. Sensors, Vol.15, 2015, 8266-8283; doi:10.3390/s150408266.
- [17] Yong Yan, Xiwang Cui, Miao Guo, Xiaojuan Han: Localization of a continuous CO2 leak from an isotropic flat-surface structure using acoustic emission detection and near-field

- beamforming techniques. *Meas. Sci. Technol.*, Vol.27, 115105, 2016, 9 pp.; doi:10.1088/0957-0233/27/11/115105.
- [18] Murvay P. S., Silea I.: A survey on gasleakdetection and localization techniques, *J. Loss Prevention Process Ind.*, Vol. 25, 2012, 966–973.
- [19] Prevorovsky Z., Krofta J., Chlada M., Farova Z., Kus V.: Progressive Approaches to Localization and Identification of AE Sources. 30th European Conf. on AE Testing & 7th Internat. Conf. on AE, Granada, Spain, 2012, CD Proc., www.ndt.net/EWGAE-ICAE 2012.
- [20] Prevorovsky Z., Krofta J., Chlada M., Kober J., Dos Santos S.: Time Reversal Signal Processing in Acoustic Emission. 11th European Conf. on Nondestructive Testing, Prague, 2014, ID=637, 33 pp., www.ndt.net/ECNDT 2014.
- [21] Prevorovsky Z., Kober J., Dvorakova Z., Krofta J., Chlada M.: How to analyze AE sources in complex structures more precisely. 31st Conf. "EWGAE 2014", September, 2014, Dresden, Germany, DGZfP-Proc. BB 149 - CD, paper Th.2.B.4, 34 pp, ISBN 978-3-940283-63-4.
- [22] Fink M, Cassereau D, Derode A, et al. Time-reversed acoustics. *Reports on Progress in Physycs*, Vol. 63(12), 2000, 1933–1995; doi:10.1088/0034-4885/63/12/202.
- [23] Kober J., Dvorakova Z., Prevorovsky Z., Krofta J.: Time reversal transfer: Exploring the robustness of time reversed acoustics in media with geometry perturbations. *J. Acoust. Soc. Am.*, Vol. 138 (1), 2015, EL 49- 53; Doi: 10.1121/1.4922623.
- [24] Kober J., Prevorovsky Z., Chlada M.: In situ calibration of acoustic emission transducers by time reversal method. *Sensors and Actuators*, Vol. A 240, 2016, 50–56. [Doi:10.1016/j.sna.2016.01.033](https://doi.org/10.1016/j.sna.2016.01.033)
- [25] Prevorovsky Z., Kober J.: Some factors affecting time reversal signal reconstruction. *Physics Procedia*, Vol. 2015, 00776-2, S1875-3892 (15). doi: 10.1016/j.phpro.2015.08.035.

Modelling of fiber break as Acoustic Emission Source in Single Fiber Fragmentation Test: comparison with experimental results

Zeina Hamam¹, Nathalie Godin¹, Claudio Fusco¹ and Thomas Monnier²

¹Univ Lyon, INSA de Lyon, MATEIS UMR 5510, F-69621 Villeurbanne, France.

²Univ Lyon, INSA-Lyon, LVA EA677, F-69621, Villeurbanne, France.

Abstract:

The objective of this work is to build a quantitative relationship between the fiber break as source of Acoustic Emission (AE) and the detected signal by unravelling the effect of each stage of the AE acquisition chain. For this purpose, an AE modelling is carried out using the Finite Element Method (FEM) and then the simulation is compared to experimental results of Single Fiber Fragmentation Test (SFFT). The SFFT is used in order to produce preferential fiber break. Two different types of transducer are used in order to gather information on a wider frequency bandwidth. The analysis of detected signals shows an important dependence of the frequency content of the signals on the propagation distance. For the modeling part, the entire geometry of the specimen is modelled. The sensor is taken into account by its transfer function. The FEM model is used to study the effects of different parameters on the signal such as the propagation medium, propagation distance and effect of sensors.

1. Introduction

The Acoustic Emission (AE) technique is widely used to detect failures in composite material. The different types of failures such as fiber breakage, interface debonding, matrix cracking and delamination are identified thanks to their AE signature. This signature is expressed by signal parameters called descriptors: amplitude, energy, peak frequency, frequency centroid, etc. Single-parameter analysis or pattern recognition techniques are usually used to classify signals belonging to the same type of failure [1-5]. In the most of studies that treat failures in polymer matrix composites, higher frequency and higher amplitude are assigned to fiber breaks as mode of failure and lower frequency and amplitude are assigned to matrix cracking.

Despite the effectiveness to these analysis methods, they are still considered as qualitative methods. Besides, in many cases, the results analysis cannot be generalized to other studies of composite failure [6-8]. Actually, in addition of type of failures, the AE signals depend on other parameters like type of sensor, geometry of the sample and the distance between source and sensor. All these parameters affect the signal recorded by AE system [9-12].

In the AE analysis, it is important to discern the role of the AE source from the effect of the transformations due to the propagation medium and the recording system. Based on experimental tests only, it is not easy to understand the contribution of the different parameters. However, modeling of AE using numerical methods allows us to go further and build a quantitative relationship between the EA source and the detected signal by unravelling the effect of each stage of the acquisition chain, namely the detection system and the propagation medium. In this context, in various works, AE signals are calculated by analytical approaches or by finite element simulations [13-23].

In this study, we focus on the identification of the features of fiber break from AE signals using Finite Element Method. For this purpose we use a model material consisting of an epoxy matrix containing a single brittle carbon fiber for our experimental tests and numerical simulations. The modeling of fiber breaks as AE source in polymer matrix composite material is the main

objective of this work. It presents two parts: experimental and numerical. In the experimental part, a Single Fiber Fragmentation Test (SFFT) is carried out on carbon fiber embedded in the epoxy, in order to produce preferential fiber break. Two types of resonant sensors are used. Concerning modeling parts, the entire geometry of the specimen is modelled using Finite Elements Method (FEM) by means of Abaqus software and a dynamic calculation is performed. The fiber breaks are created in different positions on the specimen. The model has been validated by comparison with experimental data. Three type of sensors are considered (point-contact and resonant sensors) in order to understand and to quantify the sensor effects on the signal waveform.

2. Description of work

2.1 Experimental Setup

The specimen is made of a single long carbon fiber T700 embedded in epoxy/amine matrix: 1,4 - Butanedioldiglycidyl ether (DGEED) / 4,4 '- Methylenebis(2-methylcyclohexylamine) (3DCM). The dimensions of the specimen are shown in **Figure 1**.

The AE monitoring is carried out by means of multiple sensors using a PCI-2 data acquisition system. In order to investigate the effects of the sensors, tensile tests are performed with two kinds of sensors (nano 30 and PicoHF sensors) located at the same position on each face of the specimen 40 mm apart. These two sensors display a good sensitivity in different frequency ranges, 200 to 900 kHz for nano 30 sensor and 500-1850 kHz for Pico HF sensor (MISTRAS Group data). In all cases, medium viscosity vacuum grease is used as coupling agent.

Each sensor is connected to a preamplifier (gain 40 dB, type 20 H) and AE signals are recorded by a PCI-2 acquisition system (MISTRAS Group). Each AE signal waveform is digitized and recorded, with a sampling rate of 2 MSPS or 5 MSPS. The acquisition threshold is set to 35 dB and the acquisition parameters are equal to 25 μ s, 50 μ s and 1000 μ s for the peak definition time (PDT), the hit definition time (HDT) and the hit lockout time (HLT). All recorded signals are filtered in the bandwidth [20 - 1200] kHz. The AE wave velocities are measured before the tests by calculating the difference in time of arrival on each sensor of several pencil lead breaks, generated at well-known positions. The velocity is found to be equal to 3500 m/s.

The SFFT is a tensile test applied on single fiber composite in axial direction, in order to create fiber breakage. Usually the debonding occurs at the same time of the fiber breaks, but in our case, because of a high interfacial strength, debonding does not occur. The SFFT is carried out using the tensile test machine (type: MTS, capacity 5 kN), at room temperature and with a deformation rate of 0.5 mm/min. The analysis of the experimental results is based on the calculation of descriptors as defined in [1, 24]. In our work, the main descriptors analyzed are amplitude, energy, frequency centroid (FC) and peak frequency (PF). Moreover, the time frequency graphs are obtained according to smoothed pseudo Wigner-Ville distribution.

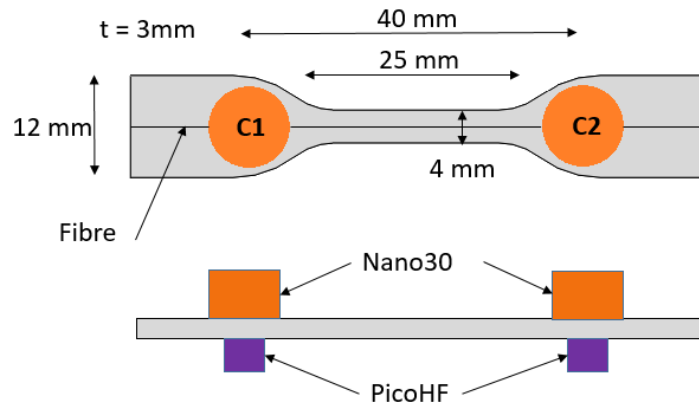


Figure 1. Dimension of specimen and sensors placement.

2.2 Numerical Setup

The single fiber fragmentation is modeled using FEM by means of Abaqus[®] software (6.14-5) with dynamic calculation. We modeled the entire geometry of the specimen: the boundary conditions are shown in **Figure 2**. The geometry is meshed using tetrahedral elements (C3D4) mainly, the element size varies between 0.01 mm and 0.2 mm and the calculation step time is 0.1 μ s. The fiber is located in the middle of the specimen.

The main properties of the material are shown in **Table 1**. Epoxy is modelled as an elastoplastic material with damping properties. The viscoelasticity of the matrix is taken into account by the Rayleigh parameters ($\alpha = 50$ and $\beta = 10^{-6}$). The fiber breakage is modelled by instantaneously separating the nodes forming fracture faces and creating a wave. During the modelling of AE signals, it was assumed that the failure process occurs without change in its rate. The numerical signals are collected on the specimen surface, at sensor positions.

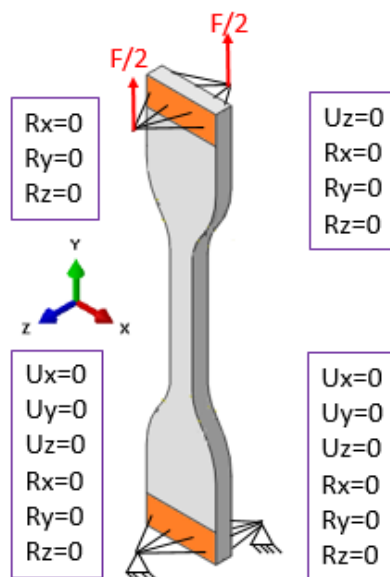


Figure 2. Scheme of the numerical specimen with the boundary conditions.

Table 1 mechanical properties of materials.

	Young Modulus (GPa)	Poisson's Ratio	Density (kg/m ³)
Carbon fiber	187	0.22	1800
DGEBD-3DCM	1.41	0.38	1034

Three types of sensor are considered in the modeling part: one point-contact sensor and two resonant sensors. The first one is considered as perfect sensor, which accurately preserves the detected signal, namely the out-of-plane velocity calculated on the node corresponding to the sensor position. The resonant sensors are taken into account by their transfer function shown in **Figure 3**, which was experimentally determined in our laboratory by the reciprocity method [25-28]. The out-of-plane velocity corresponding to the sensor surface contact is calculated then convolved with the sensor transfer function. The calculated signals then are filtered on the bandwidth [20 – 1000] kHz with a Butterworth band pass filter.

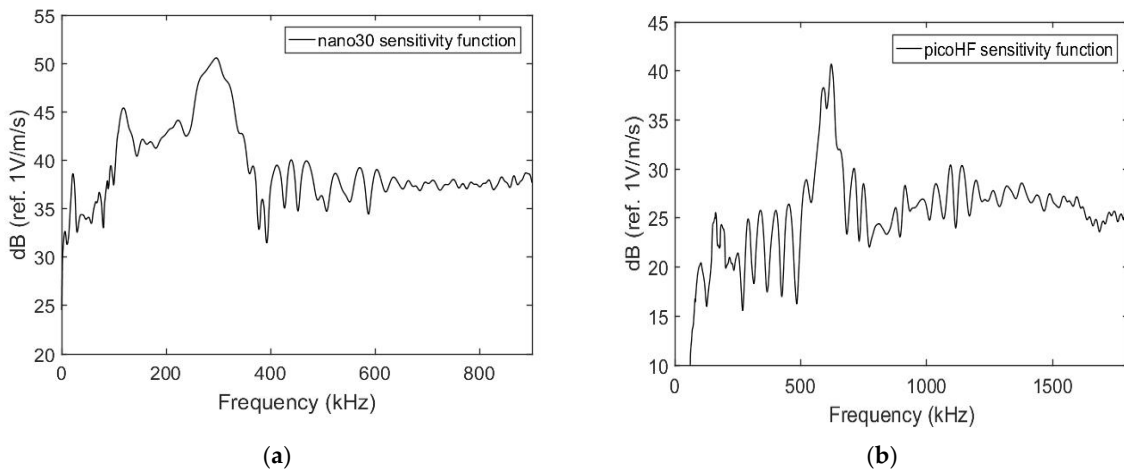


Figure 3. Transfer function of (a) nano30 and (b) picoHF, determined by reciprocity method.

3. Results and discussion

3.1 Experimental results

3.1.1 Localization of AE Sources

After waveform acquisition during SFFT, the source position of the signals is determined. A good agreement is found between the number of localized sources detected by AE and fiber breakage observed by means of transmission optical microscope (**Figure 4**). Therefore, in our tests, all located sources are ascribed to fiber breaks. In **Figure 5**, the cumulative number of localized signals are presented for the types of sensors used in our tests. The sensors have localized exactly the same sources. So, both are suitable for this test.

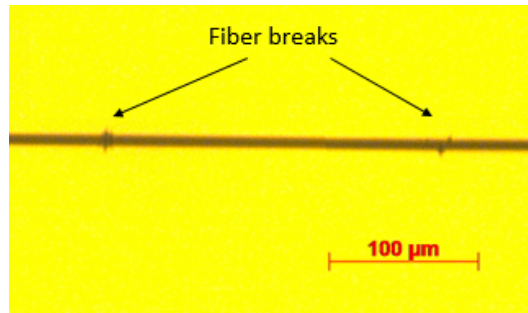


Figure 4. Fiber breaks as observed by optical microscopy.

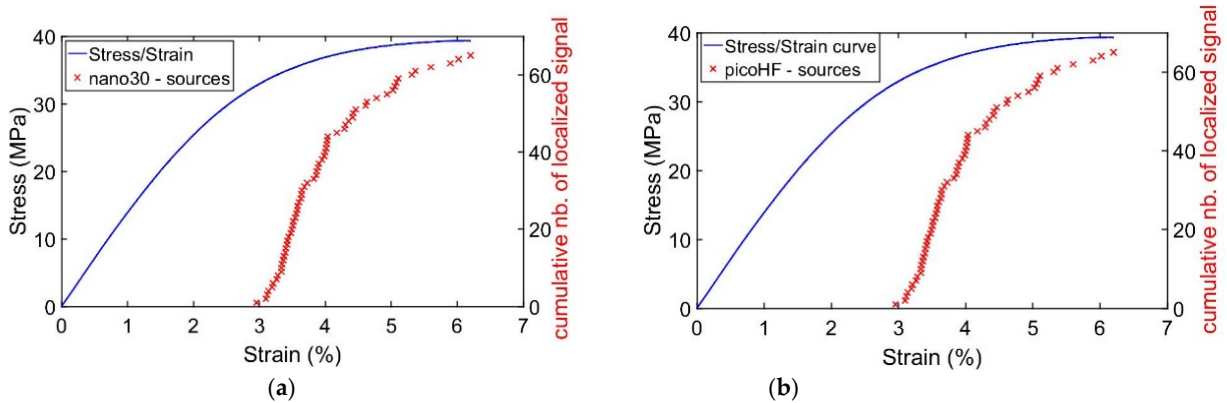


Figure 5. Cumulative localized signal during SFFT: (a) sources located by nano30; (b) by picoHF.

3.1.2 Effect of propagation distance

The calculation of descriptors shows a clear dependence on distance between the position of the source (fiber breaks) and the sensor. **Table 2** shows a summary of some descriptors for two tests. The values presented show essentially three points: the tests are reproducible, the type of sensors and the position of the AE sources affect substantially the descriptors.

Figure 6 and **Figure 7** show the evolution of temporal and frequency descriptors with the distance source/sensor. Each point on the graphs corresponds to a detected signal. The amplitude, calculated in dB, varies linearly with distance and it loses 25 dB between the nearest and the furthest fiber break. The energy decreases drastically with distance. The frequency centroid decreases linearly for 25 mm of propagation distance: from 300 kHz to 150 kHz with nano30 sensor and from 600 kHz to 200 kHz with picoHF sensor. The peak frequency takes two main values; the higher is equivalent to the resonant frequency of the sensor.

Figure 8 shows the time-frequency maps calculated with smoothed pseudo Wigner-Ville distribution for signals ascribed to fiber breaks for four positions (**Figure 10-b**). For fiber breaks close to the sensors, the content of high frequency disappears progressively when the sources are located farther away.

The frequency content of signals varies significantly with propagation distance. Some signals have only low frequency content. Due to this dependence, these results cannot allow to define an acoustic signature of fiber breakage based on frequency content.

Table 2 Descriptors calculated for two SFFT (denoted AF02 and AF03)

Descriptors	nano30				picoHF			
	Near to Sensor		Far from Sensor		Near to Sensor		Far from Sensor	
	AF02	AF03	AF02	AF03	AF02	AF03	AF02	AF03
Energy (attoJ)	2332	320	260	15.8	107	55.1	8.4	5.2
Amplitude (dB)	66.4	64	53.7	48.6	60.8	57.2	43.7	41.2
Frequency Centroid (kHz)	253	259	162	168	455	536	157	189
Peak Frequency (kHz)	251	260	70	53	351	256	50	40

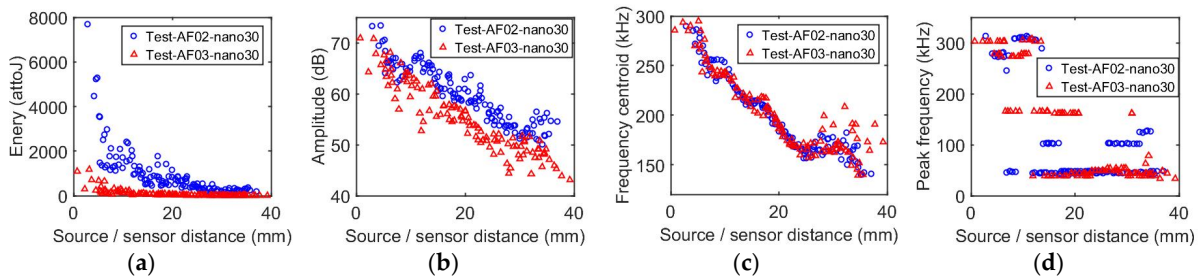


Figure 6. Temporal descriptors vs. source/sensor distance for signals detected by nano30 sensors: (a) energy in attoJ, (b) amplitude in dB, (c) frequency centroid in kHz and (d) peak frequency in kHz.

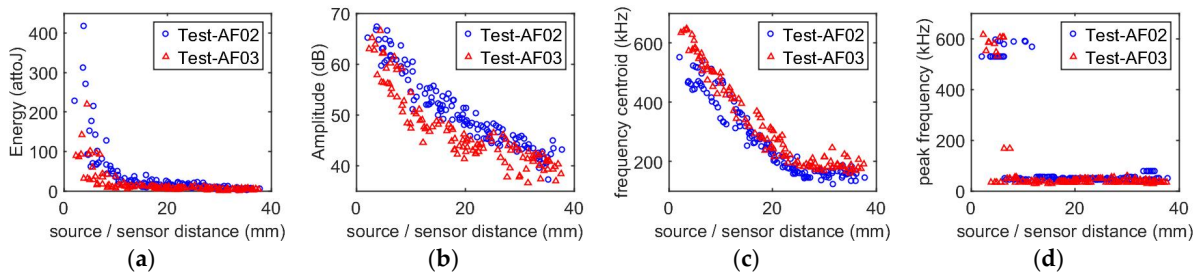


Figure 7. Temporal descriptors vs. source/sensor distance for signals detected by picoHF sensors: (a) energy in attoJ, (b) amplitude in dB, (c) frequency centroid in kHz and (d) peak frequency in kHz.

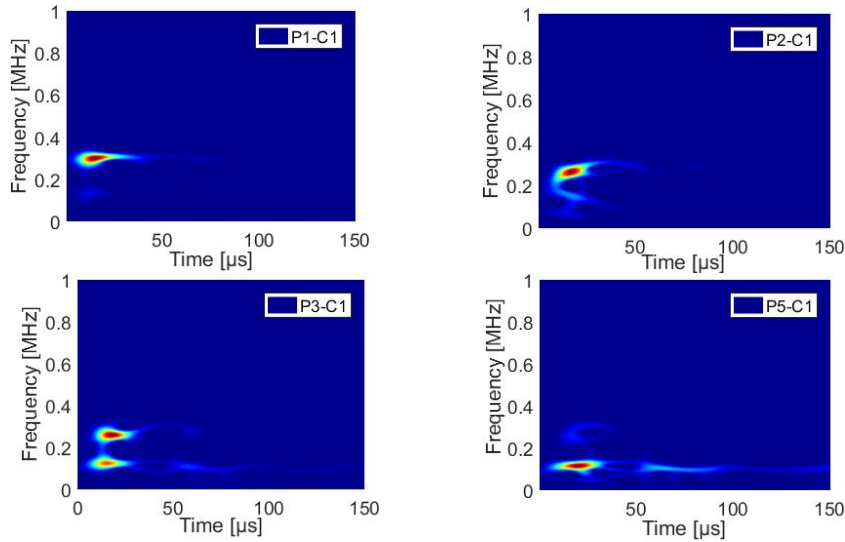


Figure 8. Time-frequency results for four source positions for signals recorded on sensor denoted C1 (P1 is the nearest position and P5 the farthest position from the sensor)

3.1.3 Effect of Sensor Type: Comparison signals of PicoHF and Nano30

The nano30 is very sensitive around 300 kHz and does not detect high frequency as from 500 kHz. However, the picoHF is very responsive around 600 kHz and detects high frequencies. In Figure 9, we compare two signals in the temporal and frequency domain, stemmed from the same source and detected by nano30 and picoHF sensors. These two sensors are equidistant from the source. Having a coefficient of correlation of 25% in the frequency domain, it is clear that those different sensors do not detect the same information, especially beyond 200 kHz. Therefore, they give certainly complementary information about the source.

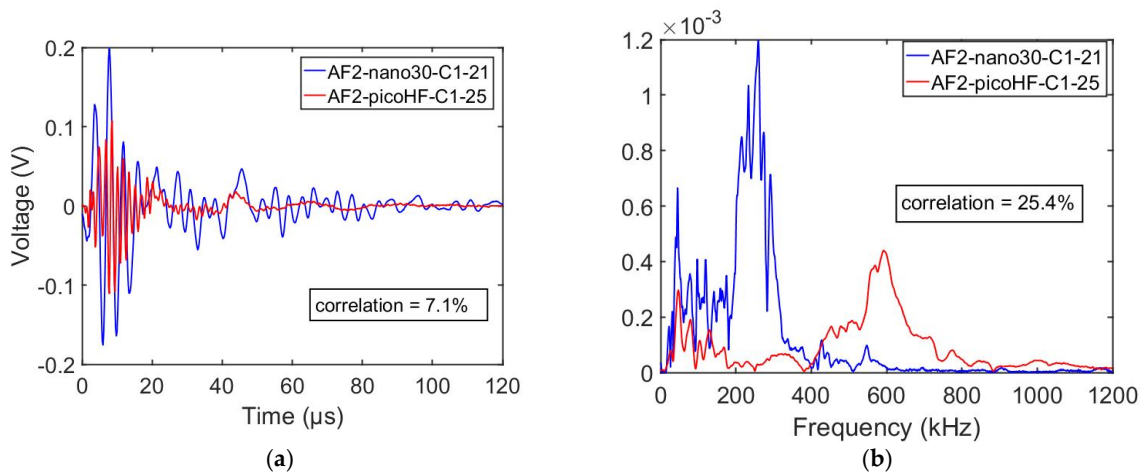


Figure 9. Temporal signals (a) and frequency spectra (b) for two types of sensors.

3.2 Simulation results

In this part, five fiber breaks are modeled at five different positions (denoted P_i) shown in the **Figure 10**. Each break is simulated for 150 μs , which is sufficient to attenuate the signal. Three different cases corresponding to three different types of sensor are considered: a perfect point-contact sensor and 2 cylindrical resonant sensors.

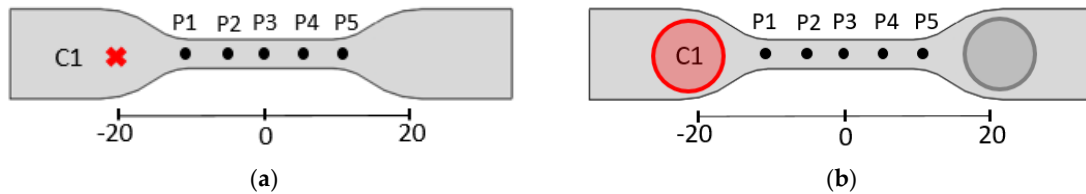
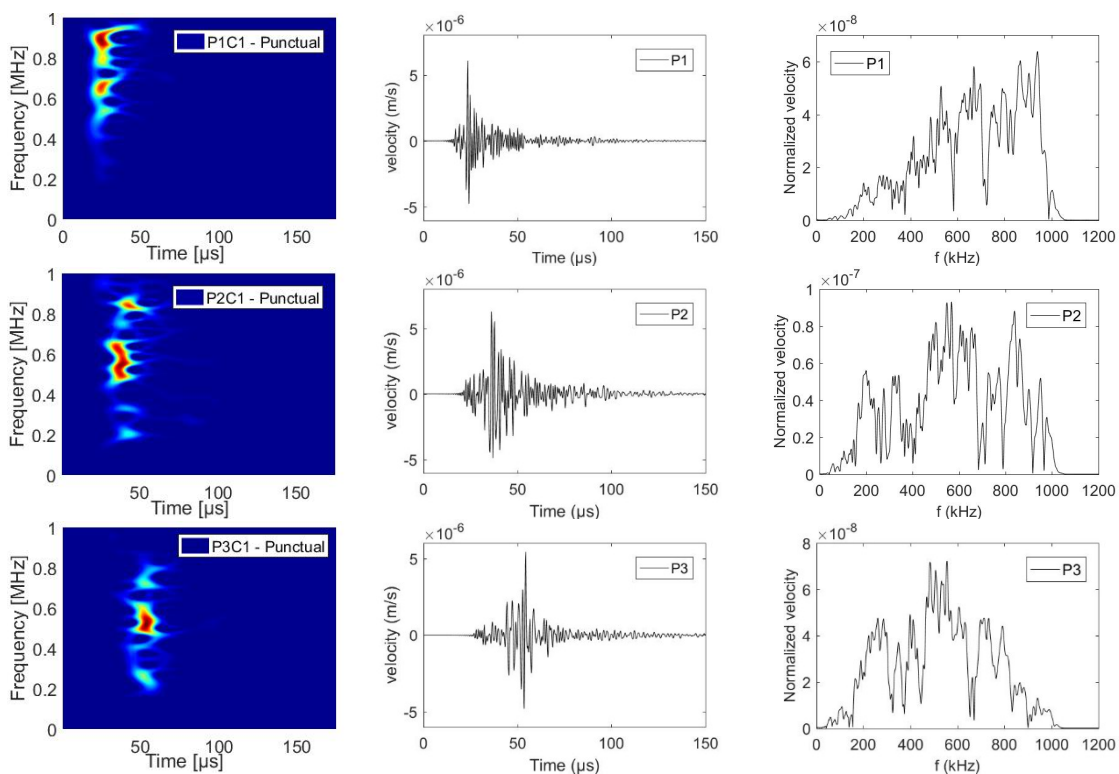


Figure 10. Position of fiber breaks and sensors: (a) point-contact sensor; (b) cylindrical sensor

3.2.1 Perfect point-contact sensor

In the model, the signal detected by perfect point-contact sensor, is the out of plane velocity of the node at sensor position (**Figure 10-a**). The advantage of studying this kind of sensor is that the signal is not altered by the sensitivity of the sensor or its aperture effect of the surface contact.

Figure 11 shows the time-frequency transforms, their corresponding signals and spectra for the five fiber breaks ($P1$ to $P5$). The frequency content of the signals is dominated by high frequency but it decreases farther away from the source.



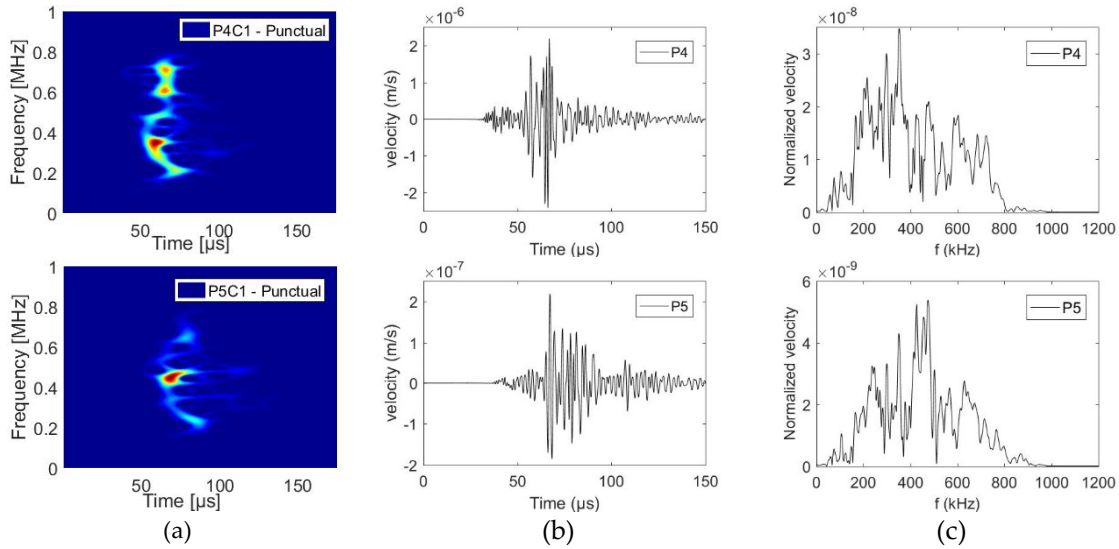


Figure 11. Results of point-contact sensor for five different fiber breaks: (a) Time-frequency graphs; (b) temporal signals; (c) signals in frequency domain

In order to better understand the evolution of AE signals with distance, the descriptors are calculated. For one fiber break, signals are calculated at nodes on the red line of **Figure 12**. It is equivalent to different sensor positions, therefore, different distance source / sensor. The descriptor curves are shown in **Figure 13**. As a first observation, there is a similarity between the decrease of experimental curves (**Figure 6 – Figure 7**) and the numerical curves, especially for energy, amplitude and frequency centroid. The main difference is the range of frequency content; for point-contact sensor, the frequency content is significantly higher (> 500 kHz) comparing to signals detected by resonant sensors (<600 kHz).

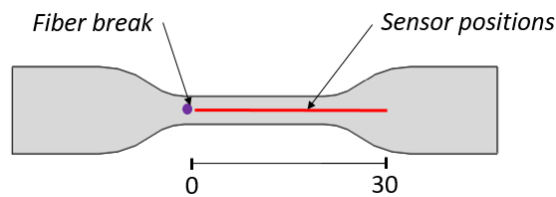


Figure 12. One fiber break and all point-contact sensor positions

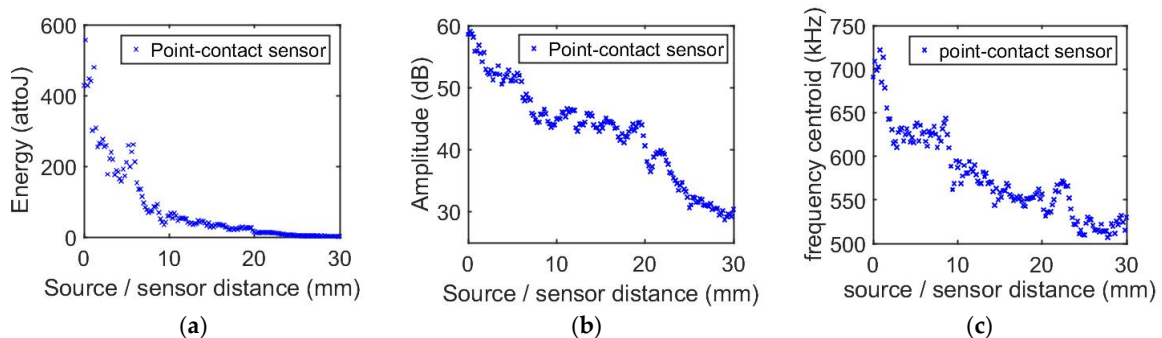


Figure 13. Model: descriptors vs. source/sensor distance for signals detected by perfect point-contact sensors: (a) energy in attoJ, (b) amplitude in dB, (c) frequency centroid in kHz

The following part is devoted to study signals detected by resonant sensors to better understand how sensors affect signals.

3.2.2 Cylindrical resonant sensors

The sensors are taken into account by their sensitivity function (**Figure 3**) by this equation:

$$V_{sensor}(\omega) = V_{surface}(\omega) \times S_{sensor}(\omega) \quad (1)$$

Where V_{sensor} is the velocity calculated by considering the effect of the sensor, $V_{surface}(\omega)$ is the average of out of plane velocity on the surface and $S_{sensor}(\omega)$ is the sensitivity function. The average of surface velocity $V_{surface}(\omega)$ is firstly calculated and compared to the velocity determined at the center of the surface. The results are presented in dB in **Figure 14** for two different sensor radii ($R_{nano30} = 3.6 \text{ mm}$ and $R_{picoHF} = 2.3 \text{ mm}$) and for two positions of fiber breaks, the nearest (P1) and the farthest (P5) from the sensor. This figure shows that the surface average of the velocity, without considering the sensor sensitivity, causes some information loss, especially in the high frequency part. For the fiber break at P1, the point contact sensor shows that the peak frequency is around 900 kHz but for the surface contact sensor the peak frequency is much lower (380 kHz).

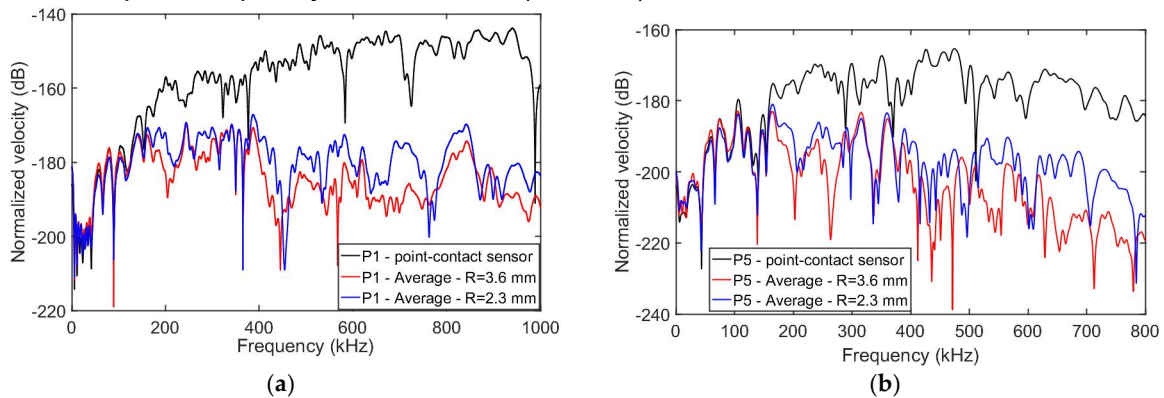


Figure 14. Velocities spectra for fiber break waves for 3 simulated cases: point-contact sensor velocity, velocity average on circular surface with 2 different radii ($R_{nano30} = 3.6$ and $R_{picoHF} = 2.3$): (a) fiber break position P1, (b) fiber break position P5

3.2.3 Comparison Numerical and Experimental Results

In this part, we calculated signals with sensor effects according to Equation (1) for the two types of sensors (nano30 and picoHF). Then, the simulated and experimental signals are compared. This comparison is carried out for signals of five fiber breaks at different positions, collected at sensor C1 position (**Figure 10-b**). The spectra are shown in **Figure 15-a** for nano30 sensor and **Figure 15-b** for picoHF. A good agreement is observed between the simulation and the experiment results despite neglecting some parameters in the calculation such as the coupling.

The descriptors corresponding to signals with nano30 sensor are calculated for 22 mm of propagation distance. The results are presented in **Figure 16**. Similarities are observed between numerical results and experimental results (**Figure 6**). The energy decreases exponentially, the amplitude loses 23 dB, the frequency centroid is higher but the rate of decrease is close to the experimental results and the peak frequency is close too. The latter corresponds to the resonance frequency of the nano30 sensor.

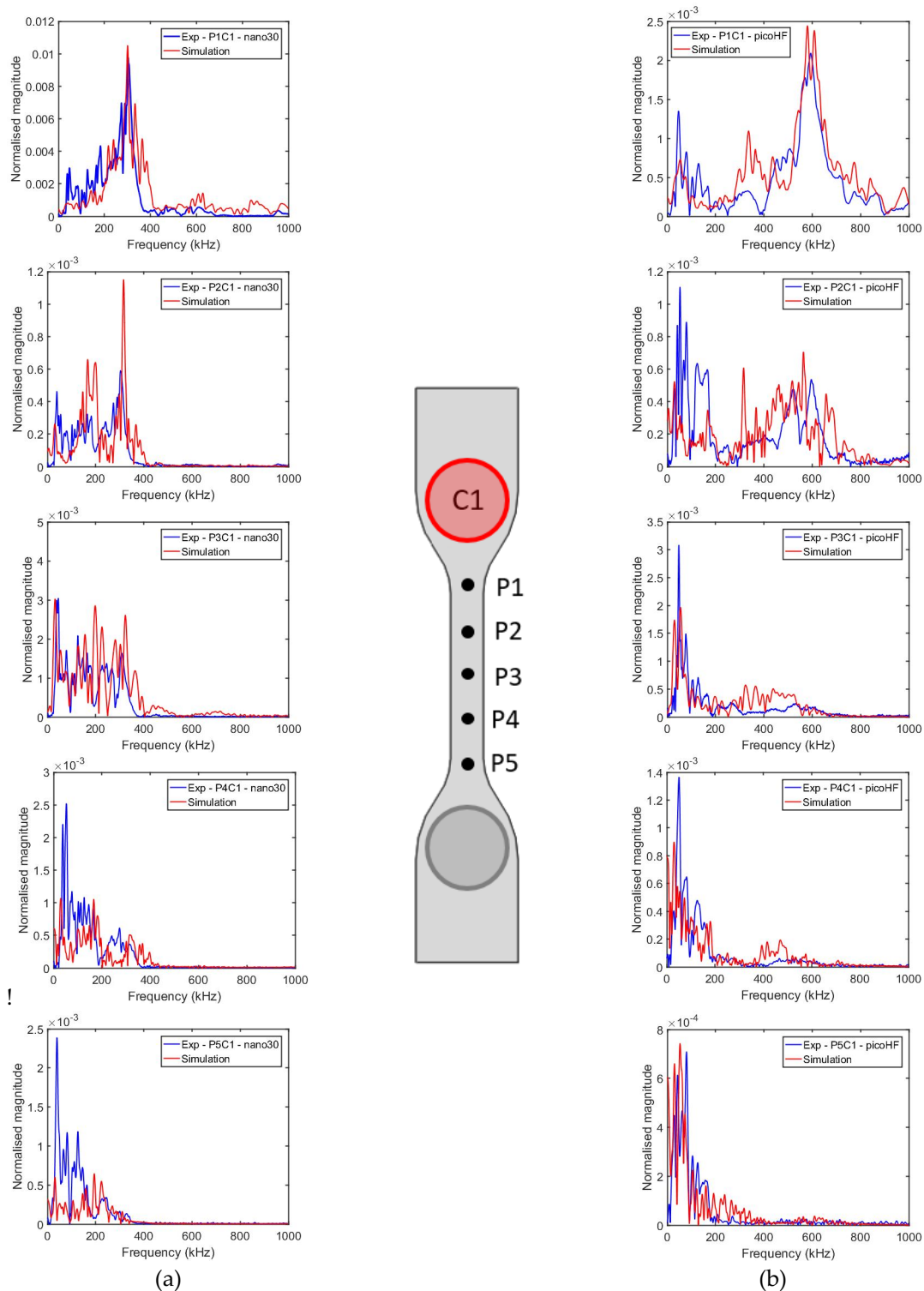


Figure 15. Comparison experimental / simulations results for 5 fiber breaks (a) results with nano30 sensor; (b) results with picoHF sensor.

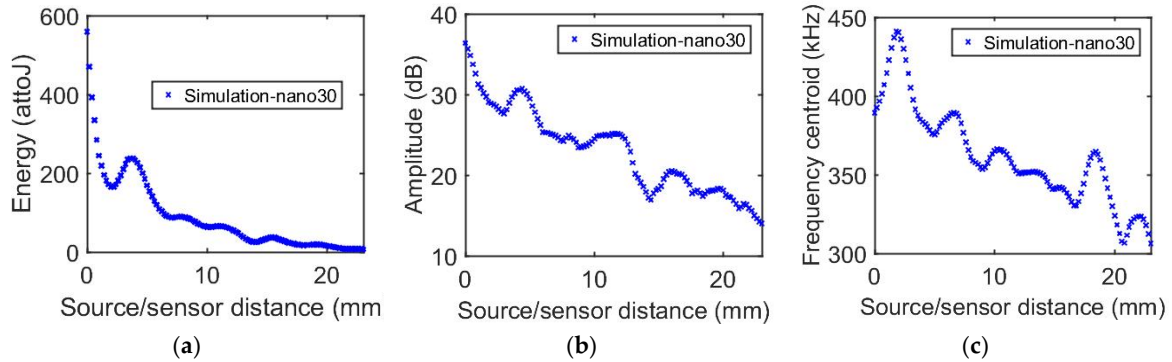


Figure 16. Model: descriptors vs. source/sensor distance for signals simulated with nano30 sensors: (a) energy in attoJ, (b) amplitude in dB, (c) frequency centroid in kHz.

4. Conclusion

The objective of this work is to build a quantitative relationship between the fiber break as source of Acoustic Emission and the detected signal by unravelling the effect of the different stages of the AE acquisition chain. Concerning experimental results, the calculation of classical descriptors does not give steady characteristics of this mode of failure. They are very dependent on the propagation distance. Their dependence is mainly due to the damping characteristic of material. The two type of sensors used in the tests detect the waves of the same sources. However, they do not give the same information. Both sensors detect low frequency (until 200 kHz) but for higher frequency, each sensor detects according to its sensitivity.

The advantage of simulating perfect point-contact sensor is to get signals not altered by the sensor effects. Therefore, the frequency content proves that the fiber breaks release waves with very high frequency content in single fiber composite specimen. Contrary to signals recorded by cylindrical sensor, the frequency reached with this type of sensor, for remotes sources, is still considered as high frequency.

The simulation results taking into account cylindrical resonant sensors show a good agreement with experimental results, highlighting the effect of propagation distance and the way that the sensor alters the detected signal. The results of this contribution highlight the limitations of the conventional source identification procedures. Modeling approaches that simulate "primitive" AE sources can be useful for (1) optimizing sensor selection and placement, (2) quantifying the wave propagation effects (3) generate training data for machine learning algorithms. With the numerical approach, it may be possible to enlarge a training set.

References:

- [1] Godin N., Reynaud P. and Fantozzi G., Acoustic Emission and Durability of Composite Materials, John Wiley & Sons, 2018.
- [2] Anastassopoulos A. and Philippidis T., Clustering methodology for the evaluation of acoustic emission from composites, Journal of Acoustic Emission, vol. 13, pp. 11-12, 1995.

- [3] Sause M., In situ monitoring of fiber-reinforced composites: Theory, basic concepts, methods, and applications. Springer series in materials science 242, 2016.
- [4] Huguet S., Godin N., Gaertner R., Salmon L. and Villard D., Use of acoustic emission to identify damage modes in glass fibre reinforced polyester, *Composites Science and Technology*, vol. 62, no. 10, pp. 1433-1444, 2002.
- [5] Gutkin R., Green C., Vangrattanachai S., Pinho S., Robinson P. and Curtis P., on acoustic emission for failure investigation in CFRP: Pattern recognition and peak frequency analyses, *Mechanical Systems and Signal Processing*, vol. 25, n° 14, pp. 1393-1407, 2011.
- [6] Oz F. E., Ersoy N. and Lomov S. V., Do high frequency acoustic emission events always represent fibre failure in CFRP laminates?, *Composites Part A: Applied Science and Manufacturing*, vol. 103, pp. 230-235, 2017.
- [7] Maillet E., Morscher G. N., Pujar V. V. and Lemanski J. R., Feasibility and limitations of damage identification in composite materials using acoustic emission, *Composites Part A: Applied Science and Manufacturing*, vol. 75, pp. 77-83, 2015.
- [8] Godin N., Reynaud P., Fantozzi G., Challenges and limitations in the identification of acoustic emission signature of damage mechanisms in composites materials. *Appl. Sci.*, 8(8), 1267, 2018
- [9] Aggelis D., Shiotani T., Papacharalampopoulos A. and Polyzos D., The influence of propagation path on elastic waves as measured by acoustic emission parameters, *Structural Health Monitoring*, vol. 11, no. 3, pp. 359-366, 2011.
- [10] Carpinteri A., Lacidogna G., Accornero F., Mpalaskas A., Matikas T. and Aggelis D., Influence of damage in the acoustic emission parameters, *Cement and Concrete Composites*, vol. 44, pp. 9-16, 2013.
- [11] Kharrat M., Placet V., Ramasso E., and Boubakar L., Influence of damage accumulation under fatigue loading on the AE-based health assessment of composite material: Wave distortion and AE-features evolution as a function of damage level. *Composites Part A: Applied Science and Manufacturing*, 109, pp. 615-627, 2018
- [12] Lhermitte T., Handley S., Holland M. and Miller J., Anisotropy of the frequency-dependent ultrasonic attenuation in unidirectional graphite/epoxy composite material, *Ultrasonics Symposium*, pp. 819-823, 1991.
- [13] Scruby C., Wadley H. and Hill J., Dynamic elastic displacements at the surface of an elastic half-space due to defect sources, *Journal of Physics D-Applied Physics*, vol. 16, pp. 1069-1083, 1983.
- [14] Ohtsu M, Ono K, A generalized theory of acoustic emission and source representations of acoustic emission. *J. acoustic Emission* 1986; 5:124-133, 1986
- [15] Giordano M., Condelli L., Nicolais L., Acoustic emission wave propagation in a viscoelastic plate, *Composites Science and Technology* 59, 1735-1743, 1999.
- [16] Sause M.G.R. and Horn S., Simulation of acoustic emission in planar carbon fiber reinforced plastic specimens, *Journal of Nondestructive Evaluation*, 29 (2), 123-142, 2010.
- [17] Hamstad M., O'Gallagher A. and Gary J., Effects of lateral plate dimensions on acoustic emission signals from dipole sources, *Journal of Acoustic Emission*, vol. 19, pp. 258-274, 2001.
- [18] Wilcox P., Lee C., Scholey J., Friswell M. I., Wisnom M. and Drinkwater B., Progress Towards a Forward Model of the Complete Acoustic Emission Process, *Advanced Materials Research* , Vols. 13-14, pp. 69-76, 2006.
- [19] Cuadra J., Vanniamparambil P., Servansky D., Bartoli I. and Kontsos A., Acoustic emission source modeling using a data-driven approach, *Journal of Sound and Vibration*, vol. 341, pp. 222-236, 2015.
- [20] Prosser W.H., Hamstad M.A., Gary J. and O'Gallagher A., Finite Element and Plate Theory Modeling of Acoustic Emission Waveforms, *Journal of Nondestructive Evaluation*, 18 (3), 83-90, 1999.
- [21] Sause M. G. and Richler S., Finite element modelling of cracks as acoustic emission sources, *Journal of nondestructive evaluation*, vol. 34, no. 1, p. 4, 2015.

- [22] Le Gall T., Godin N., Monnier T., Fusco C. and Hamam Z., Acoustic Emission modeling from the source to the detected signal: model validation and identification of relevant descriptors, *Journal of Acoustic Emission*, vol. 34, 2017.
- [23] Le Gall T., Monnier T., Fusco C., Godin N. and Hebaz S.E. , Towards quantitative acoustic emission by finite element modelling : contribution of modal analysis and identification of pertinent descriptors, *Appl. Sci.*, 8(12), 2557; 2018
- [24] Morizet N., Godin N., Tang J., Maillet E., Fregonese M. and Normand B., Classification of acoustic emission signals using wavelets and Random Forests: Application to localized corrosion, *Mechanical Systems and Signal Processing*, vol. 70, pp. 1026-1037, 2016.
- [25] Ono K., Through-Transmission Characteristics of AE Sensor Couplants, *Journal of Acoustic Emission*, vol. 34, 2017.
- [26] Goujon L. and Baboux J.-C., Behaviour of acoustic emission sensors using broadband calibration techniques, *Measurement Science and Technology*, vol. 14, no. 7, p. 903, 2003.
- [27] Monnier T., Seydou D., Godin N. and Zhang F., Primary calibration of acoustic emission sensors by the method of reciprocity, theoretical and experimental considerations, *Journal of Acoustic Emission*, vol. 30, pp. 152-166, 2012.
- [28] Hatano H. and Mori, E., Acoustic-emission transducer and its absolute calibration, *The Journal of the Acoustical Society of America*, Vol. 59, p. 344, 1976

Content

Keynotes

42 - Acoustic Emission method at the integrated structural health monitoring systems - the past, the present, the future

I. Razuvaev

86 - Acoustic Emission work over the last 10 years and relationship with Industry 4.0

M. Cherfaoui

Poster Session - Short presentation

16 - Acoustic Emission energy for condition monitoring of RC waffle slab structures subjected to bidirectional ground seismic motions

C. Abarkane, E. Suárez, F. Rescalvo, A. Benavent-Climent, A. Gallego

20 - Characterization of failure mechanisms in the wood-CFRP interface by means of Acoustic Emission during pull-off tests

F. J. Rescalvo, A. Aguilar-Aguilera, C. Abarkane, E. Suárez, A. Gallego

28 - Features of Acoustic Emission in double-walled elements of vessels pressure in the presence of cracks

I. Rastegaev, A. Chugunov

37 - Multiparametrical big data processing for Acoustic monitoring

A. Samokhvalov

44 - About new AE criteria of cracking in metal objects

I. Razuvaev, E. Suchkov

46 - Damage detection for linear pneumatic actuators using Acoustic Emission

H. Mahmoud, P. Mazal, F. Vlastic, M. Jana

47 - The parameters of Acoustic Emission signal proposed to identification of damaged and undamaged cylinders

V. Richter, H. Mahmoud, P. Mazal, V. Kratochvilova

58 - Identification of damages in composite materials during registration of Acoustic Emission signals by piezoelectric and fiber-optic sensors

O. Bashkov, I. Bashkov, A. Bryansky, T. Bashkova

62 - FEM based simulation of Acoustic Emission monitoring on oil offshore pipelines

H. Calás, J. Manuel Martin, M. Pelaez, E. Cabellos

74 - In-situ control of additive manufacturing process by Acoustic Emission

G. Perrin, J. Frechard, P. Verlet, C. Grosjean, D. Maisonnette, J. Delgado, F. Zhang

89 - Features of Acoustic Emission in double-walled elements of vessels pressure in the presence of cracks

I. Rastegaev, A. Chugunov

Monitoring in process

19 - Combination of vibration analysis & Acoustic Emission measurements to better characterize damage and mechanical behavior of aerospace high speed gear box

Y. Hebrard, A. Proust, M. Batel

79 - Advanced condition monitoring system using Acoustic Emission and vibration analysis technique

D.-H. Kim

35 - Acoustic Emission for *in situ* monitoring of laser processing

S. shevchik, T. Le Quang, B. Meylan, K. Wasmer

72 - Monitoring of stamping by Acoustic Emission (AE)

A. Saidoun, C. Hervé

Advanced composites - I

06 - Modelling of fiber break as Acoustic Emission Source in SFFT: comparison with experimental results

Z. Hamam, N. Godin, C. Fusco, T. Monnier

14 - Acoustic Emission monitoring of adhesively bonded wood joints under quasistatic and cyclic fatigue mode II flexure loads using end-notch-flexure specimens

A. J. Brunner, G. Clerc, P. Niemz

17 - Acoustic Emission analysis during bending tests of timber beams reinforced with carbon fiber composite

F. Rescalvo, C. Abarkane, E. Suárez, A. Gallego

23 - Frequency-Amplitude class of Acoustic Emission for different fracture mechanisms in C/SiC composite

D. Xiao, Y. Gao, L. Jin, F. Meng, N. Li, X. Zhou, Z. Tong, B. Jiang, T. He

24 - Mechanical behavior and Acoustic Emission technique for detecting damage in C/SiC structure

Y. Gao, L. Jin, B. Jiang, Z. Tong, D. Xiao, X. Zhou, N. Li, F. Meng

Monitoring metallic structures

27 - Study of a steel railway bridge with defects under various load conditions

M. Nowak, I. Lyasota, I. Baran

29 - Damage monitoring on a steel truck trailer using parameter-based analysis of Acoustic Emissions

J. V. Pimentel, R. Klemm, M. Dalgic, A. Irretier, K.-L. Krieger

31 - Data processing and interpretation at AE monitoring

T. Petersen, A. Samokhvalov, W. Chernigovski, D. Kurnosov

49 - Structural health monitoring using Acoustic Emission on metallic components in industrial plants

G. Lackner, H. Marihart, G. Schauritsch

51 - Acoustic Emission Testing on a rail bridge

H. Marihart, G. Lackner, M. Posch

83 - Novel AE monitoring of hydrogen induced damaged vessel and real time alarms. A case study

D. Papasalouros, K. Bollas, I. Ladis, E. Aerakis, A. Anastasopoulos, D. Kourousis

Advanced composites - II

26 - Dynamic Acoustic Emission for the Characterization of the Nonlinear Behavior of Composite Materials

X. Yu, M. Bentahar, S. Montresor, C. Mechri

55 - The influence of source depth and source-to-sensor distance on the AE signal characteristics of damaging events in thin-walled CFRP laminates

B. Kelkel, J. Vogtmann, M. Gurka

57 - Acoustic Emission behaviour on CFRP with curved fibers

Y. Mizutani, T. Ashizawa, N. Toyama, A. Todoroki

63 - Experimental investigation of the damage mechanisms in interlock reinforced composites based on AE data analysis

M. Kharrat, G. Moreau, Z. Aboura

73 - Use of AE for characterization of damage mechanisms in composite accumulator

O. Colas, C. Briançon, C. Hervé, A. Houssais

Signal Processing - Equipment and Software I

40 - Continuous recording and wireless transmission of AE waveforms by battery powered sensor nodes

K. Ito, M. Enoki

45 - Research the comparative sensitivities of fiber-optic sensors and piezoelectric sensors for detection of Acoustic Emission waves

H. Htoo Khun, O. Bashkov, V. Zaikov, R. Romashko, I. Bashkov

96 - Phased Array Modal Acoustic Emission (PA-MAE™)

B. Burks

Advanced composites - III

01 - Modal Acoustic Emission analysis of mode-I and mode-II fracture of adhesively-bonded joints

A. Crawford, M. Ghazi Droubi, N. Faisal

02 - On use of signal features for Acoustic Emission source identification in fibre-reinforced composites

M. G. R. Sause

03 - Damage diagnostic and lifetime prognosis for ceramic matrix composite with Acoustic Emission during long-term mechanical tests at intermediate temperature

N. Godin, P. Reynaud, G. Fantozzi

04 - Combination of synchrotron computed tomography and Acoustic Emission measurements for cyclic loading of fibre-reinforced composites

P. Potstada, S. Rosini, M. Mavrogordato, I. Sinclair, S. M. Spearing, M. G. R. Sause

Monitoring composites / Different applications

48 - Structural Health Monitoring of composites structures by Acoustic Emission analysis

L. Schubert, E. Schulze, R. Neubeck, B. Weihnacht

68 - Structural Health Monitoring of composite aerospace structures with Acoustic Emission

M. Lehmann, A. Bueter, O. Schwarzhaupt, C. Contell Asins

36 - Post-harvest Acoustic Emission in angiosperm leaves

S. Rosner

53 - Mechanical and Acoustic Emission characterization of lime-based masonry constituents

N. Shetty, G. Livitsanos, D. Aggelis, D. Van Hemelrijck, M. Wevers, E. Verstrynge

22 - Characterization of particle impacts using Acoustic Emission

E. Serris, L. Carrillo, A. Valentini

Material characterisation

32 - The sound of metal: Acoustic Emission during the deformation of commercially pure titanium

N. Goossens, M. Seefeldt, M. Wevers

38 - Analysis of kinking and twinning behavior in mg alloys by AE clustering method

M. Enoki, K. Tamura, T. Shiraiwa

39 - Non-threshold Acoustic Emission analysis of damage evolution in pipe segments of steel S355J2H under bending load

F. Baensch, W. Baer, P. Wossidlo, A. Habib

71 - Gallng detection by Acoustic Emission (AE) according to ASTM G98

A. Saidoun, C. Hervé, Y. Chen, T. Lesage

84 - Acoustic Emission method in nanoindentation and scratch test

R. Ctvrtlik, J. Tomastik, V. Koula, M. Drab

Corrosion

11 - AE monitoring and three-dimensional observation of stress corrosion cracking from corrosion pits

K. Wu, K. Ito, I. Shinozaki, M. Enoki

12 - Effects of media degradation on the Acoustic Emission detection

L. Calabrese, M. Galeano, E. Proverbio

18 - Application of Acoustic Emission measurements to monitor the initiation and the propagation of single or multiple Stress Corrosion Cracks (SCC)

O. Al Haj, A. Proust, J. Bolivar, M. Fregonese

64 - Acoustic Emission from gas bubble nucleation and breaking away from a flat surface

V. Kietov, M. Mandel, L. Krüger, A. Vinogradov

Pressure Vessels

05 - Lifetime tests of composite cylinders monitored by Acoustic Emission Testing

E. Duffner

69 - Application of AE technique and thermography for assessment of sludge volume inside crude oil storage tanks

I. Baran, T. Dunaj, M. Nowak

75 - New edition of GEA guideline for Acoustic Emission Testing of pressure equipments

C. Di Giulio, C. Hervé

07 - Acoustic Emission study of pressure vessels material degradation processes after long-term operation in the refinery industry

I. Lyasota, T. Ryncarz, B. Kozub

15 - Use of Acoustic Emission for inspection of various composite pressure vessels subjected to mechanical impact

F. Dahmene, O. Bardoux, S. Bittendiebel, P. Blanc-Vannet, N. Alexandre, F. Nony, M. Barcikowski, A. Maldachowska, M. Panek, P. Sheggem, A. Echtermeyer, K. Lasn

Signal Processing - Equipment and Software II

30 - Detection and identification of low-amplitude Acoustic Emissions during plastic deformation under indentation and scratch testing

A. Danyuk, D. Merson, A. Vinogradov

33 - When AE (Acoustic Emission) meets AI (Artificial Intelligence) II

K. Wasmer, F. Saeidi, B. Meylan, T. Le Quang, S. A. Shevchik

65 - AE fracturing modes classification by means of shear tensile source model

M. Petruzalek, T. Lokajicek, T. Svitek, P. Kolar, Z. Jechumtalova, J. Sileny, P. Adamova

21 - AE sensor sensitivity verification using a stimulated motion verified by laser-vibrometry

H. Vallen

Signal processing - Equipment and Software III

76 - Method for assessing the likelihood of fatigue crack detecting

V. Barat, D.V. Chernov, S.V. Elizarov

78 - Statistical non-parametrical algorithm for Acoustic Emission impulses detection adapted on the basis of modal analysis approach

V. Barat, D.A. Terentyev, S. Elizarov

80 - CFRP failure mechanisms detection using traditional and modal AE equipment's features

C. Rowland

82 - Application and Analysis of AE signals based on the EEMD-FastICA method

Y. Jiang, F. Xu, Z. Yang, J. Yu, B. Xu

10 - Evaluation of localized corrosion using Acoustic Emission signals: wavelets denoising and random forests classification

N. Morizet, M. Frégonèse, N. Godin, J. Tang, B. Normand

Civil Engineering

09 - Acoustic Emission measurements during a tensile fatigue test in reinforced concrete

G. Manthei, M. Koob, J. Minnert

59 - AE analysis of particle crushing: towards 3D analysis of soils

S. Luo

77 - Test of bending reinforced concrete structures by means of Acoustic Emission method

S.V. Elizarov, V. Bardakov, A.I. Sagaidak

81 - Assessment of infrastructures by rainy induced AE tomography with wave velocity and attenuation rate

T. Shiotani, K. Hashimoto, N. Okude, C. Granier, K. Watabe, H. Takamine

Source Location

34 - Contouring geodetically accurate Acoustic Emission sources via kernel density estimates

P. Gális, V. Kůs

41 - Analysis of AE source location precision for general sensor configurations

M. Chlada, J. Kober, Z. Prevorovsky

54 - Time reversal localization of continuous and burst AE sources under noise

Z. Prevorovsky, J. Krofta, J. Kober, M. Chlada, M. Mracko

Authors

16 - 20	ABARKANE Chihab	12 - 13	CALABRESE Luigi	06	FUSCO Claudio
63	ABOURA Zoheir	62	CALÁS Héctor	12 - 13	GALEANO Massimiliano
65	ADAMOVA Petra	22	CARRILLO Lorenzo	34	GALIS Petr
53	AGGELIS Dimitrios	71	CHEN Yanming	16 - 17 - 20	GALLEGO Antolino
20	AGUILAR-AGUILERA Antonio	86	CHERFAOUI mohammed	23 - 24	GAO Yong
18 - 19	AL HAJ Omar	31	CHERNIGOVSKI Wenceslaus	03 - 06 - 10	GODIN Nathalie
15	ALEXANDRE Noemie	76	CHERNOV D.V	32	GOOSSENS Nick
83	ANASTASOPOULOS Athanasios	41 - 54	CHLADA Milan	81	GRANIER Clement
57	ASHIZAWA Takeshi	50	CHOMYAKOV Vladimir	74	GROSJEAN Christophe
39	BAENSCH Franziska	28	CHUGUNOV Alexey	55	GURKA Martin
39	BAER Wolfram	14	CLERC Gaspard	39	HABIB Abdelkarim
50	BAKSHEEV Viktor	73	COLAS Oriane	06	HAMAM Zeina
27 - 69	BARAN Ireneusz	68	CONTELL ASINS Conchin	81	HASHIMOTO Katsufumi
76	BARAT Vera	01	CRAWFORD Alasdair	19	HEBRARD Yoann
15	BARCIKOWSKI Michal	84	CTVRTLIK Radim	15	HEGEM Per S
77	BARDAKOV V.V.	15	DAHME Fethi	71 - 72 - 73	HERVÉ Catherine
15	BARDOUX Olivier	29	DALGIC Munip	74 - 75 - 76	
58 - 45	BASHKOV Ilya	30	DANYUK Alexey	77 - 78 - 79	
58 - 45	BASHKOV Oleg	74	DELGADO Julien	80 - 82 - 83	
58	BASHKOVA Tatiana	59	DIAMBRA Andrea	85 - 86	
19	BATEL Mehdi	75	DIGIULIO Christophe	73	HOUSSAIS Alain
16	BENAVENT-CLIMENT Amadeo	84	DRAB Martin	45	HTOO KHUN Han
26	BENTAHAR Mourad	01	DROUBI Mohamad Ghazi	59	IBRAIM Erdin
15	BITTENDIEBEL Sylvie	05	DUFFNER Eric	29	IRRETIER Andree
15	BLANC-VANNET Pierre	69	DUNAJ Tomasz	11 - 40	ITO Kaita
18	BOLIVAR José	15	ECHTERMEYER Andreas	46	JANA Miroslav
83	BOLLAS Konstantinos	76 - 77 - 78	ELIZAROV Sergey.V.	65	JECHUMTALOVA Zuzana
73	BRIANÇON Christophe	11 - 38 - 40	ENOKI Manabu	23 - 24	JIANG Bo
14	BRUNNER Andreas J.	01	FAISAL Nadimul	82	JIANG Yu
58	BRYANSKY Anton	03	FANTOZZI Gilbert	23 - 24	JIN Liang
62	CABELLOS Elena	74	FRECHARD Jonathan	55	KELKEL Benjamin
		10	FRÉGONÈSE Marion	63	KHARRAT Mohamed
				64	KIETOV Volodymyr
				79	KIM Dong-Hyun

29	KLEMM Rolf	09	MINNERT Jens	07	RYNCARZ Tomasz
41 - 54	KOBER Jan	57	MIZUTANI Yoshihiro	33	SAEIDI Fatemeh
65	KOLAR Petr	06	MONNIER Thomas	77	SAGAIDAK A.I.
09	KOOB Manuel	26	MONTRESOR Silvio	71 - 72	SAIDOUN Abdelkrim
84	KOULA Vaclav	63	MOREAU Gurvan	31 - 37	SAMOKHVALOV Alexey
83	KOUROUSIS Dimitrios	10	MORIZET Nicolas	02 - 04	SAUSE Markus G. R.
07	KOZUB Barbara	54	MRACKO Michal	49	SCHAURITSCH Gert
47	KRATOCHVILOVA Vendula	48	NEUBECK Robert	48	SCHUBERT Lars
29	KRIEGER Karl-Ludwig	14	NIEMZ Peter	48	SCHULZE Eberhard
54	KROFTA Josef	15	NONY Fabien	68	SCHWARZHAUPT Oliver
64	KRÜGER Lutz	10	NORMAND Bernard	32	SEEFELDT Marc
31	KURNOSOV Dmitry	27 - 69	NOWAK Marek	22	SERRIS Eric
34	KŮS Václav	81	OKUDE Nobuhiro	53	SHETTY Naveen
49 - 51	LACKNER Gerald	15	PANEK Maciej	33 - 35	SHEVCHIK Sergey A.
15	LASN Kaspar	50	PANIN Vladimir	11	SHINOZAKI Ippei
33 - 35	LE QUANG Tri	83	PAPASALOUROS Dimitrios	81	SHIOTANI Tomoki
68	LEHMANN Martin	62	PELAEZ Miguel	38	SHIRAIWA Takayuki
71	LESAGE Thibault	74	PERRIN Guillaume	50	SHULATOV Aleksandr
23 - 24	LI Naitian	31	PETERSEN Tatiana	65	SILENY Jan
53	LIVITSANOS Georgios	65	PETRUZALEK Matěj	04	SINCLAIR Ian
65	LOKAJICEK Tomas	29	PIMENTEL Joao Vitor	04	SPEARING S. Mark
59	LUO Sha	49	POSCH Michael	44	SUCHKOV Evgeny
07 - 27	LYASOTA Igor	04	POTSTADA Philipp	16 - 17	SUÁREZ Elisabet
46 - 47	MAHMOUD Houssam	41 - 54	PREVOROVSKY Zdenek	65	SVITEK Tomas
74	MAISONNETTE Daniel	18	PROUST Alain	81	TAKAMINE Hidefuji
15	MALDACHOWSKA Agnieszka	12	PROVERBIO Edoardo	38	TAMURA Kengo
64	MANDEL Marcel	33 - 35	QUANG Tri Le	10	TANG Junlei
09	MANTHEI Gerd	28	RASTEGAEV Igor	78	TERENTYEV D.A.
49 - 51	MARIHART Heribert	42 - 44	RAZUVAEV Igor	57	TODOROKI Akira
62	MARTIN José Manuel	16 - 17 - 20	RESCALVO Francisco J.	84	TOMASTIK Jan
04	MAVROGORDATO Mark	03	REYNAUD Pascal	23 - 24	TONG Zongkai
46 - 47	MAZAL Pavel	47	RICHTER Vladislav	57	TOYAMA Nobuyuki
26	MECHRI Charfeddine	45	ROMASHKO Roman	22	VALENTINI Andrea
23 - 24	MENG Fanchao	04	ROSINI Sebastian	21	VALLEN Hartmut
30	MERSON Dmitry	36	ROSNER Sabine	53	VAN HEMELRIJCK Danny
33 - 35	MEYLAN Bastian	80	ROWLAND Chris	74	VERLET Philippe